THE GEOLOGICAL EVOLUTION OF NEUMAYERSKARVET IN THE NORTHERN KIRWANVEGGEN, WESTERN DRONNING MAUD LAND, ANTARCTICA

by

PHILIP DAVID HARRIS

THESIS

Submitted in fulfilment
of the requirements for the degree

DOCTORATE

in

GEOLOGY

in the

FACULTY OF SCIENCE

at the

RAND AFRIKAANS UNIVERSITY

SUPERVISOR: PROF D D VAN REENEN
CO-SUPERVISOR: DR A B MOYES

MAY 1999

ABSTRACT

Neumayerskarvet forms a continuous outcrop of high-grade gneiss within the northern Kirwanveggen in western Dronning Maud Land, Antarctica. A detailed geological study was carried out to obtain an evolutionary history for Neumayerskarvet. The work involved field mapping to provide a structural framework for further metamorphic and isotopic investigations. U-Pb zircon SHRIMP analysis, Rb-Sr, Sm-Nd and Ar-Ar mineral analysis were used to provide absolute time constraints on different tectono-metamorphic periods and cooling histories. Petrographic investigations, coupled with mineral chemistry on kyanite-bearing leucogneisses, provided information on the P-T conditions. An understanding of the crustal evolution of the high-grade gneisses was obtained through whole-rock geochemistry and isotope analysis.

The dominant lithotectonic unit preserved at Neumayerskarvet is biotite-garnet migmatite gneiss, which is inter-fingered with quartzofeldspathic gneisses and banded quartz-feldspar gneisses. Several magmatic phases have intruded these sequences. Three tectono-metamorphic cycles have been established for the region. The first two cycles are assigned to a period between 1390 Ma and 970 Ma while the third cycle is constrained between 650 Ma and 450 Ma.

An age of *ca.* 1390 Ma for the biotite-garnet migmatite gneiss provides a maximum age for the first tectono-metamorphic cycle. Zircon growth and magmatism during this tectono-metamorphic cycle constrains deformation (D1a) between *ca.* 1160 Ma and *ca.* 1110 Ma. Deformation is marked by the development of a penetrative planar foliation and isoclinal recumbent folding. High-pressure metamorphic conditions during this cycle have been suggested from previous investigations but are not confirmed in this investigation as the kyanite-bearing leucogneisses intruded during the second tectono-metamorphic cycle. It is possible that the first and second tectono-metamorphic cycles are part of a progressive deformational cycle.

The second tectono-thermal cycle represents a major period of magmatism and tectonism constrained between *ca.* 1110 Ma and *ca.* 970 Ma. Major folding occurred during this tectonic episode, represented by isoclinal recumbent folds, sheath folds and re-folded fold interference patterns (D1b). The structural fabric elements produced a complicated relationship of transposed coplanar and colinear composite fabrics. Fabric geometries suggest NNW-SSE tectonic transport directions. Garnet-kyanite-muscovite-biotite-quartz assemblages (Mn+1 (nkv)) provide P-T estimates of 710-760 °C and 7.8-8.5 kb. Later metamorphic assemblages of sillimanite-muscovite-high Ca-garnet-biotite-quartz (Mn+2 (nkv)) provide P-T estimates of 630-690 °C and 6.0-7.4 kb. The whole-rock isotope data indicate that material accreted during the second tectono-metamorphic cycle experienced a short crustal residence time.

The third tectono-metamorphic cycle is constrained by isotopic ages between 650 Ma and 450 Ma. Deformation (D2) that re-works earlier tectonic fabrics may represent signatures of this cycle, but the exact nature of the deformation remains enigmatic. Tectonic fabric styles and geometries are similar to the more dominant D1 tectonic episode, making recognition of temporal relationships difficult. Diffusional P-T data from garnet-biotite rims (Mn+3 (nkv)) provide P-T cooling estimates of 560-570 °C and 4.4-4.6 kb. Re-working of the high-grade gneisses during the third tectono-metamorphic cycle, with no addition or accretion of new crustal material is indicated by the isotopic data. A final tectonic episode (D3) comprising late brittle deformation and uplift is equated to Gondwana break-up.

DECLARATION

I hereby declare that this thesis submitted for the Doctorate degree to the Rand Afrikaans University, apart from the help recognised, is my own work and has not been formerly submitted to another university for a degree.

PHILIP DAVID HARRIS

25th day of MAY, 1999.

'That's it, sir . . . we've eaten the last of the geologists!'

(Courtesy of Punch)

CONTENTS

APPENDIX

Titanite electron microprobe analyses

PH92003.cdr:
Electron microprobe spot positions and measurement numbers for sample PH92003

PH92005.cdr:
Electron microprobe spot positions and measurement numbers for sample PH92005

PH92018_1.cdr:
Electron microprobe spot positions and measurement numbers for sample PH92018 Site 1

PH92018_2.cdr:
Electron microprobe spot positions and measurement numbers for sample PH92018 Site 2

PH93195_1.cdr:
Electron microprobe spot positions and measurement numbers for sample PH93195 Site 1

PH93195_2.cdr:
Electron microprobe spot positions and measurement numbers for sample PH93195 Site 2

PH93195_5.cdr:
Electron microprobe spot positions and measurement numbers for sample PH93195 Site 5

STRUCTURAL

Neumayer_92.doc:
Structural measurements taken during the 91-92 field season

Neumayer_93.doc:
Structural measurements taken during the 92-93 field season

Neumayer_95.doc:
Structural measurements taken during the 94-95 field season

LIST OF FIGURES

Chapter 3

Chapter 4

Chapter 5

Chapter 6

Chapter 7

LIST OF TABLES

CHAPTER 1

INTRODUCTION

GENERAL

Understanding of the geological evolution of Antarctica plays a significant role in Gondwana and Rodinia reconstructions, since in most of these it is the key central fragment around which amalgamation and dispersion are postulated to have taken place. It is therefore essential to obtain as much geological information as possible from the continent. There is little rock exposed through the polar ice cap, and thus accessible outcrops must be examined in as much detail as possible. Since it is an inhospitable region, geological investigations are risky and safety aspects can limit accessibility of certain areas. Due to the difficulty of access and the limited time period for field work, the maximum amount of information must be obtained from the area under investigation as returning to that locality may be difficult, costly and near impossible in certain instances.

The geological investigation presented in this thesis was conducted within a small area (5 km^2) of the northern Kirwanveggen of western Dronning Maud Land (WDML). This region comprises a package of high-grade gneisses that have undergone differing degrees of deformation and metamorphism. The introductory section presented in this chapter provides a general background to the nature of the geological work presented in the rest of the thesis.

OBJECTIVES OF PRESENT STUDY

Several objectives have been outlined for this thesis and are detailed below:

- To provide information on the nature of deformation and metamorphism experienced by the high-grade gneisses, with a view to a better understanding of the geological evolution of this region;
- To place constraints on the timing of deformation within the high grade gneiss terrain in this area, in order to make regional comparisons;
- To obtain chronological data from the various lithotectonic units within the metamorphic belt of the Kirwanveggen for regional and world-wide comparisons;
- To provide constraints on the possible timing of the metamorphic events within the Kirwanveggen, and relating these to data obtained from other isotopic techniques;
- To elucidate possible source ages and areas prior to high grade gneiss formation;
- To contribute to the thermochronological understanding of the Kirwanveggen, thereby relating this information to the region as a whole.

STUDY AREA

An area was selected for detailed geological investigation in the northern Kirwanveggen, WDML, Antarctica. A region of continuous outcrop in the central portion of Neumayerskarvet provided an ideal site for detailed structural, metamorphic and isotopic investigation (see Figure 1.1). The study area consists of an escarpment approximately 2.5km long, with exposures at the base of the escarpment at a height of ~1900m abutting against the plateau at ~2400m (see Figure 1.2). Previous reconnaissance investigations in this region highlighted areas of interest for further investigation that are examined here (Gavshorn and Erasmus, 1975). The Neumayerskarvet nunatak forms an extensive area of outcrop within the northern Kirwanveggen and is suitably representative of the nature of the high-grade gneisses of this area.

ANTARCTIC FIELDWORK

The South African National Antarctic Program (SANAP) has been conducting geological research within WDML for many years. Funding for the research is provided on a five-year period, where specific program aims are established and subsequently addressed. The fieldwork for this geological investigation was conducted during the period from 1991 to 1996 where the Kirwanveggen geological exposures were the focus of this program. Several researchers were involved in this program in order to examine various aspects of these high-grade gneiss exposures. Three field seasons were completed during the program in the austral summer period, which extended approximately from November to March. Although Neumayerskarvet in the northern Kirwanveggen was the focus of this research, several other areas in the region were also visited in order to place these rocks within the context of the surrounding geological domains.

Fieldwork was typically conducted by teams of two geologists working together. Tented camps were established in suitable areas for access to the regions under investigation. Transportation involved the use of skidoos with sledges for the necessary equipment and supplies. Camp localities used during this investigation are shown on the accompanying map of the Kirwanveggen (Figure 1.2).

METHODS OF INVESTIGATION

In order to fulfil the requirements of this study detailed geological mapping and sampling formed the basis to the investigation. Further hand specimen and petrographic work allowed more detailed descriptions of rock types. Electron microprobe work on selected samples was conducted at the Geology Department at Rand Afrikaans University under the supervision of Prof. D.D. van Reenen. Major and trace element geochemistry was carried out at the University of Natal in Pietermaritzburg. Isotopic investigations involving Rb-Sr and Sm-Nd analyses were conducted at the Bernard Price Institute of Geophysics, University of the Witwatersrand under the supervision of Dr A.B. Moyes. Ion microprobe (SHRIMP) zircon analyses were carried out at the Australian National University in Canberra, Australia in collaboration with Dr F.M. Fanning. Ar-Ar step heating analyses were conducted at the University of Houston in Texas by Dr T. Spell.

LAYOUT OF THESIS

This thesis is written in a manner to maximise the transfer of information into a publication format. For this reason, each chapter is written in a stand-alone manner within the context of the thesis. As such there is a limited amount of repetition between chapters that is required for the ensuing discussions in that section. The work presented in this thesis is my own, but significant input in either the form of fieldwork, ideas, or analytical techniques have been made by other workers. If future manuscripts are accepted for publication, these workers will automatically obtain co-authorship to those manuscripts. Without their contribution, the work presented in this thesis could not have been completed.

ACKNOWLEDGEMENTS

In a thesis such as this the amount of people that have contributed in some form or another is extensive and to mention all of these people by name would probably be a thesis within itself. So as not to leave out somebody who has either been instrumental during the running of the project or in the final stages of completion, I extend grateful thanks to all those people for the significant role they have played in this thesis. You know who you are, and I thank you for your inspiration, motivation, stimulation, humour and support.

Special thanks must, however, go to those people who assisted during the fieldwork in Antarctica. This includes the DEA for their financial and logistical support, members of the expedition teams during the field seasons conducted, and the South African Air Force for their role in the project support. I am grateful to those people who put up with me in a tent in the middle of nowhere during those long, and often cold, summer days. Many thanks to Alastair Moyes, Warren Johnstone and Ric Lewis. Other members of the geological teams also played an instrumental role in my education and geological knowledge of the region. Special thanks must go to Branko Corner, Johan Krynauw, Chris Jackson, Gavin Ferrar, Mike Knoper and Geoff Grantham.

I must thank all the staff at the BPI at Wits for their constant support, assistance in the labs and on the machines, and for the scientific stimulation. I thank RAU for their support during data collection. Mark Fanning and Richard Armstrong are thanked for their support and friendship at the ANU in Canberra, Australia during SHRIMP analysis.

Special thanks to my supervisors Dirk van Reenen and Alastair Moyes for their constant understanding, enthusiasm and support, for which I am truly grateful.

Lastly I must thank all those people who have put up with me in circumstances where I have placed my thesis first, and often neglected the fundamental things in life. To all these people I am in your debt.

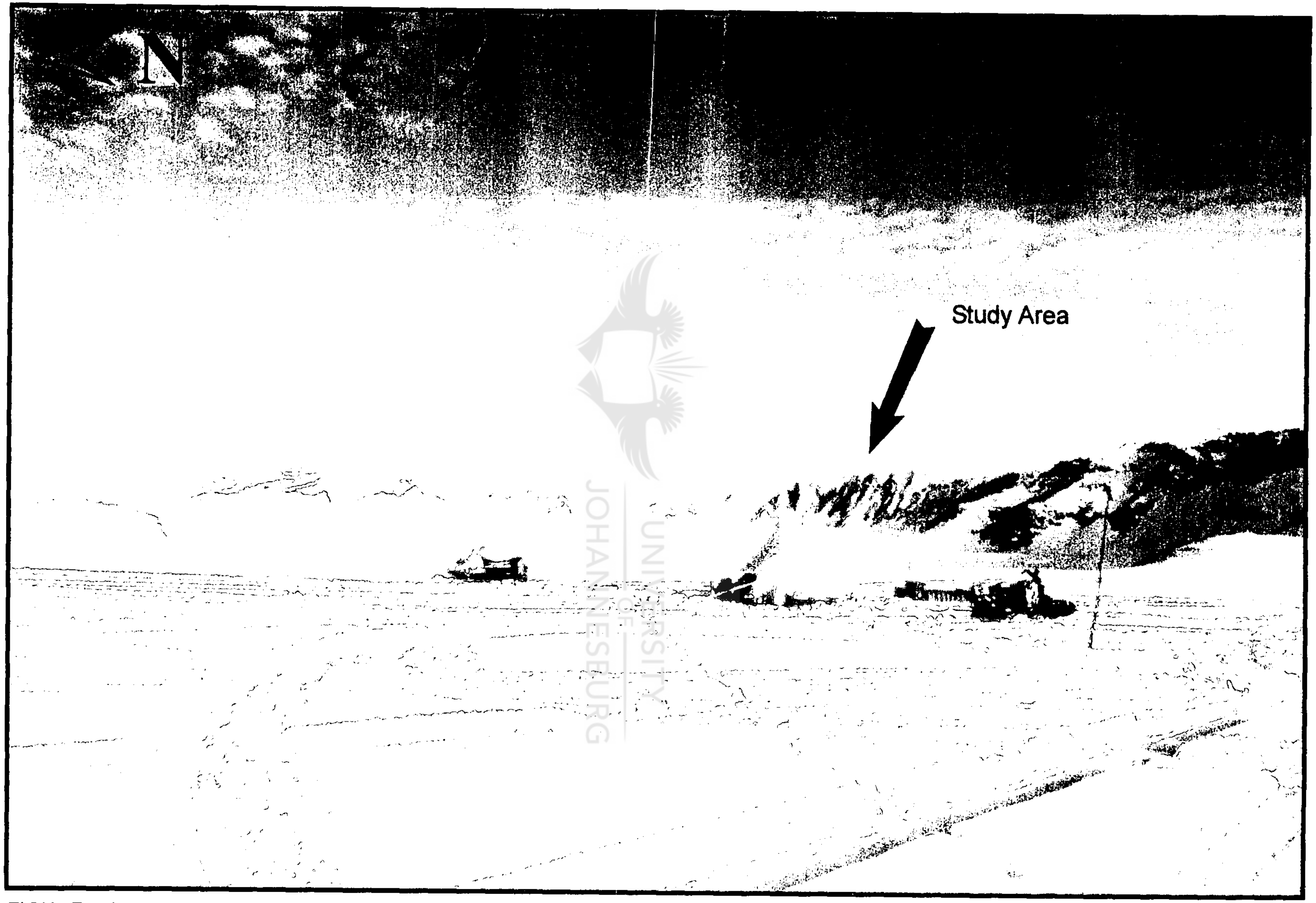

FIGURE 1.1. View of Neumayerskarvet in the northern Kirwanveggen looking east-southeast. The main area of investigation during this study is highlighted on the photograph. See Figure 1.2 for the location of Neumayerskarvet within the northern Kirwanveggen, and within western Dronning Maud Land.

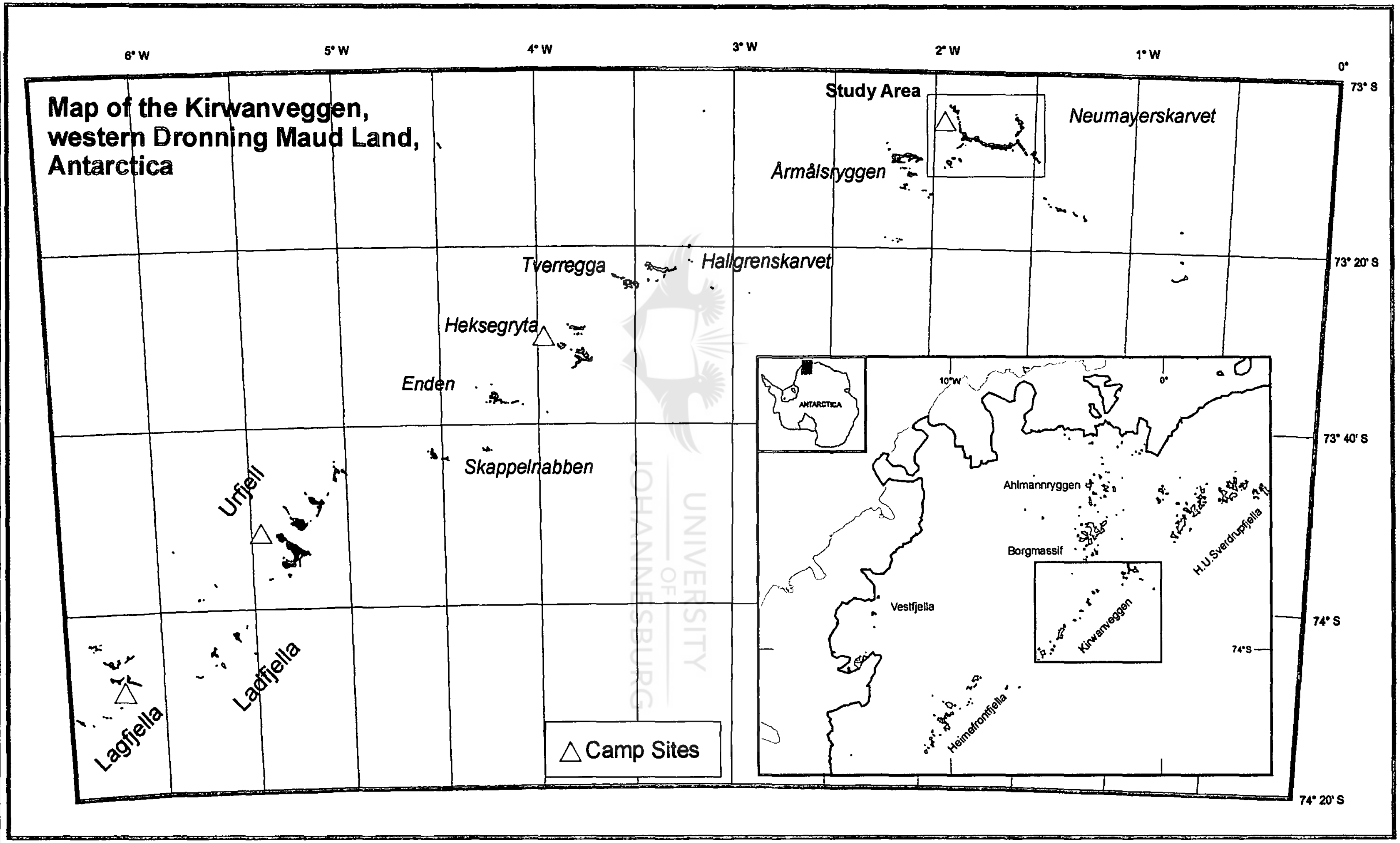

FIGURE 1.2. Geographical map of the Kirwanveggen in western Dronning Maud Land, Antarctica. The area of investigation is outlined at Neumayerskarvet in the northern Kirwanveggen. Camp site localities used during the Kirwanveggen program are also shown on the map.

CHAPTER 2

A REVIEW OF THE GEOLOGY OF WESTERN DRONNING MAUD LAND, ANTARCTICA; WITH A FOCUS ON THE HIGH-GRADE GNEISS TERRANES

INTRODUCTION

Only approximately two percent of Antarctica is exposed bedrock, with the remaining portion being covered by the polar ice cap. Most of the rock exposures occur around the edges of the continent where rock outcrop forms significant mountain ranges. Good 3-dimensional relationships and geological information can be obtained from the rock exposures since erosion in this region is dominated by mechanical rather than chemical processes. Correlation between the geological domains is complicated by the lack of exposure, and the relationships between these different domains are often obscured. Western Dronning Maud Land (WDML) does not escape these complications. Domains of contrasting geological features occur within close proximity to one another in WDML but little evidence of their inter-relationships is exposed.

The isolated and limited outcrop exposures of Antarctica are highlighted when supercontinent reconstructions are attempted (Moores, 1991; Hoffman, 1991; Dalziel, 1991; Stump, 1992; Storey, 1993; Borg and De Paolo, 1994; Storey *et al.*, 1994). Detailed understanding of the geology where exposures do occur is essential for these reconstructions, and WDML is no exception (Groenewald *et al.*, 1995; Grantham *et al.*, 1995; Jacobs *et al.*, 1993). This chapter serves as a review of the current geological understanding of WDML, and focuses on the distribution of the high-grade gneisses exposed within this portion of Antarctica. This section provides an introduction into the further detailed work that has been carried out on the high-grade gneisses within the northern Kirwanveggen. Further detailed reviews of previous work are provided, where relevant, within the individual chapters.

REGIONAL FRAMEWORK

WDML extends from approximately 5° E to 12° E and from about 70° S to 75° S. The outcrops extend from the Muhlig-Hoffmanfjella in the northeast to the Heimefrontfjella in the southwest. WDML has been subdivided into two major terranes termed the Grunehogna Province and the Maud Belt (Groenewald, 1993; Krynauw, 1996). These two major terranes are separated by the Pencksokket-Jutulstraumen glacial system (Figure 2.1), and their inter-relationships are not exposed. The following section describes the contrasting geology in terms of a lithotectonic framework providing a stratigraphic relationship for WDML.

Grunehogna Province

The Grunehogna Province comprises the Ahlmannryggen and Borgmassivet geographical regions within WDML (Figure 2.1), and three major litho-stratigraphic units are exposed:

Archaean Cratonic Fragment

An isolated set of outcrops is exposed at Annandagstoppane, approximately 200 km east of the Ahlmannryggen-Borgmassivet region. The deformed granitoid units exposed at these outcrops have been dated by Rb-Sr and Pb-Pb isotopic methods at *ca.* 3000 Ma and represent the oldest rocks exposed within WDML (Halpern, 1970; Barton *et al.*, 1987). The significance of such a small Archaean exposure is difficult to assess despite the major implications of this area for cratonic reconstructions (Krynauw, 1996). Inter-relationships with other lithologies in the Grunehogna Province are unknown.

Ritscherflya Supergroup

The Ritscherflya Supergroup crops out in the Ahlmannryggen and Borgmassivet areas of WDML. This supergroup comprises a succession of sub-horizontal sedimentary and volcano-clastic units (see Figure 2.2a), and is divided up into two groups, namely the lower Ahlmannryggen and upper Jutulstraumen groups (Wolmarans and Kent, 1982; Ferreira, 1986). The Ahlmannryggen Group is interpreted as having developed in a regressive depositional cycle from marine to braided and meandering river environments (Ferreira, 1986). The upper Jutulstraumen Group consists of basaltic rocks, pyroclastic and volcaniclastic units. A depositional or diagenetic age for the Ahlmannryggen Group sediments at Hogfonna of 1085 ± 27 Ma (Rb-Sr whole-rock) has been suggested by Moyes *et al.* (1995). In the upper portions of the Ahlmannryggen Group pyroclastic units have yielded zircon ages of *ca.* 1135 Ma (Moyes and Knoper, 1995), which support a Mesoproterozoic age for the Ritscherflya Supergroup.

Borgmassivet Intrusive Suite

The Borgmassivet Intrusive Suite have been intruded extensively into the Ritscherflya Supergroup (see Figure 2.2a). They are comprised dominantly of thick tholeiitic sills with continental geochemical signatures (Krynauw *et al.*, 1991). Textures at the contacts between the sills and the volcaniclastic rocks were interpreted by Krynauw *et al.* (1994) as indicating that intrusion occurred prior to sediment consolidation, and while the units were still water saturated. Granitoid bodies are interpreted to form as a result of partial melting of the host sediments during sill intrusion (Figure 2.2b). Geochemical signatures of the intrusive sills are similar to the Jutulstraumen volcanics of the Ritscherflya Supergroup, which tends to support this interpretation (Krynauw *et al.*, 1988; 1994). The age of intrusion of the Borgmassivet sills has been problematic and ages ranging from *ca.* 800 Ma to *ca.* 1800 Ma have been obtained (see reviews in Wolmarans and Kent, 1982; Moyes *et al.*, 1995). Moyes *et al.* (1995) suggested that crustal contamination is responsible for the observed age variations. These authors have subsequently suggested (Moyes *et al.*, 1995) that the sills intruded between *ca.* 1100 Ma and *ca.* 1000 Ma, which supports the near age equivalents of the Ritscherflya volcaniclastic units and the Borgmassivet sills.

Maud Belt

The Maud Belt (Groenewald *et al.*, 1995) is dominated by high-grade metamorphic gneisses with polyphase deformational, lithotectonic and metamorphic relationships. It extends from the Muhlig-Hoffmanfjella in the northeast, through the H.U.Sverdrupfjella and Kirwanveggen, to the Heimefrontfjella in the southwest (Figure 2.1). The major subdivisions of the Maud Belt are described below:

High-Grade Gneisses

High-grade gneisses comprise supracrustal rocks, banded leucogneisses, charnockitic rocks, intrusive leucogneisses and granitoid units (see Figure 2.2c). These rocks have been subjected to varying degrees of deformation and metamorphism. Correlation of the gneisses across the Maud Belt is difficult due to the lack of exposure between outcrops. As such, the high-grade gneisses have been differentiated into domains based on contrasting deformational and metamorphic histories, and are discussed in further detail in later sections. Isotopic data suggest major metamorphism, deformation and magmatism at *ca.* 1100 Ma with evidence of another significant event at *ca.* 500 Ma.

Urfjell Group

The Urfjell Group are almost entirely exposed in the Urfjell area, with limited outcrops recorded in isolated southerly nunataks and at Muskeg Cliff. No other exposures of this unit have been reported elsewhere in WDML. The Urfjell Group consist predominantly of quartzites, conglomerates and pebble lags with minor shale units. The quartzites and conglomerates have a distinctive light green colour, while the shale units tend to exhibit a deep red-brown colour (see Figure 2.2d). Trough cross-bedding is pervasive throughout the quartzites and conglomerates, and occasional point bar sediments are observed. Pebbles in the metasediments consist of quartz, quartzite, red shale (almost jasperlitic), chert(?), black shale, and rare fragments of orthogneiss. In the northern Urfjell area the sediments have a more dominant feldspathic component where, in several instances, pebble lags consist almost entirely of feldspar. The Urfjell Group is in tectonic contact with high-grade gneisses and other phyllonites, and sediment bedding planes are steepened due to deformation. A granitic-metamorphic provenance has been suggested from the detrital mineral assemblage, such as undulose quartz, feldspar, garnet, muscovite and rare zircon (Wolmarans and Kent, 1982). A high-energy, near shore depositional environment is suggested by the large scale cross-bedding and poorly sorted conglomerates. Previous workers suggested a Cambrian age for the

Urfjell metasediments (Aucamp *et al.*, 1972), and recent Rb-Sr isotopic work suggests an age constraint of between 688 Ma and 541 Ma (Moyes *et al.*, 1997).

Amelang Plateau Formation

Exposures of the Amelang Plateau Formation (APF) occur predominantly in the southern Kirwanveggen and in the northern Heimefrontfjella. Less than 100m of the APF is exposed in the southern Kirwanveggen. This formation consists of sandstones, poorly sorted conglomerates, pebble lags, talus slopes, diamictic and glacial deposits with lesser amounts of mudstone. These units unconformably overlie high-grade gneisses and deformed Urfjell Group sediments (see Figure 2.2f). Iron concretions are found within the trough cross-bedded and planar laminated sandstones. Poorly preserved plant fossils are observed in some of the mudstones, and trace fossils are found in the sandstones at Mount Alex du Toit. Vertebrate fossils have been reported from Concretion Point (Ahlberg *et al.*, 1992). A depositional palaeotopography has developed in the basement to the APF, where fluvial type sediments fill basement lows. Material is stripped from basement highs forming talus deposits down slope. Local variations within the APF are extreme due to limited occurrence, palaeotopography and distal nature of the sediments. A leach zone has developed on the palaeo-erosional surface for the APF where the gneisses may be leached for up 20m from the unconformity. At the basal unconformity, rip-up clasts of high-grade gneisses occur within the first 0.5m of sediment. The lower portions of the APF are interpreted as glacial deposits, grading into the upper sequences, which are typical of a braided-river system (Ahlberg *et al.*, 1992). Similar lithologies have been reported from the Vestfjella and Milorgfjella in the Heimefrontfjella (Larsson *et al.*, 1990). An Early Permian age is interpreted for the palaeontological data within the sediments at Milorgfjella (Larsson *et al.*, 1990), and similarities are observed with the APF, although no direct evidence has yet been obtained for the age of the APF. No structural deformation has been observed or reported in the APF. The APF is equated with the Karoo Sequence in southern Africa.

Kirwanveggen Formation

The Kirwanveggen lavas are exposed in the southern Kirwanveggen and the northern Heimefrontfjella within WDML. Basaltic lavas of the Kirwanveggen Formation appear to conformably overlie the sediments of the APF, but unconformably overly the basement gneisses in the southern Kirwanveggen (see Figure 2.2e). Amygdales are often documented in the basalt lava flows. A K-Ar age of 172 ± 10 Ma has been reported for the lavas by Aucamp *et al.* (1972). Recent Ar-Ar work supports the Mesozoic age for the Kirwanveggen Formation (Harris, 1995). Sand lenses have also been reported in the lower portion of the Kirwanveggen Formation (Harris *et al.*, 1990).

Alkaline Complexes

Several alkaline complexes are exposed within the high-grade gneisses of the Maud Belt. These alkaline complexes are found in the northern Kirwanveggen and in the western Sverdrupfjella. The Straumsvola nepheline syenite complex has been dated at 170 Ma (Ar-Ar method) and crops out within the western Sverdrupfjella (Harris and Grantham, 1993).

GEOLOGICAL DOMAINS WITHIN WDML

Antarctic geology is renowned for its good exposures that have undergone little chemical weathering. These areas are, however, isolated due to the extensive ice cover over the region, which makes correlations and geological relationships between exposures difficult to interpret. Geological and structural features often do not extend beyond the outcrop, limiting the extent to which geological domains can be extrapolated. WDML is no exception, and workers in this region tend to view outcrops as individual geological domains. The timing of the juxtaposition of these different domains may vary, often invoking a distinct evolutionary history. In the following section the geology of individually defined geological domains is discussed (see Figure 2.3). The distinction of different geological domains is based on previous work or work carried out during the current investigation.

Grunehogna Province

Annandagstoppane (ANDP)

The Annandagstoppane domain is marked by a series of small isolated outcrops in the western extremities of WDML, and is predominantly granitic material that has produced Archaean ages (See Table 2.1). Whole rock Pb-Pb data for all the samples provide an age of 2937 ± 84 Ma (MSWD=42), although removal of some scatter produces an older age of 3111 ± 78 Ma (MSWD=6.5). Rb-Sr muscovite analyses yield a mean age at 2945 ± 72 Ma (Barton *et al.*, 1987). This domain records the only currently documented Archaean age from WDML, and has been interpreted as a fragment of cratonic material. Rb-Sr analysis of two biotites yield ages of 1250 and 1100 Ma (Barton *et al.*, 1987). Chloritised biotite yield Rb-Sr ages of about 460 Ma while final cooling of this domain has been documented by apatite fission track ages of 303 ± 22 Ma (Barton *et al.*, 1987; unpublished data quoted in Barton and Moyes, 1990). Little data are available on the tectonic nature of the Annandagstoppane domain.

Ahlmannryggen-Borgmassivet (AH-BM)

The Ahlmannryggen-Borgmassivet domain covers an extensive geographical area that is dominated by sediments, volcanics and volcaniclastics of the Ritscherflya Supergroup and have been extensively intruded by the Borgmassivet Intrusive Suite. The sequences exposed in this domain are interpreted as Mesoproterozoic sequences that unconformably overlie the basement Archaean gneisses, although no geological relationships are exposed (see Table 2.1).

The Ritscherflya Supergroup is generally flat lying with little dip to the strata. Towards the Pencksokket and Jutulstraumen glacial systems, however, there is a tendency for an increase in deformation (Wolmarans and Kent, 1982). Moderate intensity folding has been recorded in the southeastern Borgmassivet (see Figure 2.6a) affecting the Ritscherflya Supergroup (see Wolmarans and Kent, 1982). Steep shear fabric development and associated folding have also been documented at Straumsnutane in the northeastern Ahlmannryggen (Watters, 1972; Speath and Fielitz, 1987). Shear fabrics and upright open folds have NE-SW trends, while NE-SW striking overthrusts post-dating the steep shear fabrics have WNW and ESE vergence directions (Speath and Fielitz, 1987). K-Ar white mica ages from mylonites in these steep shears provide ages of *ca.* 525 Ma (Peters, 1989). As similar K-Ar ages outside the steep shears provide somewhat older ages, the *ca.* 525 Ma age may represent an age for the deformation rather than a minimum age resulting from thermal overprinting. Lineations are poorly preserved in the steep fabric structures making interpretation on the style of deformation difficult. Block faulting has been inferred within the Ahlmannryggen-Borgmassivet domain to explain the inconsistent nature of the volcaniclastic sequence.

Maud Belt

Gjelsvikfjella and Muhlig-Hoffmanfjella (G-HFM)

The Gjelsvikfjella and Muhlig-Hoffmanfjella domain is dominated by high-grade gneisses with characteristics similar to those in the surrounding domains (see Figure 2.1 and Table 2.1). The Gjelsvikfjella is dominated by micaceous gneissic supracrustals (biotite-quartz-feldspar±garnet-cordierite-Al-silicate gneisses) in the north, with migmatitic gneisses dominating in the south (Ohta *et al.*, 1990). The rocks have a distinct gneissosity and strong lineation development. Isoclinal folding and foliation transpositions are refolded by later tight folds with approximate NW-SE trends. Steep late-stage faulting is also recorded within the Gjelsvikfjella (Ohta *et al.*, 1990). Isotopic work by Moyes (1993) has shown that these gneisses have undergone isotopic decoupling resulting in Sm-Nd whole-rock ages of *ca.* 1153 Ma and Rb-Sr ages of *ca.* 535 Ma.

Charnockitic gneisses, granitic gneisses and migmatites dominate in the western Muhlig-Hoffmanfjella. The charnockites are particularly dominant and are interpreted to intrude the metamorphic complex within this area (Ohta *et al.*, 1990). The charnockites have variable grain sizes, common xenoliths, and have a sheet-like nature in certain areas. A patchy flame-like texture of charnockitic material (orthopyroxene-bearing) is also observed. Charnockites from

Svarthamaren in the western Muhlig-Hoffmanfjella have provided Rb-Sr whole-rock ages of *ca.* 500 Ma, which have been interpreted as the age of crystallisation (Ohta *et al.*, 1990).

In the Muhlig-Hoffmanfjella Bucher-Nurminen and Ohta (1993) examined metapelitic rocks that are intruded by the *ca.* 500 Ma (Rb-Sr) charnockitic rocks (Ohta *et al.*, 1990). They concluded that two interpretations were possible from their metamorphic investigation, which depended on the timing of the metamorphic episodes recognised during their study. Orthopyroxene-garnet granulites revealed pressures of ~8 kb and temperatures of ~750 °C. These pressure and temperature (P-T) conditions are not preserved in the cordierite-bearing gneisses that indicate equilibration conditions of ~4 kb at ~650 °C. P-T conditions within the cordierite-bearing gneisses are interpreted as assemblages that have recrystallised and completely re-equilibrated from the early metamorphic event. The early high P-T phase may either be part of a Mesoproterozoic assemblage that has been overprinted by a younger *ca.* 500 Ma event, or alternatively these metamorphic episodes represent signatures of a single Palaeozoic orogenic cycle (Bucher-Nurminen and Ohta, 1993).

H.U.Sverdrupfjella

The H.U.Sverdrupfjella has been sub-divided into two major domains based on lithological, structural and metamorphic evidence (Grantham *et al.*, 1988; Groenewald and Hunter, 1991). The following sections outline the similarities and differences recognised between these two domains.

<u>Eastern Sverdrupfjella (EHUS)</u>

The eastern Sverdrupfjella is dominated by high-grade gneisses and granitic gneisses that extend the length of the H.U.Sverdrupfjella (see Figure 2.4). The supracrustal units comprise garnet-sillimanite/kyanite gneisses and quartzofeldspathic gneisses (Grantham *et al.*, 1995). A volcanic origin has been ascribed to the more felsic gneisses. In the westerly exposures of the eastern Sverdrupfjella outcrops of Fugelfjellet gneisses are dominated by metacarbonates (Groenewald *et al.*, 1995). Several periods of granitic magmatism have been recorded in the eastern Sverdrupfjella domain (Groenewald *et al.*, 1995). Early magmatism that has been affected by the major regional deformation produced tabular granitoids with calc-alkaline affinities. Extensive isotopic investigations in this domain indicate that these lithotectonic units are Mesoproterozoic in age with subsequent disturbance at *ca.* 500 Ma (see Table 2.1 and references therein). SHRIMP zircon data provide support for magmatism at ca. 1130 Ma within the high-grade gneisses (Harris *et al.*, 1995). Late granitic magmatism within the eastern Sverdrupfjella domain is represented by the Brattskarvet Granitoid Suite, which is dated at *ca.* 520 Ma by Rb-Sr and Sm-Nd methods (Moyes *et al.*, 1993b). This granitoid suite comprises alkaline to peralkaline A-type granites interpreted to be related to extension or underplating

(Moyes *et al.*, 1993a). Although deformation is documented in the Brattskarvet Granitoid Suite, it is not as intense as that recorded within the supracrustal units (Moyes *et al.*, 1993b).

Three major deformational episodes have been documented within the Kirwanvegggen-H.U.Sverdrupfjella areas (Grantham *et al.*, 1995). An early D1 event is characterised by intense fabric development and transposition, isoclinal folding and colinear progressive re-folding, and the development of SE plunging mineral elongation lineations. Isotopic data constrain this early event between *ca.* 1150 Ma and *ca.* 800 Ma (see Grantham *et al.*, 1995 and references therein). High-strain zones with top-to-the-NW movement directions are recognised within this domain. This thrusting resulted in the metamorphic inversion observed within the eastern Sverdrupfjella domain (Grantham *et al.*, 1988). The second deformational event (D2) is characterised by shallow NE plunging tight to isoclinal folds and local refoliation that is recognised within the *ca.* 520 Ma Brattskarvet Granitoid Suite. Regional open upright folding on NE axes is also observed. Late brittle deformation features have been assigned to the D3 Mesozoic Gondwana break-up event (Grantham *et al.*, 1995).

Metamorphic studies in the eastern Sverdrupfjella have lead to the recognition of four metamorphic episodes (Grantham *et al.*, 1995). In the eastern domain garnet-clinopyroxene-plagioclase-quartz assemblages (M1) provide high-pressure (10-14 kb and 675-750 °C) metamorphic conditions (Groenewald and Hunter, 1991). The M1/2 metamorphic episodes have been assigned to the Mesoproterozoic deformational event. The M3 metamorphic episode is recognised by fabrics defined by biotite and amphibolitised mafic intrusives that have been assigned to the *ca.* 500 Ma event. Temperatures and pressures of 650 °C and 6.5 kb are typically recorded for the M3 event. Late M4 metamorphism is characterised by chloritisation and saussuritisation that has been assigned to effects of the Mesozoic crustal fragmentation. Sm-Nd garnet ages clustering around 680 to 415 Ma have been obtained from the eastern Sverdrupfjella domain (Moyes and Groenewald, 1996), and are interpreted as reset ages, masking isotopic evidence for the *ca.* 1100 Ma metamorphic event.

<u>Western Sverdrupfjella (WHUS)</u>

Hornblende-biotite Jutulrora gneisses (Figure 2.4) dominate the western Sverdrupfjella domain. A SHRIMP age from the Roerkulten granite yields an age of 1103 ± 13 Ma providing evidence of magmatism during this period within western H.U.Sverdrupfjella (Harris *et al.*, 1995). These gneisses are intruded by sheet-like granitic units of the Dalmatian granite. The Dalmatian granite has been dated using Rb-Sr mineral and whole-rock samples at 469 ± 5 Ma (Grantham *et al.*, 1988). The Tvora Mesozoic alkaline complex intrudes the high-grade gneisses within the northwestern regions of this domain. Isotopic data from the western Sverdrupfjella domain provide typical Mesoproterozoic ages with cooling or reset ages at *ca.* 500 Ma (see Table 2.1 and references therein).

Four metamorphic episodes have also been recognised within the western Sverdrupfjella high-grade gneiss terrane (Grantham *et al.*, 1995). The early metamorphic episode differs between the eastern and western portions of the H.U.Sverdrupfjella. Conditions of 620-700 °C and 3-9 kb have been suggested for the M1 metamorphic episode in the western Sverdrupfjella. This metamorphism is followed by an M2 metamorphic episode with cpx-hbl-grt-pl-qtz assemblages and estimated P-T conditions of 600-700 °C and 7-9.5 kb (Groenewald and Hunter, 1991; Grantham *et al.*, 1995). M3 temperatures and pressures in the east and western Sverdrupfjella domains appear to be similar with ~650 °C and 6.5 kb, which is similar to that recorded in the Kirwanveggen by Wolmarans and Kent (1982). The M3 metamorphic period in the H.U.Sverdrupfjella has been assigned to a *ca.* 500 Ma event. The M4 metamorphic episode of Grantham *et al.* (1995) is characterised by local chlorite and saussurite development, which they assigned to a younger *ca.* 180 Ma event. The deformation recognised within the western Sverdrupfjella domain has been assigned a similar deformational history as that of the eastern Sverdrupfjella domain by Grantham *et al.* (1995) although the early D1 top-to-the–NW thrusting is typically absent.

Kirwanveggen

The Kirwanveggen has been divided into three distinct geological domains (see Figure 2.5). These domains are differentiated based on lithological, metamorphic and structural distinctions. Although much of the work is ongoing in this region, a summary of the current understanding is presented in the following sections.

Northern Kirwanveggen (NKVN)

The northern Kirwanveggen domain, specifically Neumayerskarvet, is the focus of this investigation. For completeness the following section will briefly outline the geology of the domain based on previous investigations but is influenced by the findings of the current study.

High-grade gneisses comprising predominantly biotite-garnet migmatite gneisses and quartzofeldspathic gneisses dominate the northern Kirwanveggen domain. These lithotectonic units are interleaved and intruded by orthogneissic units, megacrystic orthogneisses that are locally charnockitic in nature, and amphibolitic dykes (Gavshon and Erasmus, 1975 and the current study). These units have produced Mesoproterozoic ages for most of the gneisses with isotopic evidence related to the *ca.* 500 Ma event also being recorded (see Table 2.1 and references therein).

Deformation in the northern Kirwanveggen displays somewhat different structural styles and geometries to that in the eastern Sverdrupfjella and central Kirwanveggen domains (Grantham *et al.*, 1995). Isoclinal folding and upright open to tight refolding re-orientates the regional gneissic foliation in this domain. This results in changes in the foliation geometries from moderately SE plunging fabrics in the adjacent domains to steep and variable fabrics at high angles within the northern Kirwanveggen (see Figure 2.6b). Although a similar deformational history has been interpreted for this domain, it has been suggested that the change in structural styles may reflect a deep-seated lateral ramp to the thrusts observed in the adjacent geological domains (Jackson and Jacobs, 1995).

The first description of the metamorphism of the Kirwanveggen was presented in Wolmarans and Kent (1982). The mineralogy of some of the major lithologies in the Kirwanveggen provide an indication of the metamorphic conditions experienced by these rock units. Biotite-garnet geothermometry has also been applied by Wolmarans and Kent (1982). Their findings and interpretations are discussed below. Within the leucogneisses in the Kirwanveggen the scarcity of muscovite, along with the presence of microcline, indicated that the orthoclase isograd was reached. This suggests that the leucogneisses have been metamorphosed to upper amphibolite facies metamorphic conditions. The biotite-garnet plagiogneisses contain co-existing kyanite and sillimanite. The hornblende plagiogneisses and amphibolites contain green hornblende and calcic plagioclase (anorthite-rich plagioclase) which define amphibolite facies metamorphism. Brown hornblende, found in central Neumayerskarvet, suggests higher grades of metamorphism, probably in the amphibolite/granulite facies transition. The mineral assemblages of the calc-silicates are generally characteristic of amphibolite facies metamorphism, and the co-existence of wollastonite with quartz and grossular garnet suggests that fluid compositions of XCO_2=0.2 were attained. The use of biotite-garnet geothermometers also supports the high grade of metamorphism in the Kirwanveggen. Metamorphic pressure and temperature conditions in the Kirwanveggen have been interpreted as 6.4 ± 0.5 kb and 640 ± 50 °C by Wolmarans and Kent (1982).

Ferrar (1995) has distinguished four metamorphic events within a region of the northern Kirwanveggen. The three early events have been related to orogenesis while the last event is related to a greenschist facies uplift event. Assemblages of clinopyroxene + garnet + plagioclase ± hornblende preserved in metabasic rocks are indicative of an early high-pressure event at conditions of 650-700 °C and 12-13 kb. Amphibole + plagioclase + garnet assemblages represented by the M2 amphibolite facies event provides conditions of 720 °C and 6-10 kb. Ferrar (1995) assigned the M1 and M2 events to the Mesoproterozoic period that affected these high-grade gneisses. Biotitisation and re-equilibration of garnet and plagioclase rim compositions provide temperatures of ~650 °C for M3, which has been assigned to the *ca.* 500 Ma event.

Central Kirwanveggen (CKVN)

The central Kirwanveggen domain comprises biotite-hornblende gneisses and granodioritic orthogneisses that are intruded by megacrystic orthogneiss and leucogranite (Jackson *et al.*, 1997). Isotopic data indicate ages of *ca.* 1100 Ma for the gneisses of the central Kirwanveggen domain (Table 2.1). Biotite ages of *ca.* 475 Ma indicate significant disturbance of the Rb-Sr isotopic system during a younger event. The gneisses preserve evidence of amphibolite to upper amphibolite facies metamorphism but have undergone significant hydrous retrogression.

Tectonic fabric geometries in the central Kirwanveggen have striking similarities with the eastern Sverdrupfjella domain and parts of the Heimefrontfjella (Grantham *et al.*, 1995, Jackson and Jacobs, 1995). The domain is characterised by colinear fabric development and high-strain zones with typical top-to-the-NW movement directions. The high strain zones are tens to hundreds of meters wide and display southeast plunging elongation lineations developed within the mylonitic foliations. Numerous discrete shear zones transect and rework the early deformation fabrics, but display colinear fabric development. Top-to-the-NW sense of direction is also documented in many of these discrete shear structures. The colinear nature of deformational fabrics within the Kirwanveggen makes the distinction between tectonothermal episodes difficult (Jackson *et al.*, 1993 and 1994; Grantham *et al.*, 1995). A similar deformational history as that of the northern Kirwanveggen is interpreted for the central Kirwanveggen, with intense deformation during an early episode (Mesoproterozoic) and reworking of these fabrics during a younger *ca.* 500 Ma event. The nature and extent of the reworking remains enigmatic as the *ca.* 500 Ma event is poorly understood. Understanding the significance of this event is important to the development of any evolutionary history for WDML.

Southern Kirwanveggen (SKVN)

The southern Kirwanveggen has the most varied lithological components within the Kirwanveggen. High-grade gneisses, Urfjell Group sediments, phyllonitic and schist units, Amelang Plateau sediments and the Kirwanveggen lavas are all exposed at various outcrops within this domain. Geological relationships between different lithological units are exposed at several outcrops within the southern Kirwanveggen domain. Little work has been done on the Mesoproterozoic high-grade gneisses and no lithotectonic subdivisions have currently been defined. The multiply-deformed high-grade gneisses are dominated by augen-textured orthogneiss, banded biotite-amphibole-feldspar gneiss and quartzofeldspathic gneiss. These gneisses have similar characteristics to the rest of the high-grade gneisses in the Kirwanveggen. Limited isotopic data for this domain is provided in Table 2.1. No previous work has been done on the metamorphism or tectonism experienced by the gneisses in this domain. Current work has indicated that there are two contrasting fabric geometries evident in the gneisses of the southern Kirwanveggen. At Lagfjella the gneisses below the Kirwanveggen lavas exhibit gneissic and mylonitic foliations that dip shallowly towards the south with shallow southwest plunging stretching lineations. In contrast, fabric geometries at Ladfjella are consistent with those found in the central Kirwanveggen, and are characterised by SE-dipping foliation planes and SE-plunging lineations and mesoscopic fold axes.

The Urfjell Group metasediments dominate the northern outcrops of the southern Kirwanveggen domain. These sandstones, gritty quartzites and conglomeritic units have undergone varying degrees of deformation. In the northern extremities of the southern Kirwanveggen domain the sediments dip moderately towards the NE, but near vertical bedding and local overturning are recorded due to faulting (Figure 2.6c). Previous workers have inferred a tectonic contact between the high-grade gneisses and the Urfjell Group at this point (Aucamp *et al.*, 1972; Wolmarans and Kent, 1982 and references therein). The Amelang Plateau Formation and the Kirwanveggen lavas unconformably overly the deformed Urfjell lithologies and show little evidence of deformation (see Figure 2.6d). The Kirwanveggen lavas also unconformably overly the high-grade gneisses within the southern Kirwanveggen domain.

Heimefrontfjella

Jacobs *et al.* (1996) have divided the Heimefrontfjella into three domains, which have been distinguished on structural and geochemical grounds. These include (1) the Kottas terrane in the north, (2) the Sivorg terrane forming the major portion of the Heimefrontfjella, and (3) the Vardeklettane terrane exposed on the western edge of the mountain range and incorporating the Mannefalknaussane nunataks some 65 km to the west. The following discussion outlines the geology of these domains.

Kottas Terrane (KOTT)

The Kottas terrane in the northern Heimefrontfjella comprises layered supracrustal gneisses with sheeted granitoids, medium-grained banded grey tonalitic gneisses intercalated with leucocratic quartz-feldspar gneiss and minor amphibolite, garnet-mica gneiss, calc-silicates and marbles (Jacobs *et al.*, 1996). The supracrustal grey and pink gneisses are interpreted to represent metavolcanic and volcaniclastic rocks with dacitic/andesitic compositions. An U-Pb zircon age of 1093 ± 10 Ma has been obtained from a meta-rhyolite in this domain (Arndt *et al.*, 1991). The intrusive rocks are meta-tonalite and augen gneisses with ages of 1088 ± 10 Ma and pegmatites at 1060 ± 8 Ma (See Table 2.1). Mafic dykes intruding across the gneissic units have produced a biotite K-Ar age of 473 ± 11 Ma (Jacobs *et al.*, 1995).

Hornblende + plagioclase ± garnet assemblages within metabasite units provide an indication that the Kottas terrane has undergone amphibolite facies metamorphism. Calc-silicates with dolomite-calcite-tremolite-forsterite assemblages indicate temperatures around 650 °C (Jacobs *et al.*, 1996). Retrograde greenschist facies metamorphic assemblages occur adjacent to shear zones and mafic dykes in this region.

Three deformational events have been recognised in the Kottas terrane. The first two events have been assigned to the early *ca.* 1100 Ma regional event while the later event has been interpreted to be associated with the *ca.* 500 Ma regional event. The early F1 folds are homoaxially refolded by tight F2 folds with axes that gently plunge towards the SE. An axial planar foliation is developed with the F2 fold event along with SE plunging stretching lineations. The F2 folds are refolded by NE-SW trending gently to moderately NE-plunging F3 folds. A moderately dipping S3 metamorphic foliation develops in certain orthogneiss units and is related to the F3 fold event. In certain areas the S3 develops as a mylonitic foliation with S to SE trending stretching lineations. The mylonitic shears indicate a NW to NNW thrust direction. Late brittle shears are also recorded in the Kottas terrane. Jacobs *et al.* (1996) have proposed a tectonic contact between the Kottas and Sivorg terranes.

Sivorg Terrane (SIVT)

The Sivorg terrane forms the largest exposed portion of the Heimefrontfjella. The rocks comprise high-grade gneisses that have been interpreted as supracrustals, which are intruded by granitoid bodies. The oldest rocks within this domain are bimodal felsic-mafic gneisses, pelitic, quartzitic and calc-silicate gneisses. The gneisses have been interpreted as a bimodal volcanic suite (Jacobs *et al.*, 1996). K-Ar muscovite ages of between 987 and 960 Ma have been obtained from quartzites within the Sivorg terrane (Jacobs *et al.*, 1995). These ages are interpreted as cooling ages after the main deformational and metamorphic event. Granitic gneisses from this domain provide U-Pb zircon ages of 1104 ± 10 Ma and 1078 ± 30 Ma (see Table 2.1).

The Sivorg terrane is characterised by amphibolite facies metamorphism. There appears to be a north-south metamorphic gradient developed across this domain. Kyanite-staurolite assemblages for metasediments in the north, while staurolite-sillimanite and kyanite-staurolite-garnet assemblages in the south, suggest an increase in temperature and decrease in pressure towards the northern boundary of this domain. Fibrolite is observed replacing kyanite and indicates either a temperature increase or pressure decrease with time. Peak temperatures of 580 to 610 °C have been recorded from thermobarometry (Schulze, 1992). In the north, thermobarometry has indicated temperatures of 540 ± 50 °C with pressures of 4 kb (Bauer, 1995), while in the south garnet temperatures of 500 °C (rims) and 660 °C (cores) with approximately 8 kb pressures have been reported (Jacobs *et al.*, 1996).

Two structural domains have been identified within the Sivorg terrane (Jacobs *et al.*, 1996). The first structural domain, which represents the older structures, is dominated by open, tight to isoclinal folding. Early F1 folds are refolded by F2 fold structures that have gently plunging N-NNE trending fold axes. The Heimefrontfjella Shear Zone (HSZ) defines the second structural domain and rotates the early fold structures into sub-vertical orientations. The HSZ is interpreted as a NE trending steep dextral transpressive shear zone forming a boundary between mainly orthogneissic units and supracrustal rocks. The HSZ also forms the boundary between the Sivorg and Vardeklettane terranes. Lineations in the HSZ steepen towards the south where the shear zone trend changes to a NNE direction. Fabrics related to the HSZ obliterate evidence of the earlier tectonic fabrics. Different ages have been recorded from the HSZ and have been related to the effects of the *ca.* 500 Ma overprinting event (Jacobs *et al.*, 1995; 1996; 1998). The preservation of a K-Ar biotite age of 812 ± 17 Ma from a mylonitic gneiss suggests a *ca.* 1100 Ma origin for this structure (Jacobs *et al.*, 1995). Further *ca.* 500 Ma mica and amphibole K-Ar and Ar-Ar ages from the shear zone have been interpreted as the result of reworking within an older structure. Last movement on this structure is recorded at 395 ± 9 Ma by K-Ar age (Jacobs *et al.*, 1995) from psuedotachylites (see Table 2.1).

Vardeklettane Terrane (VDNT)

The Vardeklettane terrane is exposed in the southwestern extremities of the Heimefrontfjella and at isolated outcrops at Mannefallknausane. The oldest rocks within this domain are grey layered quartzites, garnet-cordierite gneisses and metabasites. These granulitic supracrustals are predominantly sedimentary in origin with U-Pb zircon ages ranging from *ca.* 1100 Ma to *ca.* 2000 Ma (see Table 2.1). Intrusive rocks within the Vardeklettane terrane are orthogneissic, and some of these units preserve charnockitic affinities. U-Pb zircon ages for some of these orthogneisses range from 1135 ± 8 Ma to 1073 ± 8 Ma (Arndt *et al.*, 1991). Granulite facies metamorphism is documented for the Vardeklettane terrane. Garnet-cordierite-sillimanite assemblages in the supracrustal sediments and metabasites contain orthopyroxene. Replacement and primary charnockites have both been recorded in this domain.

The structure of the Vardeklettane terrane is significantly different to the other domains in the Heimefrontfjella. Gneissic layering is sub-vertical trending E-W in some regions and N-S in others. Upright N verging folds with shallow E plunging fold axes are developed. Small discrete shear zones with steep SE plunging stretching lineations and top-to-the-NW displacements are also observed. Charnockites are often retrogressed to chlorite-sericite schists. Sericite within these regions produce K-Ar ages of 470 ± 10 Ma, whereas biotite from the non-mylonitised charnockite give K-Ar ages of 974 ± 20 Ma (Jacobs, 1991; Jacobs *et al.*, 1995).

DISCUSSION

Relationships between Contrasting Geological Domains

The Annandagstoppane domain preserves the oldest rocks within WDML. Although only a small area of outcrop is exposed, it is extremely significant since it represents one of the few areas where Archaean age rocks are exposed in East Antarctica. No geological relationships between other domains are exposed due to the isolated nature of the outcrops. These Archaean gneisses have been interpreted as basement to the Ritscherflya Supergroup sediments and volcaniclastic rocks (Wolmarans and Kent, 1982). This domain places important constraints on geological reconstructions of the WDML region and has subsequently played a significant part in the various scenarios presented.

The significance of the Ahlmannryggen-Borgmassivet domain has been controversial due to early isotopic age data that ranged from 1800 Ma to 800 Ma (Wolmarans and Kent, 1982; Moyes and Barton, 1990). Re-interpretation of the data, along with new isotopic data provide ages of approximately 1100 Ma for the deposition of the Ritscherflya Supergroup (Moyes *et al.*, 1995; Moyes and Knoper, 1995). The Ritscherflya Supergroup has subsequently (Moyes and Knoper, 1995) been interpreted as a foreland-fold and thrust-belt developing on the margin of the craton rather than an intracratonic sedimentary and volcanic basin within the centre of a cratonic block. Correlations of the Ritscherflya Supergroup with the Umkondo Sequence in Zimbabwe have been suggested, and the mafic intrusions in both areas provide further evidence of this (Allsopp *et al.*, 1989; Moyes *et al.*, 1995).

Grantham *et al.* (1995) and Jackson and Jacobs (1995) have carried out comparisons of structures and deformation fabrics within the Heimefrontfjella, Kirwanveggen and H.U.Sverdrupfjella. Inconsistencies are identified between several domains within this region, although similar ages are obtained from these domains. Jackson and Jacobs (1995) have outlined domains with similar structures and fabric geometries which are discussed here. The Vardeklettane and Sivorg terranes have similar structural features that are dominated by right lateral transpression along the NNE to NE trending Heimefront Shear Zone. These structures can be explained within a single regional east-west compressive regime. The Kottas, central Kirwanveggen and eastern Sverdrupfjella domains exhibit colinear fabrics and structures with top-to-the-NW thrusting within an overall SE to NW plate convergence. Fabric geometries within these domains are remarkably similar and consistent, suggesting development within a single kinematic framework (Jackson and Jacobs, 1995).

The northern Kirwanveggen domain is interpreted as a transitional domain with steepened fabrics through later folding, and intense sub-horizontal elongation lineations. This domain is interpreted as a potential lateral ramp within the overall convergence across the adjacent domains, but the possibility of a strike-slip zone within this domain cannot be ruled out. In the southern Kirwanveggen insufficient structural work has been conducted to allow correlation with the adjacent high-grade domains. Deformation observed within the Urfjell Group, however, has major significance for the interpretation of the tectonic development of the region. Deformation in the Urfjell Group is characterised by right lateral transpressive strike-slip structures, steep faulting and associated folding with potential thrusting indicated through the duplication of lithological units. Constraints on the Urfjell deposition are placed between 688 Ma and 541 Ma (Moyes *et al.*, 1997) and indicate that the deformation must post-date this period. A minimum age for the deformation is marked by the Amelang Plateau Formation that unconformably overlies the sediments and the associated deformation. These sediments are interpreted as Early Permian in age (Larsson *et al.*, 1990). The late deformation complicates correlation of structural fabrics and geometries between the various geological domains in WDML.

Possible reasons for the apparent kinematic inconsistencies across the domains of the Maud Belt have been outlined by Jackson and Jacobs (1995) and are summarised as follows:

Geochronological data may be insufficient, or the age errors may be too large to allow a regional correlation or distinction of different periods of deformation.

The extent of the *ca.* 500 Ma tectonics may be masked and may lead to misinterpretations through the correlation of unrelated tectonic events.

Deformation may be inconsistent or diachronous throughout the belt making geometrical and fabric correlations complicated.

Lastly, the possibility of local geometrical effects on structural development within a multi-plate scenario causing apparent inconsistencies cannot be ruled out.

Contrasting the *ca.* 1100 Ma and *ca.* 500 Ma Events in WDML

Isotopic age data from the geological domains of the Maud Belt have provided various ages (see Table 2.1). The *ca.* 1100 Ma ages have traditionally been interpreted as formation, crystallisation, deformation and metamorphic ages with the *ca.* 500 Ma ages representing an isotopic resetting or cooling age (Wolmarans and Kent, 1982; Groenewald *et al.*, 1991). Recent work in other parts of East Antarctica and East Gondwanaland have rejuvenated investigations into the significance of these two contrasting events (Dirks *et al.*, 1993; Shiraishi *et al.*, 1994; Holzl *et al.*, 1994; Hensen and Zhou, 1995 amongst others). These workers have provided evidence of a far more significant role for the *ca.* 500 Ma event. In many cases these workers have suggested that the earlier *ca.* 1100 Ma ages represent ages of formation, and these units are subsequently deformed and metamorphosed by the high-grade 650-500 Ma event.

The development of new approaches and more reliable and precise isotopic dating techniques have spurred these investigations in other regions, including WDML. Stuwe and Sandiford (1993), Groenewald *et al.* (1991) and Moyes *et al.* (1993a) have suggested a largely thermal effect of the *ca.* 500 Ma event described by an underplating model due to the equivocal nature of tectonism within this event. Subsequent investigations in WDML highlighted the colinear reworking observed within the high-grade gneisses, prompting some workers to suggest that significant tectonism is associated with the *ca.* 500 Ma event (Jackson *et al.*, 1993; Krynauw, 1995). At this stage, however, the significance of the contrasting *ca.* 1100 Ma and *ca.* 500 Ma events within WDML remains largely enigmatic.

The Significance of WDML in Supercontinent Reconstructions

WDML is indicated in several supercontinental reconstructions, during which several amalgamation and break-up periods have been postulated. (Moores, 1991; Hoffman, 1991; Dalziel, 1991; Stump, 1992; Storey, 1993; Borg and De Paolo, 1994; Storey *et al.*, 1994). WDML forms part of the Precambrian craton of Gondwana prior to dispersion that resulted in the development of the southern oceans during the Mesozoic (Dalziel, 1991). The final stages of Gondwana amalgamation are recorded in the Pan-African orogenies that terminated at *ca.* 500 Ma. Evidence presented by Moores (1991), and expanded on by Daziel (1991) and Hoffman (1991), suggested that the Grenville Province of eastern North America continued through the Mesoproterozoic rocks in DML prior to Gondwana break-up, thus providing a link between Laurentia and Gondwana. These supercontinent reconstructions are based on reconciliation of available data from the various regions, and subsequently highlight the importance of local outcrop scale contributions to the understanding of the geological evolution of the region as a whole. Models for the evolution of WDML therefore contribute significantly to these reconstructions. The supercontinent reconstructions provide evidence for the close proximity of several, now distant, regions during different geological periods. Rocks that are of similar age and have a direct bearing on WDML are observed in southern Africa (Namaqua-Natal and Mozambique), the Falklands, and rocks of the Grenville Province in North America. Several models have been proposed for the geological evolution of certain areas within WDML and are discussed below.

Comparison of crustal domains and geological relationships in WDML and southern Africa have lead Groenewald *et al.* (1991) to propose a Proterozoic to Mesozoic link between southeastern Africa and Dronning Maud Land. Similarities between several domains support the postulated connection. The Annandagstoppane domain has been interpreted as a fragment of the

Kalahari Craton that split away during Gondwana break-up. Similarities between *ca.* 1100 Ma terranes (Natal and H.U.Sverdrupfjella) suggested collision during this period with W and NNW directed tectonic transport (African azimuth). The orogenic belt is interpreted to reflect accretion of marginal basin-volcanic arc sequences onto older cratonic material. The late *ca.* 500 Ma event has been described as a widespread predominantly thermal event overprinting parts of this supercontinental orogenic belt. Groenewald *et al.* (1991) have proposed that these terranes have remained locked together until rifting associated with Gondwana break-up separated the regions during Mesozoic times.

Jacobs *et al.* (1993) have proposed a somewhat different reconstruction for these associated terranes based predominantly on investigations undertaken in the Heimefrontfjella. These workers proposed that the *ca.* 1100 Ma high-grade gneisses of the Namaqua-Natal-WDML belt were accreted onto the southern margin of the Kaapvaal Craton during prolonged SW-NE convergence (African azimuth). The Kaapvaal Craton was viewed as a SW-directed indentor during the *ca.* 1100 Ma event. The resultant structures and fabric geometries observed within these high-grade regions are interpreted as a consequence of the indentation during convergence. This model proposes convergence within WDML at high-angles compared to that proposed by Groenewald *et al.* (1991).

More detailed crustal evolution models have consequently been proposed for the Heimefrontfjella and the H.U.Sverdrupfjella regions based on the results of further investigations in these regions. In the H.U.Sverdrupfjella Groenewald *et al.* (1995) have advanced the detailed evolution model for WDML, and their model is summarised here. Little can be inferred from the small isolated outcrops of Archaean gneisses about their early history. Although these problems exist Groenewald *et al.* (1995) interpreted this Archaean material to be a fragment of the Kaapvaal-Zimbabwe Craton. Collision, compression and accretion of a retro-arc marginal basin occurred between 1200 Ma and 1100 Ma. High-pressure and medium-temperature conditions have been suggested from the occurrence of eclogitic material in the eastern Sverdrupfjella. The occurrence of such conditions is not typical of arc collision, but has been interpreted as a result of the collision and subsequent tectonic sandwiching of the arc assemblage (Groenewald *et al.*, 1995). Decompression and thermal relaxation to medium-pressure granulite facies results in the intrusion of volumetric orthogneisses around *ca.* 1050 Ma. Extension following the collisional period is suggested by mafic igneous activity in the H.U.Sverdrupfjella and the Ritscherflya Supergroup between 1000 Ma and 800 Ma. A period of possible break-up and dispersal is suggested during this period (Groenewald *et al.*, 1995). The *ca.* 500 Ma event is marked by the intrusion of the Brattskarvet Granitoid Suite followed by later stage S-type granite intrusion within the H.U.Sverdrupfjella. NW directed thrusting (Antarctic azimuth) of granulite facies material over lower-grade rocks results in rapid exhumation during the *ca.* 500 Ma event. The juxtaposition of high-grade gneisses and the Urfjell Group suggests the removal of 10-15 km of crust during this exhumation. Late stage extension and magmatism is associated with Gondwana break-up.

The crustal evolution model proposed by Groenewald *et al.* (1995) invokes continent collision involving juvenile crust that is reworked in the Mesoproterozoic. A second orogenic event at *ca.* 500 Ma resulted in the northwestward directed thrusting (Antarctic azimuth) onto the margin of the Archaean Kalahari Craton. Considerable shortening of the H.U.Sverdrupfjella is possible during this event. The postulated break-up of the terrane between the two orogenies suggests the possibility of a *ca.* 500 Ma belt crossing through WDML south and east of the Maud Belt, and joining up with the Pan-African collision belt of East Africa (Groenewald *et al.*, 1995).

In the Heimefrontfjella a similar, yet somewhat different evolution model is proposed (Jacobs *et al.*, 1996). Each of the three terranes have significant implications for the development of a tectono-stratigraphic evolution of the Heimefrontfjella. The Kottas terrane with predominantly metavolcanic rocks and tonalites favours an island arc setting. The Sivorg metavolcanics are significantly different and occur with thick metasedimentary sequences suggesting a back-arc basin environment. Older crust involvement is invoked for the Vardeklettane terrane from zircon population ages in the metasediments. This suggests a closer association with older basement material and, along with the charnockite development, indicates deeper crustal levels in a possible extensional environment.

The terranes within the Heimefrontfjella have been juxtaposed during a complex prolonged compressional period. East-west compression (Antarctic azimuth) is invoked for this period during plate convergence. The early deformational event produced the inverse metamorphic stacking of the Vardeklettane granulitic terrane over the amphibolite facies Sivorg terrane. Major dextral transpression occurred along the Heimefrontfjella Shear Zone, which developed at high angles and overprinted the earlier tectonic fabrics. The shear zone indicates east over west (Antarctic azimuth) compression. The development of these tectonic relationships is inferred to be the result of convergence of the Kalahari Craton in the northwest and an "East Antarctic Craton" towards the southeast (African azimuth). N- to NW-directed thrusting that overprints and retrogresses the high-grade gneisses has been assigned to the *ca.* 500 Ma event. NE trending normal faults in the Heimefrontfjella reflect Gondwana break-up.

Differences in tectonic transport directions during the *ca.* 1100 Ma event remain between these two near-adjacent domains and no suitable explanations of these inconsistencies have yet been provided.

Unresolved Problems within the high-grade Gneisses of WDML

Several unresolved geological problems remain for WDML. These are summarised as:

The distinction of the *ca.* 1100 Ma and *ca.* 500 Ma tectono-metamorphic events from one another remains equivocal. The colinear nature of these deformational events complicates the understanding of the nature of these two events.

Comparisons between the high-grade gneiss domains highlight the importance of establishing the sequence and timing of deformational and metamorphic events within WDML. This will allow further comparison to adjacent continental regions.

Conflicting tectonic transport directions from near-adjacent regions during the major tectonothermal event have yet to be resolved.

The geographical significance of the varied geological domains requires re-evaluation in terms of the understanding of the *ca.* 1100 Ma and *ca.* 500 Ma events.

The interpretation of isotopic data from the high-grade gneiss terrane remains problematic. Effects of resetting, disturbance, metamorphism and deformation continually hamper interpretations of ages within these regions. A better understanding of the age significance of the various isotopic techniques is required.

Several of these problems are addressed within the current investigation. These pertain to problems 1, 2 and 5 and certain aspects will be addressed, and elaborated on in the individual chapters of this thesis.

GEOLOGICAL MAP OF WESTERN DRONNING MAUD LAND, ANTARCTICA

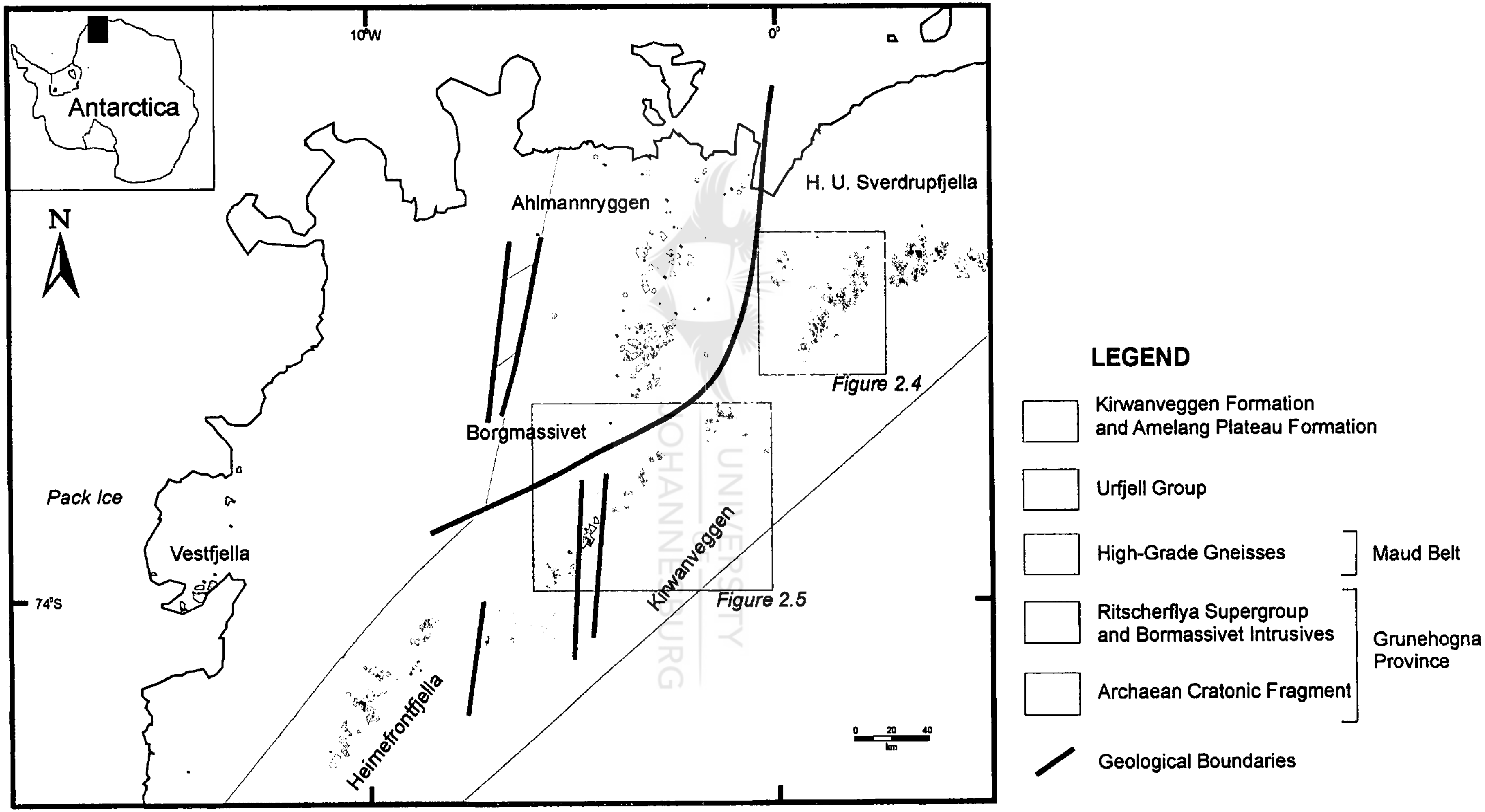

FIGURE 2.1. Geological map of western Dronning Maud Land in Antarctica. The major geology is extrapolated across outcrops (nunataks) under ice cover. Boundaries between these geological regions are interpolated. The regions that are presented as maps later, are outlined on this map.

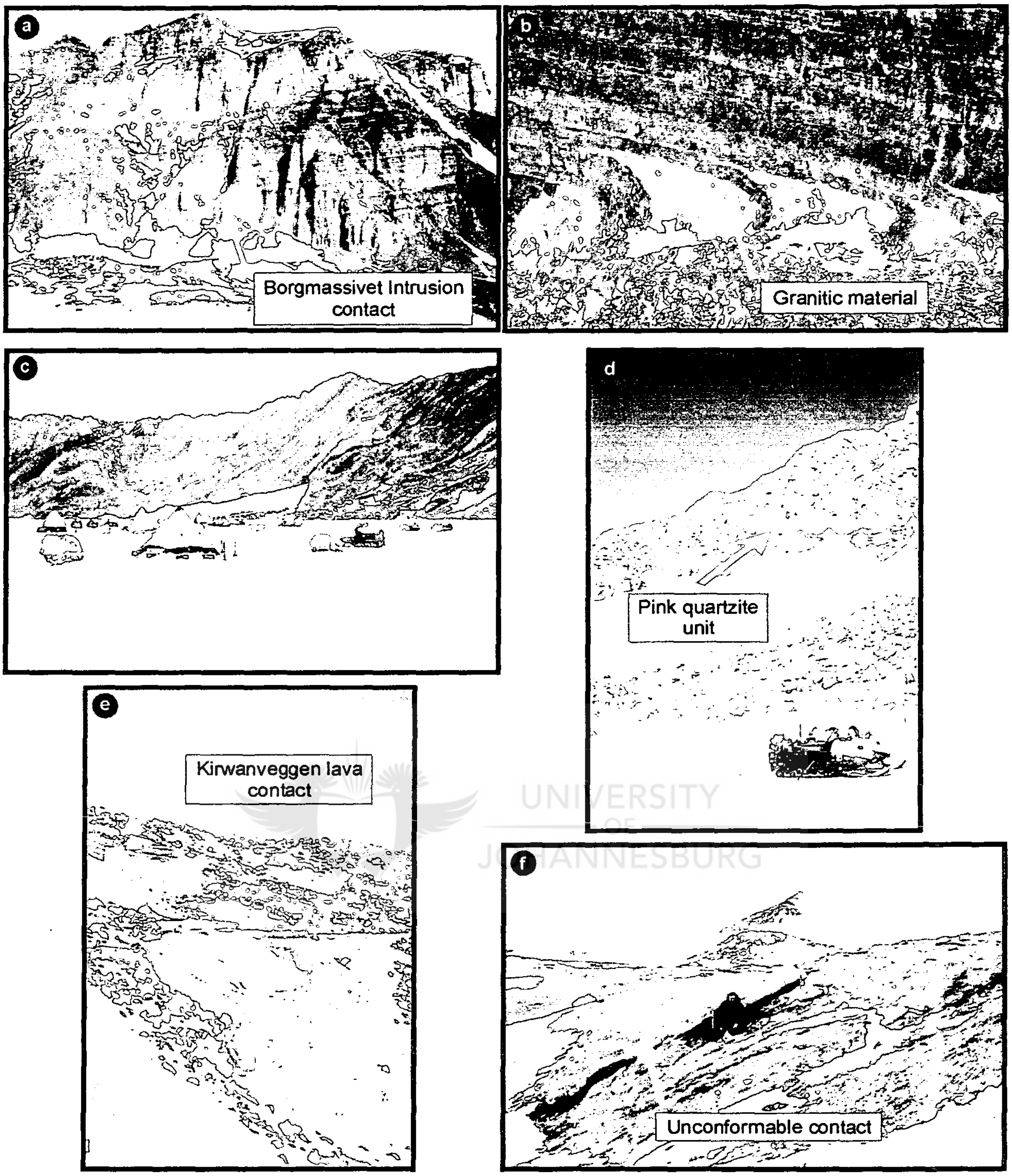

FIGURE 2.2. Photographs of different lithotectonic units found within western Dronning Maud Land.

a.) Photograph of the Ritscherflya Supergroup at Grunehogna in the Borgmassivet. The sedimentary sequence is intruded by a Borgmassivet mafic sill.
b.) Photograph of the Ritscherflya Supergroup with granitic material intruding along the bedding plane foliations. These granites have been dated at *ca.* 1000 Ma by Moyes *et al.* (1995).
c.) Photograph of the high-grade gneiss terrane exposed at Hallgrenskarvet in the central Kirwanveggen.
d.) Photograph of the Urfjell sediments exposed in the southern Kirwanveggen. The bedding planes are gently dipping and a pink quartzite unit is exposed at this outcrop.
e.) Photograph of the Kirwanveggen Formation lavas conformably overlying the Amelang Plateau Formation sediments and the leached basement high-grade gneiss contact.
f.) Photograph of the unconformable contact between the underlying high-grade gneisses and the Amelang Plateau Formation.

GEOLOGICAL MAP OF WESTERN DRONNING MAUD LAND, ANTARCTICA

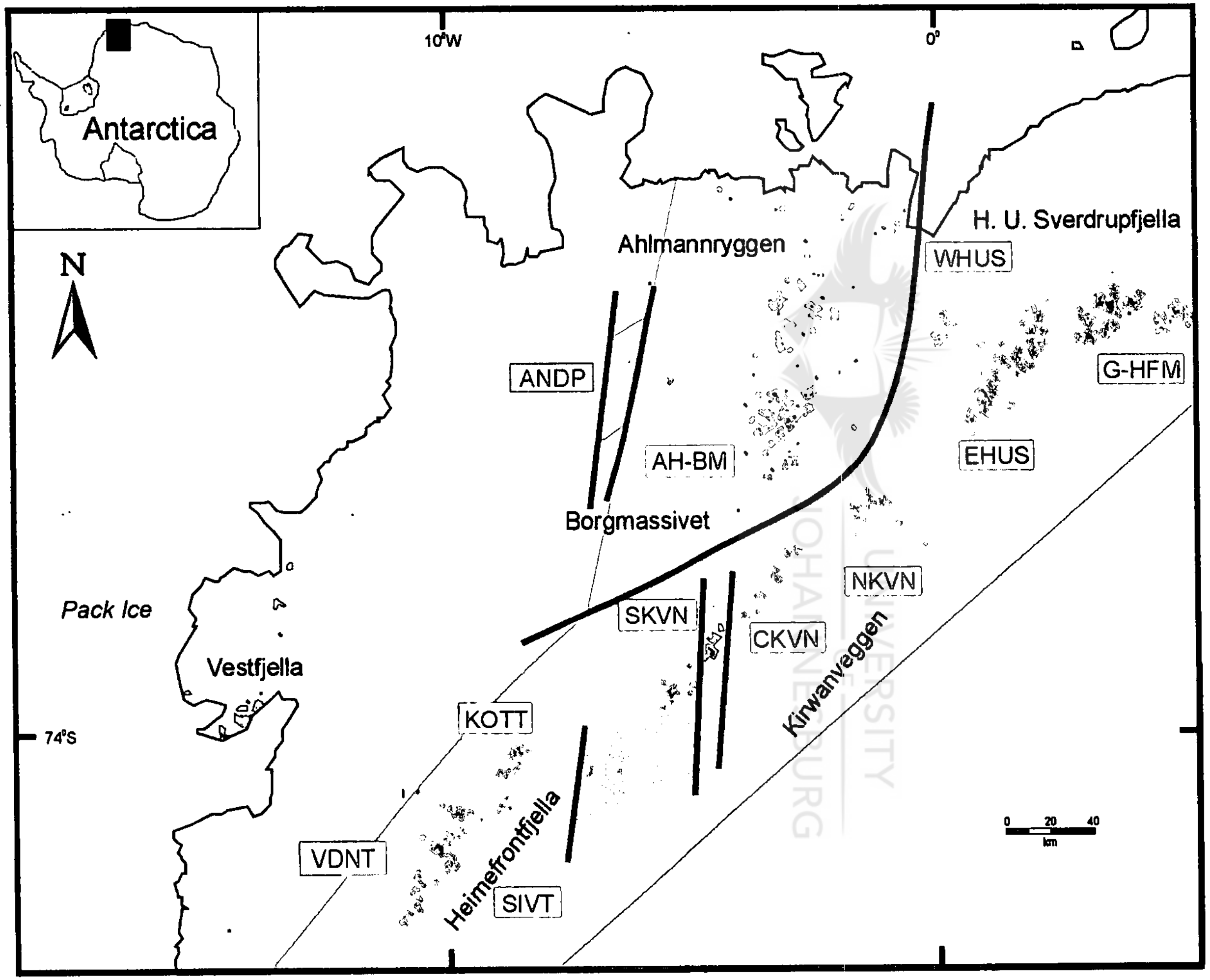

GEOLOGICAL DOMAINS IN WESTERN DRONNING MAUD LAND

ANDP : - Annandagstoppane
AH-BM : - Ahlmannryggen-Borgmassivet
G-HFM : - Gjelsvikfjella-Muhlig Hoffmanfjella
WHUS : - Western H.U.Sverdrupfjella
EHUS : - Eastern H.U.Sverdrupfjella
NKVN : - Northern Kirwanveggen
CKVN : - Central Kirwanveggen
SKVN : - Southern Kirwanveggen
KOTT : - Kottas Terrane
SIVT : - Sivorg Terrane
VDNT : - Vardeklettane Terrane
Domain Boundaries

LEGEND

Kirwanveggen Formation and Amelang Plateau Formation
Urfjell Group
High-Grade Gneisses — Maud Belt
Ritscherflya Supergroup and Bormassivet Intrusives — Grunehogna Province
Archaean Cratonic Fragment — Grunehogna Province
Geological Boundaries

FIGURE 2.3. Geological map of western Dronning Maud Land, Antarctica. The different geological domains and their boundaries are illustrated on this diagram. See text for detailed discussions of the geology of the individual domains.

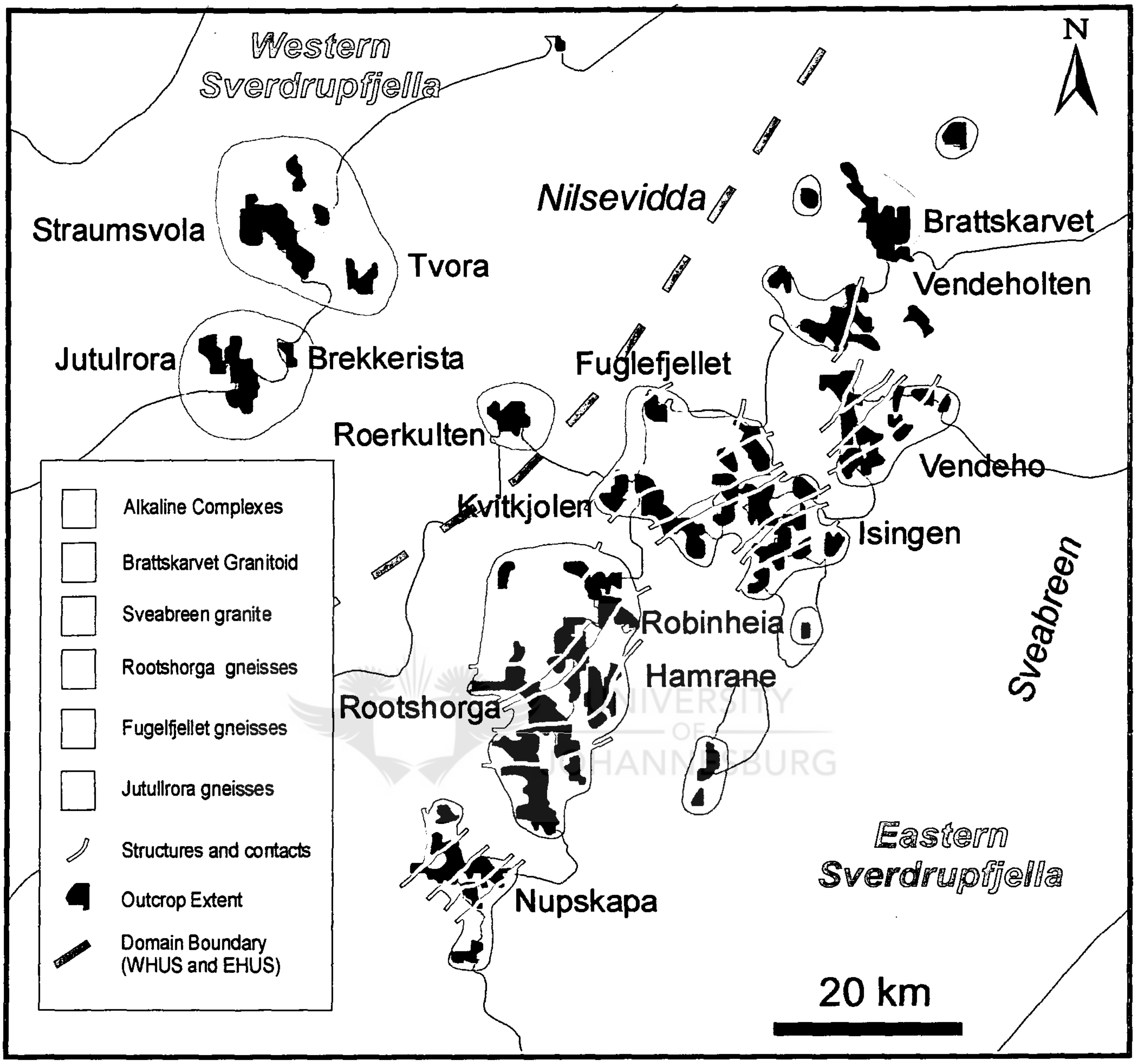

FIGURE 2.4. Geological map of the H.U.Sverdrupfjella geological region (after Grantham *et al.*, 1995 and Groenewald *et al.*, 1995). The western Sverdrupfjella (WHUS) and eastern Sverdrupfjella (EHUS) geological domains are outlined on this map. This region is dominated by major outcrops of high-grade gneisses of the Maud Belt (See text for details). The *ca.* 500 Ma Brattskarvet Intrusive Suite is outcropping in the northern part of the EHUS geological domain. Alkaline complexes of *ca.* 180 Ma are exposed in the WHUS.

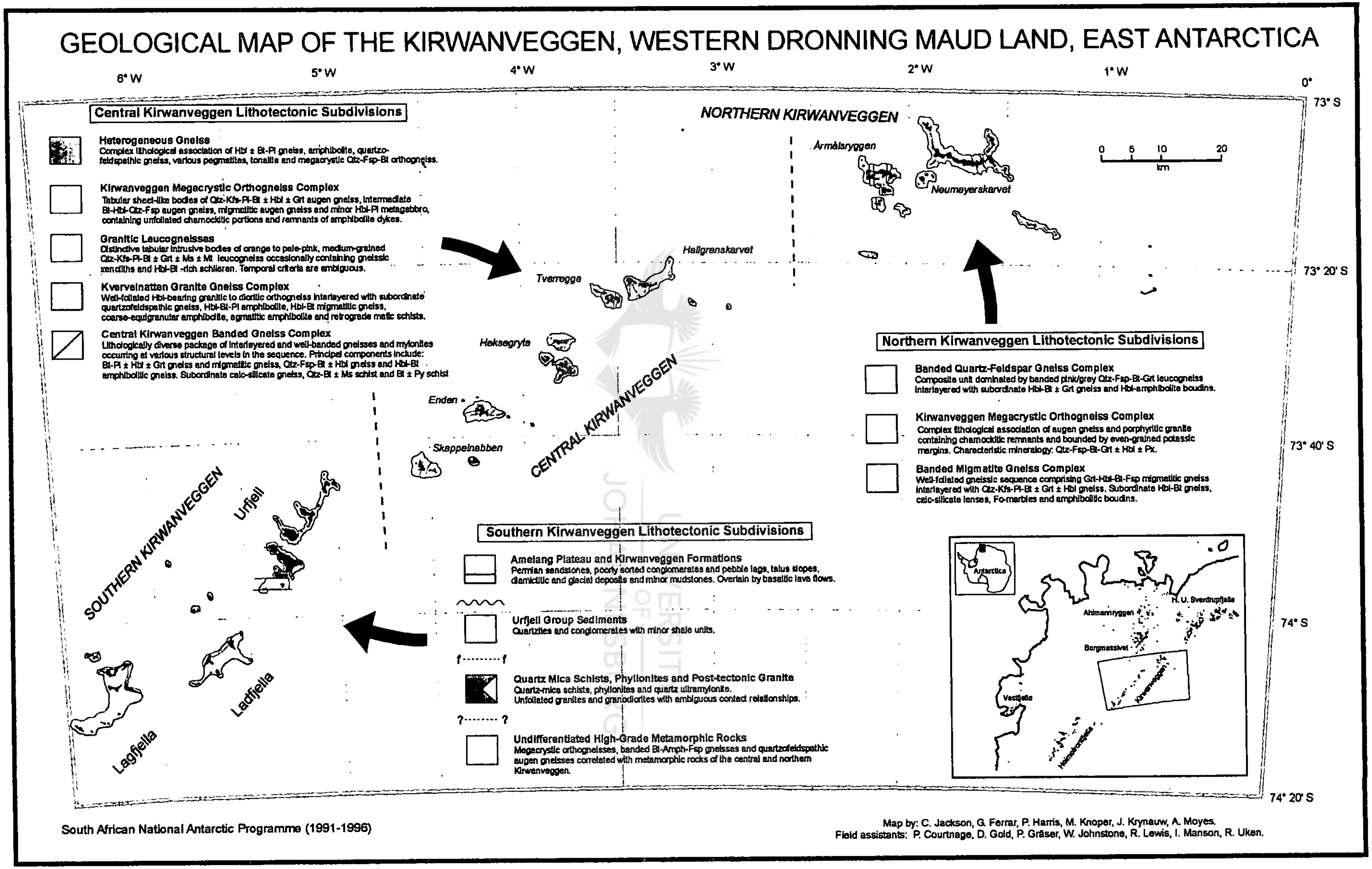

FIGURE 2.5. Geological map of the Kirwanveggen in western Dronning Maud Land, Antarctica. Outcrop areas are shown in black. The geological domains of the northern, central and southern Kirwanveggen are illustrated in terms of their lithotectonic components. This map is a compilation of geological mapping carried out by members of the Kirwanveggen program.

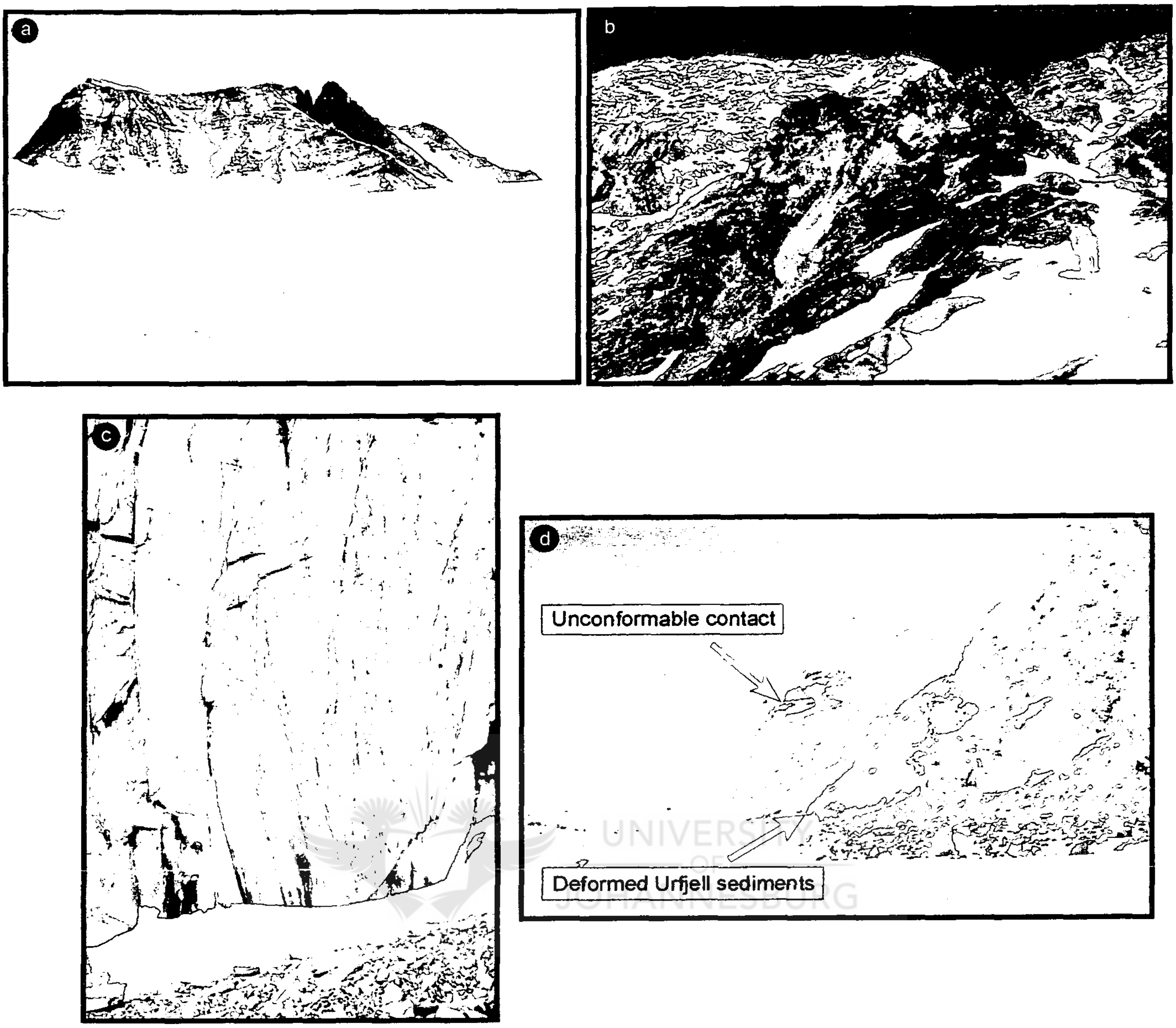

FIGURE 2.6. Photographs of different structural features observed within western Dronning Maud Land.

a.) Photograph of gentle regional folding observed within the Ritscherflya Supergroup towards the boundary with the high-grade gneisses. The boundary contact is, however, unexposed.
b.) Photograph of typical fabric formation and isoclinal folding recognised within the high-grade gneisses of western Dronning Maud Land. The photograph is of an exposure within Neumayerskarvet in the northern Kirwanveggen.
c.) Photograph of steeply dipping bedding planes from the Urfjell Group sediments at Tunga in the southern Kirwanveggen. The exposure is close to the tectonic contact with the high-grade gneisses.
d.) Photograph showing the unconformable Amelang Plateau Formation and the Kirwanveggen Formation over the tectonic contact between the Urfjell Group sediments and the high-grade gneisses. This exposure illustrates that the Amelang Plateau and Kirwanveggen Formations post-date the deformation recognised within the Urfjell sediments. The photograph was taken at Tunga in the southern Kirwanveggen.

TABLE 2.1. Geochonological data from the different geological domains within western Dronning Maud Land, Antarctica.

ANNANDAGSTOPPANE DOMAIN (ANDP)

Rock Type	Sample	Method	Age	Interpretation	Reference
Granitic gneisses forming the major unit exposed at Annandagstoppane					
Granitic gneiss	Whole-rock Muscovite Biotite Chloritised biotite Apatite	Rb-Sr/Pb-Pb Rb-Sr Rb-Sr Rb-Sr Fission Track	3100-2950Ma 3050-2830Ma 1250-1100Ma ~460Ma 303±22Ma	Intrusive age Cooling age Cooling age Cooling age Cooling age	Barton *et al.* (1987) Halpern (1970)
Mafic dyke intruding the granitic gneisses at Annandagstoppane					
Mafic dyke	Whole-rock	Rb-Sr	~390Ma	Intrusive age (?)	Moyes (*unpubl.)*

AHLMANNRYGGEN-BORGMASSIVET DOMAIN (AH-BM)

Rock Type	Sample	Method	Age	Interpretation	Reference
Ritscherflya Supergroup					
Hogfonna Sediments	Whole-rock	Rb-Sr/Sm-Nd	1200-1100Ma	Age of deposition	Moyes *et al.* (1995)
Raudberget volcaniclastic	Zircon	Evaporation	~1130Ma	Age of formation	Moyes (*unpubl.)*
Straumsnutanne Volcanics mylonites	White mica	K-Ar	522±11Ma 526±11Ma	Minimum age of deformation	Peters (1989)
Borgmassivet Intrusions					
Grunehogna gabbro	Whole-rock	Rb-Sr	~1000Ma	Approximate age of intrusion	Moyes *et al.* (1995)
Robertsskollen peridotites	Phlogopite	Rb-Sr	1134-1066Ma	Post-crystallisation resetting	Moyes and Barton (1990)

GJELSVIKFJELLA-MUHLIG HOFFMANFJELLA DOMAIN (G-HFM)

Rock Type	Sample	Method	Age	Interpretation	Reference
High-grade gneisses					
Jutulsessen granitic gneiss	Whole-rock Whole-rock Mineral (biotite)	Sm-Nd Rb-Sr Rb-Sr	~1153Ma ~535Ma 478±13Ma	Intrusive age Isotope resetting Cooling age	Moyes (1993)
Svarthameran charnockite	Whole-rock	Rb-Sr	500±24Ma	Crystallisation age (resetting??)	Otha *et al.* (1990)

EASTERN H.U.SVERDRUPFJELLA DOMAIN (EHUS))

Rock Type	Sample	Method	Age	Interpretation	Reference
High-grade gneisses					
Brattskarvet paragneiss	Whole-rock	Rb-Sr	1046±50Ma	Age of metamorphism	Moyes *et al.* (1993b)
Rootshorga gneisses	Zircon Zircon Whole-rock Whole-rock Garnetk	SHRIMP SHRIMP Sm-Nd Rb-Sr Sm-Nd	~1130Ma ~500Ma 1183±27Ma 1071±253Ma 562-415Ma	Age of formation Zircon growth Reset age	Harris *et al.* (1995) Harris *et al.* (1995) Moyes and Groenewald (1996)
Sveabreen paragneiss	Whole-rock Biotite-feldspar	Rb-Sr Rb-Sr	1170±26Ma 431±9Ma		Moyes *et al.* (1993b)
Fugitive granite	Zircon Whole-rock Garnet	SHRIMP Rb-Sr Sm-Nd	1131±25Ma 1161±98Ma 648-485Ma	Age of intrusion Reset age	Harris *et al.* (1995) Moyes and Groenewald (1996)
Sveabreen granitic gneiss	Zircon Whole-rock Garnet	SHRIMP Rb-Sr Sm-Nd	1127±12Ma 1028±94Ma 680-433Ma	Age of intrusion Reset age	Harris *et al.* (1995) Moyes and Groenewald (1996)
Late Granitic Intrusions					
Brattskarvet Intrusive Suite	Whole-rock Whole-rock Mineral (biotite)	Sm-Nd Rb-Sr Rb-Sr	522±120Ma 518±15Ma 485-465Ma	Age of intrusion (~520Ma)	Moyes *et al.* (1993b)

WESTERN H.U.SVERDRUPFJELLA DOMAIN (WHUS)

Rock Type	Sample	Method	Age	Interpretation	Reference
High-grade gneisses					
Roerkulten granite	Zircon	SHRIMP	1103±13Ma	Age of intrusion	Harris *et al.* (1995)
Late Granitic Intrusions					
Dalmation Granite	Mineral (biotite)	Rb-Sr	469±5Ma	Age of intrusion	Grantham *et al.* (1991)
Late Alkaline Complexes					
Straumsvola nepheline syenite complex	Whole-rock	Rb-Sr	170±4Ma	Age of formation	Grantham *et al.* (1988)

NORTHERN KIRWANVEGGEN DOMAIN (NKVN)

Rock Type	Sample	Method	Age	Interpretation	Reference
High-grade gneisses					
Neumayerskarvet leucogneiss	Whole-rock Zircon	Rb-Sr U-Pb (bulk)	1007±57Ma 1112±32Ma	Age of metamorphism Age of formation	Wolmarans and Kent (1982) Moyes and Barton (1990)
Neumayerskarvet bioite-garnet migmatite gneiss	Zircon	SHRIMP	~2000Ma 1157±10Ma 1100±10Ma	Inherited age Zircon growth Zircon Growth/resetting	Harris *et al.* (1995)
Neumayerskarvet megacrystic orthogneiss	Zircon	SHRIMP	1088±10Ma	Intrusive age	Harris *et al.* (1995)
Neumayerskarvet late pegmatite	Zircon	SHRIMP	1079±6Ma	Intrusive age	Harris *et al.* (1995)
Armalsryggen gneisses	Zircon	U-Pb (bulk)	1045±193Ma	Age of formation	Moyes and Barton (1990)

CENTRAL KIRWANVEGGEN DOMAIN (CKVN)

Rock Type	Sample	Method	Age	Interpretation	Reference
High-grade gneisses					
Heksegyta gneisses	Whole-rock Zircon	Rb-Sr U-Pb (bulk)	1164±78Ma 1107±127Ma	Age of metamorphism Age of formation	Wolmarans and Kent (1982) Moyes and Barton (1990)
Hallgrenskarvet gneisses	Whole-rock Mineral (Biotite)	Rb-Sr Rb-Sr	1035±18Ma 493-436Ma	Age of metamorphism Cooling afge	Wolmarans and Kent (1982)
Tverregga porphyritic dyke	Zircon	SHRIMP	1011±8Ma	Intrusive age	Harris *et al.* (1995)
Enden late pegmatite vein	Rb-Sr	Muscovite	~946Ma	Cooling age	Moyes *et al.* (1993a)

SOUTHERN KIRWANVEGGEN DOMAIN (SKVN)

Rock Type	Sample	Method	Age	Interpretation	Reference
Urfjell Sediments					
Sediments	Whole-rock Muscovite	Rb-Sr Rb-Sr	539±29Ma ~630Ma	Age of overprint or formation Source age (?)	Moyes *et al.* (1997)
Kirwanveggen Lavas					
Kirwan volcanics	Whole-rock	K-Ar	172±10Ma	Age of formation	Quoted in Aucamp *et al.* (1972)

KOTTAS TERRANE (KOTT)

Rock Type	Sample	Method	Age	Interpretation	Reference
High-grade gneisses					
Leucocratic pink gneiss	Zircon	U-Pb	1093±10Ma	Age of formation	Arndt *et al.* (1991)
Augen gneiss	Zircon	U-Pb	1088±10Ma	Age of intrusion	Arndt *et al.* (1991)
Leaboten microgranite vein	Zircon	U-Pb	1059±4Ma	Age of intrusion	Bauer (1995)
Vikenegga pegmatite	Zircon Muscovite	U-Pb K-Ar	1060±8Ma 967±21Ma	Age of intrusion Cooling age	Arndt *et al.* (1991) Jacobs *et al.* (1996)
Thrust	Biotite	K-Ar	473±11Ma	Resetting or deformation	Jacobs *et al.* (1995)

SIVORG TERRANE (SIVT)					
Rock Type	**Sample**	**Method**	**Age**	**Interpretation**	**Reference**
High-grade gneisses					
Holdorsentoppen fish granite	Zircon	U-Pb	1078±30Ma	Age of intrusion	Arndt *et al.* (1991)
Wrighthamaren granite	Zircon	SHRIMP	1104±10Ma	Age of intrusion	Arndt *et al.* (1991)
Tottanfjella Granodiorite	Zircon	U-Pb (conv)	1045±8Ma	Age of Intrusion	Arndt *et al.* (1991)
Milorgfjella Garnet Ammphibolite	Zircon Mineral (wr-amph-grt)	SHRIMP Sm-Nd	1060±8Ma 960±120Ma	Metamorphic age Metamorphic or cooling age	Arndt *et al.* (1991) Arndt *et al.* (1991)
Ristinghortane quartzites and pegmatite	Muscovite	K-Ar/Ar-Ar	987-960Ma	Cooling age	Jacobs *et al.* (1995)
Cottentoppen granite	Muscovite	K-Ar	886±19Ma	Cooling age	Jacobs *et al.* (1996)
Heimefront Shear Zone					
Type 1 mylonites	Biotite	K-Ar	812±17Ma	Cooling age	Jacobs *et al.* (1995)
Overgrowths within mylonites	Muscovite	K-Ar	~500Ma	Cooling ages	Jacobs *et al.* (1995)
Vedeklettane chlorite-sericite schist	<2um fraction	K-Ar	470±10Ma	Cooling age	Jacobs *et al.* (1995)
Pseudotachylite	<2um fraction	K-Ar	395±9Ma	Cooling age	Jacobs *et al.* (1995)
VARDEKLETTANE TERRANE (VDNT)					
Rock Type	**Sample**	**Method**	**Age**	**Interpretation**	**Reference**
High-grade gneisses					
Quartzitic gneisses	Zircon	SHRIMP	~2000Ma to ~1100Ma	Protolith and metamorphic ages	Arndt *et al.* (1991)
Vardeklettane leucogranite	Zircon	U-Pb	1135±8Ma	Age of intrusion	Arndt *et al.* (1991)
Mannefallknausane granite	Zircon	U-Pb	1073±8Ma	Age of intrusion	Arndt *et al.* (1991)
Retrogressed chlorite-sericite schists	<2um sericite separates	K-Ar	470±10Ma		Jacobs *et al.* (1995)
Charnockite	Biotite	K-Ar	974±20Ma	Cooling age	Jacobs *et al.* (1995)

CHAPTER 3

THE GEOLOGY AND DEFORMATIONAL HISTORY OF THE NORTHERN KIRWANVEGGEN

INTRODUCTION

Rock exposures in East Antarctica have been the subject of many geological investigations over several decades, since Antarctica plays a key role in Gondwana, and other supercontinent reconstructions. Problems in understanding the geological history of East Antarctica are amplified by the limited and isolated nature of the snow covered outcrops. Many regions in East Antarctica have isotopic evidence of a *ca.* 1100 Ma and a younger *ca.* 500 Ma event. The significance of these events has, however, remained controversial between different regions. As more supercontinent reconstructions are attempted, so the significance of each of these events requires resolution.

The high-grade gneisses of the Kirwanveggen have not escaped this controversy. Although isotopic data indicate the existence of both events, the structural, geological and metamorphic associations have not been clearly unravelled. The purpose of this investigation is to provide detailed geological and structural data for the high-grade gneisses of the northern Kirwanveggen. This will enable further detailed isotopic investigations into the timing of deformation within this region. The establishment of a detailed geological-structural framework will permit a better understanding of the significance of the *ca.* 1100 Ma and *ca.* 500 Ma events.

GEOLOGICAL FRAMEWORK

The northern Kirwanveggen forms part of the high-grade gneiss terrane that extends through western Dronning Maud Land (WDML) from the Muhlig-Hoffmanfjella in the northeast to the Heimefrontfjella in the southwest (Figure 3.1). The high-grade gneiss terrane is separated from the volcaniclastic, metasedimentary and mafic intrusions of the Ahlmannryggen-Borgmassivet by the Pencksokket glacial system. Isolated outcrops of Archaean age granitic gneisses are found in the western extremity of the Ahlmannryggen-Borgmassivet terrane.

Although a continuous high-grade gneiss belt is extrapolated through WDML, ice covered discontinuities separate this belt into distinct terranes. The Kirwanvegggen forms the central portion of the WDML high-grade gneiss terrane with the Heimefrontfjella to the southwest and the H.U.Sverdrupfjella to the northeast.

The Kirwanveggen forms a discontinuous escarpment that has been sub-divided into three different domains (Figure 3.2):

1. The northern Kirwanveggen, with the major outcrop patterns of Armalsryggen and Neumayerskarvet, is the area of focus for this investigation. The major lithotectonic units comprise gneisses and orthogneisses that have been subjected to various degrees of deformation.
2. A second domain within the Kirwanveggen that displays lithotectonic and structural continuity across isolated outcrops is the central Kirwanveggen. The central Kirwanveggen exhibits gneisses and orthogneisses that show similarities to the northern Kirwanveggen, but differing mineralogies and structural elements do not permit direct correlation across these domains.
3. The southern Kirwanveggen exhibits distinctly different lithotectonic units to the central and northern Kirwanveggen. The northeast portion of the southern Kirwanveggen is dominated by the Urfjell Group metasediments, which comprise quartzites, conglomerates and minor shales. These metasediments are in tectonic contact with the high-grade gneisses and are thought to be *ca.* 550 Ma in age (Moyes *et al.*, 1997). The Urfjell Group is overlain by the Permian (?) Amelang Plateau Formation, which are in turn overlain by the Kirwanveggen lavas of Mesozoic age (Harris *et al.*, 1990). In the southwestern extremities of the southern Kirwanveggen these lavas unconformably overlie the undifferentiated high-grade metamorphic rocks. The metamorphic rocks are thought to form part of the high-grade gneiss terrane observed within WDML.

LITHOTECTONIC SUBDIVISIONS OF THE NORTHERN KIRWANVEGGEN

Banded Quartz-Feldspar Gneiss

Exposures of these lithotectonic units occur at Aust Vorren in the eastern arm of Neumayerskarvet (see Figure 3.3). This unit comprises amphibole-biotite-(garnet) and quartzofeldspathic gneisses intruded by amphibolite dykes, and banded pink-grey leucogneiss with amphibolite interlayers and boudin trains. (Figure 3.4b)

Biotite-Garnet Migmatite Gneiss

Biotite-garnet migmatite gneiss forms the major lithotectonic unit exposed at Neumayerskarvet, and has also been referred to as the biotite-garnet plagiogneiss (Wolmarans and Kent, 1982). It is a fine-grained melanocratic rock, with leucosomes and melanosomes defining the gneissic foliation. The major mineralogy comprises biotite, garnet, feldspar, quartz and amphibole. The gneiss is often highly tectonised and exhibits evidence for all phases of deformation recognised in the northern Kirwanveggen (Figure 3.4c).

Calc-silicate and amphibolite boudins are often observed within the regional foliation of the biotite-garnet migmatite gneiss, and intrusive leucogneiss units are also found as lenticular bodies. Small lensoidal granitoids are found intruding into, and across the regional foliation of the gneiss, and suggest high-grade metamorphism and possible partial melting.

Vein-Network Migmatitic Gneiss

Locally within the biotite-garnet migmatite gneiss, vein-network migmatitic gneiss is observed (Figure 3.4d). The main vein-network migmatite exposure is encountered within central Neumayerskarvet (Figure 3.3). This unit grades laterally into the biotite-garnet migmatite gneiss, and no sharp structural or intrusive contact between these two units is observed. The vein-network migmatite gneiss consists of mafic phases together with leucocratic phases that show various intrusive-structural relationships. Several different phases are recorded locally within the vein-network migmatitic gneiss. Mafic material in this gneiss behaves competently during deformation, and is boudinaged or brecciated. Leucocratic gneissic material occurs with the mafic phase of the vein-network migmatitic gneiss. This material infills at the boudin necks of the mafic phase and has behaved in an incompetent manner during the deformation. The leucocratic gneissic material exhibits a strong regional foliation suggesting that it was present during the vein-network migmatisation stage. Early felsic melt material occurs in veinlets often rimming the mafic phase in the migmatite. This melt phase infills the brecciated or boudinaged material suggesting that it represents material derived during the migmatisation event. Late crosscutting felsic veining occurs as the last dominant phase in the vein-network migmatitic gneiss. This felsic veining crosscuts all the previous phases in the migmatitic gneiss and does not seem to be related to the earlier boudinage and brecciation event. This phase consists dominantly of pinkish feldspar with quartz and lesser amounts of biotite.

Quartzofeldspathic Gneiss

The quartzofeldspathic gneiss occurs interleaved with the biotite-garnet migmatite gneiss, on the western side of Neumayerskarvet (Figure 3.3). This rock unit is predominantly leucocratic and does not display the strong banding observed within the banded quartz-feldspar gneiss. A compositional banding is exhibited by the quartzofeldspathic leucogneiss consisting of small melanosomes of biotite-rich material with leucosomes of quartz-rich material (Figure 3.4a). The quartzofeldspathic gneiss comprises quartz, feldspar, and biotite with variable amounts of garnet and amphibole as the main mineralogy. Most deformational episodes are recorded within the quartzofeldspathic gneiss. Mafic boudins consisting mainly of amphibole and garnet exhibit an early foliation within the quartzofeldspathic gneiss, and these units behaved more competently during deformation of the gneissic unit. Early mafic schlieren are also observed within the more leucocratic phases of the unit. Mafic bands and leucogneissic material occur as less competent material around the mafic boudins. The mafic bands are garnet-biotite-rich, and both phases exhibit signatures of the strong regional foliation development. Melt patches of poikilitic amphibole enclosing garnet occur locally within fold closures in the quartzofeldspathic gneiss.

Megacrystic Orthogneiss

Well Foliated Augen Gneiss

A well-foliated, fine-grained augen gneiss is found at the contact between the megacrystic orthogneiss and the biotite-garnet migmatite gneiss, in central Neumayerskarvet (Figure 3.3). The unit consists of a banded fine-grained rock with quartz, feldspar, biotite and occasional garnet. The unit exhibits a strong foliation and stretching lineation development. Parasitic folds within the banded leucogneiss plunge in the same direction as the stretching lineation. Calc-silicate boudins have been observed within the well-foliated augen gneiss.

Megacrystic Orthogneiss

The Neumayerskarvet megacrystic orthogneiss is characterised by coarse-grained K-feldspar porphyroblasts and zones of remnant charnockitic material. It intruded biotite-garnet migmatite gneisses of the northern Kirwanveggen during a period of major deformation. Enclaves within the orthogneiss exhibit a strong foliation indicating that the intrusion of this body post-dates part of the deformation experienced by the high-grade gneiss terrane. These enclaves consist of migmatite gneisses and calc-silicate boudins, along with mafic enclaves of possible dyke origin. Portions of the orthogneiss are intensely deformed, producing strong linear and planar fabrics in the resulting augen-textured gneiss. These lines of evidence suggest that the megacrystic orthogneiss was intruded syn- to late-tectonically relative to the major deformation of the high-grade gneisses in the northern Kirwanveggen.

Dark chamockitic patches are preserved only in unstrained to weakly deformed areas, while in the more intensely deformed areas augen gneisses occur (Figure 3.4e). The charnockitic patches comprise only a small portion of the intrusion and are randomly dispersed throughout the megacrystic orthogneiss. Unlike patchy charnockite examples from Sri Lanka and India, this chamockite is unrelated to veins or minor shear zones and appears to form remnants that have survived deformation and rehydration. At Neumayerskarvet the preserved charnockitic patches represent the earliest recorded assemblages of the megacrystic orthogneiss. Gradational contacts are observed between the different zones of the orthogneiss, resulting in charnockitic material grading into a porphyritic granitoid, and progressing into augen gneisses. Later structures affecting the orthogneiss, including aplitic veins, provided conduits for late rehydration and retrogression of the earlier assemblages.

Several different generations and types of felsic veins crosscut the megacrystic orthogneiss. Aplitic veins that parallel the foliation are often transposed and folded, while other small granitic veins crosscut the augen gneiss. Several types of melt leucosomes have intruded across the foliations within the augen gneisses. Some of these melt leucosomes intrude into minor shear zones, while others occur as typical melt patches within the megacrystic orthogneiss.

Other Rock Types

Leucocratic Orthogneisses

Leucocratic orthogneisses are also abundant within the northern Kirwanveggen. Some of these lithologies have been previously termed leucogneiss (Gavshon and Erasmus, 1975; Wolmarans and Kent, 1982). During this study, however, several different types of leucocratic gneisses have been distinguished on their modes of occurrence, mineralogy and textures.

A series of lensoidal intrusive leucogneiss bodies occur within, and are structurally intercalated with, the biotite-garnet migmatite gneiss. These intrusive leucogneisses consist predominantly of quartz, feldspar, biotite and garnet. Large garnets are found growing within the foliation of these units. Melt segregation veinlets occur within the intrusive leucogneiss, and these are ptygmatically folded but restricted to within the intrusive leucogneiss only. The veinlets consist predominantly of quartz and feldspar, but exhibit a biotite reaction rim around their edges. A strong foliation is observed in the intrusive leucogneiss that is often folded, as are the melt veinlets developed in the orthogneiss. Consequently, the intrusive leucogneisses pre-date a major fold event, but post-date the early deformational episode recorded in the biotite-garnet migmatite gneiss into which they intrude.

Several different leucocratic orthogneisses occur within the gneissic sequence of the northern Kirwanveggen. Megacrystic orthogneisses form large pods or veins occurring within the biotite-garnet migmatite gneiss. These orthogneisses have large megacrysts of grey-blue feldspars that are set in a matrix of quartz, feldspar and occasional garnet. The grey-blue feldspars are commonly 2 to 3 cm in size, but may be up to 10 cm. Biotite schlieren are often found within these megacrystic orthogneisses. Large lensoidal pods of orthogneissic material also occur within the regional foliation of the major lithotectonic units. Some of these lensoidal leucogneiss bodies contain kyanite within and on the contact margins with the biotite-garnet migmatite gneiss. The leucogneisses either intrude within the regional foliation, or are deformed by the foliation suggesting different ages of formation for these various bodies. Their exact time of emplacement differs and therefore different structural-intrusive relationships are envisaged for all these leucocratic bodies.

Calc-Silicate Rocks

Calc-silicate rocks occur as boudins within the major gneissic units of the northern Kirwanveggen. There are two different types of calc-silicate rocks that have been observed. The dominant type is coarse-grained and consists of large diopside and garnet crystals with several other felsic phases. A fine-grained calc-silicate rock has also been observed, which is green to black in colour and exhibits a foliation parallel to the boudinaging of the unit. These units are interpreted as early phases within the original supracrustal sequence.

Amphibolite Boudins

Amphibolite boudins are commonly observed within the regional foliation of the major gneissic units. These boudins consist mainly of amphibole, biotite, pyroxene and garnet. The mineralogy of these boudins suggests that they represent early intrusives that have subsequently been deformed and boudinaged during the formation of the regional pervasive foliation.

Granitic/Dioritic Gneiss

Exposures of weakly foliated quartz-feldspar-biotite-garnet granitic/dioritic gneiss occur at Vorrkulten, in the northern section of Neumayerskarvet (Figure 3.3). The isolated nature of this outcrop makes interpretations of relationships to the northern Kirwanveggen gneisses difficult.

Metagabbros and Metadiorites

Small pods of mafic material intrude the surrounding gneisses in the southwestern extent of Neumayerskarvet (Figure 3.3). These units comprise amphibole, garnet, pyroxene, feldspar and quartz.

Granitic and Pegmatitic Veins

Several small granitic veins are found intruding into the gneissic sequence at central Neumayerskarvet. These veins exhibit various structural-intrusive relationships and are, hence, of different ages. The veins consist of quartz, feldspar, biotite and garnet.

Pegmatitic veins are observed in central Neumayerskarvet intruding across all the lithologies in the gneissic sequence (Figure 3.4f). These veins crosscut most deformational episodes recorded at Neumayerskarvet and, hence, are late in the sequence of events in the northern Kirwanveggen. Some pegmatites occur as pods within the porphyritic granitoid, while others appear to fill tension gashes within this lithology. Pegmatitic veins in the biotite-garnet migmatite gneiss are steeply dipping and intrude across pre-existing small shear structures. Vertical steeply dipping pegmatites also crosscut the migmatitic leucogneiss in the western section of central Neumayerskarvet. The granitic and pegmatitic veins consist primarily of quartz, feldspar, with lesser amounts of biotite and garnet. In some veins the garnet crystals are rimmed by biotite. A carbonate-mica vein of similar nature and age is also included in this intrusive type.

Mafic Dykes

Late mafic dykes intrude into the gneissic sequences of central Neumayerskarvet. Two different orientations of dyke emplacement have been observed. High angle dykes, showing a contact parallel foliation, intrude and crosscut the foliation within the biotite-garnet migmatite gneiss. These amphibolite dykes post-date the major regional deformation. Flat lying, shallowly-dipping mafic dykes are also observed intruding the biotite-garnet migmatite gneiss. These dykes crosscut the regional deformational fabric, but are deformed by a later phase of deformation. Both these types of dykes are late in the deformation history of central Neumayerskarvet.

STRUCTRAL FRAMEWORK

Introduction

Structural relationships and styles are complicated in high-grade gneisses that have undergone polyphase deformation. Similar structural elements could form during different deformational episodes that are unrelated in time. Only if significant intrusive-structural relationships are preserved, can these situations be recognised. In areas where these relationships are lacking, and based on observations from other localities, a composite nature to the structural element under investigation must be assumed. Similarly, structural elements of differing styles could easily form during the same deformational episode. In some areas the same deformational episode would be reflected by different structural elements, such as coeval folding and the development of high strain zones.

The development of earlier structural elements will also strongly influence the subsequent deformational response of an area. Structural fabrics tend to exploit weaknesses developed within the anisotropic material, causing areas of high and low strain with respect to a single deformational episode. If spatial or lithological relationships are not observed between areas it is difficult to define temporal relationships between structural elements. This creates another complication in the interpretation of structural elements within high-grade gneiss terranes.

Continuous deformation would also create structural fabrics of different superimposed styles. This is particularly evident with respect to fold development, since folds are continually re-folded. The reflected fold patterns may differ once deformation ceases, and folds of a similar age may be represented as upright open folds or, in other areas, as isoclinal recumbent folds. These folds would, however, exhibit the same mineral stretching lineations.

Although outcrop in Antarctica is good, the exposures tend to be isolated from one another, and extrapolation between outcrops is extremely difficult. Only through detailed mapping of intrusive, structural and spatial relationships, coupled with high precision age determinations can a realistic time-deformation-intrusive sequence be established. For these reasons the structural elements in the northern Kirwanveggen are defined by their fabric styles rather than their temporal relationships. A structural map for Neumayerskarvet is provided in Figure 3.5. A relative time frame of the intrusive-structural relationships is established at the end of this section.

Fabric Elements

Foliations

Several different types of foliations have been defined within the northern Kirwanveggen:

1. A planar penetrative foliation forms the dominant regional structural fabric within the majority of the lithological units. This planar penetrative foliation is defined by different characteristics within the different lithological units. In rock units with abundant phyllosilicates (biotite-garnet migmatite gneiss) the planar foliation is represented by mineral segregations and preferential alignment of the platy minerals, producing a schistose fabric in contrast to the more uniform, finer-grained lithologies. Melt segregations developing within the planar foliation enhance the planar and penetrative nature of the fabric. Within the coarser-grained quartz-feldspar-rich rock units (quartzofeldspathic gneiss) the planar foliation comprises discontinuous laminae and compositional layering defined by the segregation of minerals into individual bands. A gneissic foliation is developed within these coarse-grained units, and augen textures are developed where grain sizes vary.

   A composite planar penetrative foliation is developed when earlier foliations are reoriented, stretched and tightened within the high strain zones. At certain localities the melt segregations defining the planar fabric have also undergone intense deformation. The planar foliation develops as a mylonitic foliation with similar geometry to the earlier foliation in this case. In other instances, late intrusive phases, cross-cutting the regional planar foliation in the areas, are deformed and pulled into parallelism with the planar foliation. In these examples the pre-existing foliation is exploited by a later deformational episode indicating that these fabrics are often composite in nature. Planar penetrative foliations of similar geometries may, therefore, be temporally unrelated.

2. A further foliation type recognised in the northern Kirwanveggen is an axial planar foliation. This foliation develops in fold closures and can be defined by axial planar melt veins.

Within fold closures the regional foliation must be regarded as a composite foliation of earlier fabrics superimposed by the fold related axial planar foliation.

3. Brittle structures displace the gneissic lithotectonic units and are related to late deformation. Cataclasites and fault gauges are locally developed.

Lineations

Three types of lineations are observed within Neumayerskarvet:

1. Elongation lineations are defined by quartz ribbon elongations developing a stretching lineation. Preferential mineral alignment develops another type of elongation lineation which is commonly defined by micaceous minerals, amphibole or kyanite, depending on the host rock.
2. Intersection lineations are defined by crenulations, macro- and micro-folding and local inconsistencies of the fabric undergoing deformation. Intersection lineations often develop parallel to elongation lineations and result in the development of composite lineations during the progression of deformation.
3. Slickensides develop on the planes of brittle structures observed within Neumayerskarvet and define a third lineation style in the region. The slickensides indicate brittle-ductile behaviour of the late structural elements.

Folds

Four styles of folds are observed at Neumayerskarvet. Three of the four fold styles are diagrammatically represented in Figure 3.7 for clarity:

1. Type I folds are megascopic isoclinal recumbent cylindrical folds of the pre-existing compositional layering. These folds result in large scale duplication of compositional layering within the region, much of which is not recognised due to the tight fold closures not being exposed or preserved.
2. Highly elongate isoclinal sheath folds define type II folding at Neumayerskarvet and their fold axes develop parallel to the type I folds (Figure 3.6a and 3.6b). An elongation lineation develops parallel to the type I and II fold styles.
3. Open to tight upright folding defines the type III style of folding. Fold axes develop parallel to the earlier fold phases and re-fold the fold types I and II, forming Ramsay type III interference patterns (Figure 3.6c). Re-folding of earlier folds by the type III fold style is observed at megascopic regional scale, and as outcrop macroscopic re-folded interference patterns. Type III fold axes parallel regional composite lineations.

4. The type IV fold styles develop as cross folds with fold axes at a high angle to the pre-existing fold styles. Mushroom-type interference folds are observed at various locations.

Fabric Relationships and Geometries

Composite lineations in the eastern and central part of Neumayerskarvet plunge gently to the NNW and SSE. In the western part of Neumayerskarvet the composite lineations have more variable geometries and tend to plunge gently NNW-SSE to NNE-SSW (see Figure 3.5). Geometrical relationships of some fabric elements are displayed in Figure 3.8.

Fold axes of fold types I, II and III develop parallel to the composite lineation at Neumayerskarvet. In the eastern and central portion of Neumayerskarvet the fold axes are near horizontal, plunging gently NNW and SSE. The geometries of type I, II, and III fold axes show more variability in the western portion of Neumayerskarvet, as with the composite lineations. In the west, it is difficult to distinguish type I, II and III fold axes from type IV fold styles unless earlier folding is recognised. Type IV fold styles are recognised in the north western portion of Neumayerskarvet where the fold axes plunge gently towards the NNE and SSW (see Figure 3.5).

The fold axial planes of type I and II fold styles parallel the regional composite foliation. Type II fold style axial planes are steeply dipping towards the ENE. Axial planes of type IV fold styles also tend to be near vertical, but little geometrical information has been obtained from this fold style.

Planar fabrics within Neumayerskarvet are generally gently dipping, but become steep towards fold closures and several of the high strain zones. A broad girdle distribution of the planar fabrics is observed and indicates folding of these elements around type I, II and III fold styles (see Figures 3.5 and 3.8). Certain high strain zones are recognised by the steepening of planar composite fabrics as seen in the central portion of Neumayerskarvet (Figure3.6d). Displacement of the pre-existing fabric into steeper attitudes occurs, but lineation geometries remain consistent. The planar composite fabrics are intensified and stretched within these zones. High strain zones parallel to the earlier regional planar fabrics are recognised only through the deformation of crosscutting intrusive units (see Figure 3.6e and f). Fabric elements and geometries of these zones tend to be indistinguishable from the earlier pre-existing elements (Figure 3.8).

Intrusive-Structural Relationships

A complicated temporal relationship of the tectonic fabrics is indicated by the similarity of fabric elements and geometries. Temporal information can only be obtained where these fabric elements displace one another, or where structural-intrusive relationships are observed. It is therefore necessary to document these temporal relationships in order to develop a sequence of events within the northern Kirwanveggen, and the relationships that have been recorded during this investigation are presented in Figure 3.9.

The earliest major lithotectonic unit in Neumayerskarvet is the biotite-garnet migmatite gneiss. The quartzofeldspathic gneiss occurs parallel to the planar fabric within the biotite-garnet migmatite gneiss. No crosscutting or intrusive relationships are observed between the biotite-garnet migmatite gneiss and quartzofeldspathic gneiss. The banded quartz-feldspar gneiss occurs only within the eastern portion of Neumayerskarvet. The relationship between the biotite-garnet migmatite gneiss and banded quartz-feldspar gneiss is equivocal, as these lithotectonic units are not seen in contact together. All these lithotectonic units do, however, exhibit the early fabric elements displayed at Neumayerskarvet.

Small leucogneiss units intrude across the planar foliation within the biotite-garnet migmatite gneiss, but are also intensely deformed. Some of these intrusive leucogneisses are folded by type I and III fold styles. Although the planar fabrics in the intrusive leucogneiss post-date the planar foliation in the biotite-garnet migmatite gneiss they exhibit similar geometries. Likewise, the composite lineations observed in the intrusive leucogneiss show similar geometries to the lithotectonic units into which they intrude. Minor granitoid bodies (granitoid bodies I on Figure 3.9) intrude into the biotite-garnet migmatite gneiss, crosscutting the pre-existing planar composite foliation. The granitoid units only exhibit type III fold style and associated fabric elements. Felsic veins and mafic dykes crosscut regional planar fabrics and represent the youngest lithologies recognised within Neumayerskarvet. Planar foliations and composite lineations (elongation and intersection lineations) are developed in these intrusive units. Similar structural element styles are observed throughout the temporally distinct intrusive sequence that is recognised at Neumayerskarvet. The geometrical relationships of these fabric styles are important in order to establish whether these fabric styles are related in time or not.

Planar and composite foliation styles can be observed within all of the lithotectonic and intrusive units, although different geometries may be recorded. Axial planar foliations are seen in most units that have experienced type I, II and III style folding. Axial planar melting is not common for the later crosscutting type IV fold style.

Composite lineations are seen within all the lithotectonic and intrusive phases at Neumayerskarvet. Fold interference patterns aid in the recognition of time relationships between the different fold styles described from the area. Later intrusive bodies are deformed by type III and IV fold styles only (granitic veins II and granitic/pegmatitic veins III in Figure 3.9). Type I and II fold styles are only recognised in the early lithotectonic and intrusive units.

Discrete zones of brittle faulting develop locally at Neumayerskarvet, cross-cutting the early ductile deformation fabric. Cataclastic fabrics and slickensides characterise these brittle structures.

Deformational Stages

This section details individual deformational stages that can be distinguished at Neumayerskarvet based on the relationships of Figure 3.9. The deformational stages described here relate to a structurally distinct pattern of fabric elements and geometries, and the distinction of a deformational stage does not necessarily indicate a hiatus between the development of these fabric element relationships. The relationships of these deformational stages have been established in areas where relative temporal differences are clearly observed, and a summary of the deformational fabrics and stages recognised at Neumayerskarvet are shown in Figures 3.10 and 3.11. The subscript (nkv) has been used for clarification and correlation purposes with other areas of WDML.

D1nkv Deformational Stage

The D1nkv deformational stage is marked by the development of a penetrative planar foliation (S1 P). A possible early fold phase (F1) may be represented by repetitions of the quartzofeldspathic gneiss and biotite-garnet migmatite gneiss lithotectonic units. An elongation lineation (L1 E) is also developed at this stage but intense late lineation development obscures the recognition of these fabrics.

D2nkv Deformational Stage

The D2nkv deformational stage is characterised by L>S fabric development. Isoclinal, recumbent folds (F2) and sheath folds (type I and II fold styles) develop during this stage. Earlier penetrative fabrics are folded, and axial planar foliations and associated melt veins develop. Intense elongation lineations (L2a E) develop parallel to type I and II style fold axes. The enhancement and development of planar foliations during D2nkv results in a composite nature of the regional foliations and lineations. Intersection lineations develop locally where pre-existing inconsistencies and fabric elements intersect the newly developed foliations. In areas less affected by later deformation the foliation generally dips at a shallow angle, with lineations showing consistent NNW-SSE plunges.

Strain partitioning during D2nkv is represented by areas of high strain (HSZ2). These high strain zones may develop due to competency contrasts of different lithotectonic units, and form along contacts between different units. The high strain zones form parallel to the regional fabric elements. The different deformational fabric elements formed during D2nkv are colinear and coplanar to the early D1nkv stage.

D3nkv Deformational Stage

The D3nkv deformational stage is characterised by type III fold styles (F3) that refold the earlier D2nkv deformational stage type I and II fold styles (F1 and F2). The type III style folds also develop as upright folds that tighten up locally. Fold axes of the type II fold styles parallel the type I and II fold axes orientations, but the axial planes tend to develop at high angles forming refolded interference patterns. The fold axes plunge shallowly NNW-SSE, while the axial planes dip steeply towards the NE in the eastern portion of Neumayerskarvet where evidence of this folding is best preserved.

Axial planar foliations (S3 AP) and melt veins develop at fold closures. The strong pre-existing anisotropy imparted on the rocks during earlier deformation influences the fabric orientations and their geometries. The rock anisotropy results in the tightening up and stretching of earlier fabrics enhancing the composite nature of these fabrics (L3 C). Intersection lineations also develop parallel to the type III style fold axes. The D3nkv deformational stage is coaxial to the earlier deformational stages.

D4nkv Deformational Stage

Two significant deformation styles develop during the D4nkv deformational stage. These are (1) high strain zones and (2) type IV fold styles:

1. In the central portion of Neumayerskarvet discreet high strain zones (Myl4) are observed, and form the D4(a)nkv deformational stage. These ductile high strain zones disrupt early shallow dipping fabrics. The high-strain zones (Myl4) trend SE-NW, dipping steeply towards the SW, and displace the composite foliation. Early type III Ramsey refolded interference patterns are displaced by these structures. Lineations within the high strain zones (L4b MS) parallel the early lineation orientations outside these zones even though the planar fabrics are strongly re-orientated. In areas where earlier D2nkv and D3nkv stages have steepened up the composite fabrics, these high strain zones are sub-parallel to the earlier fabrics and distinguishing these features is difficult. Fabrics in the high strain zone are a composite of newly formed, tightened and stretched early foliations. Lineations within the high strain zones (L4b MS) are also composite and the orientations may be significantly influenced by the strong pre-existing anisotropy. In central Neumayerskarvet

the steep discreet high strain zones are colinear to the early deformational stages but are not coplanar.

2. Type IV fold styles (FIV) are best observed within the western portion of Neumayerskarvet and form a second deformational style termed the D4(b)nkv deformational stage. These folds cross-fold the earlier types I, II and III fold styles, and mushroom interference fold patterns are developed in outcrop. Fold axes trend approximately ENE-WSW, and this fold style results in the scatter and girdle distributions of earlier fabric element geometries. This deformation style is non-coaxial to the earlier deformational stages.

The high strain zones and the type IV fold styles have been placed together within the D4nkv deformational stage as their relative temporal relationships are indistinguishable. Placing these deformation styles into the same deformational stage does not imply that they are structurally related. Rather, these deformation styles fall within a period that is temporally distinct but their inter-relationships are unknown. The same stress regime is not implied for these different deformation styles.

D5nkv Deformational Stage

The D5nkv deformational stage is characterised by the reworking of earlier deformational stage fabrics. Discreet high strain zones (Myl5) develop that are colinear and coplanar to the regional composite fabrics. This deformational stage has been recognised in the central portion of Neumayerskarvet where late pegmatite veins intrude across the D4nkv stage high strain zones but are themselves deformed. Without these structural-intrusive markers this deformational stage would not be easily distinguished.

D6nkv Deformational Stage

Late brittle fault structures (Cat6) have been documented in the northern Kirwanveggen (Wolmarans and Kent, 1982; Grantham *et al.*, 1995). This deformational stage displaces the ductile deformation recognised in the area. Slickensides are developed on the fault planes.

DISCUSSION

Structural Synthesis

Placing fabric elements and geometries into a tectonic framework in a region that has undergone polyphase deformation is difficult. The effects of older deformational features on the formation or re-orientation of other features can complicate the interpretation. In this section an attempt is made, where possible, to understand the tectonic implications of the structural features described above.

Early D1nkv deformation develops a planar penetrative foliation that, in areas less affected by later deformation, tends to be sub-horizontal. Characterisation of earlier linear elements is not possible due to later deformation overprinting. The early D1nkv foliations develop sub-parallel to lithotectonic contacts and mineralogical changes within the units. These foliations could either be controlled by early structural features, or by primary structures within the lithotectonic units. No reliable geometrical information can be obtained from the D1nkv deformational stage.

D2nkv deformation is characterised by L>S fabric development. Sheath folds and tight isoclinal recumbent folds have fold axes parallel to the strong elongation lineation. This association may be the result of extension parallel to the fold axes. This relationship may be explained by the fact that the folds become strain hardened (lock-up buckling), and cease to become an effective mechanism of shortening. This translates into an elongation lineation parallel to the fold axes. Alternatively, extension parallel to the fold axes can occur during the growth of a fold when boundary conditions are such that extension in a direction normal to layering is more difficult than parallel to the fold axes (Price and Crosgrove, 1991).

Sheath folds are thought to develop as a result of passive amplification of initial perturbations in a layer subject to layer-parallel shear (Cobbold and Quinquis, 1980; Price and Crosgrove, 1991). There is an early period of layer-parallel flattening where the layer-parallel compression thickens the layers. Buckling is then initiated with fold axes normal to the stretching lineation direction. With continued shortening the folds are stretched and rotated into parallelism with the stretching lineation until such time as the fold strain hardens due to intense buckling (lock-up buckling), and folding eventually ceases. Further shortening takes place by post-buckle flattening. These stages of fold development are thought to be responsible for the fabric geometries and relationships seen in the northern Kirwanveggen during D2nkv. The shallow NNW-SSE trends of D2nkv fold axes and lineations suggest a movement direction parallel to this trend during this deformational stage.

Later ductile deformation in the northern Kirwanveggen is strongly influenced by the pre-existing anisotropy caused by lithological contrasts and structural fabrics formed during earlier deformation. When a strong bending anisotropy is present it results in later folding forming sub-parallel to the linear fabrics (Cobbold and Watkinson, 1981). The later fold fabric orientations are strongly dependent upon pre-existing linear fabric orientations, and less on the attitude of the principle stresses.

Similar effects of the pre-existing rock anisotropy can be envisaged during the development of D4(a)nkv and D5nkv discrete high strain zones. The D4(b)nkv cross-folding re-orientates the composite linear fabrics producing the scatter of geometrical data observed in the western portion of Neumayerskarvet. The D4(b)nkv cross-folds are more gentle folds that are interpreted as being formed normal to the maximum compression direction during this deformational stage.

All the ductile deformation identified in the northern Kirwanveggen can be formed within a consistent stress regime. However, the effect of the strong rock anisotropy imparted on the structural elements may hinder the recognition of changes in the principal stress orientations during later deformation. During the D2nkv deformational stage, stretching and elongation in a NNW-SSE direction is interpreted from the structural fabrics identified. Later ductile deformation may develop within the same stress regime, but equally could have changed orientation, although recognition of this may be masked by the D2nkv (and D1nkv?) rock anisotropy.

Late brittle faulting in the northern Kirwanveggen has been related to Gondwana break-up (Grantham *et al.*, 1995). Little geometrical evidence has been obtained during this investigation to allow interpretation of these structures.

Regional Correlations

The structural complications developed in high-grade gneiss terranes make regional correlations difficult without absolute age constraints. Comparison of similar structural fabrics may or may not indicate similar times of formation. Likewise different structural fabrics may not imply different times of formation. Correlation of northern Kirwanveggen structural features with other areas is made tentatively, and is largely dependent on age constraints for these features. Correlations are based primarily on the similarity of structural features documented in this chapter and similar structures recorded in the literature.

Three deformational episodes have been described by Grantham *et al.* (1995) for the Kirwanveggen-H.U.Sverdrupfjella areas of WDML. The first deformational episode (D1) is characterised by intense fabric development and colinear refolding parallel to regionally developed SE plunging elongation lineations. Isotopic data poorly constrain the D1 episode between *ca.* 1150 Ma and *ca.* 800 Ma (see Grantham *et al.*, 1995 for discussion). Similarities of fabric geometries have been used to correlate structural elements within the D1 episode, but these correlations are problematic in high-grade gneiss terranes without structurally constrained isotopic data. Top-to-the-NW movement senses are indicated for several regions across this belt. Deformational stages D1nkv through to D4(a)nkv in the northern Kirwanveggen are tentatively correlated here with the regional D1 episode of Grantham *et al.* (1995).

The extent of the D2 episode in the Kirwanveggen-H.U.Sverdrupfjella varies considerably throughout the region. In the H.U.Sverdrupfjella, asymmetrical cross-folding and discrete shear zones with consistent top-to-the-SE sense of vergence are observed (Grantham *et al.*, 1991). These shear zones are seen to displace the 469 ± 5 Ma Dalmatian granite (Grantham *et al.*, 1991). In the central Kirwanveggen numerous discrete shear zones rework the early D1 fabric elements. A top-to-the-NW shear sense has been interpolated for these discrete shear zones (Grantham *et al.*, 1995). The D2 episode has been assigned to the *ca.* 500 Ma tectonothermal event that has been recorded by several isotopic systems and investigations (Moyes and Barton, 1990; Grantham *et al.*, 1991; Moyes *et al.*, 1993a). Deformational stages 4(b)nkv and D5nkv in the northern Kirwanveggen are tentatively correlated here with the regional D2 episode of Grantham *et al.* (1995).

The D3 episode in the Kirwanveggen-H.U.Sverdrupfjella is interpreted as deformation related to Mesozoic brittle extension in response to the rifting of Gondwana (Grantham *et al.*, 1995). Structural elements in the D3 episode are steep fractures, joints and normal faults. Cataclasis and brecciation are commonly observed associated with these structures. Alkaline complexes that have intruded at *ca.* 180 Ma in the region have been associated with the D3 episode. The D6nkv deformational stage is tentatively correlated here with this D3 episode.

CONCLUSIONS

- Neumayerskarvet comprises lithotectonic units of supracrustal material that have been extensively intruded by syn- to late-deformational magmatism.
- Several different fold styles have been recognised ranging from isoclinal folds through to open cross-folds.
- Transposition of earlier penetrative planar foliations is commonly documented in the region. Without time distinct markers such as crosscutting intrusive units the younger colinear deformation is difficult to recognise.
- Lineations develop as a composite lineation and display consistent geometries through several different deformational periods identified at Neumayerskarvet.
- Six relative time distinct deformational stages have been identified based on crosscutting and re-working relationships identified within the study area.

GEOLOGICAL MAP OF WESTERN DRONNING MAUD LAND, ANTARCTICA

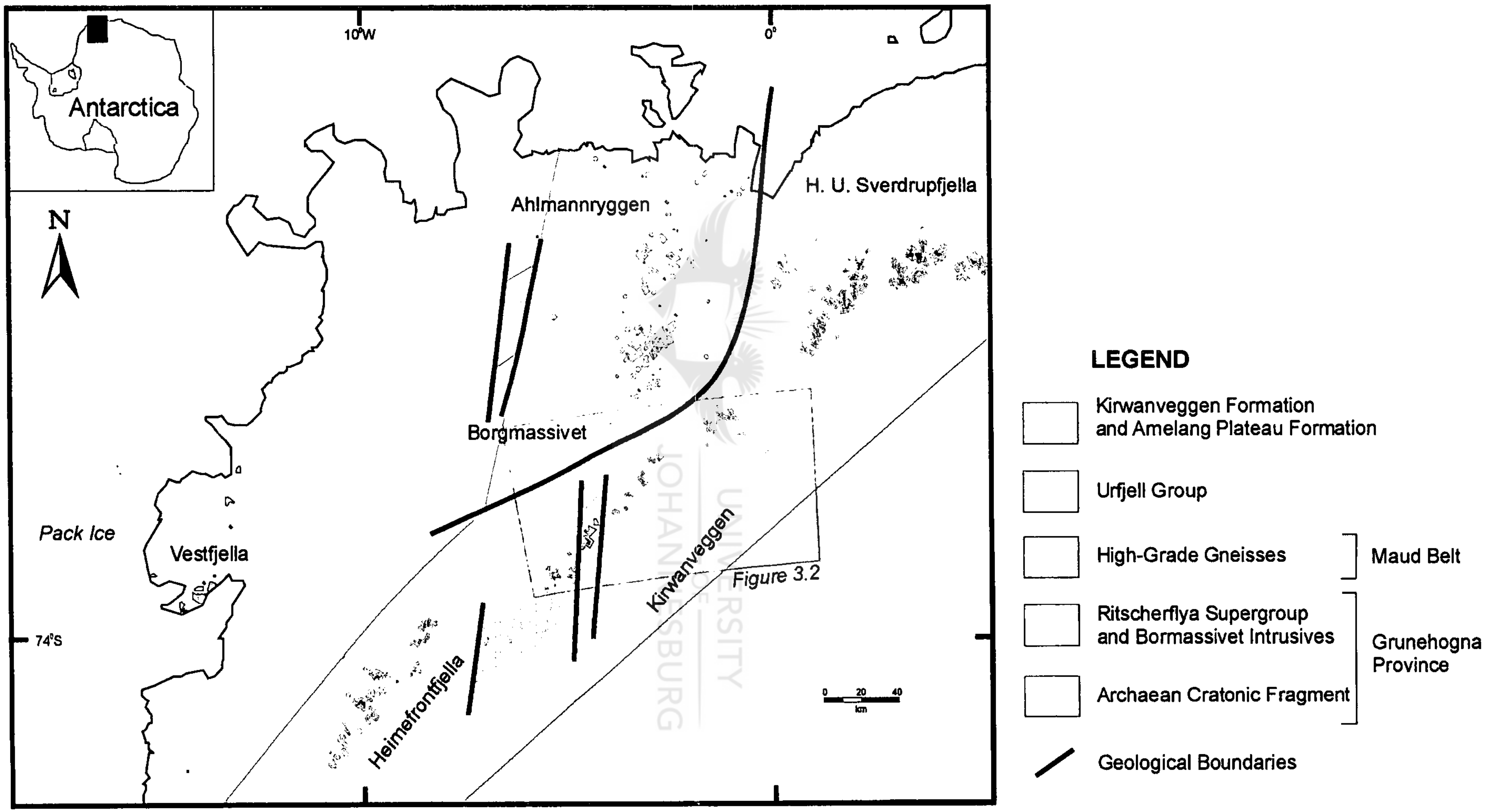

FIGURE 3.1. Geological map of western Dronning Maud Land in Antarctica. The major geology is extrapolated across outcrops (nunataks) under ice cover. Boundaries between these geological regions are interpolated. The locality of Figure 3.2 is displayed on this map for reference.

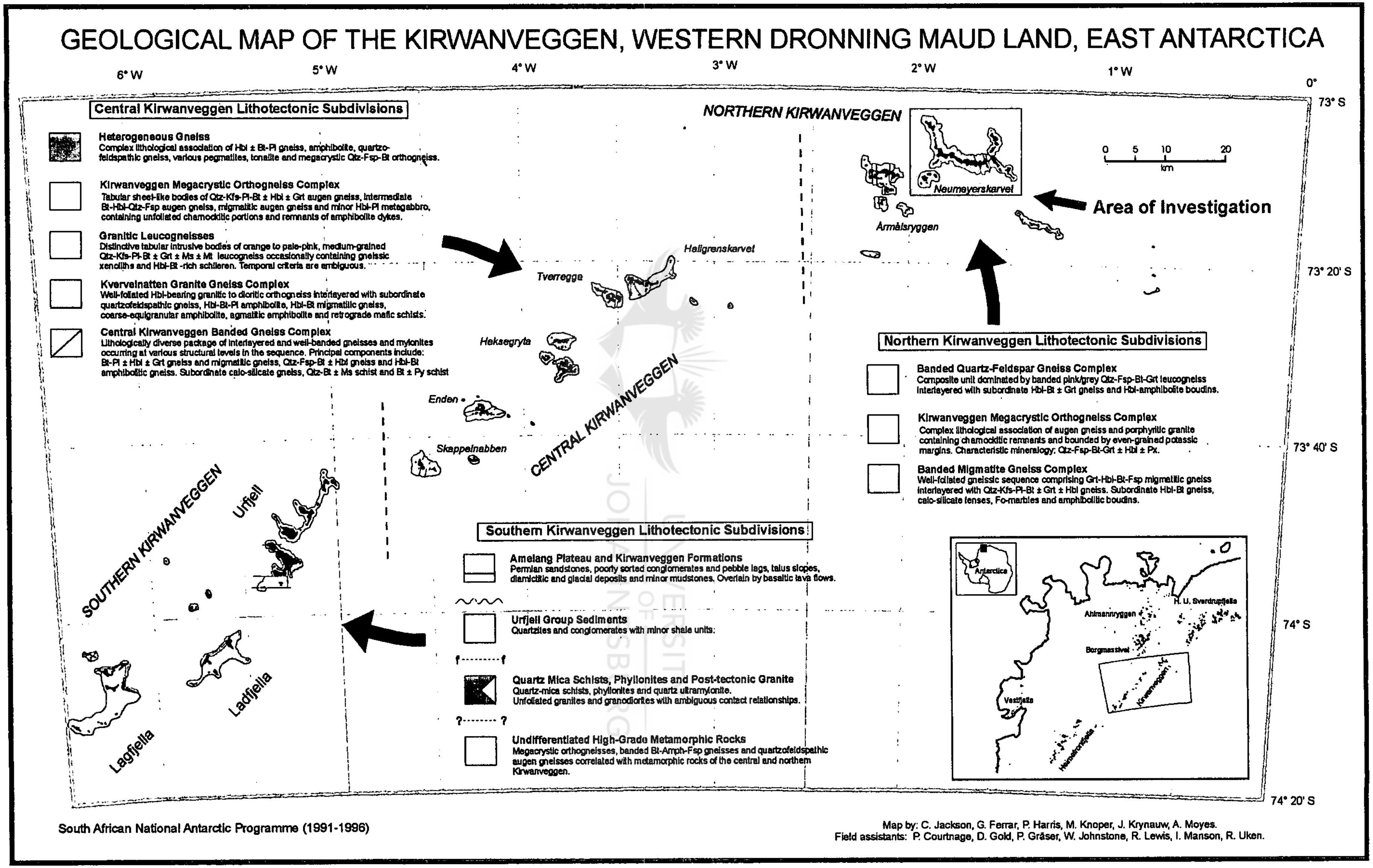

FIGURE 3.2. Geological map of the Kirwanveggen, WDML, Antarctica. Outcrops are illustrated in black on the map. The sub-division of the northern, central and southern Kirwanveggen outcrop patterns and the associated lithotectonic units are also illustrated on this map. The Neumayerskarvet outcrop pattern, which is the major area of focus in the northern Kirwanveggen, is outlined for location purposes.

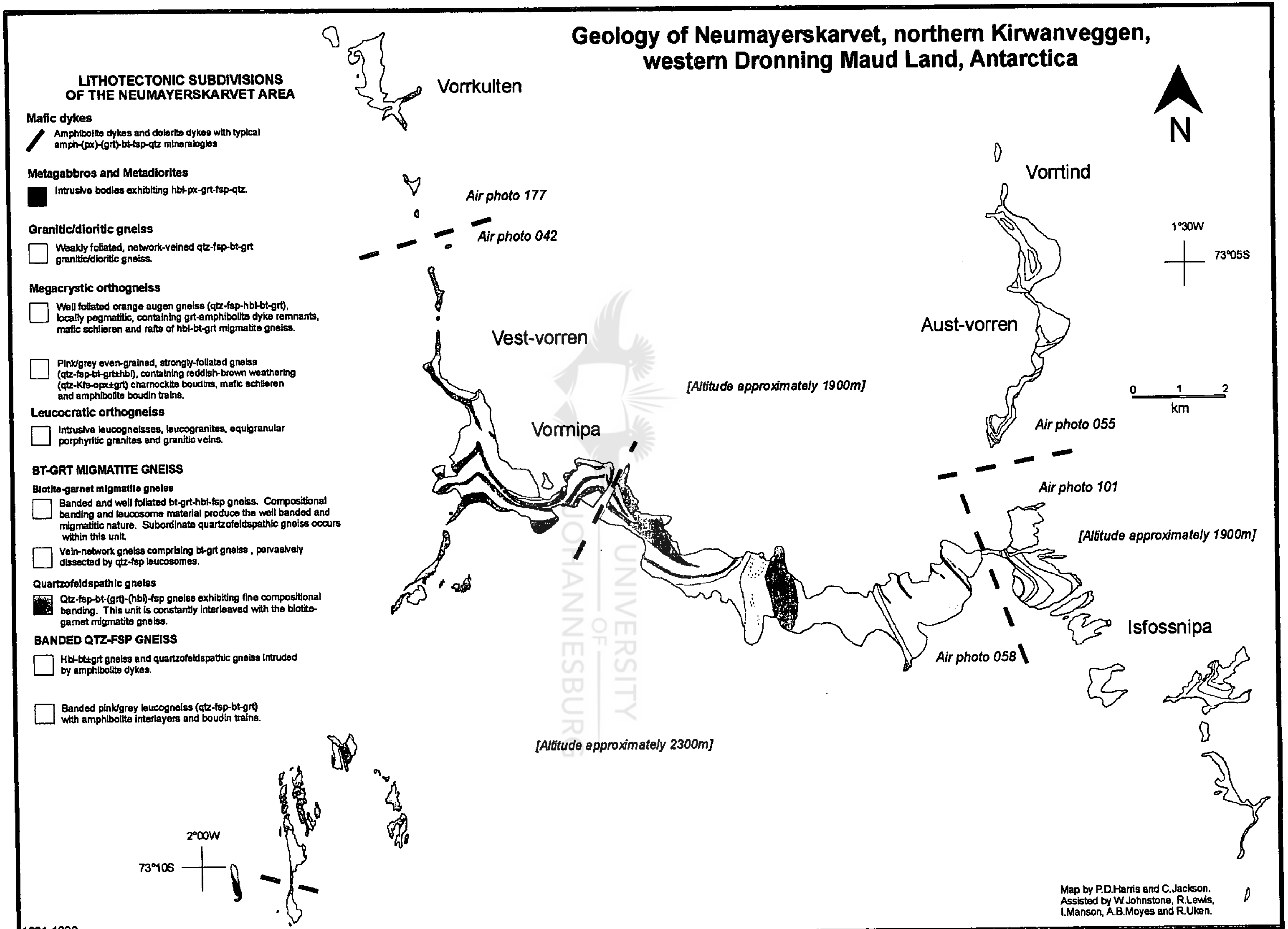

FIGURE 3.3. The geology of Neumayerskarvet in the northern Kirwanveggen. The map has been constructed using aerial photographs as no suitable topographical map at this scale is currently available. Boundaries are marked where different photographs were used for the mapping. A brief lithotectonic subdivision is illustrated on the map but further detail is provided within the text.

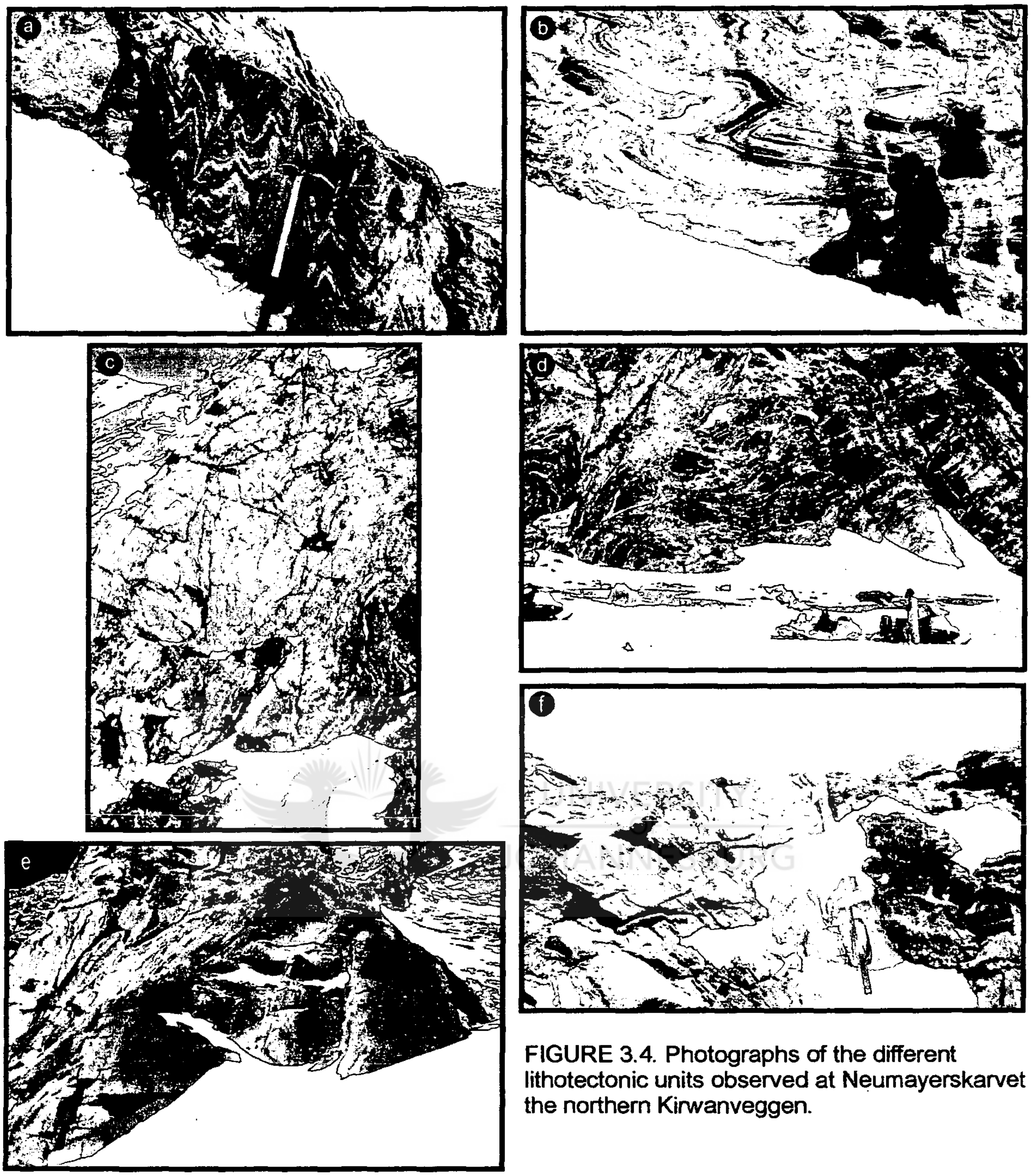

FIGURE 3.4. Photographs of the different lithotectonic units observed at Neumayerskarvet in the northern Kirwanveggen.

a.) Mesoscopic folds in the quartzofeldspathic gneiss of central Neumayerskarvet (Type I and III folds). The photograph is taken looking northwards.
b.) Photograph of the banded quartzofeldspathic gneiss found at Aust-Vorren in the eastern portion of Neumayerskarvet (See map for location of this lithotectonic unit).
c.) Garnet-biotite migmatite gneiss found throughout the central and western portion of Neumayerskarvet. Typical gneissic banding (S1 P) and folding (F2) of this lithotectonic unit can been seen in the photograph.
d.) Vein-network migmatite gneiss found in the central portion of Neumayerskarvet (See map for location of this lithotectonic unit).
e.) Photograph of the megacrystic orthogneiss of central and southeastern Neumayerskarvet. The brown-stained areas are less deformed and preserve typical charnockitic mineral assemblages. Retrogression of this unit is associated with deformation (D3 nkv) and veining that crosscuts the megacrystic orthogneiss.
f.) Photograph of a late pegmatitic dyke found within the central portion of Neumayerskarvet. This dyke intrudes across the different generations of gneissic foliations (S1 P through to S4 M) developed within the garnet-biotite migmatite gneiss.

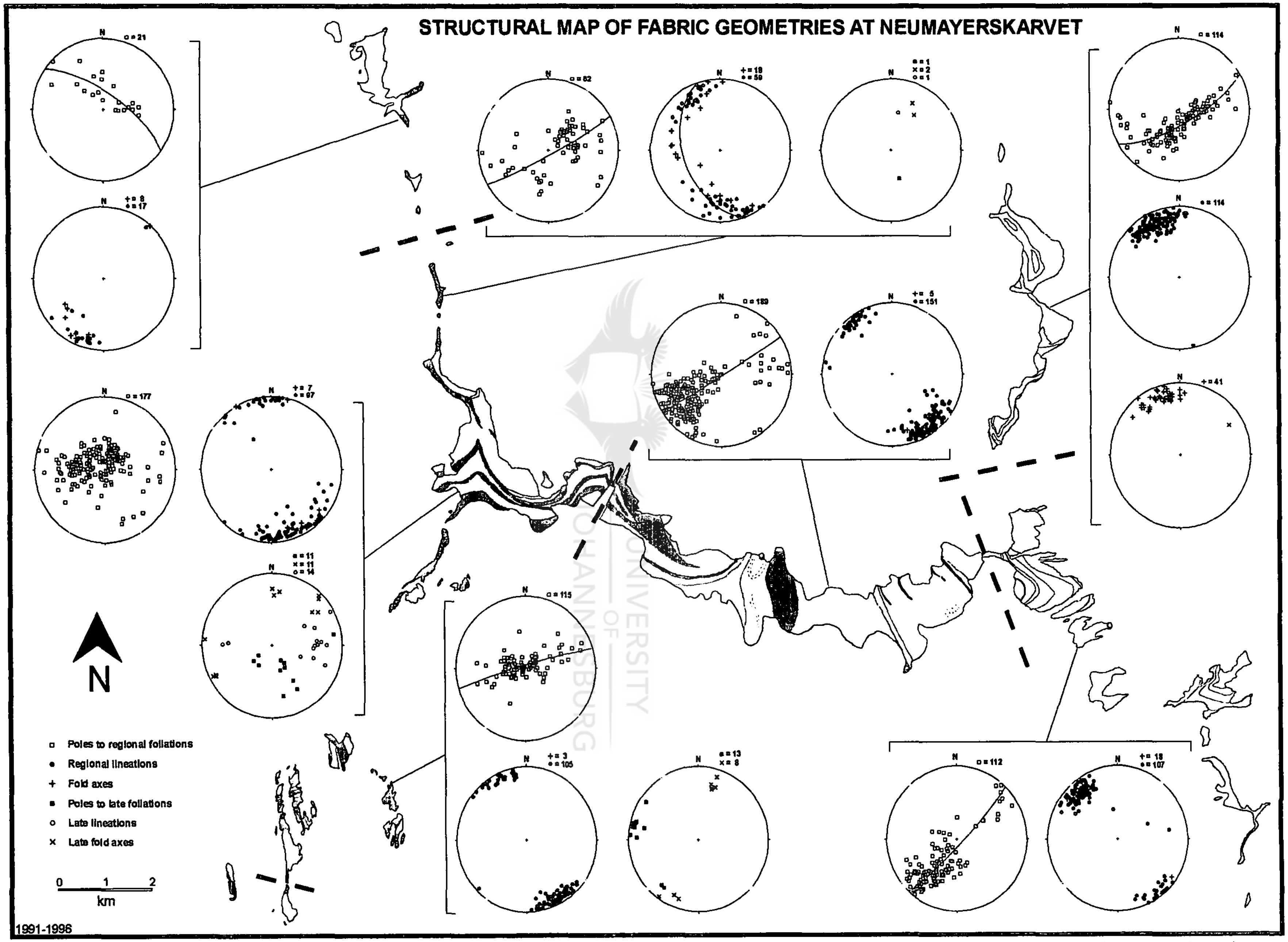

FIGURE 3.5. Structural map showing fabric geometries documented at Neumayerskarvet in the northern Kirwanveggen. Foliations are plotted as poles to planes, and the description of the symbols used in the stereonets is outlined in the accompanying legend. Interpretation of the geometrical relationships of the fabric elements is provided in the text.

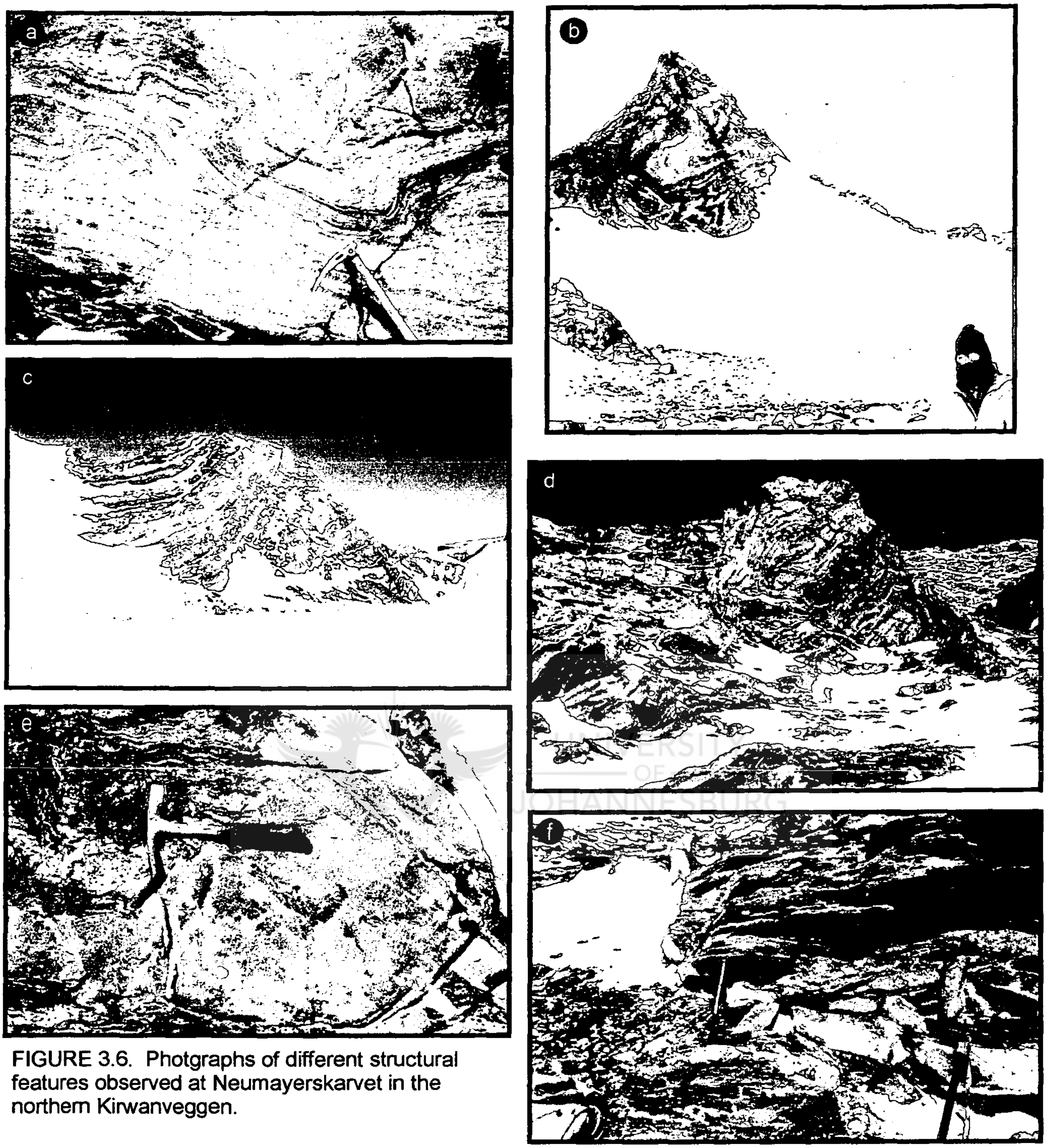

FIGURE 3.6. Photgraphs of different structural features observed at Neumayerskarvet in the northern Kirwanveggen.

a.) Sheath folding (F2 type II folds) within the biotite-garnet migmatite gneiss in the central portion of Neumayerskarvet.
b.) Photograph of cylindrical isoclinal recumbent folds (F2 type I folds) at Aust-Vorren within Neumayerskarvet.
c.) Photograph of re-folding of earlier isoclinal recumbent folds (F2 type I folds) by a later more upright fold phase (F3 type III folds). The photograph was taken from the southern exposures of Aust-Vorren at Neumayerskarvet.
d.) Reorientation of foliations (S1 and S2) by steeply dipping high-strain zones (S4 M). The photograph was taken in the central portion of Neumayerskarvet and is looking southwards.
e.) Late granitic vein cross-cutting the planar penetrative fabrics (S1 and S2) within the biotite-garnet migmatite gneiss. The vein has subsequently been folded during a later deformation phase.
f.) Reorientation of a late crosscutting pegmatitic dyke by a late discrete high-strain zone (S5 M). The reworking of the early penetrative fabric within the late high-strain zone is only recognised by the reorientation of the crosscutting dyke.

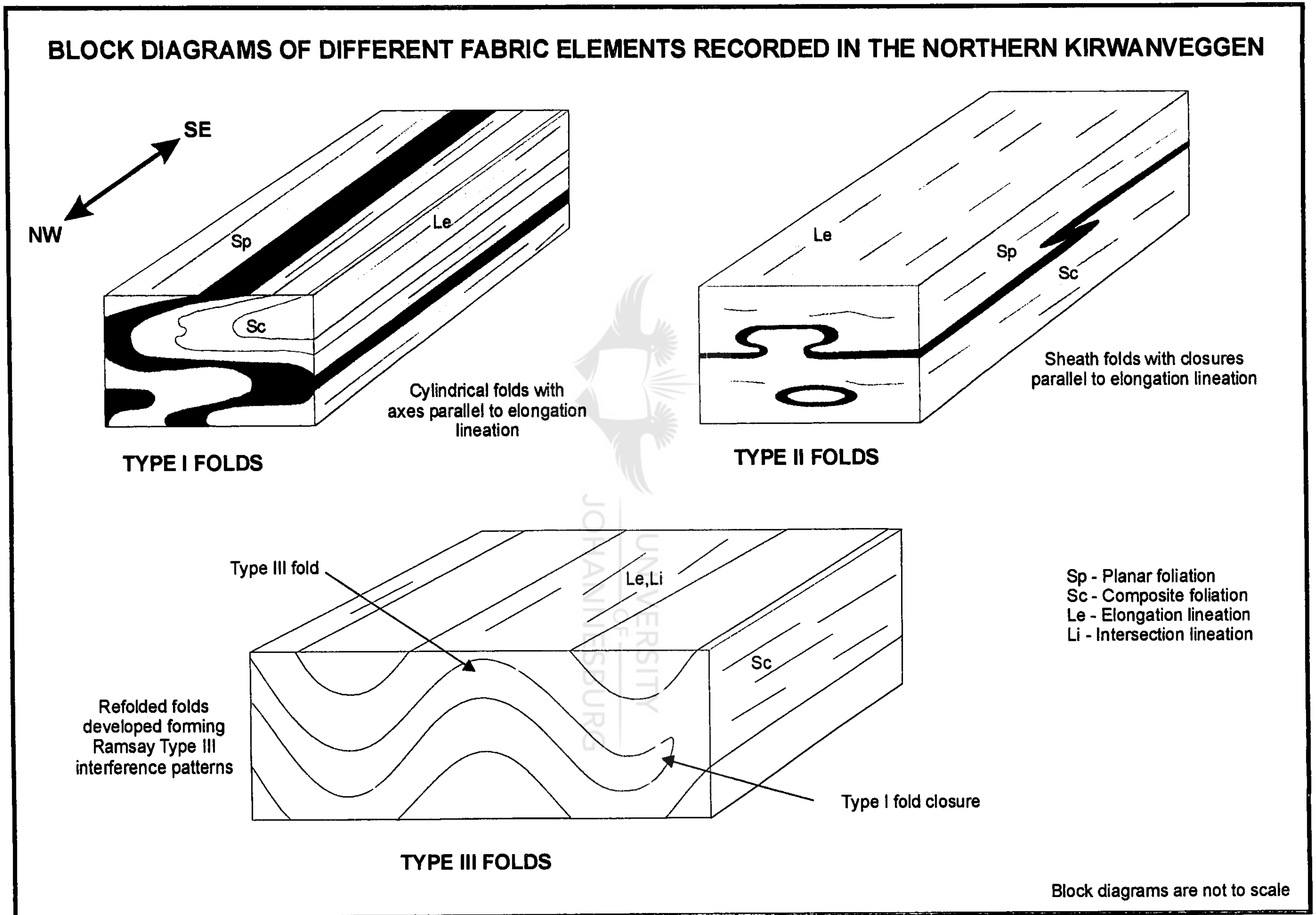

FIGURE 3.7. Block diagrams illustrating different fabric elements recorded in the northern Kirwanveggen. Descriptions of the fold styles illustrated here, along with the fabric elements, are detailed in the text.

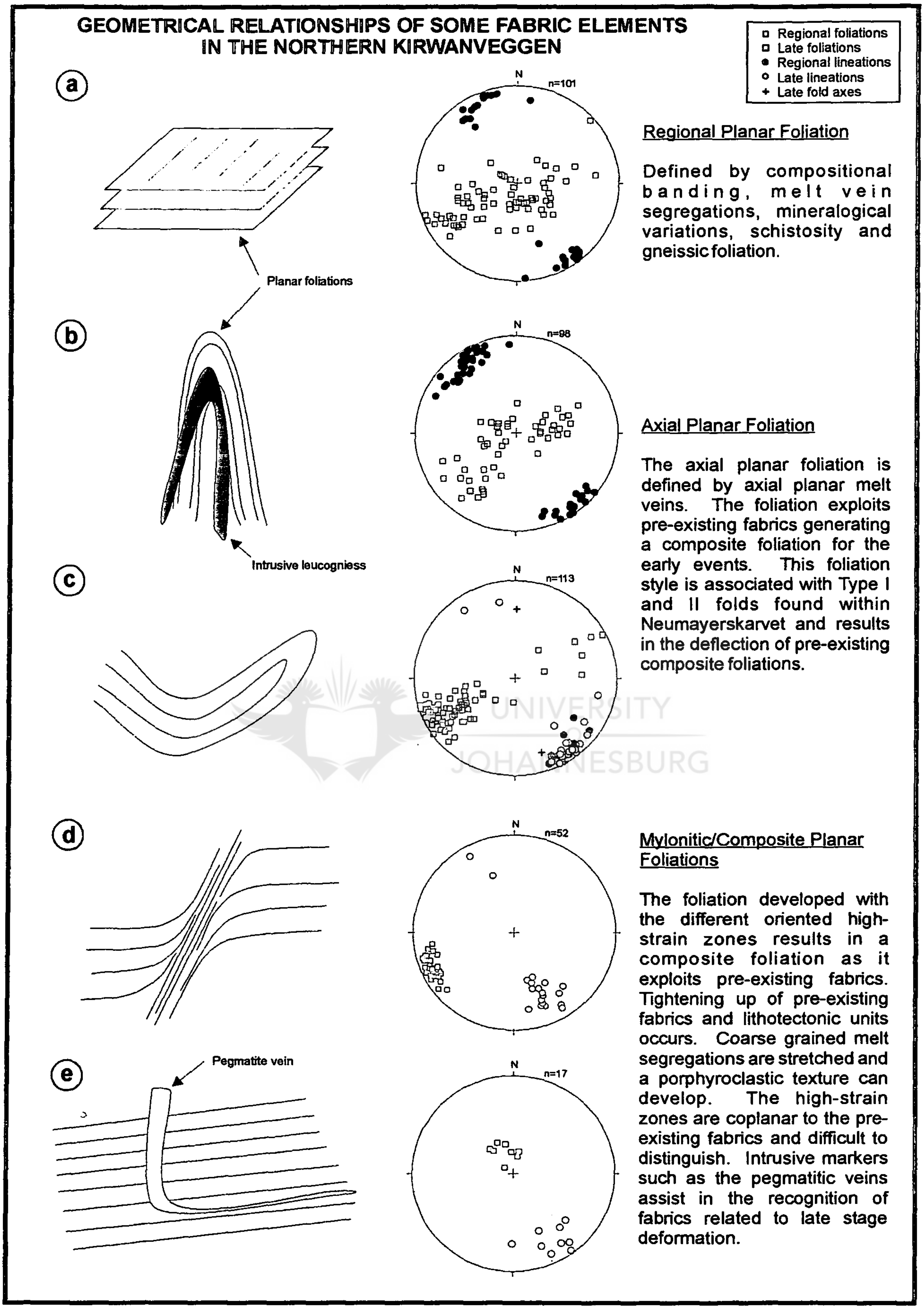

FIGURE 3.8. Geometrical relationships of some fabric elements observed within the northern Kirwanveggen. A sketch of the fabric relationships is provided with the fabric geometrical data.

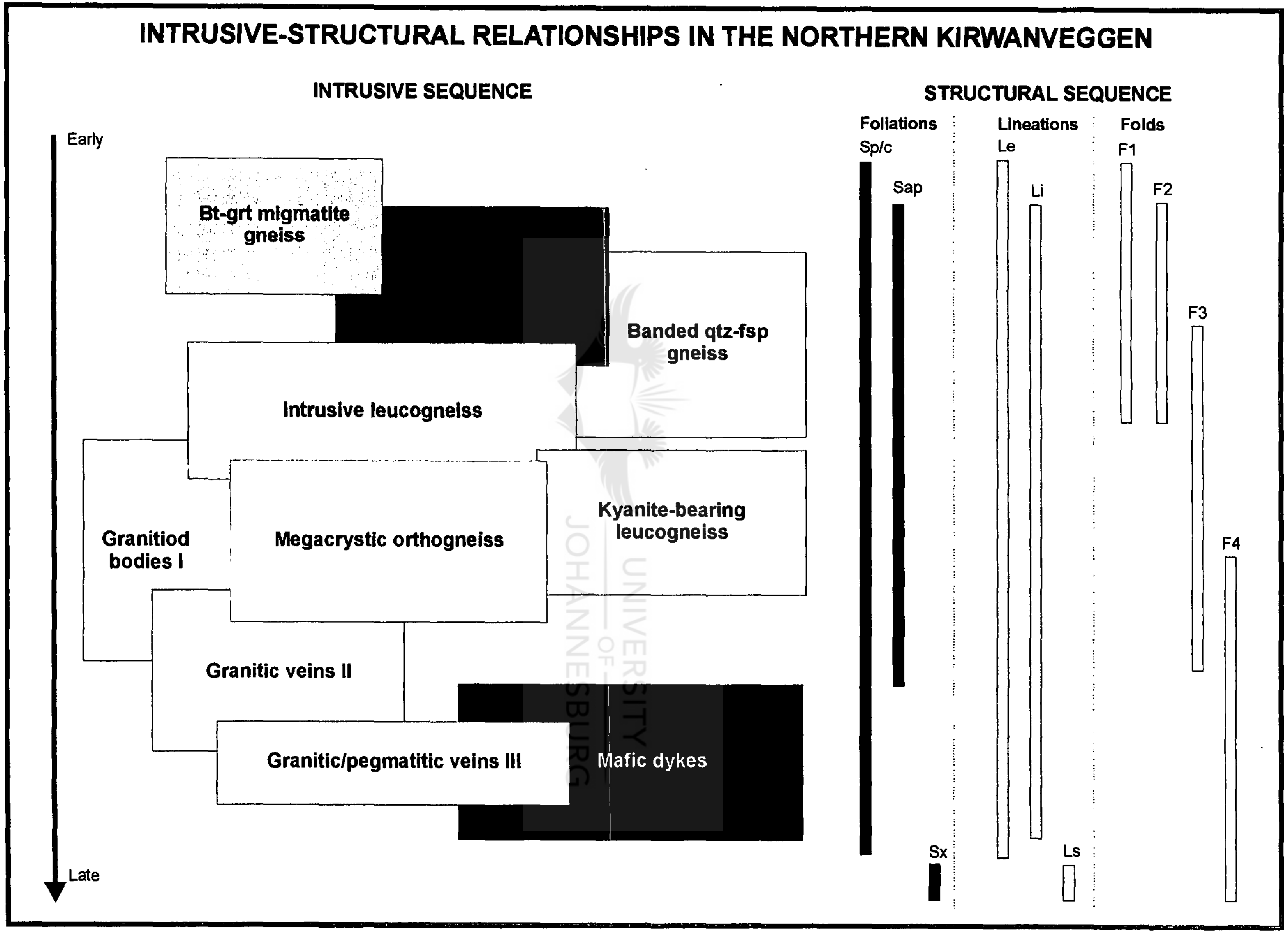

FIGURE 3.9. Intrusive-structural relationships observed for Neumayerskarvet in the northern Kirwanveggen. Fabrics displayed are: planar composite foliations (Sp/c), axial planar foliations (Sap), cataclastic foliations (Sx), elongation lineations (Le), intersection lineations (Li) and slickensides (Ls). Fold sequences F1 to F4 are described in the text.

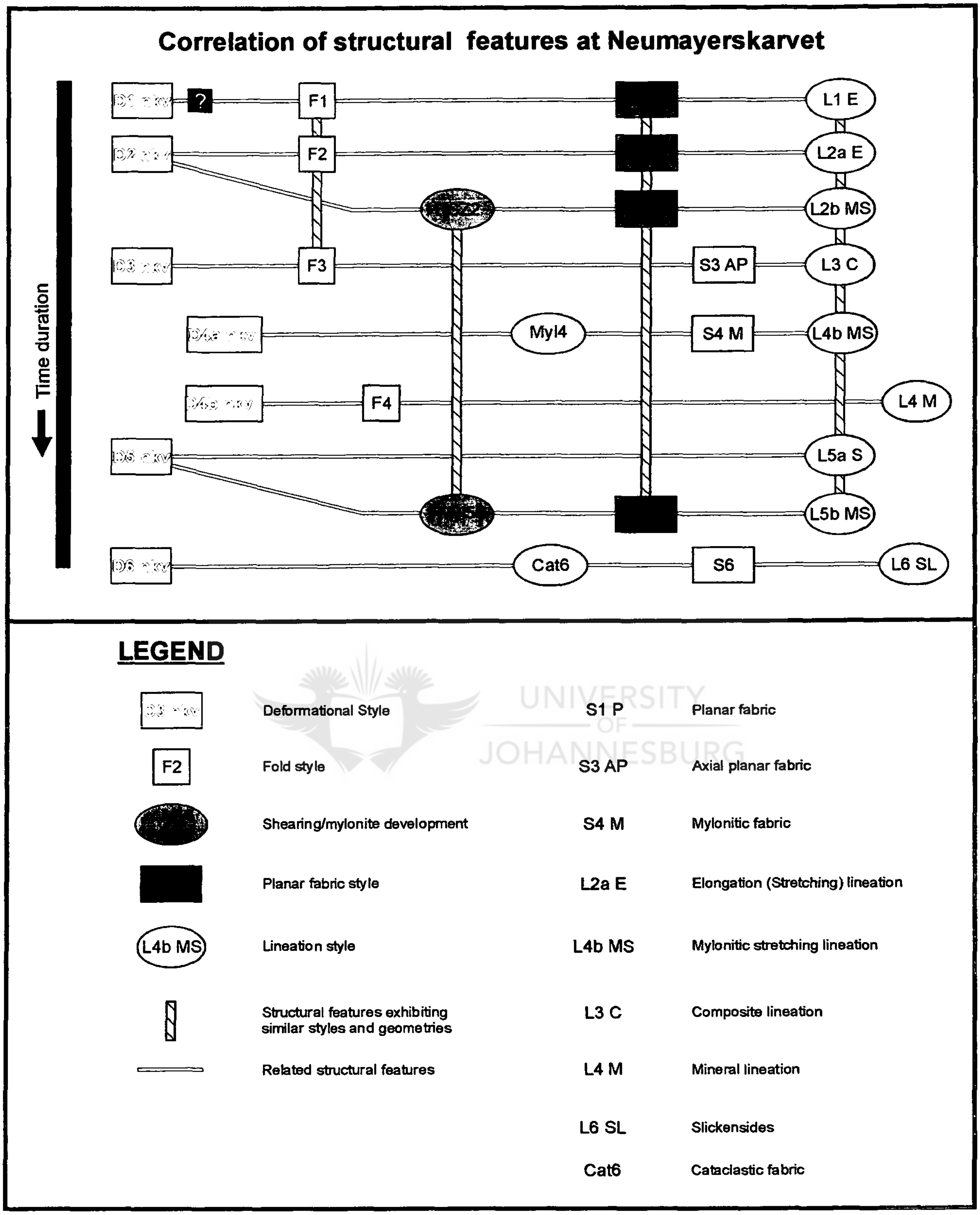

FIGURE 3.10 Illustration of the relationships between structural style, fabric elements, and their geometries, within a relative structural time framework.

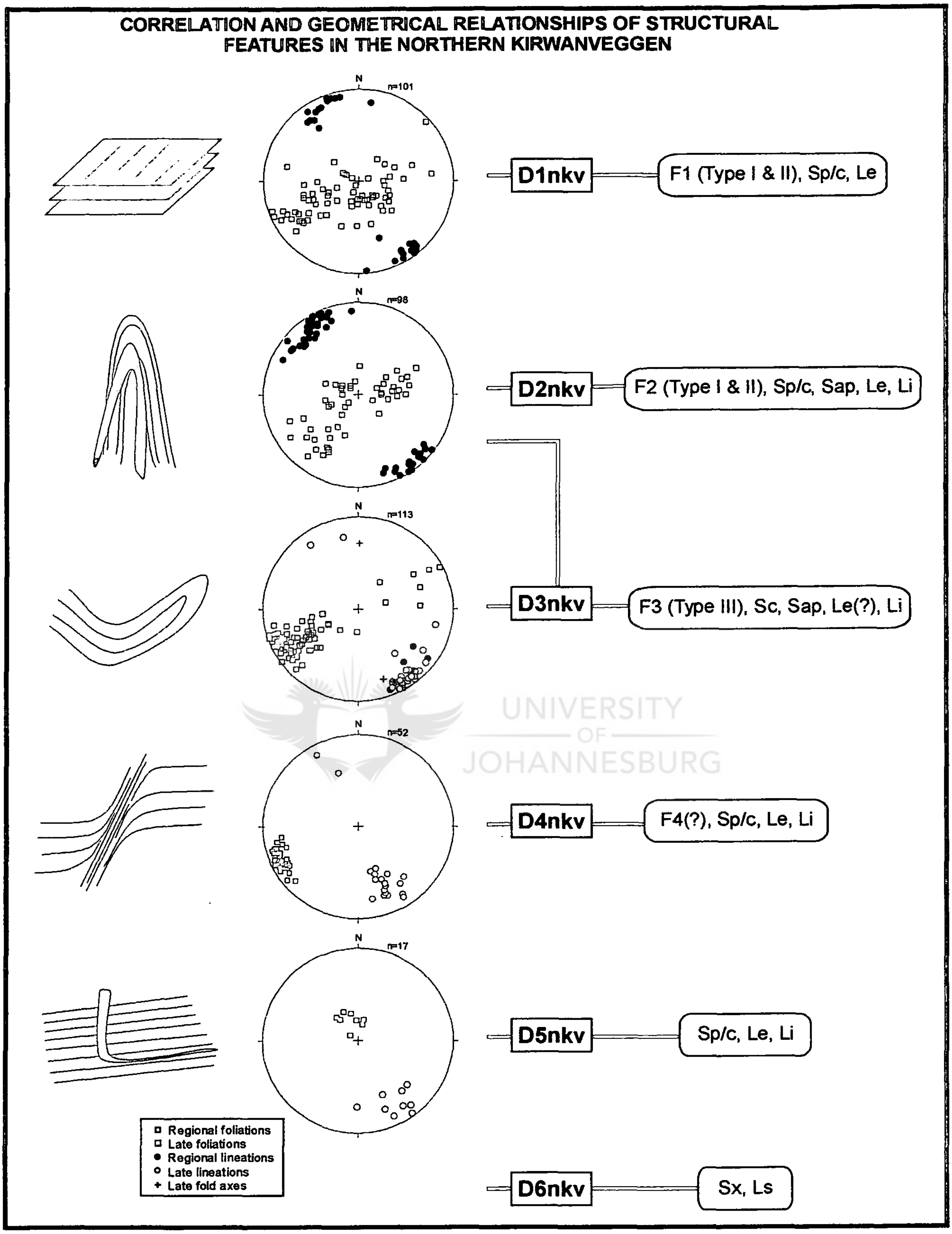

FIGURE 3.11. Correlation of geometrical relationships observed at Neumayerskarvet with the relative structural time sequence established. Codes for structural fabric elements are the same as those in Figure 3.9 and are: planar composite fabrics (Sp/c), axial planar foliations (Sap), cataclastic foliations (Sx), elongation lineations (Le), intersection lineations (Li) and slickensides (Ls). Fold sequences FI to FIV are described in the text.

CHAPTER 4

CONSTRAINTS ON THE TIMING OF DEFORMATION AT NEUMAYERSKARVET

INTRODUCTION

Western Dronning Maud Land (WDML) lies in the northeastern portion of East Antarctica, extending approximately 5° west and east of the Greenwich Meridian. On the eastern side it is bounded by the Muhlig-Hoffmanfjella while the Heimefrontfjella marks the southeastern extent of WDML. WDML can be broadly subdivided into two regions. Firstly, the Ahlmannryggen-Borgmassivet which comprises Archaean granitic gneisses with ages of approximately 3000 Ma (Barton *et al.*, 1987), and domains of younger metasediments, metavolcanics, metavolcaniclastics and mafic intrusives of broadly 1000 Ma (Moyes *et al.*, 1995). Adjacent to this region, separated by the Jutulstraumen-Pencksokket glacial system, is a high-grade gneiss terrain that extends from the Heimefrontfjella in the southwest, through the Kirwanveggen and H.U.Sverdrupfjella into the Gjelsvikfjella and Muhlig-Hoffmanfjella in the northeast.

Rb-Sr and Sm-Nd whole-rock ages for the high-grade gneiss terrane suggest *ca.* 1100 Ma ages, and a period magmatism, metamorphism and deformation has been interpreted from these data (Moyes and Barton, 1990; Groenewald *et al.*, 1991; Moyes *et al.*, 1993a and b; Grantham *et al.*, 1995; Groenewald *et al.*, 1995 amongst other references). On the other hand, Rb-Sr mineral ages (Moyes *et al.*, 1993b), K-Ar and Ar-Ar whole rock and mineral ages (Wolmarans and Kent, 1982) and Sm-Nd garnet ages (Moyes and Groenewald, 1996) provide *ca.* 650-450 Ma ages for the same high-grade gneiss terrane. The above data have led workers to interpret the gneiss terrane as a *ca.* 1100 Ma age metamorphic belt that has undergone resetting during a thermal or tectonothermal event during 550-450 Ma.

Recent research on metamorphic terranes within older portions of East Antarctica and adjacent Gondwana fragments have re-interpreted older isotopic age data after evaluation with new U-Pb zircon ages. In several areas the *ca.* 500 Ma event has not been recognised as a high-grade event due to older *ca.* 1100 Ma ages and difficulties in defining the timing of metamorphism and deformation within these high-grade rocks. In the Lutzow-Holm Complex (LHC) and the Yamato-Belgica Complex (YBC) between 30° and 45° east in Antarctica, regional high-grade metamorphism and associated folding is shown to occur between 521 ± 9 Ma and 553 ± 6 Ma based on zircon ion microprobe analyses (Shiraishi *et al.*, 1994). This interpretation is in contrast to that of Hiroi *et al.* (1991) where regional metamorphism and folding was considered to be Mesoproterozoic from Rb-Sr whole-rock isochron ages. Thermal resetting was invoked by Hiroi *et al.* (1991) to account for the *ca.* 500 Ma mineral ages obtained within the LHC and YBC.

Similar work in Sri Lanka has provided U-Pb zircon age data showing that granulite facies metamorphism occurred after *ca.* 600 Ma (Holzl *et al.*, 1994). Rb-Sr whole-rock ages ranging between 1200 and 1000 Ma have been reinterpreted as intrusive ages rather than regional metamorphic ages. In contrast to these findings, Arndt *et al.* (1991) have obtained *ca.* 1100 Ma U-Pb zircon ages for the metamorphic rocks within the Heimefrontfjella, and suggest that high-grade regional metamorphism occurred during the Mesoproterozoic. K-Ar and Ar-Ar mineral and whole-rock ages from this region again indicate 550-450 Ma ages, but in light of the U-Pb zircon data these ages are interpreted as reset ages during a younger retrograde event (Jacobs *et al.*, 1995).

The Kirwanveggen high-grade gneiss terrane lies between these contrasting, and age distinct terranes. This has prompted the detailed U-Pb ion microprobe investigation presented in this section. Detailed and focussed structural work in the northern Kirwanveggen permits the isotope data to be better constrained in order to understand the tectonic evolution of this portion of the high-grade gneiss terrane (Figure 4.2). The current SHRIMP research is aimed at unravelling the complexities of the tectono-metamorphic events, and to establish an evolutionary history for this portion of WDML. Detailed structural interpretations combined with precise age constraints are currently one of the most suitable methods for understanding the geological evolution, and are presented in this section.

GEOLOGICAL FRAMEWORK

Previous Isotopic Investigations

Initial Rb-Sr whole-rock analyses have been carried out on several lithotectonic units within the Kirwanveggen by Elworthy (in Wolmarans and Kent, 1982). Samples were taken from Neumayerskarvet, Hallgrenskarvet and Heksegryta within the Kirwanveggen (See Figure 4.1 and Table 4.1). Six Rb-Sr whole-rock samples of leucocratic gneiss from Neumayerskarvet define an isochron (MSWD=1.04) equivalent to an age of 1015 ± 24 Ma, with an initial $^{87}Sr/^{86}Sr$ (R_0) of 0.704. Five Rb-Sr whole-rock samples of high-grade gneiss from Heksegryta scatter (MSWD=11.2) about a line equivalent to an age of 1164 ± 78 Ma with R_0=0.704. At Hallgrenskarvet 13 gneiss samples were analysed for Rb-Sr isotopic ratios and compositions. The data define two isochrons equivalent to an age of 1017 ± 12 Ma (MSWD=0.7, R_0=0.705) and 869 ± 63 Ma (MSWD=2.7, R_0=0.709). Elworthy (in Wolmarans and Kent, 1982) described the second and younger date as enigmatic. All the whole-rock Rb-Sr ages suggest the existence of an event dated at between 1200 and 1000 Ma.

Zircons have been extracted from several of the gneisses in the Kirwanveggen (unpublished data quoted in Moyes and Barton, 1990), and the data are also presented in Table 4.2.

Conventional U-Pb zircon concordia ages are quoted as 1112 ± 32 Ma (MSWD=9.5) for Neumayerskarvet, 1045 ± 193 Ma (MSWD=548) for Armalsryggen, and 1107 ± 127 Ma (MSWD=260) for Heksegryta. $^{207}Pb/^{206}Pb$ ages of 1071 ± 74 Ma (MSWD=90), 1061 ± 66 Ma (MSWD=108), and 1075 ± 60 Ma (MSWD=127) for gneisses at Neumayerskarvet, Armalsryggen and Heksegryta respectively. Biotite separates from Hallgrenskarvet show a narrow range of mineral ages between 485 Ma and 460 Ma (Elworthy in Wolmarans and Kent, 1982). These seven samples produce a mean age of 475 ± 14 Ma, and a resetting of this isotope system has been suggested at this time.

A summary of the present isotope data for the high-grade gneiss terrane in WDML is presented in Tables 4.1 and 4.2. The isotope data indicate that a significant event occurred in the Mesoproterozoic (1200-1000 Ma) that is represented by metamorphic zircon growth, whole rock ages and intrusive ages for extensive magmatism. Evidence of a Mesoproterozoic event is unequivocal throughout the WDML high-grade gneiss terrane. Limited magmatism and post-orogenic or metamorphic mineral ages represent a Mesoproterozoic-Early Palaeozoic event (650-450 Ma).

Review of the Deformational History at Neumayerskarvet

Six deformational stages have been identified at Neumayerskarvet and are discussed in Chapter 3 and summarised in this section. The deformational stages relate to a structural pattern of fabric elements and geometries that can be temporally distinguished (Figure 4.3). The distinction of individual deformational stages does not necessarily imply that there is a hiatus between these stages. The stages may represent a continuum of fabric transposition identified within individual localities of the northern Kirwanveggen. Absolute age data presented in this chapter may discriminate between structurally similar deformation episodes. The following section outlines characteristics of these deformational stages.

D1nkv Deformational Stage

The earliest deformation recognised within the biotite-garnet migmatite gneiss is marked by the development of a penetrative planar foliation. Repetition of certain lithotectonic units may indicate an early phase of isoclinal recumbent folding associated with the D1nkv deformational stage. Later deformational stages re-orientate and intensify the D1nkv fabrics making geometrical interpretations of this deformational stage difficult. An elongation lineation is interpreted as developing during D1nkv.

D2nkv Deformational Stage

The D2nkv deformational stage is characterised by intense L>S fabric development. Tight isoclinal, recumbent folds and sheath folds develop at this deformational stage, and are recognised by the re-orientation of earlier fabrics and associated lithotectonic repetition. The penetrative planar foliation intensifies the pre-existing fabrics, and new planar fabrics are developed in fold closures and associated with D2nkv high-strain zones. An intense elongation lineation develops parallel to the fold axes, which dips gently NNW to SSE in areas less affected by later deformation.

D3nkv Deformational Stage

The D3nkv deformational stage results in the refolding of earlier fold phases about similar orientated fold axes. Ramsay Type III fold interference patterns are developed regionally and in outcrop. D3nkv fold axes plunge shallowly NNW-SSE while the axial planes dip steeply towards the NE in the eastern part of Neumayerskarvet where evidence of this fold phase is best preserved. Axial planar foliations and melt veins develop in the fold closures. The strong pre-existing fabric anisotropy influences the fabric geometries and D3nkv results in the stretching and tightening up of the earlier deformational fabrics. Composite intersection and elongation lineations develop parallel to fold axes and pre-existing fabric orientations. D3nkv is coaxial to the early deformational stages.

D4nkv Deformational Stage

The D4 deformational stage comprises two different deformational styles. These two deformational styles have not been temporally distinguished and have therefore been placed within the D4nkv. This does not, however, imply that these two deformational stages are related, and as such these are discussed separately.

The D4(a)nkv deformational stage is recognised by discrete high-strain zones within the central portion of Neumayerskarvet. The high-strain zones disrupt early shallowly dipping planar fabrics re-orientating and enhancing these fabrics into a NW-SE trend. The refolded fold Ramsay Type III interference patterns developed during the D3nkv deformational stage are deformed during D4(a)nkv deformation. Lineations within the high-strain zones parallel early fabric orientations outside of these zones. D4(a)nkv is colinear to earlier deformational stages.

The D4(b)nkv deformational stage is marked by the development of folds that cross-fold the earlier fold phases. This results in the development of mushroom interference patterns in outcrop. Fold axes trend roughly ENE-WSW and this folding results in the scatter or double plunge patterns seen in the pre-existing fabric elements. Mineral lineations tend to develop sub-parallel to the D4(b)nkv fold axes, possibly due to flexural-slip associated with the folding.

D5nkv Deformational Stage

The D5nkv deformational stage reworks early flat lying fabric elements by colinear and coplanar high-strain zones. Examples of these high-strain zones are recognised in central Neumayerskarvet where late pegmatite veins are re-orientated by the D5nkv high-strain zones. Without these intrusive-structural markers this deformational stage would be difficult to distinguish.

D6nkv Deformational Stage

Late brittle faulting and fracturing has been assigned to the D6nkv deformational stage, which post-dates earlier ductile deformation. Slickensides develop on the surfaces of the fault planes.

STRUCTURAL CORRELATION OF SAMPLES

Six samples were selected for detailed isotopic analysis to provide information on the timing of deformation in the northern Kirwanveggen. These samples were selected from the central portion of Neumayerskarvet where distinct structural relationships are recognised. Sample localities are indicated in the cross-sectional photographic mosaic of central Neumayerskarvet (Figure 4.4). The following section provides a description of the lithotectonic unit, and outlines the structural constraints available for these samples. The schematic diagram of Figure 4.6 illustrates the intrusive-structural correlations for these units in central Neumayerskarvet.

Biotite-Garnet Migmatite Gneiss

The biotite-garnet migmatite gneiss was selected as it represents a major unit in the northern Kirwanveggen, and possible correlatives occur within the H.U.Sverdrupfjella (Grantham *et al.*, 1995). The biotite-garnet migmatite gneiss comprises quartz, feldspar, biotite and garnet with abundant felsic melt and intrusive phases (Figure 4.5a). This unit has been exposed to all the deformational stages identified at Neumayerskarvet and provides a maximum age for the deformation currently observed. As this lithotectonic unit has been subjected to all the deformational stages, it may preserve complex age data related to the magmatic, metamorphic and tectonic events experienced during the evolution of this portion of the high-grade gneiss terrane (Figure 4.6).

Felsic Segregation or Leucosome

A felsic segregation or leucosome forming within the biotite-garnet migmatite gneiss was also selected for isotopic analysis. These quartz-feldspar-dominated units form along the penetrative planar foliation of the biotite-garnet migmatite gneiss (Figure 4.5b). This unit may either form with the development of the planar foliation, or intrude into it at a later stage. As the foliation in the biotite-garnet migmatite gneiss is composite in nature the leucosome provides a broad constraint for deformation in the region. The leucosome is syn- or post-D1nkv deformation but was subsequently deformed during D3nkv deformation (see Figure 4.6). If the leucosome develops during D2nkv composite foliation enhancement it may provide a time constraint for the D2nkv deformation.

Intrusive Leucogneiss

The intrusive leucogneiss comprises a lensoidal felsic unit that is structurally intercalated with the biotite-garnet migmatite gneiss (Figure 4.5c). This unit comprises quartz, feldspar, biotite and garnet. Melt segregation veinlets occur within the intrusive leucogneiss and are ptygmatically folded by later deformation. Felsic pressure shadows often develop around the large garnets in this unit, and are elongated parallel to the regional lineation orientation. The intrusive leucogneiss intrudes across the penetrative planar foliation developed in the biotite-garnet migmatite gneiss but has subsequently been intensely deformed. A penetrative planar foliation develops in the intrusive leucogneiss and is accompanied by an intense elongation lineation. The fabrics within the intrusive leucogneiss are parallel, and are coplanar and colinear to the older fabrics developed in the biotite-garnet migmatite gneiss. The fabric elements developed within the intrusive leucogneiss are interpreted as forming during D2nkv deformation where intense L>S fabrics are developed. The earlier fabrics transected by the intrusive leucogneiss are related to D1nkv. Fabric element geometries are displayed in Figure 4.7. The intrusive-structural relationship of the intrusive leucogneiss is illustrated in Figure 4.6.

Kyanite-Bearing Leucogneiss

The kyanite-bearing leucogneiss intrudes across the structural fabrics and several intrusive phases observed within the biotite-garnet migmatite gneiss (Figure 4.5d). The unit comprises quartz and feldspar with variable amounts of biotite, muscovite, garnet, kyanite and sillimanite. A planar fabric is developed within the kyanite-bearing leucogneiss, and these units have been subjected to D3nkv deformation at Neumayerskarvet. Phyllosilicates and aluminosilicates within the kyanite-bearing leucogneiss are aligned, and define the elongation lineation developed within this unit. The kyanite-bearing leucogneiss is potentially a melt segregation phase related to D2nkv deformation. Broad structural constraints indicate that this unit post-dates D1nkv but pre-dates D3nkv deformation.

Megacrystic Orthogneiss

The megacrystic orthogneiss comprises augen-textured gneisses with relatively undeformed charnockitic remnants. The lithotectonic unit comprises quartz, feldspar, biotite and garnet, with or without pyroxene (Figure 4.5e). The megacrystic orthogneiss intrudes into the biotite-garnet migmatite gneiss during a major period of deformation. Enclaves within the less deformed portions of the megacrystic orthogneiss exhibit earlier deformational fabrics. The megacrystic orthogneiss is interpreted to post-date D1nkv, and is either syn- to post-D2nkv, but pre-dates D3nkv deformation.

Late Pegmatite Veins

Late pegmatite veins form the final phase of igneous activity currently recognised in the northern Kirwanveggen. The pegmatites comprise quartz, feldspar, biotite and muscovite with variable amounts of garnet. The veins crosscut the flat lying composite fabrics in central Neumayerskarvet at a high angle (Figure 4.5f). The veins intrude across the steep high-strain zones of D4(a)nkv (see Figures 4.8 and 4.9), but are subsequently deformed by D5nkv deformation colinear and coplanar to earlier structural fabrics.

ANALYTICAL TECHNIQUES

Zircons were separated using standard crushing, heavy liquid and magnetic separation techniques. Representative zircon grains were handpicked and mounted in epoxy with a chip of the standard zircon SL13. Ion-microprobe analyses were carried out using SHRIMP II in collaboration with Dr F.M.Fanning at the Research School of Earth Sciences at the Australian National University in Canberra. The analyses consisted of either five or seven scans through the mass range. Data reduction methods follow standard procedures described by Compston *et al.* (1984, 1986, and 1992) and Williams and Claesson (1987). The U/Pb and Th/U ratios have been normalised to a value of 0.0928 for the $^{206}Pb/^{238}U$ ratio for the standard zircon SL13, which is equivalent to an age of 572 Ma. The 'unknowns', where present, have been corrected for isobaric interferences at mass 204 and 207, the latter for $^{206}PbH^+$. Ages quoted here are calculated using constants recommended by the IUGS Sub-Commission on Geochronology, and ages are quoted at the 95% (2σ) confidence limits. Uncertainties given in the ion microprobe tables, however, are at the 1 σ level.

Whole-rock powders were prepared using standard rock crushing techniques at the Bernard Price Institute of Geophysics (BPI). Mineral concentrates were separated using standard crushing, heavy liquid and magnetic separation techniques. Biotite, muscovite and feldspar samples were hand picked to select the most suitable separate for isotope analysis and sample fractions weighed approximately 0.1g. The mineral separates were cleaned in 2N HCl for five minutes in an ultrasonic container.

Chemical dissolution of approximately 0.1g of the whole rock powder was carried out using clean open Teflon® beakers for the Rb-Sr analyses. Approximately 0.05g to 0.1g of mineral concentrate was dissolved in screw-top Teflon® PFA (Savillex) beakers. Rb and Sr Isotope tracers were added prior to dissolution. Chemical dissolution was achieved with an HF-HNO_3 mix (3:1) for three days on a hot plate, and then taken up in 6N HCl. Separation of Rb and Sr was attained using standard cation exchange in an HCl medium. All reagents used in these procedures were prepared and purified at BPI. Rb concentrations were measured on a

Micromass® MM30 mass spectrometer, while $^{87}Sr/^{86}Sr$ ratios and Sr concentrations were measured on a Micromass® VG354 mass spectrometer. Measured total method blank levels were less than 1ng for Rb and Sr and no corrections to the data were made. Values obtained for $^{87}Sr/^{86}Sr$ during the course of this study from international standards SRM987 and Eimer & Amend® were 0.71021 ± 0.00003 and 0.70800 ± 0.00005 respectively.

The processing and regression of the Rb-Sr isotopic data was carried out using the program "*GEODATE*" of Eglington and Harmer (1991). Precision parameters at the 2σ level used in the regression techniques were: $^{87}Rb/^{86}Sr$ – 2%; $^{87}Sr/^{86}Sr$ – 0.0002. The correlation coefficient used for Sr whole-rock analyses was 1.0, and mineral separates was 0.99. Throughout the text all ages, initial ratios and errors are quoted at the 2σ (95% confidence) levels. Isochrons are defined here as occurring when the mean sum of the weighted deviates (MSWD) is less than a critical F value determined by the number of samples regressed and based on 60 replicate analyses (formulae from Ludwig, 1983; 1990). Where the MSWD exceeds this F value the errors have been augmented by $(MSWD/Critical\ F)^{1/2}$. Decay constant used for ^{87}Rb is $1.42 \times 10^{-11} y^{-1}$.

SAMPLE DESCRIPTIONS AND U-Pb ZIRCON ION MICROPROBE DATA

PH93161 (Biotite-Garnet Migmatite Gneiss)

Sample PH93161 was taken from the biotite-garnet migmatite gneiss, which comprises quartz, feldspar, biotite, garnet and amphibole. A complex zircon population is found within this sample, although the majority are clear, rounded amber coloured grains that display considerable size variations. Some milky dark brown fragments are also recognised. Another zircon type recognised displays growth zones and overgrowths developing subhedral terminations, or short and fairly stubby crystals. A total of 33 spots were analysed on 26 zircons, sampling a wide range of forms and zones within individual grains.

The results of the analyses are presented in Table 4.3 and are shown on the concordia plot of Figure 4.10a. Microphotographs of several of the analysed zircons are also displayed in Figure 4.10b to d. Three analyses lie on or near concordia between ~1880 Ma and ~2040 Ma (spots 5.1, 16.1 and 24.1). These zircons are simple clear rounded grains with a maximum $^{207}Pb/^{206}Pb$ age of ~2040 Ma. Several discordant analyses scatter between these ages and the large clustering of analyses between ~1100 Ma and ~1200 Ma. These discordant analyses can be attributed to multi-stage lead loss and represent 'inherited' components within the sample. Spot analysis 26.1 provides a near concordant $^{207}Pb/^{206}Pb$ age of ~1390 Ma.

The majority of zircon analyses cluster on or near concordia between ~1200 Ma and ~1100 Ma. These analyses can be statistically divided into two populations: (1) the older population provided a weighted mean $^{207}Pb/^{206}Pb$ age of 1157 ± 10 Ma, whereas (2) the younger population gives a mean $^{207}Pb/^{206}Pb$ age of 1100 ± 10 Ma. Although these two clusters can be distinguished statistically, the geological significance of these ages is uncertain. There is a continual spread of analyses between the statistical populations, and it is quite possible that further zircon analysis from this sample would not differentiate these two age populations. It is clear, however, that multi-stage lead loss has affected the majority of these zircons.

The SHRIMP analyses of the major cluster spread along or near concordia from the near concordant $^{207}Pb/^{206}Pb$ ages of ~1159 Ma (20.1) and ~1178 Ma (9.1) through to the youngest near concordant $^{207}Pb/^{206}Pb$ age of ~1029 Ma (3.1). Discordant analyses 1.1, 14.1 and 15.1 indicate late-stage lead loss and have been excluded from the statistical analysis. A near concordant spot analysis (3.1) provides a $^{207}Pb/^{206}Pb$ age of ~1029 Ma. Several other concordant and near concordant analyses give $^{207}Pb/^{206}Pb$ ages of ~1063 Ma (20.2), ~1074 Ma (22.1) and ~1069 Ma (7.1).

Overgrowths are observed on several of the analysed zircons from this sample. Some of these overgrowths are seen clearly through SEM cathodoluminescence investigations (Figure 4.11). Zircon overgrowth ages range from ~1260 Ma (13.1, discordant) through ~1120 Ma (12.2, near concordant) to ~1050 Ma (12.1, discordant) and ~1000 Ma (1.1, discordant) (Figures 4.10 and 4.11). Although several of these analyses are discordant (probably due to lead loss) they indicate that overgrowths accompanied separate zircon growth between ~1050 Ma to ~1160 Ma. Grain 13 shows an intact overgrowth with a discordant $^{207}Pb/^{206}Pb$ age that is older than the main analyses cluster (Figure 4.11d). The question arises as to whether this rim formed *in situ* or was inherited during deposition/extrusion of the biotite-garnet migmatite gneiss. Rims also develop on older inherited cores which display typical growth zoning often indicative of igneous generation (Figure 4.11a).

PH92009 (Leucosome in Biotite-Garnet Migmatite Gneiss)

The leucosome sample PH92009 consists mainly of quartz and feldspar. A wide variety of clear dark brown prismatic zircons, with sub-rounded terminations and irregular fracturing, are found within this sample. Several of the zircons display distinct cores, which are often inclusion filled and fractured, displaying narrow zircon growth zoning. A total of 17 spot analyses were obtained from 11 zircon grains derived from sample PH92009.

The U-Pb results are presented in Table 4.4, and the concordia plot is displayed in Figure 4.12a. Except for 2 analyses the data form a close $^{207}Pb/^{206}Pb$ grouping and cluster around concordia. The grouping gives a weighted mean $^{207}Pb/^{206}Pb$ age of 1098 ± 5 Ma.

The discordant samples (4.1 and 6.1) are analyses of the small cores to some of these zircons (Figure 4.12b and c). It is possible that they belong to an older population that has been subject to lead loss during intrusion, melting or metamorphism. These data suggest that there is an inherited component preserved in this sample, the age of which is indeterminable from the current analyses.

A younger near concordant analysis gives a $^{207}Pb/^{206}Pb$ age of ~1040 Ma (7.2). This spot analysis is of the zircon overgrowths around a core (see Figure 4.12c), and may represent evidence for later, post-crystallisation, metamorphism.

The $^{207}Pb/^{206}Pb$ age of 1098 ± 5 Ma from the main analyses grouping provides the best estimate for the formation age of this unit. The age could represent the timing of partial melting that resulted in the formation of this leucosome.

PH93148 (Intrusive Leucogneiss)

The intrusive leucogneiss sample comprises quartz, feldspar, biotite and garnet. A fairly complex zircon population is obtained from this sample. Several large sub-rounded zircon grains with overgrowths are identified (Figure 4.13b, c and d). The major population comprises small subhedral prismatic needle-like forms with growth zoning. This population has cloudy appearances due to the presence of inclusions, growth zones and occasional fractures. A total of 15 analyses on 11 zircon grains were obtained from this sample.

Analytical results are presented in Table 4.5 and represented in the concordia plot of Figure 4.13a. The SHRIMP analyses from this sample are mainly discordant making interpretation of the isotopic results difficult.

The sub-rounded larger zircon grains provide core ages, although discordant, that are older than the needle-like subhedral grains (see Figure 4.13). These analyses suggest that there is an inherited zircon component present in this sample (spots 2.1, 5.1, 6.1 and 11.1). These analyses have been excluded from the mean $^{207}Pb/^{206}Pb$ age estimate shown in Figure 4.13a. A statistical analysis of the remaining data (excluding spots 2.2, 7.1 and 9.1) provide a weighted mean $^{207}Pb/^{206}Pb$ age of 1101 ± 13 Ma, but the analyses are fairly discordant. In this spot analyses population, only two analyses are near concordant (spots 10.1 and 10.2) and provide ages of ~1137 Ma and ~1119 Ma respectively. The mean $^{207}Pb/^{206}Pb$ age of 1101 ± 13 Ma is interpreted as a minimum age of crystallisation for the intrusive leucogneiss. The near concordant analyses suggest an age closer to ~1130 Ma for intrusion of this unit. Regression of these analyses provides an upper intercept age of 1130 ± 24 Ma and a lower intercept age of 465 ± 24 Ma.

Spot analysis 9.1 lies near concordia and has a $^{207}Pb/^{206}Pb$ age of ~1049 Ma. This analysis is from a rim overgrowth to a sub-rounded zircon grain and may suggest a younger period of zircon growth. The spot analysis 2.2 is also of a rim growth to a sub-rounded grain with an older core (see Figure 4.13d). This spot is fairly discordant but gives a $^{207}Pb/^{206}Pb$ age of ~484 Ma. This is the first analysis that has provided evidence of zircon growth during a younger *ca.* 500 Ma event. A highly discordant spot analysis (7.1) may occur on a lead loss line between the *ca.* 1100 Ma zircon population and the *ca.* 500 Ma zircon growth. The discordance of a large number of these analyses may be a result of lead loss during a younger *ca.* 500 Ma geological event.

PH92020 (Kyanite-Bearing Leucogneiss)

The kyanite-bearing leucogneiss sampled for this investigation consists of 0.5 to 1 cm quartz and feldspar grains, small garnets, with bands of biotite and minor kyanite. The kyanite is randomly distributed throughout the kyanite-bearing leucogneiss bodies. Zircons from this sample comprise large strongly fractured and fragmented subhedral prismatic grains. The zircons are clear with an amber colour and inclusions are rare. The smaller zircons are also subhedral prismatic grains with rounded terminations, possibly due to the effects of metamorphism. Growth zoning is commonly seen within these zircons (Figure 4.14b). 15 SHRIMP spot analyses were made on 11 different zircon grains from this sample.

The results of the SHRIMP analyses are presented in Table 4.6 and the individual spot analyses are presented on the concordia plot of Figure 4.14a. The total spot analyses form a fairly tight grouping in $^{207}Pb/^{206}Pb$ and have a mean age of 1097 ± 10 Ma, but there is a small scatter in excess of experimental uncertainties. Removal of the more discordant samples (1.1, 4.1 and 5.2), and of the lower concordia-plotting sample 2.1, produces an indistinguishable mean $^{207}Pb/^{206}Pb$ age of 1096 ± 10 Ma for the remaining population. This age is interpreted as the age of crystallisation for the kyanite-bearing leucogneiss. A younger near concordant $^{207}Pb/^{206}Pb$ age of ~984 Ma (spot 2.1) does not display significantly different U or Pb concentrations. It is possible that this age represents a period of disturbance or metamorphism where Pb loss or zircon recrystallisation or growth took place.

PH92005(Megacrystic Orthogneiss)

This sample is of a reddish-brown portion of the megacrystic orthogneiss and represents a remnant of chamockitic material. The sample consists of large feldspar porphyroblasts with a coarse matrix of quartz, feldspar, pyroxene, garnet and biotite. Zircons from this sample are large needle-like and are euhedral to slightly subhedral in form. A small degree of rounding of the crystal edges appears to have taken place (see Figure 4.15b). The zircons are clear with a slight brown tinge. Growth zoning is preserved in the inclusion-rich zircon grains. Dark inclusion spots and needle-like features are seen in these zircons (Figure 4.15b). 14 spot analyses were made on 11 zircon grains from this sample.

The SHRIMP results are summarised in Table 4.7 and plotted on the concordia diagram of Figure 4.15a. Except for analysis 5.1 the analyses form a close grouping of $^{207}Pb/^{206}Pb$ that clusters around concordia. These analyses have a mean $^{207}Pb/^{206}Pb$ age of 1088 ± 10 Ma, which is interpreted as a crystallisation age for this sample.

Analysis 5.1 lies near concordia and has a $^{207}Pb/^{206}Pb$ age of ~977 Ma. There is no significant difference of the U and Pb concentrations for this analysis. The younger $^{207}Pb/^{206}Pb$ age is interpreted as representing a period of either lead loss or, more likely, a period of recrystallisation and re-growth during a younger time period.

PH92006/PH93140 (Late Pegmatite Vein)

Two samples from the same pegmatitic vein were combined in order to increase the net zircon population obtained for this investigation. The pegmatitic vein consists of quartz and feldspar with variable amounts of garnet and biotite. Small elongate needle-like zircons have been obtained from these samples. The zircons are near euhedral but display some degree of rounding of the crystal edges. Narrow growth zoning patterns are typically displayed in these zircons (Figure 4.16b). A total of 19 analyses were made, 14 grains from sample PH93140 and 5 zircon grains from sample PH92006.

A summary of the U-Pb results for the zircon ion probed data from these samples is provided in Table 4.8. A concordia diagram for the pegmatitic vein sample is plotted in Figure 4.16a. The zircons have high U concentrations, which are typical of highly fractionated late stage granitic magmas. The high U contents cause radiation damage and large errors for several analyses have been obtained. The highly discordant analyses (spots 3.1 and 5.1 from PH92006) and the analyses with large errors (spot 2.1, 7.1, 9.1 and 11.1 from PH93140) have been excluded from further isotopic evaluations. The discordant sample 3.1 (from PH93140) and the strongly reverse discordant spot 8.1 (from PH93140) have also been excluded for the age determination of this sample. The remaining analyses form a tight $^{207}Pb/^{206}Pb$ clustering across concordia and provide a mean $^{207}Pb/^{206}Pb$ age of 1079 ± 6 Ma. This age is interpreted as a crystallisation age for the pegmatitic vein sample.

Rb-Sr SYSTEMATICS

No magmatic phases were identified that post-date the pegmatite veins in the northern Kirwanveggen. The only units that may potentially be younger than the pegmatitic veins are a series of mafic dykes that transect central Neumayerskarvet at high angles (Figure 4.4). No zircons were, however, recovered from these samples. Rb-Sr mineral isotope systematics have been used in this investigation to try and provide some form of age constraint for the deformation that post-dates the pegmatitic veins. Minerals from 3 different intrusive units have been analysed for their Rb-Sr isotope systematics. The major mineral in these samples is biotite, and due to the highly radiogenic nature typical of this mineral, it dominates the slope of the regression line. The Rb-Sr data are given in Table 4.9 and a summary of the age determinations are provided in Table 4.10 and Figure 4.17. The following section describes the Rb-Sr isotopic results for the different intrusive units.

Of specific interest to the Rb-Sr investigation are the pegmatitic veins. These veins are the youngest intrusive phase recognised at Neumayerskarvet. An example of a pegmatitic vein that is deformed within D5nkv high strain zone is illustrated in Figure 4.9. Minerals from the deformed mylonitic textured pegmatitic veins were selected for Rb-Sr analysis (PH92012). The Rb-Sr systematics of the minerals within the high-strain zone are expected to be reset or disturbed. If there is no other later event significant enough to disturb the Rb-Sr systematics, which post-dates the high-strain zones, then the Rb-Sr mineral age may relate to the timing of this deformation. In order to evaluate the implications of the Rb-Sr mineral data from within the high-strain zones, several background samples were also selected for similar analysis. These samples are of the pegmatitic veins outside the D5nkv high-strain zones (PH92007), the intrusive leucogneiss (PH93148, SHRIMP sample) and the kyanite-bearing leucogneiss (PH92020, SHRIMP sample).

Two analyses were made from sample PH92012, which is of the pegmatitic veins within the D5nkv deformational stage high-strain zones. The whole-rock-biotite 2 point line (Figure 4.17b) has an equivalent age of 474 ± 10 Ma (R_0=0.7332).

Rb-Sr analyses of whole-rock-feldspar-biotite from the pegmatitic veins (PH92007) away from the D5nkv high-strain zone scatter (MSWD=39.6) about a line equivalent to an age of 459 ± 29

Ma (R_0=0.7596). The highly radiogenic biotite sample controls the slope of the line and hence the age determination (Figure 4.17a).

Feldspar, biotite and muscovite were analysed for their Rb-Sr isotopic composition from the kyanite-bearing leucogneiss sample PH92020 (Figure 4.17c). The minerals plot on an isochron MSWD=1.04) equivalent to an age of 479 ± 7 Ma (R_0=0.7538).

Rb-Sr isotopic data were obtained from the whole-rock sample, feldspar, biotite and muscovite samples from the intrusive leucogneiss sample PH93148 (Figure 4.17d). The minerals and whole-rock plot on an isochron (MSWD=1.06) equivalent to an age of 471 ± 7 Ma (R_0=0.7166).

All the Rb-Sr mineral data provide similar ages of *ca.* 475 Ma. These determinations are dominated by the highly radiogenic biotite samples, and can in essence be regarded as biotite ages. There is no distinguishable difference in the Rb-Sr mineral age data between the deformed and earlier undeformed units. This is in contrast to the considerably older SHRIMP zircon ages for these samples. The uniformly similar ages suggest a region-wide disturbance of the Rb-Sr mineral systematics rather than being related to localised ductile deformation in the region. It is therefore interpreted that the Rb-Sr mineral ages of *ca.* 475 Ma provide a minimum age to the ductile deformation recognised within the northern Kirwanveggen.

DISCUSSION

The Effects of Poly-Phase Deformation and Metamorphism on U-Pb Zircon Systematics

Lead loss in zircons from high-grade gneiss terranes has been commonly observed (Black *et al.*, 1986; Kroner *et al.*, 1987 and 1994; Williams and Claesson, 1987; Rudnik and Williams, 1987; Holzl *et al.*, 1994; amongst others). The lead loss is also variable between grains and between domains of individual grains. The lead loss generates discordant zircon isotope analyses. The extent of lead loss has, however, been subjected to some debate. Black *et al.* (1986) documented progressive recrystallisation and complete resetting of U-Pb isotopic systems in Archaean granulite grade zircons. Severe and widespread lead loss with new zircon growth at the same time period has been recorded by Holzl *et al.* (1994). Kroner *et al.* (1994) have suggested that lead loss can result in the loss of original lead compositions within the zircons, making lead evaporation techniques problematic on these types of materials. Mezger and Krogstad (1997), however, felt that complete resetting by diffusion is not achieved. These authors conclude that the major causes of discordance in zircons are a result of multiple growth events or metamictisation. Williams and Claesson (1987) have recorded an example where a metamorphic event has caused growth of new zircon, or partial recrystallisation of an older zircon component.

There is consensus that upper age intercepts from discordant data represent the crystallisation age (Holzl *et al.*, 1994; Kroner *et al.*, 1994; Mezger and Krogstad, 1997), but interpretation of the lower intercept is more equivocal. The lower intercept age could represent a period of resetting or recrystallisation but other geochronological techniques would be required to evaluate its geological significance.

Intrusion of magmatic phases synchronous to metamorphism may result in only minor morphological modifications, but a dynamic environment is created which could modify age determinations. In this situation, age uncertainties of ± 5 Ma or greater are to be expected (Young *et al.*, 1995). A similar situation is envisaged during this investigation and the resultant ages have large error estimates with respect to zircon U-Pb age determinations.

There are currently two hypotheses to explain the spread of data along concordia:

1. Young *et al.* (1995) have proposed that superimposed metamorphic events may lead to lead loss in early-formed zircons. If the ages of zircon crystallisation and metamorphism are close together then lead loss would not lead to discordance but would rather track along concordia between these two events.
2. Mezger and Krogstad (1997), however, interpreted zircons that have been held above their annealing temperature (600-650 °C) as remaining concordant during repair to the crystal lattice structure soon after decay damage. Zircons that have cooled below this annealing temperature will be subjected to radiation damage, and during re-heating or recrystallisation the lead will be dispelled from the lattice and thus causes discordance. Mezger and Krogstad (1997) feel that at high temperatures, zircons that spread along concordia are most likely a result of multistage growth rather than diffusion of lead in pre-existing grains. Complicated discordance patterns in zircons would therefore develop as a result of alternating low and high temperatures.

These two ideas concerning the spread of data along concordia would suggest widely differing tectonic environments and have significantly different implications. Alternating low and high temperatures would suggest episodic deformation and metamorphism. This is not unrealistic and similar scenarios have been reported in the literature (Collins and Williams, 1995; Stuwe *et al.*, 1993). The tracking of lead loss along concordia as proposed by Young *et al.* (1995) would provide no ages of geological significance, except for the upper and possibly lower ages or 'intercept ages' that can be identified. This method does not necessarily require episodic events.

Another interesting aspect of zircons in high-grade gneisses is that certain samples display Pb loss, zircon re-growth and recrystallisation while other samples do not. Several scenarios can be envisaged to explain this occurrence. One scenario is that the two adjacent samples have undergone different tectonic and metamorphic events. In cases where good structural information is available this scenario is unlikely. Another explanation is that the different rock fabrics affect the permeability and influence the migration of metamorphic fluids. This could also relate to the chemistry of the different rock units. During metamorphism, if Zr is not released then zircon cannot form during that specific event. This raises the question of the metamorphic significance of the new zircon growth. Fraser *et al.* (1997) have suggested that new zircon growth, as a result of hornblende or garnet breakdown, is not expected to record the time of peak metamorphism but rather will record the time of a particular metamorphic reaction. It is possible, therefore, that zircon growth periods may not represent different metamorphic events, but rather reactions taking place during a metamorphic cycle. Obviously both scenarios are possible and caution must be observed when making interpretations. *In-situ* analysis of zircons, which have petrogenetic information and significance, would be important to provide constraints of these issues.

Clearly the interpretation of zircon ages is complex in high-grade gneiss terranes. The above discussions have highlighted some of these complications and controversies. Zircon age data from Neumayerskarvet are interpreted with these concepts in mind in the following section.

Interpretation of the Isotope Data

In this discussion, the ages that are more readily interpreted are discussed first. Through the understanding of the more readily interpreted ages of certain units, a clearer interpretation of the more complex U-Pb zircon systematics is possible. The younger units have not been subjected to the same amount and degree of deformation and metamorphism that the older units have experienced. As such, this discussion will start with interpretations from the younger units and will finish with the older units dated at Neumayerskarvet. A summary diagram of the relationships between the zircon ages is provided in Figure 4.18.

The pegmatite vein sample (PH92006/PH93140) provides an age of 1079 ± 6 Ma, which is interpreted as the crystallisation age for this unit. The pegmatitic vein is the last magmatic phase distinguished in the northern Kirwanveggen, and dates the end of magmatism at least within this region of the Kirwanveggen.

A crystallisation age of 1088 ± 10 Ma is interpreted from the megacrystic orthogneiss sample (PH92005). No inherited components are identified, but a period of zircon recrystallisation or growth is suggested by the single zircon analysis with an age of ~977 Ma.

An U-Pb zircon age of 1096 ± 10 Ma has been obtained for the kyanite-bearing leucogneiss and is interpreted as a crystallisation age for this unit. A younger age of ~984 Ma is interpreted as possible evidence of later disturbance or recrystallisation and re-growth of zircons within this sample.

The leucosome in the biotite-garnet migmatite gneiss (PH92009) provides an U-Pb zircon age of 1098 ± 5 Ma. This is interpreted as the crystallisation age for this unit. A younger concordant analysis at ~1040 Ma suggests evidence of a later disturbance or recrystallisation period.

The U-Pb zircon data from the intrusive leucogneiss sample (PH93148) is difficult to interpret. The $^{207}Pb/^{206}Pb$ age of 1101 ± 13 Ma provides a minimum age of intrusion for this unit. The more concordant analyses, and the regression of the data, suggest an age closer to ~1130 Ma. Inherited components are recognised within the intrusive leucogneiss sample but the analyses do not provide age determinable results. Younger zircon ages of ~1049 Ma and ~484 Ma indicate disturbance, recrystallisation and re-growth of zircon. This is the only sample that has evidence for a younger *ca.* 500 Ma event in the U-Pb systematics.

The biotite-garnet migmatite gneiss is the oldest lithotectonic unit recorded within the northern Kirwanveggen, and it is not surprising that this fact is reflected by complicated U-Pb zircon systematics. Inherited components in the biotite-garnet migmatite gneiss sample (PH93161) have ages ranging up to ~2040 Ma providing information on the possible source for this unit. The large component of inherited ages support a supracrustal origin for this lithotectonic unit. The time period where this unit was consolidated as an unmetamorphosed and undeformed precursor is not well constrained. An intact zircon overgrowth of ~1260 Ma (minimum analytical age) suggests zircon growth *in-situ* and may provide a minimum age of formation for this unit. Rims of zircon overgrowths are recorded at ~1130 Ma and indicate, at least, a minimum age for the formation of the biotite-gamet migmatite gneiss. The major cluster of zircon analyses occurs between ~1200 Ma and ~1100 Ma. Based on the presence of a *ca.* 1100 Ma intrusive units within the biotite-garnet migmatite gneiss, this broad cluster of ages are interpreted as a major period of metamorphism and tectonism that the precursor rock has experienced. These zircons are interpreted as developing *in-situ* within the biotite-gamet migmatite gneiss.

The spread of zircon analyses along concordia in this sample is interpreted as lead loss and simultaneous growth closely following initial zircon crystallisation. The 'upper intercept' age of 1157 ± 10 Ma provides an approximate age when *in-situ* zircon growth began. It must be noted, however, that if the ~1260 Ma zircon rim age was not developed *in-situ*, then this age would indicate the maximum age of formation for the biotite-garnet migmatite gneiss. A single rounded zircon grain provides a $^{207}Pb/^{206}Pb$ near concordant age of ~1390 Ma (spot 26.1). This provides a maximum age of formation for the biotite-garnet migmatite gneiss.

Zircon growth may also be expected during the tectono-metamorphic event/ s(?) responsible for the lead loss tracking along concordia. The 'lower intercept' or statistical cluster at 1100 ± 10 Ma suggests a significant event during this period. This is supported by the *ca.* 1100 Ma intrusive ages that have been obtained during this investigation. If the interpretations of Mezger and Krogstad (1997) are taken into consideration, then a 'cooling' period below 650-600 °C and subsequent re-heating would be required for lead loss to occur. It must be noted, however, that the effects of pressure on the zircon annealing temperature estimates are unknown. If this is the case then the biotite-garnet migmatite gneiss is interpreted to have undergone a tectonic-metamorphic event at *ca.* 1157 Ma with cooling and subsequent re-heating by a *ca.* 1100 Ma period, which is supported by major magmatism at this period. The effects of these 2 events would explain the spread of analyses along concordia between *ca.* 1200 Ma and *ca.* 1100 Ma. These data suggest an early *ca.* 1160-1130 Ma tectonothermal period, followed by a younger significant tectonothermal period, with associated magmatism between *ca.* 1100 Ma and *ca.* 1070 Ma.

Younger ages recorded from zircons in the biotite-garnet migmatite gneiss sample are interpreted as disturbed, recrystallised or re-growth periods within this sample. These ages range between ~1074 Ma and ~1029 Ma. These data indicate that later tectonothermal events affected the region after *ca.* 1070 Ma and are reflected in all of the samples used during this investigation. Similar ages are recorded in the central Kirwanveggen (Jackson *et al.*, 1997), but in this area a significant period deformation and magmatism is also documented.

Rb-Sr data provide mineral ages of *ca.* 475 Ma for the samples. These ages are obtained from within the late ductile deformation as well as outside these structures. The Rb-Sr data provide a minimum age for the ductile deformation at Neumayerskarvet.

Timing of Deformation at Neumayerskarvet

Three major tectonic episodes are distinguished in the northern Kirwanveggen, the most significant of which is the D1 episode. The regional D1 tectonic episode is sub-divided further into three periods, although these are not significantly differentiated to represent discrete episodes. All three periods could represent a continuum of deformation and metamorphism over an extended time period. They could equally, however, represent episodic periods during the major regional D1 tectonic episode. As such, the regional D1 episode has subsequently been divided into D1a, D1b and D1c periods. Further work in this region of the Kirwanveggen may better distinguish or resolve these periods. A summary of these tectonic episodes is provided in Figure 4.19.

The upper age limit of the regional D1a period is constrained by the age of the biotite-garnet migmatite gneiss, as it represents the oldest lithotectonic units recorded at Neumayerskarvet. The maximum age of the biotite-garnet migmatite gneiss is ~1390 Ma (see discussion above). A major period of zircon growth occurred at *ca.* 1160 Ma in the biotite-garnet migmatite gneiss and at this stage is interpreted as part of the regional D1a period. Zircon growth at *ca.* 1130 Ma is also assigned to the regional D1a period. During this period planar penetrative fabrics and possible early isoclinal folding occurred. There is a possibility that magmatism is associated with the regional D1a period. The intrusive leucogneiss is estimated to have an age of *ca.* 1130 Ma, although this is poorly constrained. Within WDML magmatism has been documented during a *ca.* 1130 Ma time period and may represent magmatic signatures equivalent to the regional D1a period (see Arndt *et al.*, 1991; Harris *et al.*, 1995; Moyes and Groenewald, 1996; Jacobs *et al.*, 1996; Jackson *et al.*, 1997). Inherited components from within younger magmatic phases at Neumayerskarvet may represent sampling of the regional D1a tectonic period. This period is constrained by the current data between *ca.* 1160 Ma to *ca.* 1110 Ma.

A major tectonic, metamorphic and magmatic event is recorded during the regional D1b period. The D2nkv to D4(a)nkv deformational stages represent signatures of tectonism associated with the regional D1b period. Major folding producing isoclinal recumbent folds, sheath folds and re-folded interference fold patterns form during the D1b period, and indicate major coaxiality during this period. L>S fabrics with composite planar penetrative foliations, elongation, intersection, and composite lineations define the tectonic fabrics of this period. Large magmatic bodies intrude during the regional D1b tectonic period and are marked by the intrusion of leucosomes (1098 ± 5 Ma), kyanite–bearing leucogneiss (1096 ± 5 Ma), megacrystic orthogneiss (1088 ± 10 Ma) and pegmatite veins (1079 ± 6 Ma). Disturbance of U-Pb systematics in early zircons, zircon re-growth and recrystallisation accompany the regional D1b tectonic period. This period is constrained between *ca.* 1110 Ma to *ca.* 1070 Ma during which NNW-SSE tectonic transport directions have been inferred.

The final period of the regional D1 tectonic episode is identified through zircon disturbance, recrystallisation and re-growth between *ca.* 1070 Ma and *ca.* 970 Ma. All the zircon ion microprobe samples in this investigation show signatures of the regional D1c tectonic period, but the nature of the deformation is poorly constrained. The cross-folding and high-strain zone development associated with the D4(b)nkv and D5nkv deformational stages are constrained between the pegmatite vein sample at 1079 ± 6 Ma and the Rb-Sr reset ages of *ca.* 475 Ma. These deformational fabrics may therefore form part of the regional D1c tectonic period, but it is equally possible that they are part of the regional D2 tectonic episode. It is likely that these deformational stages form a composite of signatures from the regional D1c and D2 tectonic episodes. The current data are unable to distinguish the nature of deformational fabrics associated with these two distinct tectonic episodes. Late stage magmatism has been recorded during similar periods at the regional D1c tectonic period within other parts of the Kirwanveggen (Harris *et al.*, 1995; Jackson *et al.*, 1997).

Zircon growth and disturbance at *ca.* 500 Ma represent signatures of the regional D2 tectonic episode. Regional resetting of the Rb-Sr mineral data also occurs during this tectonic episode. As there is no age data continuum between the ~970 Ma and *ca.* 500 Ma episodes, a distinct hiatus is interpreted that separates these episodes tectonically. The nature of the deformation associated with the regional D2 tectonic event is, however, not clearly distinguished. It is possible however, that reworking of the early dominant fabric elements takes place during the regional D2 period. The regional D1 episode is however clearly the more dominant tectonic episode.

The last tectonic episode recognised in the northern Kirwanveggen is the regional D3 episode at *ca.* 180 Ma. The D6nkv deformational stage brittle fabrics are assigned to this tectonic episode. This episode has been equated to the rifting of Gondwana (Grantham *et al.*, 1995), and the timing of this episode is derived from alkaline complexes dated at *ca.* 180 Ma (see Harris and Grantham, 1993 and references therein).

Structural Correlations in Western Dronning Maud Land

The major episode of tectonism, magmatism and metamorphism that has affected the northern Kirwanveggen is dated here as a *ca.* 1100 Ma period (*ca.* 1160 Ma to *ca.* 980 Ma). This event may be episodic in nature and distinct periods of differing tectonic, metamorphic and magmatic styles exist. These ages are similar to those obtained within the H.U.Sverdrupfjella and Heimefrontfjella (see Table 4.1 and 4.2 and references therein), and are significant since they provide close constraints on the timing of deformation in this particular region. Areas that have been re-worked by intense *ca.* 500 Ma deformation may still retain older intrusive and formational ages. An example for such a case has been demonstrated by Holzl *et al.* (1994) from high-grade gneisses in India where the major metamorphism is significantly younger than the intrusive ages derived from the gneisses. Magmatism at *ca.* 500 Ma has been recognised in the H.U.Sverdrupfjella and should be focussed on to constrain deformational fabrics from that region.

This type of work will assist in resolving *ca.* 1100 Ma and *ca.* 500 Ma age deformation and metamorphism for this portion of Antarctica.

Re-working of these early tectonic fabrics has taken place during younger periods, but the extent of re-working is uncertain. The strong structural anisotropy imparted on the gneisses during the *ca.* 1100 Ma period strongly influences the signatures and recognition of younger tectonic fabrics. The geometries of the younger tectonic episodes are influenced by the fabric anisotropy, and do not permit the distinction of principal stresses during the younger tectonic events. Areas outside the high-grade gneisses would be best utilised to understand the significance and tectonic implications of the younger events. An area that has potential for understanding the nature of the younger tectonism would be in the southern Kirwanveggen where younger Urfjell Group is tectonically juxtaposed against the high-grade gneisses during a possible *ca.* 500 Ma period (Moyes *et al.*, 1997). Although the northern Kirwanveggen does not exhibit dominant *ca.* 500 Ma tectonism, this does not necessarily imply similar scenarios for other isolated high-grade gneiss outcrops within the Kirwanveggen. It is clear that re-working of tectonic fabrics during the *ca.* 500 Ma episode has occurred and that the northern Kirwanveggen may represent an older relic of the *ca.* 1100 Ma period within a dominantly re-worked *ca.* 500 Ma deformational belt. Only through significantly more detailed work within this region will this issue be resolved further. If the *ca.* 500 Ma re-working has significantly affected the northern Kirwanveggen *ca.* 1100 Ma remnant, then caution must be exercised on the tectonic significance of fabric elements generated during the older tectonic episode as re-working could re-orientate these composite fabrics.

CONCLUSIONS

- Five U-Pb SHRIMP ages have been obtained from different high-grade gneiss units within the northern Kirwanveggen.
- All the lithotectonic units provide ages reflecting the *ca.* 1100 Ma tectono-metamorphic period and are interpreted as intrusion, formation, metamorphic and deformation ages.
- Younger Rb-Sr biotite ages of *ca.* 475 Ma provide a minimum age to the deformation within the area.
- Three deformational episodes can be recognised that occur during the *ca.* 1100 ma major tectono-metamorphic cycle (D1a-c).
- Later deformation is poorly constrained and may either belong to late *ca.* 1100 Ma deformation or be related to the younger *ca.* 500 Ma tectono-metamorphic cycle.

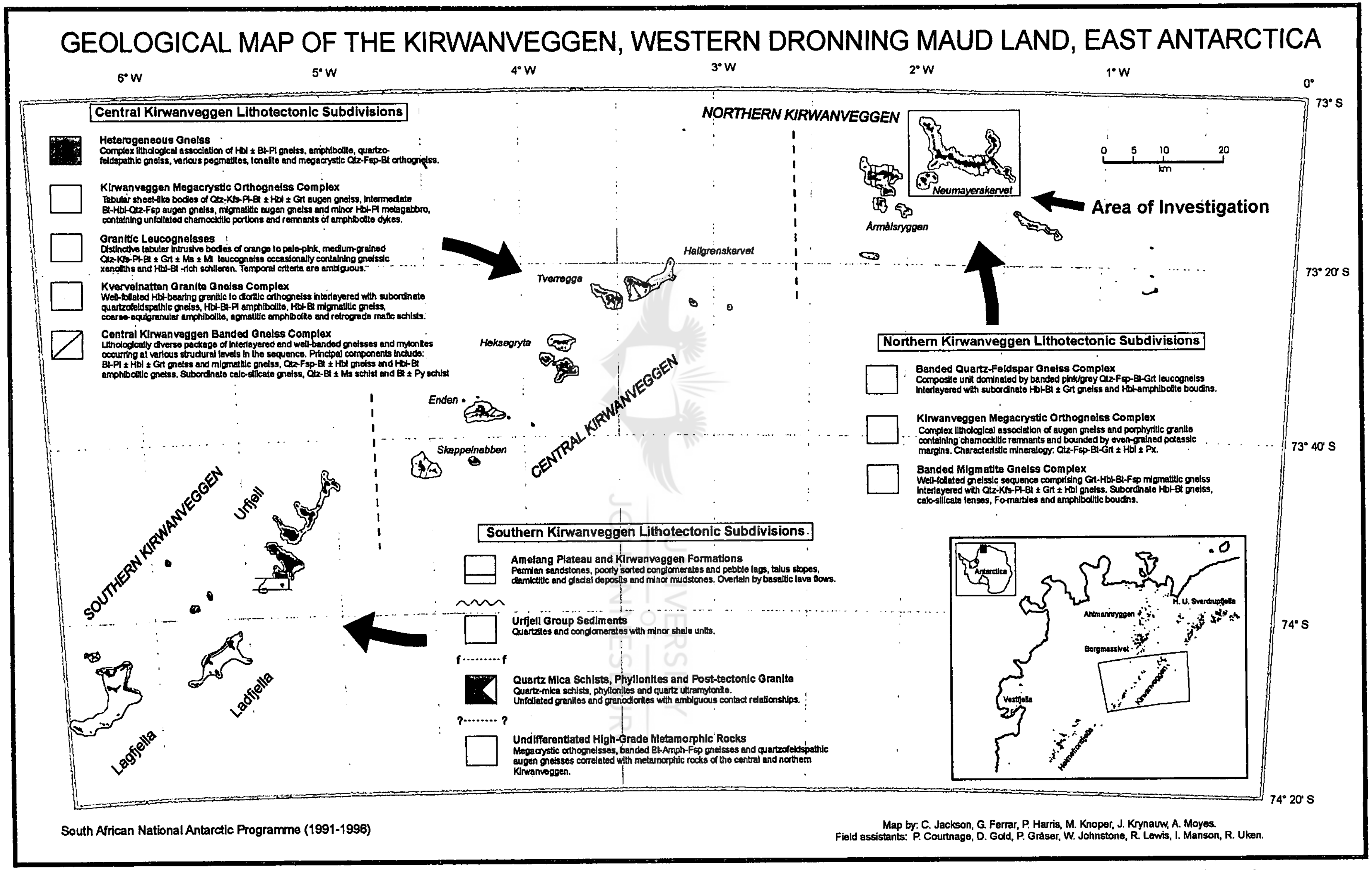

FIGURE 4.1. Geological map of the Kirwanveggen in western Dronning Maud Land, Antarctica. Outcrop regions are displayed in black on the map. The subdivision of the northern, central and southern Kirwanveggen outcrop patterns and the associated lithotectonic units are illustrated. The Neumayerskarvet outcrop pattern, which is the major area of focus in the northern Kirwanveggen, is outlined for location purposes.

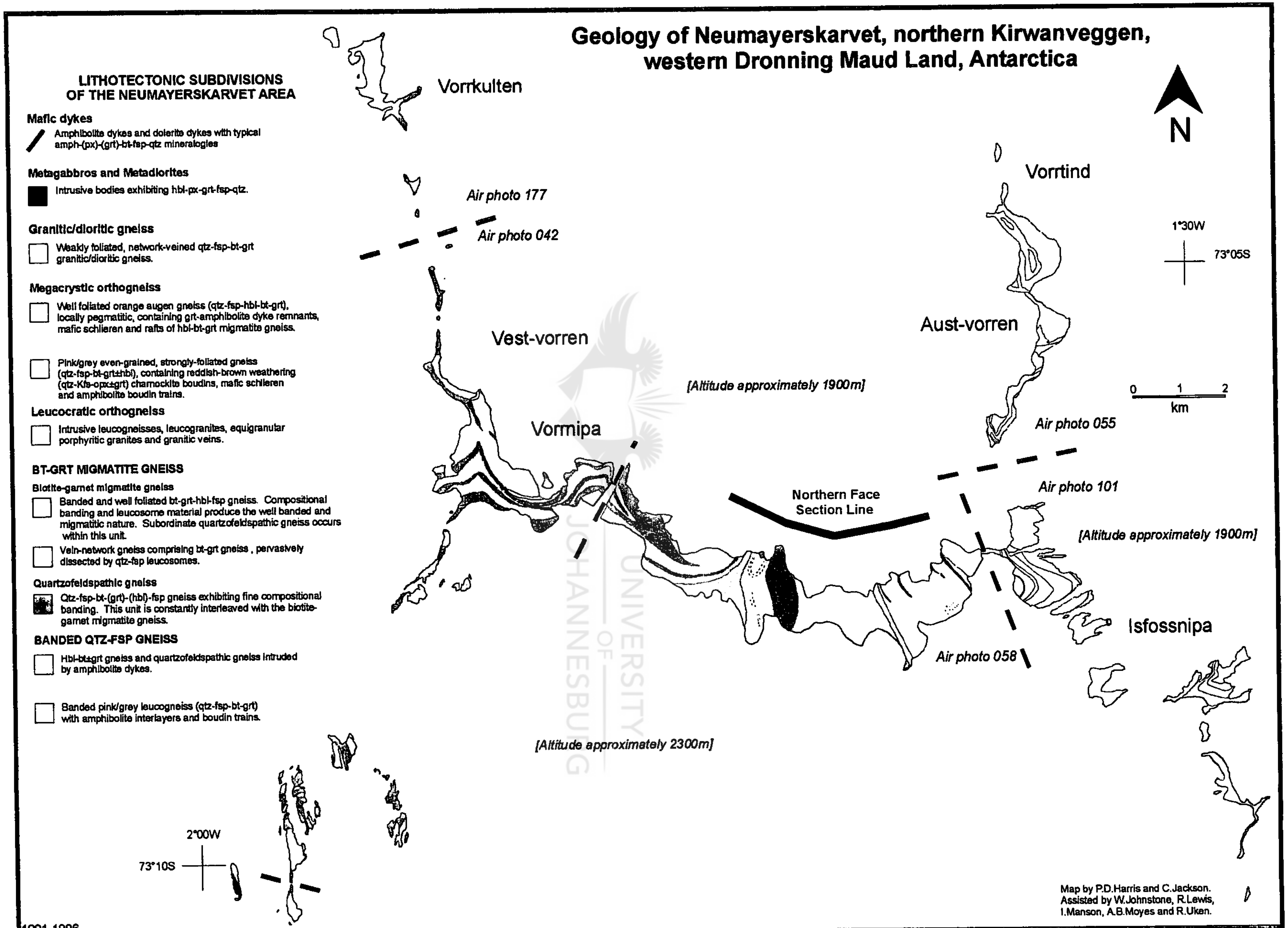

FIGURE 4.2. The geology of Neumayerskarvet in the northern Kirwanveggen. The map has been constructed using aerial photographs as no suitable topographical map at this scale is currently available. Boundaries are marked where different photographs were used for the mapping. The lithotectonic subdivision is illustrated on the map. The location of the section line displayed in Figure 4.4 is also shown on the geology map.

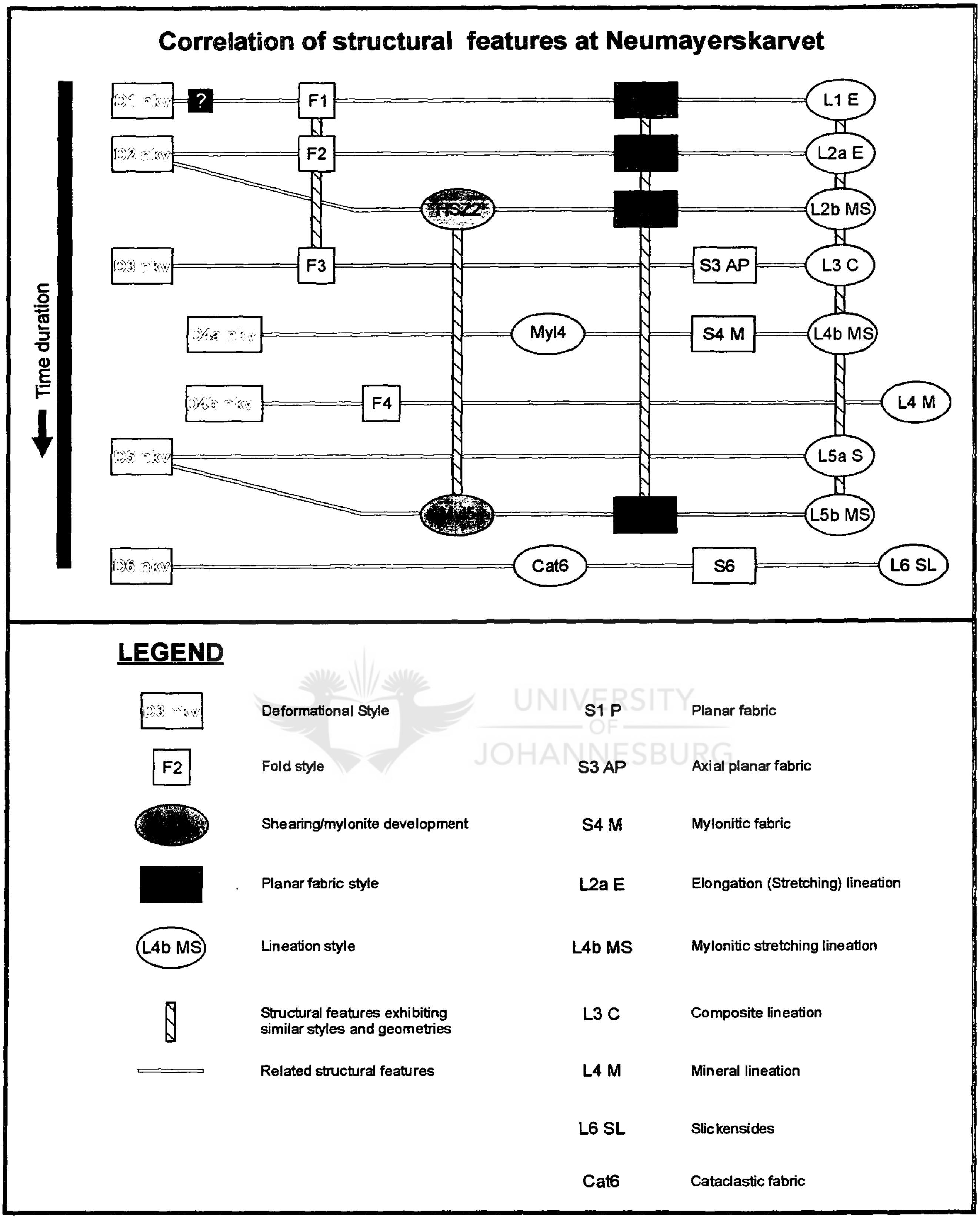

FIGURE 4.3 Illustration of the relationships between structural style, fabric elements, and their geometries, within a relative structural time framework. This diagram has been established in Chapter 3 where full details of the structural relationships and correlations are provided. These structural relationships are used to constrain the zircon samples described in this section.

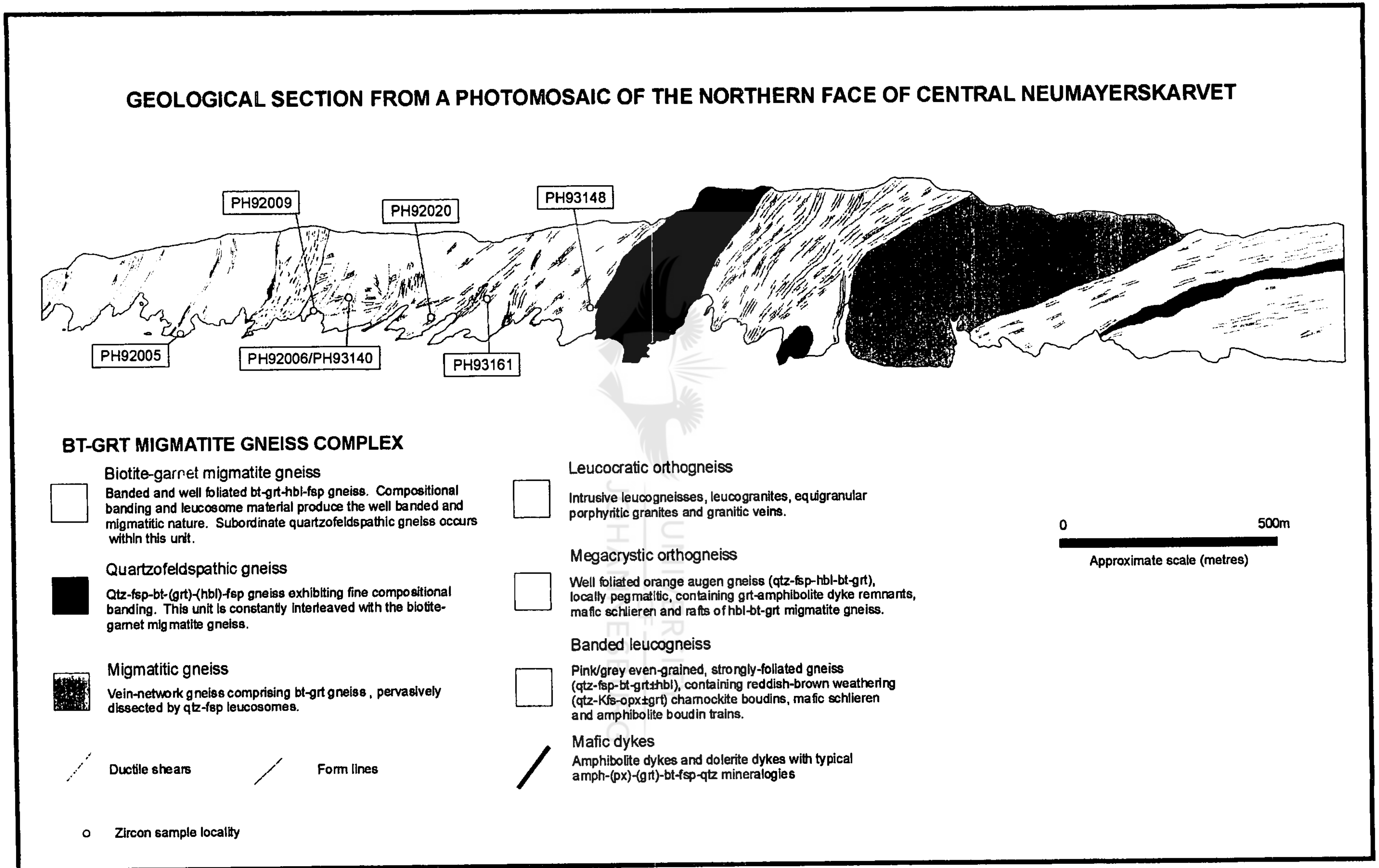

FIGURE 4.4. Cross-sectional photographic mosaic of central Neumayerskarvet showing the distribution of the different lithotectonic units. The mosaic is viewed looking southwards onto the escarpment of Neumayerskarvet. The cross-section position within the Neumayerskarvet outcrop region is shown in Figure 4.2. The sample localities for the zircon geochronological work presented within this section are also shown in this diagram.

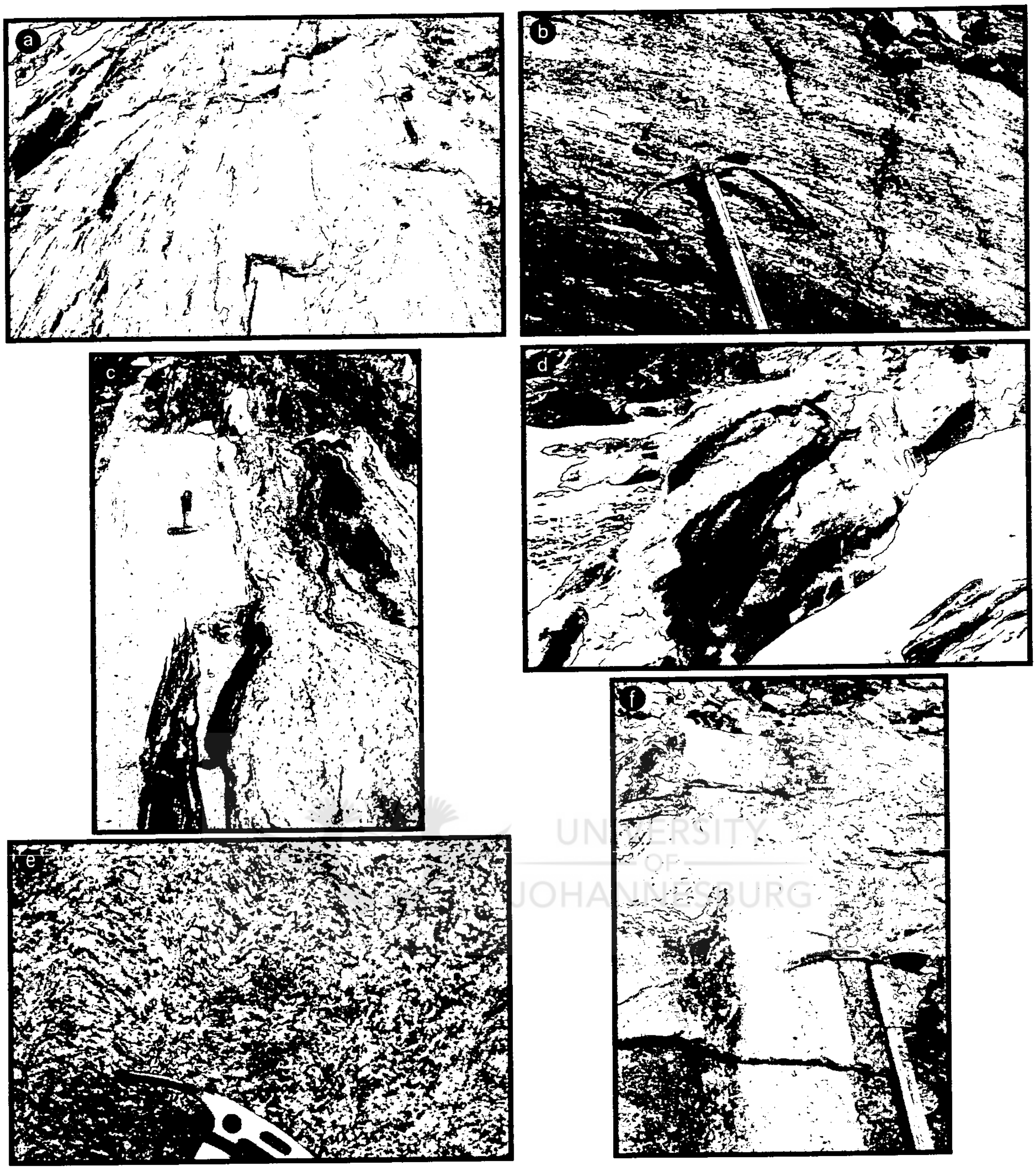

FIGURE 4.5. Photographs of the different lithotectonic units sampled for U-Pb SHRIMP analysis.
a.) Photograph of the biotite-garnet migmatite gneiss. Sample PH93161 represents the sample of this lithotectonic unit that has suitable zircon populations for the U-Pb SHRIMP investigation.
b.) Photograph of the leucosome sample (PH92009) within the biotite-garnet migmatite gneiss. The leucosomes develop within the regional gneissic foliation of the biotite-garnet migmatite gneiss.
c.) Photograph of the intrusive leucogneiss (PH93148) sample locality at Neumayerskarvet. Deformational relationships for this lithotectonic unit are discussed later.
d.) Photograph of the typical kyanite-bearing leucogneiss found at Neumayerskarvet. The leucogneiss intrudes into the biotite-garnet migmatite gneiss but is subsequently deformed. Sample PH92020, used for the zircon analysis, is from this lithotectonic unit.
e.) Photograph of the megacrystic orthogneiss exposed at Neumayerskarvet. This sample displays the typical megacrystic nature of this lithotectonic unit. The sample used for the U-Pb SHRIMP analysis is PH92005.
f.) Photograph of the pegmatitic veins that crosscut the regional foliations within the biotite-garnet migmatite gneiss at Neumayerskarvet (PH92006/PH93140).

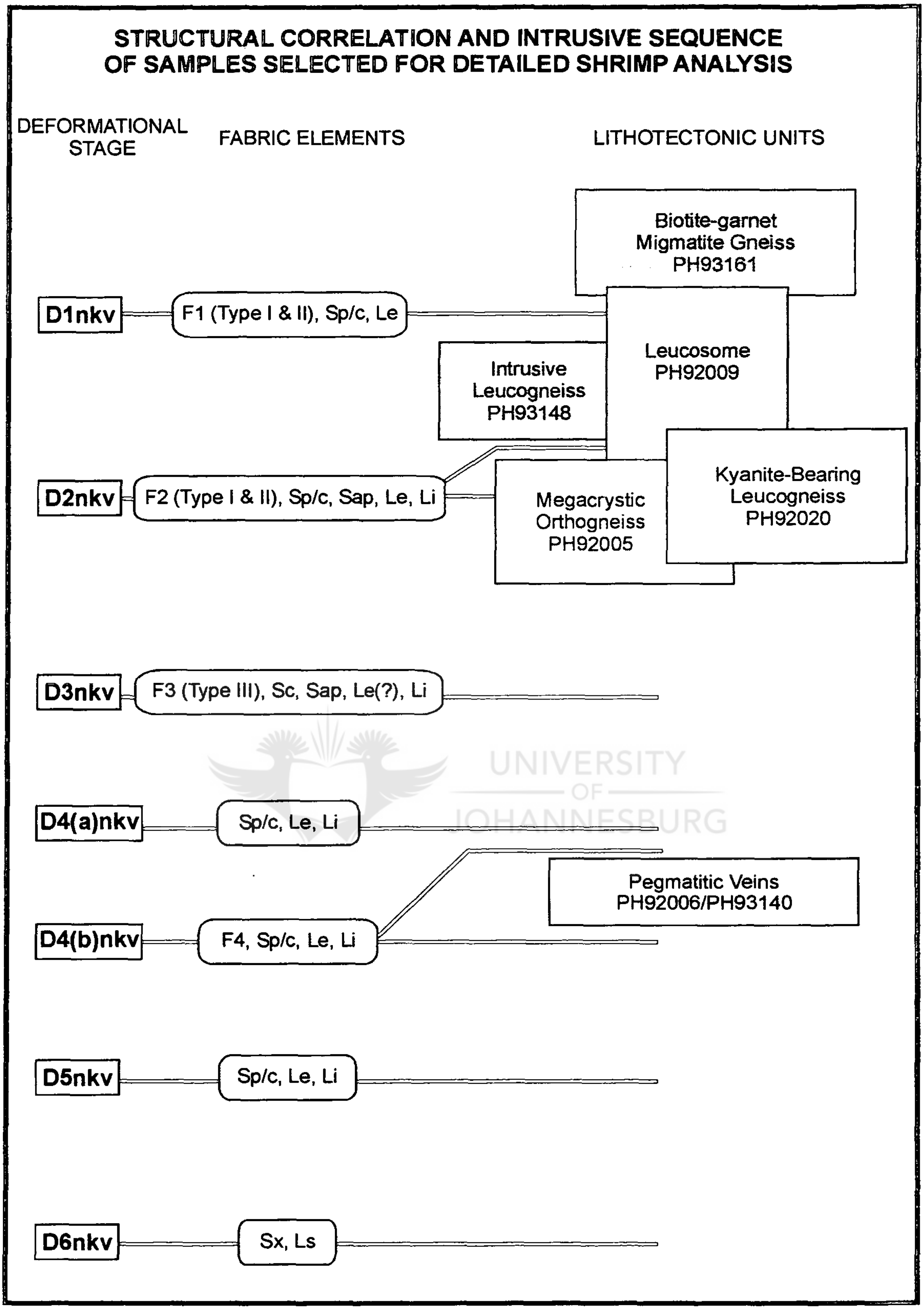

FIGURE 4.6. Structural correlation and intrusive positions of the samples selected for the zircon isotope investigation. Fabric codes displayed are: planar composite foliations (Sp/c), axial planar foliations (Sap), cataclastic foliations (Sx), elongation lineations (Le), intersection lineations (Li) and slickensides (Ls). Fold sequences observed at Neumayerskarvet are described as F1 to F4. Detailed discussion of the fabric elements and relationships are provided in Chapter 3.

D2nkv Deformation Stage at Neumayerskarvet

The photograph displays intrusive leucogneiss intruding across a pre-existing foliation in the biotite-garnet migmatite gneiss but is itself deformed during the D2nkv deformation stage.

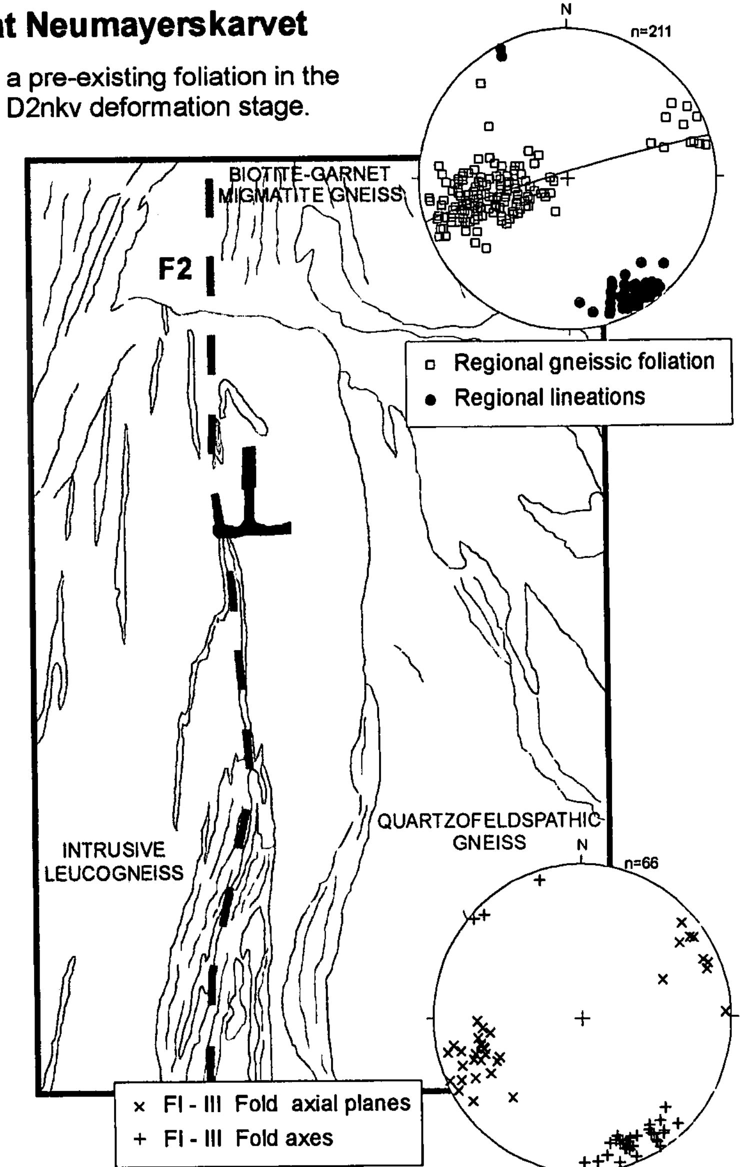

FIGURE 4.7. Structural relationships displayed by the intrusive leucogneiss at Neumayerskarvet. The location is illustrated on Figure 4.4. The diagram displays the relationship between the D1nkv and D2nkv deformational stages where the intrusive leucogneiss is the marker unit between these stages. The colinear nature of the two deformational stages is displayed by the geometrical fabric element data.

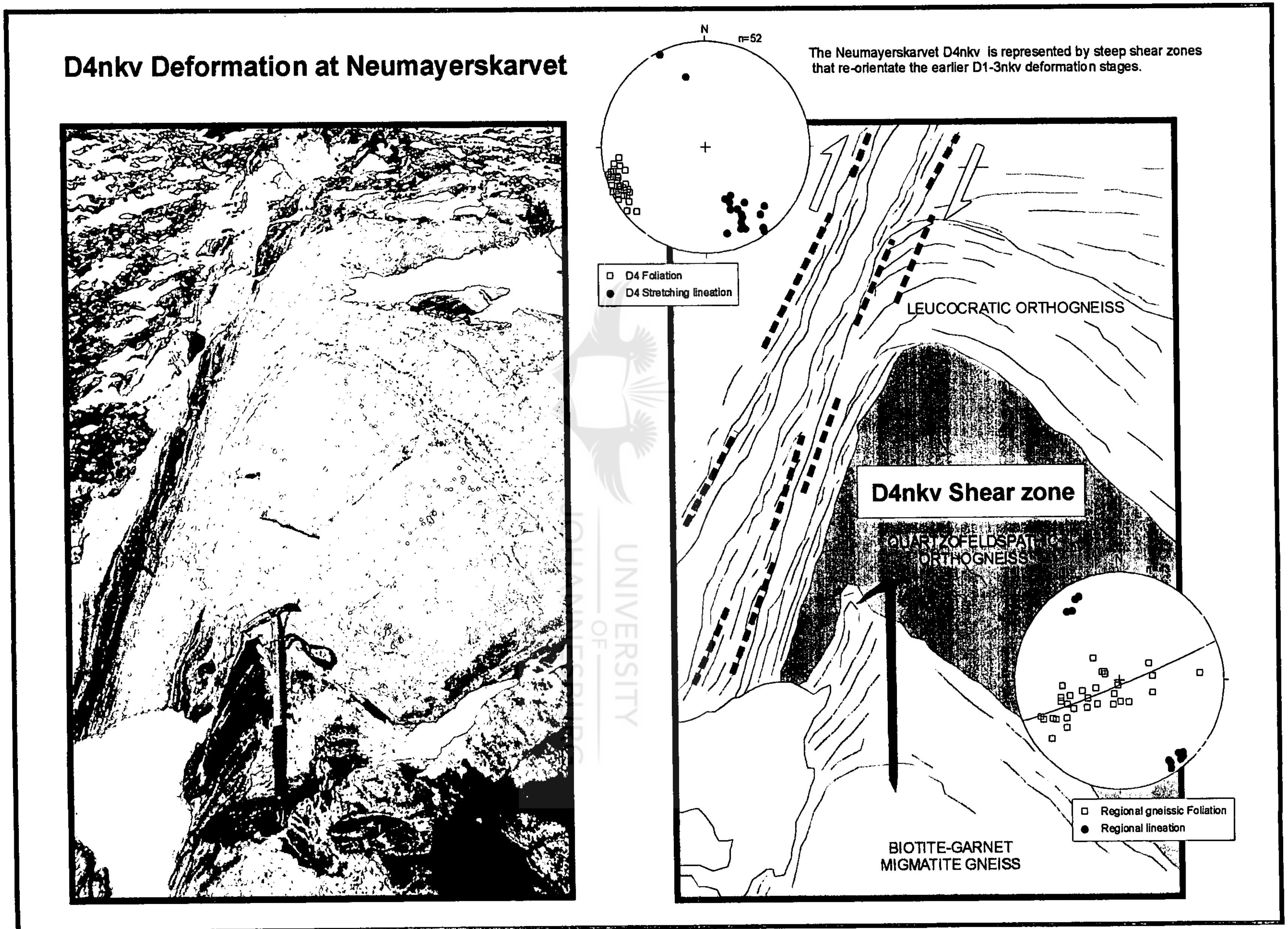

FIGURE 4.8. Illustration of the D4nkv deformational stage and its influence on the lithotectonic units. The pegmatitic veins (not illustrated in this diagram) crosscut these D4nkv discrete structures. Geometrical relationships of the various fabrics are also illustrated for clarity.

D5nkv Deformation Stage at Neumayerskarvet

The Neumayerskarvet D5nkv deformation stage is coplanar and colinear to earlier D1-3nkv fabrics which are reworked. Reorientation and mylonitisation of a late crosscutting pegmatite allows for distinction of the D5nkv stage.

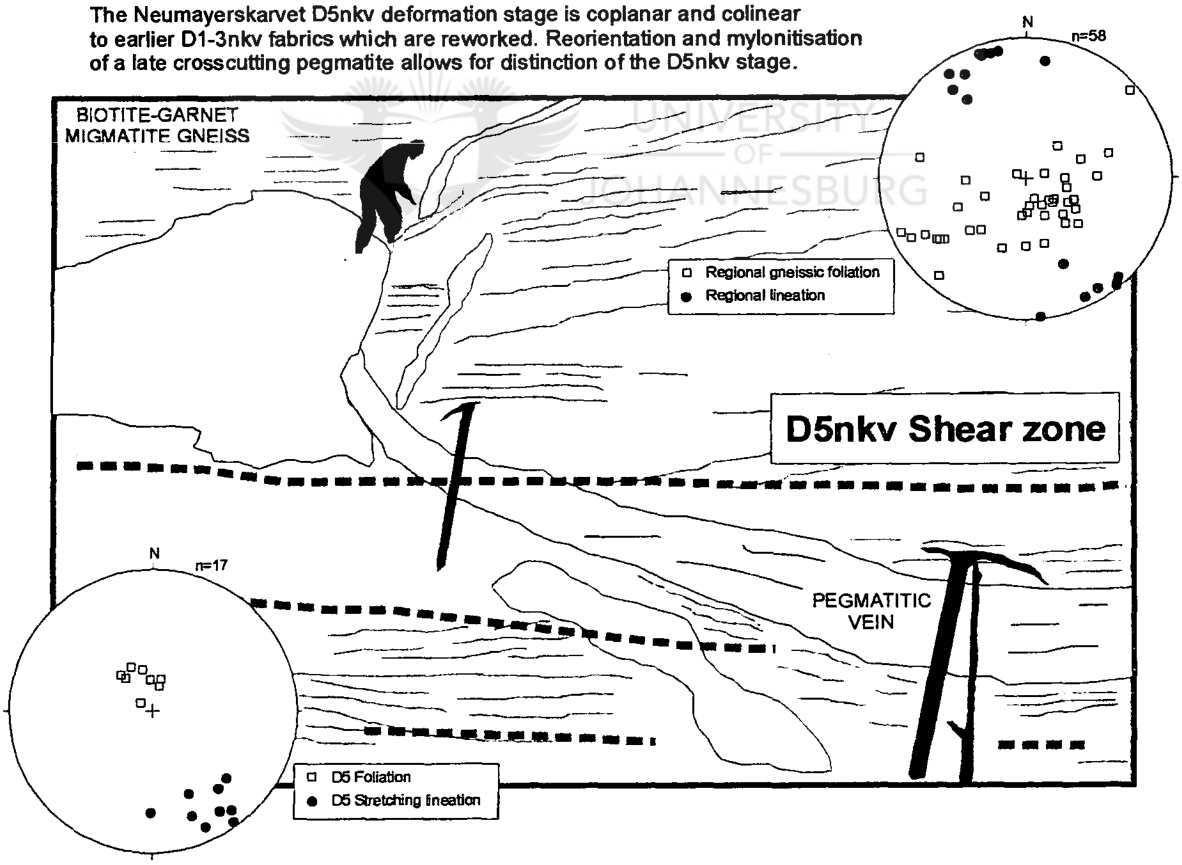

FIGURE 4.9. Illustration of the D5nkv deformational stage deforming the pegmatitic vein. The vein crosscuts the D4nkv deformational stage fabrics and is an intrusive marker between the D4nkv and D5nkv deformational stages.

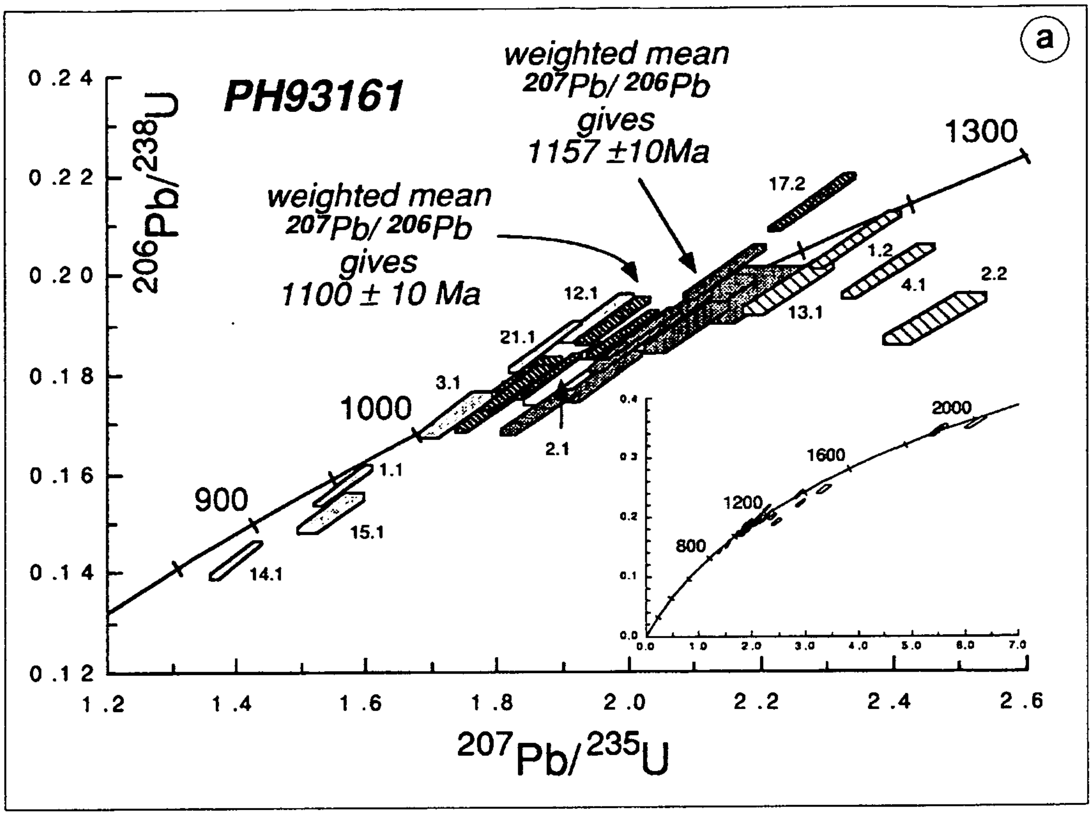

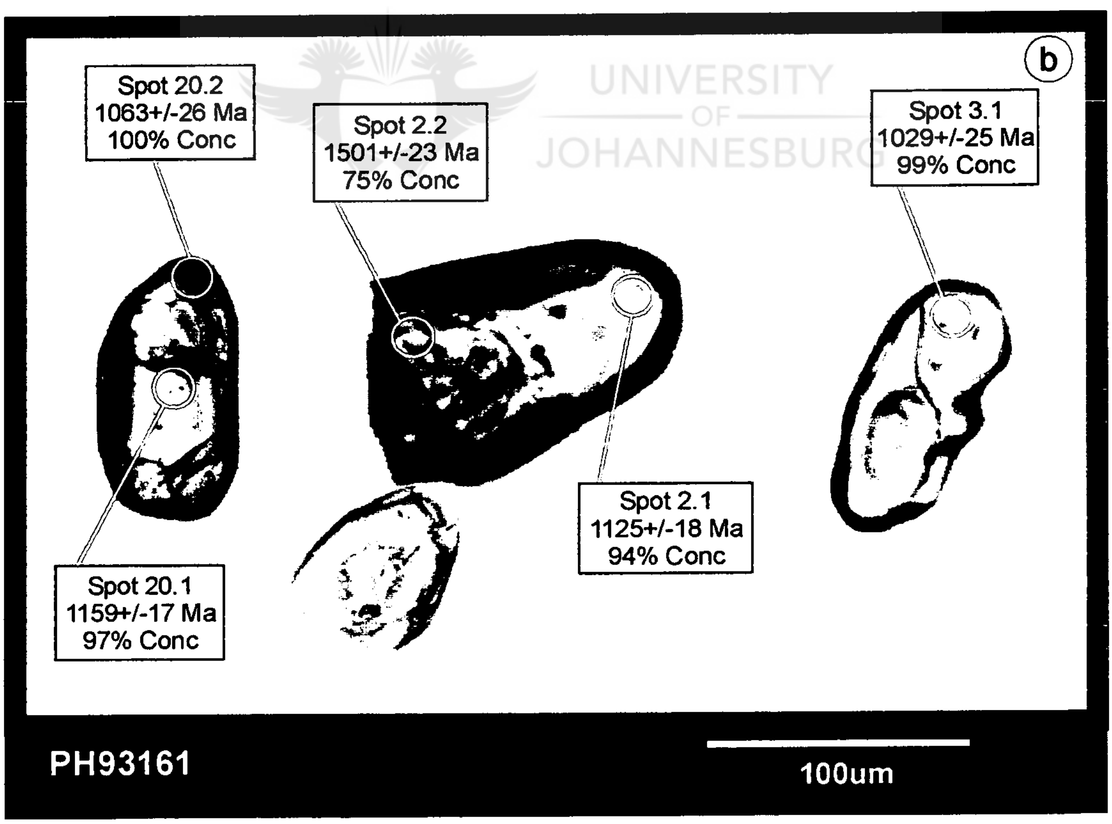

FIGURE 4.10a & b. Zircon concordia diagram and typical zircons analysed from the biotite-garnet migmatite gneiss (PH93161). The Pb-Pb ages with their individual errors, and the percentage concordance (Conc) are provided for each spot analysis.

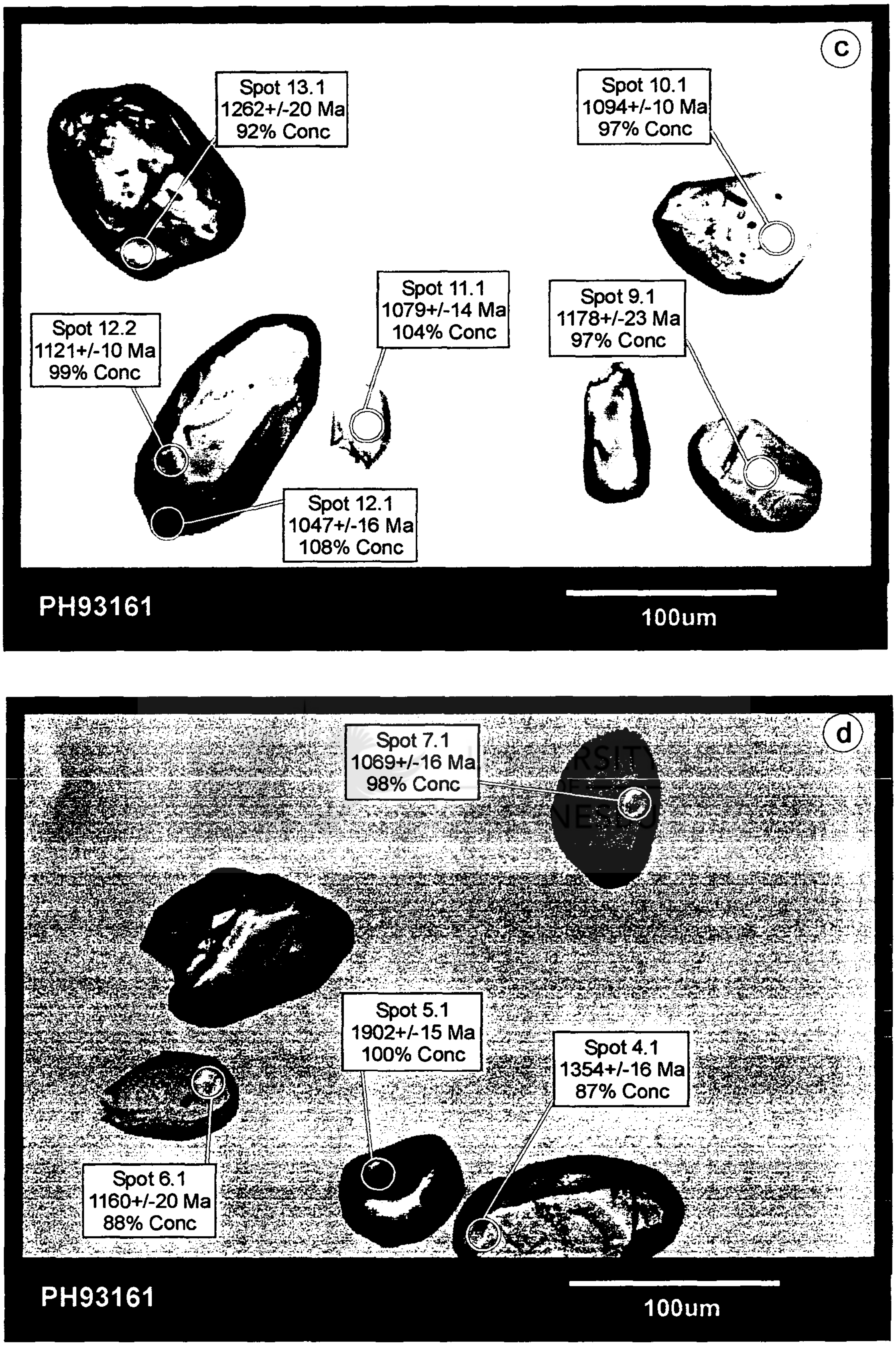

Figure 4.10c & d. Photographs of a selection of zircons analysed from the biotite-garnet migmatite gneiss sample PH93161. The Pb-Pb ages with their individual errors, and the percentage concordance (Conc) are provided for each spot analysis.

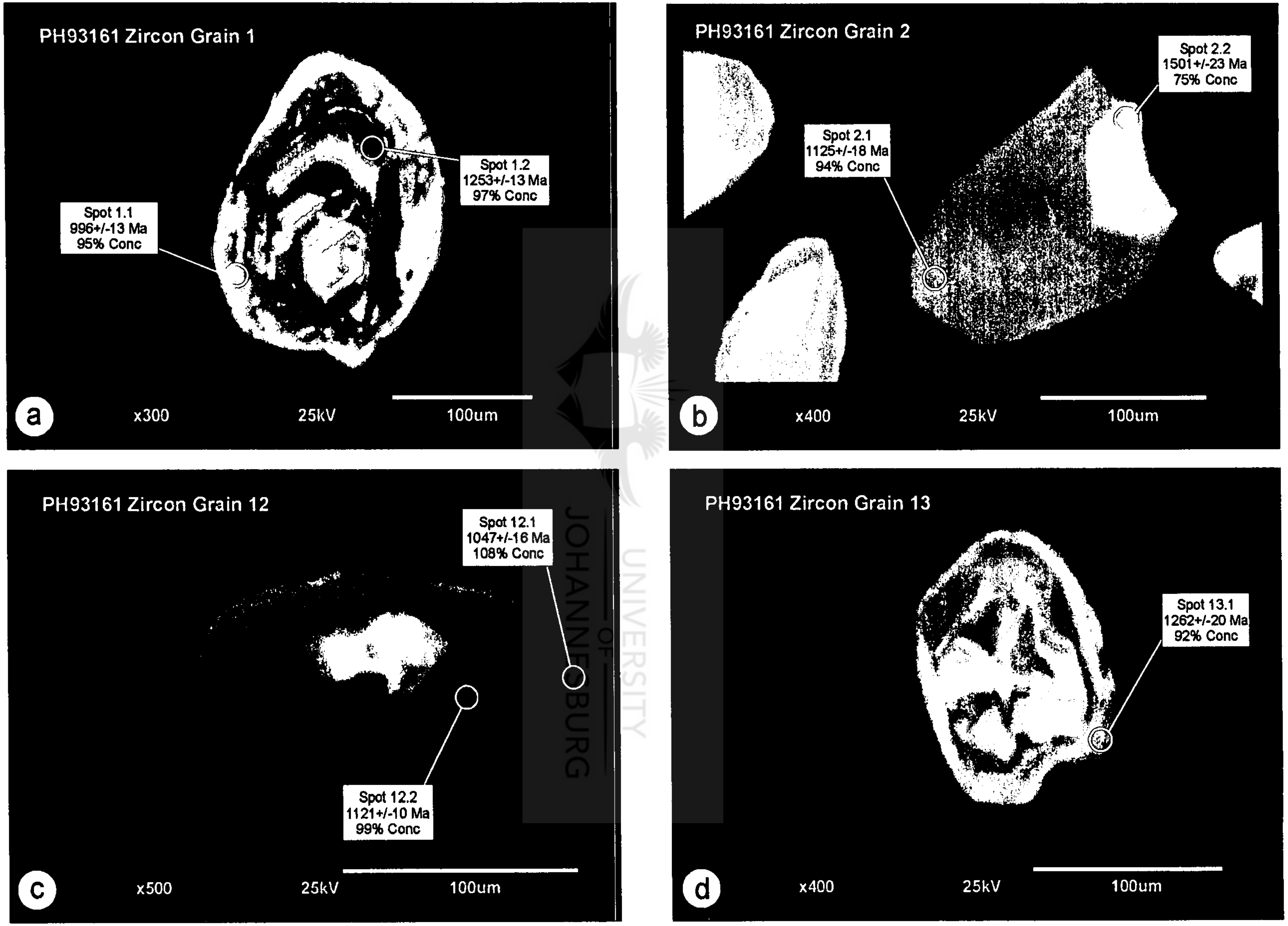

FIGURE 4.11. Cathodoluminescence of zircons from the biotite-garnet migmatite gneiss (PH93161). SHRIMP probe spots for these samples are illustrated on the photographs. The Pb-Pb ages and their individual errors are also provided, as well as an indication of the percentage concordance (Conc) for each spot.

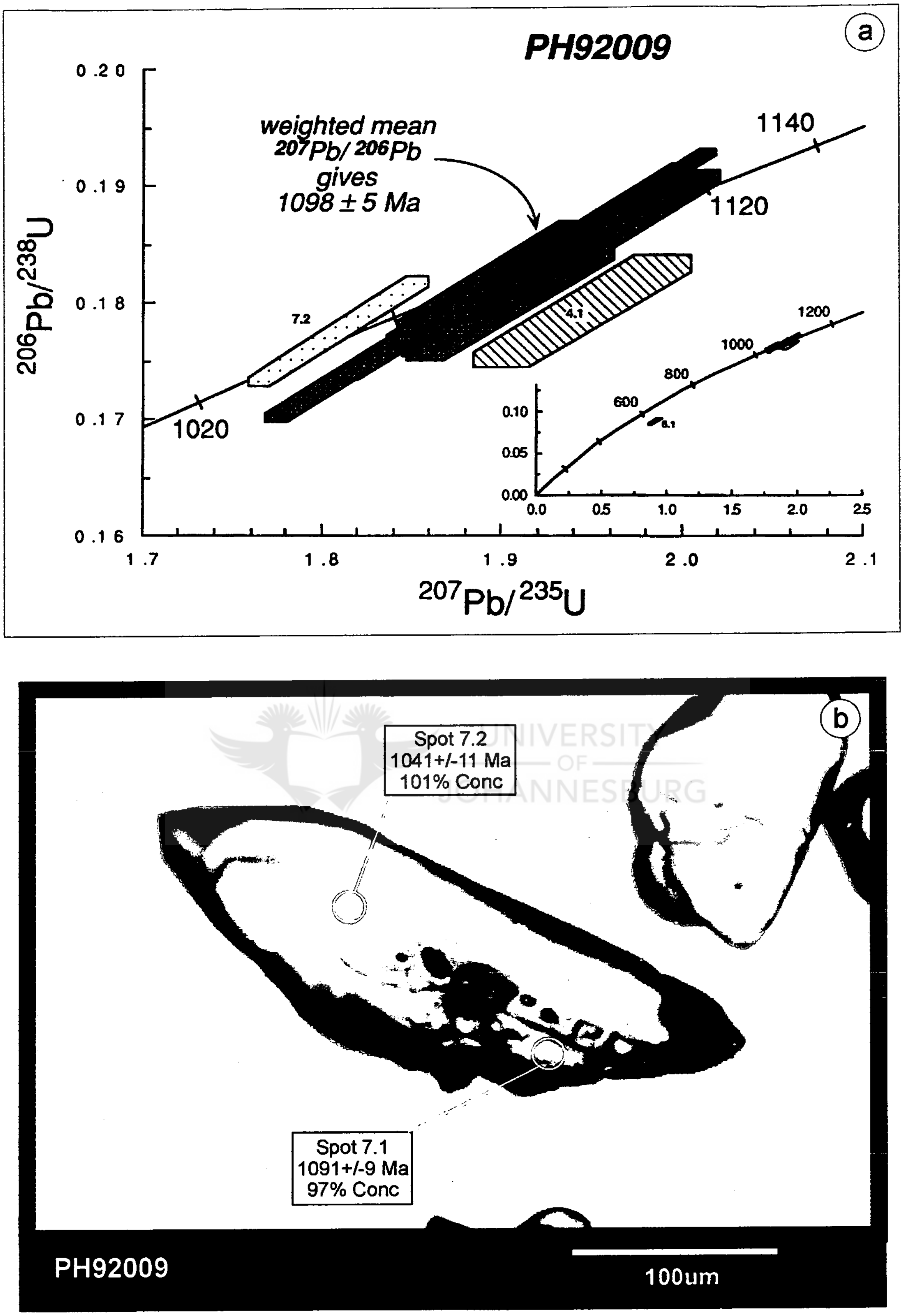

FIGURE 4.12a & b. Zircon concordia diagram and photographs of zircons analysed from the leucosome in the biotite-garnet migmatite gneiss (PH92009). The Pb-Pb ages with their individual errors, and the percentage concordance (Conc) are provided for each spot.

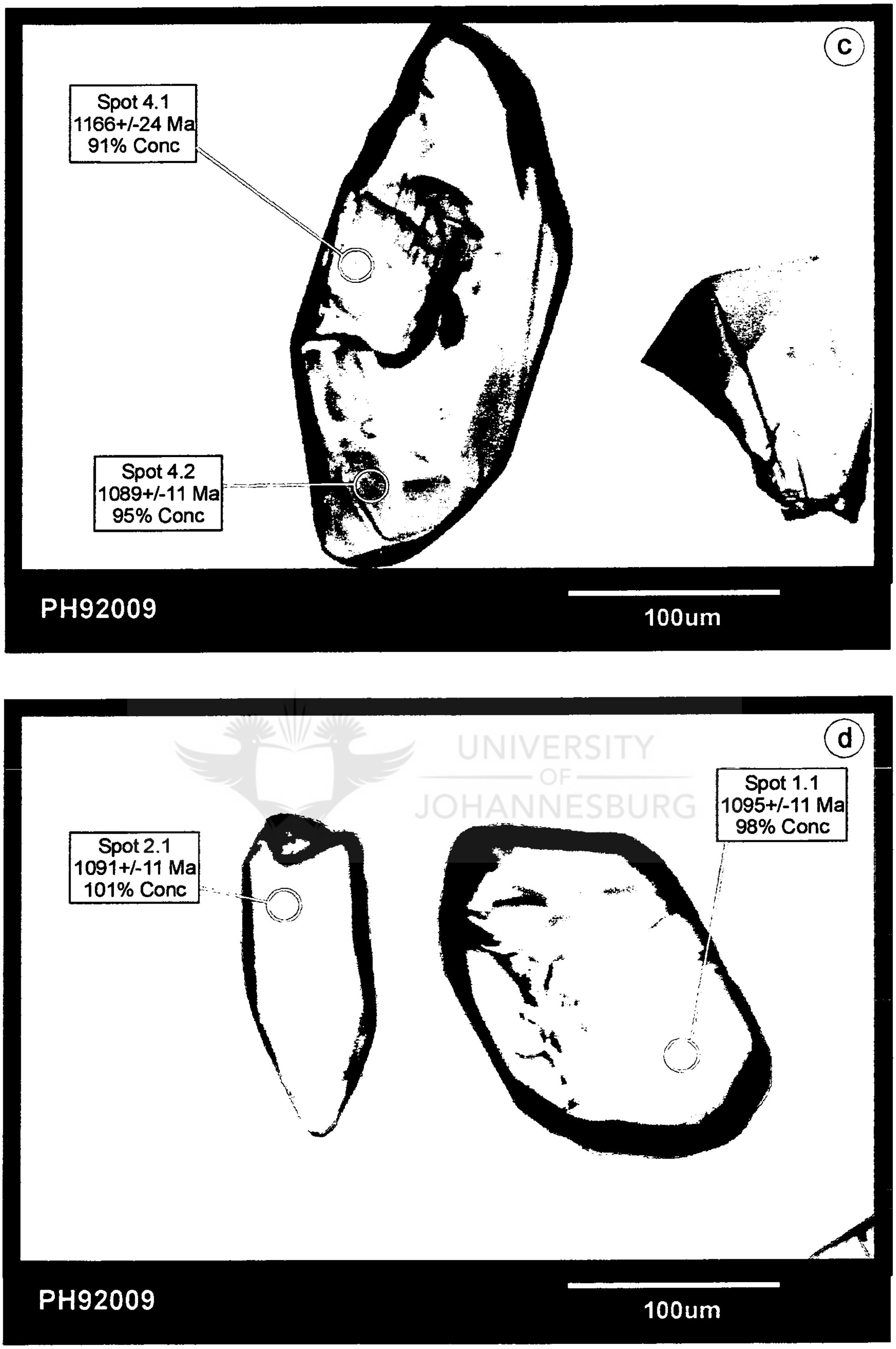

Figure 4.12c & d. Photographs of typical zircons analysed from the leucosome in the biotite-garnet migmatite gneiss (PH92009). The Pb-Pb ages with their individual errors, and the percentage concordance (Conc) are provided for each spot analysis.

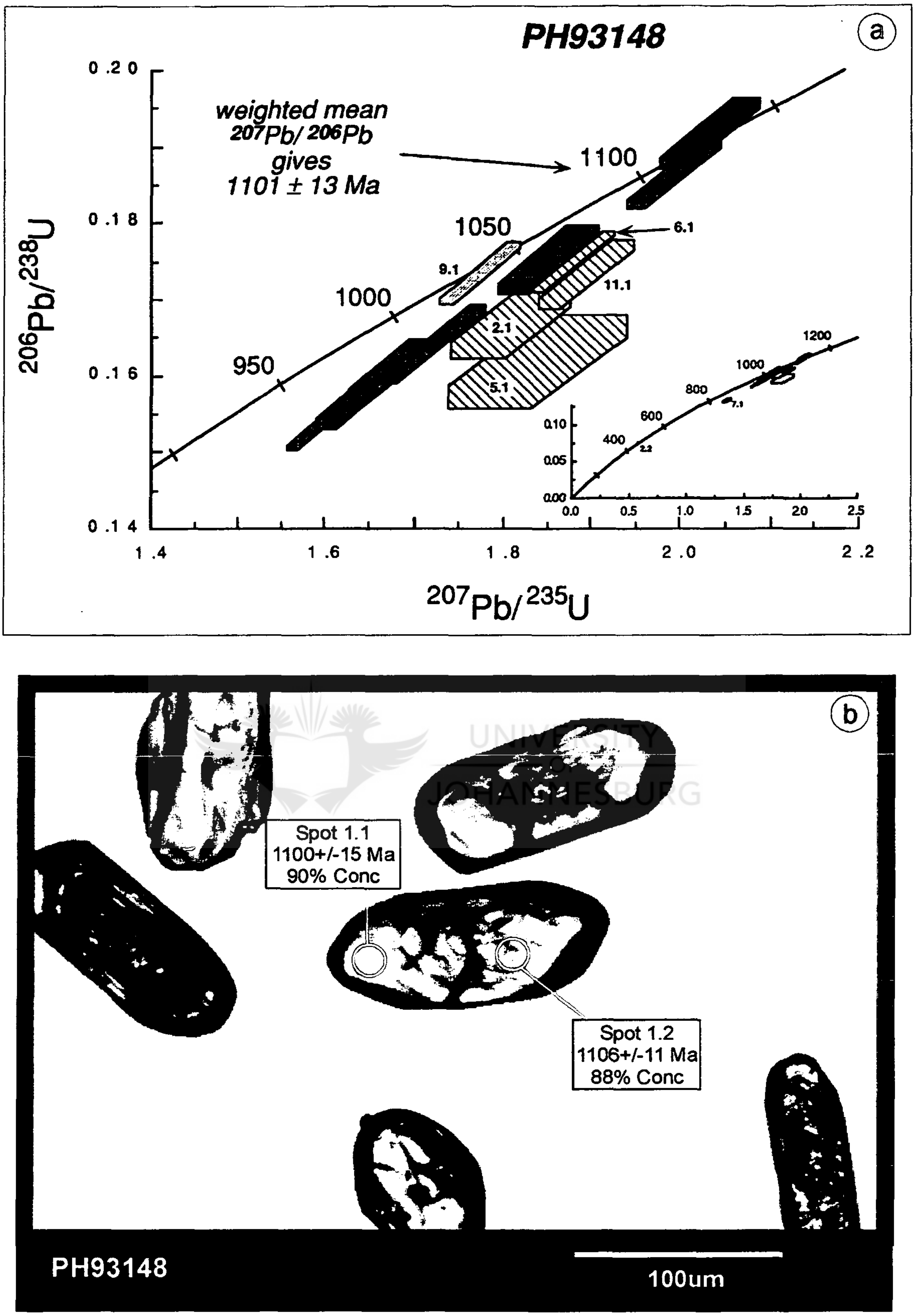

FIGURE 4.13a & b. Zircon concordia diagram and photographs of typical zircon analysed from the intrusive leucogneiss (PH93148). The Pb-Pb ages with their individual errors, and the percentage concordance (Conc) are provided for each spot analysis.

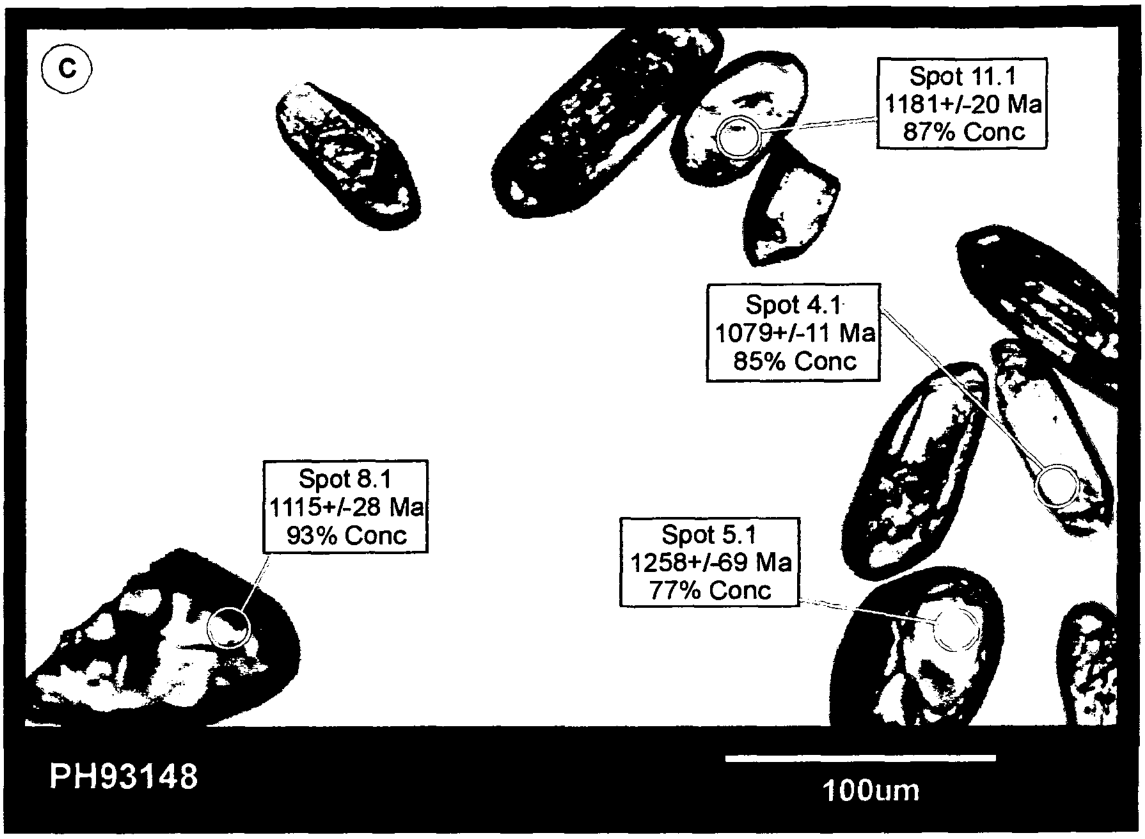

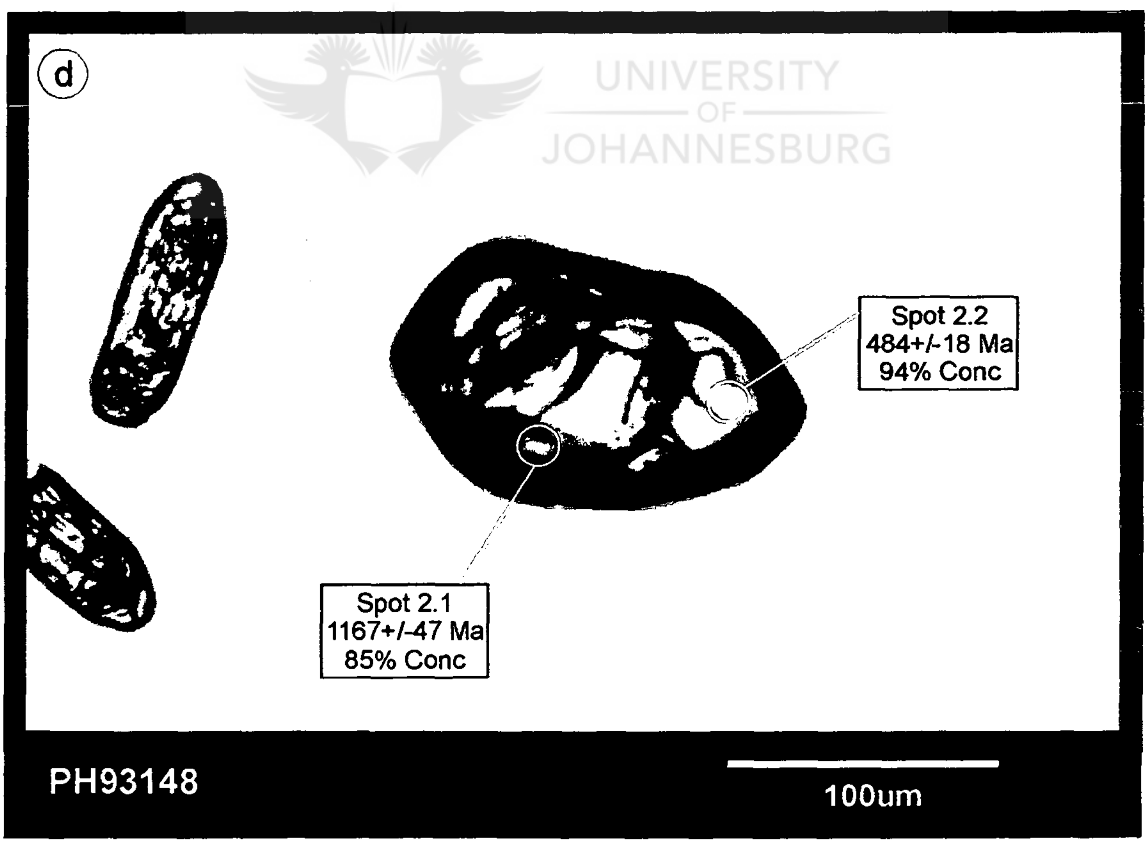

Figure 4.13c & d. Photographs of zircons analysed from the intrusive leucogneiss sample PH93148. The Pb-Pb ages with their individual errors, and the percentage concordance (Conc) are provided for each spot analysis.

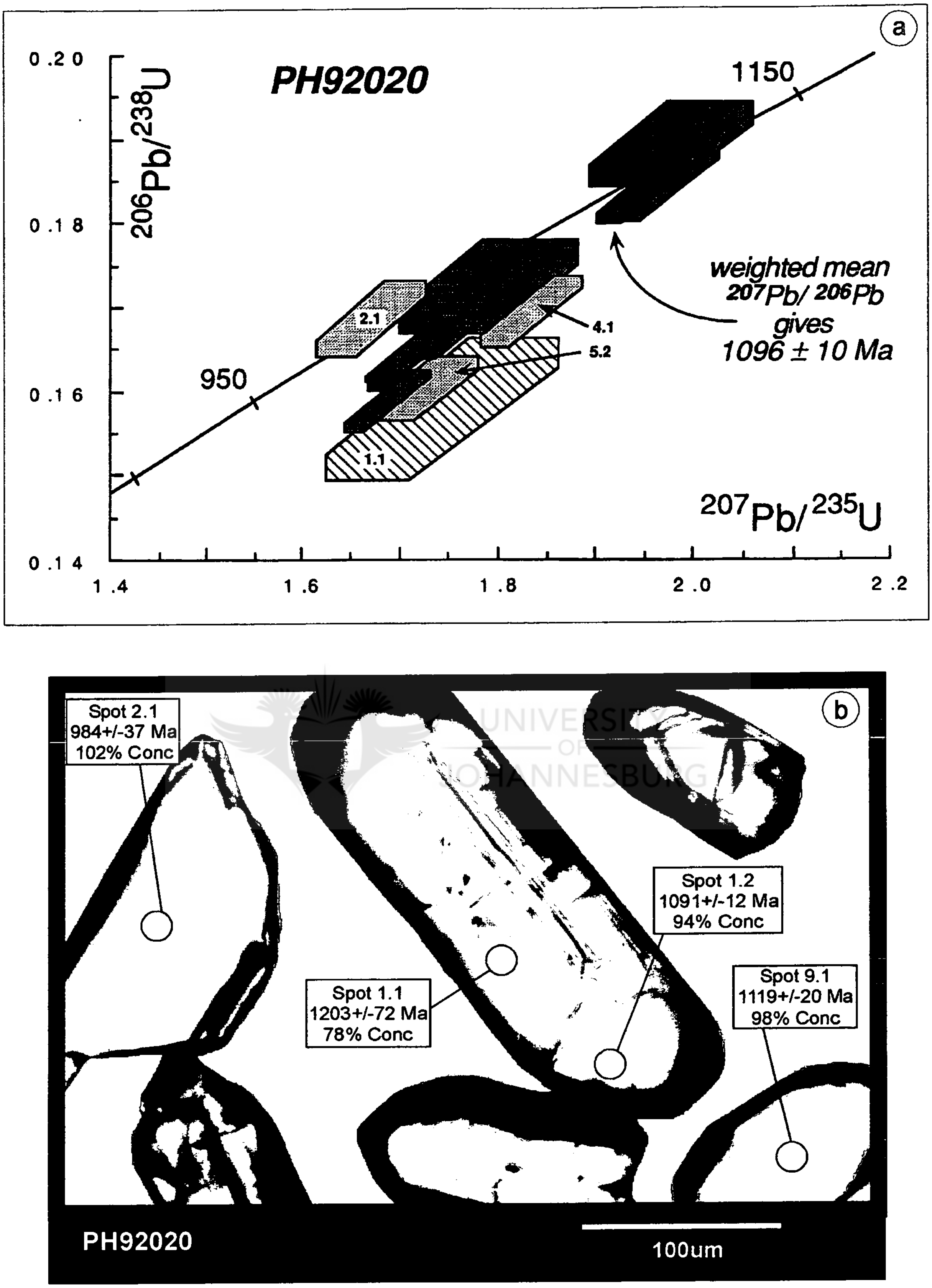

FIGURE 4.14. Zircon concordia diagram and photograph of typical zircons analysed from the kyanite-bearing leucogneiss (PH92020). The Pb-Pb ages with their individual errors, and the percentage concordance (Conc) are provided for each spot analysis.

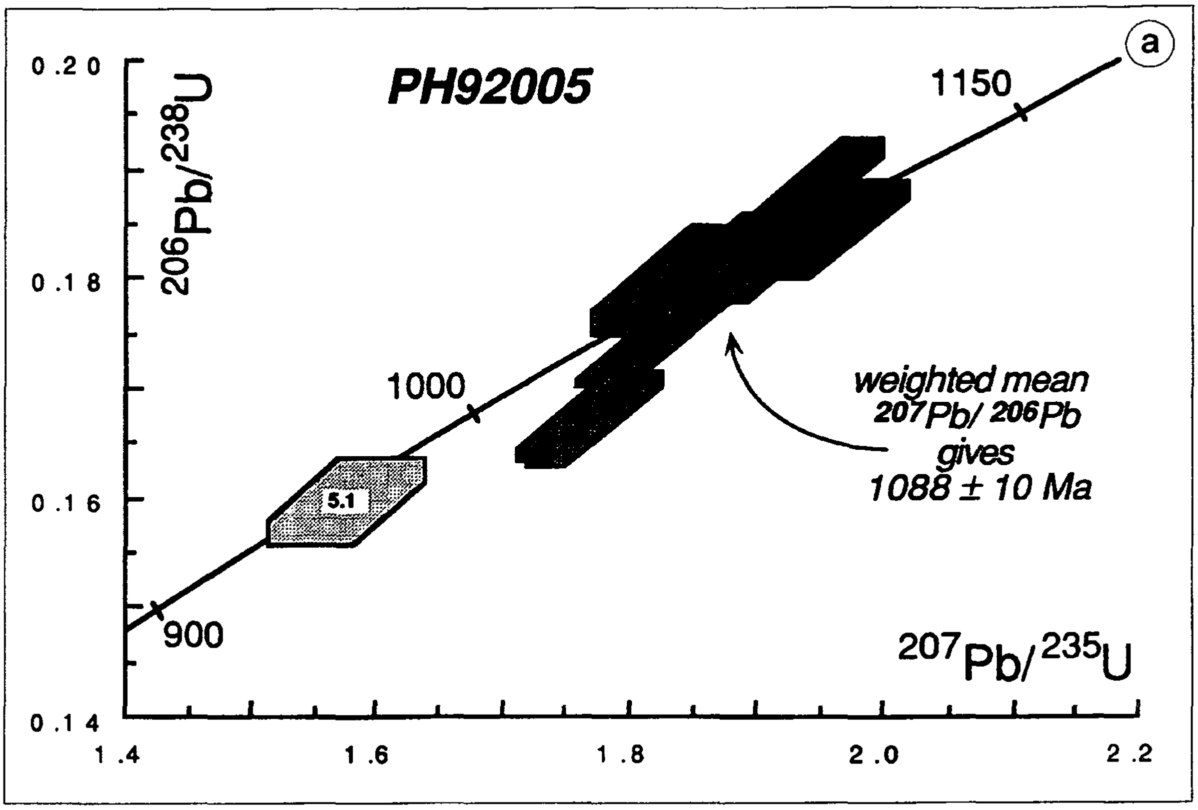

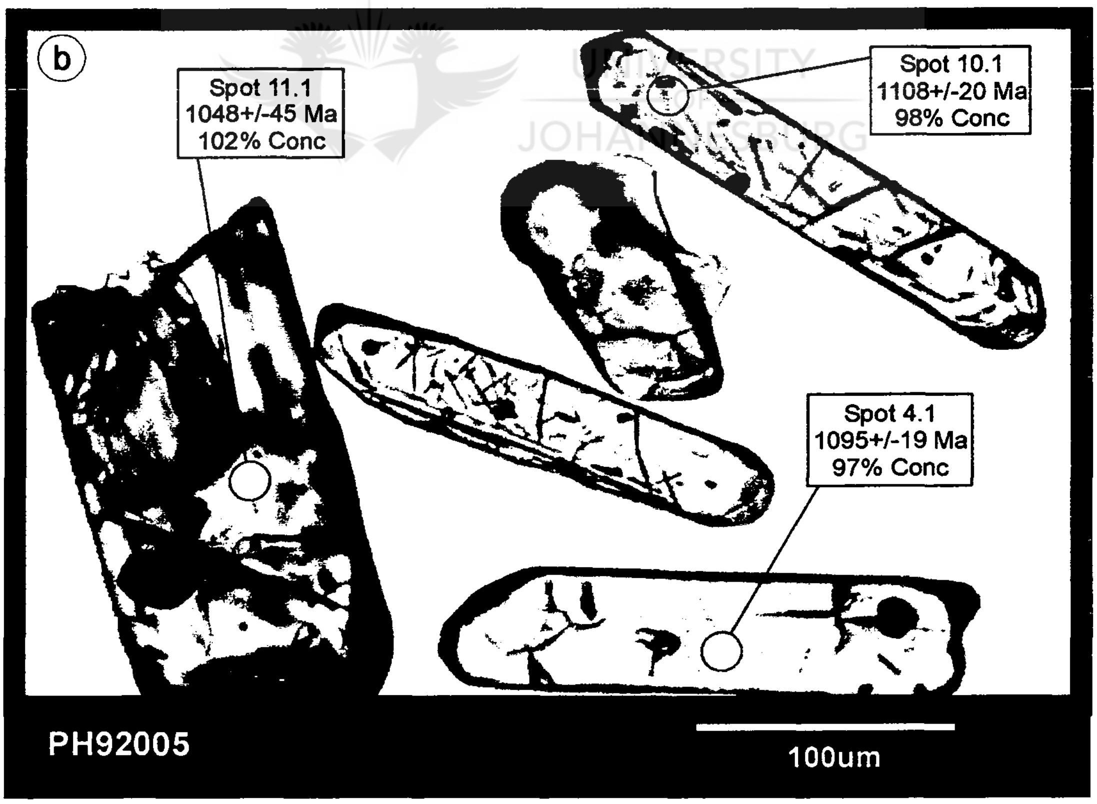

FIGURE 4.15. Zircon concordia diagram and photograph of typical zircons analysed from the megacrystic orthogneiss (PH92005). The Pb-Pb ages with their individual errors, and the percentage concordance (Conc) are provided for each analysis.

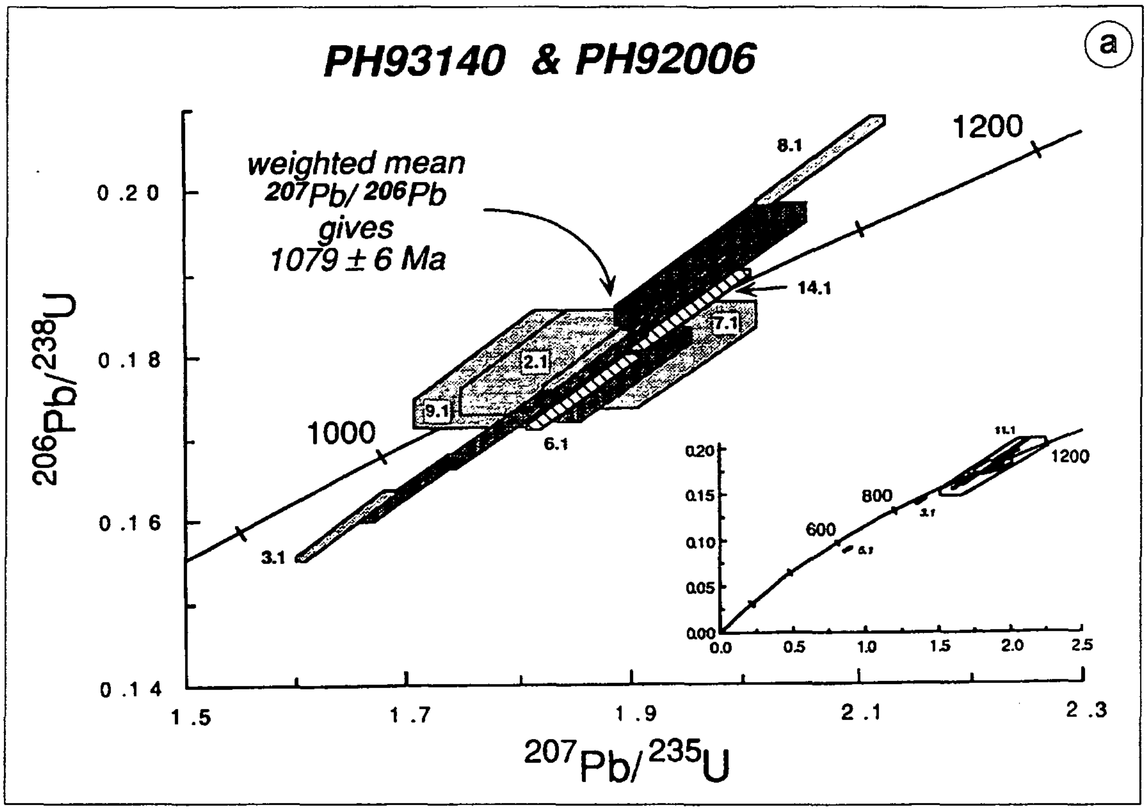

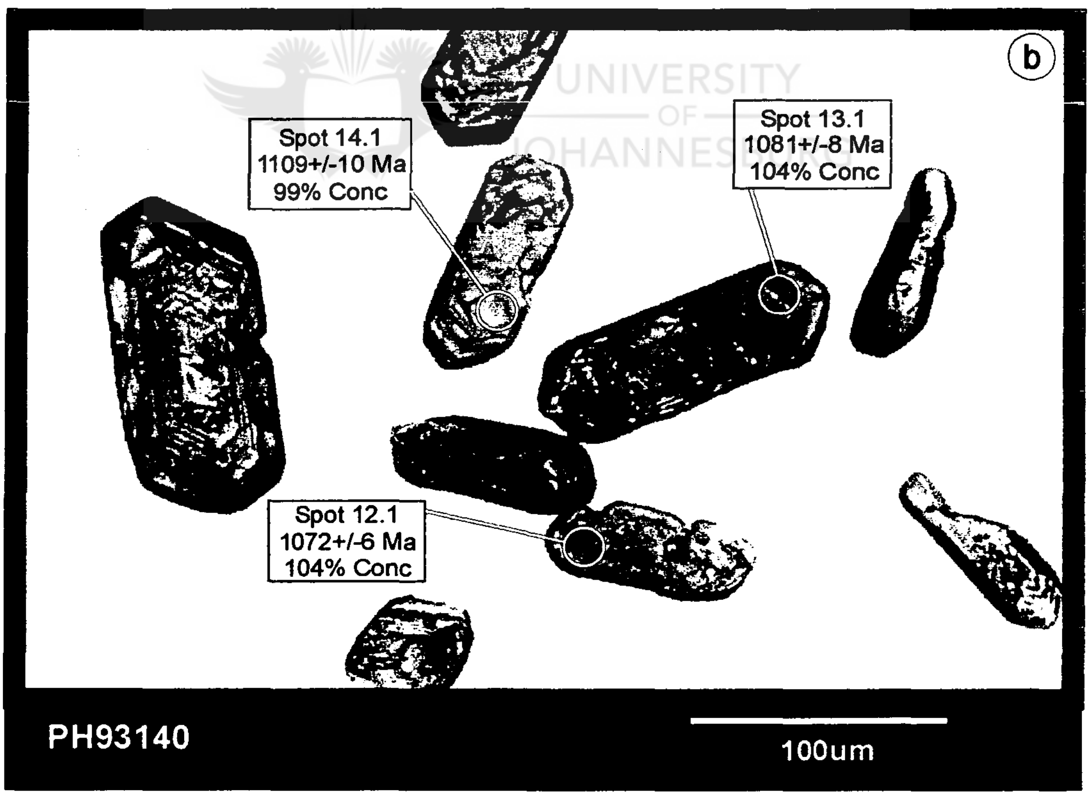

FIGURE 4.16. Zircon concordia diagram and photograph of typical zircons analysed from the pegmatitic veins (PH92006/PH93140). The Pb-Pb ages with their individual errors, and the percentage concordance (Conc) are provided for each spot analysis.

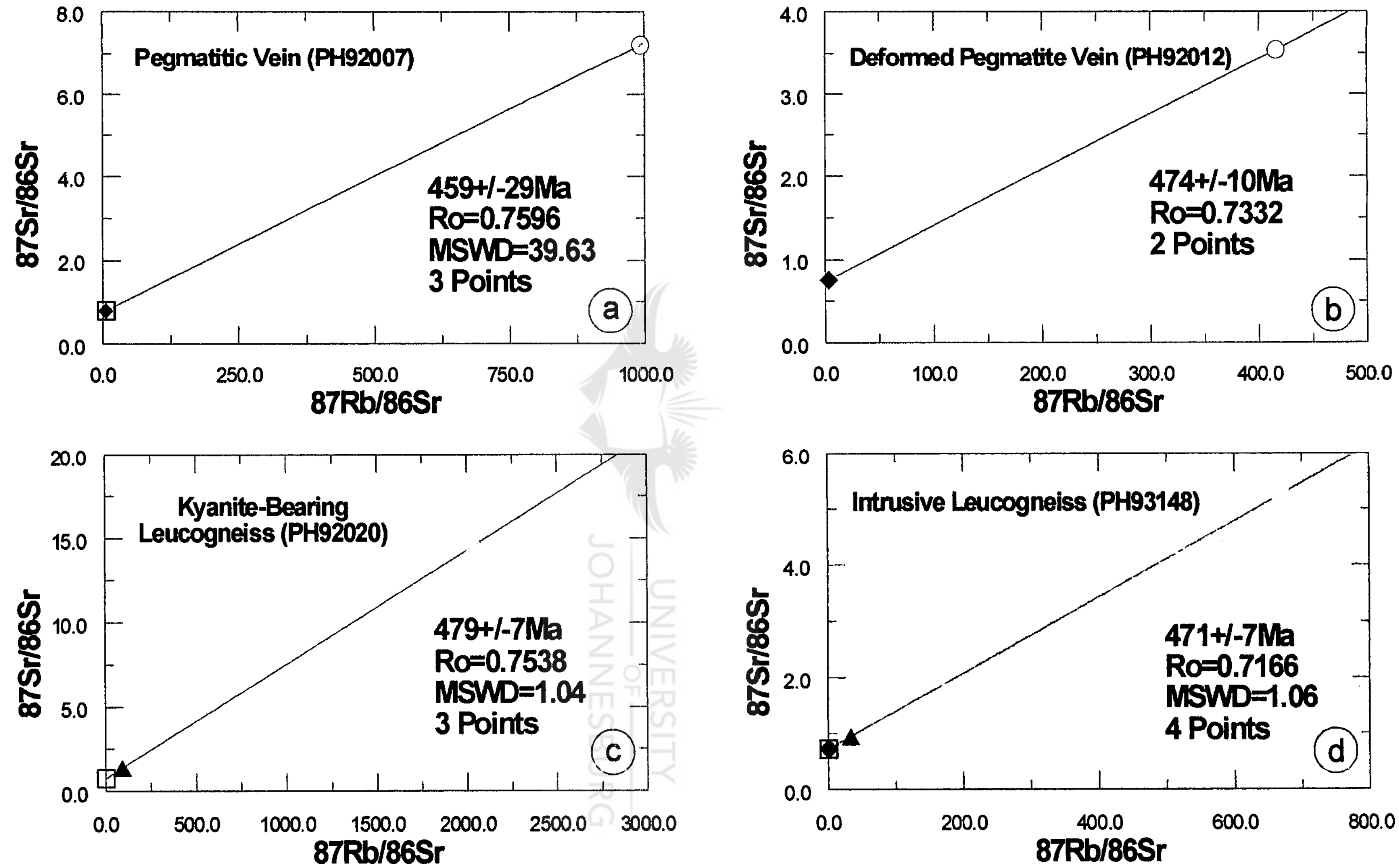

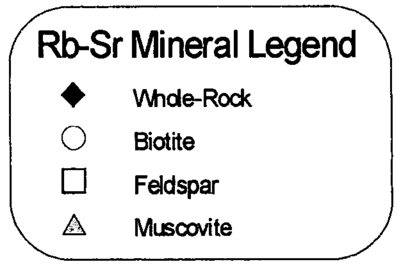

FIGURE 4.17. Rb-Sr isochron diagrams for mineral separates from a pegmatite vein (PH92007), the deformed section of the pegmatite vein (PH92012), the kyanite-bearing leucogneiss (PH92020) and the intrusive leucogneiss (PH93148).

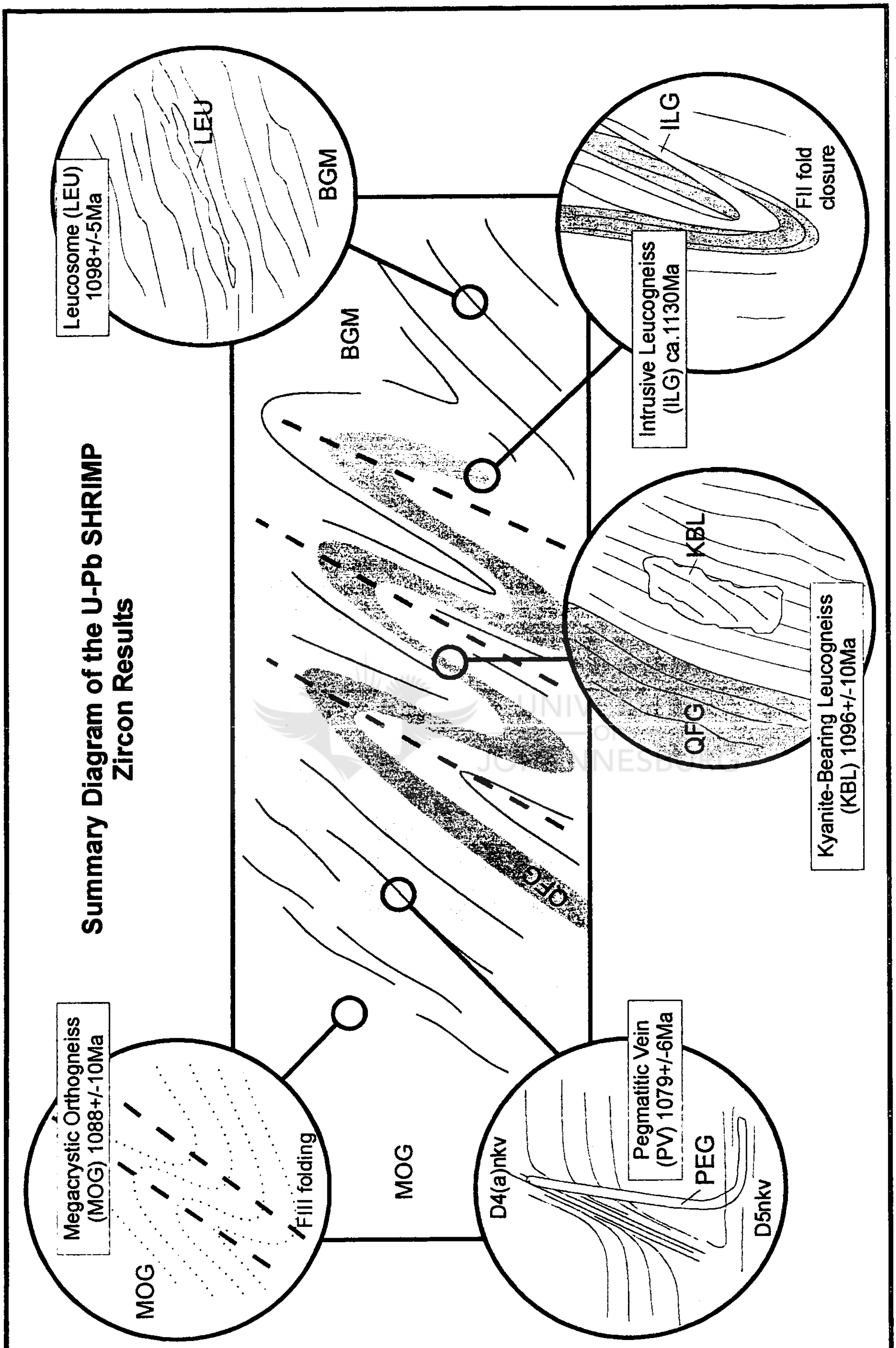

FIGURE 4.18. Summary diagram of zircon ages and structural elements recognised at Neumayerskarvet in the northern Kirwanveggen. Rock units displayed on the diagram are: biotite-garnet migmatite gneiss (BGM), quartzofeldspathic gneiss (QFG), a leucosome unit (LEU), intrusive leucogneiss (ILG), kyanite-bearing leucogneiss (KBL), megacrystic orthogneiss (MOG) and a pegmatitic vein (PEG).

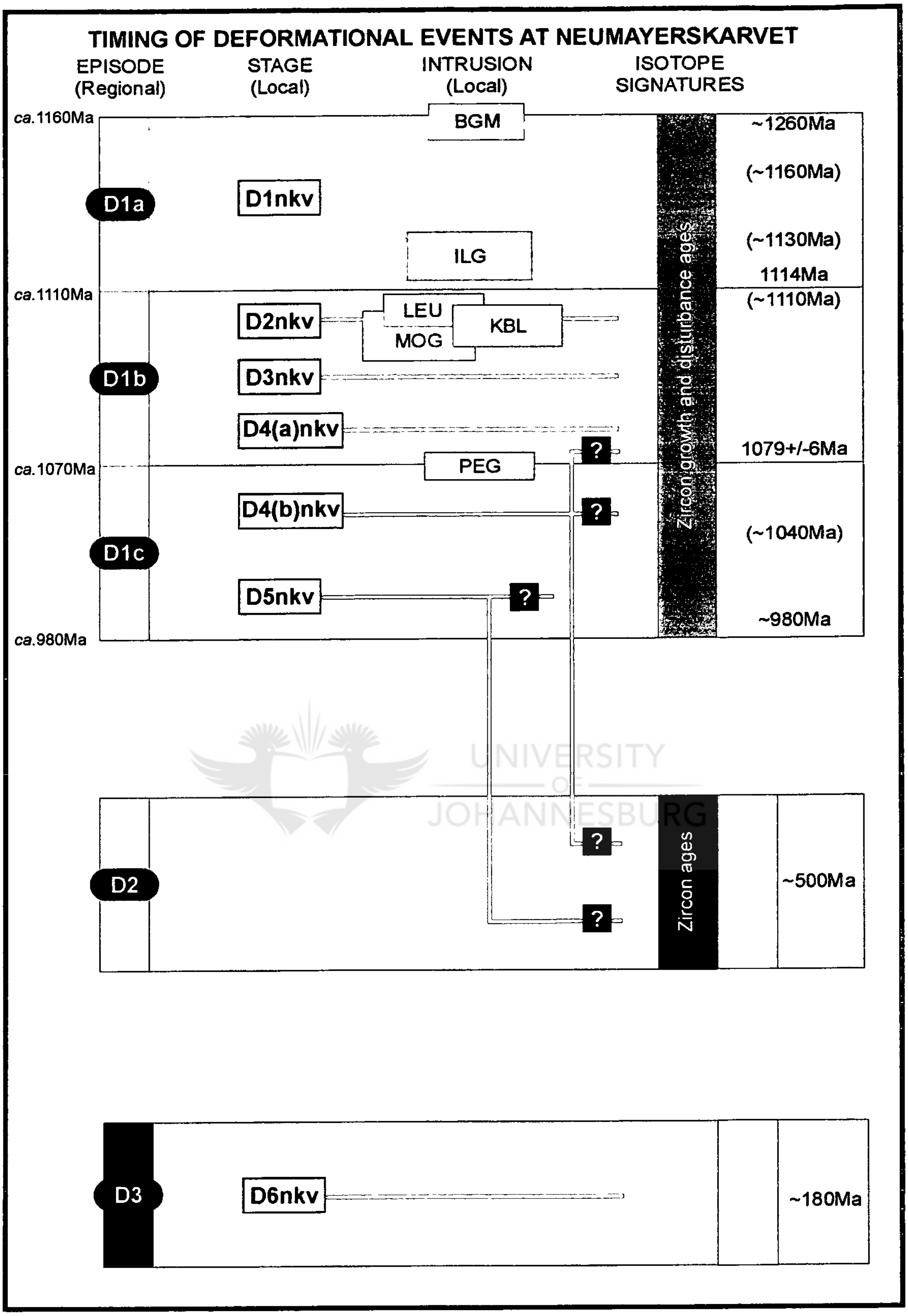

FIGURE 4.19. The timing of deformational events and intrusion of several units at Neumayerskarvet in the northern Kirwanveggen. Age constraints are based on the U-Pb SHRIMP work presented in this section. Where deformation is poorly constrained, the various options are outlined. Rock unit codes are the same as those used in Figure 4.18.

TABLE 4.1 Summary of previous whole-rock data for western Dronning Maud Land, Antarctica.

Locality	*Lithology*	*Method*	*In*	*Age (Ma)*	*MSWD*	*R_0*	*Av.ε*	*Av.Tdm*
KIRWANVEGGEN								
Heksegryta[1]	Gneiss	Rb-Sr	5	1164±78	11.2	0.704	8	
Hallgrenskarvet[1]	High-grade gneiss	Rb-Sr	13	1017±12	0.7	0.705	17	
Neumayerskarvet[1]		Rb-Sr		869±63	2.7	0.709		
Urfjell[2]	Leucocratic gneiss	Rb-Sr	6	1015±24	1.04	0.704	8.4	
	Kirwan volcanics	K-Ar	-	172±10	-	-		
H.U.SVERDRUPFJELLA								
Rootshorga paragneiss[3]		Rb-Sr	6	1183±27	2.8	0.7034	2	
		Sm-Nd	4	1071±253	0.5	0.511208	-1.0	1713(±)
Jutulrora metavolcanic[3]		Rb-Sr	25	1124±38	(±)	0.7076	60	
Fugitive granite[3]		Rb-Sr	5	1161±98	8+9	0.7036	4	
		Sm-Nd	3	1087(±)	0.01	0.51126	2	1498
Sveabreen granite[3]		Rb-Sr	5	1028±94	86	0.7065	43	
Roerkulten mafic dyke[3]		Rb-Sr	11	789±90	2.4	0.7049	16	
		Sm-Nd	16	851±220	1.9	0.51139	-3.6	1516
Midbresrabben diorite[3]		Rb-Sr	6	788±110	1.6	0.7065	39	
Brattskarvet suite[4]	Metamorphic rocks	Rb-Sr	18	518±15	(±)	0.7081	53	
		Sm-Nd	13	522±120	5.4	0.5111	-17.5	1905
Rootshorga mafic[3]		Sm-Nd	3	479(±)	(±)	0.5111	-17.8	2301
Brattskarvet xenoliths[4]	(2 isochrons)	Rb-Sr	7	1046±50	14.4	0.7105		
Sveabreen paragneiss[4]		Rb-Sr	8	1170±26	9.8	0.7036		
		Rb-Sr	3	-	-	-	-	1501
Grey gneiss complex[5]		Rb-Sr	7	1141±43	1.9	0.7081	69	
		Rb-Sr	6	1065±81	2.1	0.7066	46	
Vendeholten granite suite[5]		Rb-Sr	8	1015±73	76	0.7064	76	
Jutulsessen granitc suite[6]		Rb-Sr	8	553±13	4.2	0.7057	24	
		Rb-Sr	6	572±29	2.5	0.7064	35	
		Sm-Nd	15	1153±125	5.8	0.51117	0.37	1595

Source of data for Tables 4.1 and 4.2: 1-Wolmarans and Kent (1982), 2-Faure pers.comm. quoted in Aucamp *et al.* (1972), 3-Moyes and Barton (1990), 4-Moyes *et al.* (1993a), 5-Moyes (*unpubl.*), 6-Moyes (1993), 7-Unpublished data quoted in Moyes and Barton (1990), 8-Moyes *et al.* (1993b), 9-Grantham *et al.* (1991), 10-Arndt *et al.* (1991).

TABLE 4.2. Summary of previous mineral isotope data for western Dronning Maud Land, Antarctica.

Locality	*Lithology*	*Method*	*Mineral*	*In*	*Av.Age (Ma)*
KIRWANVEGGEN					
Heksegryta[7]	Gneiss	U-Pb^{bc}	Zircon		1107±127
Neumayerskarvet[7]	Leucocratic gneiss	U-Pb^{bc}	Zircon		1112±32
Armalsryggen[7]	Gneiss	U-Pb^{bc}	Zircon		1045±193
Hallgrenskarvet[1]	Gneiss	Rb-Sr	Bt-wr	7 pairs	468
Enden[1]	Late pegmatite	Rb-Sr	Bt	1	496
		Rb-Sr	musc	1	946
H.U.SVERDRUPFJELLA					
Sveabreen paragneiss[4]		U-Pb^{bc}	Zircon	2	~950
		U-Pb^{bc}	Zircon		$952^{+15}/_{-18}$
		Rb-Sr	Wr-bt-fsp	3	430±9
		Rb-Sr	Musc		1260
		FT	Apatite	1	121±7
Allenpiggen gneiss[8]		Rb-Sr	Wr-bt	1 pair	453
Gordonuten gneiss[8]		Rb-Sr	Wr-bt	2 pairs	454
Fugelfjellet granite[8]		Rb-Sr	Wr-bt	3 pairs	465
Fugitive granite[8]		Rb-Sr	Wr-bt	6 pairs	488
		FT	Apatite	1	143±26
Jutulsessen granitic gneiss[6]		Rb-Sr	Wr-bt-amph	3	471±9
		FT	Apatite	1	119±7
Brattskarvet granitoid suite[4,8]		Rb-Sr	Wr-bt-fsp-ttn	4	482±9
		Rb-Sr	Wr-bt-fs	3	465±14
		Rb-Sr	Wr-px-ttn(2)	4	476±9
		Sm-Nd	Wr-px-ttn	3	705±177
		FT	Apatite	1	117±8
		FT	Apatite	1	75±3
Dalmatian granite[8,9]		Rb-Sr	Bt-ms-chl	7	469±5
		Rb-Sr	Wr-ms-bt-fsp	4	457±17
		Rb-Sr	Wr-bt-fsp	3	458±12
		Rb-Sr	Wr-bt-fsp	3	470±9
Roerkulten mafic dyke[8]		Rb-Sr	Wr-bt-pl	3	455±9
		Rb-Sr	Wr-bt-pl-amph	4	488±9
		Rb-Sr	Wr-bt-pl	3	493±10
		Rb-Sr	Wr-bt-pl-amph	4	418±8
Grey gneiss complex[5]		FT	apatite	1	158±15
HEIMEFRONTFJELLA					
	Meta-rhyolite	U-Pb^{m,c}			1093±38
	Garnet amphibolite	U-Pb^{m,c}			1060±8
Amphibolite terrane[10]	Granitoids	U-Pb^{m,c}			1045±9 to 1107±16
Granulite terrane[10]	Charnockites	U-Pb^{m,c}			~1250 to ~1450
	Metasediment	Pb-Pb^{m}			1104±5 to ~2000
Granulite terrane[10]	Metaquartzite	U-Pb^{m}			960±120
	Garnet amphibolite	Sm-Nd			

Source data same as for Table 4.1.

^{Bc}-Bulk conventional techniques, ^{c}-Conventional technique, ^{m}-Ion microprobe technique, ^{e}-Evaporation technique

Table 4.3. Summary of U-Pb results for zircons ion probed from sample PH93161.

					Measured		Radiogenic Ratios						Ages				
Grain.spot	U/ppm	Th/ppm	Th/U	Pb*/ppm	204/206	% f206	206/238	±	207/235	±	207/206	±	206/238	207/235	207/206	±	%CONC
1.1	474	6	0.01	69	0.000022	0.04	0.1572	0.0042	1.568	0.044	0.0724	0.0005	941	958	996	13	95
1.2	321	314	0.98	79	0.000115	0.19	0.2067	0.0058	2.346	0.069	0.0823	0.0006	1211	1226	1253	13	97
2.1	678	12	0.02	112	0.000002	0.00	0.1782	0.0047	1.895	0.055	0.0771	0.0007	1057	1079	1125	18	94
2.2	241	68	0.28	48	0.000069	0.11	0.1907	0.0052	2.463	0.077	0.0937	0.0011	1125	1261	1501	23	75
3.1	492	6	0.01	78	0.000004	0.01	0.1715	0.0047	1.738	0.054	0.0735	0.0009	1020	1023	1029	25	99
4.1	422	67	0.16	84	0.000051	0.08	0.2001	0.0055	2.393	0.071	0.0867	0.0007	1176	1240	1354	16	87
5.1	172	140	0.81	69	0.000077	0.12	0.3441	0.0095	5.525	0.166	0.1164	0.0010	1906	1904	1902	15	100
6.1	132	39	0.29	23	-	<0.01	0.1721	0.0048	1.863	0.058	0.0785	0.0008	1024	1068	1160	20	88
7.1	568	4	0.01	93	-	<0.01	0.1768	0.0047	1.829	0.053	0.0750	0.0006	1050	1056	1069	16	98
8.1	182	116	0.63	38	0.000005	0.01	0.1890	0.0051	2.090	0.063	0.0802	0.0009	1116	1146	1202	22	93
9.1	215	102	0.48	44	0.000054	0.09	0.1946	0.0052	2.126	0.065	0.0793	0.0009	1146	1157	1178	23	97
10.1	421	4	0.01	70	0.000013	0.02	0.1793	0.0047	1.877	0.051	0.0759	0.0004	1063	1073	1094	10	97
11.1	647	3	<0.01	114	0.000029	0.05	0.1904	0.0050	1.979	0.056	0.0754	0.0005	1123	1108	1079	14	104
12.1	452	16	0.04	80	0.000147	0.25	0.1909	0.0051	1.954	0.057	0.0742	0.0006	1126	1100	1047	16	108
12.2	672	5	0.01	117	0.000037	0.06	0.1879	0.0049	1.994	0.054	0.0770	0.0004	1110	1114	1121	10	99
13.1	322	33	0.10	62	0.000087	0.14	0.1969	0.0054	2.245	0.068	0.0827	0.0008	1159	1195	1262	20	92
14.1	412	7	0.02	54	0.000128	0.22	0.1425	0.0039	1.401	0.041	0.0713	0.0006	859	889	966	17	89
15.1	453	22	0.05	64	0.000053	0.09	0.1518	0.0042	1.548	0.050	0.0740	0.0010	911	950	1041	27	88
16.1	279	250	0.89	114	0.000033	0.05	0.3431	0.0090	5.444	0.148	0.1151	0.0005	1901	1892	1881	7	101
16.2	265	115	0.43	64	-	<0.01	0.2230	0.0063	2.911	0.089	0.0947	0.0009	1298	1385	1522	17	85
17.1	645	1198	1.86	171	0.000036	0.06	0.1877	0.0051	2.019	0.057	0.0780	0.0004	1109	1122	1147	9	97
17.2	927	418	0.45	208	0.000120	0.20	0.2139	0.0058	2.280	0.065	0.0773	0.0005	1250	1206	1129	12	111
18.1	136	53	0.39	25	0.000055	0.09	0.1792	0.0052	1.961	0.062	0.0794	0.0008	1062	1102	1182	20	90
19.1	66	17	0.26	17	0.000089	0.14	0.2456	0.0078	3.338	0.131	0.0986	0.0019	1416	1490	1597	37	89
20.1	362	457	1.26	87	0.000019	0.03	0.1913	0.0051	2.070	0.060	0.0785	0.0007	1128	1139	1159	17	97
20.2	700	51	0.07	118	0.000054	0.09	0.1783	0.0051	1.838	0.060	0.0748	0.0010	1057	1059	1063	26	100
21.1	531	7	0.01	91	-	<0.01	0.1854	0.0052	1.874	0.055	0.0733	0.0005	1096	1072	1023	13	107
22.1	704	4	0.01	113	-	<0.01	0.1727	0.0047	1.791	0.053	0.0752	0.0006	1027	1042	1074	17	96
23.1	159	64	0.40	32	0.000032	0.05	0.1956	0.0059	2.173	0.091	0.0806	0.0021	1152	1172	1211	51	95
24.1	129	149	1.16	59	-	<0.01	0.3574	0.0105	6.203	0.200	0.1259	0.0013	1970	2005	2041	18	97
25.1	773	406	0.53	164	0.000018	0.03	0.2002	0.0053	2.148	0.060	0.0778	0.0005	1177	1164	1142	12	103
25.2	582	106	0.18	105	0.000070	0.12	0.1850	0.0051	2.000	0.059	0.0784	0.0006	1094	1115	1156	16	95
26.1	156	116	0.75	42	-	<0.01	0.2360	0.0068	2.875	0.089	0.0883	0.0007	1366	1375	1390	16	98

Note:
1. - denotes no 204Pb detected
2. Uncertainties given at the one sigma level

Table 4.4. Summary of U-Pb results for zircons ion probed from sample PH92009.

Grain.spot	U/ppm	Th/ppm	Th/U	Pb*/ppm	Measured 204/206	% f206	Radiogenic Ratios 206/238	±	207/235	±	207/206	±	Ages 206/238	207/235	207/206	±	%CONC
1.1	565	71	0.13	98	0.000060	0.10	0.1802	0.0047	1.888	0.052	0.0760	0.0004	1068	1077	1095	11	98
2.1	618	79	0.13	111	0.000051	0.09	0.1868	0.0049	1.954	0.054	0.0759	0.0004	1104	1100	1091	11	101
3.1	667	133	0.20	120	0.000038	0.06	0.1836	0.0048	1.941	0.053	0.0767	0.0004	1087	1095	1112	11	98
4.1	395	86	0.22	70	0.000526	0.89	0.1791	0.0048	1.945	0.060	0.0788	0.0010	1062	1097	1166	24	91
4.2	468	71	0.15	79	0.000047	0.08	0.1742	0.0046	1.820	0.051	0.0758	0.0004	1035	1053	1089	11	95
5.1	877	137	0.16	160	0.000037	0.06	0.1881	0.0049	1.966	0.053	0.0758	0.0003	1111	1104	1090	7	102
5.2	290	65	0.22	52	0.000034	0.06	0.1799	0.0050	1.906	0.058	0.0768	0.0007	1066	1083	1117	18	95
6.1	2680	67	0.02	218	0.000365	0.62	0.0878	0.0042	0.9122	0.0496	0.0754	0.0016	542	658	1079	43	50
6.2	507	69	0.14	89	0.000056	0.10	0.1834	0.0049	1.929	0.055	0.0763	0.0005	1085	1091	1103	14	98
7.1	490	57	0.12	83	0.000010	0.02	0.1780	0.0047	1.861	0.051	0.0758	0.0003	1056	1067	1091	9	97
7.2	593	86	0.15	101	0.000056	0.09	0.1774	0.0047	1.810	0.050	0.0740	0.0004	1053	1049	1041	11	101
8.1	947	38	0.04	165	0.000020	0.03	0.1864	0.0049	1.966	0.056	0.0765	0.0006	1102	1104	1107	16	100
8.2	1451	325	0.22	264	0.000020	0.03	0.1849	0.0048	1.952	0.051	0.0766	0.0002	1094	1099	1109	6	99
9.1	583	84	0.14	101	0.000004	0.01	0.1811	0.0047	1.888	0.051	0.0756	0.0003	1073	1077	1085	9	99
10.1	2378	91	0.04	407	0.000029	0.05	0.1831	0.0047	1.923	0.050	0.0762	0.0002	1084	1089	1099	6	99
10.2	454	71	0.16	80	0.000052	0.09	0.1822	0.0048	1.895	0.052	0.0755	0.0005	1079	1080	1081	13	100
11.1	609	85	0.14	106	-	<0.01	0.1800	0.0048	1.898	0.053	0.0765	0.0005	1067	1080	1107	13	96

Note:
1. - denotes no 204Pb detected
2. Uncertainties given at the one sigma level

Table 4.5. Summary of U-Pb results for zircons ion probed from sample PH93148.

					Measured				Radiogenic Ratios					Ages			
Grain.spot	U/ppm	Th/ppm	Th/U	Pb*/ppm	204/206	% f206	206/238	±	207/235	±	207/206	±	206/238	207/235	207/206	±	%CONC
1.1	544	62	0.11	86	0.000061	0.10	0.1653	0.0039	1.737	0.045	0.0762	0.0006	986	1022	1100	15	90
1.2	797	116	0.15	125	0.000073	0.12	0.1629	0.0041	1.717	0.046	0.0764	0.0004	973	1015	1106	11	88
2.1	97	80	0.83	18	0.000087	0.15	0.1666	0.0044	1.811	0.068	0.0788	0.0018	994	1049	1167	47	85
2.2	986	24	0.02	66	0.000097	0.16	0.0731	0.0017	0.5725	0.0145	0.0568	0.0005	455	460	484	18	94
3.1	1143	160	0.14	176	0.000041	0.07	0.1607	0.0038	1.674	0.045	0.0755	0.0008	961	999	1083	21	89
3.2	459	69	0.15	68	0.000171	0.29	0.1566	0.0037	1.635	0.045	0.0757	0.0008	938	984	1087	22	86
4.1	1218	891	0.73	202	0.000395	0.67	0.1537	0.0036	1.597	0.039	0.0754	0.0004	921	969	1079	11	85
5.1	36	23	0.64	6	0.000161	0.27	0.1618	0.0061	1.840	0.100	0.0825	0.0028	967	1060	1258	69	77
6.1	580	203	0.35	103	0.000055	0.09	0.1747	0.0040	1.880	0.046	0.0780	0.0004	1038	1074	1148	10	91
7.1	896	660	0.74	126	0.001551	2.62	0.1321	0.0031	1.356	0.039	0.0744	0.0011	800	870	1053	30	76
8.1	126	26	0.21	22	0.000162	0.27	0.1750	0.0045	1.852	0.057	0.0767	0.0011	1040	1064	1115	28	93
9.1	621	14	0.02	100	0.000049	0.08	0.1732	0.0041	1.774	0.044	0.0743	0.0005	1030	1036	1049	12	98
10.1	333	106	0.32	62	0.000057	0.10	0.1862	0.0045	1.993	0.052	0.0776	0.0006	1101	1113	1137	15	97
10.2	363	159	0.44	72	0.000081	0.14	0.1916	0.0046	2.032	0.056	0.0769	0.0008	1130	1126	1119	21	101
11.1	405	178	0.44	74	0.000051	0.09	0.1731	0.0044	1.895	0.054	0.0794	0.0008	1029	1079	1181	20	87

Note: 1. - denotes no 204Pb detected
2. Uncertainties given at the one sigma level

Table 4.6. Summary of U-Pb results for zircons ion probed from sample PH92020.

					Measured		Radiogenic Ratios						Ages				
Grain.spot	U/ppm	Th/ppm	Th/U	Pb*/ppm	204/206	% f206	206/238	±	207/235	±	207/206	±	206/238	207/235	207/206	±	%CONC
1.1	521	82	0.16	80	0.000113	0.19	0.1576	0.0085	1.744	0.119	0.0802	0.0029	944	1025	1203	72	78
1.2	541	124	0.23	92	0.000113	0.19	0.1730	0.0040	1.808	0.045	0.0758	0.0005	1028	1049	1091	12	94
2.1	249	28	0.11	40	0.000339	0.57	0.1686	0.0045	1.672	0.056	0.0719	0.0013	1004	998	984	37	102
3.1	1212	111	0.09	188	0.000031	0.05	0.1638	0.0038	1.711	0.042	0.0757	0.0004	978	1013	1088	11	90
3.2	706	55	0.08	110	0.000100	0.17	0.1647	0.0038	1.707	0.042	0.0752	0.0004	983	1011	1074	11	92
4.1	261	89	0.34	45	0.000163	0.28	0.1693	0.0042	1.836	0.052	0.0786	0.0009	1008	1058	1163	23	87
5.1	296	88	0.30	51	0.000152	0.26	0.1724	0.0056	1.792	0.091	0.0754	0.0027	1025	1043	1079	73	95
5.2	223	30	0.13	34	0.000131	0.22	0.1602	0.0038	1.726	0.055	0.0781	0.0014	958	1018	1150	36	83
6.1	292	25	0.08	48	0.000181	0.31	0.1736	0.0044	1.804	0.054	0.0754	0.0010	1032	1047	1079	27	96
6.2	643	65	0.10	97	0.000241	0.41	0.1588	0.0037	1.688	0.044	0.0771	0.0007	950	1004	1124	18	85
7.1	572	55	0.10	91	0.000050	0.09	0.1677	0.0040	1.767	0.044	0.0764	0.0005	1000	1033	1106	13	90
8.1	614	46	0.08	95	0.000054	0.09	0.1642	0.0038	1.719	0.042	0.0759	0.0004	980	1016	1093	12	90
9.1	375	79	0.21	68	0.000036	0.06	0.1844	0.0046	1.955	0.054	0.0769	0.0008	1091	1100	1119	20	98
10.1	462	92	0.20	83	0.000009	0.02	0.1845	0.0044	1.974	0.053	0.0776	0.0008	1091	1107	1137	20	96
11.1	534	58	0.11	96	0.000509	0.86	0.1892	0.0051	1.977	0.082	0.0758	0.0021	1117	1108	1089	57	103

Note:
1. - denotes no 204Pb detected
2. Uncertainties given at the one sigma level

Table 4.7. Summary of U-Pb results for zircons ion probed from sample PH92005.

					Measured				Radiogenic Ratios				Ages				
Grain.spot	U/ppm	Th/ppm	Th/U	Pb*/ppm	204/206	% f206	206/238	±	207/235	±	207/206	±	206/238	207/235	207/206	±	%CONC
1.1	821	191	0.23	141	0.000044	0.08	0.1742	0.0042	1.803	0.045	0.0751	0.0003	1035	1047	1071	9	97
1.2	347	81	0.23	62	0.000111	0.19	0.1821	0.0044	1.923	0.051	0.0766	0.0006	1078	1089	1111	17	97
2.1	316	71	0.22	52	0.000080	0.14	0.1673	0.0041	1.762	0.049	0.0764	0.0008	997	1032	1105	21	90
2.2	430	95	0.22	75	0.000024	0.04	0.1774	0.0041	1.856	0.046	0.0759	0.0004	1053	1066	1091	11	97
3.1	196	80	0.41	34	0.000064	0.11	0.1670	0.0043	1.773	0.053	0.0770	0.0010	996	1036	1121	25	89
3.2	505	91	0.18	84	0.000091	0.15	0.1718	0.0040	1.805	0.046	0.0762	0.0005	1022	1047	1100	14	93
4.1	364	173	0.47	68	0.000074	0.12	0.1785	0.0043	1.870	0.050	0.0760	0.0007	1059	1070	1095	19	97
5.1	213	66	0.31	34	0.001006	1.70	0.1596	0.0039	1.577	0.063	0.0717	0.0021	954	961	977	59	98
6.1	323	91	0.28	60	0.000064	0.11	0.1844	0.0045	1.958	0.060	0.0770	0.0012	1091	1101	1121	31	97
7.1	316	153	0.48	62	0.000033	0.06	0.1879	0.0047	1.942	0.057	0.0750	0.0009	1110	1096	1068	24	104
8.1	429	266	0.62	85	0.000037	0.06	0.1831	0.0044	1.903	0.049	0.0754	0.0005	1084	1082	1078	14	101
9.1	313	55	0.18	55	0.000143	0.24	0.1814	0.0044	1.870	0.055	0.0748	0.0010	1075	1071	1062	27	101
10.1	288	167	0.58	57	0.000027	0.05	0.1843	0.0045	1.944	0.053	0.0765	0.0008	1090	1096	1108	20	98
11.1	151	41	0.27	27	0.000146	0.25	0.1797	0.0051	1.840	0.069	0.0743	0.0016	1066	1060	1048	45	102

Note:
1. - denotes no 204Pb detected
2. Uncertainties given at the one sigma level

Table 4.8. Summary of U-Pb results for zircons ion probed from sample PH93140 and PH92006.

					Measured		Radiogenic Ratios						Ages				
Grain.spot	U/ppm	Th/ppm	Th/U	Pb*/ppm	204/206	% f206	206/238	±	207/235	±	207/206	±	206/238	207/235	207/206	±	%CONC
PH93140																	
1.1	1376	53	0.04	211	0.000030	0.05	0.1638	0.0042	1.706	0.046	0.0755	0.0004	978	1011	1083	11	90
2.1	810	249	0.31	146	0.000068	0.12	0.1792	0.0064	1.851	0.101	0.0749	0.0028	1063	1064	1066	77	100
3.1	872	357	0.41	154	0.000135	0.23	0.1708	0.0048	1.784	0.052	0.0758	0.0005	1016	1039	1089	12	93
4.1	1987	310	0.16	303	0.000006	0.01	0.1592	0.0042	1.647	0.045	0.0750	0.0003	953	988	1069	8	89
5.1	2452	1243	0.51	491	0.000013	0.02	0.1901	0.0055	1.965	0.058	0.0750	0.0003	1122	1104	1068	7	105
6.1	608	151	0.25	106	0.000043	0.07	0.1755	0.0046	1.859	0.052	0.0768	0.0005	1042	1067	1117	12	93
7.1	2769	1552	0.56	533	0.000008	0.01	0.1800	0.0064	1.918	0.095	0.0773	0.0024	1067	1087	1129	62	95
8.1	1523	36	0.02	287	0.000148	0.25	0.2033	0.0053	2.071	0.056	0.0739	0.0004	1193	1139	1039	10	115
9.1	855	347	0.41	156	0.000149	0.25	0.1782	0.0072	1.823	0.011	0.0742	0.0031	1057	1054	1046	88	101
10.1	988	154	0.16	170	-	<0.01	0.1783	0.0047	1.867	0.050	0.0760	0.0003	1057	1069	1094	9	97
11.1	1456	748	0.51	277	0.000002	<0.01	0.1794	0.0313	1.884	0.368	0.0762	0.0053	1064	1076	1100	146	97
12.1	3596	616	0.17	655	0.000036	0.06	0.1878	0.0048	1.945	0.051	0.0751	0.0002	1109	1097	1072	6	104
13.1	3476	2088	0.6	717	0.000077	0.13	0.1909	0.0050	1.986	0.053	0.0755	0.0003	1126	1111	1081	8	104
14.1	1867	994	0.53	368	0.000071	0.12	0.1854	0.0049	1.956	0.053	0.0765	0.0004	1096	1101	1109	10	99
PH92006																	
1.1	1268	607	0.48	236	0.000170	0.29	0.1775	0.0057	1.885	0.072	0.0770	0.0013	1053	1076	1121	34	94
2.1	1234	654	0.53	245	0.000013	0.02	0.1874	0.0049	1.952	0.052	0.0755	0.0003	1107	1099	1083	7	102
3.1	1950	592	0.3	283	0.000039	0.07	0.1418	0.0037	1.390	0.038	0.0711	0.0004	855	885	960	10	89
4.1	883	443	0.5	177	0.000017	0.03	0.1910	0.0073	1.972	0.086	0.0749	0.0012	1127	1106	1066	34	106
5.1	5595	950	0.17	495	0.001268	2.14	0.0895	0.0024	0.883	0.025	0.0716	0.0006	552	642	973	17	57

Note: 1. - denotes no 204Pb detected
2. Uncertainties given at the one sigma level

Table 4.9. Rb-Sr isotopic data for the mineral separates.

Sample	Type	Rb (ppm)	Sr (ppm)	87Rb/86Sr	87Sr/86Sr	Precision
PH92007	whole-rock	248.17	123.98	5.8414	0.795860	0.000011
PH92007/bt	biotite	1034	4.93	992.7208	7.2083	0.0008
PH92007/fs	feldspar	366.2	173.83	6.1507	0.801001	0.000013
PH92012	whole-rock	139.15	126.31	3.202	0.754772	0.000014
PH92012/bt	biotite	828.74	7.365	415.7903	3.540751	0.000051
PH92020/bt	biotite	824.9	2.76	2034.1134	14.5312	0.0042
PH92020/fs	feldspar	279.5	283.65	2.8692	0.773366	0.000012
PH92020/m	muscovite	408.8	13.76	91.6388	1.383436	0.000019
PH93148	whole-rock	102.31	244.36	1.2134	0.724727	0.000015
PH93148/bt	biotite	502.19	3.14	668.2131	5.247069	0.000079
PH93148/fs	feldspar	215.2	483.53	1.2899	0.725251	0.000013
PH93148/m	muscovite	282.2	24.623	33.9191	0.941995	0.000013

Table 4.10. Summary of Rb-Sr mineral data from Neumayerskarvet in the northern Kirwanveggen.

Sample	Description	Material	n	Age (Ma)	MSWD	Intitial Ratio
PH92007	Pegmatite vein	wr-fsp-bt	3	459±29	39.63	0.7596
PH92012	Deformed pegmatite vein	wr-bt	2	474±10	-	0.7332
PH92020	Kyanite-bearing leucogneiss	fsp-bt-musc	3	479±7	1.04	0.7538
PH93148	Intrusive leucogneiss	wr-fsp-bt-musc	4	471±7	1.06	0.7166

wr:-whole-rock
fsp:-feldspar
bt:-biotite
musc:-muscovite

TABLE 4.11. Summary of U-Pb SHRIMP zircon age data obtained during this investigation.

Sample	Age	Inheritance	Zircon Growth	Significance
PH93161 (BGM)	-	~2040 Ma (oldest age recorded) 1880-2040 Ma Possible 1500 Ma ~1390 Ma	~1260-~1000 Ma	Zircons exposed to several periods of metamorphism and deformation (High-grade between ~1260 to 1000 Ma). Unit provides a maximum age of deformation, and an indication of source material for the high-grade gneisses.
PH92009 (LEU)	1098 ± 5 Ma	Inherited component present but undetermined due to analysis discordance	~1040 Ma	Zircons provide a crystallisation age. The older component present is close to the crystallisation age. Younger zircon growth is also recorded.
PH93148 (ILG)	~1130 Ma (Not well constrained)	Inherited component present but undetermined due to analysis discordance	~1100 Ma(?) ~1050 Ma ~480 Ma	Data are discordant but possible crystallisation age of ~1130 Ma is suggested. Evidence of ~1050 Ma growth and a ~480 Ma period is present in this sample.
PH92020 (KBL)	1096 ± 10 Ma	-	~980 Ma	Crystallisation age with younger growth or disturbance documented.
PH92005 (MOG)	1088 ± 10 Ma	-	~980 Ma	Crystallisation age with younger growth or disturbance documented.
PH92006/93140 (PEG)	1079 ± 6 Ma	-	-	Crystallisation age of sample. This sample records the last magmatic event sampled at Neumayerskarvet.

CHAPTER 5

CONDITIONS OF METAMORPHISM AT NEUMAYERSKARVET IN THE NORTHERN KIRWANVEGGEN

INTRODUCTION

Neumayerskarvet lies in the northern Kirwanveggen, western Dronning Maud Land, Antarctica. This region comprises high-grade gneisses that have been subjected to several episodes of magmatism, metamorphism and deformation. In order to understand the evolution of this high-grade gneiss terrane an intimate knowledge of the metamorphic conditions is required. P-T estimates from a metamorphic terrane suffer from several problems that complicate the interpretation of the data. Geothermobarometry studies require suitable equilibrium assemblages that have not undergone late retrograde exchange. Even mineral cores may not retain peak metamorphic conditions (Fitzsimons and Harley, 1994). Inherent in these investigations is also the availability of suitably preserved mineral assemblages that provide P-T conditions for the sample under investigation. Problems also arise when geothermometers and geobarometers, based on different mineral assemblages and reactions, are combined to represent conditions within a specific temporal P-T space. These geothermobarometers may not be temporally related to one another, at least within a specific P-T space, and therefore could represent different conditions at certain instances along a P-T-t pathway. Such problems have to be addressed when metamorphic investigations are undertaken.

At Neumayerskarvet these problems are enhanced by the poly-deformational history recorded within the high-grade gneisses. Similar structural styles and geometries hinder the distinction of *ca.* 1100 Ma from *ca.* 500 Ma deformational fabric elements. Recognition of mineral assemblages representative of either tectonic episode is confused by the coaxial and colinear nature of the deformational episodes. Careful fabric analysis is therefore required before the metamorphic assemblages can be assigned to different tectonic episodes. In this investigation, structurally constrained markers are used in an attempt to unravel the P-T conditions at Neumayerskarvet. An indication of the possible effects of poly-metamorphism is also obtained in this study. The significance of these features is evaluated within the established structural context for the northern Kirwanveggen.

The kyanite-bearing leucogneiss units form the basis of this metamorphic investigation although supporting evidence from the megacrystic orthogneiss is also provided. Reaction textures in the kyanite-bearing leucogneiss can be viewed in terms of net-transfer and cation exchange reactions due to the somewhat less complicated reaction textures observed in these rocks. Reaction histories can be obtained from these rocks allowing the reconstruction of P-T conditions experienced during the evolution of Neumayerskarvet. Reactions within these rocks are essentially controlled by a combination of net-transfer reactions involving garnet, kyanite/sillimanite, biotite, muscovite, plagioclase and quartz, with cation exchange reactions between garnet and biotite (Fe-Mg).

GEOLOGICAL FRAMEWORK

Geological Background

Neumayerskarvet lies within the northern Kirwanveggen of western Dronning Maud Land (Figure 5.1). This region forms a broad belt of high-grade gneisses extending from the Heimefrontfjella in the southwest, through the Kirwanveggen and H.U.Sverdrupfjella, to the Muhlig-Hoffmanfjella in the northeast. The northern Kirwanveggen forms a geologically significant domain represented by similar lithotectonic units, structural styles and metamorphic mineral assemblages. Neumayerskarvet forms the major continuous portion of outcrop within the northern Kirwanveggen, and the geological map of this area is presented in Figure 5.2. The dominant and oldest lithotectonic unit preserved at Neumayerskarvet is the biotite-garnet migmatite gneiss. This lithotectonic unit is intercalated with quartzofeldspathic gneisses and occurs with banded quartz-feldspar gneisses. Several phases of magmatism affected the older sequences and comprise megacrystic orthogneiss, leucogneisses, granitic/dioritic gneisses, metagabbros and mafic dykes (see Figure 5.2).

Three major tectonic episodes have been distinguished in the northern Kirwanveggen (see Figure 5.3). The most significant episode is the D1 tectonic episode, which has been subdivided into 3 tectonic periods, D1a, D1b and D1c respectively. Distinction of these periods is based on magmatism, zircon growth and deformational fabrics documented in the northern Kirwanveggen (see Chapters 3 and 4). The D1a, D1b and D1c tectonic periods may either represent a continuum within a single tectonic episode, or result from episodic deformation-magmatic-metamorphic periods during the D1 tectonic episode. The current data do not provide sufficient evidence to resolve these tectonic periods.

The D1a tectonic period is constrained between *ca.* 1160 Ma and *ca.* 1120 Ma, although the exact relationships between the deformational fabrics and magmatism are not clearly resolved. A strong penetrative planar foliation is distinguished, however, that is folded by later tectonic periods. There is evidence to suggest that magmatism occurred during this period at Neumayerskarvet, but current U-Pb ion probe data are poorly constrained (see Chapter 4). Magmatism during this period has, however, been recorded in the Heimefrontfjella and the H.U.Sverdrupfjella (Arndt *et al.*, 1991; Harris *et al.*, 1995; Moyes and Groenewald, 1996).

The D1b tectonic episode represents a major period of magmatism and tectonism recorded in the northern Kirwanveggen between *ca.* 1110 Ma and *ca.* 1070 Ma. Major folding occurred during this tectonic episode and is represented by isoclinal recumbent folds, sheath folds and re-folded folds that produce Ramsay Type III interference patterns in outcrop. Strong stretching lineations and planar foliation development mark this period of tectonism. The structural fabric elements produce a complicated picture of transposed coplanar and colinear composite fabrics indistinguishable in styles and geometries from earlier fabric elements. Magmatism dominates during this time period at Neumayerskarvet with the intrusion of leucogneisses (1098 ± 5 Ma), kyanite-bearing leucogneisses (1096 ± 10 Ma) and megacrystic orthogneiss (1088 ± 10 Ma). Zircon growth and recrystallisation is also documented during this tectonic period. Fabric geometries suggest NNW-SSE tectonic transport directions within the D1b tectonic period.

Evidence for the D1c tectonic period is not clearly resolved. This tectonic period is placed between *ca.* 1070 and *ca.* 970 Ma and is distinguished primarily through U-Pb zircon growth and recrystallisation ages. Tectonism that post-dates D1b is marked by cross-folding and the development of high-strain zones that re-work earlier fabrics. These deformational styles may develop during D1c, but could equally be part of the D2 episode at *ca.* 500 Ma. Magmatism between *ca.* 1070 Ma and *ca.* 970 Ma in WDML has only been documented in the central Kirwanveggen and Heimefrontfjella (Arndt *et al.*, 1991; Harris *et al.*, 1995; Jackson *et al.*, 1997).

Zircon growth and disturbance, and the resetting of Rb-Sr mineral ages took place during the D2 episode (see Figure 5.3). Cross-folding and high strain development that re-worked earlier tectonic fabrics may represent signatures of the associated deformation, but the exact nature of the deformation remains enigmatic. Tectonic fabric styles and geometries are similar to the more dominant D1 episode, making recognition of temporal relationships difficult and only possible in isolated outcrop areas. Magmatism during D2 is only recognised in the Muhlig-Hoffmanfjella and H.U.Sverdrupfjella (Ohta *et al.*, 1990; Grantham *et al.*, 1991; Moyes *et al.*, 1993b).

The last tectonic episode that affected the northern Kirwanveggen is the D3 episode at *ca.* 180 Ma. Brittle faults and fractures at Neumayerskarvet have been assigned to this episode. Deformation during D3 is related to effects of rifting during Gondwana break-up and the age constraints are provided by alkaline complexes intruding into this region (Harris and Grantham, 1993).

Previous Metamorphic Investigations in the Kirwanveggen

The first description of the metamorphism in the Kirwanveggen is presented by Wolmarans and Kent (1982). The mineralogy of some of the major lithologies in the Kirwanveggen provided some indication of the metamorphic conditions within these rock units. Element analyses for the biotite-garnet geothermometers was also applied by Wolmarans and Kent (1982). Within the leucogneisses of the Kirwanveggen, the scarcity of muscovite and the presence of microcline, indicated that the first orthoclase isograd was reached. This suggests that the leucogneisses have been metamorphosed to the upper amphibolite facies. The biotite-garnet plagiogneisses contain co-existing kyanite and sillimanite. The hornblende plagiogneisses and amphibolites contain green hornblende and calcic plagioclase (anorthite-rich plagioclase) which define amphibolite facies metamorphism. Brown hornblende, found in central Neumayerskarvet, suggests a higher grade of metamorphism, probably in the amphibolite/granulite facies transition. High-grade metamorphic conditions are also suggested by the presence of migmatites, indicating partial melting, and granitic pegmatites. The mineral assemblages of the calc-silicates are generally characteristic of amphibolite facies metamorphism, and the co-existence of wollastonite with quartz and grossular garnet suggests fluid compositions of XCO_2=0.2 were attained (Wolmarans and Kent, 1982). The mineralogical relationships and assemblages suggest high-grade metamorphism was attained in the Kirwanveggen. The use of biotite-garnet geothermometers also supports the grade of metamorphism in the Kirwanveggen. Metamorphic pressure and temperature conditions in the Kirwanveggen have been estimated as P = 6.4 ± 0.5 kb and T = 640 ± 50 °C by Wolmarans and Kent (1982).

Ferrar (1995) distinguished four metamorphic events (M1-4) within a region of the northern Kirwanveggen. The three early events are related to orogenesis while the last event is related to a greenschist facies uplift event. M1 assemblages of cpx + grt + pl ± hbl preserved in metabasic rocks are indicative of an early high-pressure event at conditions of 650-700 °C and 12-13 kb. Amph + pl + grt assemblages representing the M2 amphibolite facies event provide metamorphic conditions of 720 °C and 6-10 kb for this event. Similar high-pressure assemblages have been recorded in the H.U.Sverdrupfjella (Groenewald and Hunter, 1991; Grantham *et al.*, 1995). Ferrar (1995) assigned the M1 and M2 events to the Mesoproterozoic period that affected these high-grade gneisses. Biotitisation and re-equilibration of garnet and plagioclase rim compositions provide temperatures of ~650 °C for the M3 event, which has been assigned to the ca. 500 Ma event (Ferrar, 1995). A summary of the metamorphic conditions interpreted for the Kirwanveggen are compared to the current structural and isotopic investigation in Figure 5.3.

SAMPLE SELECTION AND ROCK DESCRIPTIONS

The coplanar and colinear nature of the tectonic fabrics throughout the deformational history of the northern Kirwanveggen makes distinction of metamorphic assemblages on structural grounds difficult. Assemblages within planar fabrics can develop during any stage of the fabric development and transposition cycle of earlier fabrics resulting in uncertain time relationships of these assemblages. To overcome these problems, intrusive units with suitable mineralogies and definite age-constrained structural positions have been used for the metamorphic investigation. The samples studied are from the megacrystic orthogneiss and kyanite-bearing leucogneisses in the central portion of Neumayerskarvet. Localities of these samples are illustrated in the cross-sectional photo mosaic of Figure 5.4 and a list of samples studied during this investigation with their associated mineral assemblages is provided in Table 5.1.

Megacrystic Orthogneiss

The Neumayerskarvet megacrystic orthogneiss is characterised by coarse- K-feldspar porphyroblasts and zones of remnant charnockitic material. The megacrystic orthogneiss has been dated by U-Pb zircon ion probe techniques at 1088 ± 10 Ma (see Chapter 4). It intruded the biotite-garnet migmatite gneisses of the northern Kirwanveggen during a period of major deformation. Xenoliths within the orthogneiss exhibit a strong foliation, indicating the intrusion of this body post-dates part of the deformation experienced by the high-grade gneiss terrane. These xenoliths consist of migmatite gneisses and calc-silicate boudins, along with mafic enclaves of possible dyke origin. Portions of the orthogneiss are intensely deformed producing strong linear and planar fabrics in the resulting augen-textured gneiss. These lines of evidence indicate that the charnockite intruded syn- to late- the major D1 tectonic episode (D1b) in the northern Kirwanveggen.

Dark charnockitic patches are preserved only in unstrained to weakly deformed areas, while in the more intensely deformed areas augen gneisses occur. The charnockitic patches comprise only a small portion of the intrusion and are randomly dispersed throughout the megacrystic orthogneiss. This charnockite is unrelated to veins or minor shear zones and appears to form remnants that have survived deformation and rehydration (see Figure 5.5a and b). At Neumayerskarvet, the preserved charnockitic patches represent the earliest recorded assemblages of the megacrystic orthogneiss and are examined during this investigation. Gradational contacts are observed between the different zones of the orthogneiss, which result in charnockitic zones grading into porphyritic granitoid (Figure 5.5c) and subsequently augen gneisses (Figure 5.5d). The porphyritic granitoid and augen gneiss assemblages represent the retrogressed megacrystic orthogneiss material used in this study. Later structures affecting the megacrystic orthogneiss, including aplitic veins, have provided conduits for fluids that resulted in the late rehydration and retrogression of the earlier assemblages (Figure 5.5b).

Several different generations and types of felsic veins cut the megacrystic orthogneiss. Aplitic veins that parallel the foliation are often transposed and folded, while other thin granitic veins crosscut the augen gneisses. Several types of melt leucosomes migrate across the foliations within the augen gneisses. Some of these melt leucosomes migrate into minor shear zones, while others occur as typical melt patches within the megacrystic orthogneiss.

Kyanite-Bearing Leucogneisses

The kyanite-bearing leucogneisses intrude along and across early D1a foliations within the biotite-garnet migmatite gneiss at Neumayerskarvet. The leucogneisses post-date the early D1a tectonic period but intrude, and are subsequently deformed during the D1b tectonic period which is constrained between 1114 Ma and 1073 Ma. U-Pb zircon ion probe data provides an age of 1096 ± 10 Ma for one of the kyanite-bearing leucogneisses. Planar foliations and elongation lineations are observed within these units (see Figures 5.5e and f). Phyllosilicates and aluminosilicates within the kyanite-bearing leucogneisses are aligned defining a mineral lineation that parallels quartz elongation lineations observed within portions of these units.

PETROGRAPHY

Metamorphic Features and Reaction Textures

Charnockitic Remnants within Megacrystic Orthogneiss

The charnockitic remnants are progressively overprinted by retrogressive assemblages dominant in the megacrystic orthogneiss. As such it is difficult to determine the reaction and paragenetic relationships of minerals encountered in the less deformed charnockitic remnants. Minerals encountered in these assemblages are: quartz, K-feldspar, plagioclase, garnet, biotite, amphibole, clinopyroxene, orthopyroxene, ilmenite, zircon and apatite. The occurrence of pyroxene differentiates assemblages of the charnockitic assemblages from the more retrogressed portions of the orthogneiss. Clinopyroxene and orthopyroxene occur as resorbed remnants in these assemblages, where orthopyroxene occurs in the least affected zones of this gneiss. With increasing deformation orthopyroxene is replaced by clinopyroxene, and is removed from the amphibole-biotite dominant assemblages of the retrogressed megacrystic orthogneiss.

Garnet is observed surrounding orthopyroxene with symplectic/vermicular quartz intergrowths or inclusions. Quartz-plagioclase-clinopyroxene assemblages separate the garnet from the orthopyroxene (Figure 5.6a). Garnet coronas are developed around the orthopyroxene, and again contacts are separated by quartz-plagioclase-clinopyroxene assemblages. Where remnants of only clinopyroxene remain, the garnet coronas are separated by large quartz-feldspar grains. The garnet coronas all have a small grain size (0.3 mm) and display a vermicular texture with quartz. The garnet coronas tend to form around the mafic mineral clusters within the charnockitic remnants. Zoned plagioclase is observed with garnet corona textures in some of the charnockitic remnant samples (Figure 5.6c). Garnet coronas are also developed on ilmenite grains (Figure 5.6b). Similar corona textures and reactions have been described from other metamorphic terranes around the world. For example, in the high-grade gneisses of the Highlands Complex in Sri Lanka garnet + quartz reaction rims around orthopyroxene and clinopyroxene rims around orthopyroxene have been widely documented (Schumacher *et al.*, 1990; Faulhaber and Raith, 1991; Raith *et al.*, 1991; Schumacher and Schumacher, 1991). The reaction textures have led workers to suggest that these portions of the Highland Complex have experienced an episode of near-isobaric cooling (Schumacher and Faulhaber, 1994). Garnet corona reactions around orthopyroxene and plagioclase have also been documented in granulitic rocks of the Ungava Orogen in Canada (St-Onge and Ijewliw, 1996). These rocks have been subjected to a polyphase metamorphic history where the early granulite facies is overprinted in part by a younger amphibolite facies event.

Biotite and amphibole tend to overgrow the pre-existing remnant textures and are interpreted to be related to the later retrogression. No titanite is observed within the charnockitic remnants. Symplectic textures in quartz and feldspar are developed, and visible sericitisation is also observed in these rocks.

Typical reaction textures identified within the charnockitic remnants of the megacrystic orthogneiss involve the assemblage grt-plag-qtz-cpx-opx. The coronas of garnet separated by clinopyroxene can be described by the following reaction:

$$opx + plag = grt + qtz \pm cpx$$

The chemical zonation patterns observed within the plagioclase in contact with the garnet provide evidence for garnet growth during the above reactions (see Figure 5.13 and Table 5.4). Garnet coronas around ilmenite are observed within the charnockitic remnants and can be described by the following reaction:

$$pl + ilm = grt + qtz$$

(Note: quartz can either be a reactant or product within this reaction)

Retrogressed Megacrystic Orthogneiss

The range of textures withn the retrogressed megacrystic orthogneisses extends from weakly deformed porphyritic gneisses through to augen gneisses. The phenocrysts are composed of plagioclase, and as the augen-textures develop, so rims of K-feldspar representing "reverse" rapakivi-textures develop. Mineral assemblages in the retrogressed megacrystic orthogneiss comprise quartz, K-feldspar, plagioclase, biotite, amphibole, garnet, titanite, zircon, apatite and ilmenite. In these gneisses biotite, amphibole and titanite become dominant. Minor muscovite is seen intergrown with or replacing biotite. Symplectic quartz-K-feldspar textures are also commonly preserved in these gneisses. Several generations of biotite and amphibole are suggested from their relationships and textural habits.

Reaction textures observed in the retrogressed megacrystic orthogneiss involve the replacement of garnet by plagioclase with amphibole and biotite. Similar textures have been documented from the H.U.Sverdrupfjella in WDML, Antarctica (Grantham *et al.*, 1995). Small remnants of garnets often occur within a moat of plagioclase enclosed in a large amphibole grain (Figure 5.6d and e). In some samples titanite coronas around ilmenite are preserved (Figure 5.6f).

Within the retrogressed megacrystic orthogneiss samples significant reactions involve the consumption of garnet in the presence of amphibole with the development of plagioclase moats around the relic garnet. Titanite development is characteristic of the retrogression and reaction coronas of titanite develop around ilmenite within these samples. Retrogression of the Ungava Orogen granulitic rocks to amphibolite facies also produce similar reaction textures (St-Onge and Ijewliw, 1996).

Kyanite-Bearing Leucogneiss

The kyanite-bearing leucogneisses comprise quartz, K-feldspar, plagioclase, biotite, muscovite, kyanite, sillimanite and garnet with minor zircon, apatite and opaque mineral phases. The aluminosilicates and garnet are randomly distributed throughout these bodies. Kyanite is the primary aluminium phase in the leucogneisses and occurs as large needles often aligned within the foliation of the leucogneisses. Sillimanite needles and muscovite surround and replace the kyanite. Sillimanite occurs as fine needles on the rims of kyanite crystals (Figure 5.7a and b). Sillimanite also occurs on the contact between garnet and kyanite (Figure 5.7c). Kyanite concentrations are occasionally observed on the contact margins of the intrusive bodies. Kyanite blades are aligned parallel to the structural fabrics preserved in the leucogneisses. The sillimanite can exhibit either orientated replacement of the kyanite (Figure 5.7a) indicating growth within a tectonic regime, or may exhibit a radial needle-like morphology (Figure 5.7b) that does not appear to be affected and aligned by later deformation.

Large garnets (2 to 4 mm) with inclusion-rich cores and very inclusion-poor rims occur within the kyanite-bearing leucogneisses (Figure 5.7d). The major inclusions are quartz and feldspar. Rare inclusions of an early muscovite generation have been observed within some of the inclusion-rich garnet cores. Small garnets are generally inclusion free and predominate in some samples. In some thin sections garnet has a relict nature with plagioclase moats separating kyanite-sillimanite assemblages. Embayments of garnet by biotite and sillimanite are also occasionally observed. Garnet is also enclosed within large kyanite crystals. Biotite and sillimanite intergrowths are observed with muscovite and garnet. The co-existence of garnet, sillimanite, biotite, muscovite and quartz assemblages are important for P-T estimates presented later in this chapter. Intergrowths of biotite and muscovite are observed, and in some cases muscovite crosscuts the biotite, suggesting later replacement of the biotite by a late generation of muscovite (Figure 5.7e). Biotite is also replaced by chlorite. Muscovite also mantles kyanite, garnet, and replaces feldspar, suggesting late formation of the muscovite in these cases (Figure 5.7f). Symplectic intergrowths between feldspar and quartz are often recorded within these units. The plagioclase-K-feldspar concentrations vary between samples but the garnet-biotite rich zones are dominated by plagioclase.

The assemblage of pl-grt-Al_2SiO_5-qtz within the kyanite-bearing leucogneisses suggest the following reaction:

$$pl = grt + ky + qtz$$

Other reaction textures observed within the kyanite-bearing leucogneisses include the replacement of kyanite by sillimanite in some samples and the replacement of kyanite by muscovite in others. The coexistence of grt-bt-ms-sil/ky-qtz is important for the estimation of P-T conditions for these samples.

MINERAL CHEMISTRY AND ZONING PROFILES

Analytical Methods

Mineral analyses were determined by wavelength dispersive electron microprobe analysis using a Cameca CAMEBAX instrument (Link LEMAS EXL II system Oxford instrument) at the Rand Afrikaans University in Johannesburg. Analyses were performed with an accelerating voltage of 15 kV, with an absorbed beam current of 10 nA measured on brass. Data were processed using an on-line ZAF correction program. Standards used for calibrations were MicroAnalysis Consultants, Cameca and Smithsonian standards. Representative analyses of the various minerals are provided in Table 5.2 through to Table 5.7. Mineral classifications presented in the text and figures were calculated using the software program 'Minpet2'. Ferric and ferrous iron assignments were based on standard methods used within 'Minpet2' for the various mineral classifications.

The Interpretation of Mineral Reactions and Zoning Profiles

In order to apply geothermobarometry to metamorphic rocks a detailed understanding of the reaction history is required. This information may be obtained from mineral assemblages observed, coupled with the examination of chemical zoning within these phases. The interpretation of zoning profiles is, however, complicated and the reactions and conditions under which zonation formed needs to be understood. For this reason, a brief review of relevant information related to reactions and zoning is provided in this section.

Two types of reactions occur that are important for the development of zoning and ultimately the calculation of P-T conditions during metamorphism. One reaction type is an exchange reaction which results only in the change of composition of the minerals and not in the modal proportions. Equilibrium compositions on the rims of the reacting minerals could be affected by exchange reactions. Net-transfer reactions, on the other hand, result in the consumption and production of phases that results in changes to the modal proportions. Net-transfer reactions result in volume changes that are pressure sensitive whereas exchange reactions are sensitive to temperature changes.

The development of zoning patterns is strongly dependent on the minerals under investigation. Minerals such as biotite and chlorite tend to homogenise more rapidly than garnet and plagioclase due to the differences of chemical diffusivities of certain cations. In high-grade rocks biotite and chlorite tend to homogenise whereas garnet tends to preserve evidence of chemical zoning, providing some information on the P-T conditions experienced by the rock. Plagioclase also has relatively slow cation diffusion (Grove *et al.*, 1984) and therefore the plagioclase is not easily changed except by dissolution. By examination of the zoning patterns information on the formation of these minerals is obtained.

Chemical zoning can be the result of growth or diffusion zoning. Growth zoning is caused by changing external conditions such as P-T changes or bulk composition changes due to mineral (garnet) fractionation. Diffusion zoning is caused by volume diffusion. Diffusion zoning does not require the growth or consumption of the crystal and results in post-growth modification. Diffusion zoning is more dominant in high-grade rocks as it is strongly controlled by temperature (Tracy *et al.*, 1976; Woodsworth, 1977; Yardley, 1977).

Steep profiles in garnet, where concentric bell-shaped profiles develop are typical of growth zoning (see Spear, 1993 for discussion). In these cases, where a net-transfer reaction dominates, zoning across the garnet affects all phases (Fe, Mn, Ca and Mg). Flat zoning profiles in the core of garnet, with steep zoning towards the rim are more typical of diffusion zoning patterns in high-grade rocks (see Spear, 1993 for discussion). Other cases where diffusion zoning in garnet is distinguished is where zoning patterns are nearly homogenous except in the vicinity of biotite in contact with garnet. In these cases Fe and Mg display zoning modified by diffusion but similar zoning is not recorded in Mn and Ca. These zoning patterns typically result due to exchange reactions. Diffusion in Ca is considerably less than the other cations in garnet and zoning may be preserved only within this cation. These factors are taken into account when reviewing the zoning patterns observed and described below. Focus is, however, placed on the kyanite-bearing leucogneiss samples as these samples are used in the estimation of P-T conditions at Neumayerskarvet.

Charnockitic Remnants within the Megacrystic Orthogneiss

Mineral Chemistries

Pyroxene: - Pyroxene occurs only within the charnockitic remnants of the megacrystic orthogneiss. Orthopyroxene analyses plot in the clinoferrosilite field in the pyroxene quadrilateral (Figure 5.8). XFe, XMg, and XCa for orthopyroxene show little variation and range between 0.60 to 0.65, 0.33 to 0.36 and <0.05 respectively. The Al contents are extremely low in orthopyroxene and are therefore not presented in the traverse of Figure 5.13. Orthopyroxene profiles are relatively flat, with changes only being observed where clinopyroxene develops a reaction corona between orthopyroxene and garnet. At these localities the fine intergrowths of orthopyroxene and clinopyroxene are not sufficiently isolated from one another, resulting in a mixed analysis. Examples of these mixed pyroxene analyses are shown on the pyroxene classification diagram of Figure 5.8 where pseudo-compositions occur between the orthopyroxene and clinopyroxene end members. Similar mixed analyses were obtained from the contacts between the pyroxene in the microprobe traverse lines of Figure 5.13.

Clinopyroxene occurs either in isolation where no orthopyroxene is present in the more retrogressed samples, or as reaction coronas around the large orthopyroxene grains (Figure 5.6a). Clinopyroxene plots in the hedenbergite classification field at the boundary with the diopside field. Grains of clinopyroxene are small and little zonation was recognised in the analysed samples.

Garnet: - Two potential generations of garnet are seen within the charnockitic remnants. A garnet core enclosed by orthopyroxene with clinopyroxene reaction coronas between these minerals represents a potential rare early garnet generation. Garnet typically forms coronas around the orthopyroxene with clinopyroxene, quartz and plagioclase. There is no chemical difference between the two garnet types, suggesting that the observed textural relationship of the core garnet may be a function of the 2-dimensional thin-section rather than a different generation of garnet. Garnets are almandine–rich (Figure 5.9). Zoning profiles are relatively flat as shown in Figure 5.13, but the detailed garnet zoning profile from the charnockitic remnant shows some evidence of zoning (Figure 5.20). Traverse line A-B represents the "core" garnet while traverse line C-D represents the coronitic rim garnet (see Figure 5.13 and 5.20). The XFe content shows a slight increase towards the rims of the garnet in contact with pyroxene. Garnet in contact with plagioclase shows a sharp increase close to the rim at position D. The coronitic garnet displays an asymmetric distribution of XFe from the pyroxene contact to the feldspar contact. XMg decreases towards the rims of the garnet in contact with pyroxene. The garnet-plagioclase contact has higher XMg values but also displays a rapid decrease at the rim, and a similar asymmetrical distribution for the XMg is observed in the coronitic garnet. Flat patterns with irregular spikes are observed in the XCa profiles for the charnockitic remnant garnets. No real zoning patterns are discernible. Similarly, XMn profiles for these garnets tend to be erratic and no distinct zoning patterns are identified.

Feldspar: - Plagioclase and K-feldspar are observed within the charnockitic remnants of the megacrystic orthogneiss. Plagioclase An contents range from 18 to 30 (Figure 5.10) and typically show an increasing An zoning pattern away from garnet (see Figure 5.20). Strong zoning of the plagioclase is observed in contact with garnet, suggesting the involvement of the plagioclase in the garnet generation (see Figure 5.20).

Biotite: - Biotite is fairly rare in the charnockitic remnants and tends to form as a product of retrogression within the samples. Compositions are fairly constant throughout the biotites, with XFe values ranging between 0.64 and 0.66.

Ilmenite: - Ilmenite is typically surrounded by garnet coronas. Such garnet has a similar chemistry to the coronitic and "core" garnets described above. Typical analyses of these ilmenites are provided in Table 5.7.

Retrogressed Megacrystic Orthogneiss

Mineral Chemistries

Amphibole: - Amphiboles analysed from the retrogressed megacrystic orthogneiss are calcic group amphiboles and tend to plot within the ferro-pargasite field of Figure 5.11. Al varies from 2.16 to 2.33 with Si ranging from 6.15 to 6.30, and XMg values ranging from 0.17 to 0.19 in the suite of samples analysed. The amphiboles tend to be typically unzoned within these samples. Selected amphibole analyses are provided in Table 5.5.

Biotite: - Biotite classifications and representative compositions are provided for the retrogressed megacrystic orthogneiss in Figure 5.12 and Table 5.6 respectively. XFe values range from 0.71 to 0.73 with XMg values between 0.27 to 0.28. Biotites typically display flat profiles within the retrogressed megacrystic orthogneiss (see Figure 5.14).

Feldspar: - Plagioclase coronas develop between amphibole and garnet, and result from reactions involving these two mineral phases. The plagioclase An contents vary from 21 to 37, and tend to show an increase in An content towards the rim in contact with garnet (see Figures 5.10 and 5.14). K-feldspar is also observed within several areas of the plagioclase and quartz matrix. Typical feldspar compositions are presented in Table 5.4.

Garnet: - Garnet typically occurs as remnants surrounded by plagioclase moats within the larger amphibole grains within the retrogressed megacrystic orthogneiss. Garnet is typically corroded within the retrogressed samples and this suggests that garnet consumption was active during the retrogression. The garnets are almandine-rich (see Figure 5.9 and 5.14 and Table 5.3) with XFe, XMg and XCa ranging from 0.58 to 0.62, 0.03 to 0.06 and 0.29 to 0.32 respectively. Garnet zoning profiles are relatively flat but rapid changes at the contacts of the garnets with other minerals are observed (see Figures 5. 14 and 5.21). The XFe value decreases rapidly when in contact with biotite or plagioclase. XMg also tends to decrease at the garnet rim in contact with biotite and plagioclase. XCa decreases moderately at the garnet rim but shows an asymmetrical distribution with the higher Ca contents preserved closer to the plagioclase contact than the biotite contact. An increase in the XMn values is also observed towards the rims of the garnet (see Figure 5.21). The zoning profiles of the garnet within the retrogressed megacrystic orthogneiss tend to be fairly flat with sharp changes observed close to the garnet rim in contact with plagioclase and biotite.

Ilmenite and Titanite: - Ilmenite within the retrogressed portion of the megacrystic orthogneiss is often enclosed by a titanite corona. Representative analyses of ilmenite and titanite are provided in Table 5.7. Titanite becomes abundant in the retrogressed samples studied within the northern Kirwanveggen.

Kyanite-Bearing Leucogneisses

The kyanite-bearing leucogneiss is the major rock unit used for detailed metamorphic interpretation. As such the reaction textures and zoning profiles are discussed in considerable detail in order to provide information for the derivation of P-T conditions for this area. In this section the chemistry and zoning patterns of the individual minerals are discussed for each sample site selected for further detailed analysis. In this way a detailed reaction history is established in a later section for further geothermobarometry. The chemical signatures of garnet, feldspar and biotite are displayed in Figures 5.9, 5.10 and 5.12, and Tables 5.3, 5.4 and 5.6 respectively. Changes in mineral compositions due to different paragenetic relationships are also discussed in later sections.

Mineral Chemistries

Biotite: - Biotite classifications are shown in Figure 5.12 for the kyanite-bearing leucogneisses. Several generations of biotite are observed. Biotites are typically unzoned and XFe values range from 0.56 to 0.58. Biotite within the weak fabric observed in the kyanite-bearing leucogneiss displays slightly lower Al contents than biotite in contact with garnet. Very few chemical differences are seen between the different biotites analysed from the samples under investigation.

Feldspar: - The An content of the plagioclase varies from 10 to 29 within the kyanite-bearing leucogneisses (see Figure 5.10). K-feldspar is also abundant throughout the kyanite-bearing leucogneisses.

Garnet: - Garnets from the kyanite-bearing leucogneisses are almandine-rich but differ in composition from garnet within the megacrystic orthogneiss (see Figure 5.9). The profiles indicate the presence of at least two generations of garnets within these samples. The inclusion rich cores have compositions typically about 0.73, 0.17 and 0.04 for XFe, XMg and XCa respectively. The smaller garnets and inclusion free regions have XFe, XMg and XCa values of between 0.72 to 0.76, 0.13 to 0.15 and 0.03 to 0.06 respectively. Individual mineral zoning patterns are discussed in more detail in the following sections.

Muscovite: - Muscovite is observed in all of the kyanite-bearing leucogneiss samples used during this investigation (see Table 5.1) and occurs as several generations. Rare inclusions of early muscovite have been found within the cores of large garnets. Muscovite also occurs in association with kyanite, sillimanite, garnet and biotite. A late stage muscovite mantles kyanite and garnet, and replaces feldspar.

Sample PH92018

Site 1: - A sketch of the mineral assemblages at this site is illustrated in Figure 5.15. Minerals in contact with one another are plagioclase, garnet and sillimanite. In this sample sillimanite replaces kyanite, but kyanite remnants are still observed in the sample. A microprobe spot traverse was measured across the garnet and through the plagioclase (traverse A-B-C in Figure 5.15). The plagioclase displays a relatively flat profile with an increase in An content at the plagioclase-garnet contact. The chemical zoning across the garnet is shown in Figure 5.15, but a more detailed zoning profile for this sample is provided in Figure 5.22. In Figure 5.22 the zoning profile (A1-B1) displays a very slight increase in XFe with a flat XMg and XMn profile. XCa displays an increase from garnet rim to garnet core. In general the garnet displays a flat homogenous chemical zoning profile except for Ca which preserves some of the original zoning within the garnet. These zoning patterns are most likely the result of net-transfer reactions between the associated mineral phases, as the assemblages here do not support the existence of exchange reactions.

Site 2: - This locality exhibits an assemblage of garnet, plagioclase, quartz and biotite (see Figure 5.16). A microprobe spot traverse has been carried out across the plagioclase and through the entire garnet from the plagioclase-garnet contact to the garnet-plagioclase contact (B-F in Figure 5.16). A second traverse was measured from the garnet core to the garnet-biotite contact and across the biotite (traverse line C-D-E in Figure 5.16). Plagioclase (traverse A-B) displays a relatively flat profile in Figure 5.16. An increase in the Ab content occurs towards the plagioclase-garnet rim. Orthoclase content also increases slightly towards the plagioclase rim. Biotite exhibits a relatively flat zoning profile with slight variations, but generally provides an homogenous profile (profile D-E in Figure 5.16).

The garnet profile from the plagioclase-garnet contact through to the garnet-plagioclase rim exhibits similar profile chemistries to that observed at site 1 (see profile B2-F2 compared to profile A1-B1 in Figure 5.22). The distinct similarity of the zoning profiles across this traverse, and the similar mineral associations, suggest that net-transfer reactions were dominant during the development of this chemical profile. Profile C2-D2 (Figure 5.22) is taken from the garnet core through to the garnet-biotite contact and displays a somewhat different zoning pattern. The XCa zoning pattern is similar to that observed away from the biotite contact. The XFe and XMg profiles, on the other hand, exhibit a steep zoning pattern developed towards the rim garnet-biotite contact. XFe increases sharply whereas the XMg decreases sharply towards the garnet-biotite contact. XMn also shows an increase towards the garnet-biotite contact. Profile C2-D2 suggests significant cation exchange reactions took place between the garnet and biotite in contact with one another, which results in the zoning profiles observed. The zoning profile away from the garnet-biotite contact is very similar to that observed at site 1 where no biotite is observed, suggesting that the garnet zoning profile observed at this locality is the result of a combination of net-transfer and cation exchange reactions.

Sample PH93195

Site 1: - A microprobe analysis traverse was measured across a large garnet in contact with plagioclase within sample PH93195 of the kyanite-bearing leucogneiss. The profile extends across A-B and is illustrated in Figure 5.17. The garnet at this site has an inclusion-rich core with inclusion-free rims (see Figures 5.7d and 5.17). The feldspar zoning displays a mixture of plagioclase and K-feldspar across the grains. On both sides of the garnet traverse the feldspar composition changes rapidly between plagioclase and K-feldspar. The garnet profile is displayed individually in figure 5.23 to obtain a clearer picture of the zoning patterns across the garnet (traverse A1-B1). XFe, XMg and XMn exhibit flat profiles across this large garnet from rim to rim. The XCa profile, however, shows a significant zoning pattern. The inclusion-rich core of the garnet exhibits a flat and low XCa profile. Across the inclusion-free rims the XCa content increases sharply and then decreases steeply right at the adjacent garnet-plagioclase rim. The XCa profile displays evidence of a garnet overgrowth on the inclusion-rich core whereas XFe, XMg and XMn are essentially homogenous. Net-transfer reactions would dominate at this locality but homogenisation of all zoning patterns apart from Ca has taken place.

Site 3: - An assemblage of garnet, plagioclase, quartz, K-feldspar and biotite are present at site 3 in sample PH93195 (Figure 5.18). The garnet does not display an inclusion-rich core but rather is generally uniform and inclusion-free. Two main chemical profiles were measured across these assemblages (Figure 5.18). Profiles A-B-C extends from the biotite core (A) through the biotite-garnet contact (B) and into the centre of the garnet (C). The second profile extends from the garnet rim through the core to the garnet-plagioclase contact and into the plagioclase (F-D-E). The plagioclase profile (D-E in Figure 5.18) is predominantly flat with small irregular chemical changes across the grain. An increase in the An content at the plagioclase-garnet contact is possible, but not clearly resolved. The biotite also displays a flat zoning profile from core to biotite-garnet contact (profile A-B in Figure 5.18). The biotite composition is similar to the biotite that occurs in sample PH92018 site 2 (see Figure 5.16).

Two different profiles were measured across the garnet in sample PH93195 site 3. One profile extends from plagioclase-garnet contact through the garnet core and to the garnet-plagioclase contact (profile F3-D3 in Figure 5.23). The second profile extends from the garnet core to the garnet rim that is in contact with biotite (profile C3-B3 in Figure 5.23). The two profiles display fairly similar patterns although they are related to different minerals in contact with the garnet. The XFe profile increases sharply at the contact with biotite and at one rim zone in contact with plagioclase. XMg decreases sharply at the biotite contact, is less so at the one plagioclase contact, and is flat at the second plagioclase contact. XCa shows a bell-shaped zoning pattern from rim to rim across both profiles. Sharp increases in the XMn zoning pattern towards the garnet rim are present at the garnet and plagioclase contacts. The garnet displays a somewhat different chemical zoning pattern to the garnet studied in sample PH93195 site 1. The data suggest that a combination of net-transfer and cation exchange reactions influenced these mineral zoning patterns.

Site 4: - Although no diagram is presented here from site 4 it is an important site as a large biotite grain occurs within the feldspar and quartz matrix. This isolated biotite has a similar but slightly different chemistry to the biotite in contact with garnet. The biotite is incorporated within the regional foliation observed in this sample and indicates an early generation of biotite. A profile across the biotite indicates that the zoning pattern is essentially flat and homogenous for this biotite. XFe ranges from 0.56 to 0.57 with XMg of between 0.42 to 0.44.

Site 5: - Site 5 displays a garnet with an inclusion-rich core and inclusion-free rims within a feldspar and quartz matrix (Figure 5.19). Plagioclase displays little zoning with a slight increase in An towards the centre (profiles B-C in Figure 5.19). The garnet exhibits similar zoning patterns as the large garnet at site 1. This garnet also has an inclusion-rich core with a rim of inclusion-free garnet (Figure 5.23). The XFe and XMg profiles are flat with a sharp increase and decrease at one plagioclase rim contact respectively. XMn displays a flat profile across the garnet in profile B5-A5 in Figure 5.23. The XCa profile is flat across the garnet core with subsequent increasing XCa values at the rims. XCa decreases at the immediate garnet rim contact. Zoning patterns are only preserved within the XCa profile within this garnet. The associated assemblages indicate that net-transfer reaction would dominate but all profiles except the XCa are homogenised.

ESTIMATION OF P-T CONDITIONS

Geothermobarometry in the Kyanite-Bearing Leucogneiss

Careful selection of mineral chemistries that are in equilibrium with one another is required before geothermobarometry can be attempted. One of the problems inherent in exchange reactions is that diffusion between the two phases may continue well below the peak metamorphic conditions, resulting in diffusive profiles and incorrect temperature estimates being obtained. Another problem in the determination of P-T paths is that the controls for pressure and temperature calculations differ and may therefore not be related in time to one another. These reactions most likely quench at different P-T conditions and the P-T paths deduced from the combination of exchange and net-transfer reactions may give misleading results (See Frost and Charcko, 1989; Harley, 1989; Spear and Florence, 1991 for examples).

Several considerations have to be addressed before meaningful interpretations can be made using the calculated results obtained from geothermobarometry (Spear and Peacock, 1991). These involve firstly an evaluation of the state of equilibrium of minerals within the samples. Secondly, the effects of re-equilibration during cooling on the geothermometer or geobarometer needs to be assessed. Exchange reactions tend to continue during cooling from high-grade conditions. Lastly the accuracy of the geothermometer or geobarometer calibration needs to be evaluated. The suitable chemical range of the minerals involved must be within the constraints provided by the calibration set during the establishment of the geothermobarometer. Inconsistencies in and between calibrations of different geothermobarometers may lead to errors in the determination of P-T conditions for the samples under investigation. Wherever possible independent methods of evaluating the geothermometer should be used.

Geothermobarometry describes the techniques used to infer P and T conditions using the pressure and temperature dependence of the equilibrium constant (Spear, 1993). Geothermometers are reactions that show considerable T sensitivity and small P sensitivity (small change in volume), whereas geobarometers are reactions that show little T dependence but significant P dependence (large volume changes). Equilibrium constants for certain reactions can be calculated using the compositions of the mineral phases involved (Spear, 1993). Lines of constant equilibrium between co-existing phases can be calculated and imply that the sample equilibrated at some point on this line. By using two different equilibrium lines based on a P and a T sensitive reaction, a P-T point of equilibration can be obtained from the intersection of these two lines. The problem here is that the P and T calculations are done using different calibrations, which introduces uncertainties that are difficult to evaluate. Errors are generally reduced, although not eliminated, through the use of internally consistent thermodynamic data sets as is the case with GeoPath version 1.2 software (Gerya and Perchuk, 1991).

Many geothermometers are based on cation exchange reactions such as the garnet-biotite Fe-Mg exchange thermometer. The exchange reactions can be written in terms of the exchange components only, and typically make good geothermometers as they display small volume changes (Spear, 1993). In these types of reactions the distribution of Fe and Mg between garnet and biotite is a function of P and T.

Geobarometers, on the other hand, are typically based on net-transfer reactions (Spear, 1993). These reactions cause the consumption and production of phases resulting in large volume changes, which translate to pressure sensitive equilibrium constants. There are numerous geobarometers involving garnet and plagioclase where the grossular component in garnet and the anorthite component in plagioclase have been balanced against many different components (Al_2SiO_5, quartz, muscovite, biotite, amphibole and pyroxene). Such a barometer is the An = grs + ky + qtz (GASP) geobarometer. The application of the GASP geobarometers involves the measurement of co-existing garnet and plagioclase which are used to infer the activity for each phase. A simple ionic solution model predicts the activity-composition relationships, but garnet and plagioclase are non-ideal solutions and corrections are required for the GASP geobarometer.

Calculation of P-T conditions for the samples used in this investigation are based on similar principles as outlined above. GeoPath version 1.2 (Gerya and Perchuk, 1991) has been used for P-T calculations during this investigation. This program is designed to calculate a variety of geological processes using a wide range of internally consistent geothermometers and geobarometers (Gerya and Perchuk, 1991). Temperature estimates made during this investigation were obtained from the experimentally calculated biotite-garnet thermometer (Perchuk, 1989 and 1990). Pressure estimates are based primarily on the empirical ms-qtz-bt-grt-Al_2SiO_5 barometer (Perchuk and Krotov, 1998) which was corrected with respect to the bt-grt thermometer (Perchuk, 1977). The barometer is based on the reaction:

$$Grt + ms = bt + Al_2SiO_5 + qtz \text{ (Perchuk and Krotov, 1998)}$$

The thermodynamics of this reaction are controlled by the participation of the variety of Al_2SiO_5 polymorph present (Holland and Powell, 1990).

Applying the various geothermobarometers to the appropriate sample sets and minerals assemblages from the northern Kirwanveggen produced a wide range of P-T conditions for these samples. Table 5.8 summarises the ranges of pressures and temperatures obtained from the different samples. Geothermobarometry for the megacrystic orthogneiss are also provided in Table 5.8 for comparison to the data generated for the kyanite-bearing leucogneiss samples.

The extremely high pressures obtained from the GASP (grt-ky-pl-qtz) geobarometer suggest unrealistic conditions that are not compatible with other P-T calculations (see Table 5.8). Although the GASP geobarometer is a well studied reaction, and regarded as a reliable pressure indicator (Spear, 1993) this does not appear to be the case in the kyanite-bearing leucogneisses in this investigation. The problem of the application of the GASP geobarometer is potentially related to the chemistries of the minerals involved in this reaction. The reaction is described by:

$$An = grs + ky + qtz$$

In the kyanite–bearing leucogneiss the plagioclase content is strongly albite-rich (Ab) and the garnet composition has low grossular (grs) contents (XMg < 0.2). The low An and grs contents of the plagioclase and garnet result in the generation of high pressures as this reaction is controlled by the Ca content of the rocks. Rocks with high grs contents and low An contents indicate crystallisation at high P and low T, whereas rocks with low grs and high An content indicate low P and high T conditions (Spear, 1993). In the kyanite-bearing leucogneisses both An and grs content are low, but the relative abundance between these phases generates unrealistically high pressures. Another factor is that there is a large amount of late K-feldspar within the samples that may affect the plagioclase contents within the samples. Recrystallisation of plagioclase could be expected under these conditions resulting in disequilibrium between the co-existing mineral phases. Zoning profiles of the plagioclase in contact with garnet are relatively flat. During garnet generation An contents would typically decreases towards the contact of the garnet, but zoning profiles do not support the expected reaction profiles (see Figures 5.17 and 5.19). The relatively flat plagioclase profiles may indicate a degree of re-equilibration within the grains.

The wide range of P-T conditions calculated for the individual geothermometers and geobarometers suggest disequilibrium between co-existing phases, and the possibility of re-equilibration or diffusion during cooling from peak metamorphic conditions. Reactions and reaction textures described from the samples under investigation support the potential presence of mineral phases in disequilibrium with one another. A review of the tectonic history of the northern Kirwanveggen also indicates that poly-metamorphism is expected. Under such conditions diffusion of certain geothermometers should be anticipated making the establishment of peak P-T conditions for these rock samples equivocal.

Metamorphic History of Neumayerskarvet

Using the detailed zoning profiles a metamorphic history has been distinguished within the kyanite-bearing leucogneiss. The metamorphic stages are based on mineral reaction textures and chemical changes recorded in the mineral assemblages. The metamorphic stages of the kyanite-bearing leucogneisses only record metamorphic reactions since the time of emplacement of these units. The kyanite-bearing leucogneisses have been dated at 1096 ± 10 Ma (see Chapter 4) and the metamorphic history documented within these rocks only begins at this time. Earlier metamorphism within the northern Kirwanveggen would not be experienced by the samples under investigation. Early deformation pre-dating the intrusion of the kyanite-bearing leucogneisses has been documented (see Chapter 3 and 4), and therefore an earlier associated metamorphism can be expected. The metamorphic evolution outlined below does not include the early metamorphic history of the northern Kirwanveggen. As such, the metamorphic stages identified here are termed Mn+1 (nkv), Mn+2 (nkv) and Mn+3 (nkv) to account for the potential early metamorphic evolution of this region. The mineral reaction textures used to define the different metamorphic stages are discussed in the following section.

Mn+1 (nkv) Metamorphic Stage

Early Mn+1 (nkv) metamorphic assemblages are represented by kyanite, biotite, garnet, quartz and plagioclase with possible muscovite. The early large kyanite blades enclose garnet and provide evidence of early garnet growth in the leucogneisses. In some of the larger garnets preserved in this rock type inclusion-rich cores are preserved. These garnet cores have small inclusions of quartz and feldspar with rare muscovite inclusions in some samples. These garnet cores are interpreted as part of the early Mn+1 (nkv) metamorphic stage preserved in the kyanite-bearing leucogneisses. Examples of these inclusion-rich low XCa garnet cores are preserved in sample PH93195 sites 1 and 5 (Figure 5.23). These garnet compositions are referred to as grt1 in Figure 5.24 where a mineral paragenesis for the kyanite-bearing leucogneiss samples is established. Large biotite grains that are isolated and lie within the weak gneissic fabric of the leucogneisses are also interpreted to represent part of the early metamorphic assemblage (bt1 in Figure 5.24). This biotite type occurs at site 4 in sample PH93195. This biotite generation represents the earliest biotites identified within the samples under investigation. In these cases no contact relationships are observed between these mineral phases suggesting that cation exchange reactions are limited. The grt-bt geothermometer applied to Mn+1 (nkv) generation phases provides an indication of the temperature during this stage and is presented as reactions 21 and 22 in Figure 5.25c and Table 5.9. Pressure estimates are less well constrained. The presence of muscovite inclusions within the cores of garnet (grt1) suggests that the grt-bt-ms-ky-qtz geobarometer can be applied for the Mn+1 (nkv) metamorphic stage. If the mineral chemistries of the plagioclase were not affected by later retrogression then the grt-bt-ky-qtz geobarometer would be applicable. This is, however, not the case in the samples under investigation and pressures calculated using this geobarometer are unrealistically high for the mineral assemblages and chemistries observed, as already discussed. Pressure ranges for the Mn+1 (nkv) assemblages (grt-bt-ms-ky-qtz) using GeoPath Version 1.2 (Gerya and Perchuk, 1991) are obtained from reactions 19 and 20 in Figure 5.25c and in Table 5.9. P-T estimates for the Mn+1 (nkv) metamorphic stage are 710-760 °C and 7.8-8.5 kb (see Figure 5.25d). This metamorphic stage is interpreted to have taken place soon after formation of the kyanite-bearing leucogneisses and is interpreted to represent conditions of metamorphism at which these rock units formed.

Mn+2 (nkv) Metamorphic Stage

The Mn+2 (nkv) metamorphic stage is marked by the replacement of kyanite by sillimanite within the kyanite-bearing leucogneisses. The sillimanite grows within the fabric of the rock and is aligned parallel with the kyanite suggesting that it grew during the same, or a similar, tectonic regime. Garnet grows at the contact between the kyanite and sillimanite needles and has significantly higher Ca contents than the Mn+1 (nkv) metamorphic stage garnet (grt2 in Figure 5.24). The higher Ca-rich rims that grow around the older generation inclusion-rich garnet cores are interpreted as garnets of the Mn+2 (nkv) metamorphic stage. Biotite developed in contact and close association with garnet and is often intergrown with muscovite (bt2 and ms2 in Figure 5.24). Core assemblages of the coexisting phases are used to provide an estimate of the P-T conditions during the Mn+2 (nkv) metamorphic stage in the kyanite-bearing leucogneiss. The transition from kyanite to sillimanite during this metamorphic stage provides a pressure constraint based on the slope of the Al_2SiO_5 phase boundary. The pressure constraint is supported by the coexistence of grt-ms-bt-sil-qtz (reactions 5 and 6 in Figure 5.25), and grt-pl-qtz-sil (reactions 1, 2 and 3 in Figure 5.25a). Temperature estimates are obtained using grt-bt exchange reactions based on core mineral assemblages of core compositions of biotite and garnet in contact with one another (reactions 8 and 9 in Figure 5.25a). Temperatures and pressures obtained from cores of co-existing minerals for the Mn+2 (nkv) stage indicated conditions of 630-690 °C and 6.0-7.4 kb respectively Figure 5.25d).

Mn+3 (nkv) Metamorphic Stage

The final Mn+3 (nkv) metamorphic stage recognised within the kyanite-bearing leucogneisses is characterised by the growth of large amounts of microcline, muscovite and chlorite. The chlorite is typically seen replacing biotite, while muscovite replaces biotite, feldspar and kyanite. This stage represents cooling from the peak metamorphic conditions established for the kyanite-bearing leucogneiss samples. P-T conditions of the Mn+3 (nkv) metamorphic stage were obtained using rim compositions of grt-bt assemblages (compositions grt2b and bt2(rim) in Figure 5.24). These assemblages provide closure temperature conditions of the grt-bt exchange reaction for the kyanite-bearing leucogneiss. The exchange reaction of biotite and garnet rims in contact with one another have been used for characterisation of this metamorphic stage (reaction 10 in Figure 5.25a and reaction 16 in Figure 5.25b). Pressure conditions are less well constrained but indications of moderate pressure conditions are suggested using the co-existing grt-bt-ms-sil assemblages. Diffusional paths are developed between the Mn+2 (nkv) and Mn+3 (nkv) metamorphic stages. Large amounts of fluid migration during the Mn+3 (nkv) metamorphic stage are suggested by the pervasive generation of large microcline grains along with the abundant muscovite and chlorite replacement. Temperatures of 560-570 °C with pressures of 4.4-4.6 kb are suggested for the Mn+3 (nkv) metamorphic stage (Figure 5.25d).

The Significance of P-T Path Interpretations

The metamorphic evolution (P-T path) established for the northern Kirwanveggen from samples of kyanite-bearing leucogneisses is not significantly different from P-T paths established for other parts of the Kirwanveggen and Heimefrontfjella (Groenewald and Hunter, 1991; Ferrar, 1995; Grantham *et al.*, 1995; Groenewald *et al.*, 1995; Jacobs *et al.*, 1996). Similar metamorphic stages have been identified within a variety of different rock types using different mineral assemblages and geothermobarometers. A summary of these P-T conditions is provided in Figure 5.26 for comparison to the current conditions that have been calculated. The P-T path interpreted for Neumayerskarvet from the data presented here is shown in Figure 5.27. The data from previous investigations provide support for the P-T path established during this investigation. One significant difference between the path interpreted in this investigation and the published P-T paths is that the previous investigations have suggested that there is an early high-P metamorphic stage at *ca.* 1150 Ma (See Grantham *et al.*, 1995; Groenewald *et al.*, 1995 and Moyes and Groenewald, 1996 for discussions). This has not been identified during this investigation, but the samples used here do not record metamorphic conditions prior to *ca.* 1100 Ma, which are their intrusive ages.

The P-T path established in this investigation for the northern Kirwanveggen does not, however, take into account specific time relationships between the different metamorphic stages or reactions. Although the proposed P-T path can be interpreted as the result of retrogression from a single tectono-metamorphic event, this may not be the case. The P-T path may represent retrograde segments of unrelated tectono-metamorphic cycles that are superimposed on one another developing a seemingly continuous P-T pathway. Nor are all parts of the P-T path followed by these rocks necessarily preserved by the reaction history that has been identified. Prograde portions of the path are not observed and the P-T path only documents the retrogressive metamorphic history of this terrain.

The question of whether this retrogressive P-T path represents a single or multiple tectono-metamorphic cycle is not answered in this section. Other isotopic investigations have suggested that the P-T paths distinguished for the high-grade gneisses of WDML are a result of multiple tectono-metamorphic events similar to those recognised in other regions (Collins and Williams, 1995; Talarico and Castelli, 1995). Further isotopic work to obtain age data for this path is required to relate the metamorphic history at Neumayerskarvet to the tectonic evolution of the area. The following chapter attempts to address these problems and establish a P-T-t-d evolution for the northern Kirwanveggen.

CONCLUSIONS

- P-T estimates for conditions of metamorphism at Neumayerskarvet have been obtained from kyanite-bearing leucogneiss dated at 1096 ± 10 Ma using U-Pb SHRIMP methods.
- Three metamorphic stages have been identified, termed Mn+1 (nkv), Mn+2 (nkv) and Mn+3 (nkv), as there is an early tectonic event that pre-dates the intrusion of the kyanite-bearing leucogneiss. The existence of a possible earlier metamorphic stage cannot be discounted.
- The Mn+1 (nkv) metamorphic stage is represented by inclusion rich garnet cores, kyanite, quartz, plagioclase and biotite. Temperatures are constrained between 710 and 760 °C based on bt-grt (bt1 and grt1), but pressure conditions are less well constrained. The presence of kyanite permits conditions to be estimated at 7.8-8.5 kb based on grt-bt-ky-ms-qtz.
- The Mn+2 (nkv) metamorphic stage is marked by sillimanite replacement of kyanite. The co-existence of garnet, biotite, muscovite, plagioclase, sillimanite and quartz provides estimates of 630-690 °C (grt2-bt2) and 6.0-7.4 kb (grt-bt-sil-ms-qtz and grt-pl-qtz-sil).
- The final Mn+3 (nkv) metamorphic stage is determined using rim compositions (grt2b and bt2(rim)) and is controlled by the closure of diffusion between biotite and garnet, and represents cooling. Conditions of 560-570 °C and 4.4-4.6 kb have been estimated for this stage.

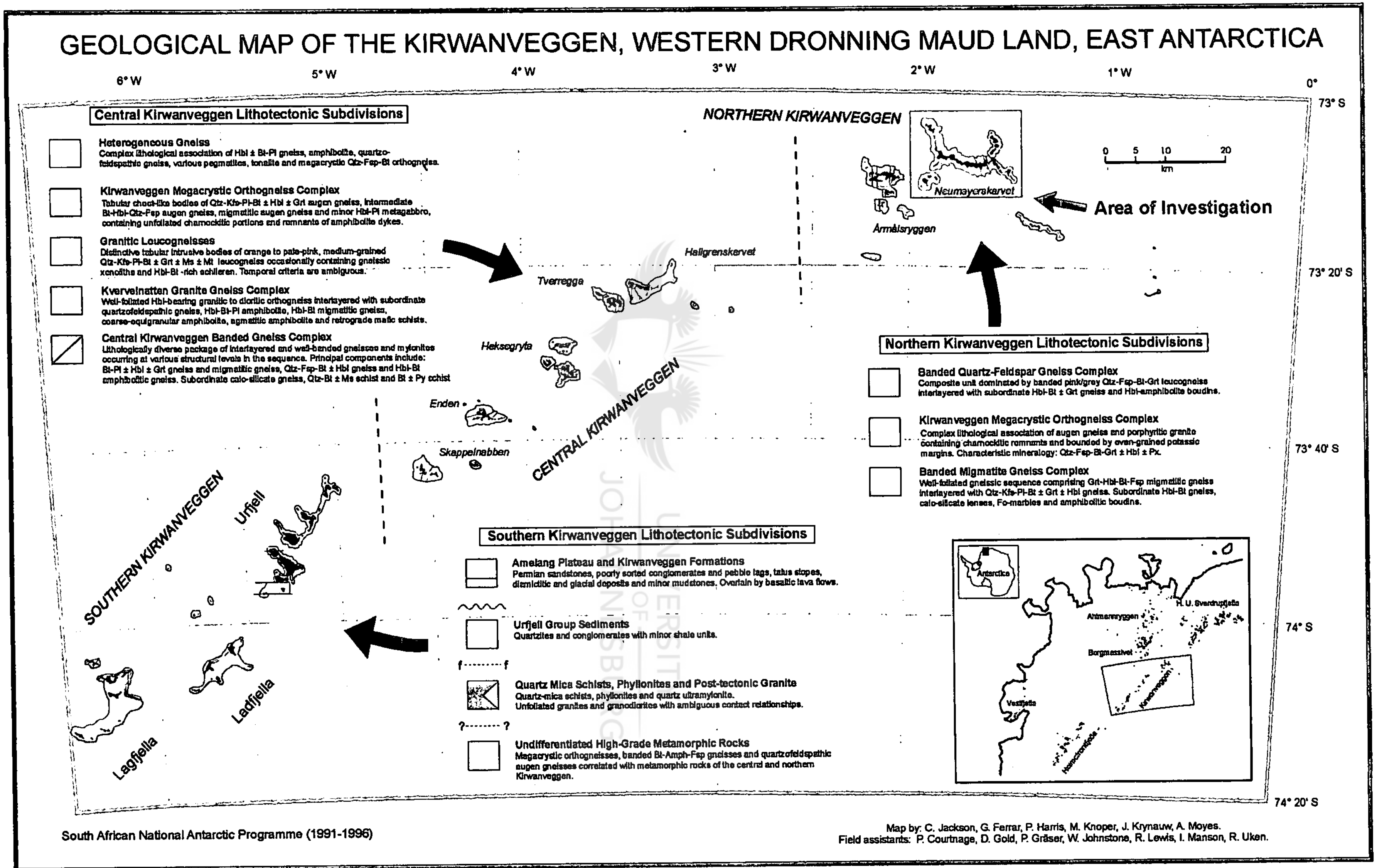

FIGURE 5.1. Geological map of the Kirwanveggen in western Dronning Maud Land, Antarctica. The subdivision of the northern, central and southern Kirwanveggen outcrop patterns and the associated lithotectonic units are illustrated. The Neumayerskarvet outcrop pattern, which is the major area of focus in the northern Kirwanveggen, is outlined for location purposes.

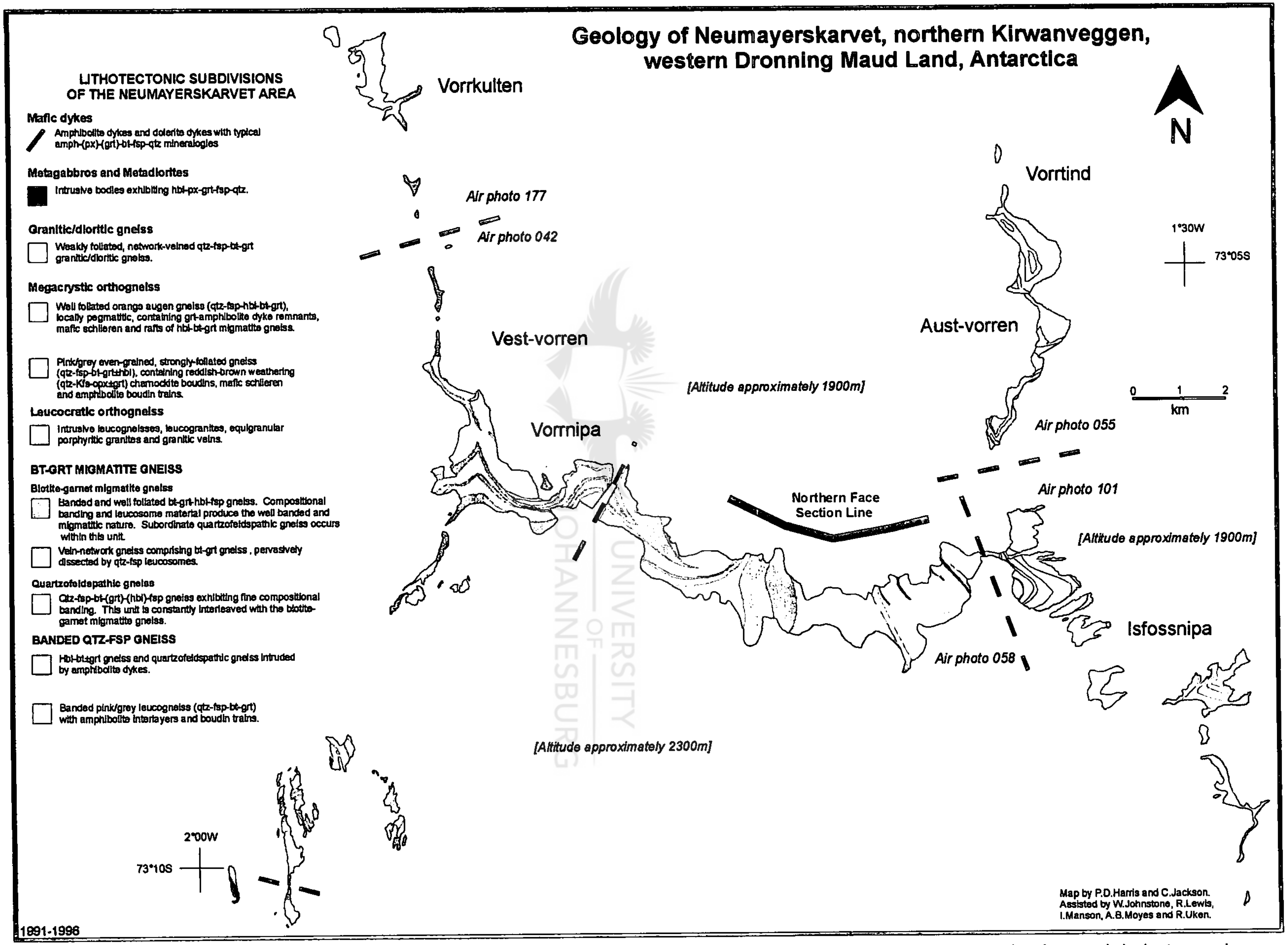

FIGURE 5.2. The geology of Neumayerskarvet in the northern Kirwanveggen. The map has been constructed using aerial photographs as no suitable topographical map at this scale is currently available. Boundaries are marked where different photographs were used for the mapping. The lithotectonic subdivision is illustrated on the map. The location of the section line displayed in Figure 5.4 is also shown on the geology map.

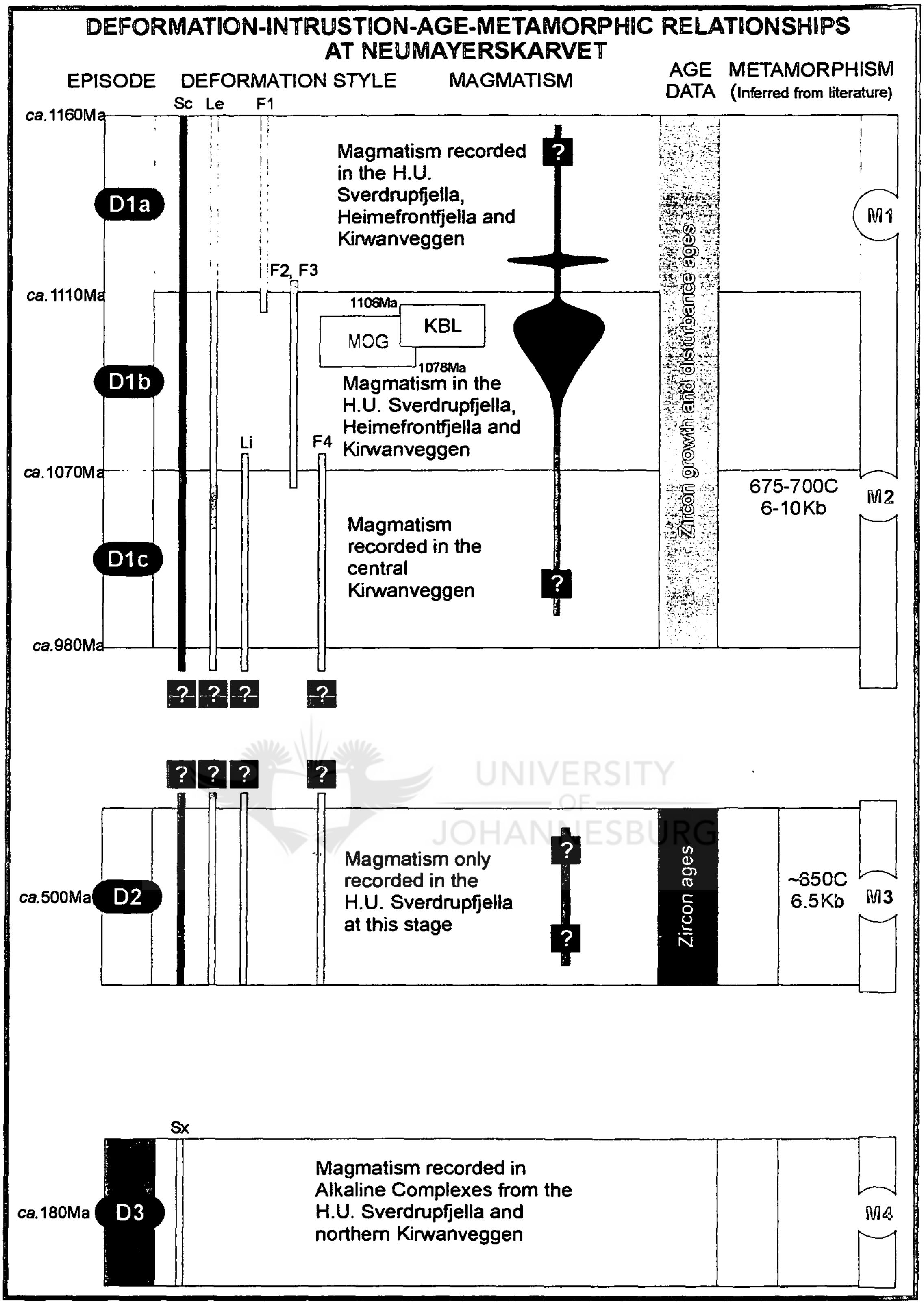

FIGURE 5.3. Deformation-isotopic-magmatic-metamorphic correlations within the northern Kirwanveggen. The deformation sequence and isotopic information have been established in Chapters 3 and 4. The metamorphic evolution is inferred from published literature and is summarised in Grantham *et al.* (1995). Intrusive units illustrated on this diagram are the kyanite-bearing leucogneiss (KBL) and the megacrystic orthogneiss (MOG).

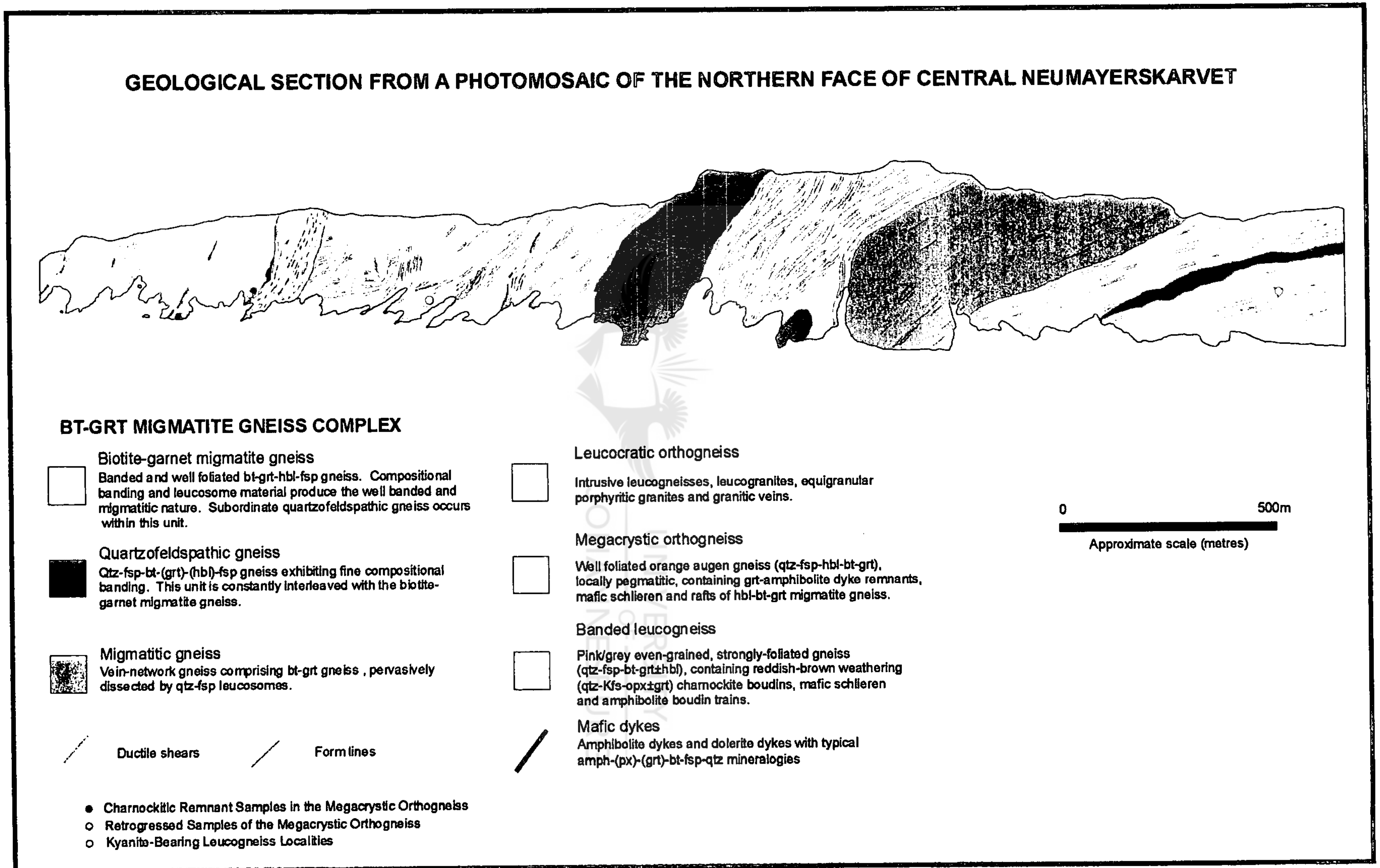

FIGURE 5.4. Cross-sectional photographic mosaic of the northern slopes of central Neumayerskarvet in the northern Kirwanveggen. The section line is viewed looking southwards. Localities of samples used for the metamorphic investigation are outlined on the diagram.

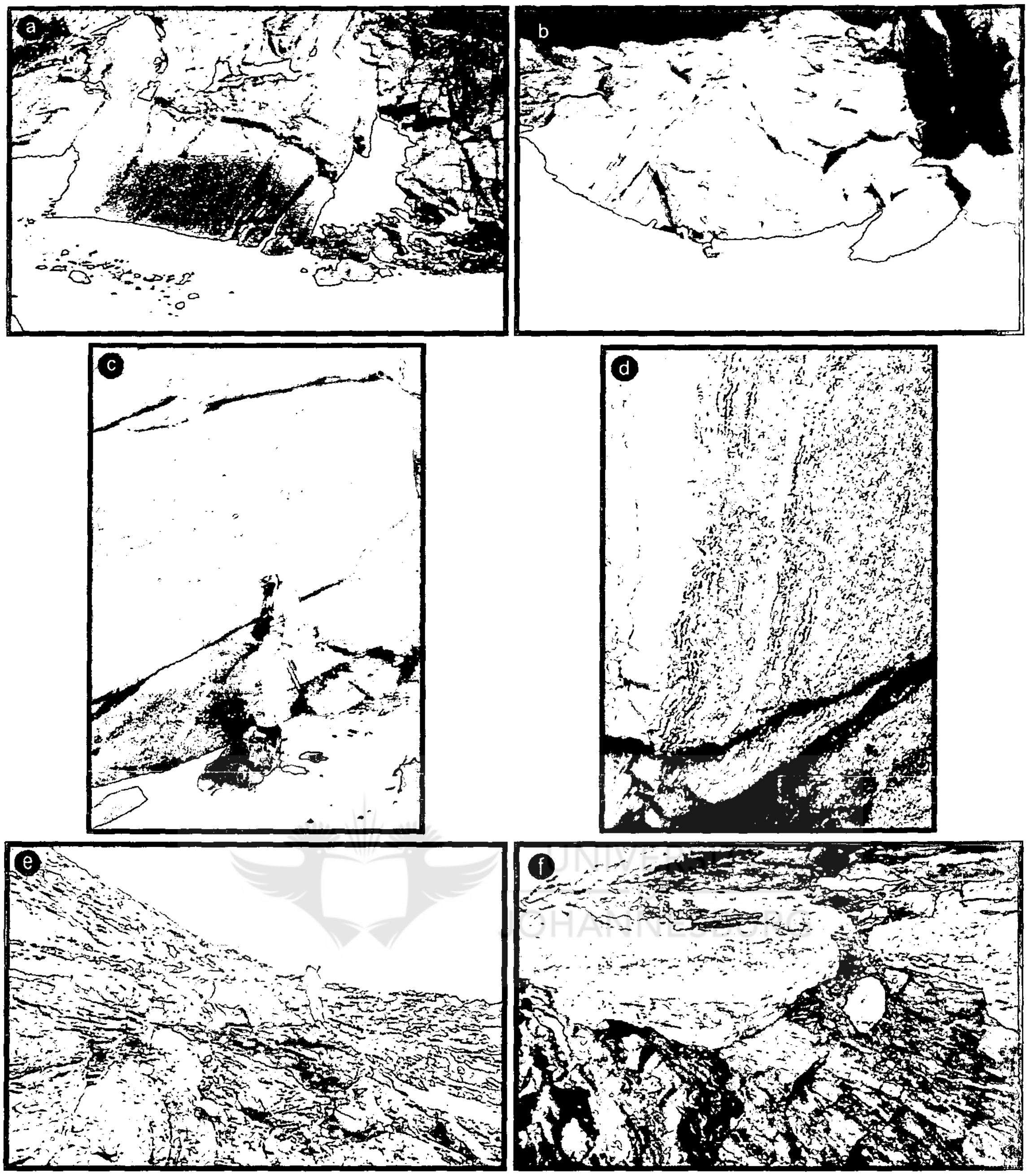

FIGURE 5.5. Photographs of the megacrystic orthogneiss and the kyanite-bearing leucogneisses at Neumayerskarvet.

a.) Photograph of the relationships between the charnockitic remnants and the retrogressed megacrystic orthogneiss. The brown coloured undeformed pod-like structure grades into porphyritic-textured granitoid and into areas of partitioned strain where augen gneiss textures develop.

b.) A photograph illustrating the retrogressed portions of the megacrystic orthogneiss that are focused around late aplitic veins or in areas of increased deformation. The low strain zones preserve the pyroxene-bearing portions of the megacrystic orthogneiss where retrogression is limited.

c.) Less deformed retrogressed megacrystic orthogneiss where a porphyritic-texture is preserved.

d.) Highly strained megacrystic orthogneiss where augen-textures develop. All evidence of the early charnockitic assemblages has been removed.

e.) The kyanite-bearing leucogneiss bodies form as elongate pods along the regional foliation of the biotite-garnet migmatite gneiss.

f.) Photograph showing a kyanite-bearing leucogneiss intruding across the pre-existing foliation, but similar oriented fabrics develop within these bodies.

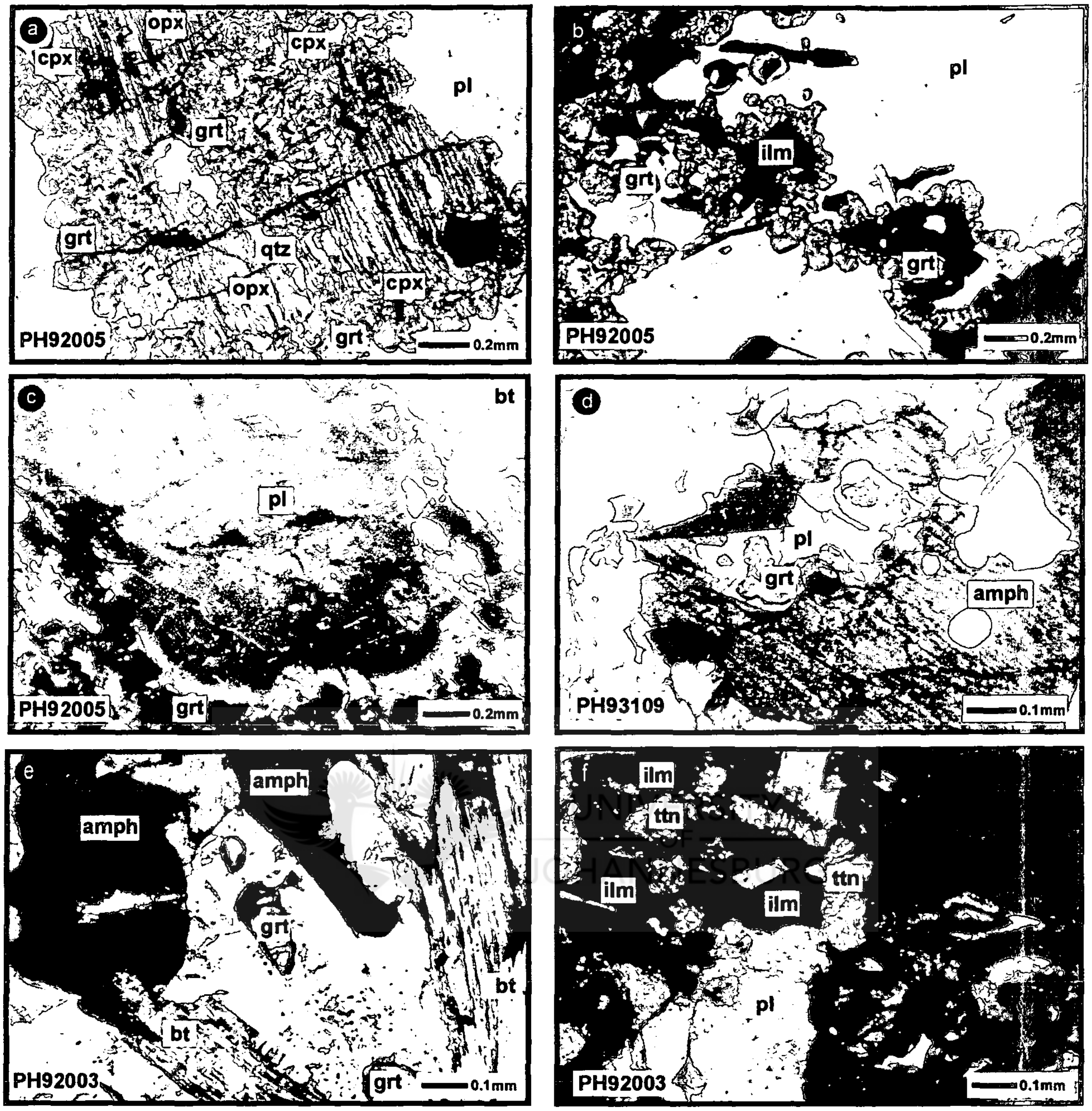

FIGURE 5.6. Microphotographs of mineral textures identified within the charnockitic remnants and retrogressed portions of the megacrystic orthogneiss.

a.) Orthopyroxene-clinopyroxene-garnet-quartz-plagioclase relationships observed within the charnockitic remnants of the megacrystic orthogneiss. Microphotograph is taken in plain polarised light.
b.) Garnet coronas developed around ilmenite within the charnockitic remnants of the megacrystic orthogneiss. Photograph is taken in plain polarised light.
c.) Garnet coronas developed around strongly zoned plagioclase within the charnockitic remnants. Photograph taken in cross-polarised light.
d.) Garnet remnants enclosed in a plagioclase mantle surrounded by amphibole in the retrogressed megacrystic orthogneiss. Photograph taken in plain polarised light.
e.) Garnet remnants mantled by plagioclase and surrounded by biotite and amphibole in the retrogressed megacrystic orthogneiss. Photograph taken in plain polarised light.
f.) Titanite coronas around ilmenite in the retrogressed megacrystic orthogneiss. Photograph taken in plain polarised light.

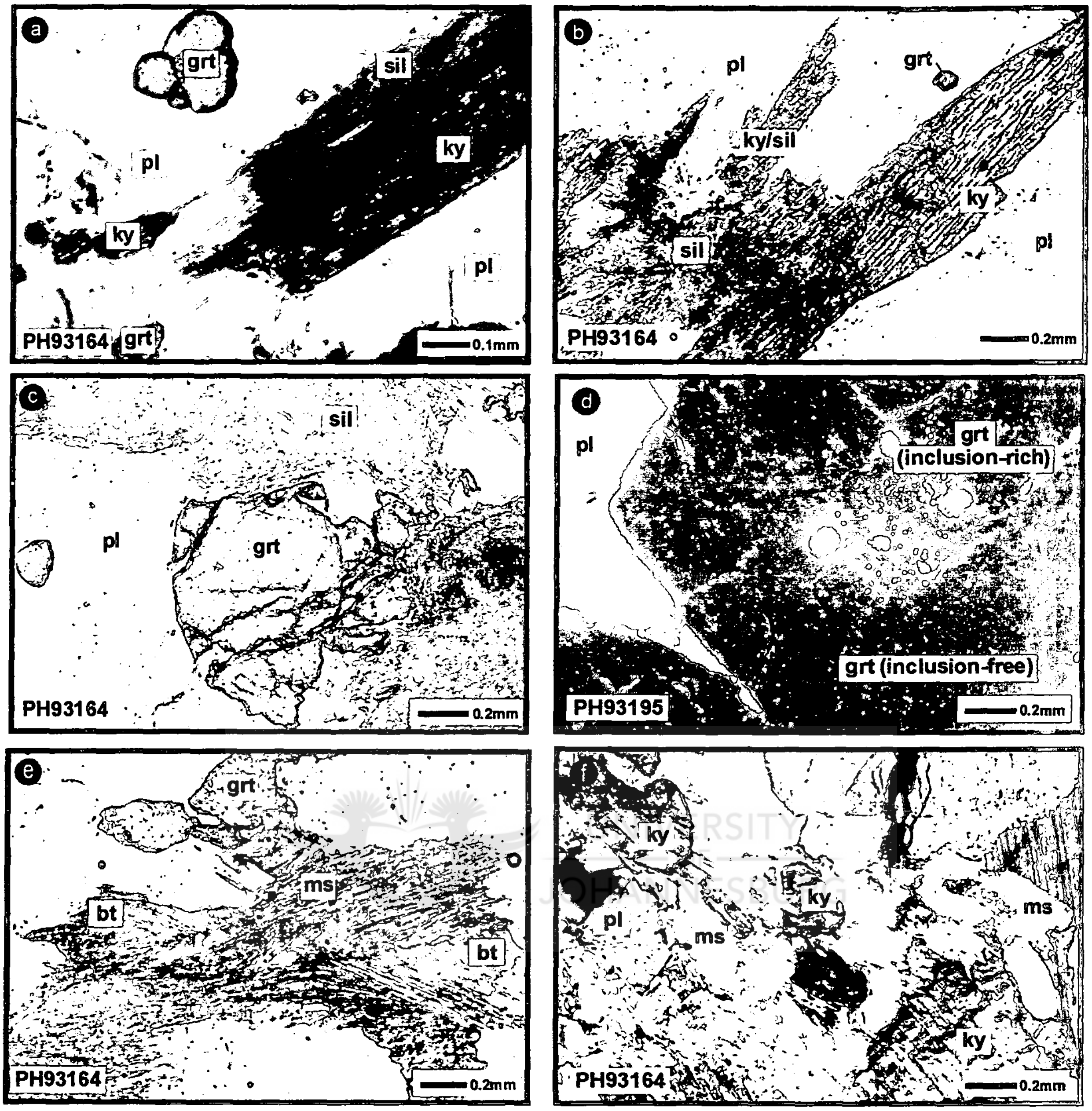

FIGURE 5.7. Microphotographs of mineral textures identified within the kyanite-bearing leucogneisses.

a.) Kyanite-sillimanite relationships within the kyanite-bearing leucogneiss. Sillimanite replaces kyanite blades but is still aligned within the foliation defined by the kyanite blades. Microphotograph is taken in plain polarised light.
b.) Intergrowths of kyanite and sillimanite within the kyanite-bearing leucogneiss. The sillimanite replaces the kyanite blades and also occurs as radiating clusters overgrowing the foliation within this sample. Microphotograph is taken in plain polarised light.
c.) Garnet in contact with sillimanite that has replaced the larger blades of kyanite. The microphotograph is taken in plain polarised light.
d.) Portion of a large garnet showing inclusion-rich core and inclusion-free rims within the kyanite-bearing leucogneiss. The microphotograph is taken in plain polarised light.
e.) Intergrowths of biotite and muscovite commonly observed within the kyanite-bearing leucogneiss. The microphotograph is taken in plain polarised light.
f.) Muscovite enclosing kyanite blades indicating late-stage of formation. The microphotograph is taken in cross polarised light.

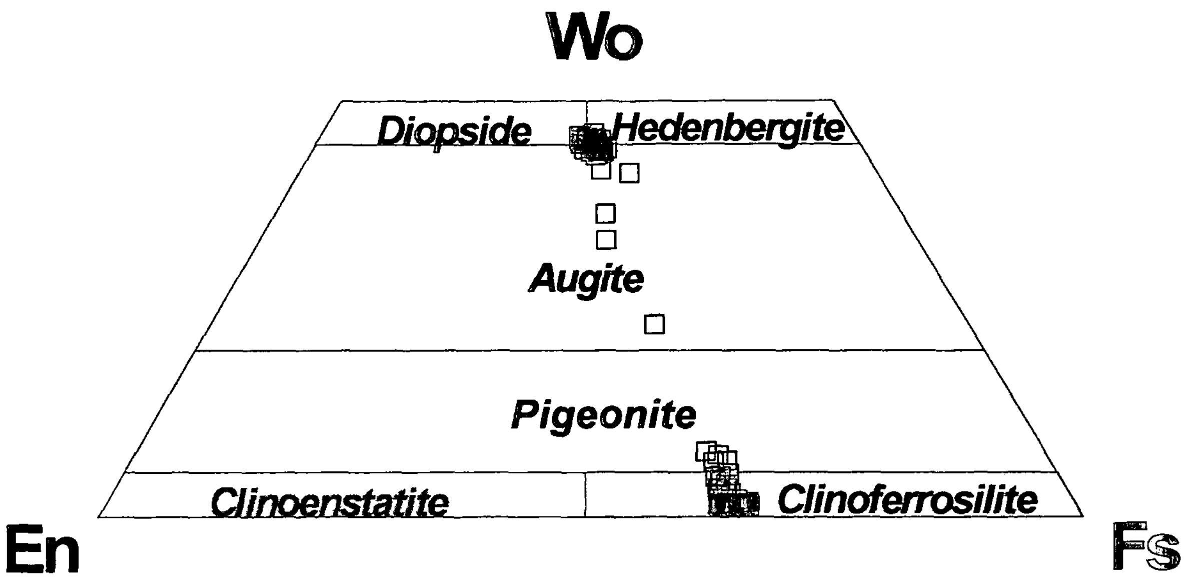

FIGURE 5.8. Plot illustrating the pyroxene compositions of analysed assemblages from samples used during this investigation. The green open square symbols represent samples from the charnockitic remnants of the megacrystic orthogniess (sample PH92005).

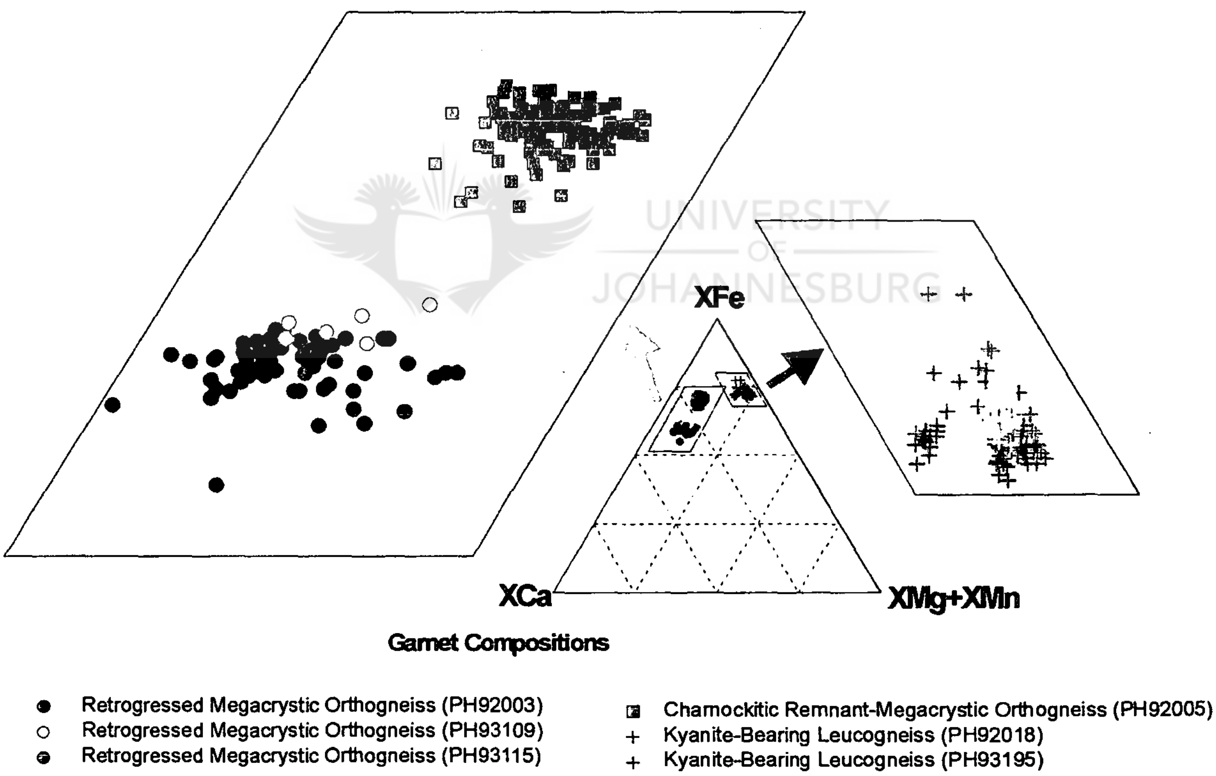

FIGURE 5.9. Plot illustrating the garnet compositions of analysed assemblages from samples used during this investigation. Samples are from the megacrystic orthogneiss (black, red and blue circles), charnockitic remnants of the megacrystic orthogneiss (green squares) and from kyanite-bearing leucogneiss samples (blue and red crosses).

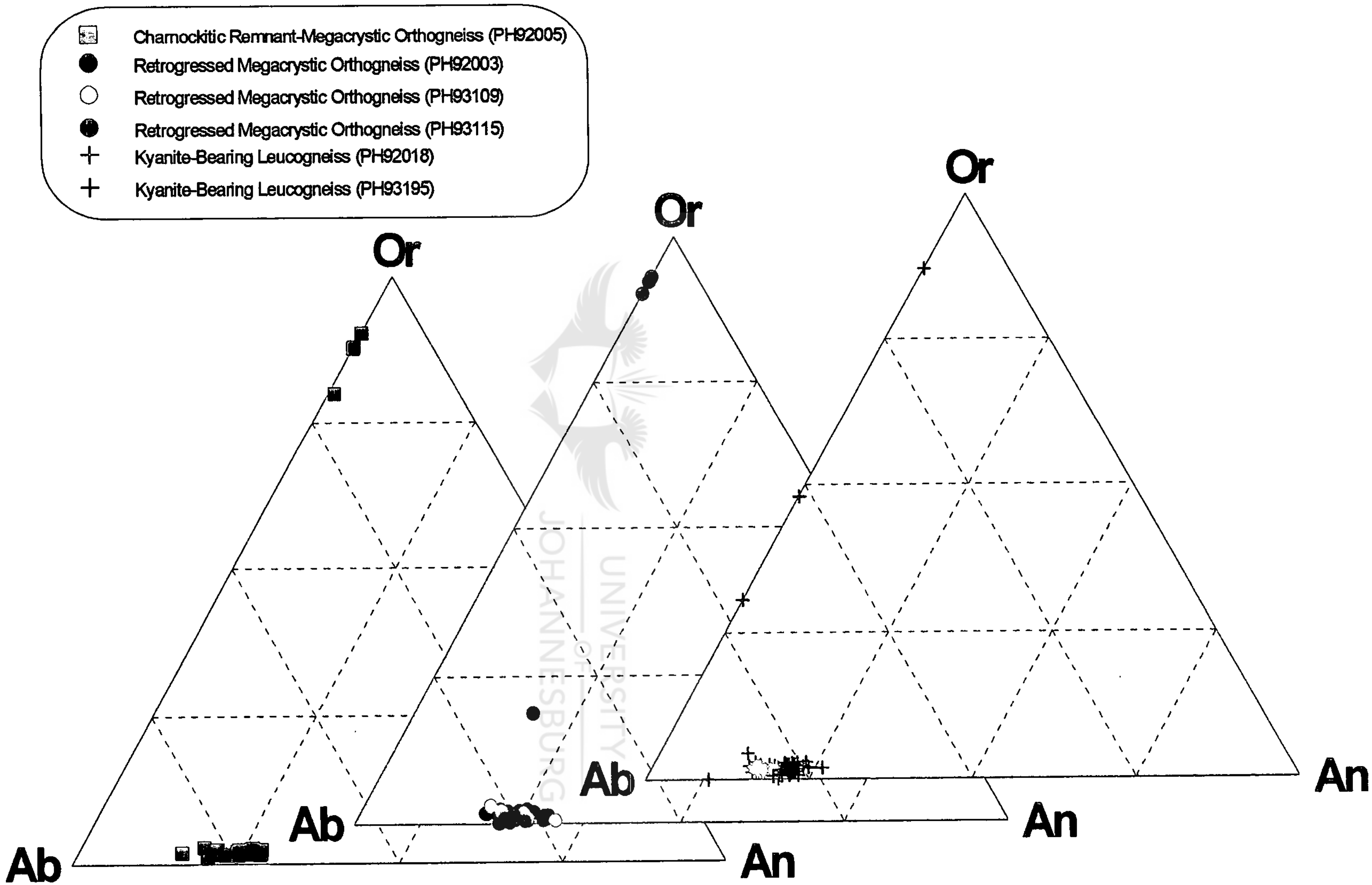

FIGURE 5.10. Plots illustrating the feldspar compositions of analysed assemblages from samples used during this investigation. The sample symbols and colours are the same as in the mineral composition diagram of Figure 5.9.

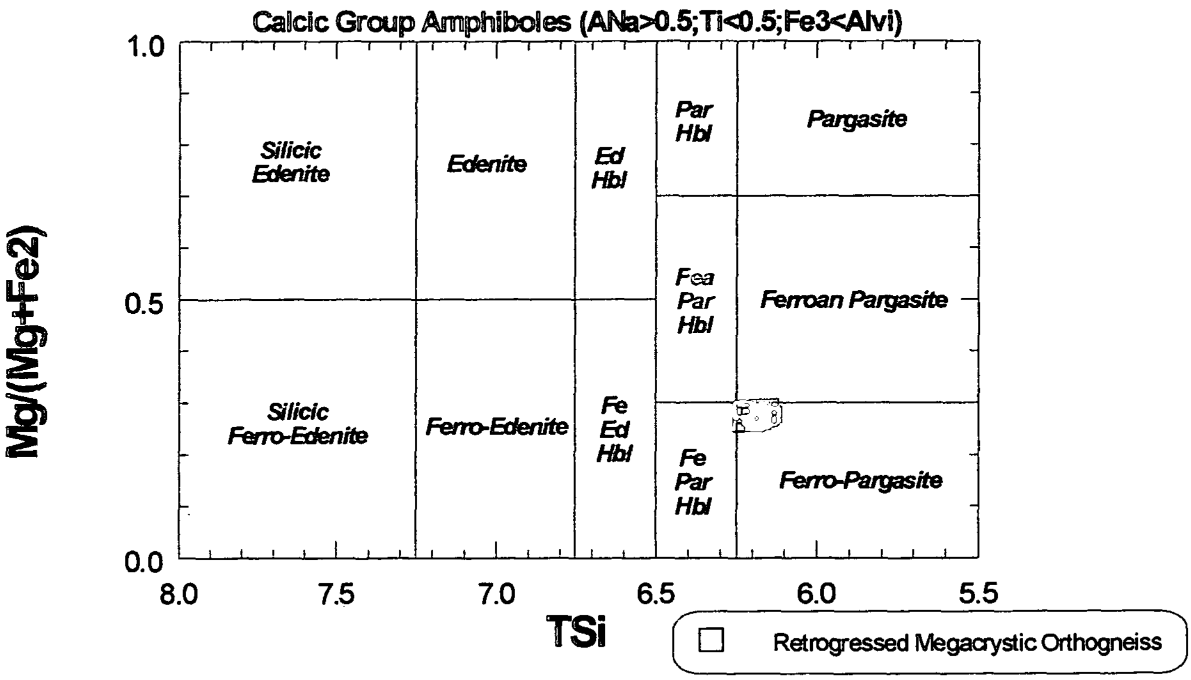

FIGURE 5.11. Plot illustrating the amphibole compositions of analysed assemblages from samples used during this investigation. The diagram is based on amphibole classification diagrams obtained in the program 'MINPET'.

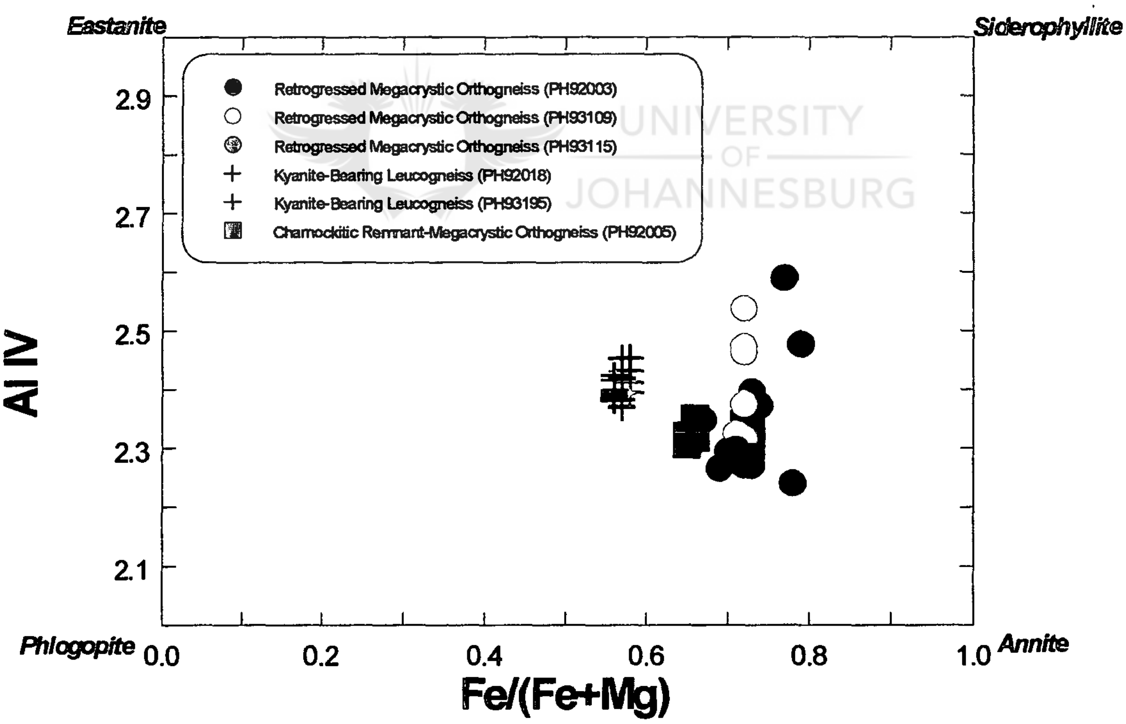

FIGURE 5.12. Plot illustrating the biotite compositions of analysed assemblages from samples used during this investigation. The diagram is based on biotite classification diagrams provided in the program 'MINPET'.

Chemistry of Mineral Textures in the Charnockitic Remnants of the Megacrystic Orthogneiss

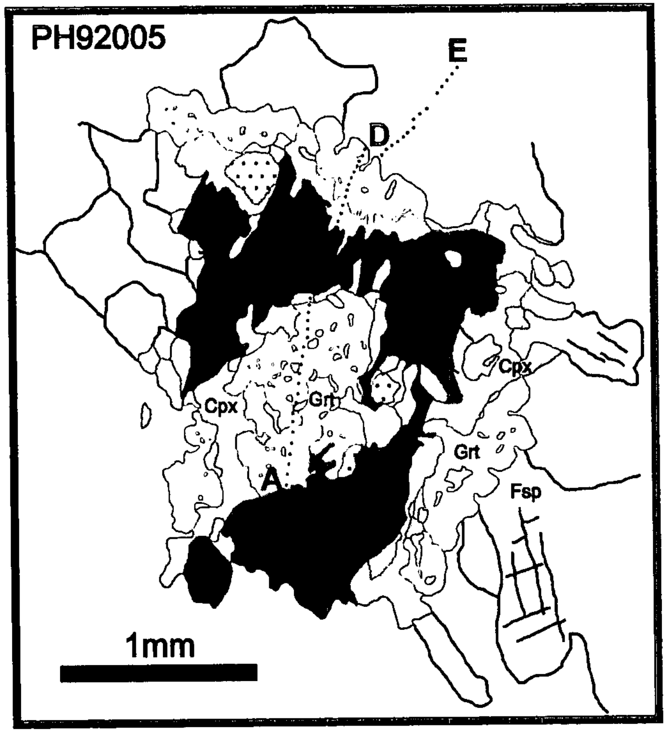

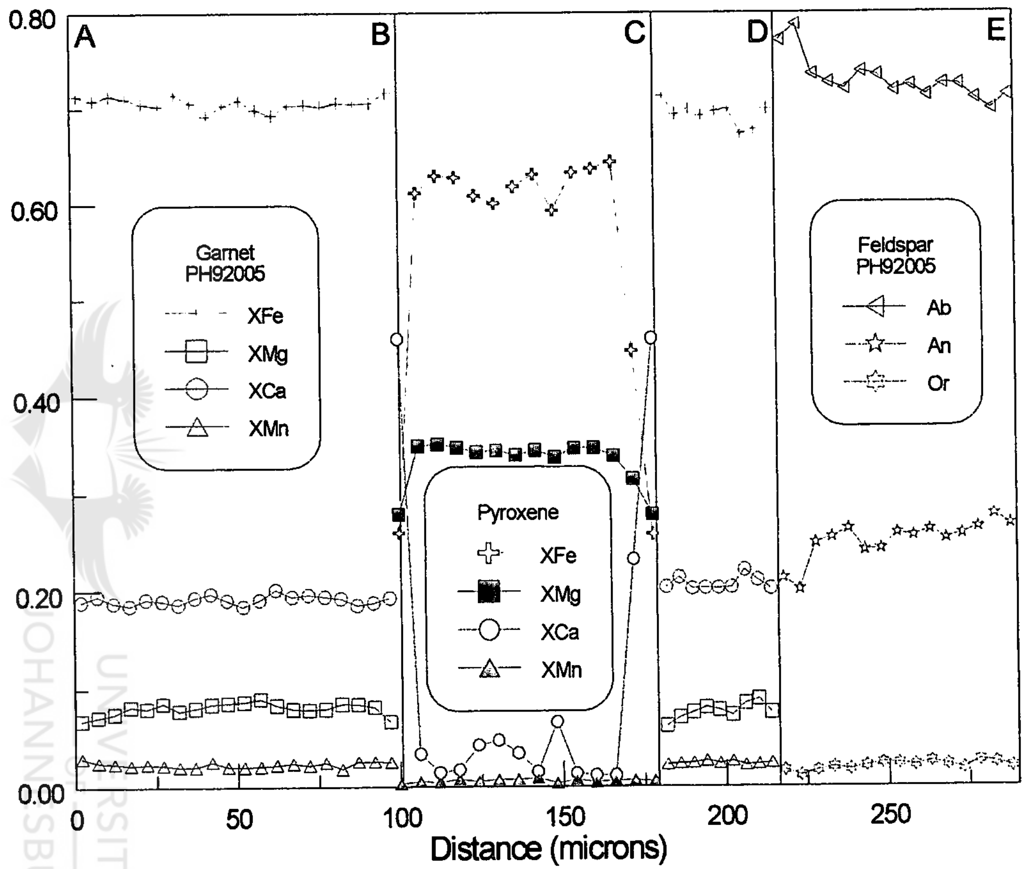

FIGURE 5.13. Zoning profiles for mineral textures within the preserved low-strain regions within the megacrystic orthogneiss. Charnockitic remnants are found within these low-strain zones. The profile extending from A through to D is displayed in the accompanying plot. Al contents of the pyroxenes is below detection and therefore not plotted on the diagram. The change in the chemistry of the orthopyroxene at the rims is due to the transition to clinopyroxene. Comparisons of the individual traverse profiles across the garnets are displayed in Figure 5.20 in order to observe the potential zoning profiles in garnet for this sample. The zoning profiles are discussed in detail within the text.

Chemistry of Mineral Textures in the Retrogressed Megacrystic Orthogneiss

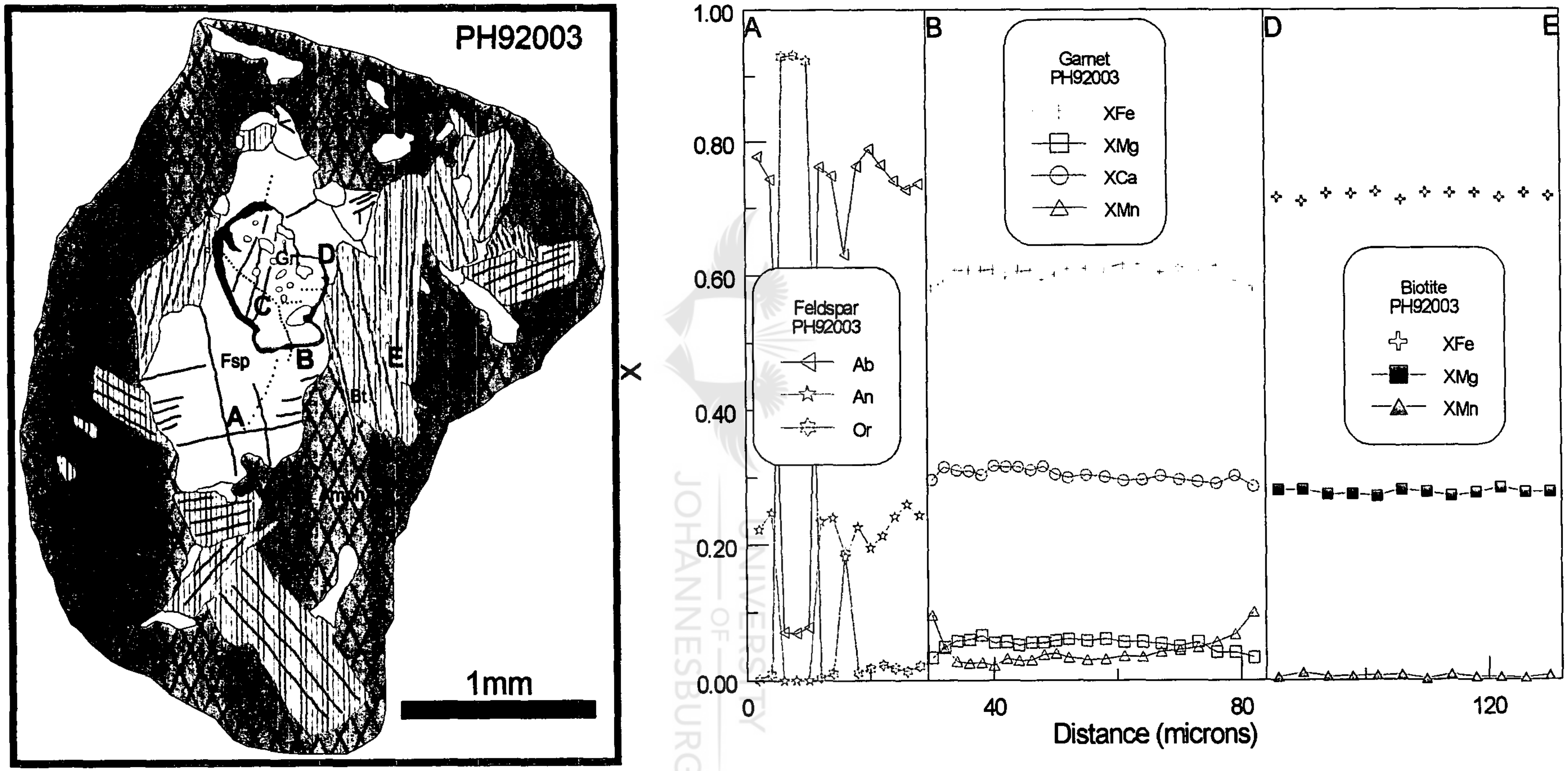

FIGURE 5.14. Zoning profiles for different mineral textures from the retrogressed megacrystic orthogneiss. The traverse line displayed on the accompanying plot extends from the plagioclase (A) through the garnet and into the biotite grain (E). Detailed zoning profiles across the garnet and in contact with different minerals are provided in Figure 5.21 for this sample. The zoning profiles are discussed in detail in the text.

Chemistry of Mineral Textures in the Kyanite-Bearing Leucogneiss

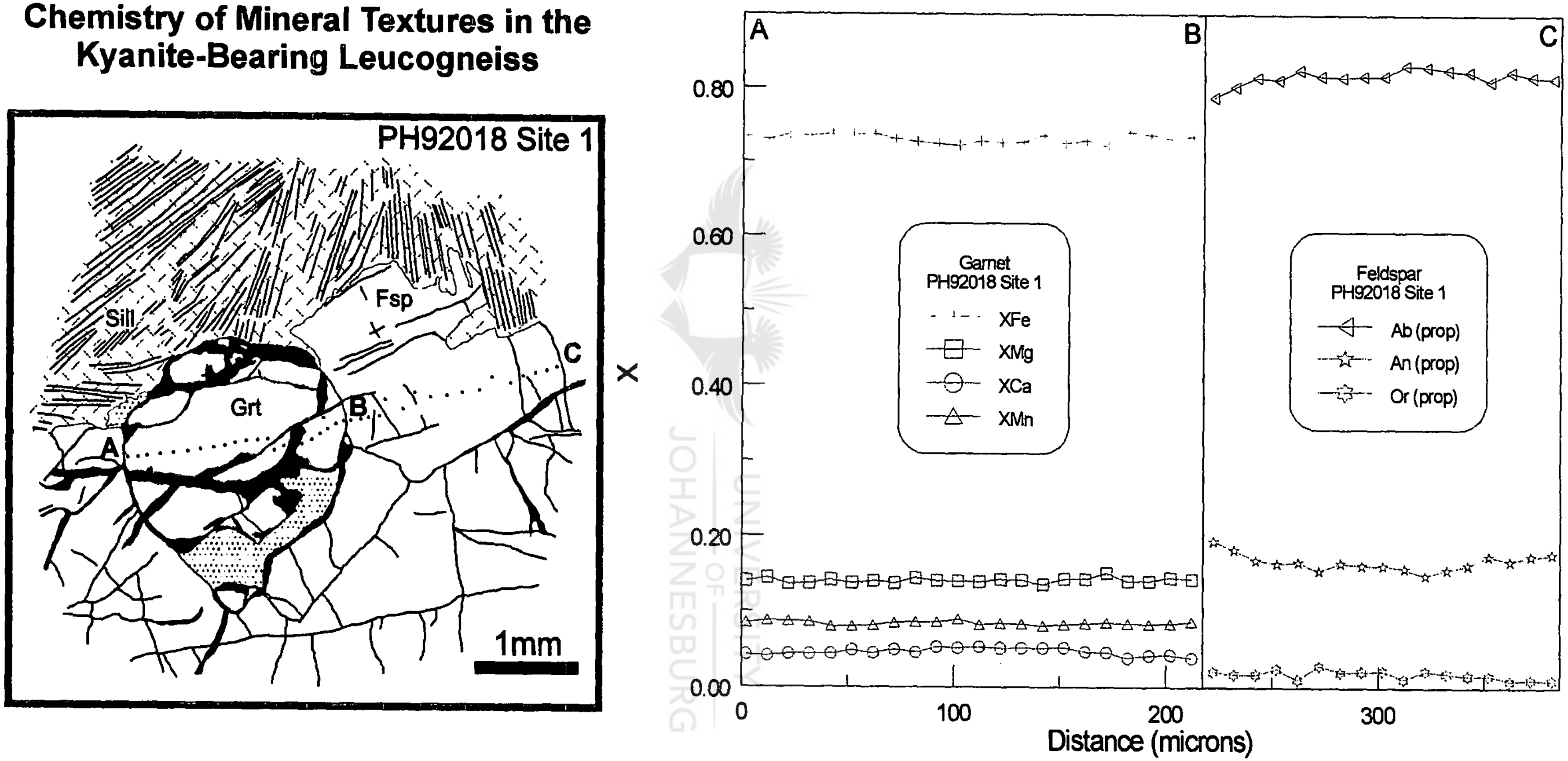

FIGURE 5.15. Zoning profiles preserved within sample PH92018 Site 1 of the kyanite-bearing leucogneisses. The profile traverse displayed runs from garnet rim to garnet rim (A to B) and across the plagioclase grain to position C. Comparison of the zoning profile of this garnet with other garnets in contact with different minerals are displayed in Figure 5.22. The detailed zoning patterns observed are described in the text.

Chemistry of Mineral Textures within the Kyanite-Bearing Leucogneisses

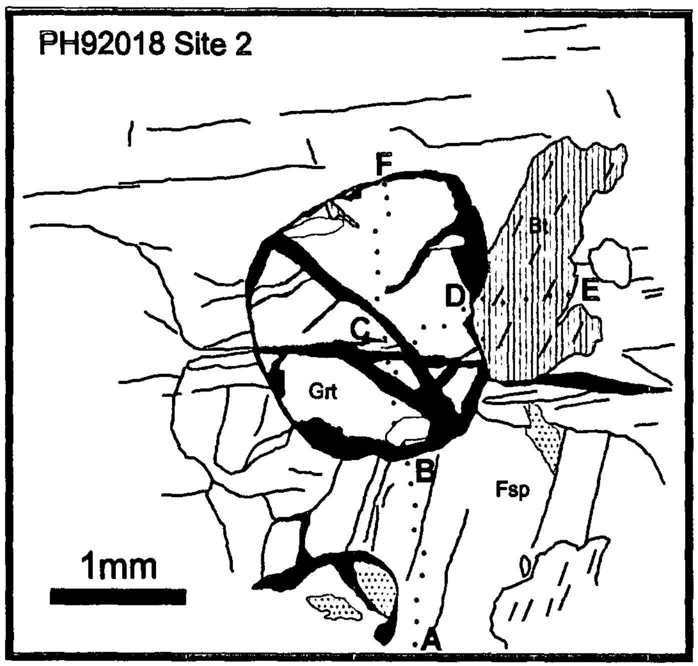

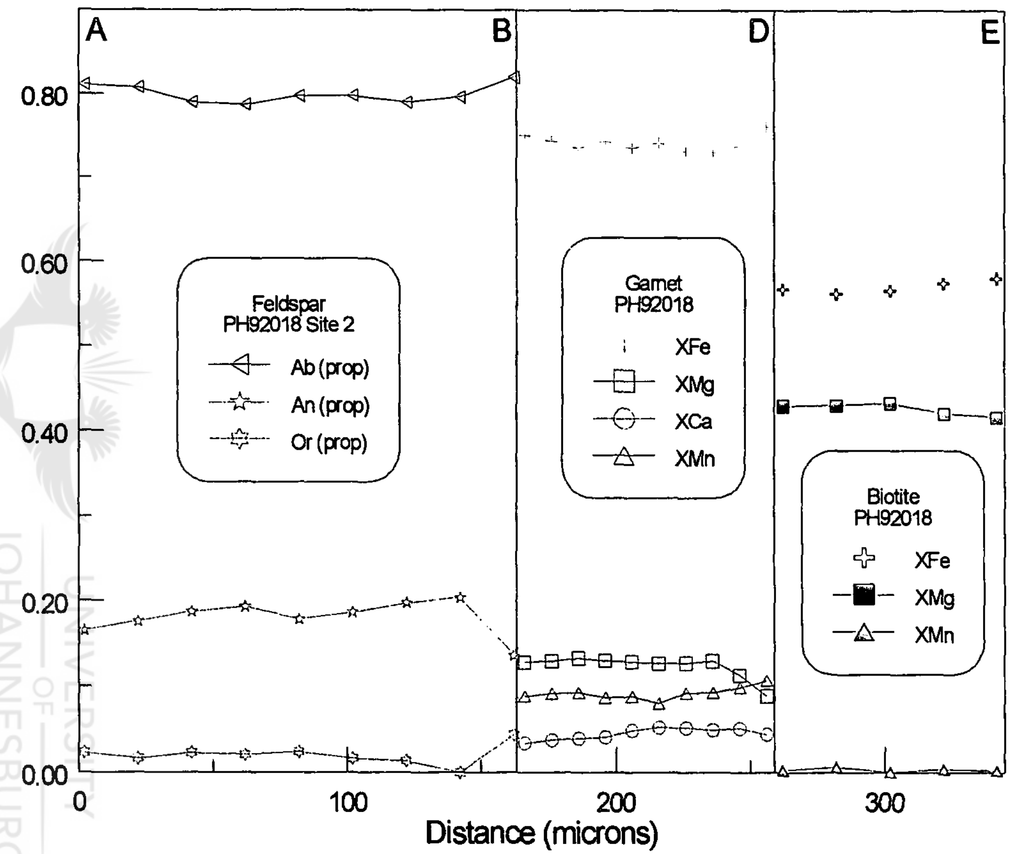

FIGURE 5.16. Zoning profiles of feldspar, biotite and garnet from sample PH92018 Site 2 of the kyanite-bearing leucogneisses. The profile displayed in this diagram begins in the plagioclase at position A, extending through the garnet from B-C-D and into the biotite to position E. The more detailed garnet zoning profile patterns are presented in Figure 5.22 and described in detail within the text.

Chemistry of Mineral Textures within the Kyanite-Bearing Leucogneisses

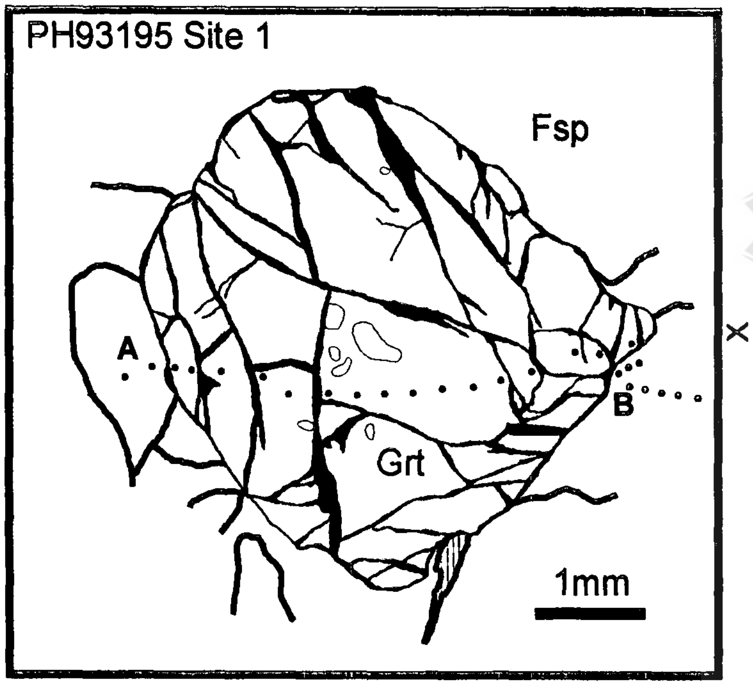

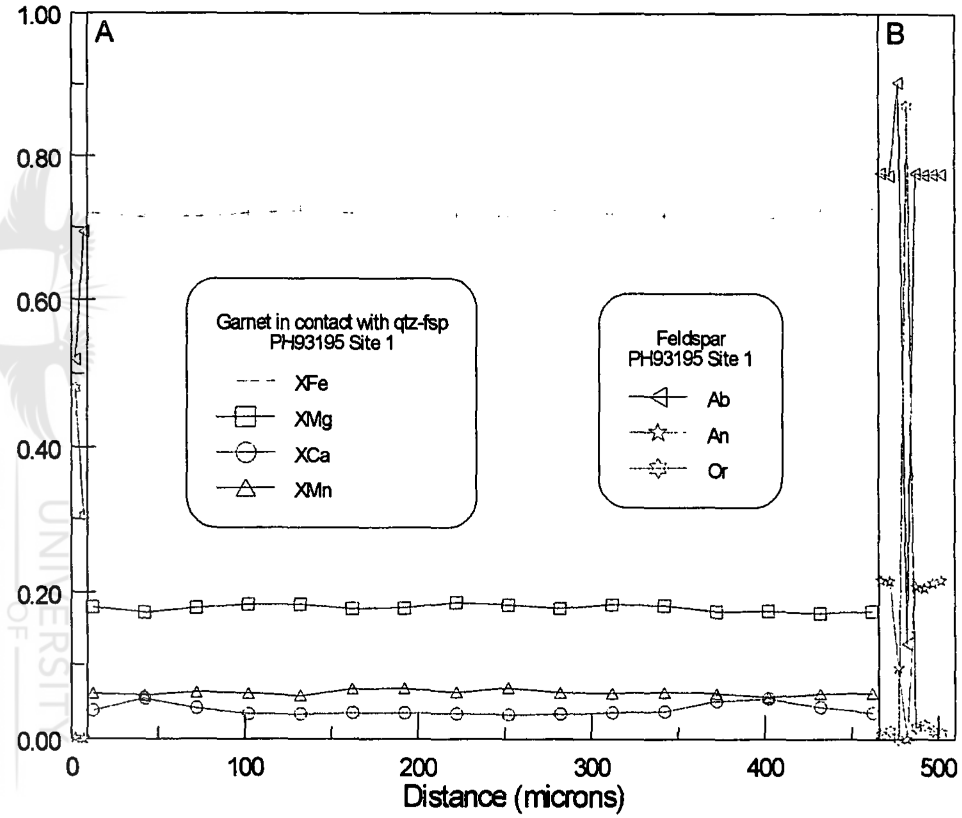

FIGURE 5.17. Zoning profiles of feldspar and garnet from sample PH93195 Site 1 of the kyanite-bearing leucogneisses. The garnet is totally enclosed within feldspar. The zoning profile presented in this diagram displays the zoning of garnet and feldspar in contact with one another. The garnet zoning profile of this sample is compared with other garnet zoning profiles within Figure 5.23 and is described in detail within the text.

Chemistry of Mineral Textures within the Kyanite-Bearing Leucogneisses

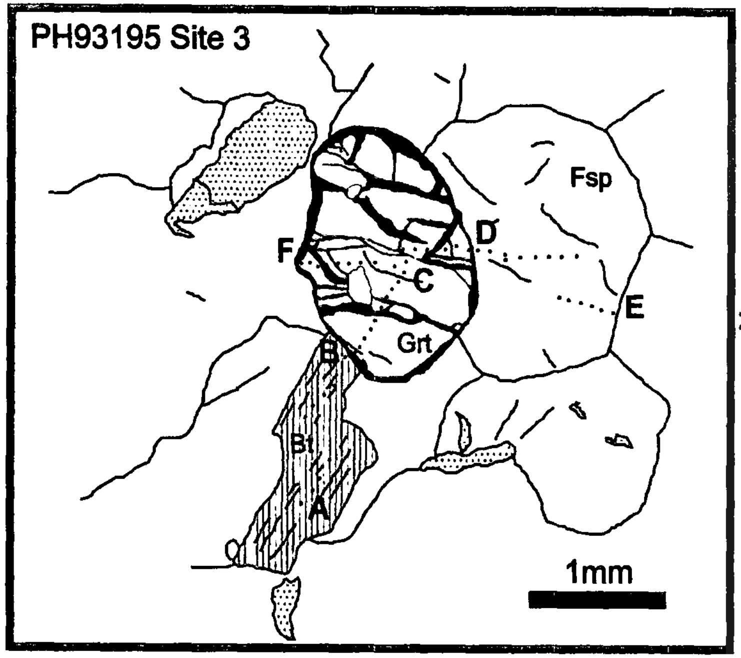

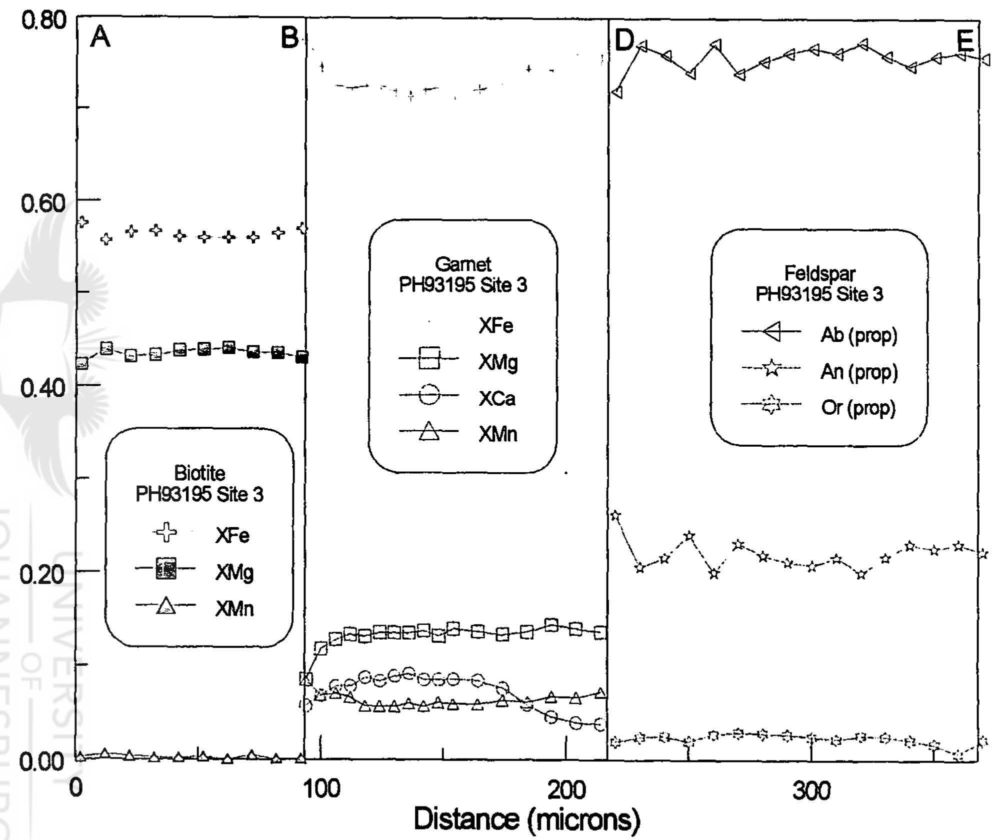

FIGURE 5.18. Zoning profiles of feldspar, biotite and garnet from sample PH93195 Site 3 of the kyanite-bearing leucogneisses. This figure illustrates the zoning relationships between biotite-garnet and feldspar (positions A-B-C-D-E). A detailed garnet zoning profile for this sample is compared to other profiles from this sample in Figure 5.23. The zoning profiles are discussed in more detail in the text.

Chemistry of Mineral Textures within the Kyanite-Bearing Leucogneisses

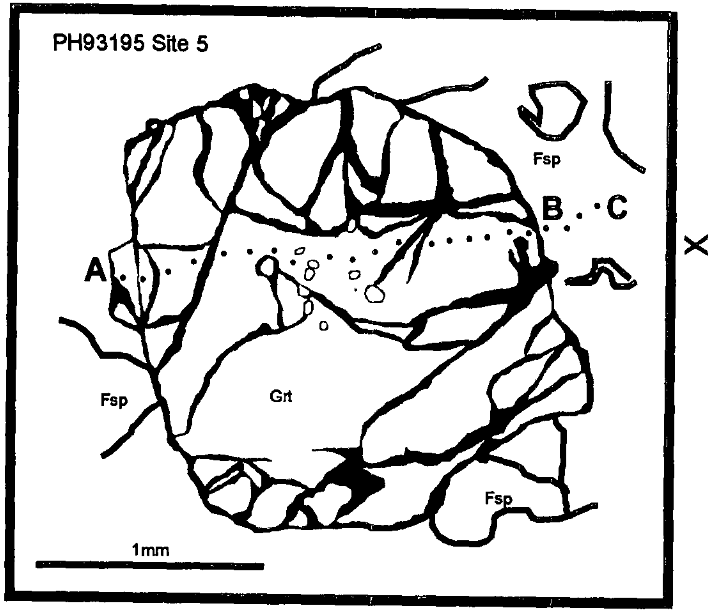

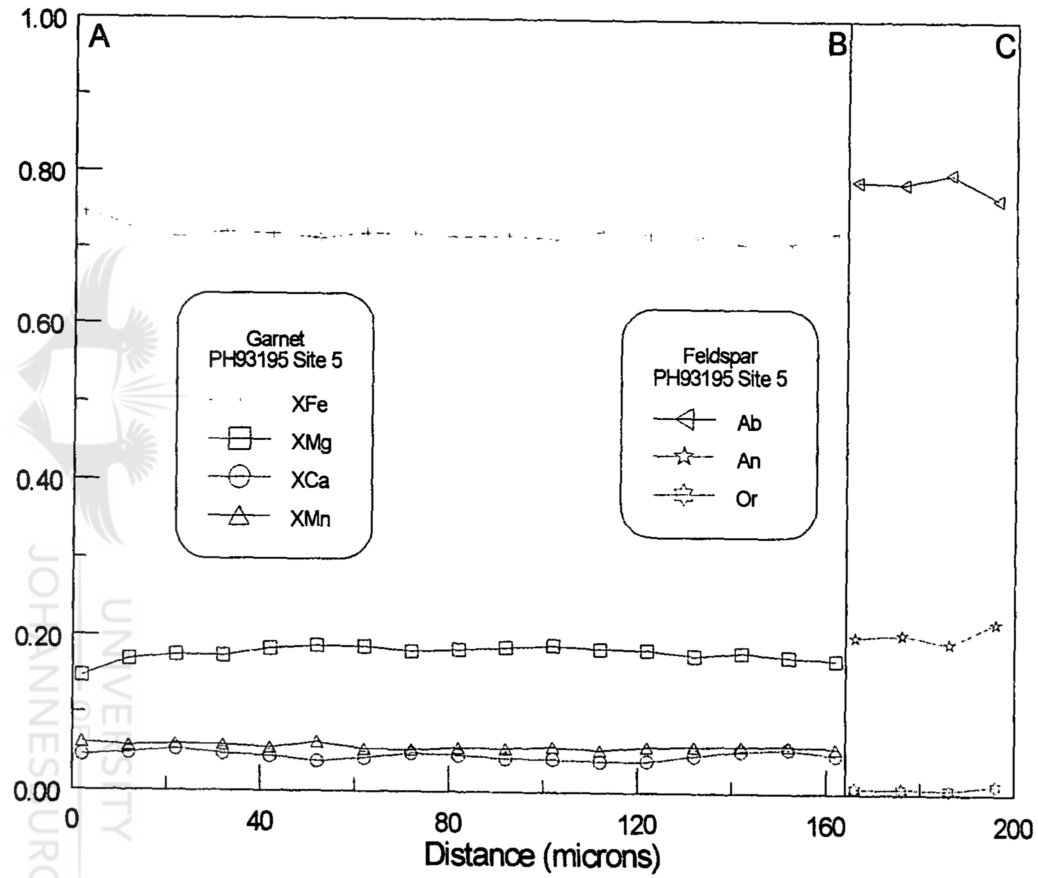

FIGURE 5.19. Zoning profiles from sample PH93195 Site 5 of the kyanite-bearing leucogneiss. The profile displays zoning patterns observed between garnet and feldspar. The profile traverse extends from position A through B in the garnet to position C within the feldspar. Detailed garnet profiles from this sample are presented in Figure 5.23 for comparison with other garnet zoning patterns. The zoning profiles are discussed in detail within the text.

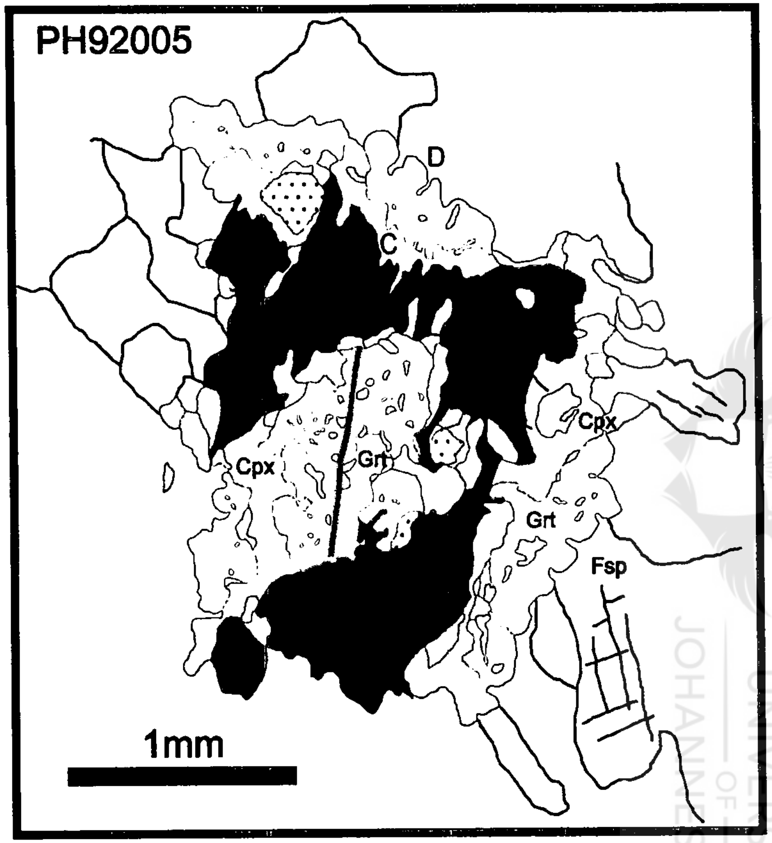

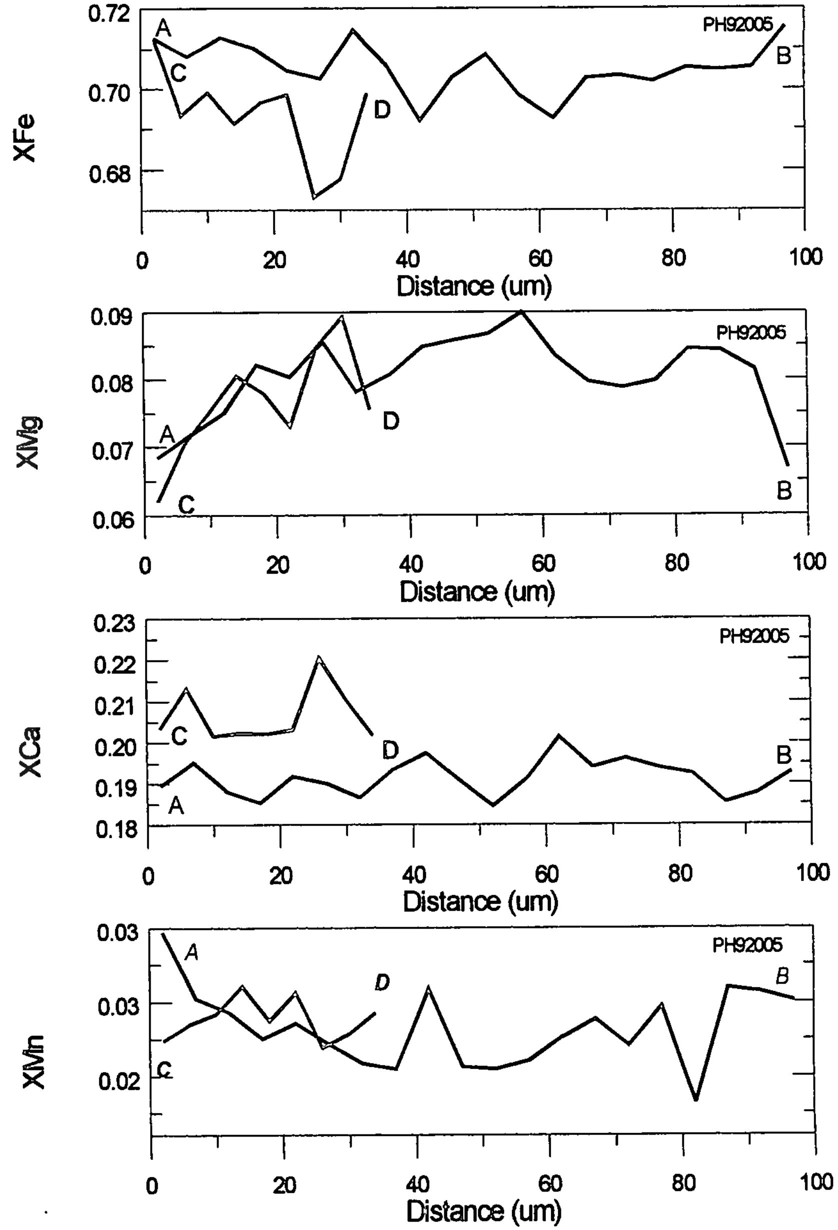

FIGURE 5.20 Garnet zoning profiles preserved within the charnockitic remnants of the megacrystic orthogneiss. The garnet profiles are displayed in the mineral sketch (from Figure 5.13) to compare the different mineral contact relationships. Garnet profile A to B is of the garnet enclosed by orthopyroxene with clinopyroxene and quartz corona texture development. The garnet profile C through D is of rim garnet in contact with clinopyroxene through to plagioclase. Zoning profile patterns are discussed within the text.

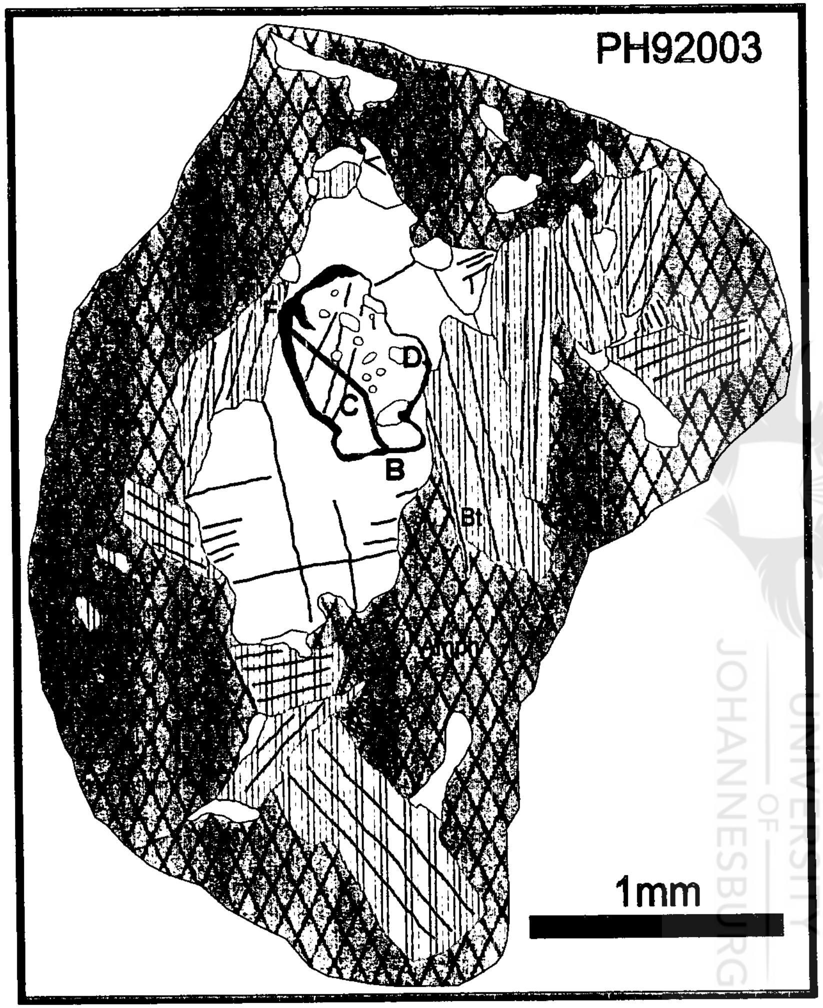

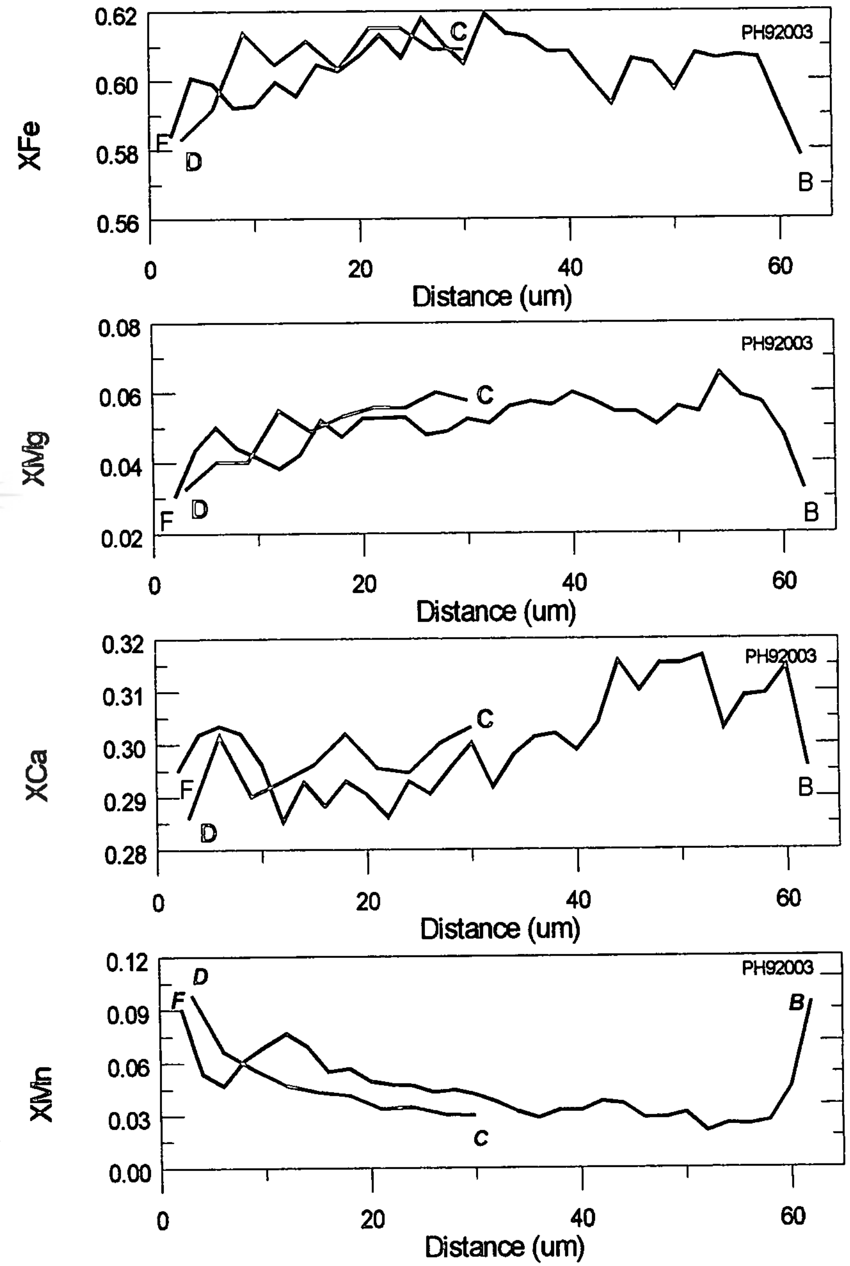

FIGURE 5.21. Garnet zoning profiles preserved within the retrogressed megacrystic orthogneiss sample PH92003. Profiles are of a garnet enclosed by biotite and amphibole with the development of a feldspar moat or corona. Profile B-F extends from plagioclase-garnet rim to garnet rim-biotite contact, while profile C-D extends from garnet core to garnet rim-biotite contact. Zoning patterns are discussed within the text.

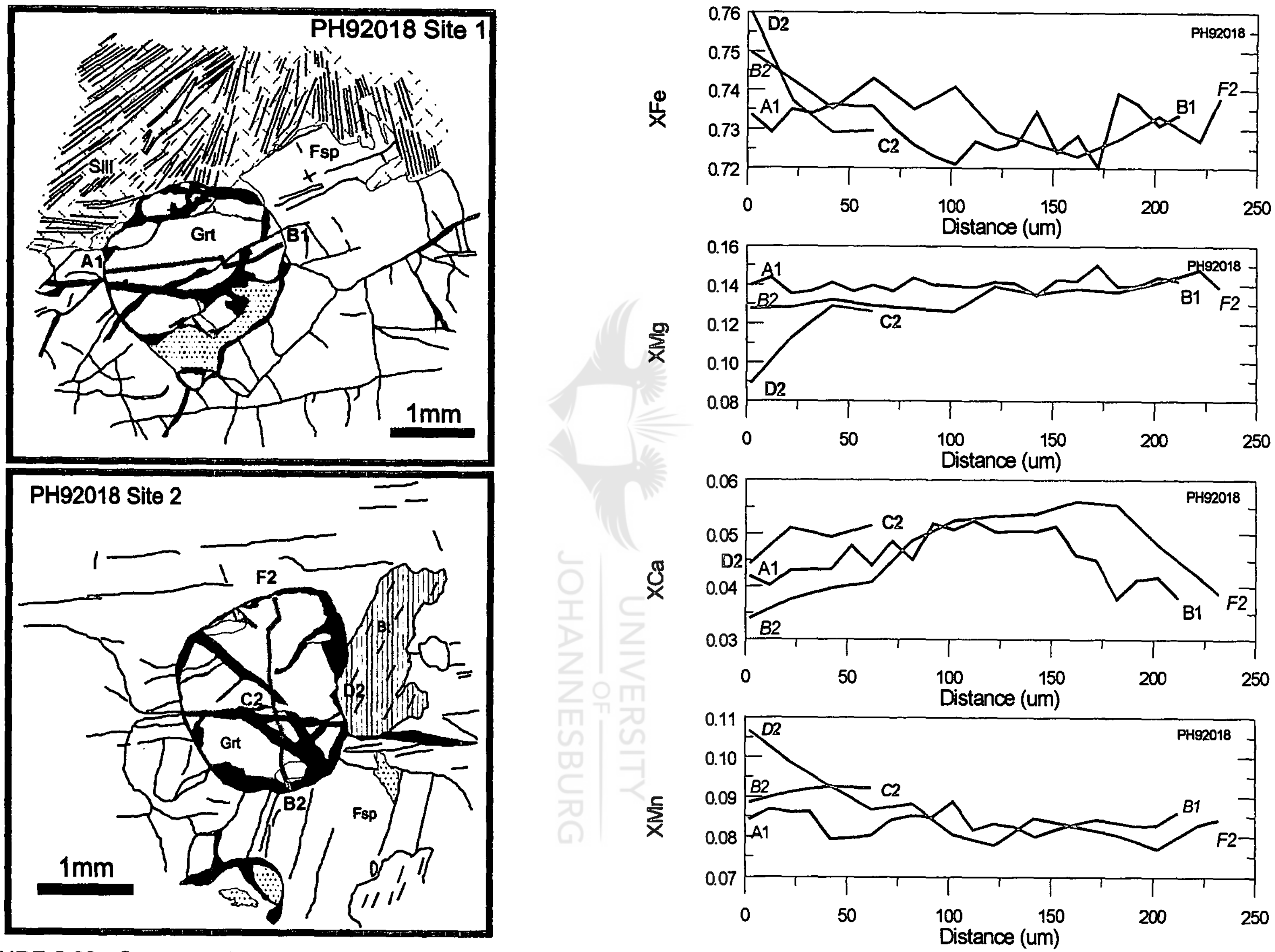

FIGURE 5.22. Garnet zoning profiles preserved within the kyanite-bearing leucogneiss sample PH92018. Sketch diagrams of the profiles are provided for comparison. Garnet zoning profile A1 to B1 is across the garnet to the contact with plagioclase. The garnet in this sample is in contact with sillimanite. Garnet zoning profile B2 to F2 is across the garnet at the plagioclase contact. The garnet is in contact with biotite. The zoning profile C2 to D2 is from garnet core to rim in contact with the biotite. The zoning profiles are discussed in detail in the text.

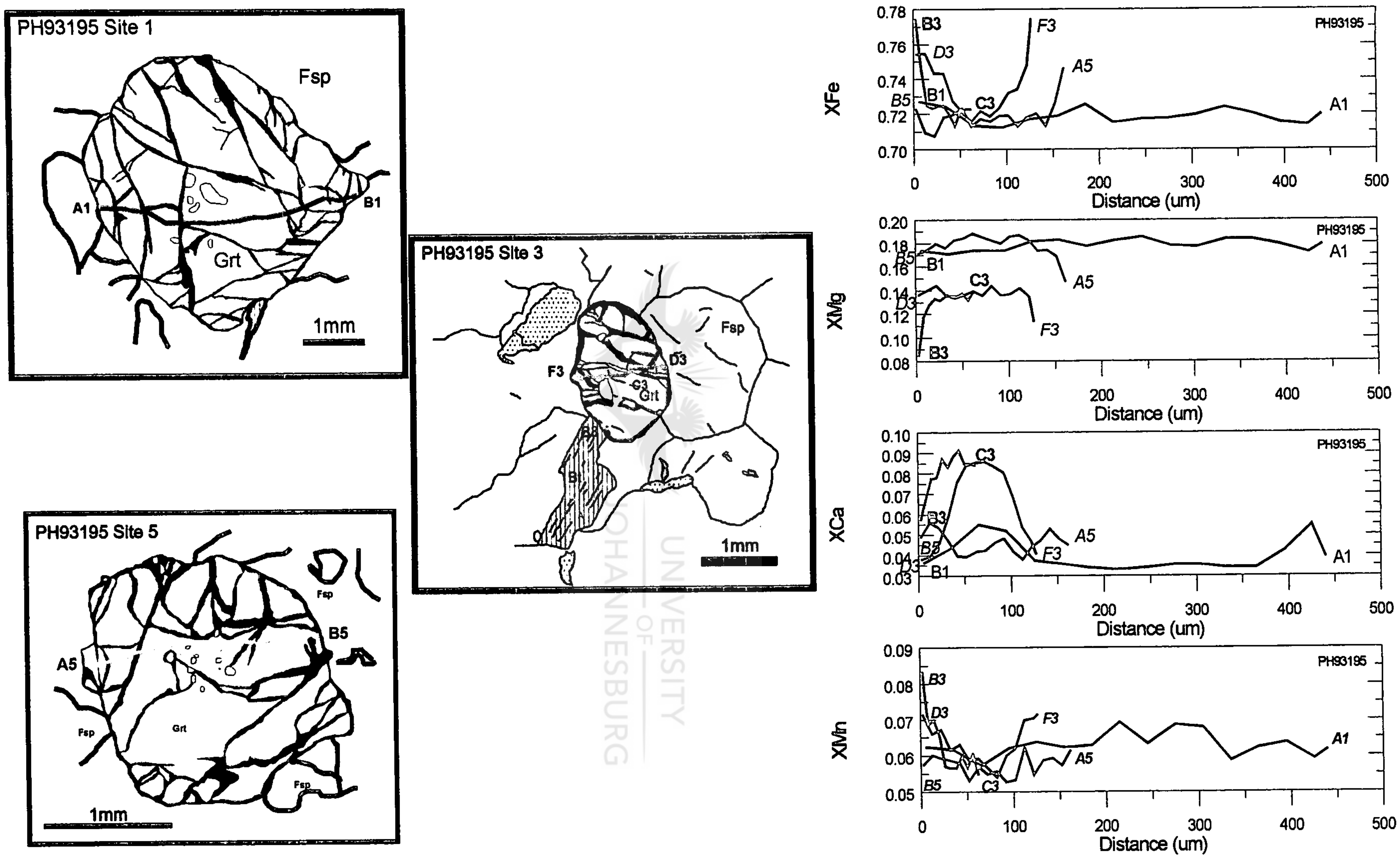

FIGURE 5.23. Garnet zoning profiles preserved within the kyanite-bearing luecogneiss sample PH93195. Garnet profile localities and mineral associations are shown in the accompanying sketches. Garnet profiles B1-A1 and B5-A5 are across large garnets with inclusion-rich cores and inclusion-free rims, and are surrounded by plagioclase. Garnet profile D3-F3 is across an inclusion-free garnet across to the plagioclase contact. This garnet is also in contact with biotite. Profile C3-B3 extends from the garnet core to the garnet-biotite contact. Zoning patterns are discussed in detail within the text.

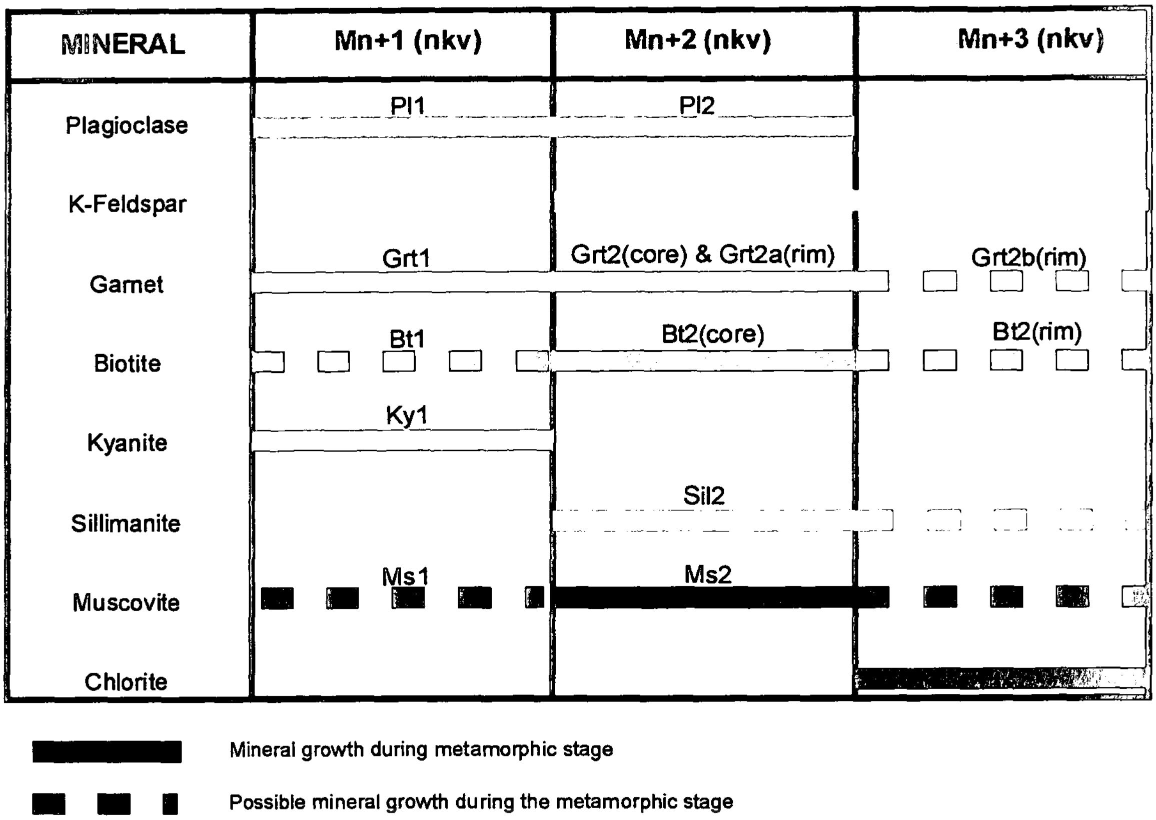

Mn+1 (nkv)
Grt1 - Low CaO core garnet (Inclusion-rich)
Bt1 - Isolated biotite
Ms1 - Muscovite inclusions in core garnet
Pl1 - Original plagioclase compositions not preserved
Ky1 - Kyanite blades aligned within regional foliation

Mn+2 (nkv)
Grt2 - High CaO rim garnet (Inclusion-free)
- Inclusion-free garnet cores
Grt2a - Garnet (Grt2) rims in contact with plagioclase
Bt2 - Biotite in contact with garnet (Grt2)
Ms2 - Large muscovite laths associated with sillimanite, garnet and biotite
Pl2 - Plagioclase core and rims in contact with garnet
Sil2 - Sillimanite replacing kyanite and in contact with garnet

Mn+3 (nkv)
Grt2b - Garnet rim in contact with biotite
Bt2(rim)- Biotite rim in contact with garnet
Ksp - K-feldspar growth within plagioclase
Chl - Chlorite replacement of biotite

Figure 5.24. Mineral paragenesis and metamorphic assemblages recorded in the kyanite-bearing leucogneiss samples. These mineral associations have been established through petrography and mineral chemistry. Discussion of the mineral assemblages is provided in the text.

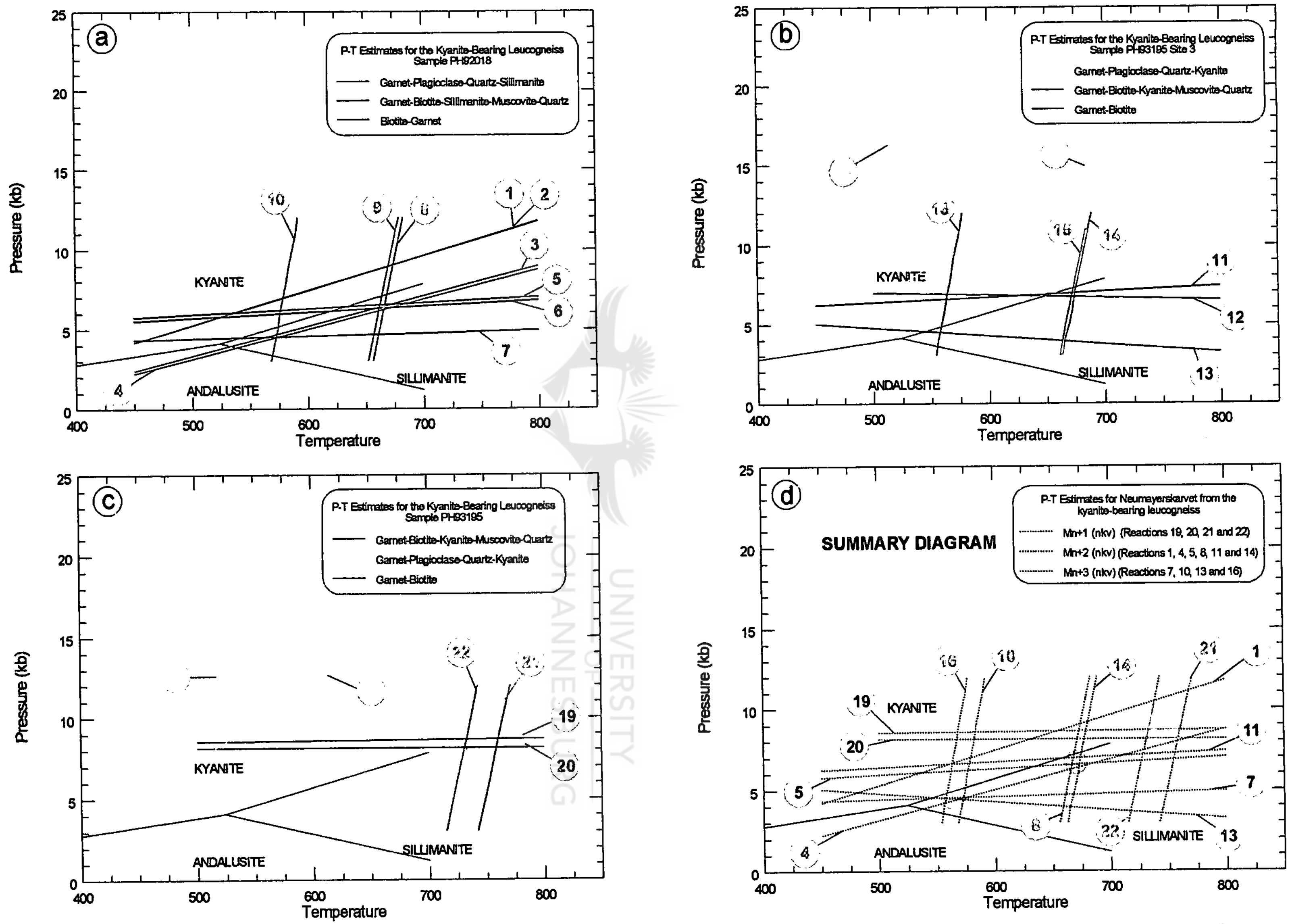

FIGURE 5.25. P-T relationships within the kyanite-bearing leucogneiss units at Neumayerskarvet. The reactions are numbered according to the information provided in Table 5.9. The reaction lines are colour coded according to the reaction type used. The mineral type used to calculate these reaction lines are outlined in Table 5.9 and Figure 5.24 illustrates the paragenetic associations of the different minerals. Detailed discussion of these P-T relationships are provided in the text.

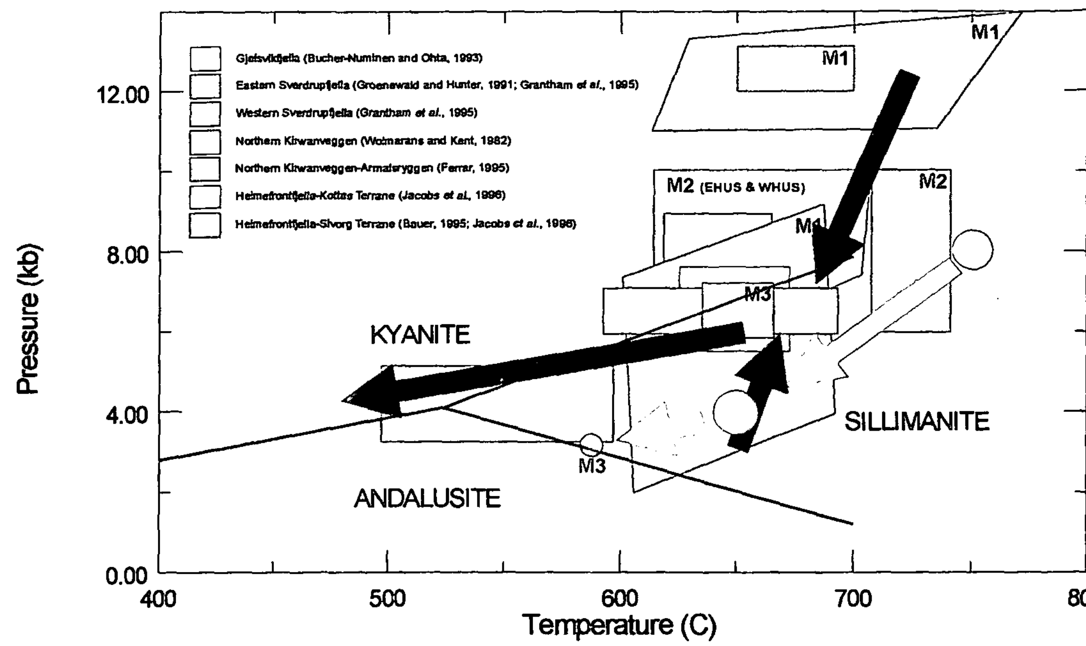

FIGURE 5.26. Previous P-T conditions estimated for different domains within WDML. Where P-T paths have been proposed these are shown in the diagram. References for the previous metamorphic work are outlined in the diagram, and a discussion of these investigations is provided in Chapter 2 and in the beginning of this chapter. The blue arrows are P-T paths proposed by Grantham *et al.* (1995) for the eastern and western Sverdrupfjella. The red arrows are the P-T path proposed by Bucher-Nurminen and Ohta (1993). All the previous P-T paths proposed have been interpreted as the result of poly-metamorphism.

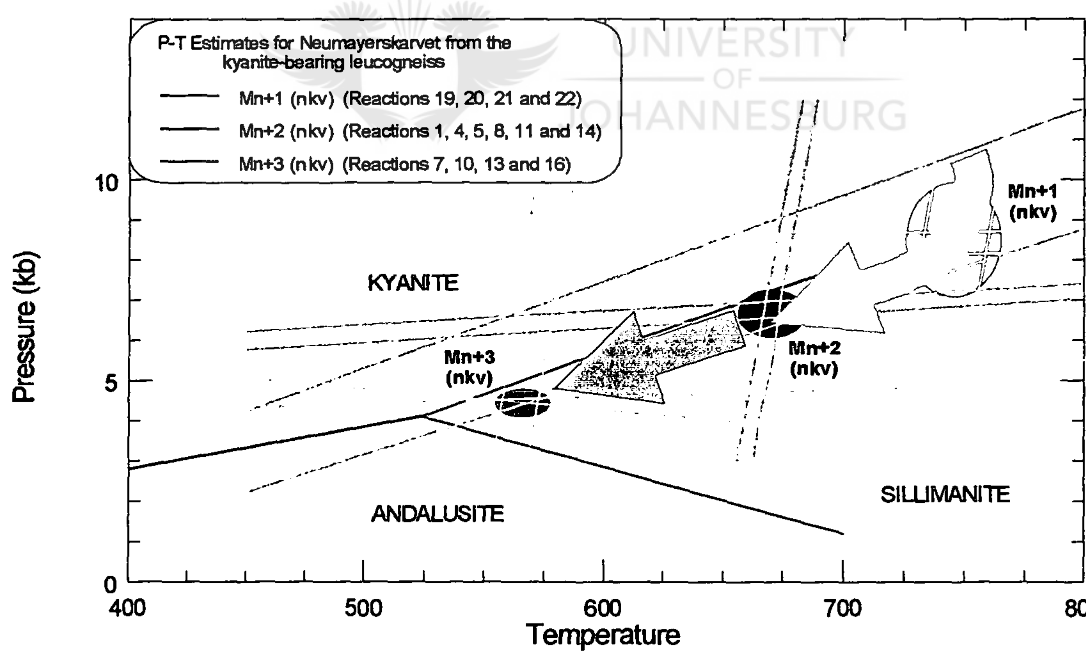

FIGURE 5.27. P-T path derived from the kyanite-bearing leucogneiss at Neumayerskarvet. The P-T estimates for Mn+1, Mn+2 and Mn+3 are shown and are summarised from Figure 5.25. Reaction lines are taken from Figure 5.25d for clarity of the P-T conditions and reactions are provided in Table 5.9. The arrows illustrate the proposed P-T path followed by these rock types. The P-T path is discussed in more detail within the text.

Table 5.1. Mineral assemblages for the megacrystic orthogneiss and kyanite-bearing leucogneiss samples under investigation.

SAMPLE	QTZ	KSP	PLAG	GRT	OPX	CPX	BT	MS	AMPH	SIL	KY	TTN	ILM
Charnockitic Remnants													
PH22005	✓	✓	✓	✓	✓	✓	✓	✗	✗	✗	✗	✗	✓
PH93108	✓	✓	✓	✓	✗	✓	✓	✗	✗	✗	✗	✗	✓
PH92110	✓	✓	✓	✓	✗	✓	✓	✗	✓	✗	✗	✗	✓
Retrogressed Megacrystic Orthogneiss													
PH92001	✓	✓	✓	✓	✗	✗	✓	✗	✓	✗	✗	✓	✓
PH92002	✓	✓	✓	✓	✗	✗	✓	✗/✓	✓	✗	✗	✓	✓
PH92003	✓	✓	✓	✓	✗	✗	✓	✗	✓	✗	✗	✓	✓
PH93102	✓	✓	✓	✓	✗	✗	✓	✗	✓	✗	✗	✓	✓
PH93109	✓	✓	✓	✓	✗	✗	✓	✗	✓	✗	✗	✓	✓
PH93115	✓	✓	✓	✓	✗	✗	✓	✓	✓	✗	✗	✓	✗/✓
Kyanite-Bearing Leucogneiss													
PH92018	✓	✓	✓	✓	✗	✗	✓	✓	✗	✓	✓	✗	✗
PH92020	✓	✓	✓	✓	✗	✗	✓	✓	✗	✗	✗	✗	✗
PH92057	✓	✓	✓	✓	✗	✗	✗	✓	✗	✗	✓	✗	✗
PH93153	✓	✓	✓	✓	✗	✗	✓	✓	✗	✗	✗	✗	✗
PH93158	✓	✓	✓	✓	✗	✗	✓	✓	✗	✓	✗	✗	✗
PH93163	✓	✓	✓	✓	✗	✗	✓	✓	✗	✗	✗	✗	✗
PH93164	✓	✓	✓	✓	✗	✗	✓	✓	✗	✓	✓	✗	✗
PH93195	✓	✓	✓	✓	✗	✗	✓	✓	✗	✗	✓	✗	✗
PH93198	✓	✓	✓	✗	✗	✗	✓	✓	✗	✗	✓	✗	✗
PH93199	✓	✓	✓	✓	✗	✗	✓	✓	✗	✗	✗	✗	✗
PH93202	✓	✓	✓	✓	✗	✗	✓	✓	✗	✗	✗	✗	✗
PH93203	✓	✓	✓	✓	✗	✗	✗	✓	✗	✗	✗	✗	✗

Table 5.2 Selected microprobe analyses of pyroxene from sample PH92005.

Sample	PH92005																			
Spot	51114a	51313	51515	524117	525T27	525T31	525T32	525T36	526116	52718	51116a	51215	51315	522110	524112	526112	525T39	525T40	527112	527114
Mineral	Opx	Opx	Opx	Opx	Opx	Opx	Opx	Opx	Opx	Opx	Cpx	Cpx	Cpx	Cpx	Cpx	Cpx	Cpx	Cpx	Cpx	Cpx
Position	rim	core	core	core	rim	core	core	rim	core	core	rim	core	core	core	core	core	rim	rim	core	rim
Rock Type	MOG	MOG	MOG	MOG	MOG	MOG	MOG	MOG	MOG	MOG	MOG	MOG	MOG	MOG	MOG	MOG	MOG	MOG	MOG	MOG
%Oxide																				
SiO_2	49.42	49.40	49.33	48.95	50.68	50.48	50.12	50.94	48.83	48.82	50.16	49.95	50.69	50.33	49.06	50.52	52.38	51.78	50.15	50.29
Al_2O_3	0.29	0.30	0.32	0.49	0.09	0.04	0.00	0.00	0.18	0.12	1.46	0.98	1.10	1.94	1.71	0.41	0.68	0.54	0.89	1.34
TiO_2	0.04	0.00	0.09	0.00	0.17	0.06	0.05	0.13	0.15	0.00	0.04	0.01	0.00	0.19	0.25	0.01	0.03	0.14	0.15	0.00
MgO	11.40	12.04	11.52	11.35	11.77	11.60	11.34	11.39	11.35	11.01	9.17	9.06	9.55	9.02	8.16	10.59	9.54	9.70	9.12	8.73
FeO	38.51	38.38	38.01	38.10	36.80	36.08	36.80	37.30	38.86	38.64	17.45	17.40	17.33	17.00	19.37	21.24	15.76	16.11	17.31	17.19
MnO	0.41	0.33	0.30	0.55	0.33	0.43	0.44	0.27	0.42	0.44	0.25	0.17	0.15	0.23	0.26	0.09	0.33	0.18	0.21	0.10
CaO	0.66	0.70	1.36	0.98	1.59	2.25	1.60	0.55	0.54	0.81	20.90	21.20	21.20	20.99	18.91	15.72	21.96	22.30	21.62	21.41
Na_2O	0.40	0.47	0.43	0.12	0.15	0.23	0.13	0.10	0.24	0.33	0.77	0.72	0.91	0.91	0.86	0.43	0.43	0.40	0.58	0.83
K_2O	0.05	0.02	0.00	0.02	0.06	0.09	0.00	0.00	0.00	0.00	0.00	0.00	0.00	0.00	0.06	0.00	0.02	0.00	0.00	0.00
Cr_2O_3	0.05	0.00	0.01	0.00	0.00	0.02	0.00	0.00	0.06	0.00	0.08	0.00	0.01	0.00	0.00	0.12	0.07	0.10	0.00	0.00
Total	101.23	101.61	101.36	100.56	101.65	101.28	100.47	100.66	100.62	100.17	100.27	99.48	100.94	100.61	98.65	99.13	101.20	101.25	100.02	99.88
Formula	6	6	6	6	6	6	6	6	6	6	6	6	6	6	6	6	6	6	6	6
Si	1.975	1.966	1.968	1.972	1.997	1.997	2.002	2.022	1.968	1.981	1.946	1.957	1.953	1.942	1.948	1.984	1.993	1.976	1.954	1.961
Al	0.014	0.014	0.015	0.023	0.004	0.002	0.000	0.000	0.008	0.006	0.067	0.045	0.050	0.088	0.080	0.019	0.031	0.024	0.041	0.062
Ti	0.001	0.000	0.003	0.000	0.005	0.002	0.001	0.004	0.005	0.000	0.001	0.000	0.000	0.005	0.008	0.000	0.001	0.004	0.005	0.000
Mg	0.679	0.714	0.685	0.681	0.692	0.684	0.675	0.674	0.682	0.666	0.530	0.529	0.548	0.519	0.483	0.620	0.541	0.552	0.530	0.507
Fe	1.287	1.277	1.268	1.283	1.213	1.194	1.229	1.238	1.310	1.311	0.566	0.570	0.559	0.549	0.643	0.698	0.501	0.514	0.564	0.561
Mn	0.014	0.011	0.010	0.019	0.011	0.015	0.015	0.009	0.014	0.015	0.008	0.006	0.005	0.007	0.009	0.003	0.011	0.006	0.007	0.003
Ca	0.028	0.030	0.058	0.042	0.067	0.095	0.069	0.023	0.023	0.035	0.869	0.890	0.875	0.868	0.805	0.662	0.895	0.912	0.903	0.895
Na	0.031	0.036	0.033	0.009	0.012	0.018	0.010	0.007	0.019	0.026	0.058	0.055	0.068	0.068	0.067	0.033	0.032	0.030	0.044	0.062
K	0.003	0.001	0.000	0.001	0.003	0.004	0.000	0.000	0.000	0.000	0.000	0.000	0.000	0.000	0.003	0.000	0.001	0.000	0.000	0.000
Cr	0.001	0.000	0.000	0.000	0.000	0.000	0.000	0.000	0.002	0.000	0.002	0.000	0.000	0.000	0.000	0.004	0.002	0.003	0.000	0.000
Total	4.033	4.049	4.040	4.030	4.004	4.011	4.001	3.977	4.031	4.040	4.047	4.052	4.058	4.046	4.046	4.023	4.008	4.021	4.048	4.051
XFe	0.641	0.628	0.627	0.634	0.612	0.601	0.618	0.637	0.646	0.647	0.287	0.286	0.281	0.283	0.331	0.352	0.257	0.259	0.281	0.285
XMg	0.338	0.351	0.339	0.336	0.349	0.344	0.340	0.347	0.336	0.329	0.269	0.265	0.276	0.267	0.249	0.313	0.278	0.278	0.264	0.258
XCa	0.014	0.015	0.029	0.021	0.034	0.048	0.035	0.012	0.011	0.017	0.440	0.446	0.440	0.447	0.415	0.334	0.459	0.460	0.451	0.455
XMn	0.007	0.005	0.005	0.009	0.006	0.008	0.008	0.005	0.007	0.007	0.004	0.003	0.003	0.004	0.005	0.002	0.006	0.003	0.003	0.002
Fe/(Fe+Mg)	0.655	0.641	0.649	0.653	0.637	0.636	0.645	0.647	0.658	0.663	0.516	0.519	0.505	0.514	0.571	0.530	0.481	0.482	0.516	0.525

Table 5.3. Selected microprobe analyses of garnets from samples under investigation.

Sample	PH92003		PH92005		PH92018						PH93195							
Spot	3111T9	111T41	525T11	525T23	181T1	81T11	182T1	182T9	82T14	82T17	1951T1	951T8	951T15	953T1	953T15	1953T24	1955T1	1955T13
Mineral	Grt	Grt	Grt	Grt	Grt	Grt	Grt	Grt	Grt	Grt	Grt	Grt	Grt	Grt	Grt	Grt	Grt	Grt
Position	core	rim	core	rim	rim	core	rim	core	rim	core	rim	core	rim	rim	rim	core	rim	core
Rock Type	MOG	MOG	MOG	MOG	KBL	KBL	KBL	KBL	KBL	KBL	KBL	KBL	KBL	KBL	KBL	KBL	KBL	KBL
Mineral Type					grt2a	grt2	grt2a	grt2	grt2b	grt2	grt2	grt1	grt2	grt2a	grt2b	grt2	grt2	grt1
%Oxide																		
SiO2	37.99	38.18	38.20	38.46	38.35	37.72	37.28	37.24	37.21	37.07	37.91	38.34	38.24	38.22	37.40	38.04	38.29	38.58
Al2O3	21.24	21.50	21.44	21.54	22.15	22.26	21.74	22.04	21.92	22.10	22.02	22.29	22.05	22.29	21.71	21.93	21.60	21.97
TiO2	0.10	0.12	0.09	0.01	0.07	0.16	0.00	0.00	0.06	0.00	0.02	0.00	0.00	0.00	0.02	0.00	0.07	0.05
MgO	1.32	0.82	2.18	1.66	3.53	3.41	3.06	3.34	2.16	3.09	4.47	4.63	4.42	3.34	2.08	3.29	4.20	4.67
FeO	28.39	26.13	31.77	31.81	32.41	31.82	32.07	31.14	32.98	31.79	33.28	32.34	32.66	32.93	33.84	32.14	31.71	31.73
MnO	1.72	4.38	1.17	1.10	3.75	3.53	3.74	3.51	4.57	3.97	2.83	3.09	2.67	3.09	3.60	2.66	2.49	2.74
CaO	10.44	10.01	7.07	6.69	1.31	1.79	1.14	1.88	1.50	1.76	1.29	1.17	1.97	1.29	1.94	2.95	1.66	1.32
Cr2O3	0.09	0.04	0.00	0.07	0.00	0.00	0.00	0.05	0.06	0.01	0.00	0.06	0.06	0.00	0.00	0.09	0.00	0.06
Total	101.28	101.17	101.93	101.35	101.57	100.69	99.01	99.20	100.45	99.78	101.81	101.92	102.07	101.16	100.59	101.11	100.02	101.12
Formula	24	24	24	24	24	24	24	24	24	24	24	24	24	24	24	24	2400%	2400%
Si	5.993	6.025	5.999	6.061	6.019	5.970	6.014	5.978	5.969	5.945	5.944	5.976	5.967	6.020	5.994	6.000	6.064	6.037
Al	3.949	3.998	3.968	4.001	4.098	4.152	4.134	4.170	4.144	4.177	4.069	4.095	4.055	4.139	4.101	4.077	4.033	4.052
Ti	0.012	0.014	0.010	0.001	0.009	0.019	0.000	0.000	0.007	0.000	0.003	0.000	0.000	0.000	0.003	0.000	0.009	0.006
Mg	0.310	0.192	0.511	0.391	0.825	0.805	0.737	0.799	0.517	0.739	1.045	1.076	1.028	0.784	0.496	0.774	0.992	1.089
Fe	3.746	3.449	4.172	4.193	4.255	4.211	4.327	4.180	4.425	4.264	4.364	4.216	4.262	4.338	4.535	4.240	4.200	4.152
Mn	0.229	0.585	0.156	0.147	0.499	0.473	0.511	0.477	0.621	0.539	0.375	0.408	0.353	0.412	0.489	0.356	0.333	0.363
Ca	1.765	1.692	1.190	1.130	0.220	0.304	0.196	0.324	0.258	0.302	0.217	0.195	0.329	0.218	0.334	0.498	0.282	0.221
Cr	0.011	0.005	0.000	0.009	0.000	0.000	0.000	0.006	0.008	0.001	0.000	0.007	0.007	0.000	0.000	0.012	0.000	0.007
Total	16.015	15.960	16.006	15.933	15.925	15.934	15.919	15.934	15.949	15.967	16.017	15.973	16.001	15.911	15.952	15.957	15.913	15.927
XFe	0.619	0.583	0.692	0.715	0.734	0.727	0.750	0.723	0.760	0.730	0.727	0.715	0.714	0.754	0.775	0.723	0.723	0.713
XMg	0.051	0.032	0.085	0.067	0.142	0.139	0.128	0.138	0.089	0.126	0.174	0.183	0.172	0.136	0.085	0.132	0.171	0.187
XCa	0.292	0.286	0.197	0.193	0.038	0.052	0.034	0.056	0.044	0.052	0.036	0.033	0.055	0.038	0.057	0.085	0.049	0.038
XMn	0.038	0.099	0.026	0.025	0.086	0.082	0.089	0.083	0.107	0.092	0.062	0.069	0.059	0.072	0.084	0.061	0.057	0.062
Fe/(Fe+Mg)	0.924	0.947	0.891	0.915	0.838	0.840	0.854	0.840	0.895	0.852	0.807	0.797	0.806	0.847	0.901	0.846	0.809	0.792

Table 5.4. Selected feldspar analyses for samples used during this investigation.

Sample	PH92004					PH92005			PH92018				PH93195								
Spot	11T56	3111T66	111T67	111T69	51218	524T3	525T50	525T63	181T23	81T32	182T25	182T32	1951T19	951T22	951T24	951T26	1953T36	1953T45	955T19	1955T22	1956T24
Mineral	Fsp	Fsp	Fsp	Fsp	Fsp	Fsp	Fsp	Fsp	Fsp	Fsp	Fsp	Fsp	Fsp	Fsp	Fsp	Fsp	Fsp	Fsp	Fsp	Fsp	Fsp
Position	rim	core	core	core			rim	core	rim	core	rim	core	rim	core	core	core	rim	core	rim	core	
Rock Type	MOG	MOG	MOG	MOG	MOG	MOG	MOG	MOG	KBL	KBL	KBL	KBL	KBL	KBL	KBL	KBL	KBL	KBL	KBL	KBL	KBL
Mineral Type									pl2	pl2	pl2	pl2	pl1	pl1	pl1	pl1	pl2	pl2	pl1(?)	pl1(?)	
%Oxide																					
SiO2	57.85	62.64	62.37	61.37	62.76	63.28	61.70	61.48	61.60	62.34	61.82	62.21	62.44	63.58	62.39	62.59	61.61	61.34	63.13	61.35	63.25
Al2O3	27.53	19.12	18.81	24.33	18.46	18.45	22.99	24.79	23.12	22.89	23.50	23.08	23.62	19.28	24.03	23.82	23.99	23.24	23.20	23.56	23.24
MgO	0.00	0.00	0.00	0.00		0.00	0.00	0.00	0.00	0.00	0.00	0.00	0.00	0.00	0.00	0.00	0.00	0.00	0.00	0.00	0.00
FeO	0.22	0.36	0.02	0.00	0.03	0.87	0.35	0.00	0.39	0.28	0.10	0.18	0.00	0.00	0.01	0.06	0.47	0.17	0.27	0.02	0.46
MnO	0.06	0.09	0.00	0.00	0.00	0.28	0.05	0.13	0.03	0.00	0.16	0.00	0.18	0.00	0.03	0.01	0.06	0.07	0.06	0.01	0.00
CaO	5.32	0.00	0.00	4.72	0.00	0.00	4.57	5.96	4.24	3.49	4.24	3.45	4.85	0.00	4.49	4.73	4.91	4.42	4.33	4.79	4.65
Na2O	8.27	0.84	0.86	9.17	1.19	1.31	9.15	8.31	9.56	10.16	9.18	9.35	9.60	1.45	9.30	9.32	7.48	9.01	9.36	9.23	9.35
K2O	0.23	17.29	17.29	0.01	16.74	14.30	0.30	0.43	0.38	0.21	0.00	0.41	0.21	14.89	0.36	0.15	0.30	0.44	0.13	0.20	0.27
Total	99.48	100.33	99.36	99.60	99.17	98.49	99.10	101.11	99.31	99.37	98.99	98.68	100.89	99.21	100.60	100.67	98.81	98.68	100.47	99.13	101.22
Formula	32	32	32	32	32	32	32	32	32	32	32	32	32	32	32	32	32	32	32	32	32
Si	10.371	11.701	11.748	10.929	11.847	11.874	11.071	10.832	11.044	11.138	11.061	11.160	11.014	11.818	11.009	11.032	11.028	11.045	11.139	10.995	11.109
Al	5.819	4.210	4.177	5.106	4.108	4.080	4.862	5.148	4.886	4.820	4.957	4.879	4.910	4.224	4.998	4.949	5.061	4.932	4.826	4.976	4.812
Mg	0.000	0.000	0.000	0.000		0.000	0.000	0.000	0.000	0.000	0.000	0.000	0.000	0.000	0.000	0.000	0.000	0.000	0.000	0.000	0.000
Fe	0.033	0.056	0.004	0.000	0.005	0.137	0.052	0.000	0.059	0.042	0.014	0.027	0.000	0.000	0.002	0.009	0.070	0.026	0.039	0.003	0.067
Mn	0.009	0.014	0.000	0.000	0.000	0.045	0.008	0.019	0.004	0.000	0.024	0.000	0.026	0.000	0.004	0.002	0.008	0.011	0.008	0.001	0.000
Ca	1.023	0.000	0.000	0.900	0.000	0.000	0.878	1.126	0.814	0.668	0.813	0.662	0.916	0.000	0.848	0.893	0.942	0.852	0.818	0.920	0.875
Na	2.876	0.304	0.314	3.165	0.434	0.477	3.185	2.839	3.324	3.521	3.184	3.251	3.284	0.523	3.183	3.187	2.595	3.146	3.204	3.206	3.184
K	0.052	4.121	4.154	0.003	4.031	3.422	0.068	0.097	0.086	0.048	0.000	0.094	0.047	3.532	0.081	0.033	0.069	0.101	0.028	0.046	0.061
Total	20.183	20.406	20.397	20.103	20.425	20.040	20.120	20.060	20.217	20.237	20.053	20.073	20.200	20.100	20.120	20.100	19.773	20.113	20.060	20.140	20.110
Ab	72.792	6.870	7.028	77.802	9.720	12.234	77.100	69.892	78.693	83.101	79.660	81.133	77.325	12.898	77.408	77.486	71.963	76.750	79.111	76.846	77.282
An	25.892	0.000	0.000	22.124	0.000	0.000	21.254	27.720	19.271	15.766	20.340	16.521	21.568	0.000	20.623	21.712	26.123	20.786	20.198	22.052	21.238
Or	1.316	93.130	92.972	0.074	90.280	87.766	1.646	2.388	2.036	1.133	0.000	2.346	1.107	87.102	1.970	0.802	1.913	2.464	0.691	1.103	1.481

Table 5.5. Selected amphibole microprobe analyses for samples under investigation.

Sample	PH92003									PH93109								PH93115		
Spot	31319	311110	311111	311112	311113	32119	321110	32111	321112	109234	109235	109236	109237	109216	109217	109241	109242	115206	115135	115136
Mineral	Amph	Amph	Amph	Amph	Amph	Amph	Amph	Amph	Amph	Amph	Amph	Amph	Amph	Amph	Amph	Amph	Amph	Amph	Amph	Amph
Rock Type	MOG	MOG	MOG	MOG	MOG	MOG	MOG	MOG	MOG	MOG	MOG	MOG	MOG	MOG	MOG	MOG	MOG	MOG	MOG	MOG
%Oxide																				
SiO2	40.46	39.40	40.61	39.76	39.89	39.84	39.76	39.46	39.58	40.65	39.92	39.65	39.99	39.64	40.57	40.67	40.06	39.59	39.44	39.67
Al2O3	12.54	12.42	12.62	12.38	12.14	12.31	12.33	12.43	12.25	12.03	12.09	12.22	11.75	11.82	11.88	12.12	12.19	12.00	12.26	12.74
TiO	1.90	1.79	1.62	1.73	1.66	2.20	1.99	2.12	2.23	1.42	1.52	2.33	2.07	1.71	1.18	1.53	2.20	1.70	1.82	1.78
MgO	4.88	4.66	4.95	4.64	4.54	4.59	4.97	4.67	4.71	5.04	5.03	4.86	5.00	4.78	5.02	5.18	5.26	4.69	4.88	4.95
FeO	25.15	24.83	25.49	25.16	25.22	24.86	24.52	24.63	24.70	25.66	25.94	24.57	25.00	25.54	25.86	26.05	24.66	25.20	25.05	24.63
MnO	0.30	0.48	0.39	0.42	0.34	0.44	0.57	0.28	0.45	0.24	0.32	0.25	0.17	0.24	0.43	0.35	0.38	0.34	0.33	0.46
CaO	11.23	11.54	11.64	11.55	11.14	11.30	11.36	11.23	11.10	11.61	11.27	11.24	11.30	11.59	11.57	11.48	11.41	11.29	11.24	11.38
Na2O	1.88	1.48	1.52	1.41	1.58	1.60	1.98	1.68	1.89	1.60	1.70	1.74	1.77	1.79	1.60	1.84	2.04	1.87	1.97	1.99
K2O	1.81	1.68	1.71	1.68	1.69	1.84	1.70	1.97	1.82	1.59	1.62	1.76	1.76	1.75	1.50	1.61	1.56	1.69	1.84	1.96
Cr2O3	0.00	0.00	0.07	0.00	0.00	0.00	0.00	0.00	0.03	0.00	0.14	0.00	0.00	0.13	0.00	0.03	0.00	0.00	0.09	0.00
Total	100.15	98.27	100.60	98.72	98.21	98.99	99.16	98.47	98.76	99.84	99.54	98.61	98.79	98.99	99.62	100.86	99.74	98.38	98.91	99.56
Formula	23	23	23	23	23	23	23	23	23	23	23	23	23	23	23	23	23	23	23	23
Si	6.225	6.191	6.222	6.217	6.273	6.211	6.185	6.182	6.186	6.280	6.208	6.193	6.242	6.209	6.298	6.235	6.187	6.228	6.170	6.154
Al	2.273	2.300	2.280	2.281	2.249	2.263	2.261	2.295	2.258	2.191	2.217	2.251	2.162	2.181	2.173	2.191	2.218	2.225	2.261	2.330
Ti	0.220	0.212	0.187	0.204	0.197	0.258	0.232	0.250	0.262	0.165	0.178	0.274	0.243	0.201	0.138	0.176	0.255	0.201	0.214	0.207
Mg	1.118	1.092	1.130	1.081	1.065	1.067	1.151	1.090	1.097	1.160	1.166	1.132	1.163	1.116	1.163	1.184	1.210	1.100	1.137	1.145
Fe	3.236	3.264	3.266	3.290	3.317	3.241	3.191	3.228	3.229	3.316	3.374	3.209	3.263	3.346	3.358	3.340	3.185	3.316	3.278	3.196
Mn	0.039	0.064	0.050	0.055	0.045	0.059	0.075	0.037	0.059	0.031	0.042	0.032	0.022	0.032	0.057	0.045	0.049	0.045	0.044	0.061
Ca	1.852	1.942	1.911	1.935	1.878	1.888	1.893	1.886	1.858	1.922	1.879	1.881	1.890	1.946	1.925	1.887	1.888	1.903	1.884	1.892
Na	0.561	0.450	0.450	0.428	0.480	0.484	0.597	0.511	0.574	0.479	0.514	0.526	0.534	0.544	0.482	0.546	0.612	0.571	0.598	0.598
K	0.356	0.337	0.335	0.335	0.339	0.365	0.337	0.395	0.363	0.314	0.321	0.351	0.350	0.349	0.297	0.315	0.307	0.339	0.368	0.387
Cr	0.000	0.000	0.008	0.000	0.000	0.000	0.000	0.000	0.004	0.000	0.017	0.000	0.005	0.016	0.000	0.003	0.000	0.000	0.011	0.000
Total	15.880	15.852	15.839	15.826	15.843	15.836	15.922	15.874	15.890	15.858	15.916	15.849	15.874	15.940	15.891	15.922	15.911	15.928	15.965	15.970
XFe	0.518	0.513	0.514	0.517	0.526	0.518	0.506	0.517	0.517	0.516	0.522	0.513	0.515	0.520	0.516	0.517	0.503	0.521	0.517	0.508
XMg	0.179	0.172	0.178	0.170	0.169	0.171	0.182	0.175	0.176	0.180	0.180	0.181	0.183	0.173	0.179	0.183	0.191	0.173	0.179	0.182
XCa	0.297	0.305	0.301	0.304	0.298	0.302	0.300	0.302	0.298	0.299	0.291	0.301	0.298	0.302	0.296	0.292	0.298	0.299	0.297	0.301
XMn	0.006	0.010	0.008	0.009	0.007	0.009	0.012	0.006	0.009	0.005	0.007	0.005	0.003	0.005	0.009	0.007	0.008	0.007	0.007	0.010
Fe/(Fe+Mg)	0.743	0.749	0.743	0.753	0.757	0.752	0.735	0.748	0.746	0.741	0.743	0.739	0.737	0.750	0.743	0.738	0.725	0.751	0.742	0.736

Table 5.6. Selected biotite microprobe analyses for samples used during this investigation.

Sample	PH92003			PH92005			PH92018			PH93109	H93115		PH93195							
Spot	3111T42	111T54	31214	51415	51416	51417	182T20	182T22	182T23	109215	115114	115115	195T26	1953T32	1953T33	1953T35	954T1	1954T2	1954T3	1954T4
Mineral	Bt	Bt	Bt	Bt	Bt	Bt	Bt	Bt	Bt	Bt	Bt	Bt	Bt	Bt	Bt	Bt	Bt	Bt	Bt	Bt
Position	rim	core	rim	core	rim	core	core	core	rim	core	rim	core	rim	core	core	core	rim	core	core	rim
Rock Type	MOG	MOG	MOG	MOG	MOG	MOG	KBL	KBL	KBL	MOG	MOG	MOG	MOG	MOG	MOG	MOG	KBL	KBL	KBL	KBL
Mineral Type								bt2	bt2								bt1	bt1	bt1	bt1
%Oxide																				
SiO2	35.14	34.81	33.79	35.02	34.43	33.70	35.41	35.47	35.20	33.42	32.36	35.00	35.68	35.89	36.20	35.98	35.78	35.24	35.76	35.48
Al2O3	15.10	14.78	15.06	13.76	13.57	13.36	19.74	19.55	19.39	15.06	17.84	16.34	20.48	20.13	20.46	20.37	19.61	19.15	19.47	19.83
TiO	4.58	4.95	3.92	5.89	5.77	5.47	3.01	3.51	3.11	4.26	1.66	3.24	2.93	3.06	3.06	3.36	4.02	4.18	3.77	4.00
MgO	5.88	5.90	5.68	7.31	7.08	6.92	8.00	7.83	8.10	6.34	5.28	4.40	8.02	8.46	8.22	8.13	8.33	8.13	8.00	8.00
FeO	26.72	27.18	28.35	24.80	25.01	24.06	18.61	19.45	19.04	28.66	30.65	27.68	19.46	19.16	18.79	19.19	19.25	19.35	18.66	19.35
MnO	0.14	0.24	0.16	0.00	0.12	0.00	0.01	0.08	0.09	0.46	0.35	0.17	0.06	0.00	0.14	0.02	0.07	0.06	0.14	0.15
CaO	0.00	0.00	0.00	0.00	0.00	0.00	0.00	0.00	0.00	0.04	0.49	0.00	0.00	0.00	0.00	0.00	0.00	0.00	0.00	0.00
Na2O	0.14	0.10	0.29	0.17	0.19	0.29	0.34	0.15	0.23	0.19	0.33	0.15	0.09	0.19	0.16	0.22	0.24	0.11	0.15	0.10
K2O	10.32	10.58	8.47	10.69	10.54	10.05	10.30	10.39	10.57	8.10	6.55	9.35	10.76	10.80	10.76	10.78	10.22	10.94	10.93	10.58
Cr2O3	0.03	0.00	0.00	0.07	0.00	0.01	0.04	0.00	0.00	0.00	0.01	0.04	0.13	0.12	0.00	0.00	0.00	0.04	0.03	0.00
Total	98.05	98.55	95.70	97.72	96.70	93.86	95.45	96.42	95.71	96.53	95.51	96.36	97.61	97.80	97.78	98.05	97.51	97.19	96.91	97.50
Formula	22	22	22	22	22	22	22	22	22	22	22	22	22	22	22	22	22	22	22	22
Si	5.450	5.401	5.388	5.440	5.422	5.447	5.384	5.361	5.364	5.295	5.175	5.517	5.326	5.341	5.372	5.337	5.334	5.306	5.374	5.305
Al	2.761	2.704	2.831	2.519	2.518	2.545	3.537	3.483	3.482	2.812	3.363	3.036	3.604	3.532	3.578	3.561	3.445	3.398	3.448	3.496
Ti	0.534	0.578	0.470	0.688	0.684	0.665	0.345	0.399	0.357	0.508	0.199	0.384	0.329	0.342	0.342	0.375	0.450	0.474	0.426	0.450
Mg	1.359	1.365	1.349	1.692	1.662	1.668	1.813	1.765	1.839	1.498	1.258	1.034	1.785	1.877	1.817	1.798	1.852	1.824	1.793	1.784
Fe	3.466	3.528	3.780	3.222	3.294	3.252	2.366	2.458	2.426	3.798	4.098	3.650	2.429	2.385	2.332	2.380	2.399	2.436	2.345	2.420
Mn	0.018	0.031	0.021	0.000	0.016	0.000	0.002	0.010	0.011	0.061	0.047	0.022	0.008	0.000	0.017	0.002	0.008	0.008	0.018	0.019
Ca	0.000	0.000	0.000	0.000	0.000	0.000	0.000	0.000	0.000	0.007	0.084	0.000	0.000	0.000	0.000	0.000	0.000	0.000	0.000	0.000
Na	0.042	0.029	0.090	0.052	0.057	0.090	0.099	0.044	0.067	0.058	0.101	0.045	0.027	0.054	0.045	0.064	0.068	0.033	0.042	0.028
K	2.042	2.095	1.723	2.119	2.119	2.072	1.999	2.004	2.054	1.637	1.335	1.881	2.049	2.050	2.037	2.041	1.943	2.101	2.095	2.018
Cr	0.004	0.000	0.000	0.009	0.000	0.001	0.005	0.000	0.000	0.000	0.001	0.005	0.015	0.014	0.000	0.000	0.000	0.005	0.004	0.000
Total	15.676	15.731	15.652	15.741	15.772	15.740	15.550	15.524	15.600	15.674	15.661	15.574	15.572	15.595	15.540	15.558	15.499	15.585	15.545	15.520
XFe	0.716	0.716	0.734	0.656	0.663	0.661	0.566	0.581	0.567	0.708	0.747	0.776	0.219	0.560	0.560	0.569	0.563	0.571	0.564	0.573
XMg	0.281	0.277	0.262	0.344	0.334	0.339	0.434	0.417	0.430	0.279	0.229	0.220	0.442	0.440	0.436	0.430	0.435	0.427	0.431	0.422
XCa	0.000	0.000	0.000	0.000	0.000	0.000	0.000	0.000	0.000	0.001	0.015	0.000	0.040	0.000	0.000	0.000	0.000	0.000	0.000	0.000
XMn	0.004	0.006	0.004	0.000	0.003	0.000	0.000	0.002	0.003	0.011	0.009	0.005	0.298	0.000	0.004	0.000	0.002	0.002	0.004	0.004
Fe/(Fe+Mg)	0.718	0.721	0.737	0.656	0.665	0.661	0.566	0.582	0.569	0.717	0.765	0.779	0.331	0.560	0.562	0.570	0.564	0.572	0.567	0.576

Table 5.7. Selected microprobe analyses of titanite and ilmenite from samples under investigation.

Sample	PH92003					PH93109					PH92003			PH92005				PH93109		
Spot	32211	32212	32213	32216	32217	1091115	1091116	1091117	1091118	1091119	32219	322110	322112	51614	51616	51618	51619	1091111	1091112	1091113
Mineral	Ttn	Ttn	Ttn	Ttn	Ttn	Ttn	Ttn	Ttn	Ttn	Ttn	Ilm	Ilm	Ilm	Ilm	Ilm	Ilm	Ilm	Ilm	Ilm	Ilm
Position	core	core	rim	core	rim	rim	rim	core	rim	core	rim	core	core	core	rim	core	rim	rim	rim	core
Rock Type	MOG	MOG	MOG	MOG	MOG	MOG	MOG	MOG	MOG	MOG	MOG	MOG	MOG	MOG	MOG	MOG	MOG	MOG	MOG	MOG
%Oxide																				
SiO2	30.10	28.97	38.75	29.26	29.33	29.67	29.42	29.86	29.31	29.58	0.12	0.20	0.16	0.17	0.24	0.17	0.30	0.14	0.19	0.19
Al2O3	1.58	1.54	1.26	1.33	1.38	1.44	1.43	1.48	1.42	1.49	0.04	0.04	0.06	0.08	0.02	0.04	0.05	0.00	0.04	0.00
TiO2	38.71	38.16	32.42	37.94	37.83	37.84	39.17	38.48	38.65	38.54	52.33	52.23	52.56	51.36	50.96	50.52	50.20	50.46	50.88	50.51
MgO	0.00	0.01	0.01	0.01	0.00	0.06	0.03	0.05	0.05	0.00	0.20	0.14	0.00	0.58	0.57	0.65	0.53	0.08	0.07	0.09
FeO	0.60	0.85	0.90	1.34	0.95	1.17	1.70	1.23	1.33	1.25	46.37	46.50	46.39	47.85	48.05	48.31	48.60	48.92	49.22	48.91
MnO	0.14	0.19	0.07	0.12	0.11	0.02	0.00	0.00	0.09	0.06	1.80	2.04	2.08	0.25	0.13	0.31	0.17	1.44	1.34	1.36
CaO	28.34	27.54	23.21	27.70	27.44	27.64	27.71	27.79	27.70	27.94	0.31	0.23	0.07	0.15	0.18	0.04	0.12	0.29	0.17	0.08
Na2O	0.06	0.10	0.16	0.05	0.09	0.04	0.09	0.07	0.02	0.05	0.23	0.09	0.15	0.11	0.19	0.14	0.42	0.16	0.10	0.17
K2O	0.00	0.00	0.06	0.03	0.04	0.00	0.06	0.06	0.06	0.05	0.03	0.01	0.00	0.00	0.08	0.00	0.01	0.04	0.02	0.04
Cr2O3	0.00	0.00	0.00	0.00	0.00	0.00	0.00	0.00	0.00	0.00	0.00	0.02	0.00	0.00	0.00	0.03	0.00	0.00	0.05	0.00
Total	99.53	97.36	96.83	97.77	97.16	97.88	99.62	99.00	98.63	98.96	101.43	101.50	101.46	100.54	100.42	100.22	100.38	101.52	102.07	101.35
Formula	6	6	6	6	6	6	6	6	6	6	6	6	6	6	6	6	6	6	6	6
Si	6.328	6.252	8.041	6.295	6.333	1.192	6.221	6.332	6.246	6.274	0.006	0.010	0.008	0.009	0.012	0.009	0.015	0.007	0.009	0.009
Al	0.391	0.392	0.307	0.336	0.352	0.068	0.357	0.370	0.357	0.371	0.002	0.002	0.004	0.005	0.001	0.002	0.003	0.000	0.003	0.000
Ti	6.120	6.192	5.060	6.138	6.143	1.143	6.229	6.137	6.194	6.149	1.966	1.961	1.973	1.947	1.937	1.928	1.918	1.916	1.918	1.920
Mg	0.000	0.005	0.004	0.004	0.000	0.004	0.009	0.015	0.017	0.000	0.015	0.010	0.000	0.043	0.043	0.049	0.040	0.006	0.005	0.007
Fe	0.106	0.153	0.156	0.241	0.171	0.039	0.300	0.217	0.237	0.222	1.937	1.941	1.937	2.017	2.031	2.050	2.065	2.065	2.063	2.068
Mn	0.024	0.036	0.013	0.021	0.020	0.001	0.000	0.000	0.015	0.011	0.076	0.086	0.088	0.011	0.005	0.014	0.007	0.062	0.057	0.058
Ca	6.384	6.367	5.161	6.386	6.349	1.189	6.279	6.314	6.325	6.351	0.016	0.012	0.004	0.008	0.010	0.002	0.006	0.016	0.009	0.004
Na	0.023	0.041	0.063	0.020	0.036	0.003	0.038	0.029	0.006	0.019	0.022	0.009	0.014	0.010	0.018	0.013	0.041	0.015	0.010	0.016
K	0.000	0.000	0.015	0.007	0.012	0.000	0.016	0.016	0.015	0.014	0.002	0.000	0.000	0.000	0.005	0.000	0.001	0.002	0.001	0.003
Cr	0.000	0.000	0.000	0.000	0.000	0.000	0.000	0.000	0.000	0.001	0.000	0.001	0.000	0.000	0.000	0.001	0.000	0.000	0.002	0.000
Total	19.376	19.438	18.820	19.448	19.416	3.639	19.449	19.430	19.412	19.412	4.042	4.032	4.028	4.050	4.062	4.068	4.096	4.089	4.077	4.085
XFe	0.016	0.023	0.029	0.036	0.026	0.032	0.046	0.033	0.036	0.034	0.948	0.947	0.955	0.970	0.972	0.969	0.975	0.961	0.967	0.968
XMg	0.000	0.001	0.001	0.001	0.000	0.003	0.001	0.002	0.003	0.000	0.007	0.005	0.000	0.021	0.021	0.023	0.019	0.003	0.002	0.003
XCa	0.980	0.970	0.968	0.960	0.971	0.964	0.953	0.965	0.959	0.965	0.008	0.006	0.002	0.004	0.005	0.001	0.003	0.007	0.004	0.002
XMn	0.004	0.005	0.002	0.003	0.003	0.001	0.000	0.000	0.002	0.002	0.037	0.042	0.043	0.005	0.002	0.007	0.003	0.029	0.027	0.027
Fe/(Fe+Mg)	1.000	0.968	0.975	0.984	1.000	0.907	0.971	0.935	0.933	1.000	0.992	0.995	1.000	0.979	0.979	0.977	0.981	0.997	0.998	0.997

Table 5.8. Geothermobarometry Results using GEOPATH program version 1.2 (Gerya and Perchuk, 1991).

ROCK TYPE	ASSEMBLAGE	PRESSURE RANGE (Kb)	TEMPERATURE RANGE (°C)
KBL, MOG	Grt-Bt[1]	(at 8Kb)	584-804
MOG	Grt-Opx[2]	(at 8Kb)	510-654
MOG	Grt-Cpx[3]	(at 8Kb)	517-609
MOG	Grt-Hbl[1]	-	520-665
MOG	Hbl-Pl[4]	6.78-7.58	756-784
KBL	Grt-Pl-Ky-Qtz[5]	13.70-21.00	(at 600°C)
KBL	Grt-Pl-Sil-Qtz[5]	5.46-7.20	(at 600°C)
KBL	Grt-Bt-Ms-Qtz-Ky[6]		(at 600°C)
KBL	Grt-Bt-Ms-Qtz-Sil[6]		(at 600°C)

KBL: - Kyanite-Bearing Leucogneiss
MOG: - Megacrystic Orthogneiss

[1]Perchuk (1989, 1990)
[2]Geopath (1991) Internally consistent thermometer
[3]Krogh (1988)
[4]Geopath (1991) Empirical Thermobarometer
[5]Aranovich (1991) quoted in GEOPATH (Gerya and Perchuk, 1991)
[6]Perchuk and Krotov (1990)

Table 5.9. Reaction pairs from the kyanite-bearing leucogneiss samples used in calculating P-T estimates illustrated in Figure 5.25.

Reaction Number	Sample Site	Site Numbers	Mineral Type	Reaction	Garnet Profile Position	Comments
1	PH92018 Site 1	181T11-181T32	grt2(core)-pl2(core)	grt-pl-qtz-sil	A1-B1 (grt core)	
2	PH92018 Site 2	182T9-182T32	grt2(core)-pl2(core)	grt-pl-qtz-sil	B2-F2 (grt core)	
3	PH92018 Site 1	181T1-181T23	grt2a(rim)-pl2(rim)	grt-pl-qtz-sil	A1-B1 (grt rim)	Grt and pl contact
4	PH92018 Site 2	182T1-182T25	grt2a(rim)-pl2(rim)	grt-pl-qtz-sil	B2-F2 (grt rim)	Grt and pl contact
5	PH92018 Site 2	182T17-182T22	grt2(core)-bt2(core)	grt-bt-sil-ms-qtz	C2-D2 (grt core)	
6	PH92018 Site 2	182T1-182T22	grt2a(rim)-bt2(core)	grt-bt-sil-ms-qtz	B2-F2 (grt rim)	Grt and pl contact
7	PH92018 Site 2	182T14-182T23	grt2b(rim)-bt2(rim)	grt-bt-sil-ms-qtz	C2-D2 (grt rim)	Grt and bt contact
8	PH92018 Site 2	182T17-182T22	grt2(core)-bt2(core)	grt-bt	C2-D2 (grt core)	
9	PH92018 Site 2	182T1-182T22	grt2a(rim)-bt2(core)	grt-bt	B2-F2 (grt rim)	Grt and pl contact
10	PH92018 Site 2	182T14-182T23	grt2b(rim)-bt2(rim)	grt-bt	C2-D2 (grt rim)	Grt and bt contact
11	PH93195 Site 3	1953T24-1953T33	grt2(core)-bt2(core)	grt-bt-ky-ms-qtz	C3-B3 (grt core)	
12	PH93195 Site 3	1953T1-1953T33	grt2a(rim)-bt2(core)	grt-bt-ky-ms-qtz	F3-D3 (grt rim)	Grt and pl contact
13	PH93195 Site 3	1953T15-1953T26	grt2b(rim)-bt2(rim)	grt-bt-ky-ms-qtz	C3-B3 (grt rim)	Grt and bt contact
14	PH93195 Site 3	1953T24-1953T33	grt2(core)-bt2(core)	grt-bt	C3-B3 (grt core)	
15	PH93195 Site 3	1953T1-1953T33	grt2a(rim)-bt2(core)	grt-bt	F3-D3 (grt rim)	Grt and pl contact
16	PH93195 Site 3	1953T15-1953T26	grt2b(rim)-bt2(rim)	grt-bt	C3-B3 (grt rim)	Grt and bt contact
17	PH93195 Site 3	1953T24-1953T45	grt2(core)-pl2(core)	grt-pl-qtz-ky	F3-D3 (grt core)	
18	PH93195 Site 3	1953T1-1953T36	grt2a(rim)-pl2(rim)	grt-pl-qtz-ky	F3-D3 (grt rim)	Grt and pl contact
19	PH93195 Site 1,4&5	1955T13-1954T2	grt1-bt1(core)	grt-bt-ky-ms-qtz	A5-B5 grt core)	Low CaO grt core, isolated bt core
20	PH93195 Site 1,4&5	1951T1-1954T4	grt2(rim)-bt1(rim)	grt-bt-ky-ms-qtz	A1-B1 (grt rim)	Grt rim and isolated bt rim
21	PH93195 Site 1,4&5	1955T13-1954T2	grt1-bt1(core)	grt-bt	A5-B5 (grt core)	Low CaO grt core, isolated bt core
22	PH93195 Site 1,4&5	1955T1-1954T4	grt2(rim)-bt1(rim)	grt-bt	A5-B5 (grt rim)	Grt rim and isolated bt rim
23	PH93195 Site 1,4&5	1951T15-1951T24	grt2(high)-pl1(core)	grt-pl-qtz-ky	A1-B1 (grt rim)	High CaO grt rim
24	PH93195 Site 1,4&5	1951T8-1951T24	grt1(low)-pl1(core)	grt-pl-qtz-ky	A1-B1 (grt core)	Low CaO grt core

CHAPTER 6

ISOTOPIC CONSTRAINTS ON METAMORPHISM IN THE NORTHERN KIRWANVEGGEN

INTRODUCTION

One of the aims of metamorphic studies is to determine the metamorphic history experienced by the rocks under investigation. To obtain these goals, detailed petrographical, fabric and geochemical data are examined in order to establish reliable P-T estimates for the assemblages or reaction textures identified. A metamorphic history is established, and a P-T path is derived. The P-T path does not, however, record the entire pathway conditions experienced by these rocks. Rather, the path represents fragments of this history preserved in the rocks. These path remnants may essentially be unrelated in time and could be the result of poly-metamorphism. To better understand the metamorphic evolution of the terrane, time constraints on the P-T path are required, which enables an interpretation of the path significance with respect to the regional geological evolution of the terrane.

The aim of this chapter is to provide age constraints for the metamorphism, and thereby temporally constrain the deformational episodes in order to elucidate the tectono-metamorphic evolution of the northern Kirwanveggen. This can be achieved through isotopic dating of different metamorphic assemblages using various mineral isotopic systems. An understanding of the closure temperature for these mineral systems is important, and is therefore described in some detail in this chapter. Through the establishment of temperature-time paths the data can be related to the metamorphic history. In combination with the deformational and metamorphic information an understanding of the tectono-metamorphic cycles that have affected the northern Kirwanveggen is established.

GEOLOGICAL SUMMARY

Neumayerskarvet has been subjected to three major tectonic episodes (see Chapters 3 and 4). The early regional D1 episode has been subdivided into three tectonic periods (D1a, D1b and D1c) based on the absolute timing of magmatism and deformational fabrics recognised at Neumayerskarvet (Chapter 4). The regional D1 episode may either represent a continuum within a single tectono-metamorphic episode, or result from episodic deformation-magmatic-metamorphic periods. D1a deformation is constrained between *ca.* 1160 Ma and *ca.* 1110 Ma and is represented by the development of a strong penetrative planar foliation. Possible magmatism occurred during this period, but the current U-Pb ion microprobe data are poorly constrained (see Chapter 4). D1b deformation represents a major period of magmatism and tectonism between *ca.* 1110 Ma and *ca.* 1070 Ma. Isoclinal recumbent folds, sheath folds and re-folded folds with associated stretching lineations and planar foliation development, dominate deformation. Fabric geometries suggest NNW-SSE tectonic transport. Evidence for D1c deformation is difficult to distinguish, but is identified through isotopic data at between *ca.* 1070 Ma and *ca.* 970 Ma. High-strain zones reworking earlier fabrics may represent deformation associated with D1c. Cross-folding and high-strain zone development reworking earlier fabrics may represent signatures of the regional D2 deformation at *ca.* 500 Ma. Late regional D3 deformation, marked by brittle faults and fractures, at *ca.* 180 Ma has been related to rifting during Gondwana break-up.

Three stages of metamorphism have been recognised within the northern Kirwanveggen based on analytical work from the kyanite-bearing leucogneisses (see Chapter 5). This unit intrudes in the gneisses at Neumayerskarvet at 1096 ± 10 Ma, and as such any pre-intrusion history associated with the D1a deformation is not documented. Garnet-kyanite assemblages are recognised within the first metamorphic stage (Mn+1 (nkv)). The early assemblages provide P-T estimates of 710-760 °C and 7.8-8.5 kb. A later metamorphic stage (Mn+2 (nkv)) overprints the early metamorphic assemblages. Kyanite replacement by sillimanite and growth of higher Ca–content garnets and garnet rims are assigned to the Mn+2 (nkv) metamorphic stage. P-T estimates for the Mn+2 (nkv) metamorphic stage are 630-690 °C and 6.0-7.4 kb. The final metamorphic stage recognised in the kyanite-bearing leucogneisses (Mn+3 (nkv)) is characterised by the growth of large microcline and muscovite grains, with the replacement of biotite by chlorite. Rim compositions of garnets and biotites provide P-T estimates of 560-570 °C and 4.4-4.6 kb.

THE APPLICATION OF RADIOGENIC ISOTOPES IN METAMORPHIC ENVIRONMENTS

Introduction

Different radiogenic isotopic systems have produced variable age data from the same region in a metamorphic terrane, and in many cases from the same sample. These data indicate that the different mineral isotopic systems behave differently during changing metamorphic conditions. An isotopic system may remain open long after peak metamorphic conditions have been achieved. During this period diffusive exchange of the daughter-parent isotopes takes place and equilibrium is maintained. Only after closure of the isotopic system is any age information recorded. The temperature at which the diffusion involving the radiogenic isotopes ceases is important for establishing temperature-time (T-t) paths for the samples under investigation. The following section discusses the closure temperature concept related to different isotopic systems, and reviews the factors that influence these closure temperatures.

The Concept of Closure Temperature

Closure temperature is the temperature at which the diffusion of a specific element ceases during cooling from crystallisation (Dodson, 1973; 1979). When a mineral system is near the temperature of crystallisation, the daughter nuclide diffuses out of the system as fast as it is produced by radioactive decay (Dodson, 1979). As the system cools past a certain temperature the daughter nuclide ceases to diffuse out of the mineral, and the daughter product accumulates without any loss out of the system. The temperature at which the system closes to daughter nuclide diffusion is regarded as the closure temperature, and the "age" obtained from the mineral will represent the time at which the system passed through its closure temperature.

Closure Temperature Estimates of Certain Mineral Systems

The data in this section summarises closure temperatures that have been suggested for certain minerals and their isotopic systems. The original values are quoted in this section and none of the values have been re-calculated for different cooling rates, grain-sizes, compositions etc. A summary of all the closure temperatures recorded in the literature are presented in Table 6.1 but the following discussion involves only those mineral systems relevant to this investigation (See Figure 6.2).

Closure Temperatures of U-Pb Mineral Systems

<ins>Zircon</ins>: - U-Pb zircon age dating has been used extensively to establish crystallisation ages of intrusive bodies, and is at present the most reliable method to date the emplacement ages of igneous rocks. Detailed morphological examinations of the zircon crystals helps to identify igneous, metamorphic, detrital zircons, and possible overgrowths. Igneous zircons are generally euhedral, but not always, while metamorphic zircons are often ovoid, very clear and multi-faceted (Passchier *et al.*, 1990). Euhedral zircons affected by metamorphism are often recognised by distinct rounding at crystal ends and by irregular grain shapes. U-Pb zircon data are usually plotted on concordia diagrams which enable the recognition of discordant data caused by radiogenic lead loss after zircon crystallisation. During high temperature metamorphism zircons lose part of their radiogenic lead. If the lead loss history is simple for the zircons then the discordant zircons generally define a straight line that can be projected back to concordia to establish the crystallisation age. A complex history, however, will generally only enable the recognition of a later event, but may not provide geologically significant age data. Likewise, if the metamorphic events are closely spaced the lead loss line may project parallel to concordia making recognition of such an event difficult (Young *et al.*, 1995). Zircons have thus far been used specifically to establish crystallisation ages and very little data is available on the potential closure temperature of this mineral and isotopic system. Mattinson (1978) has estimated closure temperature of the U-Pb zircon system for a Cretaceous plutonic terrain to be in the range of 650 to 750 °C, but there are many other studies that suggest higher age related temperatures are preserved in the U-Pb zircon systematics.

Closure Temperatures of Sm-Nd Mineral Systems

Garnet: - Conflicting data has been generated for the diffusion of rare-earth elements (REE) in garnets. Harrison and Wood (1980) established diffusion rates for Sm in pyrope garnets of grain size 4 mm at cooling rates of 2-100 °C/Ma and calculated closure temperatures between 440 and 570 °C. Similarly, closure temperatures for grossular garnet, with grain sizes of 4 mm and cooling rates of 2-100 °C/Ma, ranged between 670 and 760 °C. Using these data Humphries and Cliff (1982) estimated closure temperatures of approximately 600 °C for garnets of composition $Alm_{1.8}Py_{0.9}Gross_{0.5}$, grain sizes of 1-5 mm, and slow cooling rates of 1-3 °C/Ma from the Scourian granulites, Sutherland. These authors concluded that the diffusion of REE between mineral grains is sufficiently rapid in granulite facies conditions to prevent the preservation of Sm-Nd garnet crystallisation ages. Humphries and Cliff (1982) re-calculated the closure temperatures for garnets using the measured Sm diffusion rates, grain sizes of less than a few mm, and cooling rates of 5 °C/Ma. They calculated closure temperatures ranging from 480 °C for pyrope to 700 °C for grossular. At very rapid cooling rates of 100 °C/Ma the closure temperature of pyrope does not exceed 600 °C while for grossular the corresponding closure temperature is 775 °C (Humphries and Cliff, 1982). These data indicate that if peak metamorphism exceeds these temperatures then the Sm-Nd garnet ages will represent cooling ages rather than garnet growth ages.

Patchett and Ruiz (1987) used Sm-Nd isotopic data to date metamorphic garnets from eastern and southern Mexico. Their Sm-Nd garnet ages post-dated the 700-800 °C granulite facies metamorphism by 50-100 Ma, indicating that the closure temperature was less than 800 °C and probably less than 700 °C. Garnet compositions were not established and closure temperatures could not be accurately fixed, but these results were consistent with that of Humphries and Cliff (1982) suggesting closure temperatures of approximately 600 °C.

Cohen *et al.* (1988), Vance and O'Nions (1990) and Burton and O'Nions (1991) differ from the above authors and suggest that the diffusion of Nd and Sm in garnets is slower than the values obtained from experimental tracer diffusion experiments. These authors suggest that even in slowly cooled granulite terranes, garnets are expected to yield Sm-Nd chronologies very close to the time of mineral growth. It is thought that Sm and Nd diffusion rates are no slower than those for major elements such as Fe and Mg in garnet. Inter-diffusion rates for Fe-Mg in garnets for cooling rates of 5 °C/Ma suggest closure temperatures of 725 ± 30 °C (Freer, 1981). A more recent study by Burton *et al.* (1995) indicates that Sm-Nd garnet ages are younger than peak garnet growth times. Sm-Nd exchange ceases at different times depending on the nature of co-existing mineral phases and grain size variations (Burton *et al.*, 1995).

Other studies have suggested that Sm-Nd garnet closure temperatures are in excess of ~ 600 °C (Mezger *et al.*, 1992; Thoni and Miller, 1996) while some authors have suggested retention of Sm-Nd isotopic systematics in garnets during overprinting granulite facies metamorphism (Hensen and Zhou, 1995). Hensen and Zhou (1995) have suggested that the closure temperature for the Sm-Nd system in garnet is > 700-750 °C based on studies within the Prydz Bay region in Antarctica.

REE zoning in garnet has been examined by Brueckner *et al.* (1996). The zoning profiles from rocks from the Caledonides of Norway and the Variscides of Poland show complex profiles that indicate core preservation of growth zoning patterns with retrogressive rims. Other garnets produce flat profiles and have been interpreted to represent near-homogenisation of the REE within the garnets. Cooling rates have been described as the major influence on the varied REE zoning profiles documented within these garnets.

It is clear from the many studies and varied interpretations of the Sm-Nd garnet age significance that several factors influence the behaviour of this system, and potentially others, under different conditions. These factors vary from grain size and cooling rates, to compositional and co-existing mineral phases present within the individual samples. These and other influencing factors are discussed in more detail later within this section.

Closure Temperatures of Ar-Ar Mineral Systems

Hornblende: - The presently accepted values for the closure temperature of the Ar-Ar system in hornblende is 500 ± 50 °C for a slow cooling of 5 °C/Ma (McDougall and Harrison, 1988).

Muscovite: -The closure temperature for Ar-Ar on white micas is lower than that for hornblende but is significantly higher than that of biotite (McDougall and Harrison, 1988). For moderate cooling rates a closure temperature of about 350 °C has been established (Purdy and Jager, 1976; Jager, 1979).

Biotite: - Closure temperature estimates for biotite in the Ar-Ar system assuming slow cooling of 1 °C/Ma has been established at 250 ± 50 °C (McDougall and Harrison, 1988).

Closure Temperatures of Rb-Sr Mineral Systems

Muscovite: - Closure temperature for Rb-Sr muscovite ages have been determined by field data (Purdy and Jager, 1976; Blackenburg *et al.*, 1989), at 500 ± 50 °C, but this is not well established.

Biotite: - Harrison and McDougall (1980) have suggested a closure temperature for Rb-Sr biotite ages of 320 ± 40 °C based on the consistency of closure temperature differences between Ar, at 250 ± 50 °C, and Sr in biotite. Harrison and McDougall (1980) considered that biotite alone possessed the closing temperature of ~ 320 °C. Giletti (1991a) suggested that the next to last mineral to close controlled the distribution of Rb and Sr since their element transport depends on element exchange between another mineral or a fluid phase. If this is taken into consideration the closure temperatures for biotite and another phase such as plagioclase, may be considerably higher than ~ 320 °C.

Plagioclase: - Burton and O'Nions (1991) have calculated closure temperatures for plagioclase using experimental Sr diffusion data of Gilleti (1991b). Closure temperatures between 370 and 450 °C have been calculated for plagioclase using cooling rates of between 1 and 100 °C/Ma with grain sizes of 0.2 mm.

Closure Temperature of Fission Track Mineral Data

Apatite: - Apatite is the most widely used mineral as a fission track chronometer. This mineral has high uranium contents and occurs in many geological environments. At present apatite fission track dating is used most extensively as a geothermo-chronometer due to the relatively low thermal stability of tracks (Wagner and Van den Haute, 1992). The best estimate for the closure temperature of apatite fission track dating is 100 ± 20 °C.

Factors Influencing Mineral System Closure Temperatures

Several factors influence the closure temperature of different isotopic systems, as indicated in the equation described by Dodson (1973). These features are grain size, cooling rate, diffusion coefficient, activation energy and the mineral shape (described by the geometrical factor in the equation). The influences of these and other factors are described below.

The rate of element diffusion is controlled by the grain size of the mineral. The larger the mineral grain, the slower the rate of diffusion and therefore the higher the closure temperature. Closure temperature changes tend to be more prominent at small grain sizes whereas the closure temperature is less sensitive to size variations in larger mineral grains.

The cooling rate has a similar effect on the closure temperature. The slower the cooling rate, the lower the closure temperature for that particular mineral system. As for grain size, the closure temperature is sensitive to small variations at slower cooling rates than at faster cooling rates.

Variations in diffusion coefficients and activation energies also have a significant effect on the determination of the closure temperature. These parameters have been shown to be dependent on pressure, temperature and mineral composition. Sneeringer *et al.* (1984) have shown the dependence of the diffusion coefficient and activation energy for Sr in diopside on both temperature and pressure. Harrison and Wood (1980) have shown the effects of different garnet compositions on diffusion coefficients and activation energies for Sm. From these data it is clear that pressure, temperature and composition influence the diffusion coefficients and activation energies, and hence influence the closure temperature for different isotopic mineral systems.

A factor that must also be considered when determining the closure temperature of a mineral system is the extent of the fluid phase present during or post-dating the metamorphism. A study by Ernbert and Austerheim (1993) has shown that the re-equilibration of garnet is dependent on the presence of a fluid phase and on deformation. In areas where fluid movement was negligible the re-equilibration in the garnet chemical profiles were also negligible.

Influences of the co-existing mineral phases on the closure temperature have also been suggested by several investigations (Burton *et al.*, 1995). The closure temperature of the mineral system under investigation may be controlled by the second last mineral to close to diffusional processes. Minerals that are suitable for reaction exchange with the mineral system under investigation would affect the closure temperature at that locality. Increased diffusion rates may be expected in these types of situations. A region that has undergone reaction exchange processes may provide mineral associations that are in dis-equilibrium with one another, with resulting large age variations between samples.

A large number of factors affect the determination of the closure temperatures of different isotopic mineral systems. Theoretical determinations do not always provide data that support field observations and discrepancies are often encountered. Field data are also not entirely conclusive with respect to the closure temperatures, and differences have been recorded from various investigations. The factors discussed above all play a significant role in the determination of closure temperatures. Average estimates of the closure temperatures have been established for several geochronological mineral systems from the theoretical and field data. These estimates are presented in Table 6.1 and Figure 6.2, and are a consensus of the closure temperatures for these systems, and are used during this investigation. Influences outlined in this section must be kept in mind during the interpretation of temperature-time paths derived during this investigation.

The Significance of U-Pb Zircon Ages from High-Grade Gneisses

A detailed discussion of the effects of metamorphism on U-Pb zircon systematics is presented in Chapter 4. This section provides a summary of the discussion that is pertinent to the interpretation of the zircon data presented in this section and summarised in Table 6.2.

Lead loss in zircons from high-grade gneiss terranes has commonly been observed (Black *et al.*, 1986; Kroner *et al.*, 1987 and 1994; Williams and Claesson, 1987; Rudnik and Williams, 1987; Holzl *et al.*, 1994; amongst others). The lead loss is also variable between grains and between domains of individual grains. Most authors are in agreement that the upper age intercepts from discordant data represents the zircon crystallisation age (Holzl *et al.*, 1994; Kroner *et al.*, 1994; Mezger and Krogstad, 1997). Interpretation of the lower intercept is less certain, however. This intercept age could represent a period of resetting or recrystallisation but other geochronological techniques would be required to evaluate its geological significance. The situation is complicated further when multi-stage metamorphism, deformation and zircon growth occur. If the ages of zircon crystallisation and metamorphism are close together then lead loss would not lead to discordance but would rather track along concordia between these two events (Young *et al.*, 1995). Mezger and Krogstad (1997), however, suggested that at high temperatures, zircon U-Pb data that spread along concordia are most likely the result of multistage growth rather than diffusion of lead in pre-existing grains.

During metamorphism, if Zr is not released then zircon may not form during that specific event. This raises a question as to the metamorphic significance of the new zircon growth. Fraser *et al.* (1997) have suggested that new zircon growth, as a result of hornblende or garnet breakdown, is not expected to record the time of peak metamorphism but rather will record the time of a particular metamorphic reaction. It is possible therefore that zircon growth periods may not represent different metamorphic events, but rather reactions taking place during a metamorphic cycle.

The issues outlined above are important and must be kept in mind when interpreting the U-Pb zircon age data from a metamorphic terrane. Complicated patterns have been recognised within the U-Pb zircon systematics from the northern Kirwanveggen (see Chapter 4). The zircon data are discussed later in this chapter in terms of the metamorphic history of the northern Kirwanveggen.

SAMPLE DESCRIPTIONS

Biotite-Garnet Migmatite Gneiss

The biotite-garnet migmatite gneiss represents a major unit in the northern Kirwanveggen, and possible correlatives occur within the H.U.Sverdrupfjella (Grantham *et al.*, 1995). This unit has been exposed to all the deformational stages identified at Neumayerskarvet and provides a maximum age for the deformation currently observed.

The biotite-garnet migmatite gneiss comprises qtz + pl ± ksp + bt ± grt ± amph ± ttn ± ms ± oxides. The major feldspar is typically plagioclase except where major deformation is recorded in the samples. When late-stage deformation is recorded, microcline dominates. Strong undulose extinction patterns are often preserved in the plagioclase. Symplectic intergrowths of quartz and feldspar are also observed within these samples. Several generations of biotite have been identified. The biotite is nearly always aligned within the foliation of the biotite-garnet migmatite gneiss. Opaque phases are closely associated with biotite, and may develop along the cleavage or rim of the biotite. Zones of high biotite concentrations are accompanied by garnet. Poikiloblastic garnets are preserved in rare instances, with inclusion filled cores of quartz, feldspar and biotite, titanite and zircon. Garnet relic textures surrounded by plagioclase are preserved in most samples examined. Amphibole is rare in the biotite-garnet migmatite gneiss and is often aligned in the foliation and encloses biotite. Titanite accompanies amphibole and appears to be part of a later retrogression event. Muscovite occurs intergrown with biotite, replacing biotite and feldspar. Minerals selected for isotopic analyses from the biotite-garnet migmatite gneiss include zircon, garnet, feldspar, biotite and muscovite.

Quartzofeldspathic Gneiss

The quartzofeldspathic leucogneiss occurs interleaved with the biotite-garnet migmatite gneiss, on the western side of Neumayerskarvet. Most deformational episodes are recorded within the quartzofeldspathic gneiss, and folding of fold axes and steepening of the regional composite foliation is commonly observed.

The quartzofeldspathic gneisses preserve mineral assemblages of qtz + pl ± ksp + bt + grt ± amph ± ttn ± zrn ± ms ± oxides. Plagioclase generally forms the dominant feldspar component. Larger garnets are poikiloblastic with inclusions of quartz and feldspar with minor titanite, biotite and amphibole. Plagioclase coronas or moats develop around the small relic garnets. These reaction textures are often formed where biotite and amphibole are in contact with garnet, developing embayments in the garnet and plagioclase reaction products. Titanite occurs when amphibole is present in the sample, and forms as inclusions in amphibole or as rare inclusions preserved in garnet grains. Muscovite tends to occur as a replacement product of biotite and feldspar. Gamets are the only mineral that have been isotopically analysed for this rock type.

Intrusive Leucogneiss

The intrusive leucogneiss comprises a lensoidal felsic unit that is structurally inter-fingered with the biotite-garnet migmatite gneiss. Melt segregation veinlets occur within the intrusive leucogneisses and are ptygmatically folded by later deformation. These units intrude across the penetrative planar foliation developed in the biotite-garnet migmatite gneiss but have subsequently been intensely deformed. A penetrative planar foliation develops in the intrusive leucogneiss and is accompanied by an intense elongation lineation. The fabrics within the intrusive leucogneiss are parallel, and are coplanar and colinear to the older fabrics developed in the biotite-garnet migmatite gneiss. The fabric elements developed within the intrusive leucogneiss are interpreted as forming during the D1b deformational episode where intense L>S fabrics are developed. The earlier fabrics transected by the intrusive leucogneiss are related to the D1a deformational episode.

The mineralogical assemblages of the intrusive leucogneisses comprises qtz + pl + ksp + bt + grt ± ms ± ttn ± zrn ± ap ± opaques. Symplectic intergrowths of plagioclase and quartz are preserved in some cases. Perthitic textured K-feldspar is seen in samples that have been subjected to greater degrees of late deformation. Two generations of biotite are observed within these samples. Biotite and garnet are aligned in the foliation of several samples. Garnets occur as relics and have embayments of biotite with plagioclase rims preserved. The cores of some garnets have quartz and feldspar inclusions. Muscovite generally tends to occur as a replacement product of feldspar and biotite. Zircon, biotite, feldspar, muscovite and garnet mineral separates were used for isotopic determinations from the intrusive leucogneisses.

Kyanite-Bearing Leucogneiss

The kyanite-bearing leucogneiss intrudes across the structural fabrics, and several intrusive phases were observed within the biotite-gamet migmatite gneiss. Phyllosilicates and aluminosilicates within the kyanite-bearing leucogneiss are aligned, and define the elongation lineation developed within this unit. The kyanite-bearing leucogneisses are potentially melt segregations related to the D1b deformational episode.

Detailed mineralogical descriptions for these rock units have been provided in Chapter 5, but are briefly summarised in this section. The kyanite-bearing leucogneisses comprise quartz, K-feldspar, plagioclase, biotite, muscovite, kyanite, sillimanite, and garnet with minor zircon, apatite and opaque mineral phases. The alumino-silicate and garnets are randomly distributed throughout these bodies. Kyanite is the primary phase in the leucogneisses and occurs as large blades often aligned within the foliation of the leucogneisses. Relic natured kyanite also occurs within a quartz matrix. Sillimanite needles and muscovite surround and replace the kyanite. Sillimanite occurs as fine needles on the rims of kyanite crystals. Sillimanite also occurs on the contact between garnet and kyanite. Kyanite concentrations are occasionally observed on the contact margins of the intrusive bodies. The sillimanite can either exhibit orientated replacement of the kyanite indicating growth within a tectonic regime, or may exhibit a radial needle-like texture that does not appear to be affected and aligned by later deformation. Minerals used for isotopic analysis include zircon, garnet, biotite, muscovite and feldspar.

Megacrystic Orthogneiss

The megacrystic orthogneiss comprises augen-textured gneisses with relatively undeformed charnockitic remnants. This unit intrudes into the biotite-garnet migmatite gneiss during a major period of deformation.

The range of retrogressed megacrystic orthogneisses extends from weakly deformed porphyritic textured gneisses through to augen textured gneisses. Mineral assemblages in the retrogressed megacrystic orthogneiss comprise quartz, K-feldspar, plagioclase, biotite, amphibole, garnet, titanite, zircon, apatite and ilmenite. In these gneisses biotite, amphibole and titanite become dominant. Minor muscovite is seen intergrown or replacing biotite. Symplectic quartz-K-feldspar textures are also commonly preserved in these gneisses. Several generations of biotite and amphibole are suggested from their relationships and textural changes. Reaction textures observed in the retrogressed megacrystic orthogneiss involve the replacement of garnet by plagioclase and amphibole with biotite. Small remnants of garnets often occur within a moat of plagioclase enclosed in a large amphibole grain. In some samples titanite coronas around ilmenite are preserved. Garnet, biotite, amphibole, zircon and feldspar have been used from this rock unit for isotopic analyses presented later in this section.

Pegmatite Veins

Late pegmatite veins form the final phase of igneous activity currently recognised in the northern Kirwanveggen. The veins intrude across the steep high-strain zones of the D1b deformation episode, but are subsequently deformed by the D1c deformational stage colinear and coplanar reworking of earlier structural fabrics.

The pegmatite veins comprise quartz, K-feldspar, plagioclase, biotite, garnet, muscovite with minor zircon assemblages. Zircon, biotite, feldspar, muscovite and calcite have been used for further isotopic investigations.

Mafic Dykes

Late mafic dykes intrude into the gneissic sequences of central Neumayerskarvet. Two different orientations of dyke emplacement have been observed. Sub-vertical dykes, showing a contact parallel foliation, intrude and cross-cut the foliation within the biotite-garnet migmatite gneiss. Both these types of dykes are late in the history of events at central Neumayerskarvet.

Mineral assemblages for the late mafic dykes consist of quartz, plagioclase, amphibole, biotite, titanite, garnet, and opaques. Garnet has plagioclase rims when included within amphibole. Very small garnet remnants are preserved in plagioclase grains. Plagioclase grains are strongly zoned. Amphibole encloses biotite, garnet and titanite. Mineral separates used in this isotopic investigation include biotite and amphibole.

ISOTOPE DATA

Analytical Techniques

Isotopic analyses were carried out at the Bernard Price Institute of Geophysics (BPI) in the University of the Witwatersrand, Johannesburg. Whole rock powders were prepared using standard rock crushing techniques. Mineral concentrates were separated using standard crushing, heavy liquid and magnetic separation techniques. Garnet, biotite, amphibole and feldspar samples were hand picked to select the most suitable separate for isotope analysis and sample fractions weighed approximately 0.1 g (see Figure 6.3). The garnet separates were then leached in hot distilled 6N HCl for 4 to 6 hours prior to dissolution. Biotite, amphibole and feldspar mineral separates were cleaned in 2N HCl for five minutes in an ultrasonic container.

All the Sm-Nd mineral samples were digested in screw-top Teflon® PFA (Savillex) beakers, with an HF-HNO_3 mix (3:1), for 3 days on a hot plate, and then taken up in 6N HCl. When the ^{146}Nd tracer was used the solution was split into two aliquots in a 2:1 ratio for analysis of the isotopic composition and for concentrations by isotope dilution respectively. Sm and Nd were separated using a variation of the method described by Richard *et al.*, (1976). Concentrations were measured on a Micromass® MM30 mass spectrometer, while $^{143}Nd/^{144}Nd$ ratios were measured on a Micromass® VG354 mass spectrometer. During later work a ^{150}Nd tracer was used. For these samples the spike was added prior to dissolution, separation techniques remained the same, while the ratio and concentration measurements were all carried out on a Micromass® VG354 mass spectrometer. Whole rock Sm-Nd samples were digested in white Teflon® beakers with an HF-HNO_3 mix and procedures followed those for the garnet concentrates. Blank levels during the Sm and Nd separation were below 500pg and no correction was made.

Chemical dissolution of approximately 0.1g of the whole rock powder was carried out using clean open Teflon® beakers for the Rb-Sr analyses. Approximately 0.05g of mineral concentrate was dissolved in screw-top Teflon® PFA (Savillex) beakers. Rb and Sr Isotope tracers were added prior to dissolution. Chemical dissolution was achieved with an HF-HNO_3 mix (3:1) for three days on a hot plate, and then taken up in 6N HCl. Separation of Rb and Sr was attained using standard cation exchange in an HCl medium. All reagents used in these procedures were prepared and purified at the BPI. Measured total method blank levels were less than 1ng for Rb and Sr and no corrections were made.

$^{40}Ar/^{39}Ar$ analysis was carried out by Dr T.L.Spell at the University of Houston. Mineral separates were wrapped in Al foil and stacked in a 6 mm ID Pyrex tube. Individual sample packets averaged 3 mm thick and 77-600 hornblende neutron fluence monitors (Tetley, 1978; McDougall and Harrison, 1988) were placed approximately every 6 mm along the tube. Synthetic K-bearing glass (obtained from B. Turrin, U.S. Geological Survey) and optical-grade CaF_2 were included in the irradiation package to monitor neutron induced argon interferences from K and Ca, respectively. Samples were irradiated for 67 hours in the Ford nuclear reactor at the University of Michigan where they received a fast neutron fluence of ~5 x 10^{12} n cm^2 s^{-1}. Correction factors for interfering neutron reactions on K and Ca were determined by analysis of K-glass and CaF_2 fragments. Measured $(^{40}Ar/^{39}Ar)_K$ values were 0.022 ± 0.002 thus a correction for the $^{40}K(n,p)$ ^{40}Ar of 0.022 was made. Ca correction factors were $(^{36}Ar/^{37}Ar)_{Ca}$ = 0.00026 ± 0.00002 and $(^{39}Ar/^{37}Ar)_{Ca}$ = 0.0007 ± 0.00005. J factors were determined by analysis of 77-600 hornblende fluence monitors. Variation in neutron flux along the ~80 mm length of the irradiation tube was ~3%. An error of 0.5% was used in age calculations.

Irradiated samples and monitors were fused in a double vacuum resistance furnace (see Staudacher et. al., 1978) with heating steps of 15 minutes duration. Reactive gases were removed by a 50 L s^{-1} SAES getter prior to being admitted to a MAP 215-50 mass spectrometer by expansion. The relative volumes of the extraction line and mass spectrometer allow up to ~80% of the sample gas to be admitted to the mass spectrometer. Peak intensities were measured on a Faraday cup by peak hopping through seven cycles; initial peak heights were determined by linear regression to the time of admission. Mass spectrometer sensitivity and discrimination were monitored by repeat analysis of atmospheric argon aliquots from an on-line pipette system. The sensitivity of the mass spectrometer was ~2 x 10^{-15} mol mV^{-1}. Extraction line blanks were measured routinely and were found to be insignificant below 1200 °C with levels increasing to 2.5 x 10^{-13} mol (m/e = 40) and 1.7 x 10^{-15} mol (m/e = 36) at 1500 °C. The entire sample analysis is computer automated and final data reduction and age calculations were done using Macintosh-based software written by A. Deino (Berkeley Geochronology Center). An age of 414.1 Ma was used for the 77-600 hornblende standard (Tetley, 1978; McDougall and Harrison, 1988) in calculating ages for samples.

Values obtained for $^{87}Sr/^{86}Sr$ during the course of this study from international standards SRM987 and Eimer & Amend® were 0.71021 ± 0.00003 and 0.70800 ± 0.00005 respectively. International standards used during the course of this work provided $^{143}Nd/^{144}Nd$ values of 0.511821 ± 0.000019 for the Johnson & Mathey® standard, 0.512645 ± 0.000021 for BCR-1 and 0.511835 ± 0.000022 for La Jolla. The $^{146}Nd/^{144}Nd$ ratio was corrected to 0.7219 in all samples.

The processing and regression of the Rb-Sr and Sm-Nd isotopic data was carried out using the program "*GEODATE*" of Eglington and Harmer (1991). Precision parameters at the 2σ level used in the regression techniques were: $^{87}Rb/^{86}Sr$ – 2%; $^{87}Sr/^{86}Sr$ – 0.0002; $^{147}Sm/^{144}Nd$ – 0.2% and $^{143}Nd/^{144}Nd$ – 0.01%. The correlation coefficient used for Sr and Nd whole-rock analyses was 1.0, and Sr and Nd mineral separates was 0.99. Throughout the text all ages, initial ratios and errors are quoted at the 2σ (95% confidence) levels. Isochrons are defined here as occurring when the mean sum of the weighted deviates (MSWD) is less than a critical F value determined by the number of samples regressed and based on 60 replicate analyses (formulae from Ludwig, 1983; 1990). Where the MSWD exceeds this F value the errors have been augmented by $(\text{MSWD/Critical F})^{1/2}$. Bulk earth comparisons are based on the following constants: $^{87}Rb/^{86}Sr$ = 0.0847 and $^{87}Sr/^{86}Sr$ = 0.7047; $^{147}Sm/^{144}Nd$ = 0.1967 and $^{143}Nd/^{144}Nd$ = 0.512638. Model age data for Sm-Nd and Rb-Sr compared to depleted mantle are based on the following values: $^{87}Rb/^{86}Sr$ = 0.0459 and $^{87}Sr/^{86}Sr$ = 0.702 (Faure, 1986); $^{147}Sm/^{144}Nd$ = 0.222 and $^{143}Nd/^{144}Nd$ = 0.513114 (Richard *et al.*, 1976). Decay constants are: $^{87}Rb = 1.42 \times 10^{-11} y^{-1}$, and $^{147}Sm = 6.54 \times 10^{-12} y^{-1}$.

Isotopic Results

Introduction

The U-Pb SHRIMP zircon ages have been presented in Chapter 4 and a summary of these results are provided in Table 6.2. Seven different units at Neumayerskarvet have been used for Sm-Nd mineral isotopic analyses. The units range from the oldest biotite-garnet migmatite gneiss samples through to the kyanite-bearing leucogneisses and the megacrystic orthogneiss. Mineral and whole-rock samples have been regressed together and are presented in Figure 6.5 and Table 6.4. The results of the Rb-Sr isotopic analyses are presented in Table 6.3 and isochron diagrams for the various samples are presented in Figure 6.4. A total of 15 samples were analysed using Rb-Sr systematics during this investigation.

Biotite-Garnet Migmatite Gneiss (PH92031, PH93161)

The biotite-garnet migmatite gneiss (PH93161) is the oldest unit identified at Neumayerskarvet and exhibits complicated U-Pb zircon populations. Inherited components are abundant and have ages ranging back to ~2040 Ma. An intact zircon rim with an age of ~1260 Ma suggests a period of *in-situ* growth and provides a minimum age for the metasediments. Rims of zircon are recorded at ~1130 Ma with the main cluster of zircon ages ranging between ~1200 Ma and ~1100 Ma. This period of zircon growth or resetting occurs during an intense period of deformation and metamorphism. A leucosome in the biotite-garnet migmatite gneiss (PH92009) provides a zircon SHRIMP age of 1098 ± 5.

Two samples of biotite-garnet migmatite gneiss were used for Sm-Nd mineral isotopic systematics. Sample PH92031 (whole-rock-garnet) provides a line with an age equivalent to 605 ± 138 Ma (R_0=0.5118), while data for sample PH93161 (whole-rock-feldspar-garnet) scatter about a line equivalent to an age of 617 ± 96 Ma (MSWD=1.93, R_0=0.5114).

Three samples comprising whole-rock-muscovite-biotite were used for the Rb-Sr determination from the biotite-garnet migmatite gneiss sample PH92031. The data scatter about a line with an age equivalent to 466 ± 8 Ma (MSWD=2.87, R_0=0.7179). The line is strongly controlled by the highly radiogenic biotite sample. The muscovite and biotite Rb-Sr systematics are essentially equivalent with the whole-rock-muscovite data providing a line equivalent to 458 Ma with the whole-rock-biotite line equivalent to 471 Ma.

Quartzofeldspathic Leucogneiss (PH92050)

A single two-point Sm-Nd line has been obtained from a sample of the quartzofeldspathic leucogneiss. These Sm-Nd analyses are from sample PH92050 and the whole-rock-garnet samples plot along a line equivalent to an age of 568 ± 38 Ma (R_0=0.5119).

Intrusive Leucogneiss (PH93148)

The SHRIMP zircon data from the intrusive leucogneiss sample PH93148 are difficult to interpret. Regression of the discordant data with the more concordant data suggest an age of ~1130 Ma for the intrusion of this unit. Younger ages of ~1049 Ma and ~480 Ma indicate later periods of zircon crystallisation, re-growth or disturbance.

Two Sm-Nd whole-rock samples, one biotite, feldspar and garnet separates from the intrusive leucogneiss sample PH93148 scatter about a line with an age equivalent to 486 ± 11 Ma (MSWD=4.31, R_0=0.5117). Rb-Sr isotopic data were obtained from one whole-rock sample, a feldspar, biotite and muscovite sample for the intrusive leucogneiss sample (PH93148). The minerals and whole-rock plot on an isochron equivalent to an age of 471 ± 7 Ma (MSWD=1.058, R_0=0.7166). The whole-rock-muscovite samples plot on a line equivalent to 466 Ma, whereas the whole-rock-biotite line represents an age of 476 Ma. These ages are close to the mineral isochron age and are essentially indistinguishable, yet they have different closure temperatures (see discussion above and Table 6.1). The mineral isochron line is strongly controlled by the highly radiogenic biotite sample.

Kyanite-Bearing Leucogneiss (PH92020, PH92057, PH93200, PH93203)

A zircon SHRIMP age from the kyanite-bearing leucogneiss (PH92020) provides an age of 1096 ± 10 Ma, which is interpreted as an intrusive age indicating magmatism during this period. Two samples of kyanite-bearing leucogneiss have been analysed for their Sm-Nd mineral systematics. Sample PH92020 has a whole-rock sample, biotite and two garnet samples that scatter about a line equivalent to an age of 602 ± 16 Ma (MSWD=9.60, R_0=0.5118). The two garnet separates show markedly different Sm-Nd ratios but provide similar age estimates to one another. Sample PH92057 has also been analysed and the combined whole-rocks and garnet samples produce a line equivalent to an age of 413 ± 43 Ma (MSWD=0.95, R_0=0.5124).

Feldspar, biotite and muscovite from the kyanite-bearing leucogneiss sample (PH92020) plot on an isochron equivalent to an age of 479 ± 7 Ma (MSWD=1.044, R_0=0.7538). A two-point line of feldspar-muscovite plot along a line equivalent to an age of 482 Ma while the feldspar-biotite line provides an age of 475 Ma. Although these minerals have different closure temperatures their ages are essentially indistinguishable from the combined mineral isochron age. Sample PH92057 from a kyanite-bearing leucogneiss provides an age of 466 ± 7 Ma (MSWD=4.12, R_0=1.1428) for whole-rock, muscovite and biotite samples that scatter along a line. Whole-rock-muscovite-biotite separates plot along an isochron equivalent to an age of 477 ± 7 Ma for sample PH93200 (MSWD=0.16, R_0=0.7197). Whole-rock muscovite and whole-rock-biotite two point lines provide ages of 476 Ma and 478 Ma respectively for this sample. Sample PH93203 of a kyanite-bearing leucogneiss provides a two-point line equivalent to an age of 480 ± 10 Ma for a whole-rock-muscovite assemblage.

Megacrystic Orthogneiss (PH92003)

The megacrystic orthogneiss (PH92005) has a zircon SHRIMP age of 1088 ± 10 Ma. Only one sample was used for $^{40}Ar/^{39}Ar$ analysis. The sample was of amphibole taken from the retrogressed portion of the megacrystic orthogneiss. No isochron could be defined for this sample due to the highly radiogenic Ar present. The highly radiogenic nature of the sample implies that the proportion of trapped non-radiogenic Ar is insignificant. The first approximately 5% gas released from the amphibole gives ages ranging from 700 Ma to 1000 Ma (See Figure 6.6). After these steps the age spectrum is essentially flat. A plateau age of 509 ± 4 Ma is similar to the favoured age of steps D to J of 513 ± 5 Ma. The integrated age for this spectrum is 520 ± 5 Ma. The initial high ages could be interpreted as the result of excess argon in the system. The amphibole sample does, however, come from a unit with a SHRIMP zircon age of 1088 ± 10 Ma and may also suggest that the Ar-Ar age of 513 ± 5 Ma may be due to a strong thermal overprint.

A whole-rock-garnet Sm-Nd age of 511 ± 18Ma (R_0=0.5118) has been obtained for the retrogressed megacrystic orthogneiss sample PH92003. A retrogressed portion of the megacrystic orthogneiss was used for Rb-Sr mineral isotopic analysis (PH92003). The mineral separates used here comprised two whole-rock samples, amphibole, feldspar and biotite. The errorchron is controlled by the highly radiogenic nature of the biotite. The data scatter about a line equivalent to an age of 473 ± 11 Ma (MSWD=4.32, R_0=0.7090).

Pegmatite Veins (PH92004, PH92006, PH92007, PH92012, PH92023, PH92053, PH93140)

The youngest zircon SHRIMP age obtained from the northern Kirwanvegggen comes from a pegmatitic vein (PH92006/PH93140) that has an intrusive age of 1079 ± 6 Ma. A coarse grained pegmatite sample (PH92004) was analysed for Rb-Sr using red and white feldspar separates combined with a biotite separate. The data scatter about a line that is strongly controlled by the radiogenic biotite, with an age equivalent of 479 ± 7 Ma (MSWD=2.25, R_0=0.7097).

Two Rb-Sr analyses were made from sample PH92012, which is from a pegmatitic vein within a late high-strain zone. The age is a whole-rock-biotite two-point age that is strongly controlled by the radiogenic biotite sample. The two-point line has an equivalent age of 474 ± 10 Ma (R_0=0.7332). Rb-Sr analysis of whole-rock-feldspar-biotite from the pegmatite vein, away from the late high-strain zone (PH92007), scatter about a line equivalent to an age of 459 ± 29 Ma (MSWD=39.633, R_0=0.7596). The highly radiogenic biotite sample controls the slope of the line and hence the age determination. Pegmatite vein sample PH92023 mineral separates scatter about the Rb-Sr isochron diagram but produce an age equivalent to 481 ± 10 Ma (MSWD=13.61, R_0=0.7142). The mineral age is derived from two feldspar samples combined with a biotite sample. A late pegmatite sample of muscovite and calcite provide an Rb-Sr two point line equivalent to an age of 361 ± 7 Ma with an initial ratio R_0=0.7136. This age is significantly younger than the other pegmatite veins and suggests that this unit represents a late intrusion that is rare within the northern Kirwanveggen.

Mafic Dykes (PH92021, PH93188, PH93192)

Three mafic dyke samples were analysed for their Rb-Sr mineral isotopic systematics. The samples were all of whole-rock, biotite and amphibole samples and plot along lines equivalent to ages of 475 ± 11 Ma (4 points, MSWD=4.51, R_0=0.7100), 485 ± 10 Ma (3 points, MSWD=7.09, R_0=0.7093) and 489 ± 14 Ma (3 points, MSWD=12.96, R_0=0.7078).

DISCUSSION

Comparison of Isotope Data

A summary of all the age data from different mineral isotopic systems for the gneisses in the northern Kirwanveggen is provided in Table 6.5. The U-Pb zircon ages provide predominantly *ca.* 1100 Ma ages whereas all the other mineral systems produce younger ages ranging from *ca.* 600 Ma through to *ca.* 450 Ma. The age data for the different mineral systems and their associated errors are plotted in Figure 6.7 for comparison. The U-Pb zircon ages have been sub-divided into those ages that are interpreted as intrusive ages, and those that are related to growth, disturbance or resetting. Intrusive ages cluster close to *ca.* 1100 Ma while the zircon disturbance or growth ages range from *ca.* 1100 Ma to *ca.* 980 Ma. These data suggest that a significant tectono-metamorphic episode took place during this period. The growth ages do not necessarily imply peak metamorphic conditions but represent reaction related periods that do indicate a significant period of deformation and metamorphism affected the northern Kirwanveggen. Older growth of zircons at *ca.* 1160 Ma and even potentially at *ca.* 1260 Ma is also suggested by the U-Pb SHRIMP zircon work (See Chapter 4). Magmatism in the northern Kirwanveggen at *ca.* 1130 Ma is not significant, but this may be due to sample selection in the region rather than a lack of magmatism during this period. Ages of intrusive units within this period have been documented in the H.U.Sverdrupfjella (Harris *et al.*, 1995; Moyes and Groenewald, 1996) and in the Hiemefrontfjella (Arndt *et al.*, 1991). Deformation through this time period has been documented at Neumayerskarvet (see Chapter 3 and 4). Growth of zircon rims at *ca.* 480 Ma have been recorded in one grain from Neumayerskarvet. Although this is limited data it suggests the occurrence of another tectono-metamorphic event during this later time period.

The Sm-Nd mineral ages are pre-dominantly controlled by the more radiogenic garnet samples, and as such may be interpreted as garnet Sm-Nd mineral ages. These ages from the northern Kirwanveggen are considerably younger than the U-Pb zircon ages. The Sm-Nd garnet ages range from *ca.* 600 Ma to *ca.* 450 Ma. Two broad clusters of ages are suggested from the data, but are not fully distinguishable from one another. An earlier *ca.* 600 Ma age is suggested with a 500-450 Ma age range being suggested from other samples. Moyes and Groenewald (1996) noted similar broad clusters from Sm-Nd garnet data from the H.U.Sverdrupfjella of *ca.* 660 Ma and *ca.* 496 Ma. Although the ages vary slightly, similar trends are observed from both data sets.

Duplicate samples show variable Sm-Nd contents and ratios but do not affect the age results for the sample (see discussion in Moyes and Groenewald, 1996). This indicates that there may be zoning of Sm and Nd preserved within the garnets. This would not be unexpected based on the results of Brueckner *et al.* (1996) where the authors examined the trace element zoning of garnets. The mixture and variability of the Sm-Nd mineral age data could also be explained by compositional variations within garnet, and the various generations of garnets that have been recognised within the northern Kirwanveggen (See Chapter 5).

The significance of the Sm-Nd age data is open to interpretation. Metamorphic studies of the kyanite-bearing leucogneisses have shown that there are several generations of garnet in these samples with chemistries that are not dissimilar (See Chapter 5). Another issue is the method of the sample analysis. The analytical technique requires a bulk sample and it is to be expected that different garnet generations are combined and potentially result in age mixtures. The consistently young ages tend not to favour the fact that different garnet Sm-Nd ages were mixed in the samples. Another possible problem is that hand-picking of the mineral separates may introduce a bias to the analytical data. The most suitable garnets for isotopic analysis are generally clear, clean and low fractured garnet fragments of a similar colour. This may result in the removal of the older garnet components that are inclusion-rich, fractured and less suited for selection.

Notwithstanding these problems, the consistency of the data suggests two main interpretations:

1. Firstly, that the garnets are all of a younger generation and that they grew during the 600 Ma to 450 Ma tectono-metamorphic period.
2. The second interpretation is that there are several different generations of garnet, but these have all been overprinted and homogenised during the later 600 Ma to 450 Ma tectono-metamorphic period.

The closure temperature of this mineral system would provide an indication of the temperature conditions for the later event. The latter is favoured, but both interpretations indicate that a significant tectono-metamorphic period affected the older *ca.* 1100 Ma high-grade gneisses.

The Ar-Ar amphibole data provides an age of 513 ± 5 Ma for the retrogressed megacrystic orthogneiss. Excess argon released at higher age plateaus could be interpreted to reflect an older amphibole that has undergone later re-heating. This age is similar to the Rb-Sr mineral data from the northern Kirwanveggen. The Rb-Sr mineral data is predominantly controlled by the highly radiogenic biotite samples and can be interpreted as a biotite mineral age. These data are consistently *ca.* 475 Ma and suggest resetting of this isotopic system during the later event. The Rb-Sr, Ar-Ar and Sm-Nd mineral data all reflect the younger tectono-metamorphic event while the U-Pb zircon data provide evidence of a pre-existing older tectono-metamorphic event.

T-t Paths for the Northern Kirwanveggen

Using the estimated closure temperatures of different isotopic mineral systems, a temperature-time path has been established for the northern Kirwanveggen. Such an interpretation is not without assumptions, and the effects and influences on the closure temperature must be kept in mind. Due to the influences that may affect the closure temperatures, no estimation of cooling rates will be attempted in this investigation. The variables, and hence permutations that could occur, complicate the derivation of cooling rates. Closure temperature estimates used in the following discussions are based on the data presented earlier in this section, and are summarised in Table 6.1. It must be noted that minerals that do not reach conditions as high as the closure temperature may therefore not record cooling paths but rather formation ages. This philosophy applies to the majority of the zircon data presented in the following sections.

Temperature estimates for the zircon samples are based on the conditions of the Mn+1 (nkv) metamorphic stage rather than on closure temperatures of U-Pb in zircon. This is based on constraints of deformation described in Chapter 4. Magmatism is associated with the *ca.* 1100 Ma tectono-metamorphic event within the northern Kirwanveggen. Figure 6.8 provides a plot of the T-t data for the northern Kirwanveggen. The Sm-Nd garnet data provides ages of 600 Ma to 450 Ma with temperatures of approximately 600 °C suggested for the closure of this system. Ar-Ar amphibole data provides ages of *ca.* 500 Ma at temperatures of approximately 500 °C, while the biotite ages of *ca.* 475 Ma correspond to a temperature estimate of *ca.* 320 °C.

The T-t path for the northern Kirwanveggen suggests the presence of two significant tectono-metamorphic cycles that affect these domains. The early cycle at *ca.* 1100 Ma is accompanied by magmatism within this region. Higher temperatures are interpreted for this tectono-metamorphic cycle. A younger but significant tectono-metamorphic cycle between 650 to 450 Ma is suggested from the mineral isotope data. The younger cycle does not appear to reach the high metamorphic conditions that are seen during the older cycles, but still has an important influence on the evolution of the northern Kirwanveggen. Two scenarios have been previously postulated (Grantham *et al.*, 1995; Moyes and Groenewald, 1996). The first scenario suggests that the rocks have been held at high temperatures until the later cycle resulted in the exhumation of this terrane. The second scenario suggests that the domain has undergone significant cooling, but was reheated and exhumed during the younger tectono-metamorphic cycle. These possibilities are investigated in the following section.

Comparison of Cooling Paths within WDML

T-t paths for the different geological domains of WDML are presented in Figure 6.9. The geological domains are sub-divided based on geological features, and these are discussed in detail in Chapter 2. Summaries of the isotope data, and references to the original data are also provided in Chapter 2. The different geological domains within WDML each experience different, yet somewhat similar T-t paths. Within WDML magmatism is documented pre-dominantly during the *ca.* 1100 Ma tectono-metamorphic cycle, but isolated occurrences of magmatism are recorded in certain domains of WDML during the 650-450 Ma tectono-metamorphic cycle. All the different domains provide evidence of the two tectono-metamorphic cycles recorded within the northern Kirwanveggen. Evidence for the 650-450 Ma tectono-thermal cycle is more strongly defined in the eastern areas of WDML. A recent study within central Dronning Maud land has shown significant magmatism and deformation during this period and provides support to the WDML data (Jacobs *et al.*, 1998).

A compilation of all the data into one diagram provides a significant improvement for the interpretation in WDML. (Figure 6.10). As each geological domain in WDML has undergone a somewhat different tectono-metamorphic history, each domain will preserve different parts or portions of the evolutionary history. By combining the data the full affects of the different cycles can be evaluated. This does not, however, mean that all the domains have undergone the same deformation and tectonism. Each domain preserves a portion of the regional history for WDML. Although the data are unrelated spatially, the implications are that cooling occurred post-the *ca.* 1100 Ma tectono-metamorphic cycle prior to re-heating during the later cycle. In certain regions the later event attained conditions sufficient to obliterate any evidence of the early tectono-metamorphic cycle cooling path. The combined data provide evidence for the cooling paths of two distinct tectono-metamorphic cycles relating to the *ca.* 1100 Ma and 650-450 Ma cycles. A younger event is recorded in the fission track apatite data and suggests disturbance and final uplift of portions within this region during, or related to Gondwana break-up. The T-t data for WDML suggest a re-heating or re-working of an older *ca.* 1100 Ma metamorphic belt during a younger 650-450 Ma tectono-metamorphic cycle. The younger event is not as intense as the older cycle, but reworks the older domains within the region.

P-T-t-d Path estimates for the Northern Kirwanveggen

The T-t Path information derived from the isotopic data is combined with the deformational and metamorphic histories determined in Chapters 3, 4 and 5 to provide an estimate of the pressure-temperature-time-deformation (P-T-t-d) path for the northern Kirwanveggen. These data are presented in the P-T diagram of Figure 6.11. Four potential tectono-metamorphic cycles are inferred from the data in the northern Kirwanveggen, and the geological events related to each of these cycles is summarised in Table 6.6.. These cycles are referred to as the **1st**, **2nd**, **3rd** and **4th** cycles in Figure 6.11. The **1st** tectono-metamorphic cycle is not determined through the data of this investigation but is inferred from previous studies in the region, combined with other available data. An older D1a tectonic period is interpreted from the current investigation and occurs between 1160 and 1110 Ma (U-Pb zircon SHRIMP ages). Metamorphism for this period cannot be obtained from the current samples (Chapter 5) as these units intrude post-D1a but during the D1b tectonic period. Metamorphic conditions for this tectono-metamorphic cycle can only be inferred from the literature. In light of the current metamorphic investigation (Chapter 5), and the recognition of mineral assemblage chemistries that generate erroneous high-pressure conditions, caution should be exercised in the interpretation of previous high-pressures obtained for this region. A feasible means to explain these data is to invoke a high-pressure event that occurred prior to the development of mineral assemblages investigated in Chapter 5. High-pressure metamorphic conditions are attributed here to the **1st** tectono-metamorphic cycle (Groenewald and Hunter, 1991; Ferrar, 1995; Grantham *et al.*, 1995; Moyes and Groenewald, 1996).

A second tectono-metamorphic cycle (**2nd**) is inferred from the current data presented in this investigation. Deformation (D1b) during this cycle is dated at between 1110 Ma and 1070 Ma (U-Pb zircon SHRIMP ages) and units intruding during this cycle record the metamorphic conditions. The Mn+1 (nkv) metamorphic stage recorded in the kyanite-bearing leucogneisses is assigned to the **2nd** tectono-metamorphic cycle. The possibility that the older D1a deformation period is part of the progressive deformation associated with the **2nd** tectono-metamorphic cycle cannot be discounted. Subsequently an alternative interpretation that the *ca.* 1150 Ma D1a deformation is part of the **2nd** tectono-metamorphic cycle is also presented (Figure 6.11). The **2nd** tectono-metamorphic cycle represents the upper portion of the clockwise P-T path derived in Chapter 5. Cooling during this cycle is recorded by zircon ages that range from *ca*. 1070 Ma to *ca*. 970 Ma (Table 6.2).

The **3rd** tectono-metamorphic cycle is interpreted as the lower portion of the P-T path derived in Chapter 5, and its distinction is based primarily on the recognition of younger isotopic age data with possible associated deformation (D2). Sm-Nd garnet ages, Ar-Ar amphibole ages and Rb-Sr biotite ages provide constraints for the **3rd** tectono-metamorphic cycle. Diffusional P-T data from garnet-biotite pair rims provide an indication of the P-T conditions during the younger tectono-metamorphic cycle. This tectono-metamorphic cycle results in the exhumation of the high-grade gneiss terrane. A **4th** tectono-metamorphic cycle is recorded in the fission track data between 200 Ma and 100 Ma, and is related to uplift and magmatism associated with Gondwana break-up.

CONCLUSIONS

- Two major tectono-metamorphic cycles have been distinguished at Neumayerskarvet within the northern Kirwanveggen, WDML.
- The existence of an older high-pressure metamorphic event at *ca.* 1150 Ma cannot be refuted or supported from the current data presented for this investigation.
- The older tectono-metamorphic cycle is more dominant with the most significant metamorphic conditions, deformation and magmatism at *ca.* 1100 Ma. This cycle is supported by intrusive ages and U-Pb SHRIMP zircon growth and disturbance ages.
- The younger tectono-metamorphic cycle is difficult to characterise fully, but is placed between 650 and 450 Ma. Ages for this cycle are obtained from Sm-Nd garnet ages, Ar-Ar amphibole ages, Rb-Sr biotite ages and limited U-Pb SHRIMP zircon data.
- Late uplift documented at *ca.* 100 Ma is recorded through fission track apatite ages from the literature.

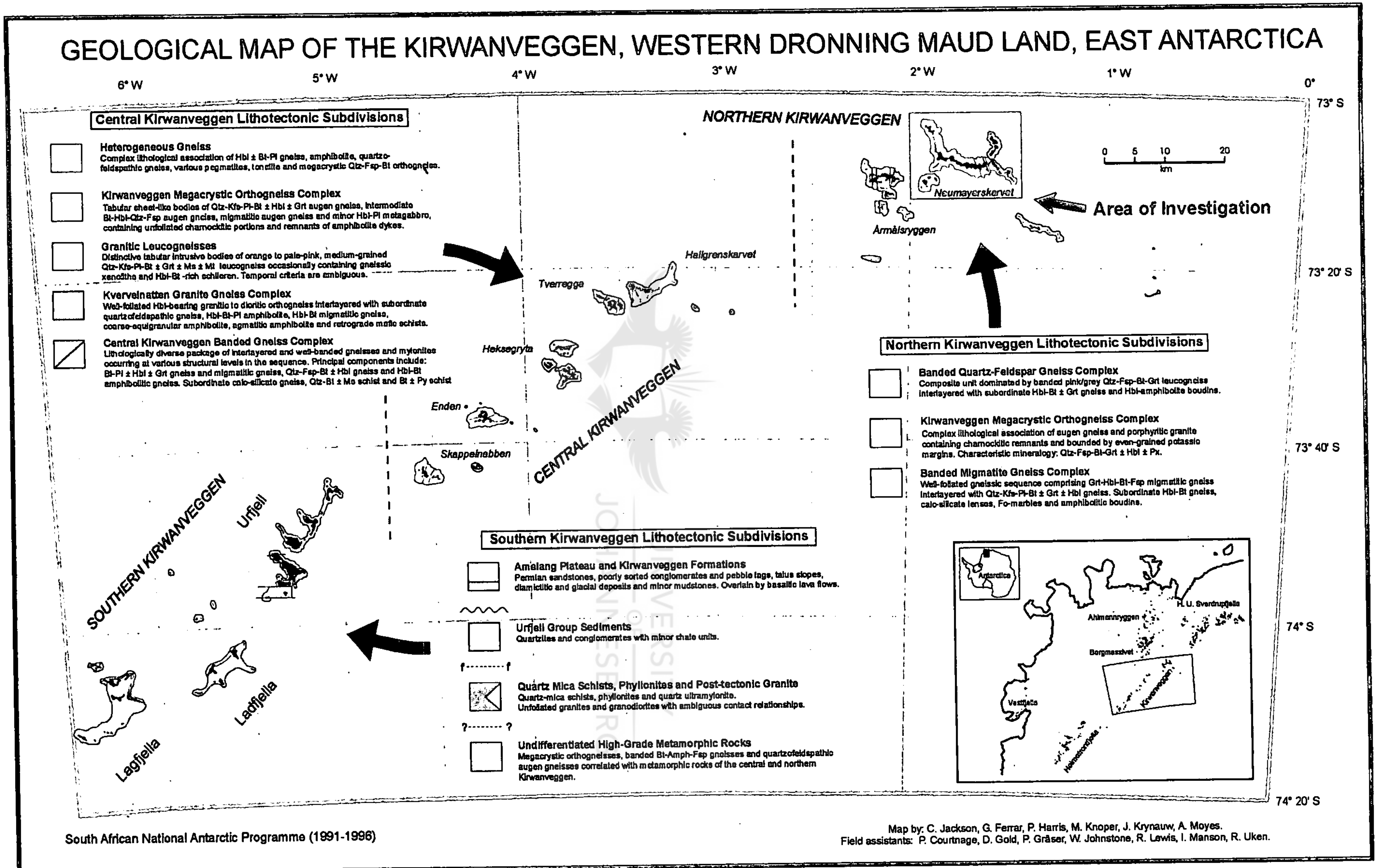

FIGURE 6.1. Geological map of the Kirwanveggen in western Dronning Maud Land, Antarctica. The subdivision of the northern, central and southern Kirwanveggen outcrop patterns and the associated lithotectonic units are illustrated. The Neumayerskarvet outcrop pattern, which is the major area of focus in the northern Kirwanveggen, is outlined for location purposes.

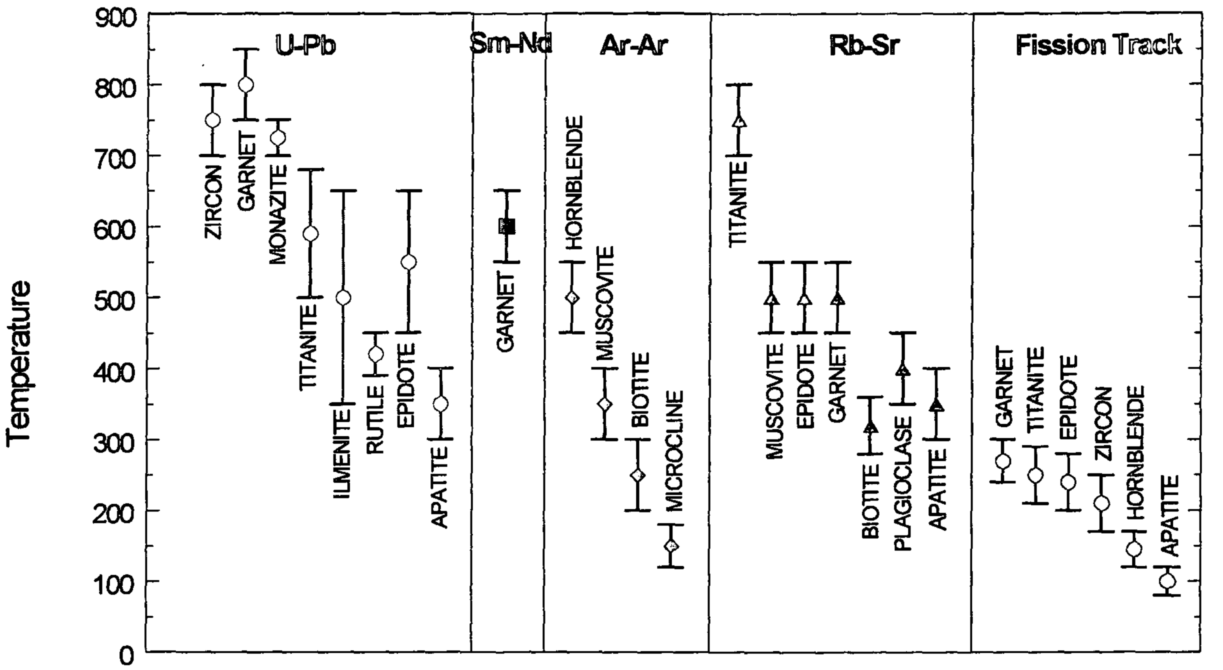

FIGURE 6.2. Closure temperature estimates for different isotopic mineral systems. The source of the data presented in this diagram are provided in Table 6.1.

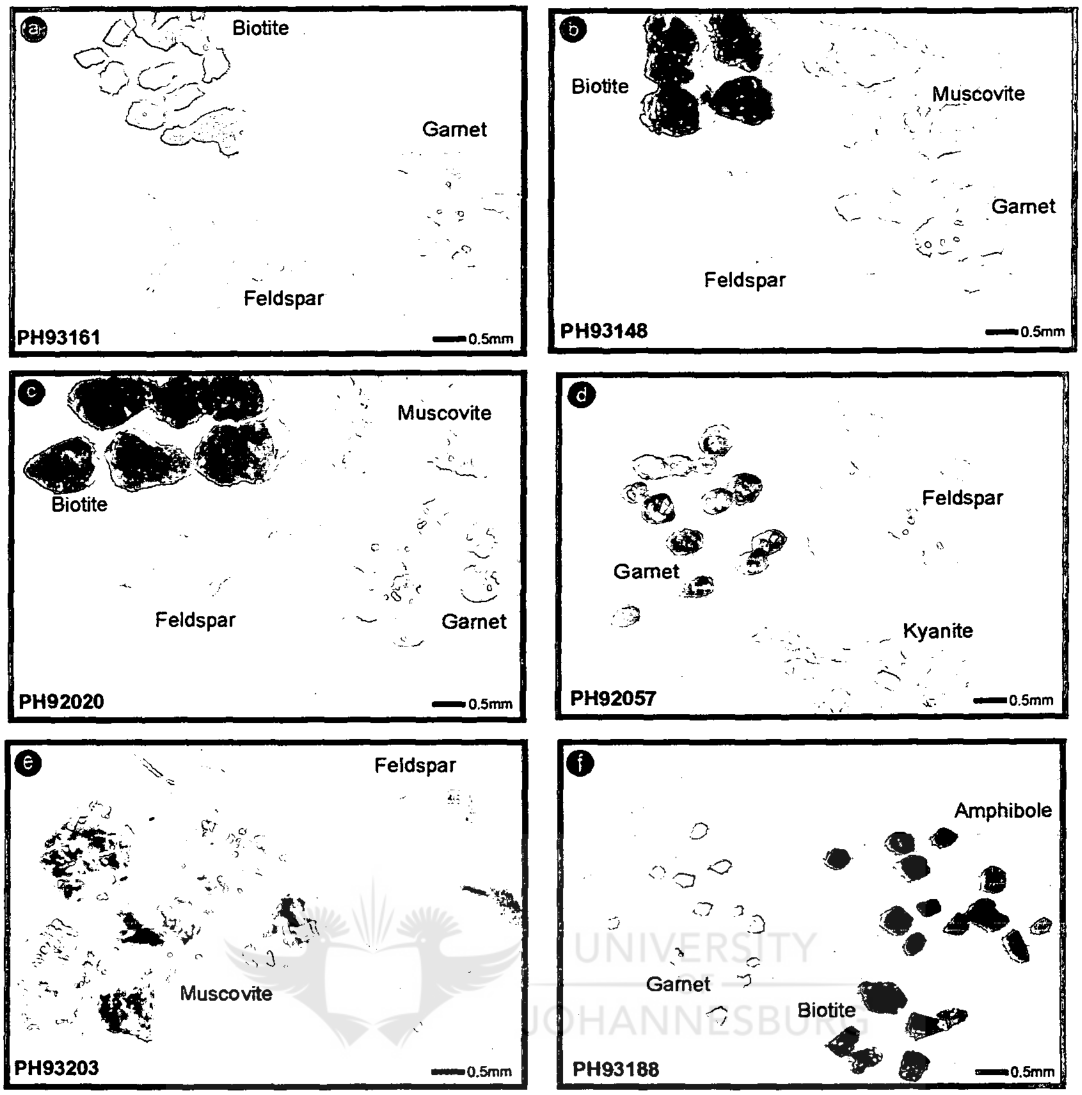

FIGURE 6.3. Photographs of typical mineral separates used for further isotopic analysis. Mineral separates were hand-picked based on grain quality, size and colour.

a.) Mineral separates from the biotite-garnet migmatite gneiss (PH93161). Minerals used for further isotopic work for this sample were garnet, biotite, feldspar and a whole-rock sample. Muscovite was found in another biotite-garnet migmatite gneiss sample (PH92031) and was used for further analytical work. Sample PH93161 was also used for U-Pb zircon SHRIMP analysis.
b.) Typical mineral separate concentrations for an intrusive leucogneiss sample (PH93148). Minerals used for isotopic analysis include biotite, garnet, muscovite and feldspar. These analyses were combined with a whole-rock analysis for this sample. This sample was also used for U-Pb zircon SHRIMP analysis.
c.) Typical mineral separate concentrations used for the isotopic analyses of the kyanite-bearing leucogneisses. These mineral separates are from sample PH92020, which has also been used for U-Pb SHRIMP zircon analysis. Minerals used for isotopic analysis were biotite, garnet, feldspar, muscovite and a whole-rock sample.
d.) Mineral concentrations from the kyanite-bearing leucogneiss sample PH92057 which include garnet, feldspar and kyanite. Biotite, which is not included in the photograph was also used for isotopic analysis. Kyanite was not dissolvable and therefore not used further.
e.) Mineral separates from the kyanite-bearing leucogneiss sample PH93203. Minerals for this sample include muscovite, feldspar and a whole-rock sample. No biotite was present in this portion of the kyanite-bearing leucogneiss, and garnet was of too low abundance.
f.) Mineral separates typical of mafic dyke units within the northern Kirwanveggen. This mafic dyke sample includes mineral concentrates of garnet, biotite and amphibole from sample PH93188.

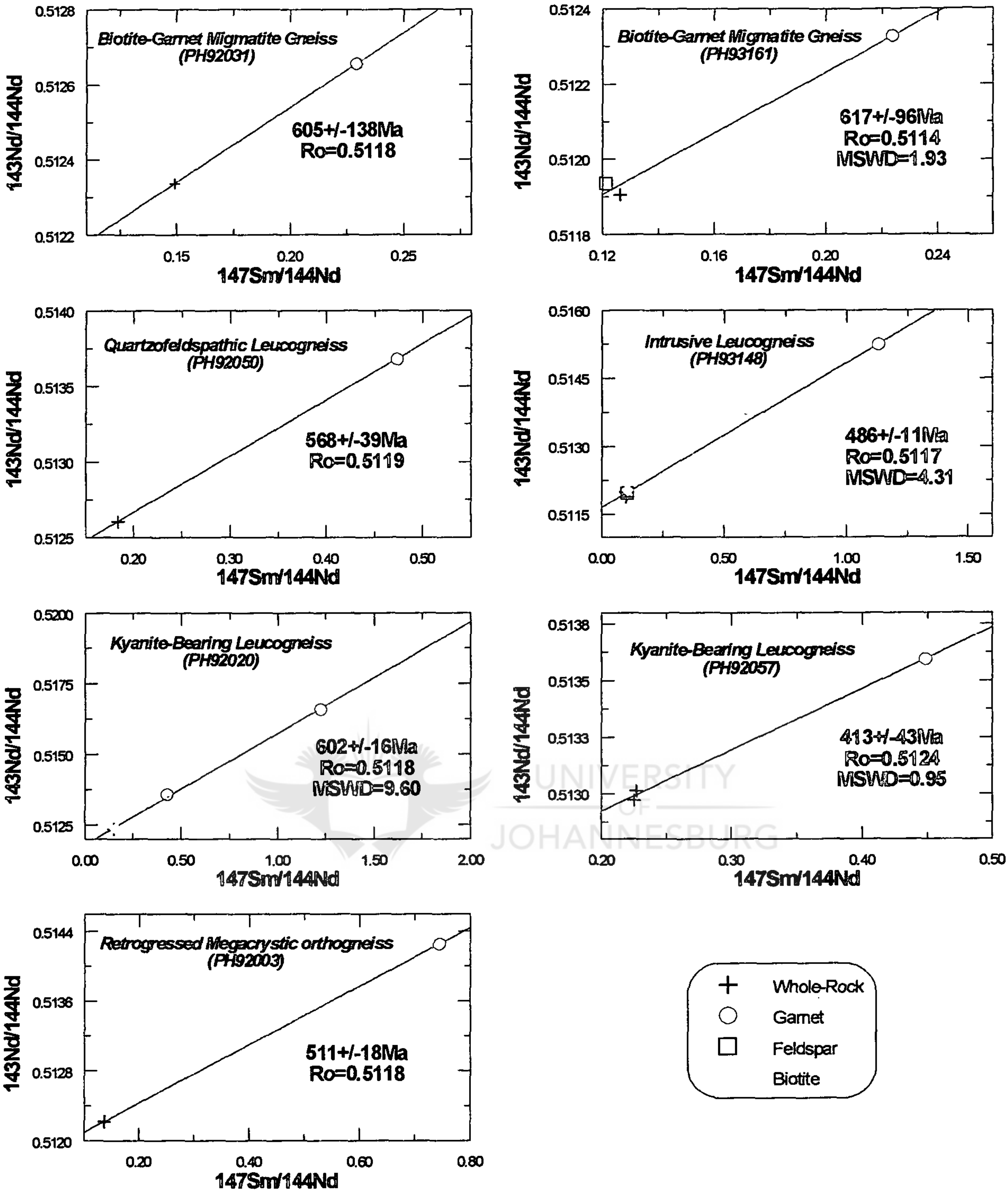

Figure 6.4. Sm-Nd mineral isochron diagrams for samples analysed from Neumayerskarvet in the northern Kirwanveggen.

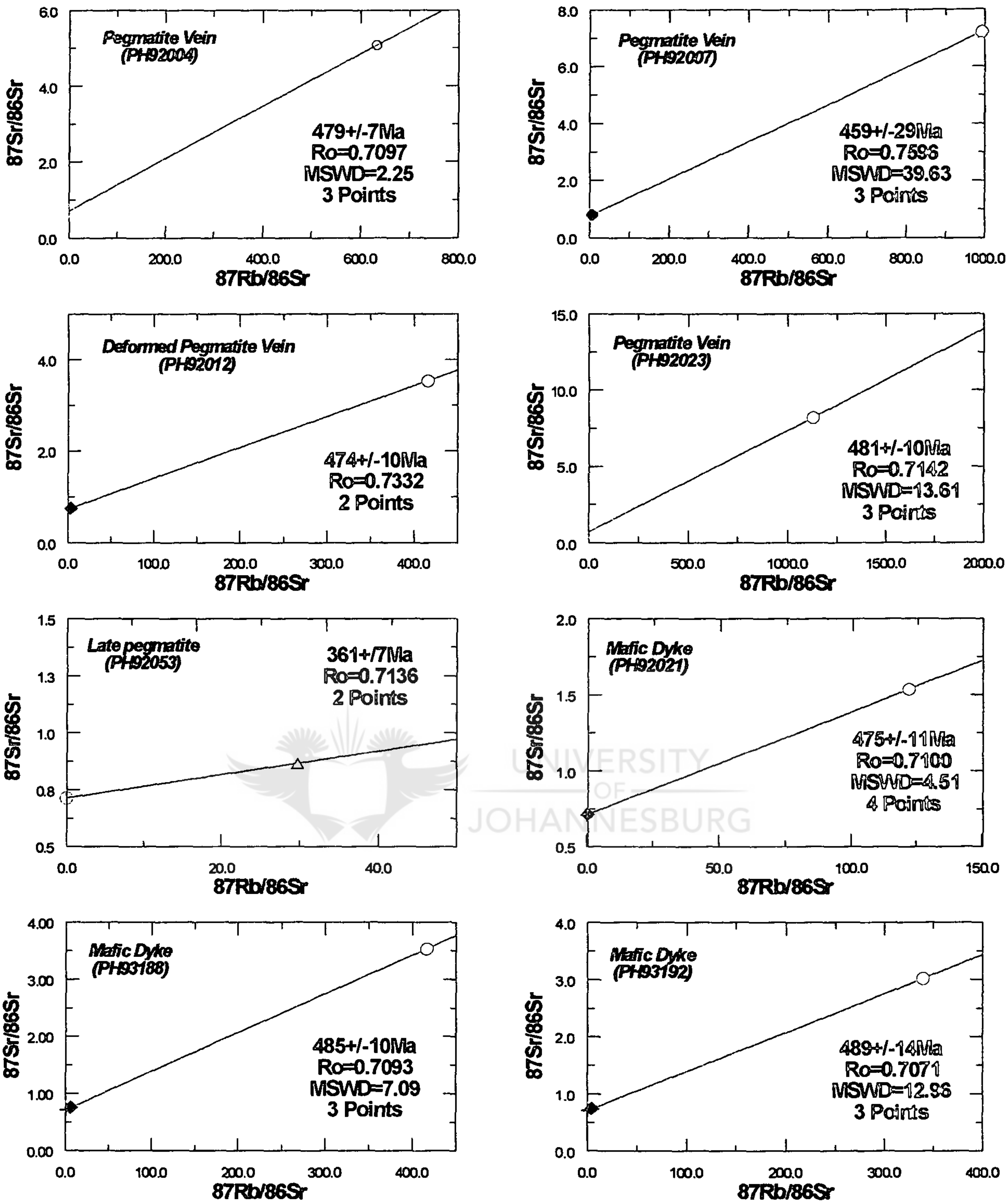

Figure 6.5. Rb-Sr mineral isochron diagrams for samples analysed from Neumayerskarvet in the northern Kirwanveggen. The diagram is continued overleaf.

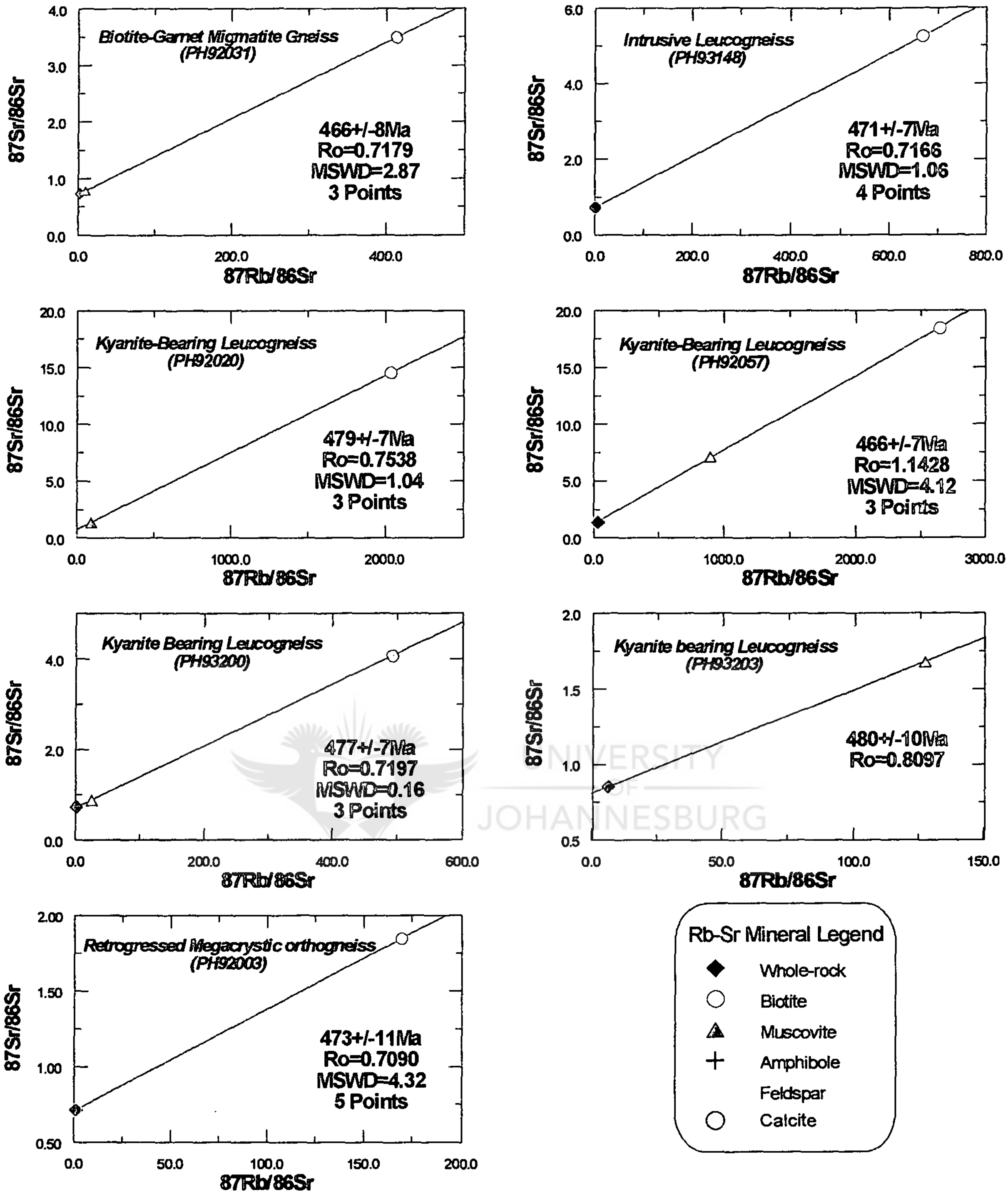

Figure 6.5. Continued. Rb-Sr mineral isochron diagrams for samples analysed from Neumayerskarvet in the northern Kirwanveggen.

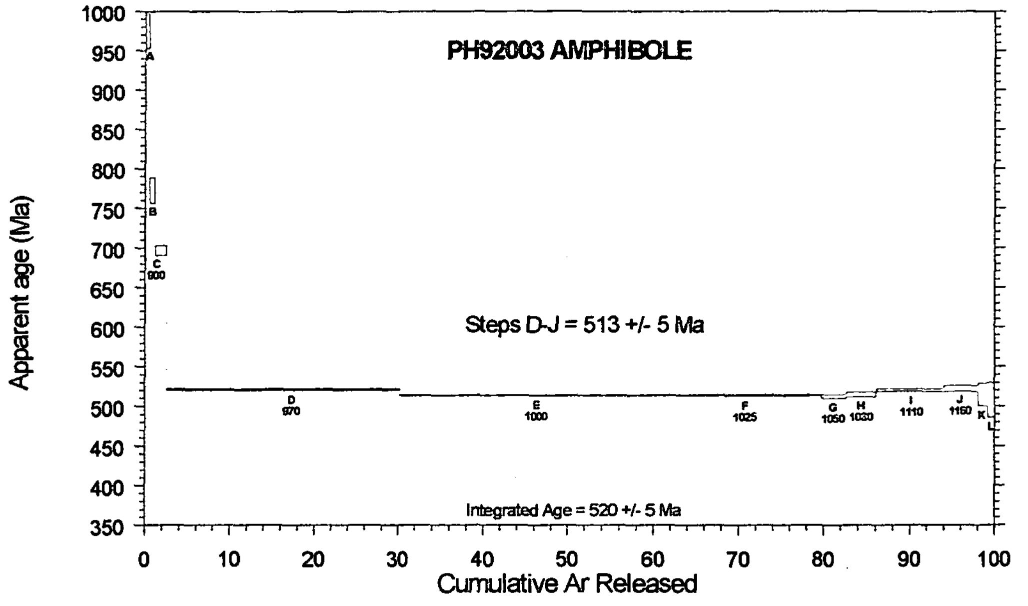

Figure 6.6. Ar-Ar diagram for amphibole from the retrogressed megacrystic orthogneiss.

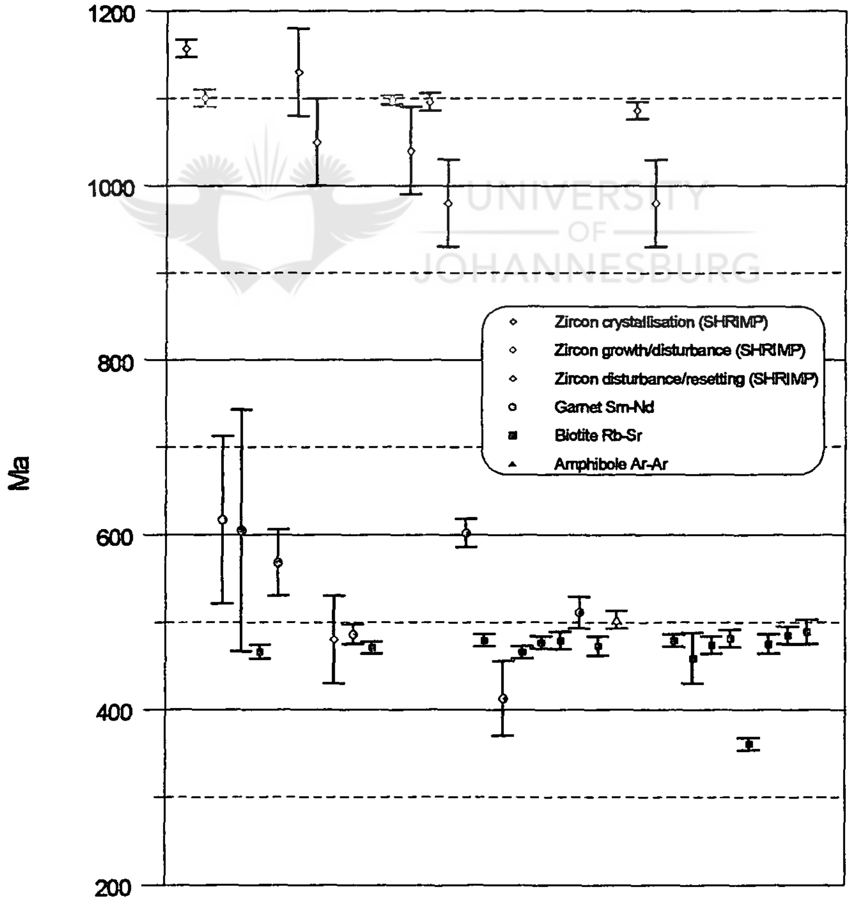

Figure 6.7. Summary diagram of isotopic age data obtained from Neumayerskarvet during this investigation. Zircon ages have been presented in Chapter 4, while the Sm-Nd, Rb-Sr and Ar-Ar mineral ages are presented in this chapter.

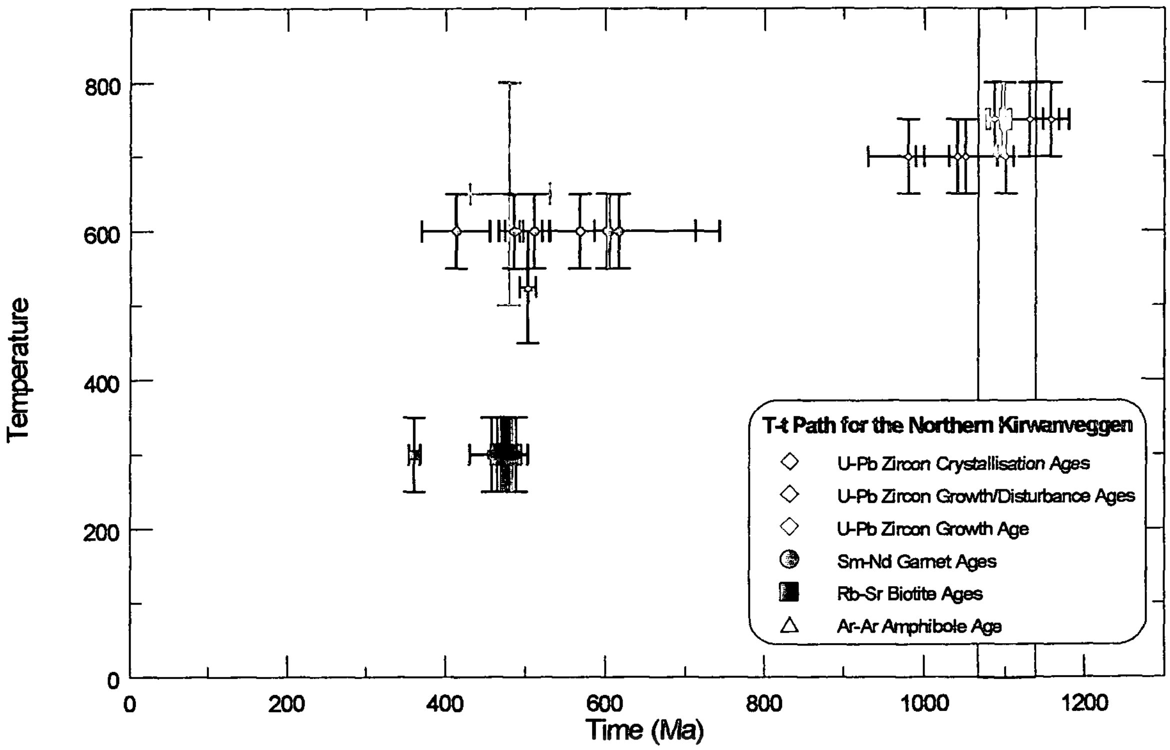

Figure 6.8. Temperature-time (T-t) path derived from the isotopic age data and the closure temperature estimates for Neumayerskarvet in the northern Kirwanveggen. Closure temperature estimates used in this diagram are taken from Table 6.1. Associated magmatism in the northern Kirwanveggen is outlined in the yellow block.

GEOLOGICAL MAP OF WESTERN DRONNING MAUD LAND, ANTARCTICA

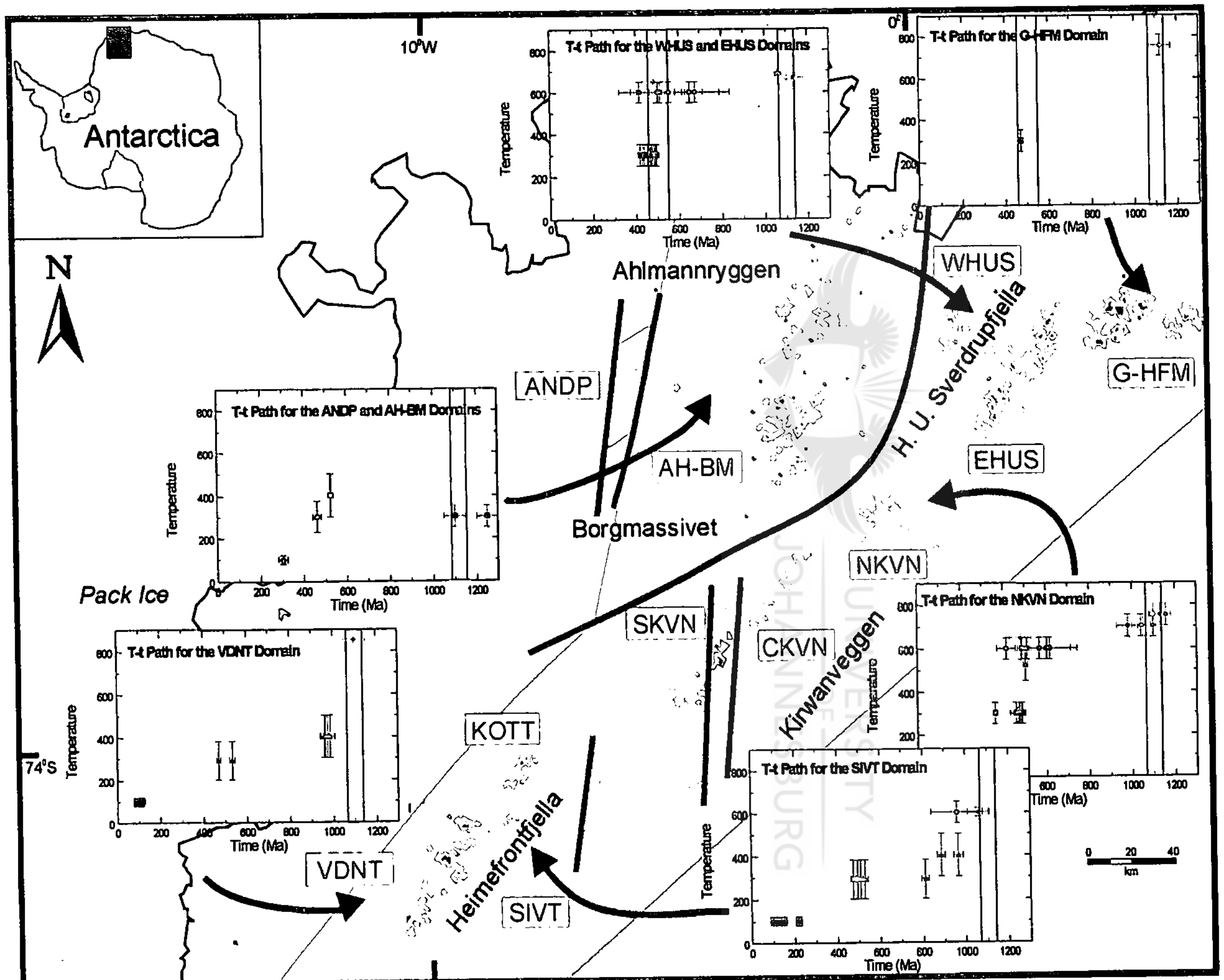

GEOLOGICAL DOMAINS IN WESTERN DRONNING MAUD LAND

ANDP : - Annandagstoppane
AH-BM : - Ahlmannryggen-Borgmassivet
G-HFM : - Gjelsvikfjella-Mulig Hoffmanfjella
WHUS : - Western H.U.Sverdrupfjella
EHUS : - Eastern H.U.Sverdrupfjella
NKVN : - Northern Kirwanveggen
CKVN : - Central Kirwanveggen
SKVN : - Southern Kirwanveggen
KOTT : - Kottas Terrane
SIVT : - Sivorg Terrane
VDNT : - Vardeklettane Terrane

LEGEND

- Kirwanveggen Formation and Amelang Plateau Formation
- Urfjell Group
- High-Grade Gneisses
- Ritscherflya Supergroup and Bormassivet Intrusives
- Archaean Cratonic Fragment

FIGURE 6.9. Geological map of western Dronning Maud Land, Antarctica. The different geological domains and their boundaries are illustrated on this diagram along with several Temperature-time paths derived from the different domains. T-t path codes of minerals are the same as for Figure 6.10, but includes fission track data in black. The source of the data is outlined in Table 2.1 of Chapter 2. Associated magmatism in the domains is illustrated by a yellow box on the T-t diagrams. Volcanic and sedimentary activity experienced in the Ritscherflya Supergroup is illustrated by a green box for the ANDP and AH-BM geological domains.

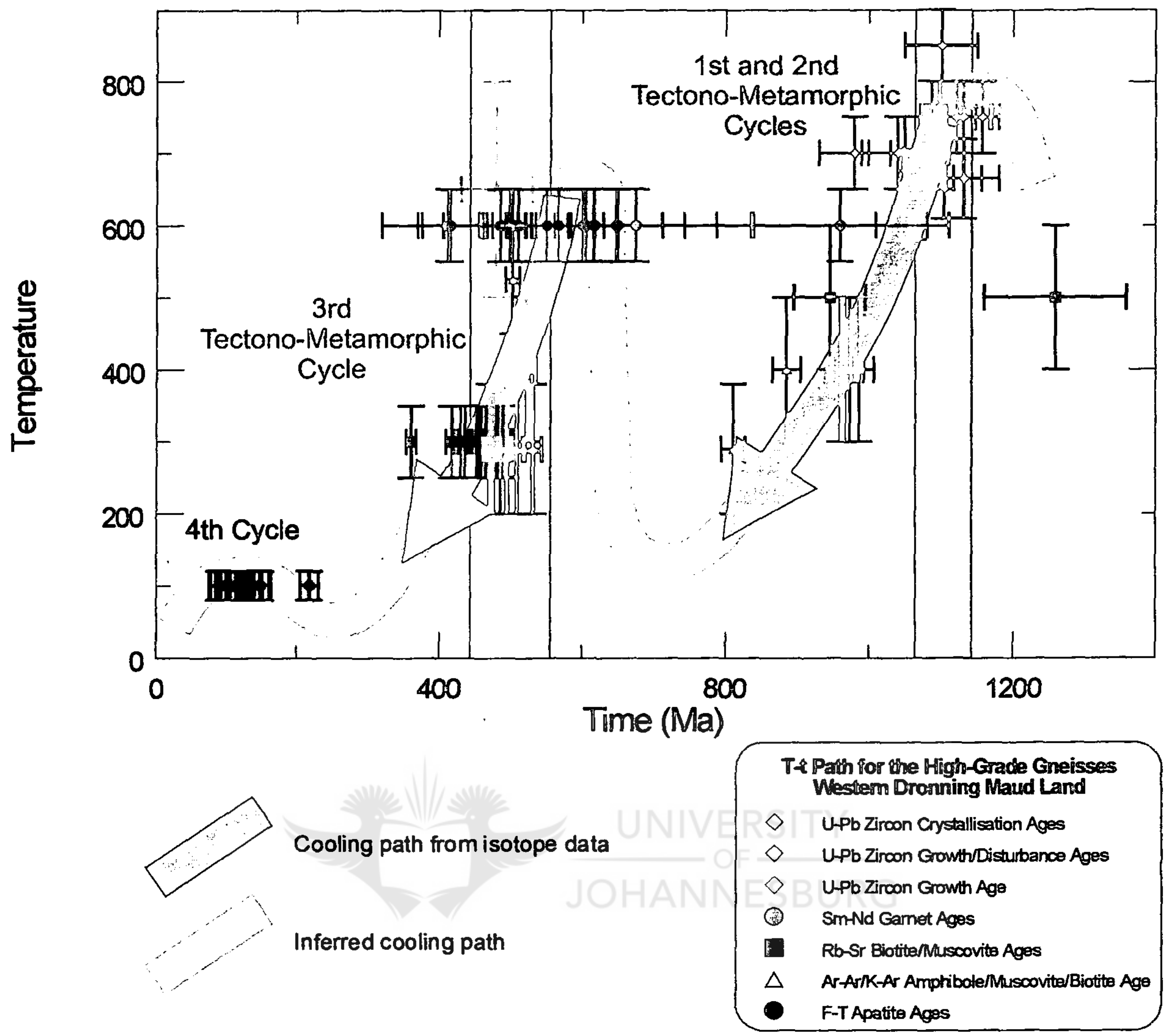

FIGURE 6.10 Summary of the T-t cooling diagrams for WDML. The T-t path is a combination of the data used in Figure 6.9. Isotopic closure temperature estimates used in these diagrams are provided in Table 6.1. The T-t path shown in this diagram is a summary of conditions experienced within the different domains of WDML. Not all the domains will have experienced the full path conditions, but the diagram provides an indication of the effects of different tectono-metamorphic cycles within WDML. Isotope data are from this study and previous investigations referenced in Table 2.1.

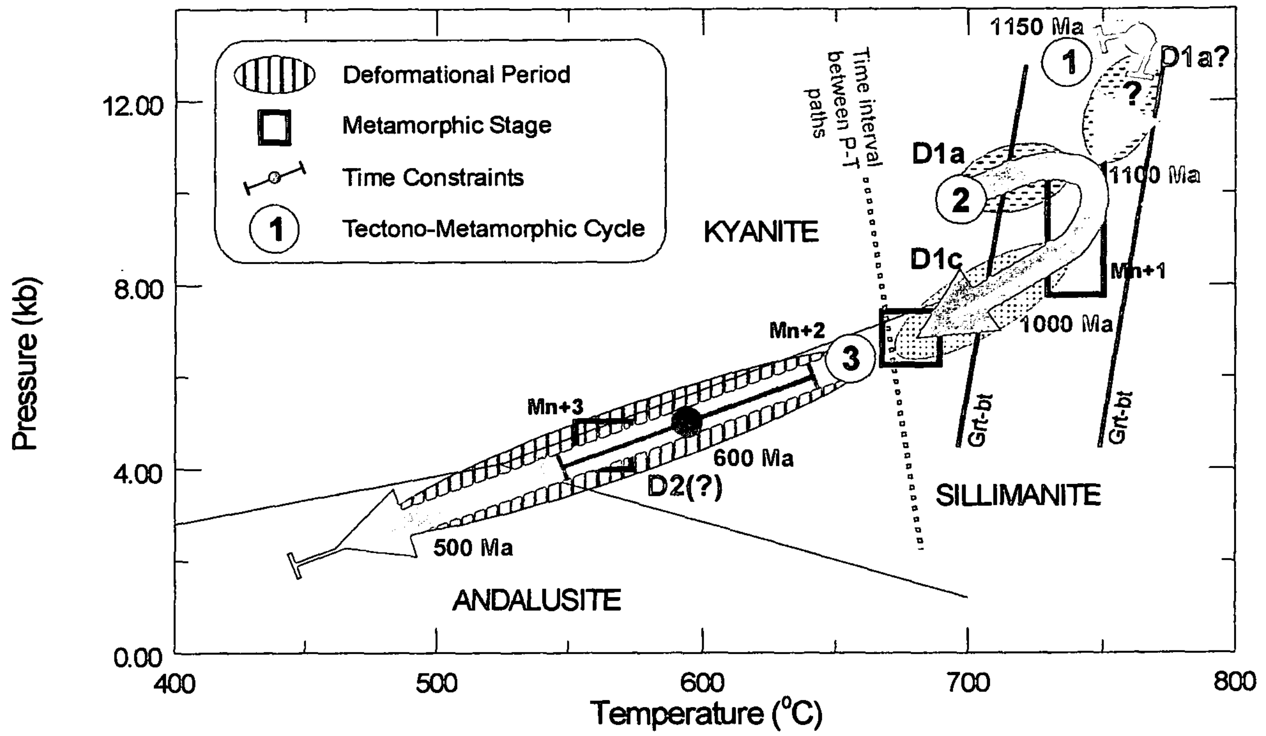

FIGURE 6.11. P-T-t-d pathway derived for Neumayerskarvet in the northern Kirwanveggen. P-T conditions and metamorphic stages have been described and determined in Chapter 5. Deformational periods and deformational time constraints have been established and described in Chapters 3 and 4. An approximately 450 Ma time interval is experienced between the end of the 2nd tectono-metamorphic cycle and the start of the 3rd tectono-metamorphic cycle. The significance of the various tectono-metamorphic cycles are discussed in the text.

Table 6.1. Closure temperature estimates for different mineral systems.

Mineral	Grainsize	Cooling Rate	Closure Temperature (Literature)	Closure Temperature (Used in this study)
U-Pb				
Zircon			700 ± 50 °C[1]	750 ± 50 °C
Garnet	1-10 mm		> 800 °C at 7.5 kb[2]	800 ± 50 °C
	1 mm		> 500 °C at 7.5 kb[3]	
Monazite			725 ± 25 °C[4]	725 ± 25 °C
Titanite	Depending on		500-680 °C[5]	590 ± 90 °C
	grainsize		> 550 °C[6,8]	
Ilmenite			350-675 °C[9]	500 ± 150 °C
Rutile	0.09-0.21 mm	1-2 °C/Ma	420 ± 30 °C[7]	420 ± 30 °C
	0.07-0.09 mm	1-2 °C/Ma	~ 380 °C[7]	
Epidote			> 550 °C (?)[6,8]	550 ± 50 °C
Apatite			~ 500 °C (?)[10]	350 ± 50 °C
			~ 350 °C (?)[11]	
Sm-Nd				
Garnet				600 ± 50 °C
Pyrope	4 mm	2-100 °C/Ma	440-570 °C[12]	
	~ 1 mm	5 °C/Ma	~ 480 °C[3]	
Grossular	4 mm	2-100 °C/Ma	670-760 °C[12]	
	~ 1 mm	5 °C/Ma	~ 725 °C[3]	
Alm, Py,Gross	1-5 mm	1-3 °C/Ma	~ 600 °C[13]	
Py,Alm(Fe-Mg)		5 °C/Ma	725 ± 30 °C[14]	
Ar-Ar				
Hornblende		5 °C/Ma	500 ± 50 °C[15]	500 ± 50 °C
Muscovite		slow cooling	350 ± 50 °C[15]	350 ± 50 °C
Biotite		1 °C	250 ± 50 °C[15]	250 ± 50 °C
Microcline				
Microperthite			150 ± 30 °C[16]	150 ± 30 °C
Rb-Sr				
Titanite		1 mm	750 °C[19]	750 ± 50 °C
Muscovite			500 ± 50 °C[17,18]	500 ± 50 °C
Epidote			≥ 500 °C (?)[3]	500 ± 50 °C
Garnet		~ 1 mm	≥ 500 °C (?)[3]	500 ± 50 °C
Biotite			320 ± 40 °C[*,16]	320 ± 40 °C
Plagioclase		1-100 °C/Ma	370-450 °C[3]	400 ± 50 °C
Apatite			~ 350 °C (?)[11]	350 ± 50 °C
Fission Track				
Garnet				
Andradite-rich			270 ± 30 °C[20]	270 ± 30 °C
Titanite			250 ± 40 °C[20]	250 ± 40 °C
Epidote			240 ± 40 °C[20]	240 ± 40 °C
Zircon			210 ± 40 °C[20]	210 ± 40 °C
Hornblende			145 ± 25 °C[20]	145 ± 25 °C
Apatite			100 ± 20 °C[20]	100 ± 20 °C

[1]Mattinson (1978), [2]Mezger *et al.* (1989a), [3]Burton and O'Nions (1991), [4]Parrish (1990), [5]Mezger *et al.* (1991), [6]Cliff and Cohen (1980), [7]Mezger *et al.* (1989b), [8]Cliff (1985), [9]Burton and O'Nions (1990), [10]Watson *et al.* (1985), [11]Ghent *et al.* (1988), [12]Harrison and Wood (1980), [13]Humphries and Cliff (1982), [14]Freer (1981), [15]McDougall and Harrison (1988), [16]Harrison and McDougall (1980), [17]Purdy and Jager (1976), [18]Blackenburg *et al.* (1989), [19]Morishita *et al.* (1989), [20]Wagner and Van den Haute (1992).

TABLE 6.2. Summary of U-Pb SHRIMP zircon age data. The table is reproduced from Table 4.11 of Chapter 4.

Sample	Age	Inheritance	Zircon Growth	Significance
PH93161 (BGM)	-	~2040 Ma (oldest age recorded) 1880-2040 Ma Possible 1500 Ma ~1390 Ma	~1260-~1000 Ma	Zircons exposed to several periods of metamorphism and deformation (High-grade between ~1260 to 1000 Ma). Unit provides a maximum age of deformation, and an indication of source material for the high-grade gneisses.
PH92009 (LEU)	1098 ± 5 Ma	Inherited component present but undetermined due to analysis discordance	~1040 Ma	Zircons provide a crystallisation age. The older component present is close to the crystallisation age. Younger zircon growth is also recorded.
PH93148 (ILG)	~1130 Ma (Not well constrained)	Inherited component present but undetermined due to analysis discordance	~1100 Ma(?) ~1050 Ma ~480 Ma	Data are discordant but possible crystallisation age of ~1130 Ma is suggested. Evidence of ~1050Ma growth and a ~480 Ma period is present in this sample.
PH92020 (KBL)	1096 ± 10 Ma	-	~980 Ma	Crystallisation age with younger growth or disturbance documented.
PH92005 (MOG)	1088 ± 10 Ma	-	~980 Ma	Crystallisation age with younger growth or disturbance documented.
PH92006/93140 (PEG)	1079 ± 6 Ma	-	-	Crystallisation age of sample. This sample records the last magmatic event sampled at Neumayerskarvet.

Table 6.3 Rb-Sr mineral isotopic data from Neumayerskarvet.

Sample	Type	Rb (ppm)	Sr (ppm)	87Rb/86Sr	87Sr/86Sr	Precision	Age
Garnet-Biotite Migmatitie Gneiss							
PH92031	wr	133.03	192.17	2.0081	0.731324	0.000012	
PH92031/bt	biotite	435.47	3.88	413.1086	3.490014	0.000037	0.7179
PH92031/m	muscovite	162.46	50.89	9.3007	0.778887	0.000030	466±8Ma
Intrusive Leucogneiss							
PH93148	wr	102.31	244.36	1.2134	0.724727	0.000015	
PH93148b	wr		244.26		0.724860	0.000019	
PH93148/bt	biotite	502.19	3.14	668.2131	5.247069	0.000079	
PH93148/fs	feldspar	215.2	483.53	1.2899	0.725251	0.000013	0.7166
PH93148/m	muscovite	282.2	24.623	33.9191	0.941995	0.000013	471±7Ma
Kyanite-Bearing Leucogneiss							
PH92020/bt	biotite	824.9	2.76	2034.1134	14.5312	0.0042	
PH92020/fs	feldspar	279.5	283.65	2.8692	0.773366	0.000012	0.7538
PH92020/m	muscovite	408.8	13.76	91.6388	1.383436	0.000019	479±7Ma
PH92057	wr	266.19	23.54	34.8491	1.37389	0.00082	
PH92057/bt	biotite	1772.0	5.3	2645.1178	18.4374	0.0017	1.1428
PH92057/m	muscovite	1058.5	5.59	893.3165	7.153435	0.000098	466±7Ma
PH93200	wr	83.60	200.14	1.2109	0.727927	0.000006	
PH9200/bt	biotite	529.9	4.14	492.2613	4.07359	0.00011	0.7197
PH93200/m	muscovite	246.1	29.41	24.6342	0.886623	0.000015	477±7Ma
PH93203	wr	211.18	97.21	6.3749	0.853291	0.000011	0.8097
PH93203/m	muscovite	535	13.29	127.566	1.681513	0.000038	479±10Ma
Megacrystic Orthogneiss							
PH92003	whole-rock	81.32	359.05	0.6556	0.713255	0.000009	
PH92003b	whole-rock	95.32	465.38	0.5929	0.713295	0.000010	
PH92003/a	amphibole	12.47	48.64	0.7422	0.713970	0.000012	
PH92003/bt	biotite	374.44	7.11	169.3447	1.846485	0.000017	0.7090
PH92003/fs	feldspar	74.53	668.24	0.3228	0.711034	0.000016	473±11Ma
Granitic Veins							
PH92004/bt	biotite	665	4.34	632.6862	5.074060	0.000110	
PH92004/rf	feldspar	203.14	416.9	1.4114	0.719336	0.000011	0.7097
PH92004/wf	feldspar	2.357	131.48	0.0519	0.710160	0.000007	479±7Ma
PH92007	whole-rock	248.17	123.98	5.8414	0.795860	0.000011	
PH92007/bt	biotite	1034	4.93	992.7208	7.2083	0.0008	0.7596
PH92007/fs	feldspar	366.2	173.83	6.1507	0.801001	0.000013	459±29Ma
PH92012	whole-rock	139.15	126.31	3.202	0.754772	0.000014	0.7332
PH92012/bt	biotite	828.74	7.365	415.7903	3.540751	0.000051	474±10Ma
PH92023/bt	biotite	587	2.61	1128.316	8.21059	0.00031	
PH92023/fs	feldspar	3.07	154.19	0.0576	0.714446	0.000012	0.7142
PH92023/gr	feldspar	244.6	198.07	3.5839	0.738975	0.000011	481±10Ma
PH92053/cc	calcite	0.008	48.67	0.0005	0.713580	0.000150	0.7136
PH92053/m	muscovite	358.1	35.40	29.7222	0.866454	0.000016	361±7Ma

Sample	Type	Rb (ppm)	Sr (ppm)	87Rb/86Sr	87Sr/86Sr	Precision	Age
Amphibolite Dykes							
PH92021	whole-rock	37.66	354.67	0.3073	0.711939	0.000011	
PH92021b	whole-rock	37.93	357.14	0.3074	0.712333	0.000011	
PH92021/a	amphibole	10.17	133.33	0.2208	0.711409	0.000013	0.7100
PH92021/bt	biotite	588.05	15.05	122.2069	1.535825	0.000019	475±11Ma
PH93188	whole-rock	156.34	70.59	6.4373	0.754707	0.000008	
PH93188/a	amphibole	12.14	30.53	1.1516	0.717274	0.000009	0.7093
PH93188/bt	biotite	459.86	4.08	416.3015	3.535151	0.000032	485±10Ma
PH93192	whole-rock	74.91	49.34	4.406	0.738669	0.000007	
PH93192/a	amphibole	11.364	60.23	0.5461	0.710864	0.000010	0.7071
PH93192/bt	biotite	606.6	6.34	339.3734	3.017525	0.000029	489±14Ma

Table 6.4 Sm-Nd mineral isotopic data from samples at Neumayerskarvet.

Sample	Type	Sm (ppm)	Nd (ppm)	147Sm/144Nd	143Nd/144Nd	Precision	Age
Biotite-Garnet Migmatite Gneiss							
PH92031	whole-rock	7.47	30.285	0.1491	0.512337	0.000006	
PH92031b	whole-rock	7.39			0.512356	0.000013	0.5117
PH92031/g	garnet	6.34	16.72	0.2292	0.512655	0.000009	605±138Ma
PH93161	whole-rock	7.143	34.221	0.1262	0.511906	0.000007	
PH93161/g	garnet	1.70	4.594	0.2237	0.512327	0.000017	0.5114
PH93161/f	feldspar	0.4833	2.411	0.1212	0.511936	0.000029	617±96Ma
Quartzofeldspathic Leucogneiss							
PH92050	whole-rock	1.598	5.256	0.1838	0.512607	0.000014	0.5119
PH92050/g	garnet	2.798	3.579	0.4728	0.513680	0.000030	568±38Ma
Intrusive Leucogneiss							
PH93148	whole-rock	10.21	62.69	0.0984	0.511888	0.000057	
PH93148b	whole-rock	9.532	59.8	0.0964	0.511996	0.000014	
PH93148/bt	biotite	2.476	14.50	0.1032	0.512040	0.000010	
PH93148/f	feldspar	0.1025	0.6093	0.1017	0.511975	0.000017	0.5117
PH93148/g	garnet	2.105	1.127	1.1299	0.515249	0.000030	486±11Ma
Kyanite-Bearing Leucogneiss							
PH92020	whole-rock	2.125	8.542	0.1504	0.512359	0.000010	
PH92020/bt	biotite	1.405	5.341	0.1590	0.512372	0.000012	
PH92020/g	garnet	2.682	1.328	1.2221	0.516588	0.000056	0.5118
PH92020/g	garnet	2.987	4.228	0.4272	0.513573	0.000029	602±16Ma
PH92057	whole-rock	8.77	23.617	0.2246	0.512972	0.000006	
PH92057b	whole-rock	8.995	24.001	0.2266	0.513013	0.000008	0.5124
PH92057/g	garnet	9.73	13.13	0.4481	0.513594	0.000010	413±43Ma
Megacrystic Orthogneiss							
PH92003b	whole-rock	11.7	51.69	0.1368	0.512218	0.000009	0.5118
PH92003/g	garnet	4.564	3.71	0.7440	0.514252	0.000016	511±18Ma

Table 6.5. Summary of isotopic age data from samples selected during this investigation.

Sample	U-Pb Zircon Intrusive Age	Zircon Growth	Sm-Nd Garnet	Rb-Sr Mineral	Ar-Ar Amphibole
Biotite-Garnet migmatite Gness		~1260-1000 Ma			
PH92031			605 ± 138 Ma	466 ± 8 Ma	-
PH93161			617 ± 96 Ma	-	-
Quartzofeldspathic Leucogneiss					
PH92050			568 ± 38 Ma	-	-
Intrusive Leucogneiss					
PH93148	~1130 Ma (Poorly constrained)	~1100 Ma,~1050 Ma, ~480 Ma	486 ± 11 Ma	471 ± 7 Ma	-
Kyanite-Bearing Leucogneiss	1096 ± 10 Ma	~980 Ma			
PH92020			602 ± 16 Ma	479 ± 7 Ma	-
PH92057			413 ± 43 Ma	466 ± 7 Ma	-
PH93200			-	477 ± 7 Ma	-
PH93203			-	479 ± 10 Ma	-
Megacrystic Orthogneiss					
PH92003			511 ± 18 Ma	473 ± 11 Ma	513 ± 5 Ma
PH92005	1088 ± 10 Ma	~980 Ma	-	-	
Pegmatitic Veins					
PH92004			-	479 ± 7 Ma	-
PH92006/PH93140	1079 ± 6Ma	-	-	-	-
PH92007			-	459 ± 29 Ma	-
PH92012			-	474 ± 10 Ma	-
PH92023			-	481 ± 10 Ma	-
PH92053			-	361 ± 7 Ma	-
Mafic Dykes					
PH92021			-	475 ± 11 Ma	-
PH93188			-	485 ± 10 Ma	-
PH93192			-	489 ± 14 Ma	-

Table 6.6. Correlation table of related events discussed within various chapters of the thesis.

Tectono-Metamorphic Cycle	Deformation (Regional)	Deformation (Neumayerskarvet)	Metamorphism (Neumayerskarvet)	Time (Ma)	Discussion
1st Cycle	D1a	D1nkv	?	1160 Ma to 1110 Ma	• Possible high-pressure metamorphism. • Development of strong planar penetrative foliation and early isoclinal folding. • Possible early magmatism.
2nd Cycle	D1b	D2nkv D3nkv D4(a)nkv	Mn+1 (nkv) 710-760 °C 7.8-8.5 kb	1100 Ma to 1070 Ma	• Major period of deformation represented by strong lineation and foliation development, isoclinal recumbent folding, sheath folds and refolded folds. NNW-SSE tectonic transport directions are suggested during this cycle. • Magmatism dominates during this cycle at Neumayerskarvet and is represented by orthogniesses charnockitic rocks and kyanite-bearing leucogneisses. • Period of major metamorphism.
	D1c	D4(b)nkv (?) D5nkv (?)	Mn+2 (nkv) 630-690 °C 6.0-7.4 kb	1070 Ma to 970 Ma	
3rd Cycle	D2	D4(b)nkv (?) D5nkv (?)	Mn+3 (nkv) 560-570 °C 4.4-4.6 kb	650 Ma to 450 Ma	• Difficult to characterise the deformational styles associated with this cycle, and exact nature enigmatic. • This cycle is distinguished through reset isotopic systems
4th Cycle	D3	D6nkv		200 Ma to 100 Ma	• Related to the break-up of Gondwana. • Period of uplift, tectonism and magmatism recorded throughout WDML.

CHAPTER 7

GEOCHEMISTRY AND CRUSTAL EVOLUTION OF THE NORTHERN KIRWANVEGGEN

INTRODUCTION

Geochemical and isotopic data can provide information on the nature and characteristics of most rock types but a large proportion of this information is lost from rocks that have undergone deformation and metamorphism. Recognition of primary textures and structures is made difficult by the intense fabric development and the metamorphic growth of new mineral phases. Isotopic data provides information on the crustal evolution of the terrane, providing insights into the terrane amalgamation and distinguishing between old re-worked and juvenile material.

Although deformation can significantly alter the geochemistry of the rocks, important information on the origin of the gneissic material may still be obtained. Rb-Sr systematics are also subjected to changes in the crust, as this system can be affected by magmatic differentiation, metamorphism, weathering and sedimentation (Muller *et al.*, 1998). The Rb-Sr isotopic results are often difficult to interpret, but coupled with other data may provide significant information for the characteristics of the rocks under investigation. Sm-Nd isotopes provide important information for the evolution of the crustal material. This isotopic system is important as it provides model mantle extraction ages that are little affected by normal crust forming processes (De Paolo, 1988). Major fractionation of Sm and Nd concentrations occur during melt extraction from the mantle and later crustal processes tend not to significantly alter the Nd/Sm ratios, thus providing valuable insights into mantle extraction ages. Partial melting and high-grade metamorphism may, however, have significant effects on these isotopic ratios and may alter the model mantle extraction ages. The Nd model ages are best interpreted as minimum ages for extraction from mantle.

This investigation assesses the geochemical and isotopic data from high-grade gneisses in the northern Kirwanveggen in order to provide an insight into the crustal evolution of this domain. The data are integrated with other data sets to assist in the interpretation of these results. The evolution of the northern Kirwanveggen high-grade gneisses is viewed in terms of its significance within WDML, and assists in placing constraints on the evolution of this portion of Antarctica.

GEOLOGICAL FRAMEWORK

Geological Summary

Detailed geological investigations in the northern Kirwanveggen high-grade gneisses have revealed a complex evolutionary history. At least two tectono-metamorphic cycles have affected this area based on structural, metamorphic and geochronological studies (see Chapters 4 through to 6). The early tectono-metamorphic cycles occurred at *ca.* 1100 Ma and are characterised by intense deformation, magmatism and partial melting, and high-grade metamorphism. A younger tectono-metamorphic cycle affected the gneisses at *ca.* 550 Ma, and resulted in the resetting of many mineral isotopic systems. The nature of the deformation and metamorphism associated with this tectono-metamorphic cycle is equivocal. Deformation and metamorphism is however less intense during this cycle and results in the exhumation of the high-grade gneisses. No magmatism associated with the *ca.* 550 Ma cycle is recognised in the northern Kirwanveggen, but has been documented in the eastern and western H.U.Sverdrupfjella (Grantham *et al.*, 1991; Moyes *et al.*, 1993b). Further crustal characterisation of the high-grade gneisses is achieved from Nd, Sr and geochemical analyses presented in this chapter.

Crustal Evolution Models for WDML

The age of the Ritscherflya Supergroup has been critical in the geological interpretation of WDML. Early work suggested that the volcanic and sedimentary sequence was older than the adjacent high-grade gneisses (see Moyes *et al.*, 1995 for discussions and new interpretation of the isotope data). Two terranes were distinguished: (1) the cratonic fragment with associated Proterozoic sediments and (2) the metamorphic belt (see Groenewald *et al.*, 1991 for review). The region was viewed as a continental collision zone at *ca.* 1100 Ma where the cratonic material was juxtaposed against the high-grade gneisses of the Maud Belt. Revision of the age for the Ritscherflya Supergroup has resulted in the crustal evolution model for WDML being modified (see Moyes and Knoper, 1995; Groenewald *et al.*, 1995, Knoper *et al.*, 1995).

Moyes and Knoper (1995) proposed a foreland fold and thrust-belt (FFTB) model for the Ritscherflya Supergroup contemporaneous, and associated with the high-grade gneisses. The model places the different lithologies within a single tectogenic process. The metamorphic rocks are regarded as representing the magmatic arc, fore arc and back arc basins with associated magmatism found during continental collision (Moyes and Knoper, 1995; Groenewald *et al.*, 1995). Reactivation during a later period (*ca.* 500 Ma) results in uplift and exposure of the metamorphic terrane. The cratonic margin was interpreted to lie between Annandagstoppane and Ahlmannryggen-Borgmassivet (Corner, 1994; Moyes and Knoper, 1995) where the Ritscherflya Supergroup formed on the craton margin.

Groenewald *et al.* (1995) have modified the interpretation based on geochemical and geochronological data from the H.U.Sverdrupfjella. The isolated and small nature of the Archaean outcrop at Annandagstoppane makes it difficult to infer any information about the evolutionary history for this terrane. Groenewald *et al.* (1995) do not favour the possibility that this terrane was part of a microplate during the Mesoproterozoic (*ca.* 1100 Ma) orogeny as proposed by Barton *et al.* (1987). Rather, these authors prefer the interpretation that Annandagstoppane forms part of the Kalahari Craton that has subsequently broken away during later Gondwana fragmentation at *ca.* 180 Ma.

The Ritscherflya Supergroup sediments and volcanic rocks accumulated on the platform provided by the Kalahari Craton (Groenewald *et al.*, 1995). These rocks were deposited during the Mesoproterozoic Grenvillian orogeny (*ca.* 1100 Ma). The generation of a foreland basin during collision at the same time period would be expected. Groenewald *et al.* (1995) suggest that the nature of the sediments in the Ritscherflya Supergroup tend to support an intracratonic provenance rather than a foreland basinal environment.

The Maud Belt has characteristics compatible with collision and accretion of a volcanic arc and retro-arc marginal basin. The high-grade gneiss terrane was relatively juvenile prior to collision and high-grade metamorphism, which is supported by the Sr and Nd isotopes (see Groenewald *et al.*, 1995 for reviews). The metamorphic P-T path derived from the H.U.Sverdrupfjella indicates initial high pressures followed by decompression and thermal relaxation. The early high pressures are problematic for a retro-arc basin as subduction would not produce these conditions. Groenewald *et al.* (1995) proposed an orogeny involving collision and sandwiching of a young arc-complex between colliding continents. These authors cite the Kohishan portion of the Himalayan belt (Bard, 1983) as an example of such an orogeny. Evidence for cratonic material to the south or east of the Maud Belt is lacking for this model, however, since an absence of outcrop in this area makes evaluation of the underlying geology difficult.

Supercontinent assembly took place at *ca.* 1100 Ma followed by a period of extension with mafic magmatism (Borgmassivet Intrusive Suite and mafic dykes in western H.U.Sverdrupfjella) between 1000 and 800 Ma. Break-up and dispersal was tentatively proposed during this period (Groenewald *et al.*, 1995). The Brattskarvet Intrusive Suite provides evidence for the next significant event that affected WDML at ~520 Ma. Most mineral isotopic systems were reset during this period (see Chapter 6). Deformation in the H.U.Sverdrupfjella is suggested to indicate another period of collision at *ca.* 500 Ma. Deformation associated with the *ca.* 500 Ma event tends to increase towards the east and northeast. The ca. 500 Ma event represents a period of rapid cooling and exhumation and Groenewald *et al.* (1995) postulated overthrusting during this orogeny. Rapid uplift is also suggested by the deposition of the Urfjell Group sediments during this period (Moyes *et al.*, 1997).

RESULTS

Analytical Techniques

Whole rock powders were prepared using standard rock crushing techniques. Geochemical analyses were carried out at the University of Natal, Pietermaritzburg, using standard XRF techniques. Isotope analyses were carried out at the Bernard Price Institute of Geophysics, University of the Witwatersrand, Johannesburg.

Whole rock Sm-Nd samples were digested in white Teflon® beakers with an HF-HNO_3 mix (3:1), for 3 days on a hot plate, and then taken up in 6N HCl. When the ^{146}Nd tracer was used the solution was split into two aliquots in a 2:1 ratio for analysis of the isotopic composition and for concentrations by isotope dilution respectively. Sm and Nd were separated using a variation of the method described by Richard *et al.*, (1976). Concentrations were measured on a Micromass® MM30 mass spectrometer, while ^{143}Nd/^{144}Nd ratios were measured on a Micromass® VG354 mass spectrometer. During later work a ^{150}Nd tracer was used. For these samples the spike was added prior to dissolution; separation techniques remained the same, while the ratio and Sr and Nd concentration measurements were carried out on a Micromass® VG354 mass spectrometer. Rb, Sm and several Nd concentrations were obtained by isotope dilution on a Micromass® MM30 mass spectrometer using solid source thermal ionisation techniques. Blank levels during the Sm and Nd separation were below 500pg, and no corrections have been made.

Chemical dissolution of approximately 0.1g of the whole rock powder was carried out using clean open Teflon® beakers for the Rb-Sr analyses. Rb and Sr isotope tracers were added prior to dissolution. Chemical dissolution was achieved with an HF-HNO_3 mix (3:1) for three days on a hot plate, and then taken up in 6N HCl. Separation of Rb and Sr was attained using standard cation exchange in an HCl medium. All reagents used in these procedures were prepared and purified at the BPI. Measured total method blank levels were less than 1ng for Rb and Sr, and no corrections have been made.

Values obtained for ^{87}Sr/^{86}Sr from international standards SRM987 and Eimer & Amend® were 0.71021 ± 0.00003 and 0.70800 ± 0.00005 respectively. International standards used during the course of this work provided ^{143}Nd/^{144}Nd values of 0.511821 ± 0.000019 for the Johnson &

Mathey® standard, 0.512645 ± 0.000021 for BCR-1 and 0.511835 ± 0.000022 for La Jolla. The $^{146}Nd/^{144}Nd$ ratio was corrected to 0.7219 in all samples.

The processing and regression of the Rb-Sr and Sm-Nd isotopic data was carried out using the program "*GEODATE*" of Eglington and Harmer (1991). Precision parameters at the 2σ level used in the regression techniques were: $^{87}Rb/^{86}Sr$ – 2%; $^{87}Sr/^{86}Sr$ – 0.0002; $^{147}Sm/^{144}Nd$ – 0.2% and $^{143}Nd/^{144}Nd$ – 0.01%. The correlation coefficient used for Sr and Nd whole-rock analyses was 1.0. Throughout the text all ages, initial ratios and errors are quoted at the 2σ (95% confidence) levels. Isochrons are defined here as occurring when the mean sum of the weighted deviates (MSWD) is less than a critical F value determined by the number of samples regressed and based on 60 replicate analyses (formulae from Ludwig, 1983; 1990). Where the MSWD exceeds this F value the errors have been augmented by (MSWD/Critical F)$^{1/2}$. Bulk earth comparisons are based on the following constants: $^{87}Rb/^{86}Sr = 0.0847$ and $^{87}Sr/^{86}Sr = 0.7047$; $^{147}Sm/^{144}Nd = 0.1967$ and $^{143}Nd/^{144}Nd = 0.512638$. Model age data for Sm-Nd and Rb-Sr compared to depleted mantle are based on the following values: $^{87}Rb/^{86}Sr = 0.0459$ and $^{87}Sr/^{86}Sr = 0.702$ (Faure, 1986); $^{147}Sm/^{144}Nd = 0.222$ and $^{143}Nd/^{144}Nd = 0.513114$ (Richard *et al.*, 1976). Decay constants are $^{87}Rb = 1.42 \times 10^{-11}y^{-1}$, $^{147}Sm = 6.54 \times 10^{-12}y^{-1}$.

Geochemical and Isotopic Signatures

Several different geochemical plots are used in this section to display the chemical variations of the samples analysed. Caution must, however, be exercised when reviewing these diagrams as these rocks have undergone high-grade metamorphism and deformation that will have affected the geochemical signatures of these samples. Harker diagrams for the samples from this investigation are plotted in Figure 7.2, and geochemical discrimination diagrams discussed in more detail are presented in Figure 7.3. The geochemical data for these samples are provided in Table 7.1. Conventional isochron diagrams for Rb-Sr whole-rock samples are displayed in Figure 7.4. The Rb-Sr data are provided in Table 7.2. Isochron plots for Sm-Nd whole-rock samples are presented in Figure 7.5, while the data are provided in Table 7.3. The isotopic signatures of the different lithotectonic units analysed during this investigation are discussed below.

Biotite-Garnet Migmatite Gneiss

The biotite-garnet migmatite gneiss forms the major lithotectonic unit exposed in the northern Kirwanveggen. It is also the oldest unit recognised, and hence exhibits all phases of deformation. The gneiss comprises leucosomes and melanosomes mixed with various intrusive units within the gneissic foliation. A complex zircon population has been recognised from samples of the biotite-garnet migmatite gneiss (see Chapter 4). The zircons are often rounded and exhibit zircon overgrowths. U-Pb SHRIMP data display inherited components with ages ranging up to ~2040 Ma. Rims with zircon ages of ~1130 Ma provide a minimum age for this lithotectonic unit. The large component of inherited ages and the nature of the zircon grains supports a supracrustal origin for the biotite-garnet migmatite gneiss. Overgrowths of zircon are interpreted as being the result of post-formation metamorphism experienced by this lithotectonic unit.

Geochemistry of the biotite-garnet migmatite gneiss supports a sedimentary origin for this lithotectonic unit based on the diagram of Werner (1987) displayed in Figure 7.3. Two samples plot near the magmatic-sedimentary boundary defined in this diagram, which may be the result of complex tectonic interleaving of supracrustal material with magmatic components. Harker diagrams for the data analysed during this investigation are shown in Figure 7.2.

Only one sample of the biotite-garnet migmatite gneiss was analysed for Rb-Sr. The depleted mantle model age for this sample is 1007 Ma, which is close to the metamorphic zircon ages obtained from this lithotectonic unit (see Chapter 4).

Four biotite-garnet migmatite gneiss samples, three quartzofeldspathic gneiss samples, one mafic boudin and one leucosome sample (PH92009) have been analysed for their Sm-Nd isotopic compositions (Table 7.3). These data have been plotted in a conventional isochron diagram for comparison (Figure 7.5). Due to the nature of the samples no isochron could be defined but an 1100 Ma line is shown for reference. Nd T_{DM} range from 1621 Ma to 2013 Ma with present day ε Nd values between –14.28 and –5.87 (See Table 7.3 and Figure 7.6). The leucosome sample PH92009 produces a Nd T_{DM} age of 1435 with a present day ε Nd value of +1.37.

Quartzofeldspathic Gneiss

The quartzofeldspathic gneiss is interleaved with the biotite-garnet migmatite gneiss. These lithotectonic units are leucocratic and exhibit similar deformational fabrics as those displayed by the biotite-garnet migmatite gneiss (see Chapter 3). No previous isotopic age data have been obtained for this unit. The quartzofeldspathic gneiss is interpreted as an old lithotectonic unit within the northern Kirwanveggen, but no indication of the nature of origin for this unit was obtained from field observations.

Limited samples have been obtained from this unit for geochemical analysis. On the plot of Figure 7.3 (Werner, 1987) these samples plot in the magmatic field. The samples plot across the tonalite and granodiorite field within the Streckeisen plot shown in Figure 7.3. In the discrimination diagrams of Pearce *et al.* (1984) the samples plot within the volcanic arc granite

(VAG) field (Figure 7.3). At this stage it is uncertain as to whether this lithotectonic unit has an extrusive or intrusive protolith.

Three samples of the quartzofeldspathic gneiss have been analysed for Rb-Sr and provide depleted mantle model ages ranging from 1150 Ma to 1616 Ma. All these samples have been plotted on the isochron diagram in Figure 7.4. These data do not define an age but scatter about a line with a slope equivalent to an age of 1100 Ma. The quartzofeldspathic gneiss has Nd T_{DM} ages of 1233 Ma and 1282 Ma with ε Nd values of +3.72 and +4.38.

Intrusive Leucogneiss

The intrusive leucogneiss intrudes across the fabrics within the biotite-garnet migmatite gneiss but has subsequently been deformed. The SHRIMP zircon age data for the intrusive leucogneiss are difficult to interpret. A Pb-Pb age of 1101 ± 13 Ma provides a minimum age for this unit, but more concordant samples suggest an age closer to 1130 Ma for intrusion of this unit.

The samples analysed from these lithotectonic units plot within the magmatic field in Figure 7.3, within the granite field, and at the border between the VAG and within plate granite (WPG) fields on the discrimination diagrams (Figure 7.3).

Seven samples of intrusive leucogneiss where analysed for Rb-Sr isotopic compositions during this investigation. The isotopic data scatter widely (MSWD = 88.9) about a line equivalent to an age of 1315 ± 151 Ma with an initial ratio (R_0) of 0.7020 (Figure 7.4). This age is older than the U-Pb SHRIMP zircon estimate of ~ 1130 Ma for intrusion. This unit is strongly deformed and has undergone at least one period of high-grade metamorphism and it is probable that the isotopic signatures have been affected during these events. Depleted mantle Sr model ages range between 1155 Ma and 1502 Ma for these samples (Table 7.2).

Eight intrusive leucogneiss samples have been analysed for their Sm-Nd isotopic compositions. The data scatter (MSWD = 5.47) about a line equivalent to an age of 1443 ± 754 Ma with an R_0 = 0.5110. The limited spread in Sm-Nd isotopic compositions result in the large error estimate for this age. Nd T_{DM} ages for the intrusive leucogneiss range from 1291 Ma to 1509 Ma and present day ε Nd values range between –0.88 to +2.93 (see Table 7.3).

Kyanite-Bearing Leucogneiss

The kyanite-bearing leucogneisses are intrusive bodies that are discordant to the early tectonic fabrics but have subsequently been deformed. These units intrude during the peak of the Mn+2 (nkv) metamorphic stage (see Chapters 5 and 6). A kyanite-bearing leucogneiss from the central portion of Neumayerskarvet produced a U-Pb zircon SHRIMP age of 1096 ± 10 Ma, which is interpreted as an age of intrusion for this unit.

Geochemical samples for these units plot within the monzogranite field on the Streckeisen diagram in Figure 7.3. The data spread broadly across the VAG and WPG fields on the discrimination diagrams of Pearce *et al*. (1984), as shown in Figure 7.3. The Nb contents within these units are low and near the detection limits, which may explain the large variation exhibited by this lithotectonic unit.

Three samples of kyanite-bearing leucogneiss have been analysed for their Rb-Sr isotopic signatures. Two of the three samples display high radiogenic $^{87}Sr/^{86}Sr$ ratios. The T_{DM} ages range from 1344 Ma to 1651 Ma for these samples. The samples are plotted in Figure 7.4 but do not define an isochron. An 1100 Ma reference line is illustrated in the diagram for comparison.

Seven kyanite-bearing leucogneiss samples have been analysed for Sm and Nd during this investigation. Many of the samples display high $^{147}Sm/^{144}Nd$ ratios that produce unrealistic model ages. The data scatter on the isochron diagram in Figure 7.5 and do not provide any age information. Nd depleted mantle model ages for three samples range from 1604 Ma to 2874 Ma.

Megacrystic Orthogneiss

The megacrystic orthogneiss is a large intrusive unit that occurs predominantly within the eastern sections of the northern Kirwanveggen. The unit varies in nature due mainly to the extent of deformation that this unit has undergone. Undeformed remnant portions within the megacrystic orthogneiss are charnockitic. These units grade into a porphyritic granitoid and ultimately into augen-textured gneiss as deformation increases. The megacrystic orthogneiss intrudes during the peak of metamorphism (Mn+2 (nkv)) identified within the northern Kirwanveggen (see Chapter 5). A U-Pb zircon SHRIMP age of 1088 ± 10 Ma has been obtained from this lithotectonic unit and is interpreted as the age of intrusion.

The geochemical samples for the megacrystic orthogneiss plot within the quartz-monzonite, quartz-monzodiorite and monzogranite fields shown in Figure 7.3. In the Pearce *et al.* (1984)

discrimination diagrams the samples plot across the boundary between the VAG and WPG fields (Figure 7.3).

Twenty-one samples of megacrystic orthogneiss have been analysed for their Rb-Sr isotopic compositions (Table 7.2). The data are plotted on an isochron diagram in Figure 7.4 and scatter (MSWD = 16.99) about a line equivalent to an age of 1099 ± 52 Ma with R_0 = 0.7033. This age is within error of the U-Pb SHRIMP zircon age and is interpreted to represent the age of intrusion for the megacrystic orthogneiss. T_{DM} Sr ages range from 838 Ma to 1673 Ma for these samples (Table 7.2).

Seventeen samples of different portions of the megacrystic orthogneiss have been analysed during this investigation for their Sm and Nd isotopic compositions. The data scatter about a line equivalent to an age of 1085 ± 217 Ma (MSWD = 4.55, R_0 = 0.5113). Although the error is large it is within the age obtained from U-Pb SHRIMP zircon isotope analysis (See Chapter 4). Nd T_{DM} ages range from 1329 Ma to 1634 Ma for these samples with present day ε Nd values ranging from –0.25 to +2.84.

Pegmatite Veins

Pegmatite veins are identified within the central portion of Neumayerskarvet that intrude across the dominant tectonic fabrics recognised within the northern Kirwanveggen. These units intrude late during the older tectono-metamorphic cycle and have been dated at 1073 ± 6 Ma by U-Pb SHRIMP zircon methods (see Chapter 4). This age is regarded as the age of intrusion for these units.

The pegmatite veins plot within the granite field of the Streckeisen diagram (Figure 7.3). These samples again plot across the border between the VAG and WPG fields of the Pearce *et al.* (1984) discrimination diagrams.

Six pegmatitic vein samples were analysed for Rb-Sr isotopic compositions, and the data are presented in Table 7.2. The data are plotted on an isochron diagram in Figure 7.4, and the six points scatter about a line equivalent to an age of 999 ± 17 Ma (MSWD = 4.09, R_0 = 0.7103). This age is younger than the U-Pb SHRIMP zircon age obtained from one of these veins. The inconsistency between the isotopic age data may be the result of the pegmatitic samples being taken from slightly different age units. The possibility that late D1c or D2 deformation affected the isotopic systematics cannot be discounted. Sr T_{DM} data range from 1100 Ma to 1713 Ma for these samples.

Four pegmatitic vein samples were analysed for their Sm-Nd isotopic compositions. The data (Figure 7.5) scatter about a line equivalent to an age of 1025 ± 239 Ma (MSWD = 5.85, R_0 = 0.5114). The Sm-Nd whole-rock age has a relatively large error but is within the age obtained through U-Pb SHRIMP zircon dating of one of these samples. Nd T_{DM} ages range from 1268 Ma through to 1576 Ma, with ε Nd values of +2.01 and +3.03 for these samples.

Mafic Dykes

Six samples of mafic dyke material were collected from several localities within the central portion of Neumayerskarvet. The data do not define an isochron, but reference lines equivalent to 1100 Ma and 550 Ma have been drawn in Figure 7.4 for comparison. Two samples are radiogenic and plot close to the 550 Ma reference line. These analyses may be influenced by high biotite contents seen within some of these samples. Biotite Rb-Sr systematics typically display *ca.* 500 Ma ages for gneisses within western Dronning Maud Land (Wolmarans and Kent, 1982; Moyes *et al.*, 1993a; Chapter 6). The remaining whole-rock samples plot in a tight cluster and do not display sufficient isotopic variation to define an isochron. Sr T_{DM} ages fall into two groups, one ranging between 568 Ma and 574 Ma, with the older range extending from 1198 Ma through to 2462 Ma.

Three mafic dyke samples have been analysed for their Sm and Nd isotopic compositions. The data are limited and do not define an isochron in Figure 7.5. Depleted mantle model ages for Nd are 1818 Ma and 1707 Ma for two of these samples.

Sr and Nd Signatures

A Nd evolution diagram for the high-grade gneiss samples used in this investigation is displayed in Figure 7.6. Formation ages for the lithotectonic units were taken as 1100 Ma based on U-Pb SHRIMP zircon ages of most units, and on structural-intrusive relationships recorded in the area (Chapter 4). Nd T_{DM} ages range from approximately 1100 Ma to 2800 Ma, with the majority of the data ranging between approximately 1200 Ma and 1700 Ma (Figure 7.8). The kyanite-bearing leucogneiss has variable and high Sm/Nd ratios that result in the generation of unrealistically old model ages (Table 7.3). Where the ages are unrealistic these have been excluded from further data comparison.

Where possible Sr and Nd isotopic data for the various rock samples have been combined, and the results are presented in the ε Nd and ε Sr diagram of Figure 7.7. ε Nd values calculated for the formation age of the samples under investigation range from –0.88 to +4. ε Sr values calculated from these units at 1100 Ma are more varied, and range from –482 for a mafic dyke sample to +1736 from the kyanite-bearing leucogneiss.

Sr and Nd T_{DM} ages for the samples are plotted against one another in Figure 7.8. This diagram indicates that the Nd T_{DM} ages tend to be older than the Sr T_{DM} ages. The Nd T_{DM} ages are interpreted to represent the age of the source of the material whereas the Sr T_{DM} ages may reflect the age of formation (metamorphism, magmatism, re-melting, sedimentation) of these units. Nd T_{DM} ages for the rocks under investigation are presented in the histogram of Figure 7.9.

DISCUSSION

Evidence for ca. 2.1 Ga Crust

There are several lines of evidence that suggest that a *ca.* 2.1 Ga crust has been involved in the evolution of WDML, although no direct outcrop of this material has yet been found. The Borgmassivet Intrusive Suite in the Ahlmannryggen-Borgmassivet (Figure 7.10) are mantle derived units with consistent Nd T_{DM} ages of 2.0 Ga to 2.1 Ga (Moyes *et al.*, 1995). The Hogfonna Formation sediments from the Ritscherflya Supergroup are interpreted to have been laid down around *ca.* 1.1 Ga, but these rocks also have *ca.* 2.1 Ga Nd T_{DM} ages (Moyes *et al.*, 1995; Moyes and Knoper, 1995). The younger 520 Ma Brattskarvet intrusive suite has Nd T_{DM} ages between 1.8 Ga and 1.9 Ga (Moyes *et al.*, 1993b). Geochemical signatures indicate that this unit formed by remelting of antique crust (Moyes *et al.*, 1993b).

U-Pb SHRIMP zircon data from paragneisses in this investigation also provide evidence of older material ranging back to 2.05 Ga (Chapter 4). These data are supported by metasediments in the high-grade gneisses of the Heimefrontfjella, which also show older zircon ages ranging back to ca. 2.1 Ga (Arndt *et al.*, 1991).

These independent lines of evidence suggest the involvement of *ca.* 2.1 Ga crust in the evolution of WDML. The only crustal material that is exposed in WDML, and which is older than the Ritscherflya Supergroup and the high-grade gneisses, is the Archaean material exposed at Annandagstoppane (Figure 7.10). This granitoid gneiss has been dated at *ca.* 3.0 Ga (Barton *et al.*, 1987) and this material does not explain the isotopic signatures observed in the Ritscherflya Supergroup or the high-grade gneisses. It is possible that the East Antarctic craton, which has been postulated towards the southeast of the high-grade gneisses, has a component of *ca.* 2.1 Ga crust attached.

Crustal Domains in WDML

To better understand the significance of the Sr and Nd isotopic data generated during this investigation, an understanding of the crustal evolution within WDML is required. To do this isotopic data from previous investigations have been collated and recalculated using similar models where required. Data used here has been obtained from the Gjelsvikfjella and Muhlig-Hoffmanfjella (Moyes, 1993), the eastern H.U.Sverdrupfjella (Moyes *et al.*, 1993a and b), the Ahlmannryggen-Borgmassivet (Moyes *et al.*, 1995), and the Kottas, Sivorg and Vardeklettane (Arndt *et al.*, 1991) geological domains (see Figure 7.10). Comparison of the data from the northern Kirwanveggen geological domain with other high-grade gneiss domains in WDML indicates that these areas have similar isotopic characteristics (Figure 7.10). The only unit that shows significant differences is the younger *ca.* 520 Ma Brattskarvet granitoid. Nd T_{DM} data from the *ca.* 1100 Ma high-grade gneisses ranges between 1192 Ma and 2055 Ma. Model age data for the Brattskarvet granitoid ranges between 1745 Ma and 2004 Ma.

The Ritscherflya Supergroup sediments (Hogfonna Formation) have distinctly different Nd T_{DM} ages that range between 1905 Ma and 2184 Ma. These ages tend to be somewhat older than the ages from the *ca.* 1100 Ma high-grade gneisses, and slightly older than the *ca.* 520 Ma Brattskarvet granitoid depleted mantle ages. Unfortunately no data are available from the Archaean cratonic fragment exposed at Annandagstoppane. A diagram summarising the Nd T_{DM} data is presented in Figure 7.10.

Although WDML can be divided into many geological domains based on geographical and geological distinctions, the Nd isotope data does not reflect these small domains. Rather, the isotope data relates more to the broad geological regions encountered within WDML. Within the *ca.* 1100 Ma high-grade gneisses the Nd isotopic signatures are similar. No evidence is present that indicates the existence of crustal domain boundaries within this portion of the high-grade gneiss terrane. Crustal domain boundaries can however be placed between the high-grade gneisses and the Ritscherflya Supergroup based on their isotopic signatures. Another important boundary can be inferred between the Ritscherflya Supergroup and the Archaean cratonic fragment at Annandagstoppane although isotopic data are not available for comparison. This boundary is defined on the basis of the large age differences between the *ca.* 3000 Ma granitoid gneisses and the *ca.* 1130 Ma volcano-sedimentary sequence.

Implications for Crustal Evolution of the Northern Kirwanveggen

The isotopic data presented here provide significant insights into the evolution of the different lithotectonic units exposed in the northern Kirwanveggen. Combined with precise age dating, structural data, field relationships and metamorphic histories, an evolution for this crustal material can be established. The current evidence from the biotite-garnet migmatite gneiss indicates that this unit comprises supracrustal material and suggests a sedimentary protolith. A maximum age of formation for the biotite-garnet migmatite gneiss is *ca.* 1390 Ma (see Chapter 4). This age could be younger due to the presence of *ca.* 1260 Ma zircon rims, but the preferred interpretation is that these rims were developed in-situ. The mixed detrital zircon age populations ranging from *ca.* 1300 Ma to *ca.* 2050 Ma indicate the involvement of young juvenile material mixed with antique crust. As such the Nd T_{DM} ages are expected to represent mixed ages falling between the age of sedimentation and the older crustal source. The biotite-garnet migmatite gneiss is the oldest unit recognised in the northern Kirwanveggen and has undergone all phases of deformation. It is intensely deformed and tectonic interleaving may result causing this unit to comprise a potential mixture of units of different origin. It is quite possible that sedimentary, volcanic and plutonic components be encountered within this lithotectonic unit.

The quartzofeldspathic lithotectonic unit has not been dated during this investigation, but is constrained by intrusive-structural relationships between the biotite-garnet migmatite gneiss and the intrusive leucogneiss. The quartzofeldspathic gneiss is formed early during the *ca.* 1100 Ma tectono-metamorphic cycle. The low ε Nd values obtained for this lithotectonic unit, although limited, indicate that it comprises juvenile material. The Nd isotopic signatures suggest that it is either a direct differentiate of mantle material, or that it forms from rapidly recycled material with little crustal residence time. It is uncertain if this unit is an extrusive or intrusive magmatic body.

The intrusive leucogneiss and the megacrystic orthogneiss are granitoid units that intrude the supracrustal sequence in the northern Kirwanveggen during the *ca.* 1100 Ma tectono-metamorphic cycle. The ε Nd and Sr values for these units are low and suggest the derivation of these units from direct differentiates of mantle material or from rapidly recycled material with little crustal residence time. The Nd isotopic data mitigates against the generation of granitic liquids from older continental crustal sources.

The kyanite-bearing leucogneisses have different isotopic signatures from the other intrusive units from the northern Kirwanveggen. The variable geochemical signatures, coupled with the aluminous nature of the rocks suggest that these units formed as partial melts during metamorphism. The high Sr values and elevated Nd values supports the derivation of these units through partial melting.

Relationships between Geological Terranes in WDML

The first issue that has to be addressed when invoking a crustal evolution model for WDML is the relationships between the major geological terranes. In WDML three distinct geological terranes are recognised. These comprise, firstly the Archaean cratonic fragment exposed at Annandagstoppane in the west-northwest of WDML. The second terrane is the Ritscherflya

Supergroup exposed in the Ahlmannryggen-Borgmassivet region. These rocks have been dated at *ca.* 1100 Ma based on the Borgmassivet Intrusive Suite (Moyes *et al.* (1995) and unpublished U-Pb zircon ages from a volcaniclastic unit in the Raudberget Formation of the Ritscherflya Supergroup (unpublished data of Moyes and Knoper). The third major geological terrane comprises the high-grade gneisses exposed in the northeast of WDML, and includes the northern Kirwanveggen. No contact relationships between these three units are exposed. Geophysical modelling has, however, provided evidence that no geological break occurs between the Annandagstoppane and Ahlmannryggen-Borgmassivet geological domains (Corner, 1994). The modelling has also provided evidence of thrusting of the high-grade gneisses onto the Archaean craton where the boundary is delineated by the Pencksokket-Jutulstraumen glacial system.

It has been speculated that the Archaean fragment in WDML is part of the Kaapvaal-Zimbabwe Craton in Southern Africa (Groenewald *et al.*, 1991; Groenewald *et al.*, 1995 amongst others). These ideas are based on the close proximity of the Kalahari Craton to the Annandagstoppane granite in Gondwana reconstructions and the remarkable similarity of the age and lithology of the Ritscherflya Supergroup and the Umkondo Group in Zimbabwe. Unfortunately the inter-relationships between these supercontinental fragments are not preserved. It could therefore also be speculated that the WDML Archaean fragment is a portion of unrelated cratonic material that has been emplaced into its current geographical location by younger tectonism (i.e. autochthonous).

Previous workers have proposed that the Ritscherflya Supergroup accumulated on an Archaean platform where the Annandagstoppane granite provides exposure of this platform (Wolmarans and Kent, 1982; Groenewald *et al.*, 1995). Although there is limited data from geographically diverse locations within the Ritscherflya Supergroup, the current data suggest the source extraction age from the mantle was *ca*. 2.1 Ga (see discussion above and Moyes *et al.*, 1995). These data suggest the derivation of the sediments from a *ca.* 2.1 Ga crustal source that is not exposed, or identified within WDML. None of the current data from the Ritscherflya Supergroup provide evidence for any involvement of Archaean crustal material in its formation.

The Ritscherflya Supergroup is separated from the high-grade gneisses by the Pencksokket-Jutulstraumen glacial system. Geophysical modelling, along with field relationships, suggests a significant crustal boundary occurs along this glacial system (Corner, 1994). Evidence of increased tectonism has been reported along the northeastern flank of the Pencksokket-Jutulstraumen within the Ritscherflya Supergroup (Wolmarans and Kent, 1982; Speath and Fielitz, 1987). K-Ar white mica ages from mylonites in steep shears within Straumsnutane provide ages of *ca.* 525 Ma (Peters, 1989). Although these ages may not represent deformation ages, but rather reflect cooling ages, a significant thermal event must be invoked at *ca.* 525 Ma. On the northeastern side of the Pencksokket-Jutulstraumen, the Midbresrabben diorites crop out close to the glacial confluence. Unpublished Rb-Sr whole-rock ages for six samples provide an age of 788 ± 110 Ma (Moyes, *pers. comm.*). This age is younger than the ages obtained from the high-grade gneisses in the H.U.Sverdrupfjella (Moyes *et al.*, 1993a) and may be related to a period of mafic magmatism and dispersion. This period would relate well to the break-up of the Rodinia Supercontinent prior to Gondwana Supercontinent amalgamation during the *ca.* 500 Ma event. It is also possible that this age represents partial resetting of this system during a younger tectonic event. Support for this interpretation is obtained from the Roerkulten granite in the eastern H.U.Sverdrupfjella from which Rb-Sr whole-rock ages range around 850 Ma (Moyes, *unpubl.*) while the U-Pb SHRIMP zircon data provides an age of 1103 ± 17 Ma (Harris *et al.,* 1995.).

In the southern Kirwanveggen the high-grade gneisses are tectonically juxtaposed against the Urfjell Group metasediments. This area is unique, for WDML, in that two geologically distinct terranes are tectonically juxtaposed, yet the contact relationships are preserved. The age of sedimentation for the Urfjell Group has been constrained between 688 Ma and 541 Ma based on Rb-Sr whole-rock and muscovite samples (Moyes *et al.*, 1997). This implies that tectonism juxtaposing these geological terranes is post-Urfjell Group deposition. Nd data from the sediments indicate that the Urfjell Group is isotopically very similar to the high-grade gneisses, but distinct from the Ritscherflya Supergroup (Moyes *et al.*, 1997). The Urfjell Group was interpreted as being composed of recycled rocks very similar in isotopic composition to the high-grade gneisses.

The above discussions outline the problematic nature of the major terrane boundaries present within WDML. Evidence exists that these boundaries have been significantly affected by later tectonism. When invoking a crustal evolution model for this region it cannot be assumed that these terranes have remained in their current geographical position since their formation. The age relationships seen in this region and some of the terrane similarities may suggest that these regions are probably more autochthonous than allochthonous with respect to one another.

Model for WDML Evolution Based on Data from the Northern Kirwanveggen

A crustal evolution model for WDML has been presented by Groenewald *et al.* (1995) based on constraints from previous investigations within the area, and data obtained during this investigation support the proposed model. The intention of this section is to incorporate the new data from the northern Kirwanveggen into the existing data to provide tighter constraints for the already existing model.

There is no evidence of the involvement of Archaean crust in the formation of the high-grade gneisses in the northern Kirwanveggen. There is evidence, however, that older crustal material is involved, but the lines of evidence discussed in an earlier section suggest that this crustal material was *ca.* 2.1 Ga in age. The data presented here indicate that the majority of the material incorporated within the high-grade gneiss terrane comprises material that has little crustal residence time. Accretion of young material and the derivation of new juvenile material during the *ca.* 1100 Ma tectono-metamorphic cycle is suggested from the data (see Figure 7.11). P-T conditions for the *ca.* 1100 Ma tectono-metamorphic cycle support the accretionary nature for this event. No evidence for mafic magmatism or break-up between 1000 and 800 Ma has been recorded in the northern Kirwanveggen. Re-working of the high-grade gneisses during the younger *ca.* 550 Ma tectono-metamorphic cycle, with no addition or accretion of new crustal material is also indicated by the data. Jacobs *et al.* (1998) identified major tectonism and magmatism between 650 Ma and 450 Ma in central Dronning Maud Land. The data suggest an increasing influence of the *ca.* 550 Ma tectono-metamorphic cycle towards the east in WDML. Disruption of lithologies takes place during the *ca.* 500 Ma tectono-metamorphic cycle, which results in rapid uplift and exhumation of the northern Kirwanveggen high-grade gneiss domain. This tectono-metamorphic cycle results in the juxtaposition of terranes formed at different crustal depths. The Urfjell Group sediments were deposited during this tectono-metamorphic cycle, and these sediments were derived from material similar to that within the high-grade gneisses. Contacts between the high-grade gneisses and the Urfjell Group are, however, tectonic. The exact evolutionary relationship between the Archaean fragment, the Ritscherflya Supergroup and the Maud Belt is equivocal. The current investigation does not address these issues with respect to the evolution of WDML.

Neumayerskarvet in an East Antarctic Context

The geological evolution of Neumayerskarvet and the northern Kirwanveggen have important implications on the evolution of East Antarctica. This section reviews the implications of the current study on the present thinking in terms of supercontinental reconstructions that involve WDML. The presence of high-grade deformation at *ca.* 1100 Ma supports the existence of a Grenvillian age belt within this portion of East Antarctica (Moores, 1991;Dalziel, 1991; Storey *et al.*, 1994). Isotope data suggest an accretionary and juvenile nature for this belt which supports the collisional orogeny proposed by several workers (Groenewald *et al.*, 1991; Jacobs *et al.*, 1993; Groenewald *et al.*, 1995). The Grenvillian age deformation in the northern Kirwanveggen provides evidence of NW-SE oriented transport directions (Antarctic azimuth) and supports accretion onto an Archaean craton that lies northwest of the Maud Belt (Groenewald *et al.*, 1991; Groenewald *et al.*, 1995). An inconsistency that arises when reviewing the northeastern and southwestern extensions of the Maud Belt is the differences of the kinematic signatures between the Heimefrontfjella and the Kirwanveggen-H.U.Sverdrupfjella high-grade gneisses (Jacobs, 1991; Jacobs *et al.*, 1993 and 1996; Grantham *et al.*, 1995; Jackson and Jacobs, 1995). Jacobs *et al.* (1993) have suggested that transport directions during the Grenvillian period were in a NE-SW direction (Antarctic azimuth) from work within the Heimefrontfjella. Further focussed work in key areas would be required to resolve these problems.

It has been shown in this study that the *ca.* 500 Ma event, often referred to as the Pan-African in a regional context (Jacobs *et al.*, 1995; Moyes and Groenewald, 1996), influences the Grenvillian age orogenic belt. Although the exact expression of the Pan African remains elusive within the northern Kirwanveggen, the current data provides some constraints on the nature of this event. The decreasing effect of the Pan African from central Dronning Maud Land (CDML) through WDML and into the Natal-Namaqua Mobile Belt has been proposed by previous workers and is supported through this study (Jacobs *et al.*, 1995 and 1996). Deformation of the Urfjell Group sediments in the southern Kirwanveggen, along with the juxtaposition of different crustal levels across the Pencksokket-Jutulstraumen glacial system, indicates significant reworking during the Pan African period (Peters, 1989; Jacobs *et al.*, 1995; Moyes *et al.*, 1997). These data imply that caution should be exercised when viewing the different crustal domains of WDML in terms of their geographical position, although an autochthonous relationship is possible. Different crustal levels are exposed across the Heimefront Shear Zone (HSZ) in the Heimefrontfjella, and isotope data support a significant Pan African age of movement along this structure. Previous workers have proposed that the HSZ is a significant Grenvillian age structure (Jacobs, 1991; Jacobs *et al.*, 1993), but also recognise the presence of later Pan African reworking through the isotopic data (Jacobs, 1991; Jacobs *et al.*, 1995; Jacobs *et al.*, 1996). Knowing that the HSZ has been active during the Pan African poses a problem with regard to the significance of the kinematic indicators and geometries within the structure. The previous workers propose that the structural elements within the HSZ are a reflection of signatures of the Grenvillian event. It is, however, possible that the structural elements preserved within the shear zone provide information relating to the final movement experienced by this structure. Further work may resolve these questions and assist in reconciling the kinematic geometries within the high-grade gneisses of WDML.

Recent work in CDML has provided evidence of significant Pan African magmatism and deformation within the Grenvillian gneisses (Jacobs *et al.*, 1998). These data again support the decreasing effect of the Pan African towards the west of Dronning Maud Land within East Antarctica. The effects of the Ross orogeny (*ca.* 500 Ma) from the Transantarctic Mountains through the Shackleton Range may also have a significant influence on WDML (Goodge *et al.*, 1993; Kleinschmidt and Buggisch, 1993; Buggisch *et al.*, 1994).

The poly-metamorphic nature of the high-grade gneisses in the northern Kirwanveggen complicates the interpretation of metamorphic conditions for all these events. The current study highlights the presence of disequilibrium between assemblages preserved in these rocks. If the disequilibrium was not detected between certain assemblages of the kyanite-bearing leucogneisses then high-pressure metamorphism would have been suggested for this terrane. Although the kyanite-bearing leucogneisses do not record the entire history of the Neumayerskarvet high-grade gneisses they do highlight the importance of detailed petrographic and mineral chemical studies. Whether or not the high-pressure conditions previously recorded in portions of this terrane (Groenewald and Hunter, 1991; Ferrar, 1995; Grantham *et al.*, 1995) are realistic cannot be evaluated through the current work. It does, however, suggest that these high-pressure assemblages should be reviewed to ensure that these conditions are realistic for this high-grade terrane.

Isotopic data presented in this study, coupled with previous investigations (Arndt *et al.*, 1991; Jacobs *et al.*, 1995; Moyes *et al.*, 1995) indicate the presence of a *ca.* 2.1 Ga source within WDML. It is possible that the portion of the East Antarctic Craton involved during the Grenvillian collisional orogeny comprised *ca.* 2.1 Ga crustal material. The Maud Belt may represent a collisional zone between an Archaean craton (Kalahari Craton?) in the northwest (Antarctic azimuth) and a *ca.* 2.1 Ga cratonic block (East Antarctic Craton?) within the southwest, while incorporating juvenile (arc?) crust accreted during the process.

Regional Implications

A Pan-African suture zone along which east and west Gondwana amalgamated is postulated within DML (see discussions in Moyes *et al.*, 1993a). The geological data from Neumayerskarvet indicates limited Pan-African deformation in comparison to the effects of the Grenvillian-aged deformation. Regional data does provide some evidence of late structures developed during the Pan-African but a major suture zone is not recognised in this portion of WDML. The placement of a major suture zone of this nature is most likely to occur eastwards of Neumayerskarvet. Increasing effects of Pan-African deformation and magmatism are seen within CDML (Jacobs *et al.*, 1998). Based on the data from Neumayerskarvet the Pan-African signature suggests limited exploitation of earlier fabrics in which the pre-existing crustal material is reworked by continental-style tectonics distal to the Pan-African suture/collisional/accretionary zone. The increasing effects of the Pan-African observed towards the west of Neumayerskarvet suggest that the suture zone is being approached, while almost no effects are recorded within the Natal-Namaqua Belt in South Africa. Neumayerskarvet indicates that major accretion of juvenile material and crust formation took place during the Grenvillian-aged period. The Pan-African resets and reworks the pre-existing crustal material, which is also supported by the data of Jacobs *et al.* (1998).

The preservation of high-grade assemblages with less retrogression observed than those within the central Kirwanveggen suggest that this region has escaped some of the effects of a later tectono-metamorphic event. Neumayerskarvet may be a low strain zone within a reworked Pan-African belt, but this is not substantiated though the available regional data. The exact timing of this event is as yet unresolved. This study suggests that NW-SE tectonic transport directions were experienced during the Grenvillian-aged period. Data from H.U.Sverdrupfjella support this interpretation (Grantham et al., 1995; Groenewald et al., 1995) but, as previously discussed, it is not supported by data from the Heimefrontfjella or the Natal-Namaqua regions (Jacobs *et al.*, 1993, 1996). At Neumayerskarvet these fabrics pre-date *ca.* 1070 Ma and are representative of Grenvillian-age kinematics. Reconciliation of the data from these regions is required in order to resolve these issues and better understand the evolution of this portion of East Antarctica.

CONCLUSIONS

- Geochemical data from the high-grade gneisses in the northern Kirwanveggen are similar to data reported from other regions of high-grade gneisses in WDML.
- Protolith information for the lithotectonic units under investigation are supported by the geochemical and isotopic data. The biotite-garnet migmatite gneiss has a sedimentary protolith whereas all the other lithotectonic units are magmatic in origin.
- Nd isotope data indicate that the majority of the source material for the lithotectonic units represents juvenile material with little crustal residence time.
- Several lines of evidence suggest the involvement of *ca.* 2.1 Ga crust in the evolution of WDML.
- The isotopic data suggest that major accretion of juvenile material, as either rapidly recycled material or as direct differentiates, occurred during the ca. 1100 Ma tectono-thermal cycle.
- The younger ca. 550 Ma tectono-metamorphic cycle did not involve new crust formation but rather re-worked the pre-existing crustal material in the northern Kirwanveggen. Increased effects of this cycle are seen in the H.U.Sverdrupfjella and in central Dronning Maud Land.

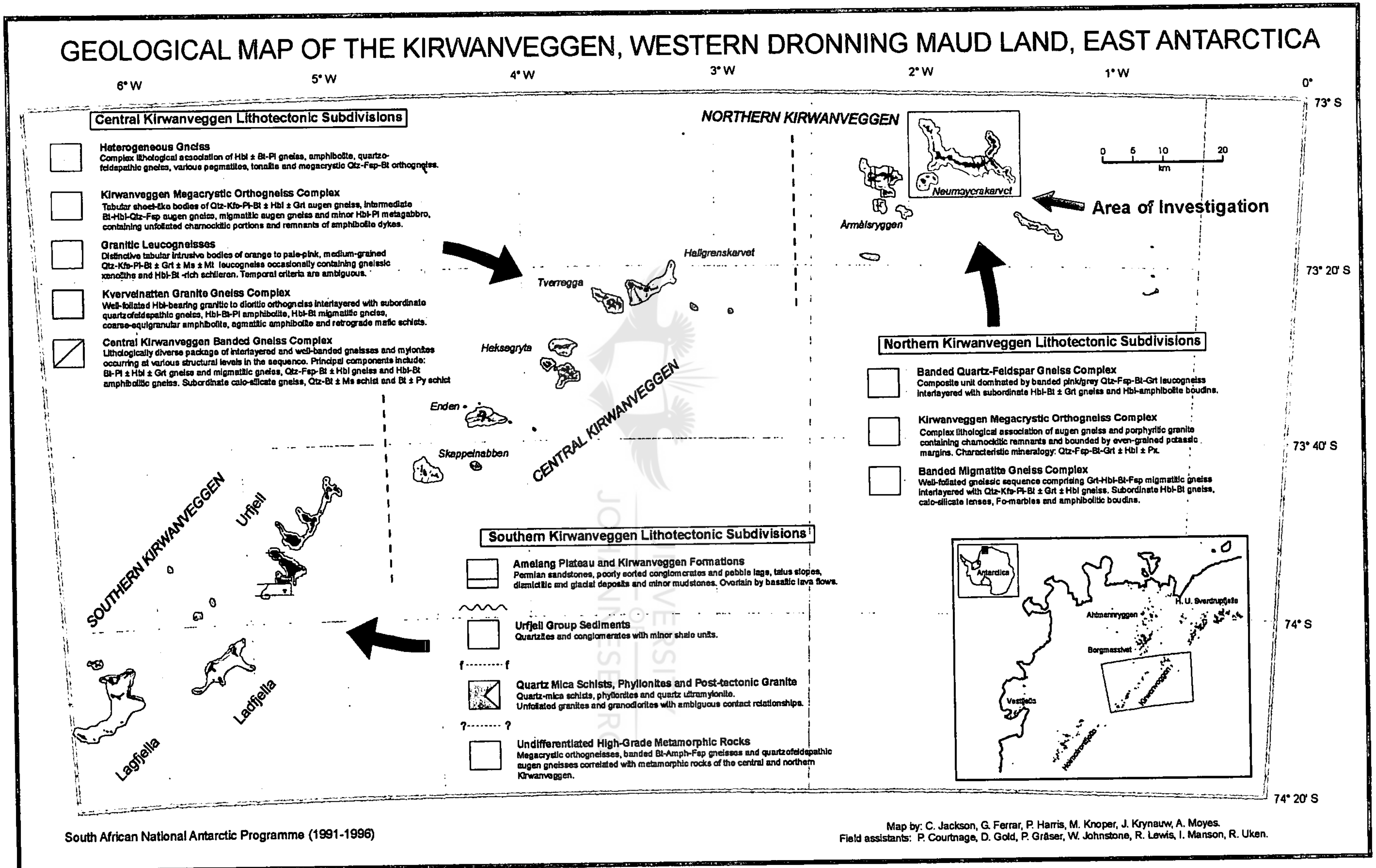

FIGURE 7.1. Geological map of the Kirwanveggen in western Dronning Maud Land, Antarctica. The subdivision of the northern, central and southern Kirwanveggen outcrop patterns (in black on the map) and the associated lithotectonic units are illustrated. The Neumayerskarvet outcrop pattern, which is the major area of focus in the northern Kirwanveggen, is outlined for location purposes.

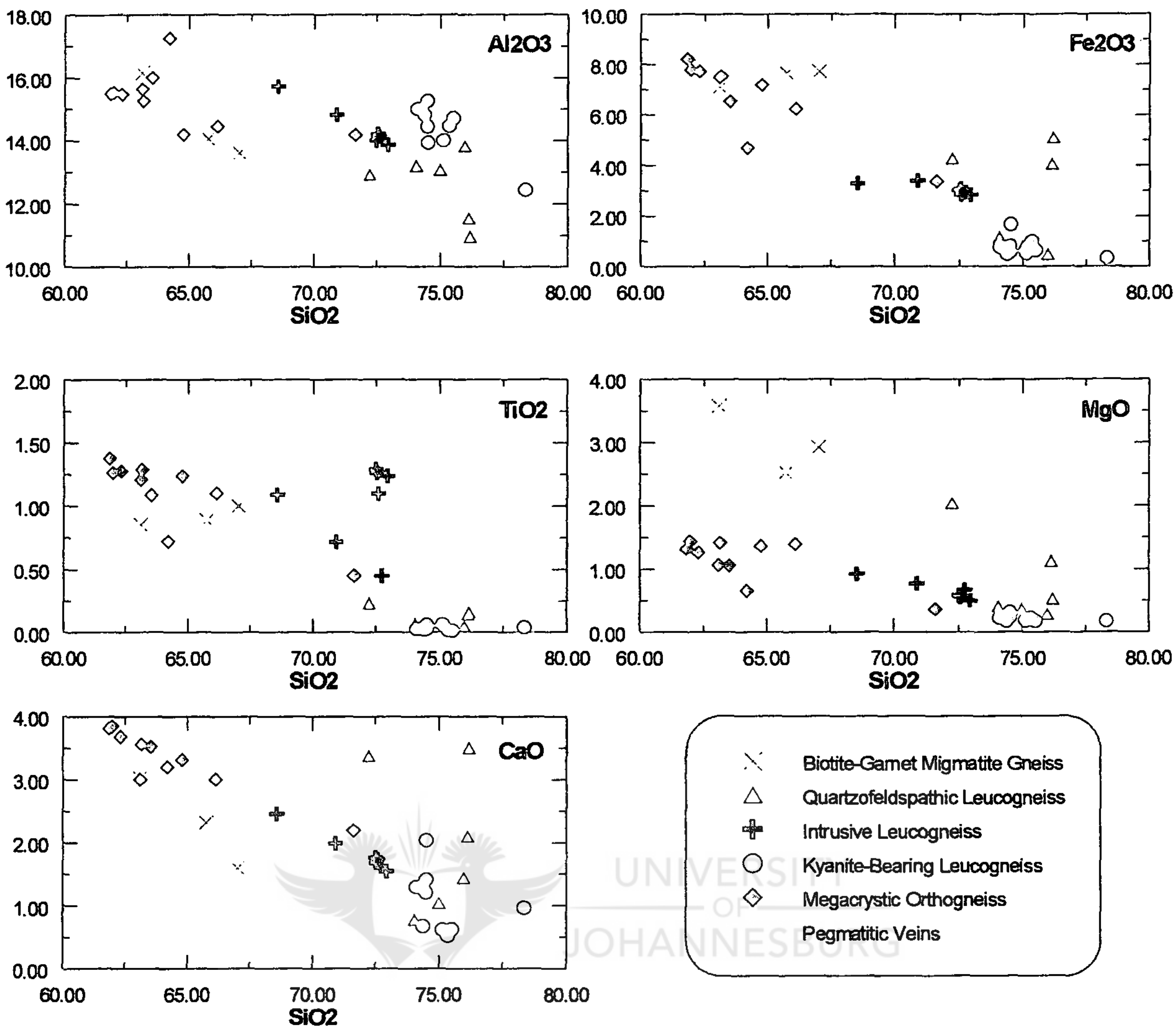

FIGURE 7.2 Harker diagrams for gneisses at Neumayerskarvet in the northern Kirwanveggen, WDML.

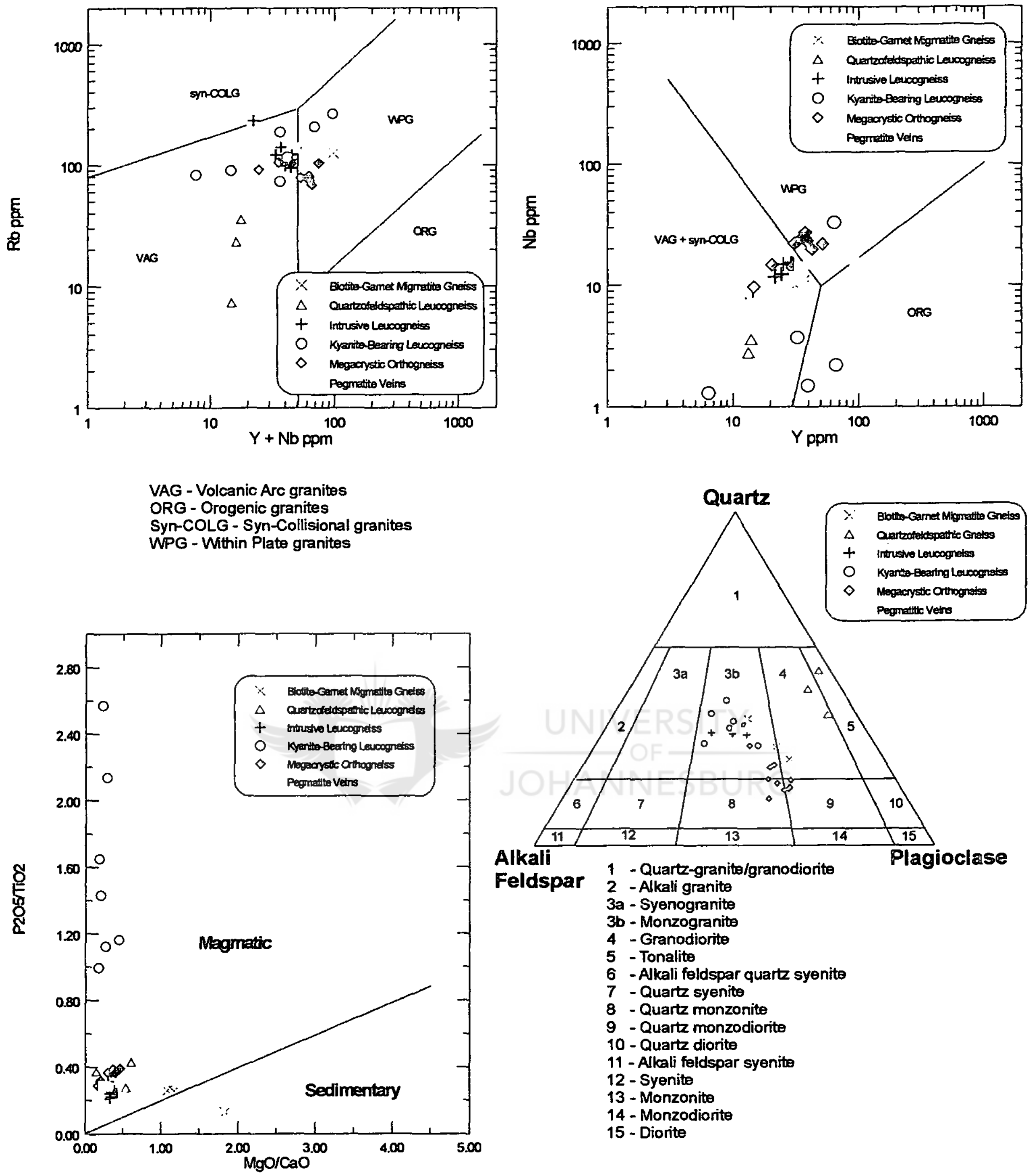

Figure 7.3. Geochemical discrimination diagrams for the high-grade gneisses from the northern Kirwanveggen. These diagrams are from Pearce *et al.* (1984), Werner (1987) and Streckeisen (1976). The data is discussed in detail within the text.

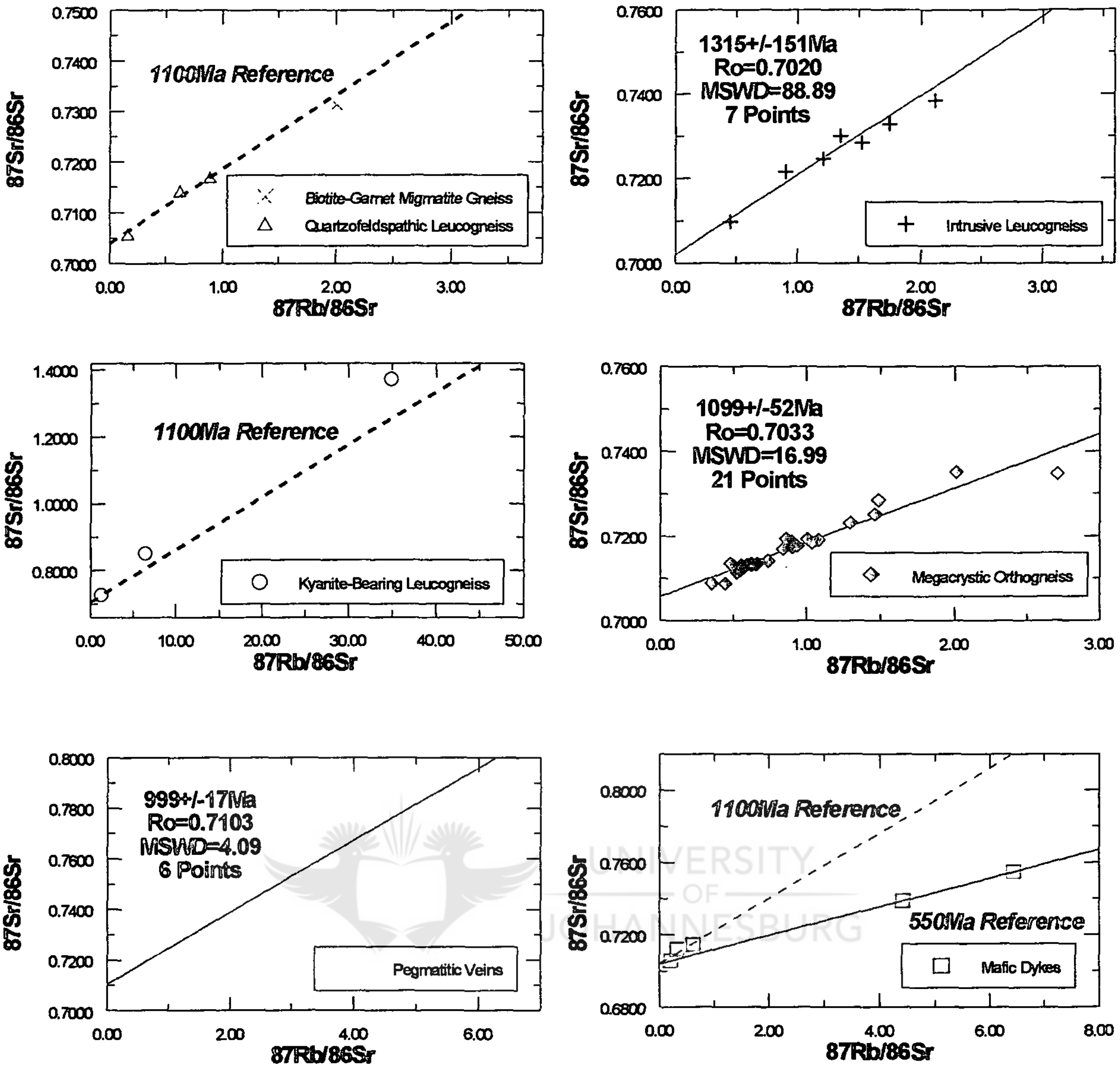

Figure 7.4 Rb-Sr whole-rock isotopic data for samples from Neumayerskarvet in the northern Kirwanveggen. Description of the samples and the age significance of these isochron diagrams are discussed in the text. Data presented here are provided in Table 7.2.

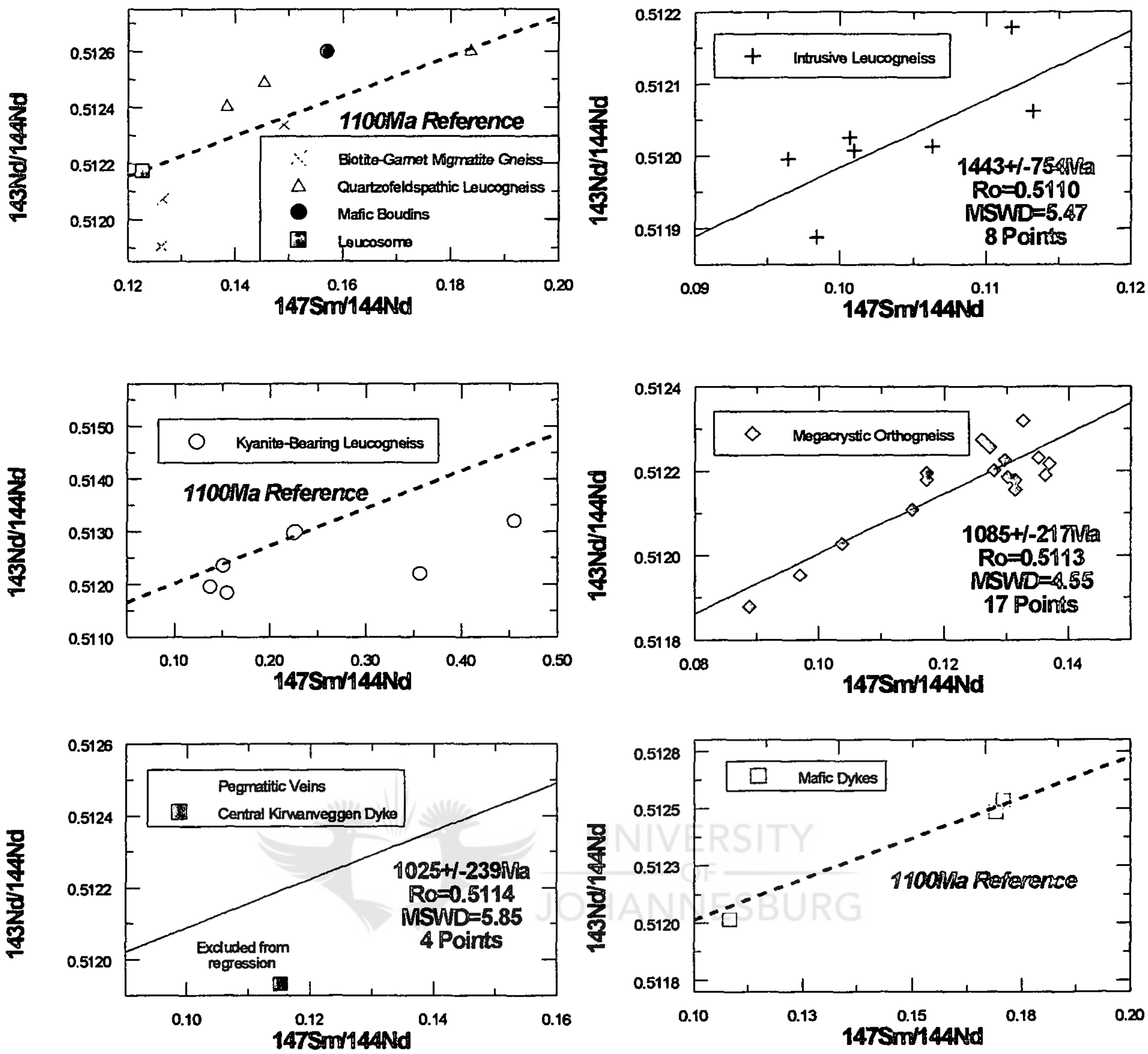

FIGURE 7.5. Sm-Nd whole-rock data for samples from Neumayerskarvet in the northern Kirwanveggen. Description of the samples and the age significance of these isochron diagrams are discussed in the text. Data presented here are derived using the data in Table 7.3.

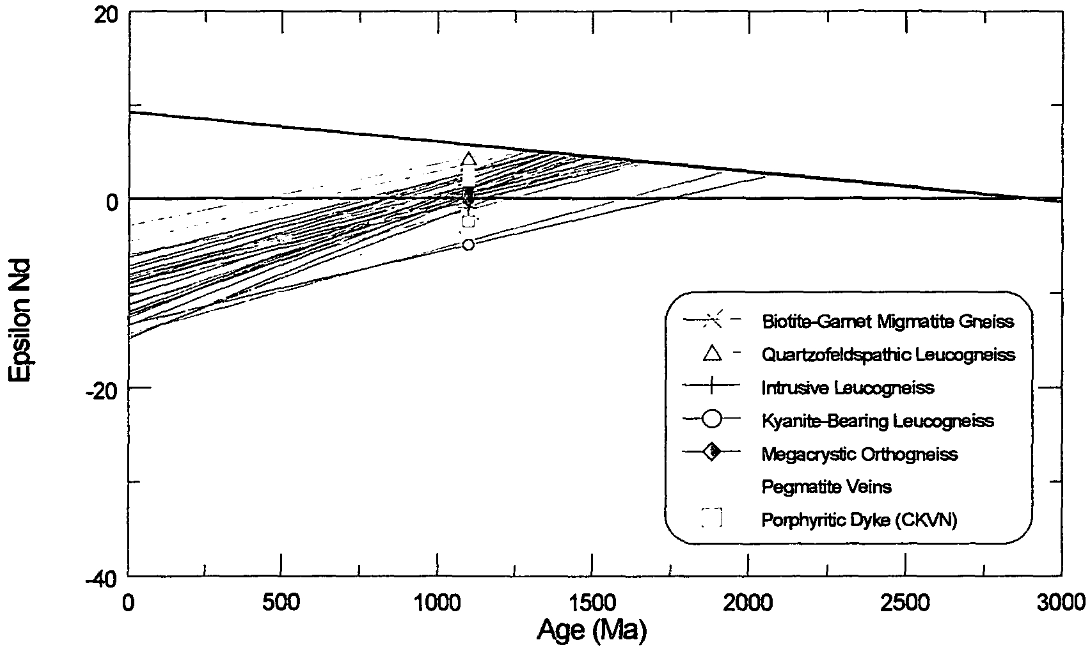

FIGURE 7.6. Nd evolution diagram for the high-grade gneisses from Neumayerskarvet in the northern Kirwanveggen. Ages of formation are based on U-Pb SHRIMP zircon work and structural-intrusive relationships (see Chapters 3 and 4), and have been plotted at 1100 Ma in this diagram.

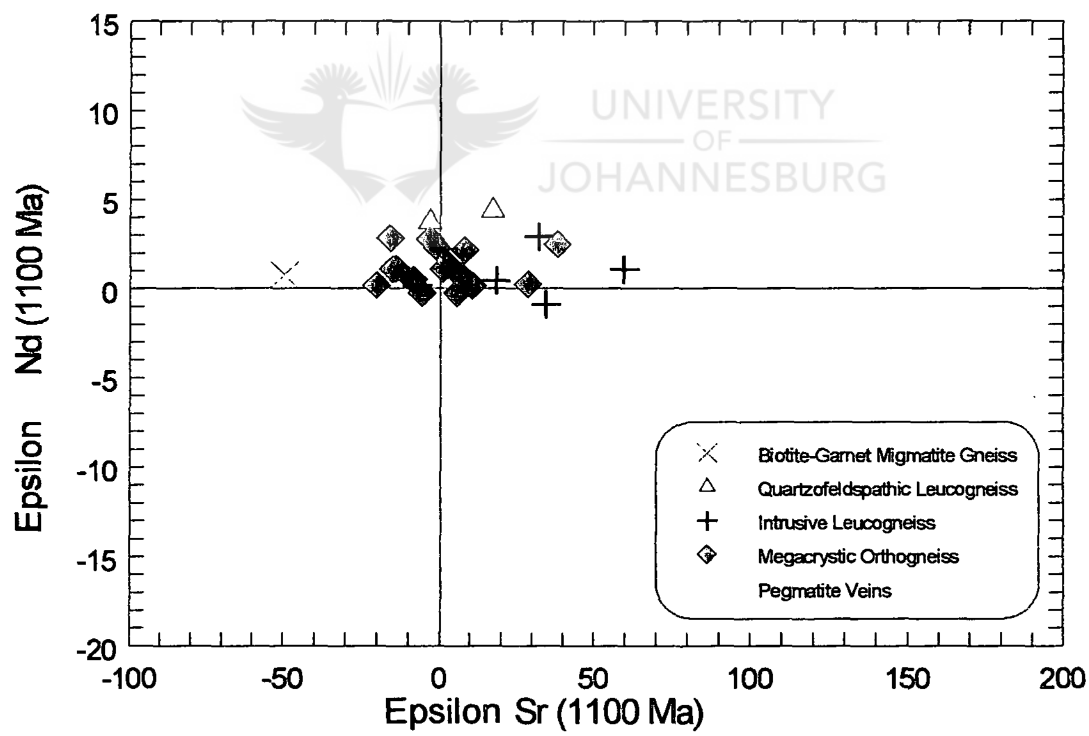

FIGURE 7.7 Epsilon values of Nd and Sr of the high-grade gneiss samples used during this investigation. Data used here are provided in Tables 7.2 and 7.3. The isotope values are expressed in terms of epsilon values after correction for decay. The low epsilon Nd and Sr values for these rocks suggest the derivation of these units from direct differentiates of mantle material or from rapidly recycled material with little crustal residence time.

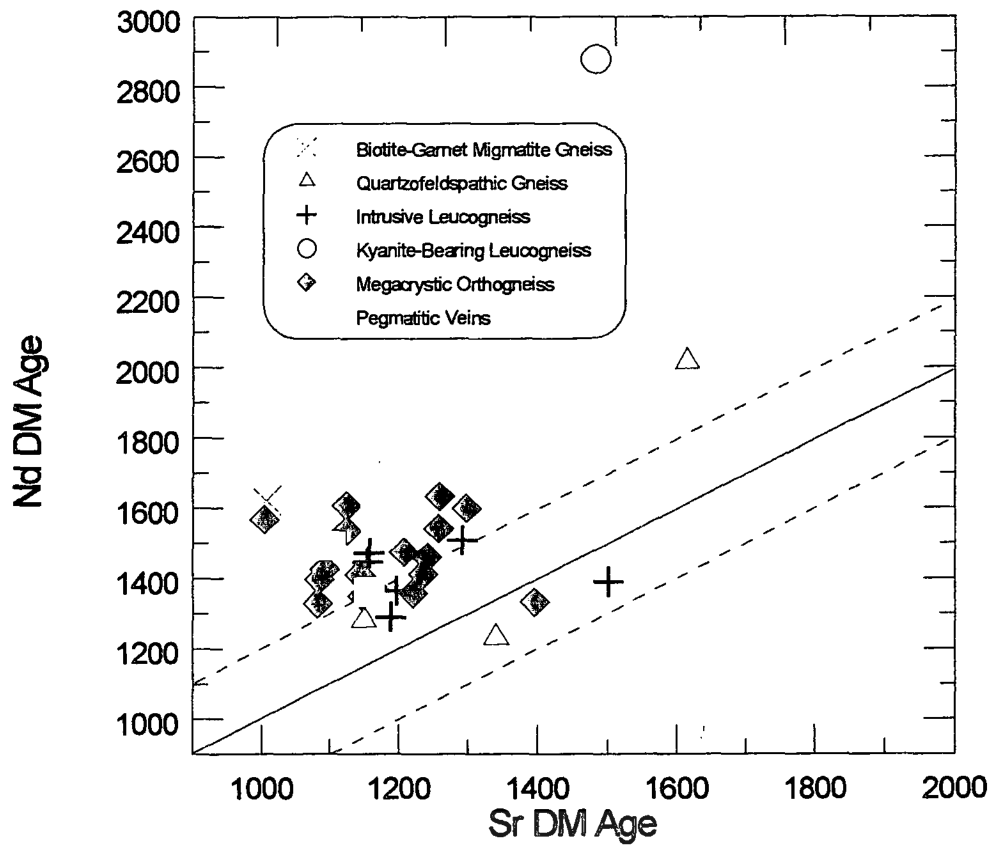

FIGURE 7.8. Comparison between Nd model ages and Sr model ages obtained from gneisses at Neumayerskarvet in the northern Kirwanveggen. In most cases Nd model ages tend to be slightly older than the Sr model ages. Sr model ages are similar to the intrusive ages interpreted from U-Pb zircon SHRIMP data for the same lithotectonic units.

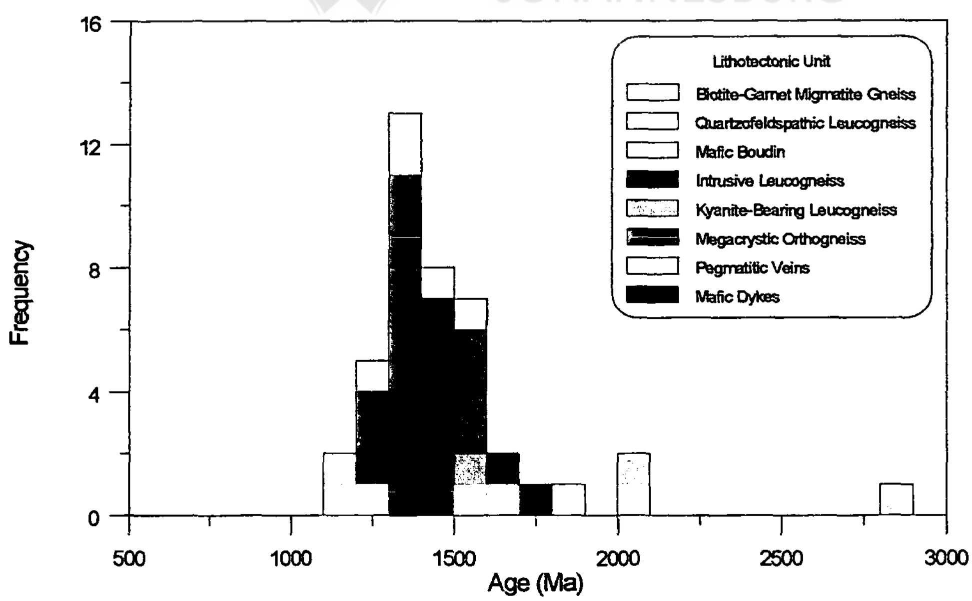

FIGURE 7.9. Histogram plot of Nd model ages from all data collected during this investigation. These data are compared to similar Nd data from other domains in WDML in Figure 7.10.

GEOLOGICAL MAP OF WESTERN DRONNING MAUD LAND, ANTARCTICA

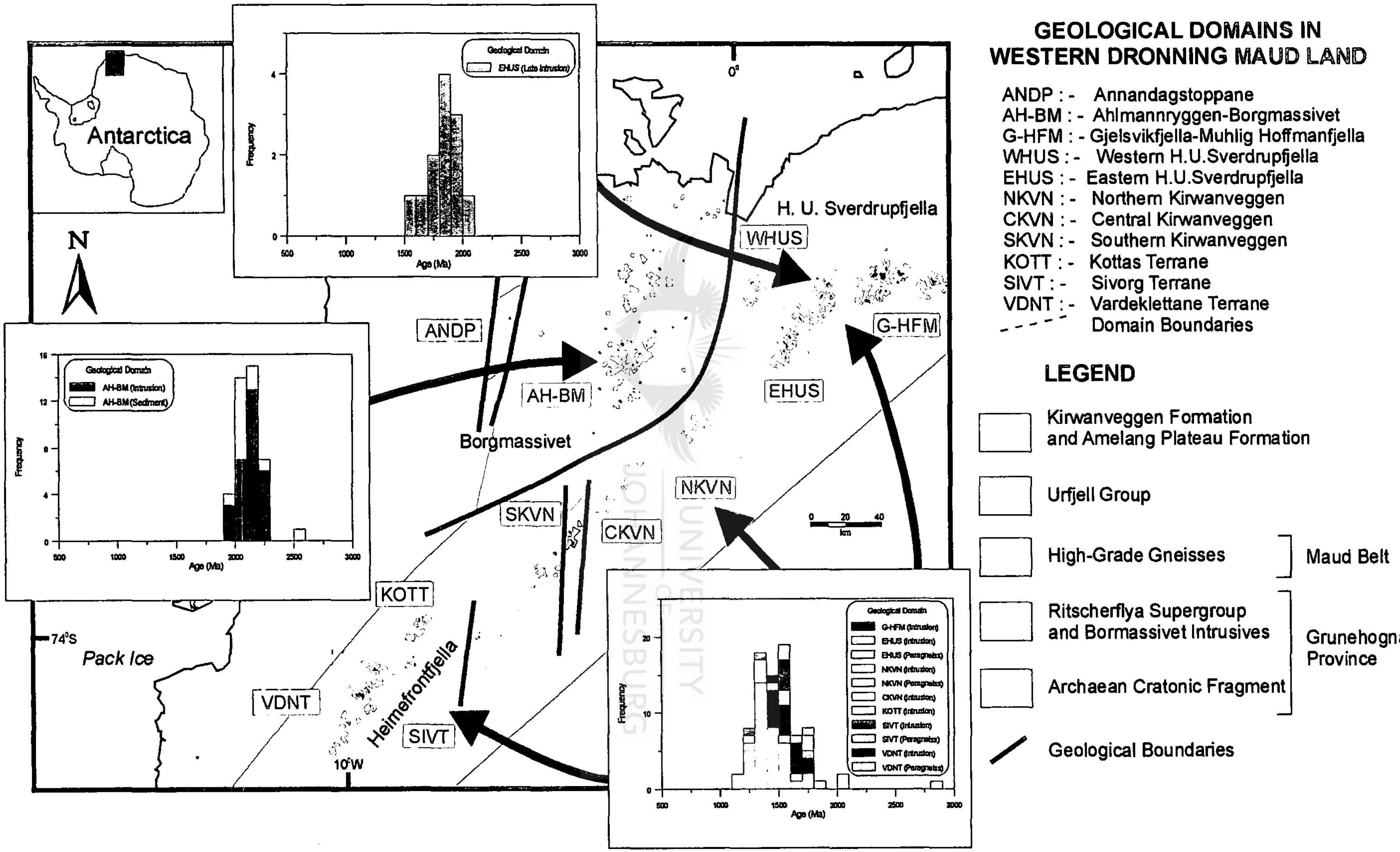

FIGURE 7.10. Geological maps of western Dronning Maud Land, Antarctica (WDML). The different geological domains and their boundaries distinguished in WDML are illustrated on this diagram. Nd model ages for similar domains are provided in the diagram and reference sources are provided in the text. Differences in the Nd model ages have been highlighted by separating those domains that differ from one another within the current data set. Further discussions of this data are provided in the text.

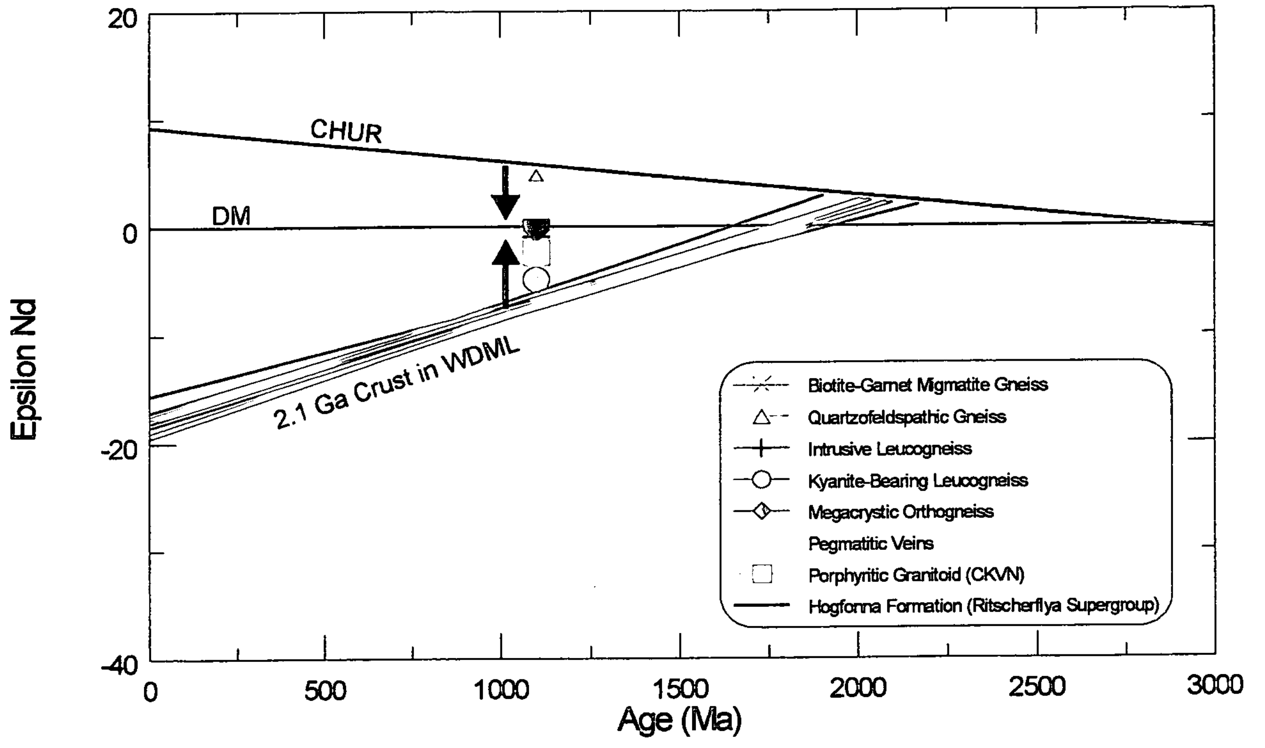

FIGURE 7.11. Nd evolution diagram of the high-grade gneisses under investigation from the northern Kirwanveggen. Included on the diagram are the Nd data from the Hogfonna Formation in the Ritscherflya Supergroup for comparison. The Hogfonna Formation data is from Moyes *et al.* (1995). The data presented here suggest the accretion of material with little crustal residence time, and the derivation of new juvenile material during the *ca.* 1100 Ma tectono-metamorphic cycle. See text for further discussion.

Table 7.1 Geochemical data for the high-grade gneisses used during this investigation.

Sample	PH92031	PH93151	PH93161	PH92050	PH92054	PH92055	PH93141	PH93194	PH92063	PH93146	PH93147	PH93148	PH93149	PH93155	PH93163	PH92020	PH92057
Rock	BGM	BGM	BGM	QFG	QFG	QFG	BOU	BOU	ILG	ILG	ILG	ILG	ILG	ILG	ILG	KBL	KBL
SiO2	65.77	63.11	67.04	76.19	72.22	76.15	50.41	54.58	72.59	72.95	72.51	72.55	70.9	72.74	75.14	74.11	75.36
Al2O3	14.06	16.15	13.61	10.96	12.92	11.55	13.72	15.4	14.14	13.87	14.01	14.22	14.83	14.04	14.01	15.01	14.46
Fe2O3	7.64	7.12	7.74	5.11	4.29	4.07	10.84	12.73	2.85	2.84	3.04	3.11	3.41	2.96	0.53	0.78	1.01
MnO	0.11	0.11	0.1	0.11	0.06	0.05	0.18	0.17	0.04	0.04	0.04	0.03	0.06	0.05	0.02	0.03	0.09
MgO	2.53	3.58	2.93	0.53	2.04	1.13	9.83	5.34	0.56	0.5	0.59	0.57	0.77	0.67	0.19	0.23	0.23
CaO	2.32	3.03	1.6	3.51	3.38	2.10	10.5	8.58	1.74	1.55	1.77	1.68	1.99	1.62	0.62	1.3	0.52
Na2O	3.03	2.92	2.23	2.83	3.69	3.54	2.5	0.7	2.79	2.76	2.61	2.68	2.8	2.83	2.76	3.96	3.20
K2O	3.28	2.98	3.54	0.41	1.05	1.26	0.84	0.9	4.71	5.32	5.08	4.91	4.63	4.78	6.39	4.8	5.08
TiO2	0.8846	0.8547	1.0013	0.1601	0.2327	0.1436	0.6097	1.4598	0.3776	0.3726	0.3918	0.4066	0.4554	0.4073	0.0635	0.0301	0.0172
P2O5	0.23	0.22	0.13	0.06	0.10	0.04	0.19	0.16	0.08	0.09	0.1	0.09	0.12	0.1	0.02	0.03	0.02
L.O.I.	0.78	0.85	0.65	0.19	0.72	0.56	0.41	0.72	0.07	0.05	0.07	0.17	0.21	0.28	0.45	0.37	0.41
TOTAL	99.86	100.08	99.91	99.87	99.96	100.02	99.61	100	99.88	100.3	100.13	100.25	99.97	100.19	99.73	100.28	100.00
Ba	719.8	539.7	591	130.9	200.2	245.3	228.2	79.6	1660.6	1612	1987.3	1890.1	1953.1	1824.6	352	1024.4	91.4
Rb	126.2	120	127.8	7.4	23.5	35.8	12.8	23.3	141.2	122.4	121.6	99.4	95.4	110.8	233.9	116.9	266.5
Sr	196.9	246	127.5	180.7	118.7	128.3	189.4	197.7	195	208	236.8	243.7	305.9	244.3	81	194.2	23.9
Y	74.5	31.7	37.9	14.2	13.4	14.0	14.1	18.6	24.5	30.2	21.8	25.4	30	29.2	14.4	39.8	63.9
Zr	317.9	175.4	238	43.1	55.6	64.4	34	48.7	307.1	300.9	320.6	342	382.3	326.6	3.6	28.9	17.0
Nb	22.8	10.1	11.4	0.7	2.8	3.6	1.2	2	12.4	15	11.8	15	14.6	15.3	7.9	1.5	33.0
U	4.6	0.9	0	0.7	0.5	0.1	0.7	1.5	0.6	2.8	2.6	2	2.9	2.2	0.4	2	15.2
Th	13.0	11.6	12.4	1.8	0.5	0.0	2.3	2.7	30.7	29.7	34.5	29.7	36.6	28.3	1.2	8.3	11.2
Pb		18	21				11	16							63	55	
La	32.6	20	22.2	0.7	2.4	8.6	1.2	0.3	68.7	45.1	59.4	54.5	70.2	63.9	0	2.8	4.7
Ce		80	58				0	5							0	3	
Nd		34	25				0	0							0	0	
Ga		20.1	19.4				14.8	23.5							22.6	19.9	
Zn	127.3	104.5	124.1	22.3	63.6	22.0	82.6	134.2	47.1	47.2	46.9	44.3	44.6	37.4	3.2	7	9.8
As		7	5				3	3							28	23	
Cu	0.0	15	3.3	15.4	2.8	0.0	0	20.5	0	0	5.7	28.7	5.4	0	0	2.1	0.0
Ni	39.3	84.2	55.5	0.2	9.1	0.1	151.4	107.8	3	1.3	5.8	11.8	4.2	3.3	0.3	18.1	1.7
V	167.0	145.6	155.1	12.9	57.7	10.2	257.4	200.1	25.9	27.1	35.3	28.2	35.9	30.7	3.1	3	1.2
Cr	270.4	235.7	323.5	315.8	322.0	248.4	612.4	259.7	158.2	89.4	139.1	243.4	173.3	151.7	98.9	151.6	168.8
Sc	21.1	20	22.5	14.1	15.5	11.4	41.2	21.4	4.4	5.1	6.2	6.1	6.2	6.2	2	0.9	3.7
Co		25	19				49	39							1	6	
F		0.04	0.09				0.11	0.04							0.02	0	
Cl		183	275				151	363							52	50	
S		0.01	0.04				0.01	0.03							0.01	0	

Sample	PH93198	PH93199	PH93200	PH93203	PH93204	PH92001	PH92002	PH92003	PH92005	PH93101	PH93102	PH93105	PH93108	PH93109	PH93110	PH92006	PH92007
Rock	KBL	KBL	KBL	KBL	KBL	MOG	MOG	MOG	MOG	MOG	MOG	MOG	MOG	MOG	MOG	PEG	PEG
SiO2	74.5	74.52	78.35	75.53	74.38	66.14	64.77	63.15	61.99	64.2	71.63	63.52	61.86	62.32	63.11	75.16	73.19
Al2O3	14.45	13.94	12.45	14.71	14.83	14.44	14.20	15.27	15.53	17.25	14.18	16.01	15.5	15.48	15.65	13.50	14.69
Fe2O3	0.83	1.68	0.35	0.65	0.5	6.23	7.20	7.55	7.79	4.68	3.36	6.55	8.22	7.75	7.51	1.46	0.78
MnO	0.03	0.12	0	0.03	0.01	0.08	0.12	0.11	0.10	0.07	0.05	0.1	0.12	0.11	0.11	0.03	0.02
MgO	0.25	0.32	0.18	0.18	0.18	1.40	1.37	1.42	1.44	0.66	0.37	1.06	1.32	1.27	1.07	0.38	0.29
CaO	1.21	1.42	0.97	0.62	0.68	3.00	3.32	3.57	3.85	3.2	2.19	3.53	3.82	3.68	3.01	1.28	0.58
Na2O	2.87	3.08	2.48	2.39	2.73	3.38	3.14	3.56	3.47	3.79	3.09	3.41	3.52	3.61	3.31	3.35	2.80
K2O	5.44	4.72	5	5.78	6.98	4.03	4.12	3.63	4.04	5.21	4.93	4.3	3.85	3.81	4.38	4.69	7.69
TiO2	0.0559	0.0311	0.0424	0.0187	0.0267	1.0990	1.2396	1.2900	1.2642	0.7182	0.4491	1.0894	1.379	1.2758	1.2107	0.1404	0.0777
P2O5	0.08	0.08	0.07	0.04	0.03	0.43	0.46	0.47	0.49	0.23	0.13	0.4	0.51	0.47	0.45	0.04	0.02
L.O.I.	0.41	0.34	0.41	0.8	0.63	0.93	0.99	0.45	0.14	0.15	0.01	0.02	0.04	0.41	0.54	0.32	0.40
TOTAL	99.71	99.9	99.89	99.95	100.34	100.23	99.93	99.95	99.96	100	100.39	99.97	100.1	99.77	99.79	100.03	100.13
Ba	1126	1299.2	1296.4	365.7	914.7	1593.4	1602.9	1715.4	1932.2	2146.4	1937.1	2229.4	2213.9	1905.2	2164.9	736.1	1168.0
Rb	91	73.7	83	206.4	189	103.2	104.1	75.5	80.7	105.5	91.5	78.8	69	80.3	80.8	145.7	237.9
Sr	180.3	222.6	203.8	98.9	183.5	313.3	319.0	367.3	377.2	371	270.6	392.4	388.1	379.2	372.5	134.7	127.4
Y	13.8	36.5	6.4	66.6	32.8	30.2	51.9	38.9	42.7	20.6	14.7	31.2	38	36.3	37.8	89.2	14.6
Zr	36.4	161.8	51	21.7	18.1	399.7	505.0	520.6	576.6	408.6	297.1	486	619.5	542.4	539.8	146.6	74.5
Nb	0.8	0	1.3	2.2	3.7	14.0	22.0	23.4	20.0	14.9	9.8	22.3	27.4	25	24.7	16.9	7.0
U	0	2	0.2	1.9	0.2	2.5	2.0	1.9	0.4	1.9	2	1	2.2	2.6	2.9	4.3	5.7
Th	4.5	8	2.3	6.2	10.3	1.0	0.9	0.0	0.3	0.1	2.7	1.1	1.5	1.1	2.9	21.3	5.5
Pb	45	48	42	67	67												
La	3.2	4	0	0	0	33.5	35.1	32.0	36.5	14.5	30.2	18.9	32.8	24	31.5	21.8	0.0
Ce	5	20	0	0	4												
Nd	0	5	0	0	0												
Ga	13.8	11.2	10	21.6	22.5												
Zn	14.6	5.1	5.1	2.9	3.3	112.8	125.3	139.7	144.6	78.7	61.2	118.5	155.6	140.6	140.8	27.2	12.7
As	19	17	18	28	32												
Cu	0	1.3	1.8	9.8	6.7	0.0	0.0	0.0	0.0	0	0	2.6	5.7	3.2	4.9	0.0	0.0
Ni	0.4	8.8	14.1	11.8	8.1	0.5	0.2	0.0	0.5	0	0	0	0	0	0.8	1.5	2.7
V	6.1	5.4	6.3	4.7	4.1	55.2	64.7	60.0	68.1	34.3	17.2	50.6	65.7	58	59.9	8.2	6.8
Cr	136.3	180.5	132.3	125.4	150	164.6	156.4	178.5	187.0	118.6	208	180.2	229.7	195.8	281.8	139.8	156.1
Sc	2.1	7.4	0.9	1.8	1.3	10.3	16.4	16.4	16.8	7.8	4.5	16.3	20.3	20.6	21.4	3.4	1.2
Co	0	2	5	5	3												
F	0	0	0.01	0.01	0.02												
Cl	36	34	26	30	25												
S	0.01	0.1	0.03	0.01	0.07												

Sample	PH92011	PH92012	PH92013	PH93140	PH92021	PH93171	PH93174	PH93187	PH93188	PH93190	PH93192	PH93193	PH93197	PH92040	PH92043	PH92008	PH92014
Rock	PEG	PEG	PEG	PEG	MD	MD	MD	MD	MD	MD	MD	MD	MD				
SiO2	75.35	75.58	73.34	75.08	50.69	50.45	68.56	50.46	45.37	47.25	44.72	51.1	74.51	75.00	74.06	52.57	75.99
Al2O3	13.62	13.42	14.39	13.66	12.93	12.9	15.73	16.28	11.9	12.85	13.45	17.03	15.27	13.07	13.21	14.92	13.83
Fe2O3	1.10	0.86	2.19	1.77	12.96	12.97	3.3	12.12	17.49	17.06	19.99	10.83	0.6	0.79	1.17	12.82	0.49
MnO	0.04	0.03	0.04	0.04	0.18	0.18	0.06	0.17	0.34	0.25	0.31	0.19	0.01	0.01	0.04	0.21	0.01
MgO	0.32	0.31	0.71	0.25	8.29	8.95	0.93	6.07	3.93	5.91	5.6	5.37	0.24	0.36	0.41	4.32	0.29
CaO	1.35	1.16	1.78	1.19	8.91	8.85	2.46	7.75	8.45	9.61	9.54	9.01	2.04	1.04	0.78	7.90	1.44
Na2O	3.22	3.11	2.92	3.07	2.12	2.13	3.63	3.56	1.42	2.32	1.13	3.72	4.25	2.39	3.10	2.76	2.87
K2O	5.01	5.34	4.42	5.09	1.06	1.41	4.82	2.05	3.47	0.82	1.95	1.36	2.97	6.61	6.67	1.15	5.14
TiO2	0.1040	0.1051	0.2740	0.1726	2.2676	2.2376	0.6566	1.197	4.3108	3.0306	3.1806	1.1215	0.0624	0.0774	0.0707	2.6345	0.0486
P2O5	0.03	0.03	0.05	0.03	0.23	0.2	0.19	0.21	2.52	0.53	0.35	0.31	0.09	0.06	0.05	0.72	0.02
L.O.I.	0.32	0.29	0.46	0.02	0.64	1.04	0.25	0.9	1.15	0.24	0.41	0.56	0.53	0.46	0.86	0.90	0.39
TOTAL	100.15	99.95	100.12	100.36	99.63	100.29	100.33	99.85	99.18	99.64	100.21	100.05	100.04	99.42	99.57	100.00	100.11
Ba	462.9	604.9	1974.1	765.8	270.2	303.2	2607.3	512.4	1656.5	136	570.2	293.2	654.9	2101.7	1927.0	950.3	1374.8
Rb	138.1	135.4	84.0	179.2	37.0	45.9	89.3	52.3	142	14	71.8	14.9	47	107.0	119.7	23.1	97.9
Sr	113.8	132.4	316.2	111.6	357.1	209.8	599.6	271.7	68.7	205.1	46.3	416.9	204.5	428.3	213.8	627.7	296.4
Y	35.1	32.3	28.0	80.2	29.2	27	21.8	44.1	148.9	49	56.9	28.9	10.7	3.9	14.1	49.0	3.0
Zr	85.4	84.7	227.7	144.9	169.1	159.9	401.8	143.5	1315.2	206	127.5	104.8	34	25.9	146.9	241.3	8.3
Nb	13.8	11.5	7.7	23.5	16.5	16.8	12	6.9	42.5	15	12	4.9	0.6	0.0	0.5	9.9	4.6
U	1.9	3.7	4.0	3.6	0.3	0	1.6	1.4	0.9	0.3	1.3	1.7	0	1.8	1.8	2.6	0.6
Th	16.1	21.1	25.9	22.1	3.4	3.6	14.7	1.9	6.5	0.5	2.1	0.6	6.4	3.6	27.1	5.3	0.0
Pb													33				
La	7.8	14.0	66.9	21.3	12.4	17.9	81.5	13.8	63.9	10.1	14.1	6.2	7.1	11.6	46.6	30.4	0.0
Ce													23				
Nd													7				
Ga													13.5				
Zn	19.8	20.9	30.7	36.9	102.8	107.7	44.7	147.3	186.5	137.7	159.6	99.1	10.1	11.6	14.4	145.9	8.5
As													17				
Cu	0.0	9.0	1.9	0	20.8	64.5	0.8	13.5	25.2	19.3	16.7	29.7	5.3	0.0	0.0	17.9	12.3
Ni	2.9	85.1	8.9	0.6	114.3	167.4	1	56.9	3	43.3	0	16.8	20.1	3.3	5.3	4.4	16.4
V	5.8	5.7	21.9	9.8	276.8	279.8	36.6	167.2	107.8	375.4	632.9	240.3	8.6	9.4	7.6	163.3	4.1
Cr	198.6	172.8	200.2	146	528.5	598.5	124.5	205.6	62	160.4	221.4	120.5	154.4	236.6	178.6	231.0	191.1
Sc	1.3	2.7	3.4	3.3	31.6	45.3	3.2	49.5	56.2	56.7	75.3	52.3	1.1	1.0	3.6	30.2	0.8
Co													8				
F													0.01				
Cl													36				
S													0.04				

Table 7.2. Rb-Sr isotopic data.

Sample	Type	Rb (ppm)	Sr (ppm)	87Rb/86Sr	87Sr/86Sr	Precision	DM Age
Biotite-Garnet Migmatite Gneiss							
PH92031	whole-rock	133.03	192.17	2.0081	0.731324	0.000012	1007
Quartzofeldspathic Leucogneiss							
PH92050	whole-rock	9.51	174.05	0.1581	0.705736	0.000008	1616
PH92054	whole-rock	25.48	118.19	0.6241	0.714234	0.000090	1341
PH92055	whole-rock	38.86	126.55	0.8892	0.716982	0.000014	1150
Intrusive Leucogneiss							
PH92063b	whole-rock	143.05	196.28	2.115	0.738544	0.000008	1196
PH93146	whole-rock	126.3	210.20	1.7427	0.732902	0.000005	1188
PH93147	whole-rock	123.9	235.80	1.5233	0.728478	0.000014	1155
PH93148	whole-rock	102.31	244.36	1.2134	0.724727	0.000015	1292
PH93148b	whole-rock		244.26		0.724860	0.000019	
PH93149	whole-rock	95.2	304.97	0.9044	0.721639	0.000006	1502
PH93155	whole-rock	114.01	244.63	1.3514	0.730105	0.000009	1441
PH93174	whole-rock	94.84	606.65	0.4524	0.709830	0.000005	1157
Kyanite-Bearing Leucogneiss							
PH92057	whole-rock	266.19	23.54	34.8491	1.37389	0.00082	1344
PH93200	whole-rock	83.60	200.14	1.2109	0.727927	0.000006	1483
PH93203	whole-rock	211.18	97.21	6.3749	0.853291	0.000011	1651
Megacrystic Orthogneiss							
PH92001	whole-rock	109.33	308.67	0.8611	0.719446	0.000011	1396
PH92001b	whole-rock	106.61	307.04	1.0057	0.719339	0.000006	1181
PH92002	whole-rock	111.39	311.03	1.0373	0.718430	0.000009	1082
PH92003	whole-rock	81.32	359.05	0.6556	0.713255	0.000009	1163
PH92003b	whole-rock	95.32	465.38	0.5929	0.713295	0.000010	1298
PH92005	whole-rock	83.90	366.81	0.6621	0.713483	0.000011	1177
PH92005b	whole-rock	104.38	486.05	0.6217	0.713488	0.000014	1258
PH93101	whole-rock	129.77	446.53	0.8416	0.717025	0.000011	1221
PH93102	whole-rock	164.47	528.35	0.9016	0.718789	0.000017	1278
PH93105	whole-rock	86.08	437.44	0.5696	0.712566	0.000014	1260
PH93108b	whole-rock	70.53	386.76	0.5278	0.711396	0.000016	1201
PH93108	whole-rock	53.92			0.711448	0.000020	
PH93109	whole-rock	113.66	681.31	0.4829	0.713638	0.000015	1673
PH93109b	whole-rock	81.63	376.20	0.6281	0.713379	0.000005	1231
PH93110	whole-rock	104.55	544.80	0.5555	0.713076	0.000008	1362
92/10	whole-rock	99.20	265.17	1.0836	0.719205	0.000011	1085
92/14	whole-rock	91.38	357.83	0.7393	0.714246	0.000011	1124
92/16	whole-rock	84.95	392.88	0.6259	0.713136	0.000014	1208
92/17	whole-rock	72.96	386.70	0.5461	0.712011	0.000014	1242
92/18	whole-rock	95.85	307.48	0.9028	0.717348	0.000011	1161
92/19	whole-rock	101.4	313.10	0.9379	0.717747	0.000013	1147
92/34	whole-rock	135.59	303.09	1.2962	0.723211	0.000011	1124
92/35	whole-rock	132.58	262.95	1.4618	0.725237	0.000014	1093
92/36	whole-rock	88.06	567.04	0.4494	0.708864	0.000009	1004
92/36b	whole-rock	73.39	597.55	0.3554	0.708871	0.000015	1298
92/45	whole-rock	152.06	296.95	1.4846	0.728584	0.000009	1236
92/46	whole-rock	161.08	172.57	2.7078	0.734890	0.000010	838
92/46b	whole-rock	121.44	175.39	2.0087	0.735202	0.000011	1143

Sample	Type	Rb (ppm)	Sr (ppm)	87Rb/86Sr	87Sr/86Sr	Precision	DM Age
Pegmatitic Veins							
PH92006	whole-rock	148.99	130.82	3.3112	0.757608	0.000012	1166
PH92007	whole-rock	248.17	123.98	5.8414	0.795860	0.000011	1118
PH92011	whole-rock	141.9	111.86	3.6903	0.763488	0.000008	1157
PH92012	whole-rock	139.15	126.31	3.202	0.754772	0.000014	1144
PH92013	whole-rock	87.04	308.33	0.8179	0.722005	0.000011	1701
PH92013b	whole-rock	86.41	307.57	0.814	0.722046	0.000005	1713
PH93140b	whole-rock	183.26	111.42	4.7898	0.777747	0.000012	1100
Mafic Dykes							
PH92021	whole-rock	37.66	354.67	0.3073	0.711939	0.000011	2353
PH92021b	whole-rock	37.93	357.14	0.3074	0.712333	0.000011	2462
PH93171	whole-rock	50.88	241.99	0.6087	0.714650	0.000005	1427
PH93187	whole-rock	59.56	285.40	0.6042	0.714164	0.000006	1379
PH93188	whole-rock	156.34	70.59	6.4373	0.754707	0.000008	568
PH93190	whole-rock	13.99	203.72	0.1986	0.705725	0.000008	1198
PH93192	whole-rock	74.91	49.34	4.406	0.738669	0.000007	574

Table 7.3. Sm-Nd isotopic data.

Sample	Type	Sm (ppm)	Nd (ppm)	147Sm/144Nd	143Nd/144Nd	Error	DM Age	E Nd
Biotite-Garnet Migmatite Gneiss								
PH92031	whole-rock	7.47	30.285	0.1491	0.512337	0.000006	1621	-5.87
PH92031b	whole-rock	7.39			0.512356	0.000013		
PH93151	whole-rock	7.106	33.99	0.1264	0.512073	0.000006	1656	-11.02
PH93161	whole-rock	7.143	34.221	0.1262	0.511906	0.000007	2013	-14.28
PH92009	whole-rock	8.40	41.43	0.1226	0.512177	0.000011	1435	1.37
Quartzofeldspathic Leucogneiss								
PH92050	whole-rock	1.598	5.256	0.1838	0.512607	0.000014	2016	
PH92054	whole-rock	1.968	8.18	0.1454	0.512494	0.000024	1233	4.38
PH92055	whole-rock	1.974	8.62	0.1384	0.512410	0.000012	1282	3.72
Mafic Boudins								
PH93141	whole-rock	2.056	7.911	0.1571	0.512600	0.000008	1206	
Intrusive Leucogneiss								
PH92063	whole-rock	11.21	59.87	0.1132	0.512063	0.000016	1470	0.47
PH92063b	whole-rock	9.026	54.20	0.1007	0.512026	0.000015	1365	1.49
PH93146	whole-rock	7.762	42.00	0.1117	0.512179	0.000010	1291	2.93
PH93147	whole-rock	8.314	47.30	0.1063	0.512014	0.000009	1447	0.47
PH93148	whole-rock	10.21	62.69	0.0984	0.511888	0.000057	1509	-0.88
PH93148b	whole-rock	9.532	59.8	0.0964	0.511996	0.000014	1355	1.51
PH93149	whole-rock	11.115	66.53	0.1010	0.512008	0.000012	1391	1.10
PH93174	whole-rock	9.614	53.72	0.1082	0.512013	0.000015	1472	0.18
Kyanite-Bearing Leucogneiss								
PH92020	whole-rock	2.125	8.542	0.1504	0.512359	0.000010	1604	
PH92057	whole-rock	8.77	23.617	0.2246	0.512972	0.000006		
PH92057b	whole-rock	8.995	24.001	0.2266	0.513013	0.000008		
PH93163	whole-rock	0.9837	1.671	0.3559	0.512205	0.000015		
PH93198	whole-rock	1.628	7.199	0.1367	0.511960	0.000014	2055	-4.85
PH93200	whole-rock	0.826	3.223	0.1549	0.511841	0.000031	2874	
PH93203	whole-rock	4.573	6.084	0.4545	0.513195	0.000009		
Megacrystic Orthogneiss								
PH92001	whole-rock	9.584	49.4	0.1173	0.512197	0.000008	1333	2.50
PH92002	whole-rock	14.74	70.7	0.1260	0.512276	0.000008	1329	2.84
PH92003b	whole-rock	11.7	51.69	0.1368	0.512218	0.000009	1600	0.18
PH92005b	whole-rock	13.024	58.34	0.1350	0.512232	0.000008	1542	0.70
PH93101	whole-rock	7.304	37.63	0.1173	0.512180	0.000015	1358	2.17
PH93105	whole-rock	10.129	44.99	0.1361	0.512191	0.000076	1634	-0.25
92/10	whole-rock	5.62	32.73	0.1038	0.512029	0.000009	1397	1.11
92/14	whole-rock	10.92	50.7	0.1302	0.512187	0.000017	1536	0.51
92/16	whole-rock	11.94	56.41	0.1280	0.512203	0.000011	1475	1.11
92/17	whole-rock	12.18	56.75	0.1297	0.512228	0.000018	1461	1.37
92/18	whole-rock	14.95	71.0	0.1273	0.512258	0.000014	1376	2.29
92/19	whole-rock	14.09	64.24	0.1326	0.512321	0.000044	1350	2.78
92/34	whole-rock	13.34	61.39	0.1314	0.512157	0.000022	1607	-0.25
92/35	whole-rock	12.85	67.62	0.1149	0.512110	0.000008	1427	1.13
92/36	whole-rock	9.759	44.89	0.1314	0.512180	0.000010	1568	0.20
92/45	whole-rock	12.736	86.63	0.0889	0.511879	0.000011	1412	0.27
92/46	whole-rock	6.716	41.90	0.0969	0.511954	0.000025	1411	0.61

Sample	Type	Sm (ppm)	Nd (ppm)	147Sm/144Nd	143Nd/144Nd	Error	DM Age	E Nd
Pegmatitic Veins								
PH92006	whole-rock	9.35	37.68	0.1500	0.512368	0.000009	1576	
PH92011	whole-rock	3.17	12.10	0.1584	0.512545	0.000023	1362	
PH92013	whole-rock	9.823	58.38	0.1017	0.512112	0.000010	1268	3.03
PH93140	whole-rock	8.953	36.17	0.1496	0.512403	0.000018	1494	2.01
Mafic Dykes								
PH93190	whole-rock		29.13		0.512703	0.000014		
PH93192	whole-rock	9.072	32.12	0.1707	0.512538	0.000011	1707	
PH93193	whole-rock	4.642	16.61	0.1690	0.512483	0.000019	1818	
Porphyritic Granite-Central Kirwanveggen								
CJK 103	whole-rock	1.274	6.684	0.1152	0.511933	0.000009	1682	-2.37

CHAPTER 8

THE GEOLOGICAL EVOLUTION OF NEUMAYERSKARVET IN THE NORTHERN KIRWANVEGGEN:

SUMMARY

Neumayerskarvet lies within the northern Kirwanveggen of western Dronning Maud Land (WDML). This region forms a broad belt of high-grade gneisses extending from the Heimefrontfjella in the southwest, through the Kirwanveggen and H.U.Sverdrupfjella, to the Muhlig-Hoffmanfjella in the northeast and beyond. The northern Kirwanveggen forms a geologically significant domain represented by similar lithotectonic units, structural styles and metamorphic mineral assemblages. Neumayerskarvet forms the major continuous portion of outcrop within the northern Kirwanveggen. The dominant lithotectonic unit preserved at Neumayerskarvet is the biotite-garnet migmatite gneiss, which is inter-fingered with quartzofeldspathic gneisses and occurs with banded quartz-feldspar gneisses. Several phases of magmatism have intruded into the older sequences and comprise megacrystic orthogneiss, leucogneisses, granitic/dioritic gneisses, metagabbros and mafic dykes.

The current investigation involves a detailed geological study at Neumayerskarvet in the northern Kirwanveggen. The main objective of the study was to obtain an evolutionary history for this portion of the high-grade gneisses. The work involved lithological and structural mapping to obtain a structural history for the study area (detail provided in Chapter 3). The establishment of a structural history provided a framework for further metamorphic and isotopic investigations. U-Pb zircon SHRIMP analysis, Rb-Sr, Sm-Nd and Ar-Ar mineral analysis were used to provide absolute time constraints on different tectono-metamorphic periods and cooling histories experienced at Neumayerskarvet (see Chapters 4 and 6 for more detail). Petrographic investigations, coupled with mineral chemistry, provided information on the P-T conditions that were experienced by these rocks (see Chapter 5). An understanding of the crustal evolution of the high-grade gneisses was obtained through whole-rock geochemistry along with Rb-Sr and Sm-Nd isotopic analysis (see Chapter 7). The evolution of Neumayerskarvet obtained through this data is presented in this thesis and is summarised in this section.

Four tectono-metamorphic cycles are interpreted from the data in the northern Kirwanveggen. The first two tectono-metamorphic cycles are assigned to a period between 1390 Ma and 970 Ma, but it is unclear as to whether these cycles represent a continuous event or are the result of two distinct and separate events. The last tectono-metamorphic cycle has been interpreted as the result of the 650-450 Ma event that has affected the region.

The first tectono-metamorphic cycle is not well constrained, but the D1a tectonic period is associated with this cycle. D1a is constrained between *ca.* 1160 Ma and *ca.* 1110 Ma. Evidence of deformational fabrics and magmatism are not clearly resolved for the D1a tectonic period. A strong penetrative planar foliation is distinguished, however; that is folded by later tectonic periods. There is evidence to suggest that magmatism occurred during this period at Neumayerskarvet, but current U-Pb ion probe data is poorly constrained (see Chapter 4). Magmatism during this period has, however, been recorded in the Heimefrontfjella and the H.U.Sverdrupfjella (Arndt *et al.*, 1991; Harris *et al.*, 1995; Moyes and Groenewald, 1996). Metamorphism for this period cannot be obtained from the current samples (Chapter 5) as the units used for detailed metamorphic investigations intrude post-D1a but during the D1b tectonic period. Metamorphic conditions for this tectono-metamorphic cycle can only be inferred from the literature. High-pressure metamorphic conditions have been suggested from previous investigations and may be attributed to the early tectono-metamorphic cycle (Groenewald and Hunter, 1991; Ferrar, 1995; Grantham *et al.*, 1995; Moyes and Groenewald, 1996).

A second tectono-metamorphic cycle is interpreted from the data obtained during this investigation, and is supported by previous investigations in the region (Grantham *et al.*, 1995; Jacobs *et al.*, 1996). The D1b tectonic episode represents a major period of magmatism and tectonism recorded during the second tectono-metamorphic cycle at between *ca.* 1110 Ma and *ca.* 1070 Ma. Major folding occurred during this tectonic episode and is represented by isoclinal recumbent folds, sheath folds and re-folded folds that produce Ramsay Type III interference patterns in outcrop. Strong stretching lineations and planar foliation development mark this period of tectonism. The structural fabric elements produce a complicated relationship of transposed coplanar and colinear composite fabrics indistinguishable in styles and geometries from earlier fabric elements. Magmatism dominates during this time period at Neumayerskarvet and is accompanied by zircon growth and recrystallisation. Fabric geometries suggest NNW-SSE tectonic transport directions within the D1b tectonic period. Tectonism that post-dates the D1b tectonic period is marked by cross-folding and the development of high-strain zones that re-work earlier tectonic fabrics. These deformational styles may develop during the D1c tectonic period, but could equally be part of the D2 tectonic episode at *ca.* 500 Ma. Magmatism between *ca.* 1070 Ma and *ca.* 970 Ma has only been documented in the central Kirwanveggen and Heimefrontfjella (Arndt *et al.*, 1991; Harris *et al.*, 1995; Jackson *et al.*, 1997).

The Mn+1 (nkv) metamorphic stage recorded in the kyanite-bearing leucogneisses is assigned to the second tectono-metamorphic cycle. Garnet-kyanite assemblages are recognised within the first metamorphic stage (Mn+1 (nkv)). The early assemblages provide P-T estimates of 710-760 °C and 7.8-8.5 kb. The possibility that the older D1a deformation period is part of the progressive deformation associated with the second tectono-metamorphic cycle cannot be discounted. Cooling during this cycle is recorded by zircon ages that range from *ca.* 1070 Ma to *ca.* 970 Ma. A later metamorphic stage (Mn+2 (nkv)) overprints the early metamorphic assemblages. Kyanite is transformed to sillimanite and this provides a good indication of the pressure conditions during this stage. Growth of higher Ca–content garnets and garnet rims are assigned to the Mn+2 (nkv) metamorphic stage. P-T estimates for the Mn+2 (nkv) metamorphic stage are 630-690 °C and 6.0-7.4 kb.

The third tectono-metamorphic cycle is distinguished primarily on the recognition of younger isotopic age data and related deformation (D2). Zircon growth and disturbance, and the resetting of biotite Rb-Sr, amphibole Ar-Ar and garnet Sm-Nd isotopic systematics takes place during the D2 tectonic episode. Cross-folding and high-strain development that re-works earlier tectonic fabrics may represent signatures of the associated deformation, but the exact nature of the deformation remains enigmatic. Tectonic fabric styles and geometries are similar to the more dominant D1 tectonic episode, making recognition of temporal relationships difficult and only possible in isolated outcrop areas. Magmatism during the D2 tectonic episode is only recognised in the Muhlig-Hoffmanfjella and H.U.Sverdrupfjella (Ohta *et al.*, 1990; Grantham *et al.*, 1991; Moyes *et al.*, 1993). Diffusional P-T data from garnet-biotite pair rims provide an indication of the P-T conditions during the younger tectono-metamorphic cycle. The final metamorphic stage (Mn+3 (nkv)) recognised in the kyanite-bearing leucogneisses is characterised by the growth of large microcline and muscovite grains, with the replacement of biotite by chlorite. Rim compositions of garnets and biotites provide P-T estimates of 560-570 °C and 4.4-4.6 kb for the Mn+3 (nkv) metamorphic stage. The third tectono-metamorphic cycle results in the exhumation of the high-grade gneiss terrane. A final tectono-metamorphic cycle is distinguished through apatite fission track data, and is related to uplift, tectonism and magmatism during Gondwana break-up.

There is little evidence of the involvement of Archaean crust in the formation of the high-grade gneisses in the northern Kirwanveggen. There is evidence, however, for the involvement of limited *ca.* 2.1 Ga crustal material. The data indicate that the material incorporated within the high-grade gneiss terrane comprises material that has little crustal residence time. Accretion of young material and the derivation of new juvenile material during the *ca.* 1100 Ma tectono-metamorphic cycle is suggested from the data. P-T conditions for the *ca.* 1100 Ma tectono-metamorphic cycle support the accretionary nature for this event. No evidence for mafic magmatism or break-up between 1000 and 800 Ma has been recorded in the northern Kirwanveggen, although an event at this time has been suggested for the H.U.Sverdrupfjella (Groenewald *et al.*, 1995).

Re-working of the high-grade gneisses during the younger *ca.* 550 Ma tectono-metamorphic cycle, with no addition or accretion of new crustal material is also indicated by the data. Jacobs *et al.* (1998) identified major tectonism and magmatism between 650 Ma and 450 Ma in central Dronning Maud Land. The data suggest an increasing influence of the *ca.* 550 Ma tectono-metamorphic cycle towards the east in WDML. Disruption of lithologies takes place during the *ca.* 500 Ma tectono-metamorphic cycle, which results in rapid uplift and exhumation of the northern Kirwanveggen high-grade gneiss domain. This tectono-metamorphic cycle results in the juxtaposition of terranes formed at different crustal depths. The Urfjell Group sediments were deposited during this tectono-metamorphic cycle, and these sediments were derived from material similar to that within the high-grade gneisses. Contacts between the high-grade gneisses and the Urfjell Group are, however, tectonic. Until such time as the effects of the ca. 500 Ma event have been evaluated the exact evolutionary nature of the Archaean fragment, the Ritscherflya Supergroup and the Maud Belt remains equivocal.

APPENDIX 1

REFERENCES

Ahlberg, P., Bylund, G. and Larsson, K. (1992) Geological fieldwork in the Kirwanveggen area.SWEDARP, 1991/92 – Dronning Maud Land.

Allsopp, H.L., Kramers, J.D., Jones, D.L. and Erlank, A.J. (1989) The age of the Umkondo Group, eastern Zimbabwe, and implications for palaeomagnetic correlations. S. Afr. J. Geol., 92, 11-19.

Arndt, N.T., Todt, W., Chauvel, C., Tapfer, M. and Weber K. (1991) U-Pb zircon age and Nd isotopic composition of granitoids, charnockites and supracrustal rocks from Heimefrontfjella, Antarctica. Geol. Rundsch., 80, 759-777.

Aucamp, A.P.H., Wolmarans, L.G. and Neethling, D.C. (1972) The Urfjell Group, a deformed (?) Early Palaeozoic sedimentary sequence, Kirwanveggen, western Dronning Maud Land. In: Adie, R.J. (ed.): Antarctic Geology and Geophysics, 557-562, Oslo (Universitettforlaget).

Bard J.P. (1983) Metamorphism of an obducted island arc: example of the Kohistan sequence (Pakistan) in the Himalayan collided range. Earth Planet. Sci. Lett., 65, 133-144.

Barton, J.M. Jr. and Moyes, A.B. (1990) Cooling patterns in western Dronning Maud Land, Antarctica, and southeastern Africa and their implications to Gondwana. Zbl . Geol. Palaont. Teil I 1990 (1/2), 33-43; Stuttgart.

Barton, J.M., Klemd, R., Allsopp, H.L., Auret, S.H. and Copperthwaite, Y.E. (1987) The geology and geochronology of the Annandagstoppane granite, western Dronning Maud Land, Antarctica. Contrib. Mineral. Petrol., 97, 488-496.

Bauer, W. (1995) Strukturentwicklung und Petrogenese des metamophen Grundgebirges der nordlichen Heimefrontfjella (wesstliches Dronning Maud Land/Antarktika). Ber. Polarforsch., 171, 1-222.

Black, L.P., Sheraton, J.W. and James, P.R. (1986) Late Archaean granites of the Napier Complex, Enderby land, Antarctica: a comparison of Rb-Sr, Sm-Nd and U-Pb isotopic systematics in a complex terrain. Precambr. Res., 32, 343-368.

Blackenburg, F.V., Villa, I.M., Baur, H., Morteani, G. and Steiger, R.H. (1989) Time calibration of a P-T path from the western Tauern window, Eastern Alps: the problem of closure temperature. Contrib. Mineral. Petrol., 101, 1-11.

Borg, S.G. and De Paolo, D.J. (1994) Laurentia, Australia, and Antarctica as a Late Proterozoic supercontinent: Constraints from isotopic mapping. Geology, 22, 307-310.

Brueckner, H.K., Blusztajn, J. and Bakun-Czubarow, N. (1996) Trace element and Sm-Nd 'age' zoning in garnets from peridotites of the Caledonian and Variscan Mountains and tectonic implications. J. Met. Geol., 14, 61-73.

Bucher-Nurminen, K. and Ohta, Y. (1993) Granulites and garnet-cordierite gneisses from Dronning Maud Land, Antarctica. J. Met. Geol., 11, 691-703.

Buggisch, W., Kleinschmidt, G., Kreuzer, H. and Krumm, S. (1994) Metamorphic and structural evolution of the southern Shackleton Range during the Ross Orogeny. Polarforsch., 63, 33-56.

Burton K.W. and O'Nions R.K. (1990) The timescale and mechanism of granulite formation at Kurunegala, Sri Lanka. Contrib. Mineral. Petrol., 106, 66-89.

Burton K.W. and O'Nions R.K. (1991) High-resolution garnet chronometry and the rates of metamorphic processes. Earth Planet. Sci. Lett., 107, 1-21.

Burton, K.W., Kohn, M.J., Cohen, A.S. and O'Nions, R.K. (1995) The relative diffusion of Pb, Nd, Sr and O in garnet. Earth Planet. Sci. Lett., 133, 199-211.

Cliff. R.A. (1985) Isotopic dating in metamorphic belts. J. Geol. Soc. London, 142, 97-110.

Cliff, R.A. and Cohen, A. (1980) Uranium-lead isotopic systematics in a regionally metamorphosed tonalite from the Eastern Alps. Earth Planet. Sci. Lett., 50, 211-218.

Cobbold, P.R. and Quinquis, H. (1980) Development of sheath folds in shear regimes. J.Struct. Geol., 2, 119-126.

Cobbold, P.R. and Watkinson, A.J. (1981) Bending anisotropy: a mechanical constraint on the orientation of fold axes in an anisotropic medium. Tectonophysics, 72, T1-T10.

Cohen, A.S., O'Nions, R.K., Siegenthaler, R. and Griffin, W.L. (1988) Chronology of the pressure-temperature history recorded by a granulite terrain. Contrib. Mineral. Petrol., 98, 303-311.

Collins, W.J. and Williams, I.S. (1995) SHRIMP ionprobe dating of short-lived Proterozoic tectonic cycles in the northern Arunta Inlier, central Australia. Precambr. Res., 71, 69-89.

Compston, W., Williams, I.S. and Meyer, C. (1984) U-Pb geochronology of zircons from Lunar Breccia 73217 using a sensitive high mass-resolution ion microprobe. In: Proceedings of the Fourteenth Lunar and Planetary Science Conference, Part 2. J. Geophys. Res., 89, Supplement, B525-B534.

Compston, W., Kinny, P.D., Williams, I.S. and Foster, J. (1986) The age and Pb loss behaviour of zircons from the Isua supracrustal belt as determined by ion-microprobe. Earth Planet. Sci. Lett., 80, 71-81.

Compston, W., Williams, I.S., Kirschvink, J.L., Zhang, Z. and Guogan, M.A. (1992) Zircon U-Pb ages for the Early Cambrian time-scale. J. Geol. Soc. London, 149, 171-184.

Corner, B. (1994) Geological evolution of western Dronning Maud Land within a Gondwana framework - Geophysics Sub-programme. Final Project Report to SACAR [unpublished].

Dalziel, I.W.D. (1991) Pacific margins of Laurentia and East Antarctica-Australia as a conjugate rift pair: evidence for an Eocambrian supercontinent. Geology, 19, 598-601.

De Paolo, D.J. (1988) Neodymium Isotope Geochemistry. Berlin. Springer.

Dirks, P.H.M.G., Carson, C.J. and Wilson, C.J.L. (1993) The deformational history of the Larsemann Hills, Prydz Bay: the importance of the Pan-African (500 Ma) in East Antarctica. Antarctic Science, 5, 179-192.

Dodson, M.H., (1973) Closure temperature in cooling geochronological and petrological systems. Contrib. Mineral. Petrol., 40, 259-274.

Dodson, M.H. (1979) Theory of Cooling Ages. In: Jager, E. and Hunziker, J.C. (eds.) Lectures in Isotope Geology. Springer-Verlag, New York, pp. 194-202.

Eglington, B.M. and Harmer, R.E. (1991) GEODATE, Version 2.2. Council for Scientific and Industrial Research (CSIR), Report No. EMA-H 9102, 70pp.

Ernbert, M. and Austerheim, H. (1993) The effect of fluid and deformation on zoning and inclusion patterns in poly-metamorphic garnets. Contrib. Mineral. Petrol., 115, 204-214.

Faulhaber, S. and Raith, M. (1991) Geothermometry and geobarometry of high-grade rocks: a case study of garnet-pyroxene granulites in southern Sri Lanka. Min. Mag., 378, 33-56.

Faure (1986) Principles of Isotope Geology. New York. John Wiley.

Ferrar, G.R. (1995) The metamorphic geology of the Armalsryggen, northern Kirwanveggen, western Dronning Maud Land, Antarctica. Unpubl. MSc thesis, University of Natal, Pietermaritzburg, 116p.

Ferreira, E.P. (1986) The sedimentology and stratigraphy of the Ahlmannryggen Group, Antarctica. Unpubl. MSc thesis, University of Stellenbosch, Stellenbosch.

Fitzsimons, I.C.W. and Harley, S.L. (1994) The influence of retrograde cation exchange on granulite P-T estimates and a convergence technique for the recovery of peak metamorphic conditions. J. Petrol., 35, 543-576.

Fraser, G., Ellis, D. and Eggins, S. (1997) Zirconium abundance in granulite-facies minerals, with implications for zircon geochronology in high-grade rocks. Geology, 25, 607-610.

Freer, R. (1981) Diffusion in minerals and glasses: A data digest and guide to the literature. Contrib. Mineral. Petrol., 76, 440-454.

Frost, B.R. and Charcko, T. (1989) The granulite uncertainty principle: Limitations on thermobarometry in granulites. J. Geol., 97, 435-450.

Gavshon, R.D.J. and Erasmus, J.M. (1975) Precambrian metamorphic rocks of the Neeumayerskarvet area, Kirwanveggen, western Dronning Maud Land. S. Afr. Antarct. Res., 5, 2-12.

Gerya, T.V. and Perchuk, L.L. (1991) Geopath version 1.2. Institute of Experimental Mineralogy USSR Academy of Sciences, Chernogolovka, Moscow District 142432, U.S.S.R.

Ghent, E.D., Stout, M.Z. and Parrish, R.R. (1988) Determination of metamorphic pressure-temperature-time (P-T-t) paths. In: Nisbet, E.G. and Fowler, C.M.R. (eds.). Heat, Metamorphism and Tectonics. Mineral Association of Canada, Short Course Handbook, v.14, pp.155-188.

Gilletti, B.J. (1991a) Rb and Sr diffusion in alkali feldspars, with implications for cooling histories of rocks. Geochim. Cosmochim. Acta, 55, 1331-1343.

Gilletti, B.J. (1991b) Mg, Ca, Sr and Ba diffusion in plagioclase and Sr diffusion in micas. EOS, 72, 292.

Goodge, J.W., Hansen, V.L., Peacock, S.M., Smith, B.K. and Walker, N.W. (1993) Kinematic evolution of the Miller Range Shear Zone, central Transantarctic Mountains, Antarctica, and implications for Neoproterozoic to Early Paleozoic tectonics of the East Antarctic margin of Gondwana. Tectonics, 12, 1460-1478.

Grantham, G.H., Groenewald, P.B. and Hunter, D.R. (1988) Geology of the northern Sverdrupfjella, western Dronning Maud Land and implications for Gondwana reconstructions. S. Afr. J. Antarct. Res., 18, 2-10.

Grantham, G.H., Moyes, A.B. and Hunter, D.R. (1991) The age, petrogenesis and emplacement of the Dalmatian granite, H.U. Sverdrupfjella, Dronning Maud Land, Antarctica. Antarctic Science, 3 (2), 197-204.

Grantham, G.H., Jackson, C., Moyes, A.B., Harris. P.D., Groenewald, P.B., Ferrar, G. and Krynauw, J.R. (1995) P-T evolution of the HU Sverdrupfjella and Kirwanveggen, Dronning Maud Land, Antarctica. Precambr. Res., 75, 209-229.

Groenewald, P.B. (1993) Correlation of cratonic and orogenic provinces in southeastern Africa and Dronning Maud Land, Antarctica. In: Findlay, R.H., Unrug, R., Banks, M.R. and Veevers, J.J. (eds.), Gondwana 8. Balkema, Rotterdam, pp. 111-123.

Groenewald, P.B. and Hunter, D.R. (1991) Granulites of northern H.U.Sverdrupfjella, western Dronning Maud Land: metamorphic history from garnet-pyroxene assemblages, coronas and hydration reactions. In: Thomson, M.R.A., Crame, J.A. and Thompson, J.W. (eds.), Geological Evolution of Antarctica, Cambridge University Press, Cambridge, 61-66.

Groenewald, P.B., Grantham, G.H. and Watkeys, M.K. (1991) Geological evidence for a Proterozoic to Mesozoic link between southeastern Africa and Dronning Maud Land, Antarctica. J. Geol. Soc. London, 148, 1115-1123.

Groenewald, P.B., Moyes, A.B., Krynauw, J.R. and Grantham, G.H. (1995) Constraints on East Antarctic crustal evolution in western Dronning Maud Land. Precambr. Res., 75, 231-250.

Grove, T.L., Baker, M.B. and Kinzler, R.J. (1984) Coupled CaAl-NaSi diffusion in plagioclase feldspar: Experiments and applications to cooling rate speedometry. Geochim. Cosmochim. Acta, 48, 2113-2121.

Halpern, M. (1970) Rubidium-strontium date of possibly 3 billion years for a granitic rock from Antarctica. Science, 164, 977-978.

Harley, S.L. (1989) The origins of granulites: a metamorphic perspective. Geol. Mag., 126, 215-247.

Harris, C. (1995) Petrogenesis of the Sisterfjell syenite complex, Dronning Maud Land, Antarctica: Generation of low $\delta^{18}O$ magmas by crustal contamination of rift zone magmas. Extended Abstracts, Centennial Geocongress, Rand Afrikaans University, Johannesburg. 235-238.

Harris, C. and Grantham, G.H. (1993) Geology and petrogenesis of the Staumsvola nepheline syenite complex, Dronning Maud Land, Antarctica. Geol. Mag., 130, 513-532.

Harris, C., Marsh, J.S., Duncan, A.R. and Erlank, A.J. (1990) The petrogenesis of the Kirwan basalts of Dronning Maud Land, Antarctica. J. Petrol., 31, 341-370.

Harris, P.D., Moyes, A.B., Fanning, C.M. and Armstrong, R.A. (1995) Zircon ion microprobe results from the Maudheim high-grade gneiss terrane, western Dronning Maud Land, Antarctica. Extended Abstracts, Centennial Geocongress, Rand Afrikaans University, Johannesburg. 240-243.

Harrison, T.M. and McDougall, I. (1980) Investigations of an intrusive contact, northwest Nelson, New Zealand – I. Thermal, chronological and isotopic constraints. Geochim. Cosmochim. Acta, 44, 1985-2003.

Harrison, W.J. and Wood, B.J. (1980) An experimental investigation of the partitioning of REE between garnet and liquid with reference to the role of defect equilibria. Contrib. Mineral. Petrol., 72, 145-155.

Hensen, B.J. and Zhou, B. (1995) A Pan-African granulite facies metamorphic episode in Prydz Bay, Antarctica: evidence from Sm-Nd garnet dating. Aust. J. Earth Sci., 42, 249-258.

Hiroi, Y., Shiraishi, K. and Motoyoshi, Y. (1991) Late Proterozoic paired metamorphic complexes in East Antarctica, with special reference to the tectonic significance of ultramafic rocks. . In: Thomson, M.R.A., Crame, J.A. and Thompson, J.W. (eds.), Geological Evolution of Antarctica, Cambridge University Press, Cambridge, 83-87.

Hoffman, P.F. (1991) Did the breakout of Laurentia turn Gondwanaland inside out? Science, 252, 1409-1412.

Holland, T.J.P. and Powell R. (1990) An enlarged and updated internally consistent thermodynamic dataset with uncertainties and corrections: the system K_2O-Na_2O-CaO-MgO-MnO-FeO-Fe_2O_3-Al_2O_3-TiO_2-SiO_2-C-H_2-O2. J. Met. Geol., 8, 89-124.

Holzl, S., Hofmann, A.W., Todt, W. and Kohler, H. (1994) U-Pb geochronology of the Sri Lankan basement. Precambr. Res., 66, 123-149.

Humphries, F.J. and Cliff, R.A. (1982) Sm-Nd dating and cooling history of Scourian granulites, Sutherland. Nature (London), 295, 515-517.

Jackson, C. and Jacobs, J. (1995) Reconciliation of the kinematics and timing of deformation in contrasting structural domains within the 1.1 Ga terrains of western Dronning Maud Land. Abstracts Volume, VIIth International Symposium on Antarctic Earth Sciences, 10-15 September, 1995, Sienna, Italy, p208.

Jackson, C., Corner, B., Ferrar, G., Grantham, G.H., Groenewald, P.B., Harris, P.D. and Krynauw, J.R. (1993) Structural evolution of the Kirwanveggen and H.U. Sverdrupfjella, western Dronning Maud Land. Conference Abstracts, The Tectonics of East Antarctica, University of Utrecht, Holland.

Jackson, C., Harris, P.D. and Krynauw, J.R. (1994) Cryptic reworking of a 1000Ma orogenic belt in western Dronning Maud Land, Antarctica: evidence from repeated reactivation of composite shear zones. IGCP 348. Proceedings of the International Geological Field Conference, held in Mozambique orogenic belt in East Africa.

Jackson, C., Harris, P.D., Armstrong, R.A. and Fanning, C.M. (1997) The tectonic framework of the Meso-Neoproterozoic Kirwanveggen terrain, Maud Orogenic Province Antarctica: recent insights from SHRIMP U-Pb zircon geochronology. Intraplate magmatism and the Tectonics of Southern Africa. Geological Society of Zimbabwe, Harare, Zimbabwe, 23-24.

Jacobs, J. (1991) Structural evolution and cooling history of the Heimefrontfjella mountains (Western Dronning Maud Land/Antarctica). Ber. Polarforsch., 97, 141pp.

Jacobs, J., Thomas, R.J. and Weber, K. (1993) Accretion and indentation tectonics at the southern edge of the Kaapvaal Craton during the Kibaran (Grenville) orogeny. Geology, 21, 203-206.

Jacobs, J., Ahrendt, H., Kreutzer, H. and Weber, K. (1995) K-Ar, ^{40}Ar-^{39}Ar and apatite fission track evidence for Neoproterozoic and Mesozoic basement rejuvination events in the Heimefrontfjella and Mannefallknausane (east Antarctica). Precambr. Res., 75, 251-262.

Jacobs, J. Bauer, W., Speath, G., Thomas, R.J. and Weber, K. (1996) Lithology and structure of Heimefrontfjella (East Antarctica). Geol. Rundsch., 85, 800-821.

Jacobs, J., Fanning, C.M., Henjes-Kunst, F., Olesch, M. and Paech, H.-J. (1998) Continuation of the Mozambique Belt into East Antarctica: Grenville-age metamorphism and polyphase Pan-African high-grade events in central Dronning Maud Land. J. Geol., 106, 385-406.

Jager, E. (1979) Introduction to geochronology. In: Jager, E. and Hunziker, J.C. (eds.). Lectures in Isotope Geology. Springer-Verlag, New York, pp. 1-7.

Kleinschmidt, G. and Buggisch, W. (1993) Plate tectonic implications of the structure of the Shackleton range, Antarctica. Polarforsch., 63, 57-62.

Knoper, M.W., Moyes, A.B., Tucker, R.D., Amelin, Y. and Harris, P.D. (1995) Growth of pre-Gondwana crust as indicated by three crustal provinces in western Dronning Maud Land, East Antarctica. Abstracts Volume, VIIth International Symposium on Antarctic Earth Sciences, 10-15 September, 1995, Sienna, Italy, p230.

Krogh, E.J. (1988) The garnet-clinopyroxene Fe-Mg geothermometer – a reinterpretation of existing experimental data. Contrib. Mineral. Petrol., 99, 44-48.

Kroner, A., Williams, I.S., Compston, W., Baur, N., Vitanage, P.W. and Perera, L.R.K. (1987) Zircon ion microprobe dating of high-grade rocks in Sri Lanka. J. Geol., 95, 775-791.

Kroner, A., Jaeckel, P. and Williams, I.S. (1994) Pb-loss patterns in zircons from a high-grade metamorphic terrain as revealed by different dating methods: U-Pb and Pb-Pb ages for igneous and metamorphic zircons from northern Sri Lanka. Precambr. Res., 66, 151-181.

Krynauw, J.R. (1995) The role of the 1200-1000 and 550-450 Ma tectonothermal events in the geological evolution of East Antarctica. Abstracts Volume, VIIth International Symposium on Antarctic Earth Sciences, 10-15 September, 1995, Sienna, Italy, p231.

Krynauw, J.R. (1996) A review of the geology of East Antarctica, with special reference to the c.1000 Ma and c.500 Ma events. Terra Antarctica, 3, 77-89.

Krynauw, J.R., Hunter, D.R. and Wilson, A.H. (1988) Emplacement of sills into wet sediments at Grunehogna, western Dronning Maud Land, Antarctica. J. Geol. Soc. London, 145, 1019-1032.

Krynauw, J.R., Watters, B.R., Hunter, D.R. and Wilson, A.H. (1991) A review of the field relations, petrography and geochemistry of the Borgmassivet intrusions in the Grunehogna Province, western Dronning Maud Land. . In: Thomson, M.R.A., Crame, J.A. and Thompson, J.W. (eds.), Geological Evolution of Antarctica, Cambridge University Press, Cambridge, 33-39.

Krynauw, J.R., Behr, H.-J. and van den Kerkhof, A.M. (1994) Sill emplacement in wet sediments: fluid inclusion and cathodoluminescence studies at Grunehogna, western Dronning Maud Land, Antarctica. J. Geol. Soc. London, 151, 777-794.

Larsson, K., Lindstrom, S. and Guy-Ohlson, D. (1990) An Early Permian Palynoflora from Milorgfjella, Dronning Maud Land, Antarctica. Antarctic Science, 2, 331-344.

Ludwig, K.R. (1983) Plotting and regression programs for isotope geochemists, for use with HP-86/87 microcomputers. U.S.G.S. Open-file Report, 83-849, pp.94.

Ludwig, K.R. (1990) ISOPLOT: a plotting and regression program for radiogenic-isotope data, for IBM-PC compatible computers. Version 2.03. U.S.G.S. Open-file Report, 88-557, pp45.

Mattinson, J.M. (1978) Age, origin and thermal histories of some plutonic rocks from the Salinian Block of California. Contrib. Mineral. Petrol., 67, 233-245.

McDougall, I. and Harrison, T.M., (1988) Geochronology and thermochronology by the $^{40}Ar/^{39}Ar$ method, Oxford, New York, 212 p.

Mezger, K. and Krogstad, E.J. (1997) Interpretation of discordant U-Pb zircon ages: an evaluation. J. Met. Geol., 15, 127-140.

Mezger, K., Hanson, G.N. and Bohlen, S.R. (1989a) U-Pb systematics of garnet: dating the growth of garnet in the Late Archean Pikwitonei granulite domain at Cauchon and Natawahunan Lakes, Manitoba, Canada. Contrib. Mineral. Petrol., 101, 136-148.

Mezger, K., Hanson, G.N. and Bohlen, S.R. (1989b) High precision U-Pb ages of metamorphic rutile: application to the cooling history of high-grade metamorphic terrains. Earth Planet. Sci. Lett., 96, 106-118.

Mezger, K, Rawnsley, C.M., Bohlen, S.R. and Hanson, G.N. (1991) U-Pb garnet, sphene, monazite, and rutile ages: implications for the duration of high-grade metamorphism and cooling histories, Adirondack Mts., New York. J. Geol., 99, 415-428.

Mezger, K., Essene, E.J. and Halliday, A.N. (1992) Closure temperatures of the Sm-Nd system in metamorphic garnets. Earth Planet. Sci. Lett ., 113, 397-409.

Moores, E.M. (1991) The southwest U.S.-East Antarctica (SWEAT) connection: a hypothesis. Geology, 19, 425-428.

Morishita, Y., Giletti, B.J. and Fraver, J.R. (1989) Strontium and oxygen self-diffusion in titanite. EOS, 71, 652.

Moyes, A.B. (1993) The age and origin of the Jutulsessen granitic gneiss, Gjelsvikfjella, Dronning Maud Land. S. Afr. J. Antarct. Res., 23, 25-32.

Moyes, A.B., and Barton, J.M. Jr. (1990) A review of isotopic data from western Dronning Maud Land, Antarctica. Zbl. Geol. Palaont. Teil I, 1990 (1/2), 19-31; Stuttgart.

Moyes, A.B. and Knoper M.W. (1995) A Mesoproterozoic (±1100Ma) foreland fold and thrust belt in western Dronning Maud Land, Antarctica. Extended Abstracts, Centennial Geocongress, Rand Afrikaans University, Johannesburg, 257-260.

Moyes, A.B. and Groenewald, P.B. (1996) Isotopic constraints on Pan-African metamorphism in Dronning Maud Land, Antarctica. Chemical Geology (Isotope Geoscience), 129, 247-256.

Moyes, A.B., Barton, J.M. and Groenewald, P.B. (1993a) Late Proterozoic to Early Palaeozoic tectonism in Dronning Maud Land, Antarctica: its bearing on supercontinental fragmentation and amalgamation. J. Geol. Soc. London, 150, 833-842.

Moyes, A.B., Groenewald, P.B. and Brown, R.W. (1993b) Isotopic constraints on the age and origin of the Brattskarvet intrusive suite, Dronning Maud Land, Antarctica. Chemical Geology, 107, 453-466.

Moyes, A.B., Krynauw, J.R. and Barton, J.M. Jr. (1995) The age and origin of the Ritscherflya Supergroup and Borgmassivet Intrusions, Dronning Maud Land. Antarctic Science, 7, 87-97.

Moyes, A.B., Knoper, M.W. and Harris, P.D. (1997) The age and significance of the Urfjell group, western Dronning Maud Land. In: Ricci, C.A. (ed) The Antarctic Region: Geological Evolution and Processes. p.31-37.

Muller, A., Mezger, K. and Schenk, V. (1998) Crustal age domains and the evolutions of the continental crust in the Mozambique Belt of Tanzania: Combined Sm-Nd, Rb-Sr, and Pb-Pb isotopic evidence. J. Petrol., 39, 749-783.

Ohta, Y., Torudbakken, B.O. and Shiraishi, K. (1990) Geology of Gjelsvikfjella and western Muhlig-Hofmannfjella, Dronning Maud Land, East Antarcitca. Polar Research, 8, 99-126.

Parrish, R.R. (1990) U-Pb dating of monazite and its application to geological problems. Can. J. Earth Sci., 27, 1431-1450.

Passchier, C.W., Myers, J.S. and Kroner, A. (1990) Field geology of high-grade gneiss terrains. Springer-Verlag, New York. 150p.

Patchett, P.J. and Ruiz, J. (1987) Nd isotopic ages of crust formation and metamorphism in the Precambrian of eastern and southern Mexico. Contrib. Mineral. Petrol., 96, 523-528.

Pearce, J.A., Harris, N.B.W. and Tindle, A.G. (1984) Trace element discrimination diagrams for the tectonic interpretation of granitic rocks. J. Petrol., 25, 958-953.

Perchuk, L.L. (1977) Thermodynamic control of metamorphic processes. Saxena, S.K. and Bhattacharji, S. (eds) Energetics of Geological Processes. New York. Springer., pp. 285-352.

Perchuk, L.L. (1989) P-T-fluid regime of metamorphic and related magmatism with specific reference to the granulite-facies Sharyzhalgay Complex of Lake Baikal. In: Daly, J.S., Cliff, R.A. and Yardley, B.W.D. (eds.). Evolution of Metamorphic Belts. Geological Society Special Publication, 43, pp.275-291.

Perchuk, L.L. (1990) Derivation of thermodynamically consistent system of geothermometers and geobarometers for metamorphic and magmatic rocks. In: Perchuk, L.L. (ed) Progress in Metamorphic and Magmatic Petrology. Cambridge University Press, Cambridge, p.93-112.

Perchuk, L.L. and Krotov, A.V. (1998) Petrology of the mica schists of the Tanaelv Belt in the southern Texctonic Framing of the Lapland Granulite Complex. Petrol., 6, 149-179.

Peters, M. (1989) Igneous rocks in western and central Neuschwabenland, Vestfjella and Ahlmannryggen, Antarctica – Petrography, geochronology, palaeomagnetism, geotectonic implications. – Ber. Polarforsch., Bremerhaven 61, pp186.

Price, N.J. and Crosgrove, J.W. (1991) Analysis of Geological Structures. Cambridge University Press, Cambridge. p.502.

Purdy, J.W. and Jager, E. (1976) K-Ar ages on rock-forming minerals from the Central Alps. Mem. Inst. Geol. Petrol. Univ. Padova, 30, 1-321.

Raith, M. Faulhaber, S., Hoffbauer, R. and Spiering, B. (1991) Characterisation of high-grade metamorphism in the southern part of Sri Lanka, Part I. Summary of Research of the German-Sri Lankan Consortium. Geol. Surv. Dept. Sri Lanka, Prof. Pap., 5, 164-178.

Richard, P., Shimizu, N. and Allegre, C.J. (1976) $^{143}Nd/^{144}Nd$, a natural tracer: an application to oceanic basalt. Earth Planet. Sci. Lett., 31, 269-278.

Rudnik, R.L. and Williams, I.S. (1987) Dating the lower crust by ion microprobe. Earth Planet. Sci. Lett., 85, 145-161.

Schulze, P. (1992) Petrogenese des metamorphen Grundgebriges der zentralen Heimefrontfjella (westliches Dronning Maund Land/Antarktis). Ber. Polarforsch., 117, 1-321.

Schumacher, R. and Schumacher, J. (1991) Hornblende breakdown in granulite-facies rocks from the Highland Series of Sri Lanka. Geol. Soc. Am. Abstr. Programs, 23, A334.

Schumacher, R. and Faulhaber, S. (1994) Summary and discussion of P-T estimates from garnet-plagioclase-quartz-bearing granulite-facies rocks from Sri Lanka. Precambr. Res., 66, 295-308.

Schumacher, R., Schenk, V., Raase, P. and Vitanage, P.W. (1990) Granulite facies metamorphism of metabasic and intermediate rocks in the Highland Series of Sri Lanka. In: Ashworth, J.R. and Brown, M. (eds) High-Grade Metamorphism and Crustal Anatexis. Allen and Unwin, London, pp. 235-271.

Shiraishi, K., Ellis, D.J., Hiroi, Y., Fanning, C.M., Motoyoshi, Y. and Nakai, Y. (1994) Cambrian Orogenic Belt in East Antarctica and Sri Lanka: Implications for Gondwana Assembly. J. Geol., 102, 47-65.

Sneeringer, M., Hart, S.R. and Shimizu, N. (1984) Strontium and samarium diffusion in diopside. Geochim. Cosmochim. Acta, 48, 1589-1608.

Spear, F.S. (1993) Metamorphic Phase Equilibria and Pressure-Temperature-Time Paths. Mineralogical Society of America, Monograph. pp.789.

Spear, F.S. and Florence, F.P. (1991) Thermobarometry in granulites: Pitfalls and new approaches. Precambr. Res., 55, 209-241.

Spear, F.S. and Peacock, S.M. (1991) Metamorphic Pressure-Temperature-Time Paths. Short Course in Geology, v.7, American Geophysical Union.

Speath, G. and Fielitz, W. (1987) Structural investigations in the Precambrian of western Neuschwabenland, Antarctica. Polarforsch., 57, 71-92.

St-Onge, M.R. and Ijewliw, O.J. (1996) Mineral corona formation during high-P retrogression of granulite rocks, Ungava Orogen, Canada. J. Petrol., 37, 533-582.

Staudacher, T.H., Jessberger, E.K., Dorflinger, D., and Kiko, J., (1978) A refined ultrahigh-vacuum furnace for rare gas analysis, J. Phys. E: Sci. Instrum., v. 11, p. 781-784.

Storey, B.C. (1993) The changing face of late Precambrian and early Palaeozoic reconstructions. J. Geol. Soc. London, 150, 665-668.

Storey, B.C., Pankhurst, R.J. and Johnson, A.C. (1994) The Grenvillian province within Antarctica: a test of the SWEAT hypothesis, J. Geol. Soc. London, 151, 1-4.

Stump, E. (1992) The Ross Orogen of the Transantarctic Mountains in light of the Laurentia-Gondwana split. GSA Today, 2, 25-31.

Streckeisen, A. (1976) To each plutonic rock its proper name. Earth Sci. Rev., 12, 113-145.

Stuwe, K. and Sandiford, M. (1993) A preliminary model for the 500 Ma event in the East Antarctic shield. In: Findlay, R.H., Unrug, r., banks, H.R. and Veevers, J.J. (eds.) Gondwana 8. Assembly, Evolution and Dispersal. Balkema, Rotterdam, 125-130.

Stuwe, K., Sandiford, M and Powell, R. (1993) Episodic metamorphism and deformation in low-pressure, high-temperature terranes, Geology, 21, 829-832.

Talarico, F. and Castelli, D. (1995) Relic granulites in the Ross Orogen of northern Victoria Land (Antarctica): I Field occurrence, petrography and metamorphic evolution. Precambr. Res., 75, 141-156.

Tetley, N.R., (1978) Geochronology by the $^{40}Ar/^{39}Ar$ technique, unpublished Ph.D. thesis, The Australian National University, 592 pp.

Thoni, M. and Miller, C.H. (1996) Garnet Sm-Nd data from the Saualpe and the Koralpe (Eastern Alps, Austria): chronological and P-T constraints on the thermal and tectonic history. J. Met. Geol., 14, 453-466.

Tracy, R.J., Robinson and Thompson, A.B. (1976) Garnet composition and zoning in the determination of temperature and pressure of metamorphism, central Massachusetts. Am. Mineral., 61, 762-775.

Vance, D. and O'Nions, R.K. (1990) Isotopic chronometry of zoned garnets: growth kinetics and metamorphic histories. Earth Planet. Sci. Lett., 97, 227-240.

Wagner, G.A. and Van den Haute, P. (1992) Fission track dating. Solid earth sciences library, v.6, Kluwer Academic Publishers, London. 285p.

Watson, E.B., Harrison, T.M. and Ryerson, F.J. (1985) Diffusion of Sm, Sr and Pb in fluorapatite. Geochim. Cosmochim. Acta, 49, 1813-1823.

Watters, B.R. (1972) The Straumsnutane volcanics, western Dronning Maud Land. S. Afr. J. Antarc. Res., 2, 23-31.

Werner, C.D. (1987) Saxonian granulites – igneous or lithogenous. A contribution to the geochemical diagnosis of the original rocks in high-metamorphic complexes. In: Gerstenberger, H. (ed.) Contributions to the geology of the Saxonian granulite massiif (Sachsisches Granulitgebirge) Zfl-Mitteilungen Nr 133, 221-250.

Williams, I.S. and Claesson, S. (1987) Isotopic evidence for the Precambrian provenance and Caledonian metamorphism of high grade paragneisses from the Seve Nappes, Scandinavian Caledonides. II. Ion microprobe zircon U-Th-Pb. Contrib. Mineral. Petrol., 97, 205-217.

Wolmarans, L.G. and Kent, L.E. (1982) Geological investigations in western Dronning Maud Land, Antarctica - a synthesis. S. Afr. J. Antarct. Res., 18 (Supplement 2), 93pp.

Woodsworth, G.J. (1977) Homogenization of zoned garnets from pelitic schists. Can. Mineral., 15, 230-242.

Yardley, B.W.D. (1977) An empirical study of diffusion in garnet. Am. Mineral., 62, 793-800.

Young, D.N., Fanning, C.M., Shaw, R.D., Edgoose, C.J., Blake, D.H., Page, R.W. and Camacho, A. (1995) U–Pb zircon dating of tectonomagmatic events in the northern Arunta Inlier, central Australia. Precambr. Res., 71, 45-68.